VISCOUS FLUID FLOW

McGraw-Hill Series in Mechanical Engineering

Alciatore and Histand: *Introduction to Mechatronics and Measurement Systems*
Anderson: *Computational Fluid Dynamics: The Basics with Applications*
Anderson: *Fundamentals of Aerodynamics*
Anderson: *Introduction to Flight*
Anderson: *Modern Compressible Flow*
Barber: *Intermediate Mechanics of Materials*
Beer/Johnston: *Vector Mechanics for Engineers*
Beer/Johnston/DeWolf: *Mechanics of Materials*
Budynas: *Advanced Strength and Applied Stress Analysis*
Cengel and Boles: *Thermodynamics: An Engineering Approach*
Cengel and Turner: *Fundamentals of Thermal-Fluid Sciences*
Cengel: *Heat Transfer: A Practical Approach*
Cengel: *Introduction to Thermodynamics & Heat Transfer*
Crespo da Silva: *Intermediate Dynamics*
Dieter: *Engineering Design: A Materials & Processing Approach*
Dieter: *Mechanical Metallurgy*
Doebelin: *Measurement Systems: Application & Design*
Dunn: *Measurement & Data Analysis for Engineering & Science*
EDS, Inc.: *I-DEAS Student Guide*
Hamrock/Schmid/Jacobson: *Fundamentals of Machine Elements*
Heywood: *Internal Combustion Engine Fundamentals*
Holman: *Experimental Methods for Engineers*
Holman: *Heat Transfer*
Hutton: *Fundamentals of Finite Element Analysis*
Kays/Crawford/Weigand: *Convective Heat and Mass Transfer*
Meirovitch: *Fundamentals of Vibrations*
Norton: *Design of Machinery*
Palm: *System Dynamics*
Reddy: *An Introduction to Finite Element Method*
Schaffer et al.: *The Science and Design of Engineering Materials*
Schey: *Introduction to Manufacturing Processes*
Shames: *Mechanics of Fluids*
Shigley/Mischke/Budynas: *Mechanical Engineering Design*
Smith: *Foundations of Materials Science and Engineering*
Suryanarayana and Arici: *Design and Simulation of Thermal Systems*
Turns: *An Introduction to Combustion: Concepts and Applications*
Ugural: *Mechanical Design: An Integrated Approach*
Ullman: *The Mechanical Design Process*
White: *Fluid Mechanics*
White: *Viscous Fluid Flow*
Zeid: *Mastering CAD/CAM*

VISCOUS FLUID FLOW

Third Edition

Frank M. White

University of Rhode Island

ABOUT THE AUTHOR

Frank M. White is Professor Emeritus of Mechanical and Ocean Engineering at the University of Rhode Island. He is a native of Augusta, Georgia, and went to undergraduate school at Georgia Tech, receiving a B.M.E. degree in 1954. Then he attended the Massachusetts Institute of Technology for an S.M. degree in 1956, returning to Georgia Tech to earn a Ph.D. degree in mechanical engineering in 1959. He began teaching aerospace engineering at Georgia Tech in 1957 and moved to the University of Rhode Island in 1964. He retired in January 1998.

At the University of Rhode Island, Frank became interested in oceanographic and coastal flow problems and in 1966 helped found the first Department of Ocean Engineering in the United States. His research interests have mainly been in viscous flow and convection heat transfer. Known primarily as a teacher and writer, he received the ASEE Westinghouse Teaching Excellence Award in addition to seven University of Rhode Island teaching awards. His modest research accomplishments include some 80 technical papers and reports, the ASME Lewis F. Moody Research Award in 1973, and the ASME Fluids Engineering Award in 1991. He is a Fellow of the ASME and for 12 years served as editor-in-chief of the ASME *Journal of Fluids Engineering*. He received a Distinguished Alumnus award from Georgia Tech in 1990 and was elected to the Academy of Distinguished Georgia Tech Alumni in 1994.

In addition to the present text, he has written three undergraduate textbooks: *Fluid Mechanics, Heat Transfer,* and *Heat and Mass Transfer.* He continues to serve on the ASME Publications Committee and has been a consulting editor of the McGraw-Hill Encyclopedia of Science and Technology since 1992. He lives with his wife, Jeanne, in Narragansett, Rhode Island.

My wife, Jeanne Faucher White, is the key to this book.
Without her love and encouragement,
I can't even get started.

CONTENTS

PREFACE

OVERVIEW

The third edition of this book continues the goal of serving as a senior or first-year graduate textbook on viscous flow with engineering applications. Students should be expected to have knowledge of basic fluid mechanics, vector calculus, ordinary and partial differential equations, and elementary numerical analysis. The material can be selectively presented in a one-semester course or, with fuller coverage, in two quarters or even two semesters. At the author's institution, the text is used in a first-semester graduate course that has, as a prerequisite, a one-semester junior course in fluid mechanics.

The evolution of viscous-flow prediction continues toward CFD instead of physical insight and mathematical analysis. However, this book still exists to introduce viscous-flow *concepts*, not software. Dozens of new books and monographs on CFD are discussed and listed here for further specialized study. Since the second edition appeared in 1991, more than 10,000 new articles have been published on viscous flows. Clearly, the present book is an introductory textbook, not a comprehensive state-of-the-art treatment of the entire field. The goal is to make the book readable and informative and to introduce graduate students to the field.

New to this edition:

- Over 30 percent of the problems are new or revised.
- New material has been added to Chapters 1, 3, and 4 on microflows, slip in liquids, gas slip flow in tubes and channels, and a novel micropump.
- Section 2-9 on Dimensional Analysis is completely rewritten. Material has been added on Euler's equation and inviscid flow analysis and their relation to viscous flow.

- Chapter 5 begins with the classic Kelvin–Helmholtz wind-wave instability.
- Turbulence modeling in Chapter 6 is completely rewritten, expanded, and updated.
- Chapter 7 includes a detailed discussion of isentropic flow analysis to increase its relation to the understanding of viscous effects.
- References are completely updated.
- An Instructor and Student Resource Web Site is available to users of the text.

ORGANIZATION

The seven-chapter format of the book remains the same. Chapter 1 covers the basic properties of fluids and introductory concepts. New material has been added on microflows, slip in liquids, and an improved discussion of boundary conditions for flow.

Chapter 2 covers the basic equations of flow, with a bit of condensing of Secs. 2-8, 9 and 2-11, 12. Section 2-9 on Dimensional Analysis has been completely rewritten. Material has been added on Euler's equation and inviscid flow analysis and their relation to viscous flow.

Chapter 3 treats a variety of laminar-flow solutions, both analytical and numerical, of the Navier–Stokes equation. A number of new exact solutions are discussed and the Stokes paradox is illuminated a bit more. The creeping-flow discussion is updated. Two new interesting engineering CFD applications are given for liquid spheres and a novel micropump.

Chapter 4 has some obsolete material deleted, such as the Stratford separation criterion. A new section has been added on unsteady boundary layers, including acoustic streaming and the Goldstein/MRS separation criteria. Numerical solutions are covered, but the traditional integral methods remain.

Chapter 5 has dropped the beam-buckling instability analogy and now begins with the classic Kelvin–Helmholtz wind–wave instability. A great wind-shear photo by Brooks Martner has been added. The concept of pseudoresonance has been added. Section 5-4 on transition processes has been completely rewritten. New results of DNS transition prediction are now discussed.

Chapter 6 has been updated with many new references, but the basic outline of turbulent mean-flow prediction remains. Section 6-7 on modeling has been completely rewritten. The power-law overlap layer controversy is now included. DNS predictions are augmented.

Chapter 7 has two new photos of supersonic boundary-layer flow. Isentropic flow analysis is added to increase our understanding of viscous effects. There is a new discussion of Morkovin's hypothesis. Section 7-7 on compressible wall–wake laws has been rewritten.

The three Appendices are pretty much the same. More fluid property data have been added to App. A. Appendix C, a Runge–Kutta subroutine, is still useful and clarifies numerical integration. However, more and more readers are changing to spreadsheet calculations.

SUPPLEMENTS

The new Instructor and Student Resource Web Site, http://www.mhhe.com/white3e, will house general text information, the solutions to end-of-chapter problems (*under password-protection*), additional problems (*with password-protected solutions*), and helpful Web links.

ACKNOWLEDGMENTS

There are many people to thank. Much appreciated comments, suggestions, photos, charts, corrections, and encouragement were received from Leon van Dommelen of Florida State University; Gary Settles of Penn State University; Steven Schneider of Purdue University; Kyle Squires of Arizona State University; Chihyung Wen of Da-Yeh University, Taiwan; Brooks Martner of the NOAA Environmental Technology Laboratory; Jay Khodadadi of Auburn University; Philipp Epple of Friedrich-Alexander-Universität; Jürgen Thoenes of the University of Alabama at Huntsville; Luca d' Agostino of Università Degli Studi di Pisa; Raul Machado of the Royal Institute of Technology (KTH), Sweden; Gordon Holloway of the University of New Brunswick; Abdulaziz Almukbel of George Washington University; Dale Hart of Louisiana Tech University; Debendra K. Das of the University of Alaska Fairbanks; Alexander Smits of Princeton University; Hans Fernholz of Technische Universitaet Berlin; Peter Bernard of the University of Maryland; John Borg of Marquette University; Philip Drazin of the University of Bristol, UK; Ashok Rao of Rancho Santa Margarita, CA; Deborah Pence of Oregon State University; Joseph Katz of Johns Hopkins University; Pierre Dogan of the Colorado School of Mines; Philip Burgers of San Diego, CA; Beth Darchi of the American Society of Mechanical Engineers; and Norma Brennan of the American Institute of Aeronautics and Astronautics.

I have tried to incorporate almost all of the reviewer comments, criticisms, corrections, and improvements. The third edition has greatly benefited from the reviewers of the second edition text, as well as the reviewers of the third edition manuscript:

Malcolm J. Andrews, *Texas A&M University*

Mehdi Asheghi, *Carnegie Mellon University*

Robert Breidenthal, *University of Washington*

H. A. Hassan, *North Carolina State University*

Herman Krier, *University of Illinois, Urbana-Champaign*

Daniel Maynes, *Brigham Young University*

Suresh Menon, *Georgia Institute of Technology*

Meredith Metzger, *University of Utah*

Kamran Mohseni, *University of Colorado*

Ugo Piomelli, *University of Maryland*

Steven P. Schneider, *Purdue University*

Kendra Sharp, *Pennsylvania State University*
Marc K. Smith, *Georgia Institute of Technology*
Leon van Dommelen, FAMU-FSU
Steve Wereley, *Purdue University*

LIST OF SYMBOLS

English Symbols

a	speed of sound; acceleration (Chap. 2), body radius (Chap. 4)
A	area; amplitude, Eq. (5-40); damping parameter, Eq. (6-90)
b	jet or wake width, Fig. 6-35
B	stagnation-point velocity gradient (Sec. 3-8.1); turbulent wall-law intercept constant, Eq. (6-38a)
ΔB	wall-law shift due to roughness, Eq. (6-60)
c, c_i, c_r	wave phase speeds (Chap. 5)
c_p, c_v	specific heats, Eq. (1-69)
C	Chapman–Rubesin parameter, Eq. (7-20)
C_i	species concentrations (Chap. 1)
D	diameter; drag force (Chap. 4); diffusion coefficient (Chap. 1)
D_h	duct hydraulic diameter, Eq. (3-55)
D_{ij}	turbulent transport or diffusion, Eq. (6-111)
e, E	internal energy
e_t	internal plus kinetic plus potential energy, Eq. (2-113)
$\mathbf{f, F}$	force
f, F, g	similarity variables
$\mathbf{g}$	acceleration of gravity
$G(Pr)$	heat-transfer parameter, Eqs. (3-172) and (4-78)
h	enthalpy; duct width; heat-transfer coefficient
h_i	metric coefficients, Eqs. (2-58) and (4-229)
h_0	stagnation enthalpy, $h + V^2/2$
H	shape factor, δ^*/θ; stagnation enthalpy, Eq. (7-3)
H_1	alternate shape factor, $(\delta - \delta^*)/\theta$
J	jet momentum, Eqs. (4-97), (4-206), and (6-144)
k	thermal conductivity; roughness height (Chaps. 5 and 6)

K	bulk modulus, Eq. (1-84); duct pressure-drop parameter, Eq. (4-176); turbulence kinetic energy, Eq. (6-16); stagnation-point velocity gradient, Fig. 7-6
ℓ	mean-free path (Chap. 1); mixing length, Eq. (6-88)
L	characteristic length
L_{slip}	slip length of a liquid, Eq. (1-89)
m	mass; wedge-velocity exponent, Eq. (4-69)
$\dot{m}$	mass rate of flow
M	molecular weight; moment, Eq. (3-190)
n	normal to the wall; power-law exponent, Eq. (1-35)
p	pressure
$\hat{p}$	effective pressure, $p + \rho gz$
P	pressure gradient parameter, Eq. (3-42); duct perimeter
q	heat-transfer rate per unit area; turbulence level, Eq. (5-43)
Q	heat; volume flow rate, Eq. (3-35)
r	radial coordinate; recovery factor, Eq. (7-16)
r, θ, z	cylindrical polar coordinates, Eq. (2-63)
r, θ, λ	spherical polar coordinates, Eq. (2-65)
r_0	cylinder surface radius, Fig. 4-34
R	gas constant; body radius
s	entropy
S	Sutherland constant, Eq. (1-36); laminar shear parameter, Eq. (4-134); van Driest parameter, Eq. (7-130)
t	time
T	temperature; percent turbulence, Eq. (5-43)
T^*	wall heat-flux temperature, $q_w/(\rho c_p v^*)$; compressible-flow reference temperature, Eq. (7-42)
$\mathcal{T}$	surface tension coefficient
u, v, w	Cartesian velocity components
u_θ, u_r, u_z	cylindrical polar velocity components
u', v', w'	turbulent velocity fluctuations
Δu	wake velocity defect, Fig. 6-35c and Eq. (6-155)
U, W	freestream velocity components
v^*	wall-friction velocity, $(\tau_w/\rho_w)^{1/2}$
v_β	wake velocity, Eq. (6-137)
V	velocity; also U_e/U_0, Eq. (6-133)
$\mathcal{V}$	volume (Chap. 2)
w	rate of work done on an element, Eq. (2-36)
x, y, z	Cartesian coordinates
Z	gas compressibility factor, $p/(\rho RT)$

τ	boundary-layer shear stress
τ_{ij}	stress tensor
χ	hypersonic interaction parameter, Eq. (7-86)
ξ	dimensionless pressure gradient, Eq. (6-36); similarity variable, Eq. (7-19)
ω	vorticity; angular velocity; frequency
Ω_v, Ω_D	molecular potential functions, Chap. 1
Ω	angular velocity
ζ	heat-transfer coefficient, Eq. (3-14); ratio δ_T/δ, Eq. (4-24)

Dimensionless Groups

Br	Brinkman number, $\mu V^2/k\,\Delta T$
Ca	cavitation number, $(p_\infty - p_{\text{sat}})/\rho V^2$
C_D	drag coefficient, $2\,(\text{drag})/\rho V^2 A$
C_f	skin-friction coefficient, $2\tau_w/\rho V^2$
C_h	Stanton number, $q_w/\rho V c_p\Delta T$
C_L	lift coefficient, $2\,(\text{lift})/\rho V^2 A$
C_p	pressure coefficient, $2(p - p_\infty)/\rho V^2$
Ec	Eckert number, $V^2/c_p\,\Delta T$
Eu	Euler number, $2\Delta p/\rho U^2$
Fr	Froude number, V^2/gL
Gr	Grashof number, $g\beta\,\Delta T L^3/\nu^2$
Gr^*	modified Grashof number, $GrNu = g\beta q_w L^4/k\nu^2$
Kn	Knudsen number, ℓ/L
L^*	Graetz number (Sec. 3-3.8), $L/(d_0\,Re_D Pr)$
Le	Lewis number, D/α
Ma	Mach number, V/a
Nu	Nusselt number, $q_w L/k\,\Delta T$
Pe	Peclet number, $RePr$
Po	Poiseuille number, $2\tau L/\mu V$
Pr	Prandtl number, $\mu c_p/k$
Pr_t	turbulent Prandtl number, $\mu_t c_p/k_t$
Ra	Rayleigh number, $GrPr = g\beta\,\Delta T L^3/\nu\alpha$
Re	Reynolds number, $\rho VL/\mu$
Ro	Rossby number, $V/\Omega L$
Sc	Schmidt number, ν/D
St	Strouhal number, fL/V
Ta	Taylor number, Eq. (5-34)
We	Weber number, $\rho V^2 L/\mathcal{T}$

Greek Symbols

α	thermal diffusivity, $k/\rho c_p$; wedge angle (Fig. 3-32); wave number, Eq. (5-12); angle of attack
α, β, γ	finite-difference mesh-size parameters, Eq. (4-146); also compressible wall-law parameters, Eqs. (7-111)
α^*, β, ζ	compressible finite-difference mesh-size parameters, Eq. (7-67)
β	thermal expansion coefficient, Eq. (1-86); Falkner–Skan parameter, Eq. (4-71); Clauser parameter, Eq. (6-42)
γ	specific-heat ratio, c_p/c_v; finite-difference parameter Eq. (4-163) intermittency, Fig. 6-5; compressibility parameter, Eq. (7-111)
δ, δ_u	velocity boundary-layer thickness
δ^*	displacement thickness, Eq. (4-4)
δ_c	conduction thickness, Eq. (4-156)
δ_h	enthalpy thickness, Eq. (4-22)
δ_T	temperature boundary-layer thickness
δ_3	dissipation thickness, Eq. (4-128)
δ_{ij}	Kronecker delta
Δ	defect thickness, Eq. (6-43)
ϵ	perturbation parameter (Sec. 4-11); turbulent dissipation [term V of Eq. (6-17)]
ϵ_{ij}	strain-rate tensor; Reynolds stress dissipation, Eq. (6-111)
κ	Kármán constant, ≈ 0.41
λ	second viscosity coefficient (Chap. 2); Darcy friction factor, Eq. (3-38); Thwaites' parameter, Eq. (4-132); $(2/C_f)^{1/2}$ (Chap. 6)
Λ	Kármán–Pohlhausen parameter, $\delta^2 (dp/dx)/\mu U$; pipe-friction factor, Eq. (6-54)
λ_n	Graetz function eigenvalues, Table 3-1
η	similarity variable; free-surface elevation (Chap. 5)
μ	viscosity
ν	kinematic viscosity μ/ρ
π	$3.14159 \ldots$
Π	Coles' wake parameter, Eq. (6-47)
ϕ	velocity potential (Chap. 2); latitude (Chap. 3); wave angle, Eq. (5-12); dimensionless disturbance, Eq. (5-23)
Φ	dissipation function, Eq. (2-46)
ψ	stream function
θ	polar coordinate angle; momentum thickness, Eq. (4-6)
Θ	dimensionless temperature ratio, Eq. (3-167) or (4-56)
ρ	density
σ	molecular collision diameter (Chap. 1); numerical mesh parameter, Eq. (3-247); turbulent jet growth parameter, Eq. (6-147)

Subscripts

aw	adiabatic wall
∞	far field
e	freestream, boundary-layer edge
0	initial or reference value
c, crit	critical, at the point of instability
m	mean
n	normal
rms	root mean square
sep	separation point
t	turbulent, tangential
tr	transition
r	recovery or adiabatic wall
w	wall
x	at position x

Superscripts

—	time-mean
$'$	differentiation; turbulent fluctuation
*	dimensionless variable (Chaps. 2, 3, and 4)
+	law-of-the-wall variable
^	small-disturbance variable (Chap. 5)

PRELIMINARY CONCEPTS

1-1 HISTORICAL OUTLINE

By stretching a point one could say that the study of viscous fluid flow reaches back into antiquity, for it was probably in prehistoric times that human weaponry developed from simple sticks and stones into streamlined, weighted spears and slim, pointed, fin-stabilized arrows. One can conclude that primitive man recognized and solved in part the problem of viscous resistance.

The exact solution for the problem of the viscous fluid at rest was correctly given by the Greek mathematician Archimedes (287–212 B.C.) as his two postulates of buoyancy. Subsequently, in order to derive expressions for the buoyant force on various-shaped bodies, Archimedes actually developed a version of the differential calculus. At about the same time, the Romans were building their magnificent water-supply systems and in so doing demonstrated some intuitive understanding of the effect of viscous resistance in long conduits. However, the Romans contributed little to a systematic solution of this problem, and in fact no significant progress on channel resistance was made until Chézy's work in 1768.

The period from the birth of Christ to the fifteenth century produced the same impact on viscous-flow analysis as it did on other fields of science, i.e., little if any. But the mountains of conjecture and superstition accumulated in these unscientific centuries certainly contained nuggets of fact which the great thinkers of the Renaissance finally mined. In 1500, the equation of conservation of mass for incompressible one-dimensional viscous flow was correctly deduced by Leonardo da Vinci, the Italian painter, sculptor, musician, philosopher, anatomist, botanist, geologist, architect, engineer, and scientist. Leonardo's notes also contain accurate sketches and descriptions of wave motion, hydraulic jumps, free jets, eddy formation behind bluff

bodies (see Example 2 of Sec. 1-2), reduction of drag by streamlining, and the velocity distribution in a vortex.

The next notable achievement was by Evangelista Torricelli (1608–1647), who in 1644 published his theorem that the velocity of efflux of a (viscous) liquid from a hole in a tank is equal to the velocity which a liquid particle would attain in free fall from its surface. Torricelli termed his discovery "almost useless," but history has seen fit to disagree. From the point of view of this text, the efflux principle is unusually interesting, since it is one of the few flow phenomena for which viscous effects are often negligible.

The above achievements do not relate directly to viscous motion. That is, these early workers were probably studying a fluid they thought to be inviscid, or *perfect*; it happens that their results are also true for a viscous, or *real* fluid. The first to make a direct study of fluid friction was probably Edme Mariotte (1620–1684), who invented a balance system to measure the drag of a model held stationary in a moving stream, the first wind tunnel. Mariotte's text, "Traité du mouvement des eaux," was published in 1686, a year before the incomparable "Principia Mathematica" of Sir Isaac Newton.

In 1687, Newton published in his "Principia" the simple statement which delineates the viscous behavior of nearly all common fluids: "The resistance which arises from the lack of lubricity in the parts of a fluid—other things being equal—is proportional to the velocity by which the parts of the fluid are being separated from each other." Such fluids, water and air being prominent examples, are now called *newtonian* in his honor. With the law of linear viscosity thus proposed, Newton contributed the first viscous-flow analysis by deriving the correct velocity distribution about a rotating cylinder.

But the world was apparently not ready for viscous-flow theory. This was probably due to Newton himself, because of his more famous discovery, the differential calculus. Whereas those who preceded Newton were essentially limited to discussion of fluid-flow problems, those who followed him could use the calculus to attack such problems directly. It is natural that the first efforts were directed toward the idealized frictionless fluid. First to succeed was Daniel Bernoulli, who in 1738 demonstrated the proportionality between pressure gradient and acceleration in inviscid flow. Subsequently, the master of the calculus, Leonhard Euler, derived in 1755 the famous frictionless equation which now bears Bernoulli's name. Euler's magnificent derivation is essentially unchanged today in ideal-fluid theory, or *hydrodynamics*, as Bernoulli termed it. Paralleling Euler, Jean d'Alembert published in 1752 his famous paradox, showing that a body immersed in a frictionless flow would have zero drag. Shortly afterward, Lagrange (1736–1813), Laplace (1749–1827), and Gerstner (1756–1832) carried the new hydrodynamics to elegant heights of analysis.

But theoretical results such as the d'Alembert paradox were too much for practical engineers to bear, with the tragic result that fluid mechanics was rent into two parts: hydrodynamics, under whose banner mathematicians soared to new frictionless summits, and hydraulics, which abandoned theory entirely and relied on experimental measurements. This schism continued unhealed for 150 years, to the

beginning of the twentieth century. Indeed, the separation of fluid mechanics theory from experiment is not extinct even today, as witness the divergent views of the subject now held among aeronautical, chemical, civil, and mechanical engineers.

After Euler and his colleagues, the next significant analytical advance was the addition of frictional-resistance terms to Euler's inviscid equations. This was done, with varying degrees of elegance, by Navier in 1827, Cauchy in 1828, Poisson in 1829, St. Venant in 1843, and Stokes in 1845. The first four wrote their equations in terms of an unknown molecular function, whereas Stokes was the first to use the first coefficient of viscosity μ. Today these equations, which are fundamental to the subject, are called the *Navier–Stokes relations*, and this text can do little to improve upon Stokes' analysis.

The Navier–Stokes equations, though fundamental and rigorous, are non-linear, nonunique, complex, and difficult to solve. To this day, only a relatively few particular solutions have been found, although mathematicians are now taking an interest in the general properties of these remarkable equations [Constantin and Foias (1988)]. Meanwhile, the widespread use of digital computers has given birth to many numerical models and published computations of viscous flows. Certain of these models can be implemented, for simple geometries, on a small personal computer and are described here in Chaps. 3, 4, and 6. Experimentation remains a strong component of viscous-flow research because even the largest supercomputers are incapable of resolving the fine details of a high-Reynolds-number flow.

For practical fluids engineering, the biggest breakthrough was the demonstration, by Ludwig Prandtl in 1904, of the existence of a thin *boundary layer* in fluid flow with small viscosity. Viscous effects are confined to this boundary layer, which may then be patched onto the outer inviscid flow, where so many powerful mathematical techniques obtain. Boundary-layer theory applies to many, but definitely not all, engineering flows. The concept makes it possible, as Leslie Howarth said, "to think intelligently about almost any problem in real fluid flow."

The second most important breakthrough, also accomplished at the turn of the twentieth century, was to put fluid-flow experimentation on a solid basis, using dimensional analysis. Leaders in this effort were Osborne Reynolds (1842–1912), Lord Rayleigh (1842–1919), and Ludwig Prandtl (1875–1953). Modern engineering studies—and textbooks—routinely place their results in dimensionless form, thus making them applicable to any newtonian fluid under the same flow conditions.

With thousands of researchers now active in fluid mechanics, present progress is incremental and substantial. Instrumentation has advanced greatly with the inventions of the hot-wire, the hot-film, the laser-Doppler velocimeter, and miniature pressure and temperature sensors. Visualization of flow—through bubbles, smoke, dye, oil-films, holography, and other methods—is now outstanding [see, e.g., Van Dyke (1982), Nakayama and Tanida (1996), Smits and Lim (2000), and Nakayama (1988)]. Computational fluid dynamics (CFD) has grown from a special topic to infiltrate the entire field: Many user-friendly CFD codes are now available so that ordinary engineers can attempt to model a realistic two- or three-dimensional viscous flow.

. The literature in fluid mechanics is now out of control, too much to keep up with, at least for someone as dedicated as this writer. The first edition of this text had a figure to show the growth of viscous-flow papers during the twentieth century. Prandtl's 1904 breakthrough could be considered as "Paper 1," and the research output rose at a 7 percent annual rate to 70 papers per year in 1970. Well, that annual increase has continued to this day, so that thousands of papers are now being published each year. A dozen new fluids-oriented journals have been introduced, plus a half-dozen serials related to computational fluid dynamics. There are dozens of conferences and symposia every year devoted to fluids-oriented topics. Consider the following statistics:

- In 2002, the *Journal of Fluid Mechanics* printed 450 papers covering 9000 journal pages.
- In 2002, the *Physics of Fluids* printed 410 papers covering 4500 journal pages.
- In 2002, the *Journal of Fluids Engineering* printed 120 papers covering 1068 journal pages.
- In 2002, the Fluids Engineering Division of the American Society of Mechanical Engineers sponsored 650 papers.
- The *May 2003 Meetings Calendar of the Journal of Fluids Engineering* listed 38 fluids-related conferences for the coming year.
- The *2001 International Symposium on Turbulent Shear Flow Phenomena* presented 300 papers.

This situation is, of course, much the same in other pure and applied sciences. The net effect of the above incomplete statistics is that the present text can only be an introduction to some of the many topics of ongoing research into laminar and turbulent shear flows. Many specialized monographs will be cited throughout this text for further reading.

The historical details in this present section were abstracted from the excellent history of hydraulics by Rouse and Ince (1957).

1-2   SOME EXAMPLES OF VISCOUS-FLOW PHENOMENA

Before embarking upon the inevitable detailed studies of theoretical and experimental viscous flows, let us discuss four examples, chosen to illustrate both the strength and the limitations of the subject: (1) airfoil flow, (2) a cylinder in crossflow, (3) pipe-entry flow, and (4) prolate spheroid flow. These examples remind one that a textbook tends to emphasize analytical power while deemphasizing practical difficulties. Viscous-flow theory does have limitations, especially in the high-Reynolds-number *turbulent flow* regime, where the flow undergoes random fluctuations and is only modeled on a semiempirical time-mean or statistical basis.

Although geometry and fluid buoyancy and compressibility will be important, in all viscous flows, the primary controlling parameter is the dimensionless *Reynolds number*.

$$Re_L = \rho UL/\mu \qquad (1\text{-}1)$$

where U is a velocity scale, L is a characteristic geometric size, and ρ and μ are the fluid density and viscosity, respectively. Fluid properties alone can cause dramatic differences in the Reynolds number and, consequently, the flow pattern. For example, if $U = 1$ m/s and $L = 1$ m at 20°C, $Re_L = 9E3$, $7E4$, and $1E6$ for SAE-10 oil, air, and water, respectively. By adding in changes in size and speed, the Reynolds number can vary from a small fraction (falling dust particles) to $5E9$ (a cruising supertanker). For a given geometry, as Re_L increases, the flow pattern changes from smooth or *laminar* through a transitional region into the fluctuating or *turbulent* regime.

Example 1   Flow past a thin airfoil. Consider flow past a thin airfoil at small angle of incidence, $\alpha < 5°$, as sketched in Fig. 1-1a. In practical applications, the *Reynolds number*, Re_L, is large. For example, if $L = 1$ m, $U = 100$ m/s, and $\nu \approx 1.5E\text{-}5$ m²/s (air at 20°C and 1 atm), $Re_L = 6.7E6$. In these circumstances the flow creates a thin boundary layer near the airfoil surface and a thin wake downstream. The measured surface pressure distribution on the foil can be predicted by inviscid-flow theory [e.g., White (2003), Sec. 8.7], and the wall shear stress can be computed with the boundary-layer theory of Chaps. 4 to 6. The sharp trailing edge establishes the flow pattern, for a viscous fluid cannot go around such a sharp edge but instead must leave smoothly and tangentially, as shown in Fig. 1-1a.
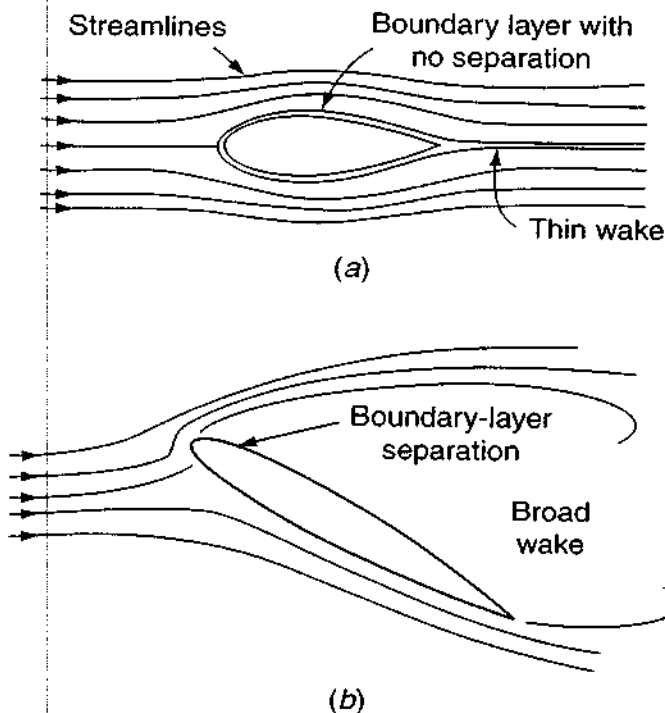
FIGURE 1-1
Flow past a thin airfoil: (a) low incidence angle, smooth flow, no separation; (b) high incidence angle, upper surface separates or "stalls," lift decreases.

According to inviscid theory, if F is the lift force per unit depth on a symmetric (two-dimensional) airfoil, the dimensionless lift coefficient C_L is given by

$$C_L = \frac{F}{\frac{1}{2}\rho U^2 L} \approx 2\pi \sin(\alpha) \tag{1-2}$$

where L is the chord length of the airfoil.

At larger incidence angles (10–15°), boundary-layer separation, or *stall*, will occur on the upper or *suction* (low-pressure) surface, as shown in Fig. 1-1b. For thicker airfoils, separation generally occurs at the trailing edge. Thin airfoils may form a partial separation, or *bubble*, near the leading edge. In stalled flow, the upper surface pressure distribution deviates considerably from inviscid theory, resulting in a loss of lift and an increase in drag force.

When an airfoil flow separates, its lift coefficient levels off to a maximum and then decreases, sometimes gradually, sometimes quickly as a short leading-edge bubble suddenly lengthens. Figure 1-2 compares typical theoretical and experimental lift curves for a symmetric airfoil.

As long as the angle of attack is below stall, the lift can be predicted by inviscid theory and the friction by boundary-layer theory. The onset of stall can be predicted. In the stalled region, however, boundary-layer theory is not valid, and one must resort either to experimentation or—with increasing success as turbulence modeling improves—numerical simulation on a digital computer.

Figures 1-1 and 1-2 are for two-dimensional airfoils—of infinite span into the paper. Practical wings of course have tips and can have leading edges *swept* or nonorthogonal to the oncoming stream. The flow over them is three-dimensional. An example is the 45° swept wing shown in Fig. 1-3. The flow on the upper surface is visualized by streaks in an oil-film coating. At $\alpha = 12°$, Fig. 1-3a, there is a leading-edge separation bubble (the white strip), but the remaining flow is attached and moves toward the (low-pressure) tip region. At 15° incidence, Fig. 1-3b, the rear surface flow moves parallel to the trailing edge, toward a separated region at the tip. Finally, at $\alpha = 20°$, Fig. 1-3c, the wing is heavily stalled and the surface flow actually moves backward or upstream toward the leading edge. Inviscid-flow computation is common for three-dimensional flows, e.g., Anderson (2001), and viscous-flow simulation of such flows is now possible with the advent of supercomputers [Chung (2002)].
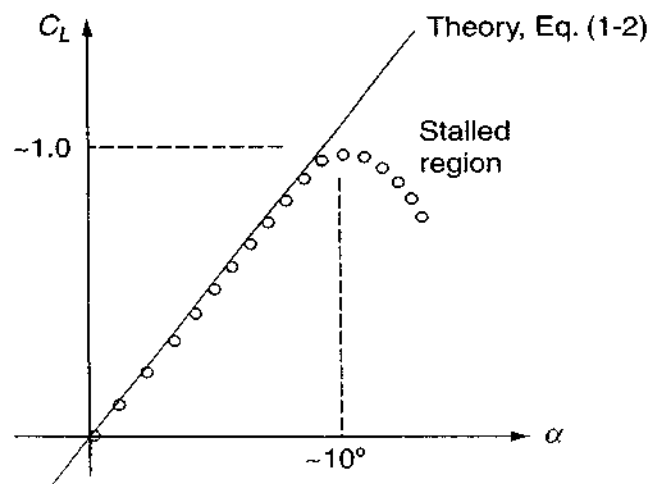
FIGURE 1-2

Typical comparison of theory and experiment for lift coefficient on a symmetric airfoil.
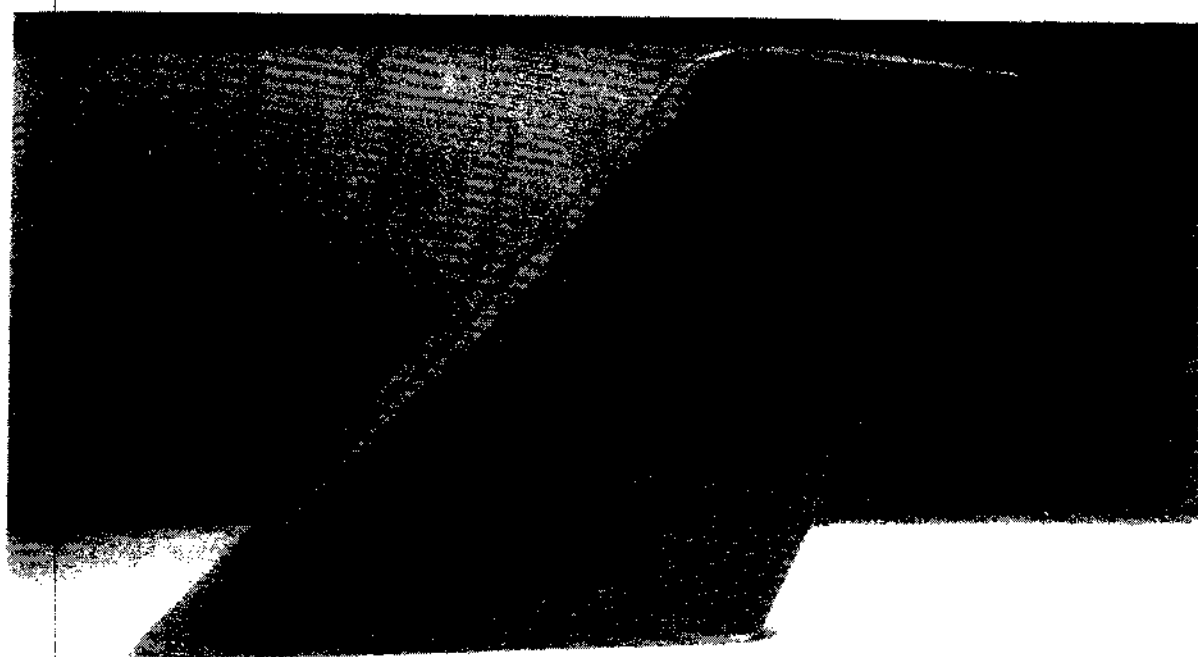
Attack   12°
angle

(a)
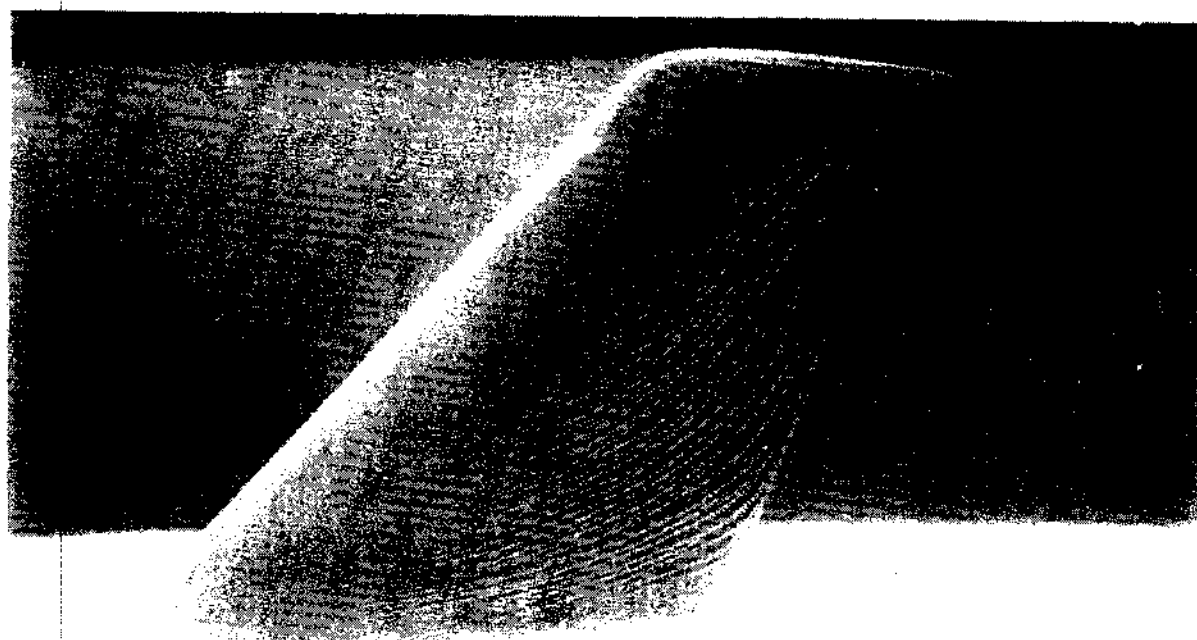
15°
(b)

FIGURE 1-3

Oil-film visualization of suction-surface flow past a 45° swept wing at $Re_L = 2.6E5$: (a) $\alpha = 12°$, flow attached except for leading-edge bubble; (b) at 15°, surface flow moves toward a stalled tip region; (c) at 20°, the wing is almost entirely stalled and surface flow moves upstream. [*From Nakayama (1988), courtesy of Hitoshi Murai, Hiroshima Institute of Technology.*]

20°

(c)
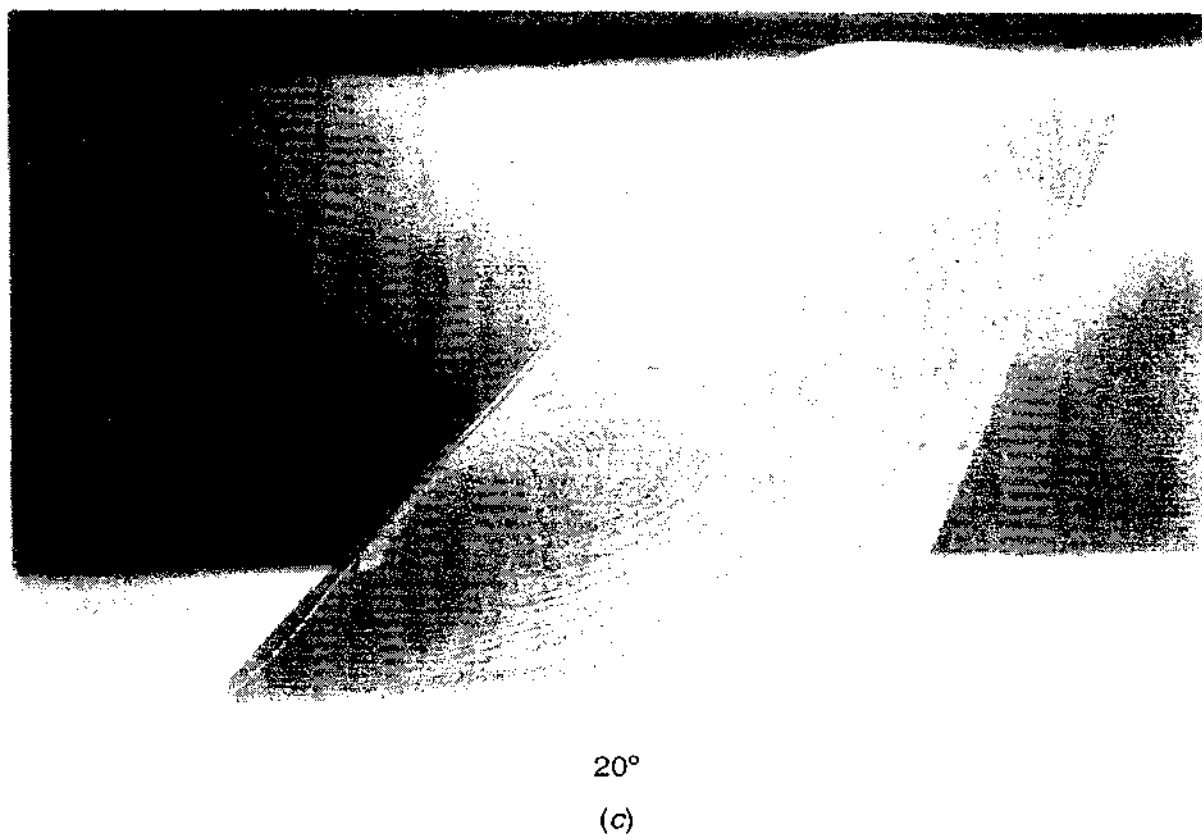
FIGURE 1-3
Continued.

Example 2   Flow past a circular cylinder. A very common geometry in fluids engineering is crossflow of a stream at velocity U_∞ past a circular cylinder of radius R. For plane inviscid flow, the solution superimposes a uniform stream with a line doublet and is given in polar coordinates by [see, e.g., White (2003), p. 537]

$$v_r = U_\infty \left(1 - \frac{R^2}{r^2}\right) \cos \theta$$

$$v_\theta = -U_\infty \left(1 + \frac{R^2}{r^2}\right) \sin \theta$$

(1-3)

The streamlines of this flow can then be plotted as in Fig. 1-4. At the surface of the cylinder, $r = R$, we have $v_r = 0$ and $v_\theta = -2U_\infty \sin \theta$, the latter velocity being finite and thus violating the no-slip condition imposed by intermolecular forces between the fluid and the solid.

The pressure distribution at the cylinder surface can be found from Bernoulli's equation, $p + \frac{1}{2}\rho V^2 = $ const, where ρ is the fluid density. The result is

$$p_s = p_\infty + \tfrac{1}{2}\rho U_\infty^2 (1 - 4 \sin^2 \theta)$$

or

$$C_p = \frac{p_s - p_\infty}{\frac{1}{2}\rho U_\infty^2} = 1 - 4 \sin^2 \theta$$
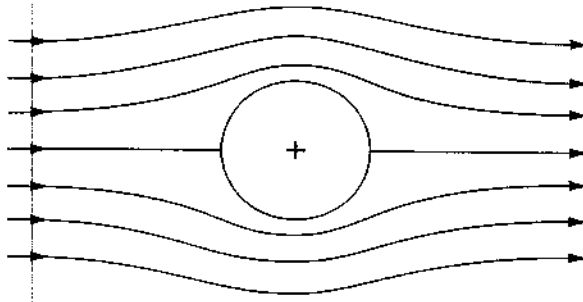
FIGURE 1-4
Perfect-fluid flow past a circular cylinder.

This distribution is shown as the dash-dot line in Fig. 1-5. Equations (1–3) illustrate a characteristic of inviscid flow without a free surface or "deadwater" region: There are no parameters such as Reynolds number and no dependence upon physical properties. Also, the symmetry of $C_p(\theta)$ in Fig. 1-5 indicates that the integrated surface-pressure force in the streamwise direction—the cylinder *drag*—is zero. This is an example of the d'Alembert paradox for inviscid flow past immersed bodies.

The experimental facts differ considerably from this inviscid symmetrical picture and depend strongly upon Reynolds number. Figure 1-5 shows measured C_p by Flachsbart (1932) for two Reynolds numbers. The pressure on the rear or lee side of the cylinder is everywhere less than the freestream pressure. Consequently, unlike the d'Alembert paradox, the real fluid causes a large pressure-drag force on the body.

Nor are the real streamlines symmetrical. Figure 1-6 shows the measured flow pattern in water moving past a cylinder at $Re_D = 170$. The flow breaks away or "separates" from the rear surface, forming a broad, pulsating wake. The pattern is visualized by releasing hydrogen bubbles at the left of the photograph, in *streaklines* parallel to the stream and *timelines* normal to the flow. Note that the wake consists of pairs of vortices shed alternately from the upper and lower part of the rear surface. They are called Kármán vortex streets, after a paper by Kármán (1911) explaining this alternation to be a stable configuration for vortex pairs. Beginning for $Re_D > 35$, the vortex streets occur in almost any bluff-body flow and persist over a wide range of Reynolds
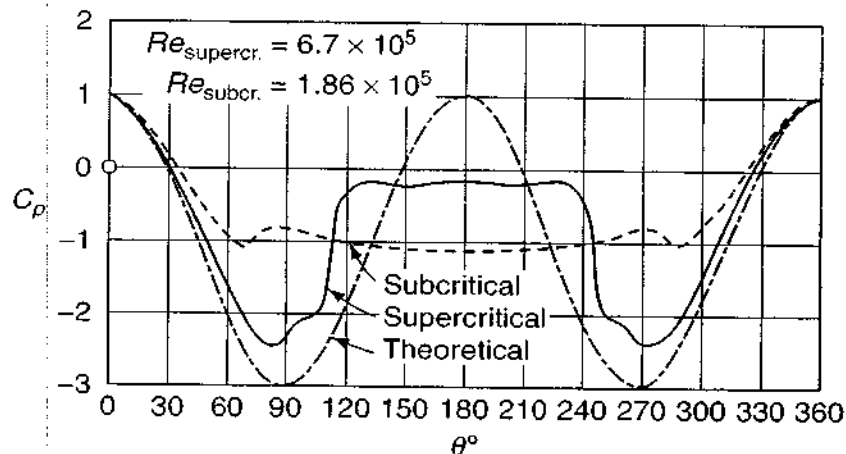
FIGURE 1-5
Comparison of perfect-fluid theory and an experiment for the pressure distribution on a cylinder. [*After Flachsbart (1932).*]
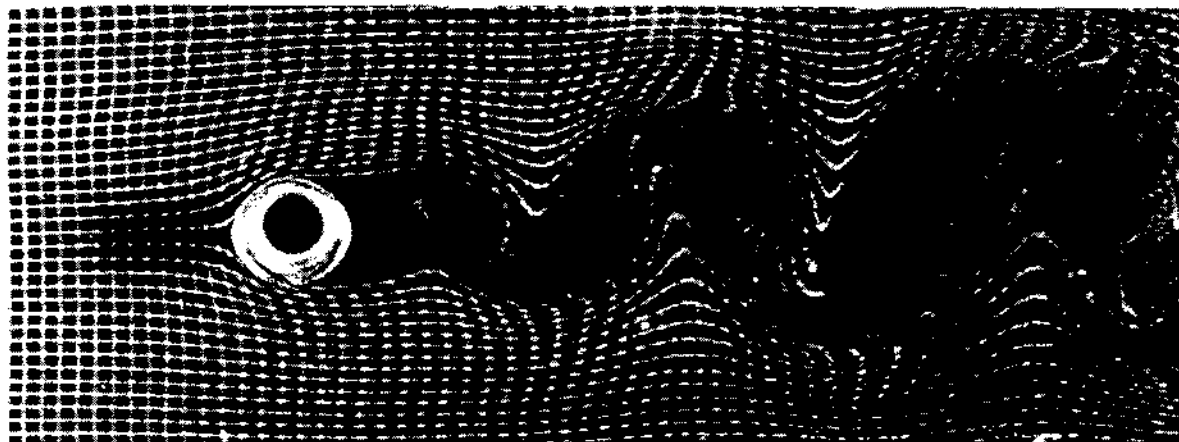
FIGURE 1-6
Timelines and streaklines for flow past a cylinder at $Re_D = 170$. [*From Nakayama (1988), courtesy of Y. Nakayama, Tokai University.*]

numbers, as shown in Fig. 1-7. As the Reynolds number increases, the wake becomes more complex—and turbulent—but the alternate shedding can still be detected at $Re = 10^7$.

As shown in Fig. 1-8, the dimensionless cylinder shedding frequency or *Strouhal number*, $St = fD/U \approx 0.2$ for Reynolds numbers from 100 to 10^5. Thus the shedding cycle takes place during the time that the freestream moves approximately five cylinder diameters. Vortex shedding is one of many viscous flows which, though posed with fixed and steady boundary conditions, evolve into unsteady motions because of flow instability. The pressure distributions in Fig. 1-5 are time averages for this reason.

$Re = 32$ $Re = 55$

$Re = 65$ $Re = 71$

$Re = 102$ $Re = 161$

$Re = 225$ $Re = 281$
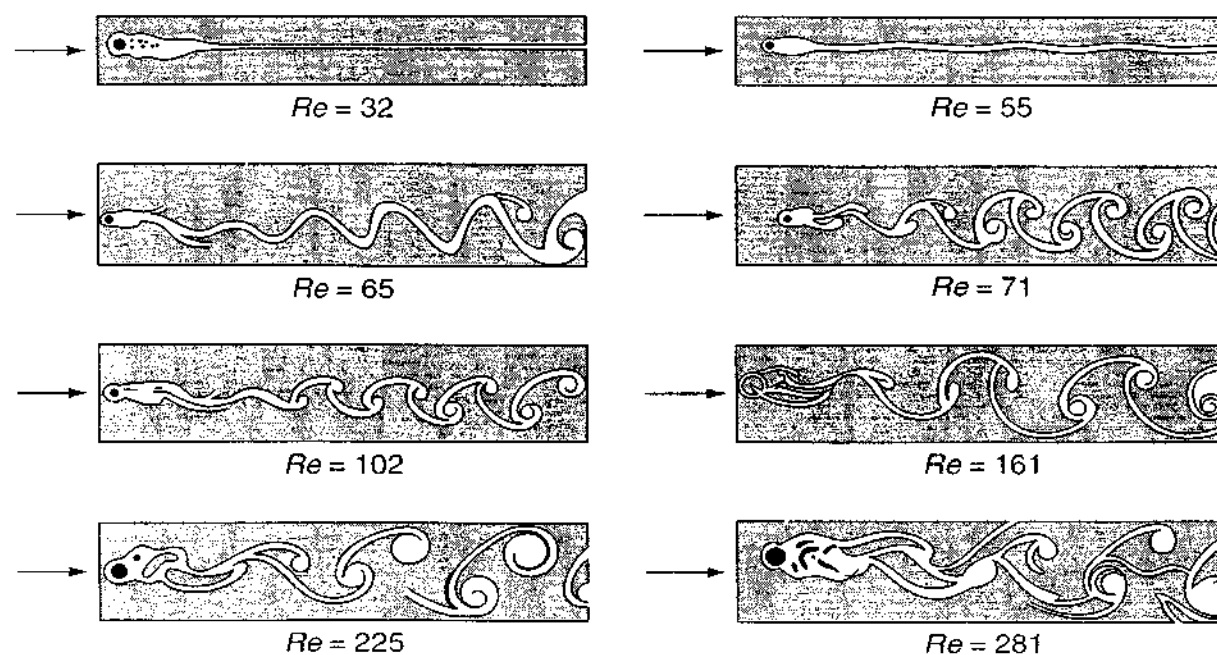
FIGURE 1-7
The effect of the Reynolds number on the flow past a cylinder. [*After Homann (1936).*]
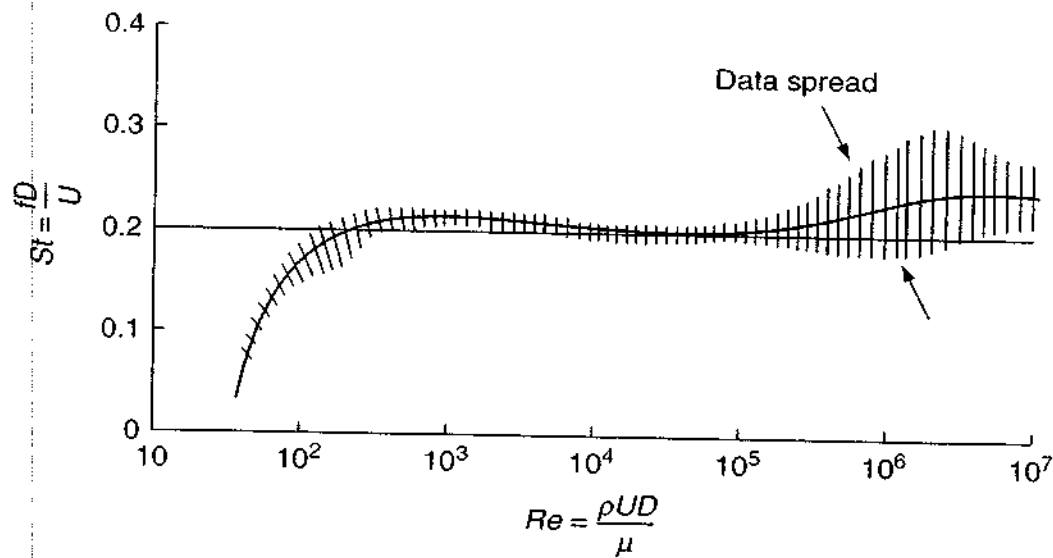
FIGURE 1-8
Measured Strouhal number for vortex shedding frequency behind a circular cylinder.

The drag coefficient on a cylinder, defined as $C_D = F/(\rho U^2 RL)$, is plotted in Fig. 1-9 over a wide range of Reynolds numbers. The solid curve, for a smooth wall, shows a sharp drop, called the *drag crisis*, at about $Re_D \approx 2E5$, which occurs when the boundary layer on the front surface becomes turbulent. If the surface is rough, the drag crisis occurs earlier, a fact exploited in sports by the deliberate dimpling of golf balls. As shown in Fig. 1-9, freestream turbulence also causes an early drag crisis.
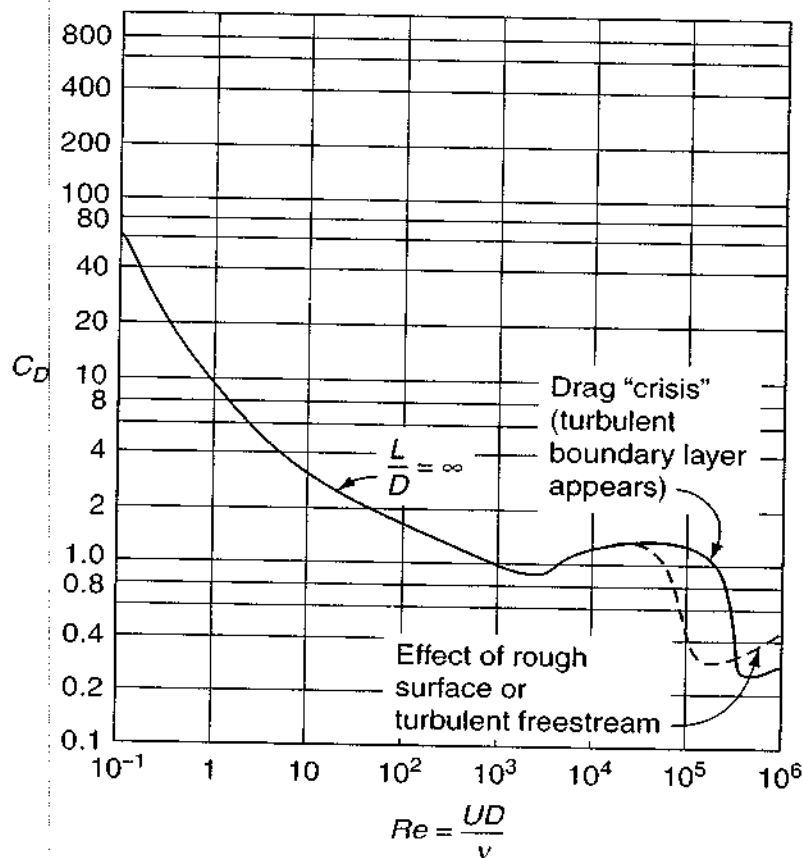
FIGURE 1-9
Drag coefficient of a circular cylinder.
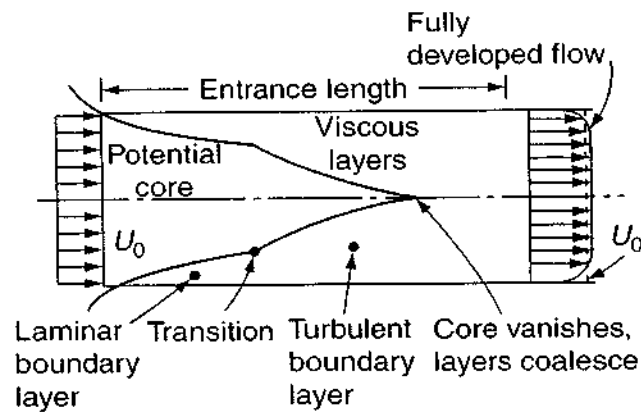
FIGURE 1-10
Flow in the entry region of a tube.

To summarize, real fluid flow past a bluff body such as a circular cylinder can differ markedly from the inviscid-flow prediction. Viscous forces which are extremely small (only a few percent of the total drag) actually control the flow by inducing separation and wake formation at the rear of the body. Boundary-layer theory can predict the onset of separation, but the surface pressure distribution changes so markedly from inviscid theory (Fig. 1-6) that Prandtl's matching scheme of Chap. 4 fails to be quantitative. For $Re \ll 1$, Stokes' creeping-flow theory can be used effectively (Sec. 3-9). For higher Reynolds numbers, both laminar and turbulent, numerical modeling on a digital computer is possible, e.g., Breuer (1998).

Example 3 Flow in a circular pipe. Consider now the flow illustrated in Fig. 1-10, where a steady viscous flow enters a tube from a reservoir. Wall friction causes a viscous layer, probably laminar, to begin at the inlet and grow in thickness downstream, possibly becoming turbulent further inside the tube. Unlike the *external* flows of Examples 1 and 2, this is an *internal* flow constrained by the solid walls, and inevitably the viscous layers must coalesce at some distance x_L, so that the tube is then completely filled with boundary layer. Slightly further downstream of the coalescence, the flow profile ceases to change with axial position and is said to be fully developed.

The developed flow in Fig. 1-10 ends up turbulent, which typically occurs for a Reynolds number $U_0D/\nu > 2000$. At lower Re, both the developing and developed regions remain laminar. Figure 1-11 shows such a laminar experiment, using hydrogen bubbles in water flow. Note that the wall flow slows down and the central core accelerates. The bubble profiles change from near-slug flow at the inlet to near-parabolic downstream.

Pipe flow is common in engineering. The theory of constant-area duct flow, for both developing and developed laminar and turbulent conditions, is well formulated and satisfying. Analytical difficulties arise if the duct diameter is tapered. Tapered flow does not become fully developed and, if the area increases in the flow direction (subsonic diffuser), separation, backflow, and unsteadiness complicate the flow pattern. A sketch of flow in a "stalled" diffuser is shown in Fig. 1-12, after Kline et al. (1959). Diffusers can now be analyzed by numerical methods, using either boundary-layer theory, Johnston (1998), or computational fluid dynamics, Muggli (1997). If the duct area *decreases* in the flow direction (subsonic nozzle), there is no flow separation or unsteadiness, and the nozzle is readily analyzed by elementary boundary-layer theory.

FIGURE 1-11
Hydrogen-bubble visualization of laminar flow in the entrance of a tube at $Re = 1600$. [*From Nakayama (1988), courtesy of Y. Nakayama, Tokai University.*]
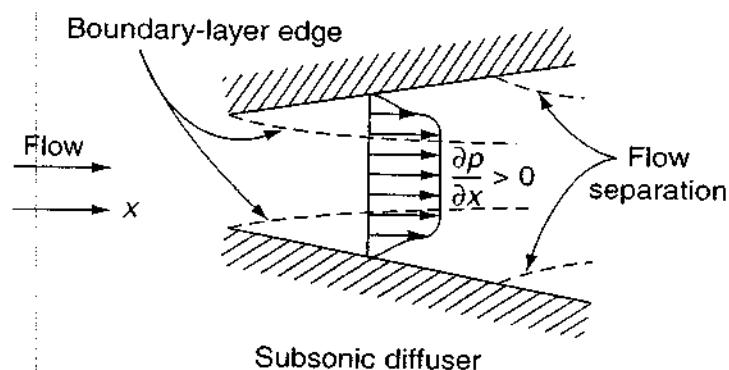
FIGURE 1-12
Flow separation in a diffuser.

Example 4   Flow past a prolate spheroid. Flows involving complicated three-dimensional effects, such as the cylinder flow of Example 2, are rightly termed *complex viscous flows* and cannot be analyzed by traditional boundary-layer methods. Complex flows are studied either experimentally or, increasingly, by computational fluid dynamics (CFD).

Figure 1-13 illustrates the computation of viscous flow past a 6:1 prolate spheroid (a slender football shape) at a high angle of attack of 20°. The angle of attack is defined as the angle between the oncoming flow and the central axis of the body. The Reynolds number is large, $\rho UL/\mu = 4.2E6$, and the flow near the body is turbulent. How might one analyze this flow with CFD? Laminar (smooth, nonfluctuating) flow can be computed accurately with a suitable fine mesh. However, the wide spectrum of random fluctuations of turbulence will yield to direct numerical simulation (DNS) only for low Reynolds numbers of order 10^4. Higher Reynolds numbers require *modeling* the small scale eddies with a time-averaging scheme (Chap. 6).

The prolate spheroid flow in Fig. 1-13 was computed using large-eddy simulation (LES) by Constantinescu et al. (2002). The authors directly simulated the large eddies but used a *turbulence model* for the fine-scale motions. The three-dimensional grid in Fig. 1-13a uses 2.6 million nodes, yet it still cannot resolve the important small fluctuations. Figure 1-13b shows the computed surface streamlines when the body is placed at a 20° angle to the freestream. The computations are in reasonable agreement
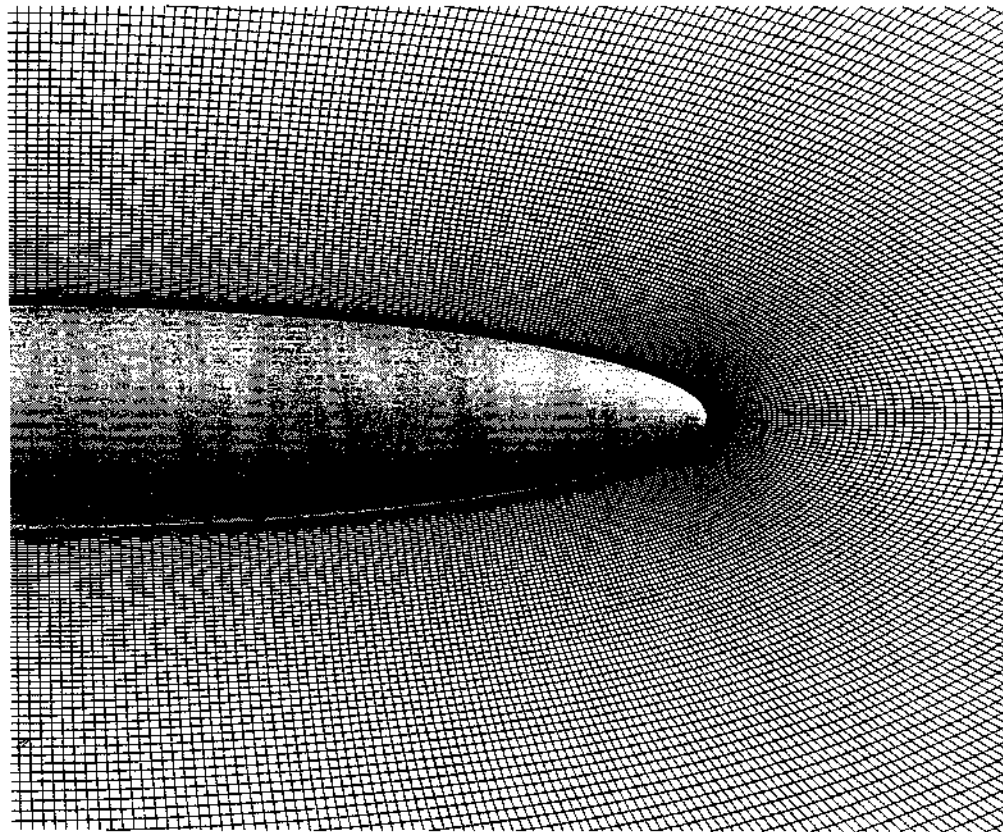
(a)
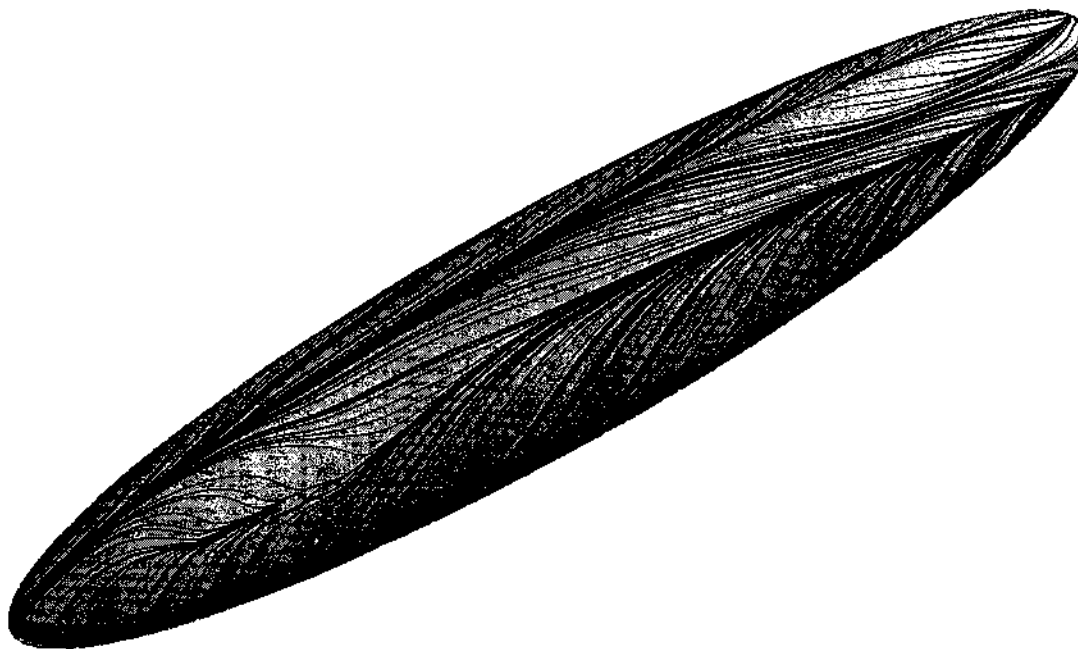
(b)

FIGURE 1-13
Computational fluid dynamics model of flow past a prolate spheroid: (a) meridian slice showing the million-node grid system; (b) surface pattern at $Re_L = 4.2E6$ and an angle of attack of 20°. [*After Constantinescu et al. (2002).*]

with the data of Chesnakas and Simpson (1997) for surface pressures and shear stresses, separation lines, and surface turning angles.

Prolate spheroid flow is a good example of fluids engineering research. Detailed *benchmark* experiments are followed by prediction methods that are gradually improved. In addition to the LES computations of Constantinescu et al. (2002), the same flow has been modeled by a multivortex simulation, Dimas et al. (1998), and by traditional turbulence modeling without large-eddy simulation, Paneras (1998).

The general subject of computational fluid dynamics is beyond the scope of the present text. We will briefly discuss CFD simulations in Chaps. 3, 4, and 6 but always refer the reader to advanced monographs for details of the subject.

1-3 PROPERTIES OF A FLUID

It is common in introductory physics to divide materials into the three classes of solids, liquids, and gases, noting their different behavior when placed in a container. This is a handy classification in thermodynamics, for example, because of the strong differences in state relations among the three. In fluid mechanics, however, there are only two classes of matter: fluids and nonfluids (solids). A solid can resist an applied shear force and remain at rest, while a fluid cannot. This distinction is not completely clear-cut. Consider a barrel full of pitch at room temperature. The pitch looks hard as a rock and will easily support a brick placed on its surface. But if the brick is left there for several days, one will have trouble retrieving the brick from the bottom of the barrel. Pitch, then, is usually classed as a fluid. Consider the metal aluminum. At room temperature, aluminum is solid to all appearances and will resist any applied shear stress below its strength limit. However, at 400°F, well below its 1200°F melting point, aluminum flows gently and continuously under applied stress and has a measurable viscosity. Nor is high temperature the criterion for fluid behavior in metals, since lead exhibits this gentle viscous creep at room temperature. Note also that mercury is a fluid and has the lowest viscosity relative to its own density (kinematic viscosity) of any common substance.

This text is primarily concerned, then, with easily recognizable fluids which flow readily under applied shear, although some slight attention will be paid to the borderline substances which partly flow and partly deform when sheared. All gases are true fluids, as are the common liquids, such as water, oil, gasoline, and alcohol. Some liquid substances which may not be true fluids are emulsions, colloids, high-polymer solutions, and slurries. The general study of flow and deformation of materials constitutes the subject of *rheology*, of which viscous flow is a special case [see, e.g., the texts by Reiner (1969), Bird et al. (2001), Hutton (1989), and Owens and Phillips (2002)].

Restricting ourselves to true fluids, we now define and illustrate their properties. These properties are of at least four classes:

1. *Kinematic* properties (linear velocity, angular velocity, vorticity, acceleration, and strain rate). Strictly speaking, these are properties of the flow field itself rather than of the fluid.

2. *Transport* properties (viscosity, thermal conductivity, mass diffusivity).

3. *Thermodynamic* properties (pressure, density, temperature, enthalpy, entropy, specific heat, Prandtl number, bulk modulus, coefficient of thermal expansion).

4. Other miscellaneous properties (surface tension, vapor pressure, eddy-diffusion coefficients, surface-accommodation coefficients).

Some items in class 4 are not true properties but depend upon flow conditions, surface conditions, and contaminants in the fluid.

The use of class 3 properties requires hedging. It is a matter of some concern that classical thermodynamics, strictly speaking, does *not* apply to this subject, since a viscous fluid in motion is technically not in equilibrium. Fortunately, deviations from local thermodynamic equilibrium are usually not significant except when flow residence times are short and the number of molecular particles few, e.g., hypersonic flow of a rarefied gas. The reason is that gases at normal pressures are quite dense in the statistical sense: A cube of sea-level air 1 μm on a side contains approximately 10^8 molecules. Such a gas, when subjected to a change of state—even a shock change—will rapidly smooth itself into local equilibrium because of the enormous number of molecular collisions occurring in a short distance. A liquid is even more dense, and thus we accept thermodynamic equilibrium as a good approximation in this text.[*]

1-3.1 The Kinematic Properties

In fluid mechanics, one's first concern is normally with the fluid velocity. In solid mechanics, on the other hand, one might instead follow particle displacements, since particles in a solid are bonded together in a relatively rigid manner.

Consider the rigid-body dynamics problem of a rocket trajectory. After solving for the paths of any three noncollinear particles on the rocket, one is finished, since all other particle paths can be inferred from these three. This scheme of following the trajectories of individual particles is called the *Lagrangian description* of motion and is very useful in solid mechanics.

But consider the fluid flow out of the nozzle of that rocket. Surely we cannot follow the millions of separate paths. Even the point of view is important, since an observer on the ground would perceive a complicated unsteady flow, while an observer fixed to the rocket would see a nearly steady flow of quite regular pattern. Thus it is generally useful in fluid mechanics (1) to choose the most convenient origin of coordinates, with luck making the flow appear steady, and (2) to study only the velocity *field* as a function of position and time, not trying to follow any specific particle paths. This scheme of describing the flow at every fixed point as a function of time is called the *Eulerian formulation* of motion. The Eulerian velocity vector field can be defined in the following Cartesian form:

$$\mathbf{V}(\mathbf{r}, t) = \mathbf{V}(x, y, z, t)$$
$$= \mathbf{i}u(x, y, z, t) + \mathbf{j}v(x, y, z, t) + \mathbf{k}w(x, y, z, t) \tag{1-4}$$

---

[*]Note, however, that flows involving chemical or nuclear reactions require an extended concept of equilibrium. Such flows typically involve knowledge of reaction rates and are not treated here.

Complete knowledge of the scalar variables u, v, and w as functions of (x, y, z, t) is often the solution to a problem in fluid mechanics. Note that we have used the notation (u, v, w) to mean velocity components, not displacement components, as they would be in solid mechanics. Displacements are of so little use in fluid problems that they have no symbol reserved for themselves.

The Eulerian, or velocity-field system, is certainly the proper choice in fluid mechanics, but one definite conflict exists. The three fundamental laws of mechanics—conservation of mass, momentum, and energy—are formulated for particles (systems) of fixed identity, i.e., they are Lagrangian in nature. All three of these laws relate to the time rate of change of some property of a fixed particle. Let Q represent any property of the fluid. If dx, dy, dz, dt represent arbitrary changes in the four independent variables, the total differential change in Q is given by

$$dQ = \frac{\partial Q}{\partial x} dx + \frac{\partial Q}{\partial y} dy + \frac{\partial Q}{\partial z} dz + \frac{\partial Q}{\partial t} dt \tag{1-5}$$

Since we are deliberately following an infinitesimal particle of fixed identity, the spatial increments must be such that

$$dx = u\, dt \qquad dy = v\, dt \qquad dz = w\, dt \tag{1-6}$$

Substituting in Eq. (1-5), we find the proper expression for the time derivative of Q of a particular elemental particle:

$$\frac{dQ}{dt} = \frac{\partial Q}{\partial t} + u\frac{\partial Q}{\partial x} + v\frac{\partial Q}{\partial y} + w\frac{\partial Q}{\partial z} \tag{1-7}$$

The quantity dQ/dt is variously termed the *substantial derivative, particle derivative*, or *material derivative*—all names which try to invoke the feeling that we are following a fixed fluid particle. To strengthen this feeling, it is traditional to give this derivative the special symbol DQ/Dt, purely a mnemonic device, not intended to frighten readers. In Eq. (1-7), the last three terms are called the *convective derivative*, since they vanish if the velocity is zero or if Q has no spatial change. The term $\partial Q/\partial t$ is called the *local derivative*. Also note the neat vector form

$$\frac{DQ}{Dt} = \frac{\partial Q}{\partial t} + (\mathbf{V} \cdot \nabla)Q \tag{1-8}$$

where ∇ is the gradient operator

$$\mathbf{i}\frac{\partial}{\partial x} + \mathbf{j}\frac{\partial}{\partial y} + \mathbf{k}\frac{\partial}{\partial z}$$

1-3.2   Acceleration of a Fixed-Identity Particle

If Q is $\mathbf{V}$ itself, we obtain our first kinematic property, the particle-acceleration vector:

$$\frac{D\mathbf{V}}{Dt} = \frac{\partial \mathbf{V}}{\partial t} + (\mathbf{V} \cdot \nabla)\mathbf{V} = \mathbf{i}\frac{Du}{Dt} + \mathbf{j}\frac{Dv}{Dt} + \mathbf{k}\frac{Dw}{Dt} \tag{1-9}$$

Note that the acceleration is concerned with u, v, and w and 12 scalar derivatives, i.e., the local changes $\partial u/\partial t$, $\partial v/\partial t$, and $\partial w/\partial t$ and the nine spatial derivatives of the form $\partial u_i/\partial x_j$, where i and j denote the three coordinate directions. Henceforth, we shall not use i, j, and k to denote unit vectors but instead use them as Cartesian indexes.

The convective terms in D/Dt present unfortunate mathematical difficulty because they are non-linear products of variable terms. It follows that viscous flows with finite convective accelerations are non-linear in character and present such vexing analytical problems as failure of the superposition principle; nonunique solutions, even in steady laminar flow; and coupled oscillating motion in a continuous frequency spectrum, which is the chief feature of a high Reynolds number, or turbulent, flow. Note that these non-linear terms are accelerations, not viscous stresses. It is ironic that the main obstacle in viscous-flow analysis is an inviscid term; the viscous stresses themselves are linear if the viscosity and density are assumed constant.

In frictionless flow, non-linear convective accelerations still exist but do not misbehave, as can be seen with reference to the valuable vector identity

$$(\mathbf{V} \cdot \nabla)\mathbf{V} \equiv \nabla \frac{V^2}{2} - \mathbf{V} \times (\nabla \times \mathbf{V}) \tag{1-10}$$

As we shall see, the term $\nabla \times \mathbf{V}$ usually vanishes if the viscosity is zero (irrotationality), leaving the convective acceleration equal only to the familiar kinetic-energy term of Bernoulli's equation. Inviscid flow, then, is non-linear also, but the non-linearity is confined to the calculation of static pressure, not to the determination of the velocity field, which is linear.

If we agree from this brief discussion that viscous flow is mathematically formidable, we deduce that a very important problem is that of modeling a viscous-flow experiment. That is, when can a velocity distribution $\mathbf{V}_1$ measured in a flow about or through a model shape B_1 be scaled by (say) a simple multiplier to yield the velocity distribution $\mathbf{V}_2$ about or through a geometrically similar but larger (say) model shape B_2? This happy condition is called *similarity*, and the conditions for achieving it or the frustrations in not achieving it are discussed in Chap. 2.

1-3.3   Other Kinematic Properties

In fluid mechanics, as in solid mechanics, we are interested in the general motion, deformation, and rate of deformation of particles. Like its solid counterpart, a fluid element can undergo four different types of motion or deformation: (1) translation; (2) rotation; (3) extensional strain, or dilatation; and (4) shear strain. The four types are easy to separate geometrically, which is of course why they are so defined. The reader familiar with, say, the theory of elasticity for solids will find the following analysis of fluid kinematic properties almost identical to that in solid mechanics. Consider an initially square fluid element at time t and then again later at time $t + dt$, as illustrated in Fig. 1-14 for motion in the xy plane. We can see by inspection the four types of motion which acted on the element. There has been translation of the reference corner B to its new position B'. There has been a counterclockwise rotation of the diagonal BD to the new position $B'D'$. There has been
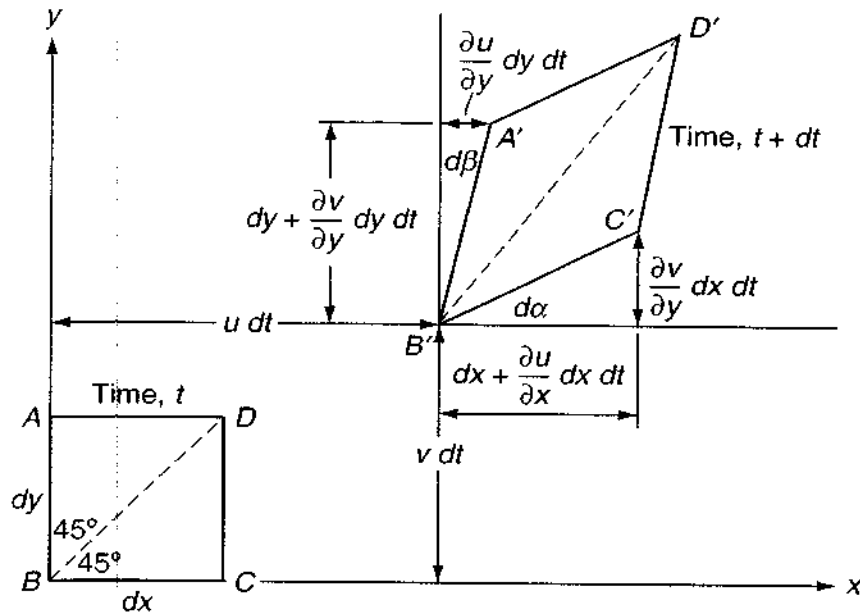
FIGURE 1-14
Distortion of a moving fluid element.

dilatation; the element looks a little bigger. There has been shear strain, i.e., the square has become rhombic.

Now put this discussion on a quantitative basis. Note in each case that the final result will be a *rate*, i.e., a time derivative.

The translation is defined by the displacements $u\,dt$ and $v\,dt$ of the point B. The *rate* of translation is u, v; in three-dimensional motion, the rate of translation is the velocity u, v, w.

The angular rotation of the element about the z axis is defined as the *average* counterclockwise rotation of the two sides BC and BA. As shown in Fig. 1-14, BC has rotated an amount $d\alpha$. Meanwhile, BA has rotated clockwise, thus its counterclockwise turn is $(-d\beta)$. The average rotation is thus

$$d\Omega_z = \tfrac{1}{2}(d\alpha - d\beta) \tag{1-11}$$

where the subscript z denotes rotation about an axis parallel to the z axis. Thus we perceived the counterclockwise rotation in Fig. 1-14 because $d\alpha$ was drawn larger than $d\beta$. Referring to Fig. 1-14, we find that both $d\alpha$ and $d\beta$ are directly related to velocity derivatives through the calculus limit:

$$d\alpha = \lim_{dt \to 0}\left(\tan^{-1} \frac{\frac{\partial v}{\partial x}\,dx\,dt}{dx + \frac{\partial u}{\partial x}\,dx\,dt} \right) = \frac{\partial v}{\partial x}\,dt$$

$$\tag{1-12}$$

$$d\beta = \lim_{dt \to 0}\left(\tan^{-1} \frac{\frac{\partial u}{\partial y}\,dy\,dt}{dy + \frac{\partial v}{\partial y}\,dy\,dt} \right) = \frac{\partial u}{\partial y}\,dt$$

Substituting Eq. (1-12) into (1-11), we find that the *rate* of rotation (angular velocity) about the z axis is given by

$$\frac{d\Omega_z}{dt} = \frac{1}{2}\left(\frac{\partial v}{\partial x} - \frac{\partial u}{\partial y}\right) \tag{1-13}$$

In exactly similar fashion, the *rates* of rotation about the x and y axes are

$$\frac{d\Omega_x}{dt} = \frac{1}{2}\left(\frac{\partial w}{\partial y} - \frac{\partial v}{\partial z}\right) \qquad \frac{d\Omega_y}{dt} = \frac{1}{2}\left(\frac{\partial u}{\partial z} - \frac{\partial w}{\partial x}\right) \tag{1-14}$$

These are clearly the three components of the angular velocity vector $d\Omega/dt$. The three factors of one-half are irritating, and it is customary to work instead with a quantity ω equal to twice the angular velocity:

$$\omega = 2\frac{d\Omega}{dt} \tag{1-15}$$

The new quantity ω, of vital interest in fluid mechanics, is called the *vorticity* of the fluid. By inspecting Eqs. (1-13) to (1-15), we see that vorticity and velocity are related by the vector calculus:

$$\omega = \text{curl } \mathbf{V} = \nabla \times \mathbf{V} \tag{1-16}$$

and hence the divergence of vorticity vanishes identically:

$$\text{div } \omega = \nabla \cdot \omega = \text{div curl } \mathbf{V} = 0 \tag{1-17}$$

Mathematically speaking, we say the vorticity vector is *solenoidal*. Note also that vorticity is intimately connected with convective acceleration through Eq. (1-10). If $\omega = 0$, the flow is *irrotational*.

Now consider the two-dimensional shear strain, which is commonly defined as the average *decrease* of the angle between two lines which are initially perpendicular in the unstrained state. Taking AB and BC in Fig. 1-14 as our initial lines, the shear–strain increment is obviously $\frac{1}{2}(d\alpha + d\beta)$. The shear–strain *rate* is

$$\epsilon_{xy} = \frac{1}{2}\left(\frac{d\alpha}{dt} + \frac{d\beta}{dt}\right) = \frac{1}{2}\left(\frac{\partial v}{\partial x} + \frac{\partial u}{\partial y}\right) \tag{1-18}$$

Similarly, the other two components of shear–strain *rate* are

$$\epsilon_{yz} = \frac{1}{2}\left(\frac{\partial w}{\partial y} + \frac{\partial v}{\partial z}\right) \qquad \epsilon_{zx} = \frac{1}{2}\left(\frac{\partial u}{\partial z} + \frac{\partial w}{\partial x}\right) \tag{1-19}$$

By analogy with solid mechanics, the shear–strain rates are symmetric, that is, $\epsilon_{ij} = \epsilon_{ji}$.

The fourth and final particle motion is dilatation, or extensional strain. Again with reference to Fig. 1-14, the extensional strain in the x direction is defined as the fractional increase in length of the horizontal side of the element. This is given by

$$\epsilon_{xx}\, dt = \frac{(dx + \partial u/\partial x\, dx\, dt) - dx}{dx} = \frac{\partial u}{\partial x}\, dt \tag{1-20}$$

with exactly similar expressions for the other two strains. Thus the three extensional strain *rates* are

$$\epsilon_{xx} = \frac{\partial u}{\partial x} \qquad \epsilon_{yy} = \frac{\partial v}{\partial y} \qquad \epsilon_{zz} = \frac{\partial w}{\partial z} \tag{1-21}$$

Taken as a whole, the strain rates, both extensional and shear, constitute a symmetric second-order tensor, which may be visualized as the array

$$\epsilon_{ij} = \begin{pmatrix} \epsilon_{xx} & \epsilon_{xy} & \epsilon_{xz} \\ \epsilon_{yx} & \epsilon_{yy} & \epsilon_{yz} \\ \epsilon_{zx} & \epsilon_{zy} & \epsilon_{zz} \end{pmatrix} \tag{1-22}$$

Although the component magnitudes vary with a change of axes x, y, and z, the strain-rate tensor, like the stress tensor [Eq. (2-14)] and the strain tensor of elasticity, follows the transformation laws of symmetric tensors [see, e.g., Aris (1990), Spain (2003), or Talpaert (2003)]. In particular, there are three invariants that are independent of direction or choice of axes:

$$I_1 = \epsilon_{xx} + \epsilon_{yy} + \epsilon_{zz}$$

$$I_2 = \epsilon_{xx}\epsilon_{yy} + \epsilon_{yy}\epsilon_{zz} + \epsilon_{zz}\epsilon_{xx} - \epsilon_{xy}^2 - \epsilon_{yz}^2 - \epsilon_{zx}^2$$

$$I_3 = \begin{vmatrix} \epsilon_{xx} & \epsilon_{xy} & \epsilon_{xz} \\ \epsilon_{yx} & \epsilon_{yy} & \epsilon_{yz} \\ \epsilon_{zx} & \epsilon_{zy} & \epsilon_{zz} \end{vmatrix} \tag{1-23}$$

A further property of symmetric tensors is that there exists one and only one set of axes for which the off-diagonal terms (the shear–strain rates in this case) vanish. These are the *principal axes*, for which the strain-rate tensor becomes

$$\begin{pmatrix} \epsilon_1 & 0 & 0 \\ 0 & \epsilon_2 & 0 \\ 0 & 0 & \epsilon_3 \end{pmatrix} \tag{1-24}$$

The quantities ϵ_1, ϵ_2, ϵ_3 are called the *principal strain rates*. For this special case, the three tensor invariants become

$$I_1 = \epsilon_1 + \epsilon_2 + \epsilon_3$$

$$I_2 = \epsilon_1\epsilon_2 + \epsilon_2\epsilon_3 + \epsilon_3\epsilon_1 \tag{1-25}$$

$$I_3 = \epsilon_1\epsilon_2\epsilon_3$$

If the invariants are known, Eqs. (1-25) are necessary and sufficient to solve for the principal strain rates, although there are actually much simpler ways to do this [see, e.g., Timoshenko and Goodier (1970)].

Finally, if we adopt the short notation $u_{i,j} = \partial u_i / \partial x_j$, where i and j are any two coordinate directions, note that any velocity derivative of this type can be split into two parts, one symmetric and one antisymmetric:

$$u_{i,j} = \tfrac{1}{2}(u_{i,j} + u_{j,i}) + \tfrac{1}{2}(u_{i,j} - u_{j,i}) \tag{1-26}$$

By comparing Eq. (1-26) with Eqs. (1-13), (1-14), (1-18), (1-19), and (1-21), we see that Eq. (1-26) can also be written as

$$\frac{\partial u_i}{\partial x_j} = \epsilon_{ij} + \frac{d\Omega_{ij}}{dt} \tag{1-27}$$

That is, each velocity derivative can be resolved into a strain rate plus an angular velocity. The angular velocity does not distort the element, so that only the strain rate will cause a viscous stress, a fact which is exploited in Chap. 2.

To summarize, we have shown that all the kinematic properties of fluid flow—acceleration, translation, angular velocity, rate of dilatation, and shear–strain rate—are directly related to the fluid velocity vector $V = (u, v, w)$. These relations are identical to the equivalent expressions from infinitesimal solid mechanics, if (u, v, w) are instead taken to be components of the *displacement* vector. This analogy between fluid and solid continuum mechanics is sometimes used to produce the equations of motion of a viscous linear fluid as a direct carryover from the equations of linear (Hookean) elasticity, with which students are often more familiar.

1-3.4   The Transport Properties of a Fluid

The three so-called transport properties are the coefficients of viscosity, thermal conductivity, and diffusion, so named because of the relation they bear to movement, or transport, of momentum, heat, and mass, respectively. Thus it is now popular in the field of chemical engineering to refer to a viscous-flow study as a problem in *momentum transport*, giving pause to the casual reader. The idea is not without merit. Each of the three coefficients relates a flux or transport to the gradient of a property. Viscosity relates momentum flux to velocity gradient, thermal conductivity relates heat flux to temperature gradient, and the diffusion coefficient relates mass transport to concentration gradient. Further, the mathematical properties of momentum, heat, and mass-flux problems are often similar and sometimes genuinely analogous. The perfect analogy, when it exists, is so striking that Bird et al. (2001) have devoted an entire textbook to an exposition of analogies among this trinity of problems. We should note now that the analogy fails in multidimensional problems because heat and mass flux are vectors while momentum flux (stress) is a tensor.

1-3.5   The Coefficient of Viscosity

The layperson knows from experience what *viscosity* means and associates it with the ability of a fluid to flow freely. Heavy oil takes a long time to flow out of a can. Light oil flows out quickly. The disastrous Boston molasses-tank explosion of 1919 [see Shank (1954)] caused one of the slowest floods in history. The idea of viscosity being proportional to time to flow has become accepted practice in the petroleum industry. Thus the motorist purchases oil with a viscosity labeled SAE 30. This means that 60 ml of this oil at a specified temperature takes 30 s to run out of a 1.76-cm hole in the bottom of a cup. This experiment is convenient and reproducible for very viscous
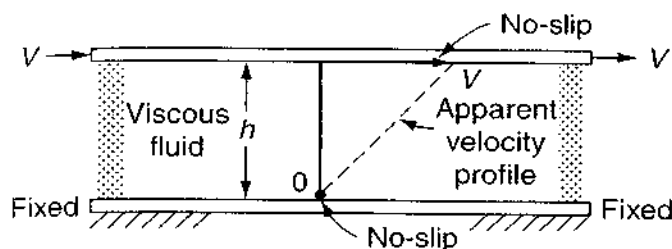
FIGURE 1-15
A fluid sheared between two plates.

liquids such as oil, but the time to flow is *not* viscosity, any more than the speed of sound is the time it takes an echo to return from a mountainside. It is an intriguing fact that the flow of a viscous liquid out of the bottom of a cup is a difficult problem for which no analytic solution exists at present.

A more fundamental approach to viscosity shows that it is the property of a fluid which relates applied stress to the resulting strain rate. The general relations are considered in Sec. 2-4. Here we consider a simple and widely used example of a fluid sheared between two plates, as in Fig. 1-15. This geometry is such that the shear stress τ_{xy} must be constant throughout the fluid. The motion is in the x direction only and varies with y, $u = u(y)$ only. Thus there is only a single finite strain rate in this flow:

$$\epsilon_{xy} = \frac{1}{2}\left(\frac{\partial u}{\partial y} + \frac{\partial v}{\partial x}\right) = \frac{1}{2}\frac{\partial u}{\partial y} = \frac{1}{2}\frac{du}{dy} \tag{1-28}$$

If one performs this experiment, one finds that, for all the common fluids, the applied shear is a unique function of the strain rate:

$$\tau_{xy} = f(\epsilon_{xy}) \tag{1-29}$$

Since, for a given motion V of the upper plate, τ_{xy} is constant, it follows that in these fluids ϵ_{xy}, and hence du/dy, is constant, so that the resulting velocity profile is linear across the plate, as sketched in Fig. 1-15. This is true regardless of the actual form of the functional relationship in Eq. (1-29). If the no-slip condition holds, the velocity profile varies from zero at the lower wall to V at the upper wall (Prob. 1-16 considers the case of a slip boundary condition). Repeated experiments with various values of τ_{xy} will establish the functional relationship Eq. (1-29). For simple fluids such as water, oils, or gases, the relationship is linear or *newtonian*:

$$\tau_{xy} \sim \epsilon_{xy}$$

or

$$\tau_{xy} = \mu\frac{V}{h} = 2\mu\epsilon_{xy} = \mu\frac{du}{dy} \tag{1-30}$$

The quantity μ, called the *coefficient of viscosity of a newtonian fluid*, is what handbooks commonly quote when listing the viscosity of a fluid (see App. A). Actually, there is also a second coefficient, λ, related to bulk fluid expansions, but it is rarely encountered in practice (see Sec. 2-4). Equation (1-30) shows that the dimensions
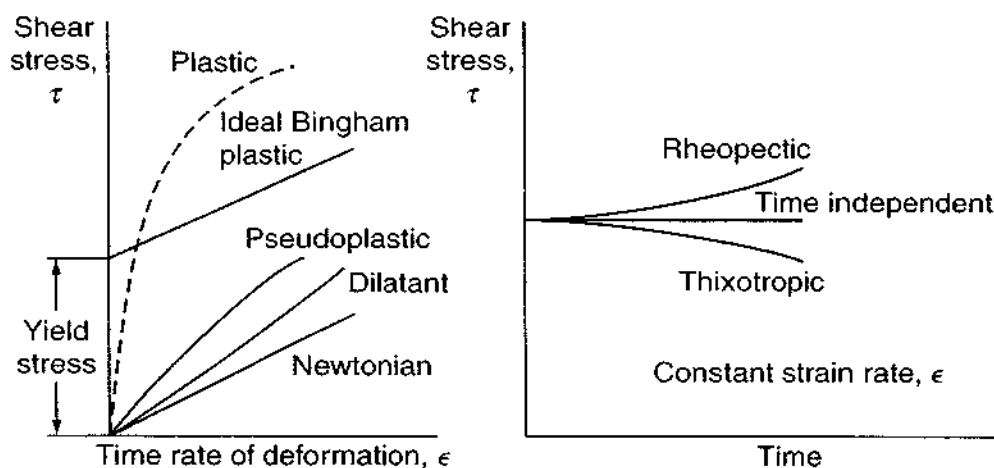
FIGURE 1-16
Viscous behavior of various materials.

of μ are stress-time: $N \cdot s/m^2$ [or $kg/(m \cdot s)$] in metric units and $lbf \cdot s/ft^2$ [or $slugs/ft \cdot s)$] in English units. The conversion factor is

$$1 \, N \cdot s/m^2 = 0.020886 \, lbf \cdot s/ft^2 \tag{1-31}$$

The coefficient μ is a thermodynamic property and varies with temperature and pressure. Data for common fluids are given in App. A.

If the functional relationship in Eq. (1-29) is nonlinear, the fluid is said to be *nonnewtonian*. Some examples of nonnewtonian behavior are sketched in Fig. 1-16. Curves for true fluids, which cannot resist shear, must pass through the origin on a plot of τ vs. ϵ. Other substances, called *yielding fluids*, show a finite stress at zero strain rate and are really part fluid and part solid.

The curve labeled *pseudoplastic* in Fig. 1-16 is said to be shear-thinning, since its slope (local viscosity) decreases with increasing stress. If the thinning effect is very strong, the fluid may be termed *plastic*, as shown. The opposite case of a shear-thickening fluid is usually called a *dilatant* fluid, as shown.

Also illustrated in Fig. 1-16 is a material with a finite yield stress, followed by a linear curve at finite strain rate. This idealized material, part solid and part fluid, is called a *Bingham plastic* and is commonly used in analytic investigations of yielding materials under flow conditions. Yielding substances need not be linear but may show either dilatant or pseudoplastic behavior.

Still another complication of some nonnewtonian fluids is that their behavior may be time-dependent. If the strain rate is held constant, the shear stress may vary, and vice versa. If the shear stress decreases, the material is called *thixotropic*, while the opposite effect is termed *rheopectic*. Such curves are also sketched in Fig. 1-16.

A simple but often effective analytic approach to nonnewtonian behavior is the power-law approximation of Ostwald and de Waele:

$$\tau_{xy} \approx 2K\epsilon_{xy}^n \tag{1-31a}$$

where K and n are material parameters which in general vary with pressure and temperature (and composition in the case of mixtures). The exponent n delineates three cases on the left-hand side of Fig. 1-16.

$$n < 1 \quad \text{pseudoplastic}$$
$$n = 1 \quad \text{newtonian} \; (K = \mu) \tag{1-31b}$$
$$n > 1 \quad \text{dilatant}$$

Note the Eq. (1-31a) is unrealistic near the origin, where it would incorrectly predict the pseudoplastic to have an infinite slope and the dilatant a zero slope. Hence many other formulas have been proposed for nonnewtonian fluids; see, e.g., Bird et al. (2001) or Hutton et al. (1989). The reader is advised to become familiar with such flows although the present text is confined to the study of newtonian flow.

1-3.6 Viscosity as a Function of Temperature and Pressure

The coefficient of viscosity of a newtonian fluid is directly related to molecular interactions and thus may be considered a thermodynamic property in the macroscopic sense, varying with temperature and pressure. The theory of the transport properties of gases and liquids is still being developed, and a comprehensive review is given by Hirschfelder et al. (1954). Extensive data on properties of fluids are given by Reid et al. (1987).

No single functional relation $\mu(T, p)$ really describes any large class of fluids, but reasonable accuracy (± 20 percent) can be achieved by nondimensionalizing the data with respect to the critical point (T_c, p_c). This procedure is the so-called principle of corresponding states [Keenan (1941)], wherein the given property, here μ/μ_c, is found to be roughly a function of T/T_c and p/p_c, the reduced temperature and pressure. This principle is *not* justified on thermodynamic grounds but arises simply from dimensional analysis and experimental observation. Since changes occur very rapidly near the critical point, T_c and p_c are known only approximately, and it is essentially impossible to measure μ_c accurately. Appendix A contains a table of critical constants (T_c, p_c, μ_c, k_c) for common fluids, which should be regarded as best-fit values.

Figure 1-17 shows a recommended correlation of reduced viscosity μ/μ_c vs. reduced temperature T/T_c and reduced pressure p/p_c. As stated, the accuracy for any given fluid is about ± 20 percent. By examining this figure, we can make the following general statements:

1. The viscosity of liquids decreases rapidly with temperature.
2. The viscosity of low-pressure (dilute) gases increases with temperature.
3. The viscosity always increases with pressure.
4. Very poor accuracy obtains near the critical point.

Since p_c for most fluids is greater than 10 atm (App. A), typical gas flow problems are at low reduced pressure and approximate the low-density-limit curve of Fig. 1-17.
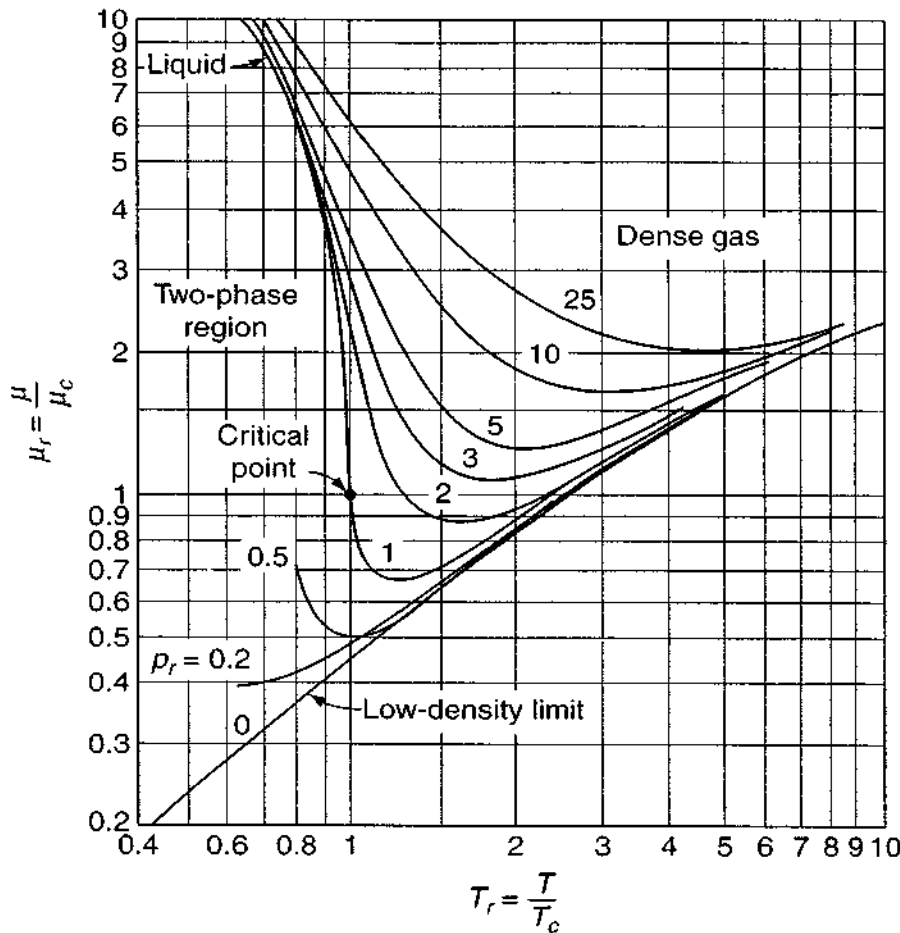
FIGURE 1-17

Reduced viscosity vs. reduced temperature for several values of reduced pressure $p_r = p/p_c$. [*After Uyehara and Watson (1944)*.]

Thus it is common in aerodynamics, for example, to ignore the pressure dependence of gas viscosity and consider only temperature variations.

1-3.7 The Low-Density Limit

The kinetic theory of dilute gases is now highly refined and has been the subject of several excellent texts, e.g., Brush (1972), Present (1958), and Hirschfelder et al. (1954). In these theories, which date back to Maxwell, the macroscopic concept of viscosity is related to a statistical average of the momentum exchange occurring between molecules of the fluid. For dilute gases, the viscosity is found to be proportional to the density ρ, the mean free path ℓ, and the speed of sound a in the gas. The accepted approximation for nonpolar gases is a slight adjustment of Maxwell's original expression:

$$\mu \approx 0.67 \rho \ell \, a \tag{1-32}$$

The product $\rho \ell$ is approximately constant for dilute gases, but more refined calculations by Chapman and Cowling (1970) show that it varies slightly with temperature due to the so-called collision integral Ω_v, computed from an approximate

intermolecular force potential between the given molecules of effective collision diameter σ. Thus the generalized kinetic-theory formula for dilute-gas viscosity is of the form.

$$\mu = \frac{2.68E-6\sqrt{MT}}{\sigma^2 \Omega_v} \qquad \text{[Chapman and Cowling (1970)]} \qquad (1\text{-}33)$$

where σ = collision diameter, Å
$\quad M$ = molecular weight of gas
$\quad \mu$ = viscosity, kg/(m · s)
$\quad T$ = absolute temperature, K

Ω_v is dimensionless and equal to unity for noninteracting molecules. Note that the mean free path can be computed by comparing Eqs. (1-32) and (1-33). In the general theory, Ω_v is found to depend upon the ratio T/T_ϵ, where T_ϵ is an effective temperature characteristic of the force potential chosen and the particular molecule. Most calculations are based either upon the Stockmayer potential or the Lennard–Jones potential function. Some calculated values of Ω_v for the Stockmayer potential function are given in Table 1-1. A curve-fit formula which fits these computed values to ±2 percent is

$$\Omega_v \approx 1.147\left(\frac{T}{T_\epsilon}\right)^{-0.145} + \left(\frac{T}{T_\epsilon} + 0.5\right)^{-2.0} \qquad (1\text{-}34)$$

The second term is negligible for T/T_ϵ greater than about 10. Values of the molecular parameters T_ϵ and σ are given in App. A for the common gases.

For routine calculations, a simpler formula than Eq. (1-33) may be desired. At higher temperatures, Eq. (1-34) indicates that $\Omega_v \sim T^{-0.145}$ and hence μ from Eq. (1-33) is proportional to $T^{0.645}$, which is approximately correct for all gases. Figure 1-17 also suggests the same power-law behavior. Thus a common approximation for the viscosity of dilute gases is the power law

$$\frac{\mu}{\mu_0} \approx \left(\frac{T}{T_0}\right)^n \qquad (1\text{-}35)$$

TABLE 1-1
Collision integrals computed from the Stockmayer potential

$T^* = T/T_\epsilon$	Ω_v	Ω_v [Eq. (1-34)]
0.3	2.840	2.928
1.0	1.593	1.591
3.0	1.039	1.060
10.0	0.8244	0.8305
30.0	0.7010	0.7015
100.0	0.5887	0.5884
400.0	0.4811	0.4811

Source: Data from Hirschfelder et al. (1954).

TABLE 1-2
Power-law and Sutherland-law viscosity parameters for gases
[Eqs. (1-35) and (1-36)][†]

Gas	T_0, K	μ_0, N·s/m^2	n	Error, %, temperature range, K		S, K	Temperature range for 2% error
Air	273	1.716E−5	0.666	±4	210–1900	111	170–1900
Argon	273	2.125E−5	0.72	±3	200–1500	144	120–1500
CO$_2$	273	1.370E−5	0.79	±5	209–1700	222	190–1700
CO	273	1.657E−5	0.71	±2	230–1500	136	130–1500
N$_2$	273	1.663E−5	0.67	±3	220–1500	107	100–1500
O$_2$	273	1.919E−5	0.69	±2	230–2000	139	190–2000
H$_2$	273	8.411E−6	0.68	±2	80–1100	97	220–1100
Steam	350	1.12E−5	1.15	±3	280–1500	1064	360–1500

Source: Data from Hilsenrath et al. (1955).

[†]No data given above maximum temperature listed. Formulas inaccurate below minimum temperature listed.

where n is of the order of 0.7 and T_0 and μ_0 are reference values. This formula was suggested by Maxwell also and later deduced on purely dimensional grounds by Rayleigh. Table 1-2 lists empirical values of n for various gases and the accuracy obtainable for a given temperature range.

A second widely used approximation resulted from a kinetic theory by Sutherland (1893) using an idealized intermolecular-force potential. The final formula is

$$\frac{\mu}{\mu_0} \approx \left(\frac{T}{T_0}\right)^{3/2} \frac{T_0 + S}{T + S} \tag{1-36}$$

where S is an effective temperature, called the *Sutherland constant*, which is characteristic of the gas. The accuracy is slightly better than that of Eq. (1-35) for the same temperature range. Values of S for common gases are also given in Table 1-2. Less common gases are tabulated in App. A.

These dilute-gas formulas are strictly valid only for a single component substance; air qualifies only because its two principal components, oxygen and nitrogen, are nearly identical diatomic molecules. For mixtures of gases of markedly different species, the mixture viscosity varies strongly with species concentration. A good discussion of transport properties of gas mixtures is given in Bird et al. (2001).

1-3.8 The Coefficient of Thermal Conductivity

It is well established in thermodynamics that heat flow is the result of temperature variation, i.e., a temperature gradient. This can be formally expressed as a proportionality between heat flux and temperature gradient, i.e., Fourier's law:

$$\mathbf{q} = -k\nabla T \tag{1-37}$$

where $\mathbf{q}$ is the vector rate of heat flow per unit area. The quantity k is our second transport coefficient, the thermal conductivity. Solid substances often show anisotropy, or directional sensitivity:

$$-\mathbf{q}_{sol} = \left(k_x \frac{\partial T}{\partial x}, k_y \frac{\partial T}{\partial y}, k_z \frac{\partial T}{\partial z} \right) \tag{1-38}$$

Fortunately, a fluid is isotropic, i.e., has no directional characteristics, and thus k is a thermodynamic property and, like viscosity, varies with temperature and pressure. Also, like viscosity, the common fluids will correlate with their critical properties, as shown in Fig. 1-18. Note that the general remarks for Fig. 1-17 also apply to Fig. 1-18 but the actual numerical values are quite different. The low-density limit for k is quite practical for the problems in this text, and the kinetic theory of dilute gases applies once more.
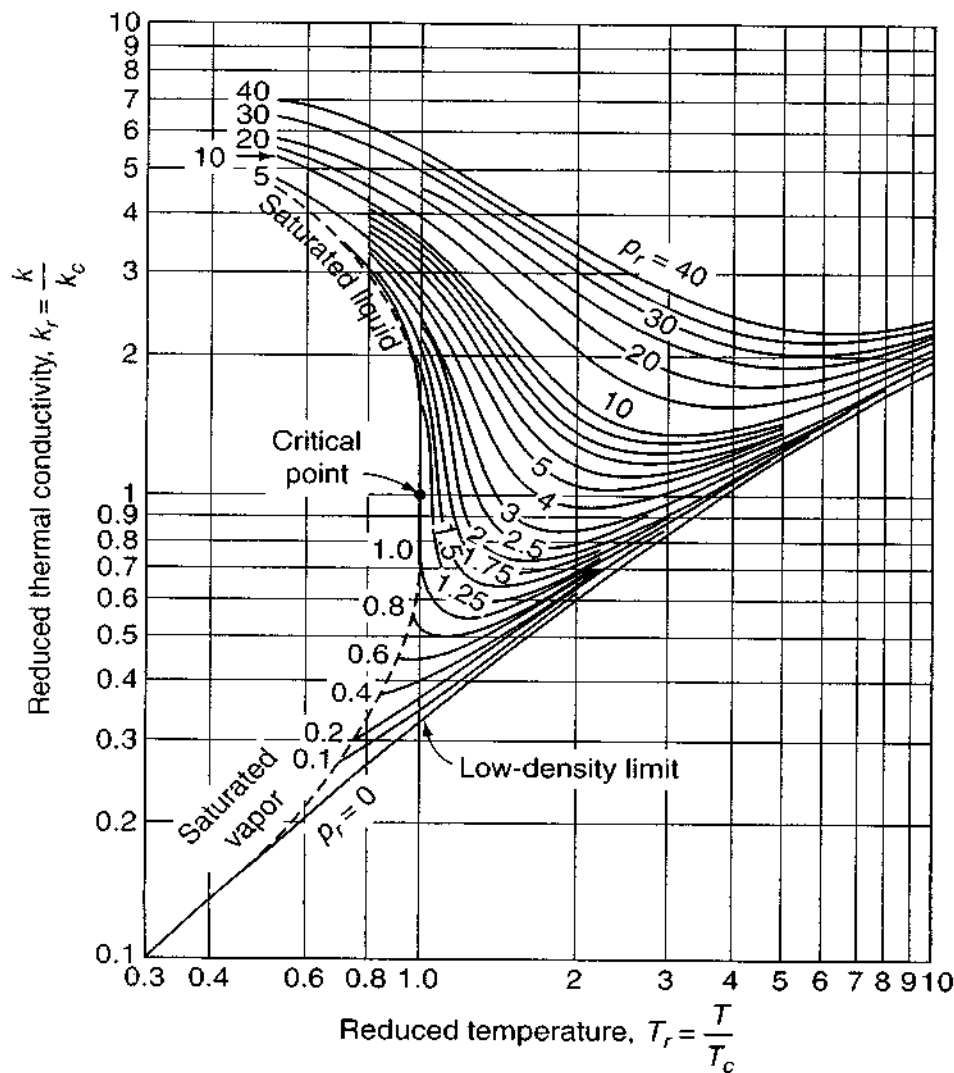
FIGURE 1-18
Reduced thermal conductivity vs. reduced temperature. [*After Owens and Thodos (1957)*.]

By inspection of Eq. (1-37), we see that thermal conductivity k should have dimensions of heat per time per length per degree, the common engineering unit being Btu/(h)(ft)(°R). The metric unit is W/(m · K), and the conversion factor is

$$1 \text{ W}/(\text{m} \cdot \text{K}) = 0.5778 \text{ Btu}/(\text{h})(\text{ft})(°\text{R}) \tag{1-39}$$

Also, k has the dimensions of viscosity times specific heat, so that the ratio of these is a fundamental parameter called the *Prandtl number*:

$$\text{Prandtl number} = Pr = \frac{\mu c_p}{k} \tag{1-40}$$

This parameter involves fluid properties only, rather than length and velocity scales of the flow. As we shall see, the Prandtl number is important in heat-transfer calculations but does not enter into friction computations.

The kinetic theory for conductivity of dilute gases is very similar to the viscosity analysis and leads to an expression similar to Eq. (1-33):

$$k \text{ W}/(\text{m} \cdot \text{K}) = \frac{0.0833 \sqrt{T}}{\sigma^2 \Omega_v \sqrt{M}} \tag{1-41}$$

where σ, Ω_v, and M have the same meanings and the same numerical values as in Eq. (1-33) and T is in kelvins. The collision integral Ω_v is again given by Table 1-1. If Eq. (1-41) is divided by Eq. (1-33), the result is

$$Pr = \frac{\mu c_p}{k} \approx \frac{4\gamma}{15\gamma - 15} \qquad \gamma = \frac{c_p}{c_v} \tag{1-42}$$

which relates the Prandtl number to the specific-heat ratio of the gas. The accuracy is only fair, however, and this relation was modified by Eucken (1913) and now serves as a purely empirical correlation formula:

$$Pr \approx \frac{4\gamma}{7.08\gamma - 1.80} = \begin{cases} 0.690 & \text{if } \gamma = 1.40 \text{ (diatomic gas)} \\ 0.667 & \text{if } \gamma = 1.67 \text{ (monatomic gas)} \end{cases} \tag{1-43}$$

This is seen to be a fair approximation to the Prandtl numbers of the gases plotted in Fig. 1-26.

For routine calculations with dilute gases, the power law and Sutherland formula, which correlated viscosity data, can also be used for thermal conductivity:

Power law:
$$\frac{k}{k_0} \approx \left(\frac{T}{T_0}\right)^n \tag{1-44a}$$

Sutherland:
$$\frac{k}{k_0} \approx \left(\frac{T}{T_0}\right)^{3/2} \frac{T_0 + S}{T + S} \tag{1-44b}$$

The accuracy is from 2 to 4 percent, depending upon the gas. Values of n, S, k_0, and T_0 are given for the common gases in Table 1-3, along with their accuracy when compared with the data compiled by White (1988).

TABLE 1-3

Power-law and Sutherland-law thermal-conductivity parameters for gases [Eqs. (1-44a) and (1-44b)]

Gas	T_0, K	k_0, W/m · K	n	Error, % temperature range, K		S, K	Temperature range for $\pm 2\%$ error, K
Air	273	0.0241	0.81	±3	210–2000	194	160–2000
Argon	273	0.0163	0.73	±4	210–1800	170	150–1800
CO_2	273	0.0146	1.30	±2	180–700	1800	180–700
CO	273	0.0232	0.82	±2	210–800	180	200–800
N_2	273	0.0242	0.74	±3	210–1200	150	200–1200
O_2	273	0.0244	0.84	±2	220–1200	240	200–1200
H_2	273	0.168	0.72	±2	200–1000	120	200–1000
Steam	300	0.0181	1.35	±2	300–900	2200	300–700

Source: Data from White (1988).

1-3.9   The Coefficient of Mass Diffusivity

The third and final transport coefficient is associated with the movement of mass due to molecular exchange. This process, called *diffusion*, constantly occurs in a fluid because of random molecular motion; the air in a given portion of a room continually loses some particles and gains others, so that the specific content of a given volume is always changing. We cannot notice the change on a macroscopic basis because the air mixture remains the same; such diffusion of nearly identical particles is called *self-diffusion*.

Diffusion becomes macroscopically evident when a variable mixture of two or more species is involved. If we stand on one side of a room while an amount of hydrogen sulfide gas is released at the other side, we soon notice the odor as the hydrogen sulfide diffuses to our side, replacing some of our air, which diffuses to the other side. The transfer of mass is equal and opposite, i.e., diffusion is an equal exchange of species, and the final state in this case would be a uniform mixture of air and hydrogen sulfide throughout the room. It is well to note that the rate of diffusion is *not* equal to the mean molecular speed $\bar{c}$ but is far slower. Many molecular collisions occur in a short distance, the mean free path; hence the hydrogen sulfide "front" advances slowly, a mean free path at a time, so to speak.

Mass diffusion occurs, then, whenever there is a gradient in the proportions of a mixture, i.e., a *concentration gradient*. There are two different definitions of concentration in frequent use: (1) the volume concentration $\rho_i = m_i/\text{volume} = \text{mass of}$ component i per unit volume and (2) the mass concentration $C_i = \rho_i/\rho = $ the mass of species i per unit mass of the mixture. The second definition or mass concentration will be more useful in this text if for no other reason than that it is a dimensionless fraction less than or equal to unity. By analogy with viscosity and thermal conductivity, we postulate that mass diffusion per unit area is proportional to concentration

gradient. In vector form, we have

$$\frac{\dot{m}_i}{A} = -D\nabla(\rho_i) \tag{1-45}$$

where $\dot{m}_i$ is the mass flux of species i in the direction of decreasing concentration (which accounts for the minus sign). The quantity D is called the *coefficient of mass diffusivity* and has dimensions of (length)^2/time, usually either square feet per second or square centimeters per second. Equation (1-45) is called *Fick's law of diffusion.*

In terms of mass concentration $C_i = \rho_i/\rho$, Eq. (1-45) becomes

$$\frac{\dot{m}_i}{A} = -\rho_i D\nabla(\ln C_i) \tag{1-46}$$

where ln denotes the natural logarithm. Since mass flux per unit area equals density times velocity, we can write, by definition,

$$\frac{\dot{m}_i}{A} = \rho_i V_i \tag{1-47}$$

where V_i is called the *diffusion velocity* of species i. In this simpler form, then, Fick's law can be written as

$$V_i = -D\nabla(\ln C_i) \tag{1-48}$$

Here we account only for concentration gradients. Rigorous kinetic theory shows that species mass fluxes may also be caused by pressure gradients or by temperature gradients, with a general expression

$$V_i = -D\nabla(\ln C_i) - D_p\nabla(\ln p) - D_T\nabla(\ln T) \tag{1-49}$$

as explained in Chapman and Cowling (1970), for example. The pressure-diffusion term is usually small because pressure gradients are smaller than concentration gradients in flow problems. The thermal-diffusion term is usually neglected because D_T is typically much smaller than D.

The diffusion coefficient D has the same dimensions as the kinematic viscosity $\nu = \mu/\rho$ or the thermal diffusivity $\alpha = k/\rho c_p$. Thus their ratios, like the Prandtl number considered earlier, are important dimensionless parameters in a fluid-diffusion problem:

$$\text{Schmidt number} = Sc = \frac{\mu}{\rho D} = \frac{\nu}{D}$$

$$\text{Lewis number} = Le = \frac{\rho c_p D}{k} = \frac{D}{\alpha} \tag{1-50}$$

The Schmidt number relates viscous diffusion to mass diffusion, and the Lewis number compares mass diffusion to thermal diffusion.

For dilute gases, kinetic theory yields the following expression for the binary-diffusion coefficient D_{12} between species 1 and 2 [Chapman and Cowling (1970)]:

$$D_{12} = \frac{0.001858 T^{3/2}[(M_1 + M_2)/M_1 M_2]^{1/2}}{p\sigma_{12}^2 \Omega_D} \tag{1-51}$$

where
D_{12} = binary-diffusion coefficient, cm^2/s
M_1, M_2 = molecular weight of two gases
Ω_D = diffusion collision integral
σ_{12} = effective collision diameter, Å
T = absolute temperature, K
p = pressure, atm

The collision integral is about 10 percent smaller than Ω_v from Table 1-1 and can be approximated closely by modifying Eq. (1-34):

$$\Omega_D \approx 1.0 T^{*-0.145} + (T^* + 0.5)^{-2.0} \tag{1-52}$$

where $T^* = T/T_{\epsilon_{12}}$. The effective temperatures and diameters are averages computed from the separate molecular properties of each species:

$$\sigma_{12} = \tfrac{1}{2}(\sigma_1 + \sigma_2)$$

$$T_{\epsilon_{12}} = (T_{\epsilon_1} T_{\epsilon_2})^{1/2} \tag{1-53}$$

The molecular properties listed in App. A are valid for these diffusion calculations also. Note that, unlike viscosity and conductivity, diffusion coefficient D varies inversely with pressure in Eq. (1-51). Thus, at low pressures, product pD is a function only of temperature. For dense gases, there is considerable pressure dependence also, but very few data are available. Figure 1-19 is a tentative plot of this pressure effect for self-diffusion D_{11} (nearly identical molecules). Note that reduced
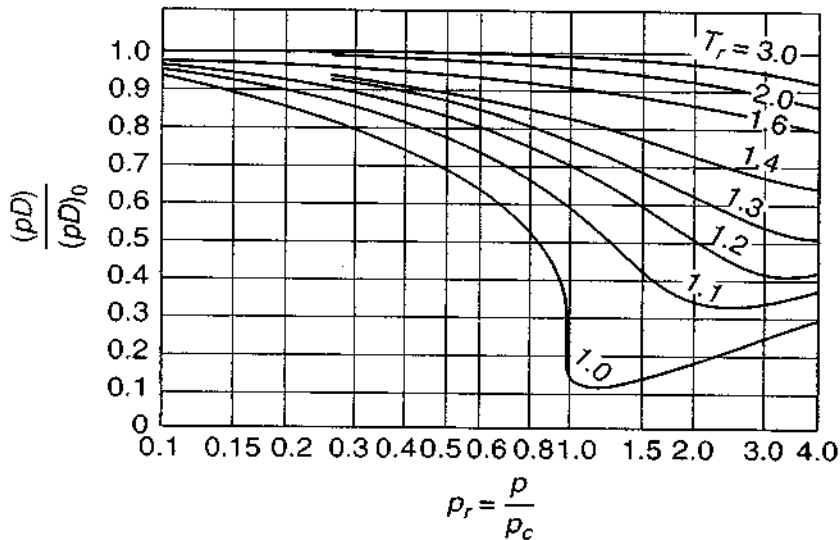
FIGURE 1-19
Tentative generalized chart for self-diffusivity of a dense gas. [*After Slattery and Bird (1958)*.]

diffusivity D/D_c cannot be used. The plot involves instead the ratio of pD to its value $(pD)_0$ at the same temperature but very low pressures.

Since binary-diffusion data are scarce, we shall not attempt to present a power law or a Sutherland formula for estimating D_{12} of dilute gases. For further information on diffusion estimates, consult Reid et al. (1987).

1-3.10 Transport Properties of Dilute-Gas Mixtures

The previous discussion of viscosity has been confined essentially to fluids of a single species. For gases, the kinetic theory has been extended, for the low-density limit, to multicomponent mixtures. The details are given by Hirschfelder et al. (1954). For routine calculations, the semiempirical formula of Wilke (1950) is recommended:

$$\mu_{\text{mix}} \approx \sum_{i=1}^{n} \frac{x_i \mu_i}{\sum_{j=1}^{n} x_j \phi_{ij}} \tag{1-54}$$

where

$$\phi_{ij} = \frac{[1 + (\mu_i/\mu_j)^{1/2}(M_j/M_i)^{1/4}]^2}{(8 + 8M_i/M_j)^{1/2}}$$

This formula is for a mixture of n gases, where M_i are the molecular weights and x_i are the mole fractions. In terms of the *mass* fractions $C_i = \rho_i/\rho$, we have

$$x_i = \frac{C_i/M_i}{\sum_{j=1}^{n}(C_j/M_j)} \tag{1-55}$$

A similar formula is recommended by Wilke for the thermal conductivity k of a mixture of n gases except that μ_i are replaced by k_i.

1-3.11 Transport Properties of Liquids

The theoretical analysis of liquid transport properties is not nearly as well developed as that for gases. The difficulty is that liquid molecules are very closely packed compared to gases and thus dominated by large intermolecular forces. Momentum transfer by collisions—so dominant in gases—is small in liquids. The kinetic theory of liquids is summarized in the texts by Bird et al. (1977) and Reid et al. (1987). However, the theory is not yet quantitative, in the sense that a given liquid's properties cannot be predicted from other thermodynamic data.

If no data are available, we recommend the reduced temperature and pressure plots, Figs. 1-17 and 1-18, for ±20 percent accuracy. If data are available for calibration, however, they may be fit accurately to the empirical formula:

Liquid: $$\ln \frac{\mu}{\mu_0} \approx a + b\left(\frac{T_0}{T}\right) + c\left(\frac{T_0}{T}\right)^2 \tag{1-56}$$

where (μ_0, T_0) are reference values and (a, b, c) are dimensionless curve-fit constants. For nonpolar liquids, $c \approx 0$, i.e., the plot is linear.
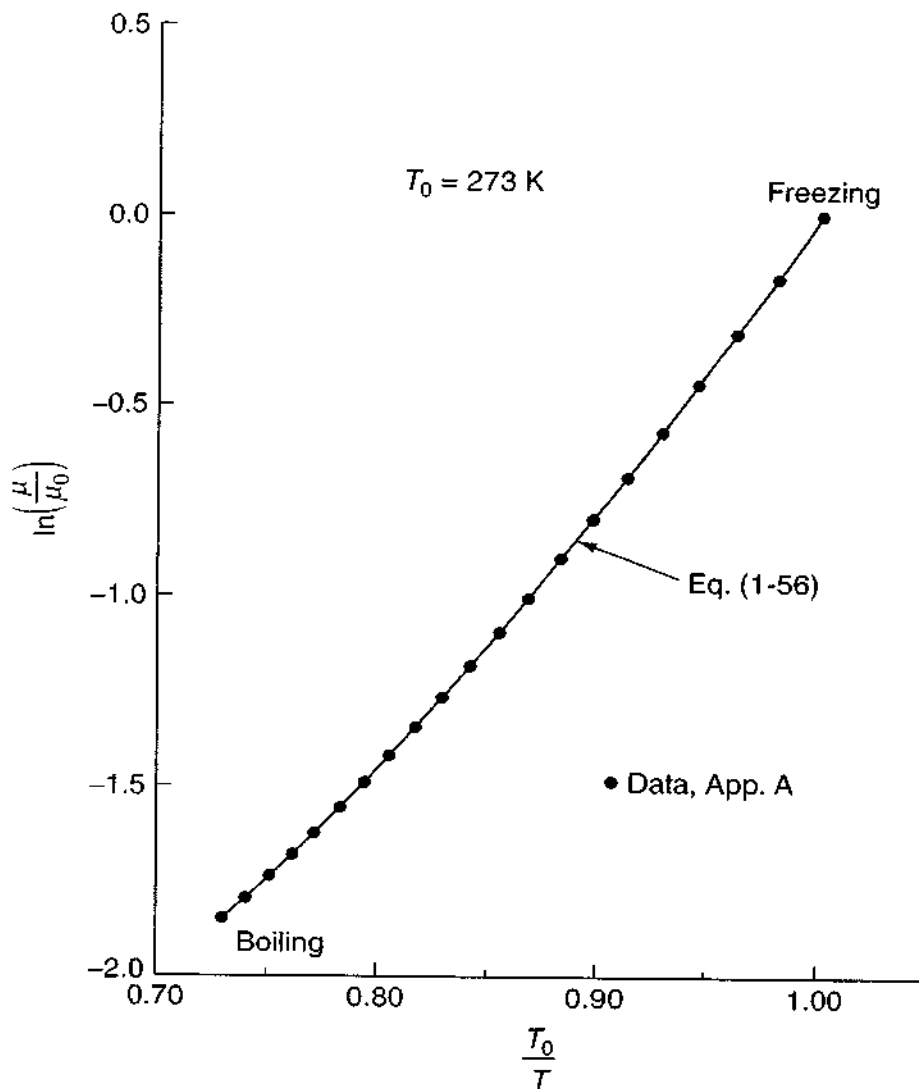
FIGURE 1-20
Empirical plot of the viscosity of water in the manner suggested by Eq. (1-56).

For example, App. A tabulates the viscosity of water at atmospheric pressure. If these data are plotted in the manner suggested by Eq. (1-56), the results are shown in Fig. 1-20. The plot is nearly linear, and the curve-fit values are

$$a = -2.10 \qquad b = -4.45 \qquad c = 6.55 \tag{1-57}$$

corresponding to $T_0 = 273$ K and $\mu_0 = 0.00179$ kg/m·s. The accuracy of the curve fit is ± 1 percent when compared to the data of App. Table A.1.

For thermal conductivity of liquids, Eq. (1-56) may not be a good fit—see, e.g., data for water in App. Fig. A-5. Reid et al. (1987) recommend the simple linear fit

$$k_{liq} \quad \text{or} \quad D_{liq} \approx a + bT \tag{1-58}$$

which will be accurate at least over a limited temperature range.

1-3.12 The Thermodynamic Properties

As stated before, by their very nature viscous flows are technically not in equilibrium, but at normal densities the deviations from equilibrium are negligible. Two exceptions to this are chemically reacting flows and very sudden state changes, as in a strong shock wave. Generally, though, it is quite reasonable to assume that a moving viscous fluid is a pure substance whose properties are related by ordinary equilibrium thermodynamics. The properties most important to this subject are pressure, density, temperature, entropy, enthalpy, and internal energy. Of these six, two may be regarded as the independent variables from which all others follow through experimental (or theoretical) equations of state. In Chap. 2, it will be convenient to consider p and T as primary variables, but technically this is a flawed choice.

The first law of thermodynamics can be written as

$$dE = dQ + dW \tag{1-59}$$

where dE = change in total energy of system
dQ = heat added to system
dW = work done on system

For a substance at rest with infinitesimal changes, we have

$$dW = -p\, d\,(\text{volume})$$
$$dQ = T\, dS \tag{1-60}$$

Substituting in Eq. (1-59) and expressing the result on a unit mass basis, we have

$$de = T\, ds + \frac{p}{\rho^2}\, d\rho \tag{1-61}$$

which is one form of the first and second laws combined for infinitesimal processes. Equation (1-61) implies that the single state relation

$$e = e(s, \rho) \tag{1-62}$$

is entirely sufficient to define a fluid thermodynamically. For, in terms of the calculus of two variables,

$$de = \frac{\partial e}{\partial s}\, ds + \frac{\partial e}{\partial \rho}\, d\rho \tag{1-63}$$

from which, by comparison with Eq. (1-61), the temperature and pressure can be calculated by

$$T = \left.\frac{\partial e}{\partial s}\right|_\rho \qquad p = \left.\rho^2\frac{\partial e}{\partial \rho}\right|_s \tag{1-64}$$

after which the enthalpy can be calculated from its definition:

$$h = e + \frac{p}{\rho} \tag{1-65}$$

Thus a single chart of e vs. s for lines of constant ρ is sufficient to calculate all thermodynamic properties. Equation (1-62) is therefore called a *canonical* equation of state.

A second and more popular canonical equation of state is obtained by using Eq. (1-65) to eliminate de in Eq. (1-61), with the result

$$dh = T\,ds + \frac{1}{\rho}\,dp \qquad (1\text{-}66)$$

Again using calculus, we find that from the canonical relation

$$h = h(s, p) \qquad (1\text{-}67)$$

all other properties can be calculated:

$$T = \left.\frac{\partial h}{\partial s}\right|_\rho \qquad \frac{1}{\rho} = \left.\frac{\partial h}{\partial p}\right|_s$$

$$e = h - \frac{p}{\rho} \qquad (1\text{-}68)$$

In this case, a chart of h vs. s for lines of constant p will define the substance completely. Such a plot is very popular and is called a *Mollier chart*, after Richard Mollier (1863–1935), a German engineering professor who first proposed it.

Figure 1-21 is a sketch of the Mollier chart for air as given by Little (1963) from many sources of data. Tabular properties for eight common gases are given by Hilsenrath et al. (1955). Figure 1-21 shows only the constant-pressure lines, which
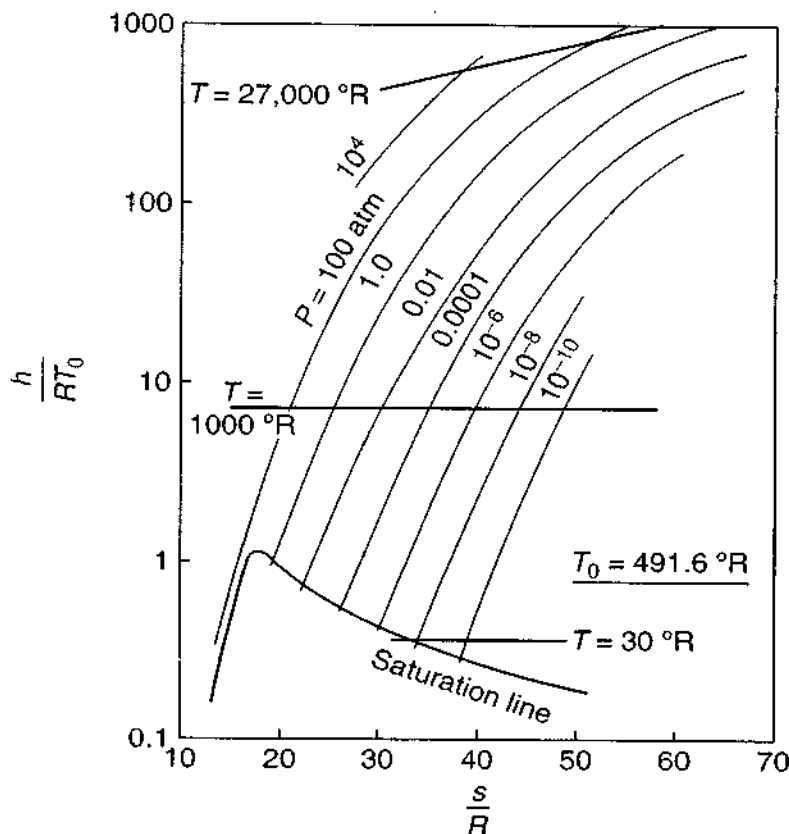
FIGURE 1-21

Mollier chart for equilibrium air.
[*After Little (1963).*]

are quite sufficient thermodynamically, as discussed previously. However, in preparing such a Mollier chart for publication, it is usual to include other lines (constant density, temperature, speed of sound). Data for water and steam are given by Parry et al. (2000).

1-3.13 Secondary Thermodynamic Properties

Still other properties are often used in flow analyses, particularly with idealized equations of state such as the perfect-gas law. Two of these are the specific heats (so-called) at constant pressure and constant volume:

$$c_p = \left.\frac{\partial h}{\partial T}\right|_p \qquad c_v = \left.\frac{\partial e}{\partial T}\right|_v \tag{1-69}$$

which of course are not heats at all but expressions of energy change. The ratio of specific heats

$$\gamma = \frac{c_p}{c_v} \tag{1-70}$$

is an important dimensionless parameter in high-speed (compressible) flow problems. This ratio lies between 1.0 and 1.7 for all fluids. For a liquid, which is nearly incompressible, $c_p \approx c_v$ and $\gamma \approx 1.0$. Figure 1-22 shows values of γ at atmospheric
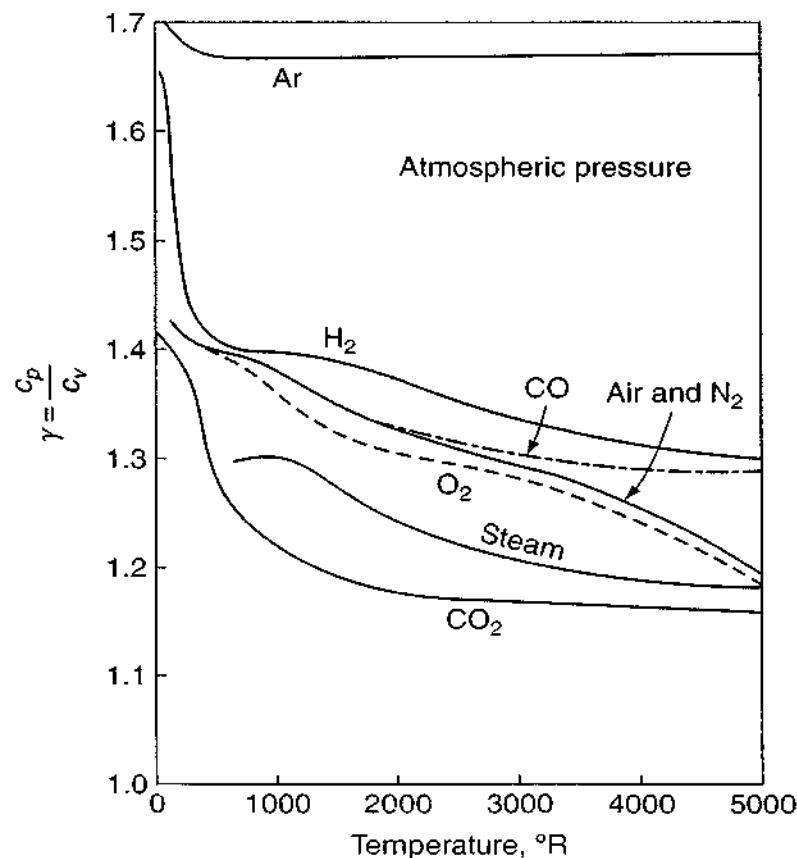
FIGURE 1-22
Specific-heat ratio for eight common gases. [*Data from Hilsenrath et al.* (*1955*).]

pressure for various gases as a function of absolute temperature. The pressure dependence of γ is very weak, and the figure shows that the approximation (γ = const) is accurate over fairly wide temperature variations.

Another minor but important thermodynamic property is the *speed of sound* a, defined as the rate of propagation of infinitesimal pressure pulses:

$$a^2 = \frac{\partial p}{\partial \rho}\bigg|_s \tag{1-71}$$

[see, e.g., White (2003), Sec. 9.2]. The partial derivative in Eq. (1-71) is often rather clumsy to handle, in which case an alternate relation can be used:

$$a^2 = \gamma\left(\frac{\partial p}{\partial \rho}\right)_T \tag{1-72}$$

The student may prove as an exercise that Eqs. (1-71) and (1-72) are thermodynamically identical. Since viscous flows are definitely *not* isentropic in general, the speed of sound is not a natural inhabitant of viscous analyses but enters instead through the assumption of perfect-gas relations, as does the Mach number.

1-3.14 The Perfect Gas

All the common gases follow with reasonable accuracy, at least in some finite region, the so-called ideal or perfect-gas law:

$$p = \rho R T \tag{1-73}$$

where R is called the gas constant. Equation (1-73) has a solid theoretical basis in the kinetic theory of dilute gases, e.g., Brush (1972), and should not be regarded as an empirical formula. The gas constant R is the ratio of Boltzmann's constant to the mass of a single molecule:

$$R = \frac{K}{m} \tag{1-74}$$

Alternately, R may be written in terms of the molecular weight M of the gas:

$$R_{\text{gas}} = \frac{R_0}{M_{\text{gas}}} \tag{1-75}$$

where R_0 is a universal constant similar to Boltzmann's constant. In metric units,

$$R_0 = 8314 \text{ J/(kg} \cdot \text{mol} \cdot \text{K)} \tag{1-76}$$

which is too many significant figures, since no gas really fits the law that well. Equations (1-73) and (1-75) are also suitable for mixtures of gases if the equivalent molecular weight is properly defined in terms of the mass fractions $C_i = \rho_i/\rho$:

$$M_{\text{mix}} = \frac{1}{\sum(C_i/M_i)} \tag{1-77}$$

In terms of the mole fractions x_i (number of moles of species i per mole of mixture), we have

$$M_{\text{mix}} = \sum x_i M_i \qquad (1\text{-}78)$$

As a classic example, air at ordinary temperatures has mole fractions of approximately 78 percent nitrogen, 21 percent oxygen, and 1 percent argon. Then, from Eq. (1-78),

$$M_{\text{air}} = 0.78(28.016) + 0.21(32.000) + 0.01(39.944) = 28.97$$

from which

$$R_{\text{air}} = \frac{8314}{28.97} = 287 \text{ J}/(\text{kg} \cdot \text{K})$$

These are the accepted values for room-temperature dry air.

According to Eq. (1-73), the so-called compressibility factor

$$Z = \frac{p}{\rho RT} \qquad (1\text{-}79)$$

should be unity for gases. Actually, Z varies from zero to 4.0 or greater, depending upon temperature and pressure. To good accuracy, Z is a function only of the reduced variables $p_r = p/p_{\text{crit}}$ and $T_r = T/T_{\text{crit}}$ referred to the critical point. This is illustrated in Figs. 1-23 and 1-24, which are representative of all gases. Examining these figures, we see that the perfect-gas law ($Z = 1$) is accurate to ± 10 percent in the range $1.8 \leq T_r \leq 15$ and $0 \leq p_r \leq 10$, which is the range of interest of the majority of viscous-flow problems. The higher temperatures should be viewed with
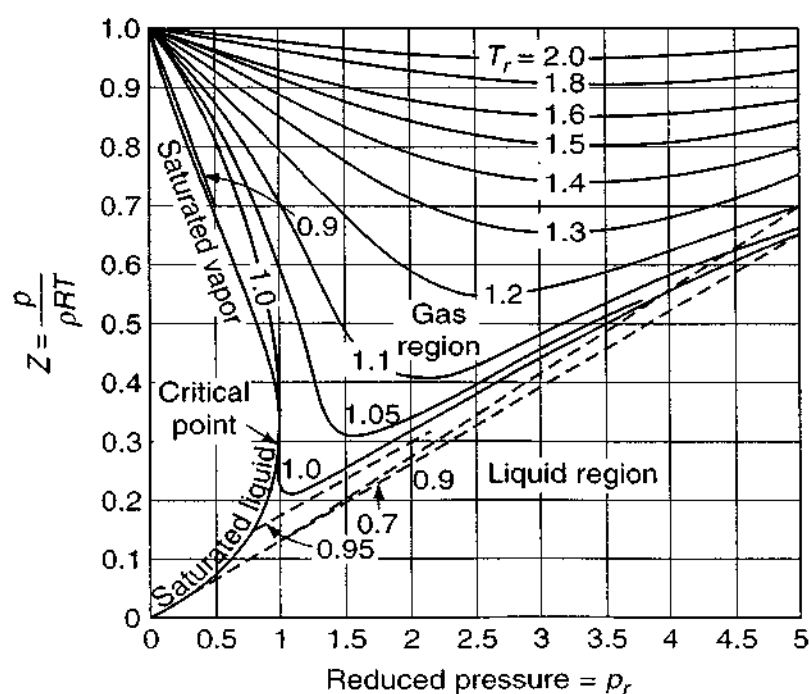
FIGURE 1-23
Compressibility factors for gases. [*After Weber (1939).*]
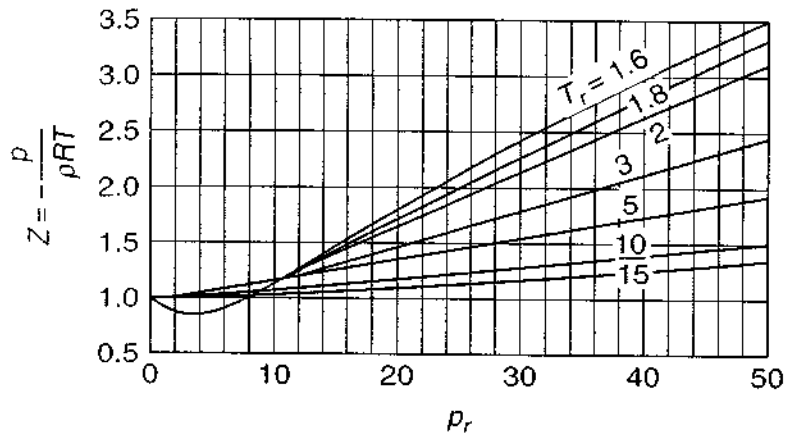
FIGURE 1-24
Compressibility at higher p_r and T_r.
[*After Weber (1939).*]
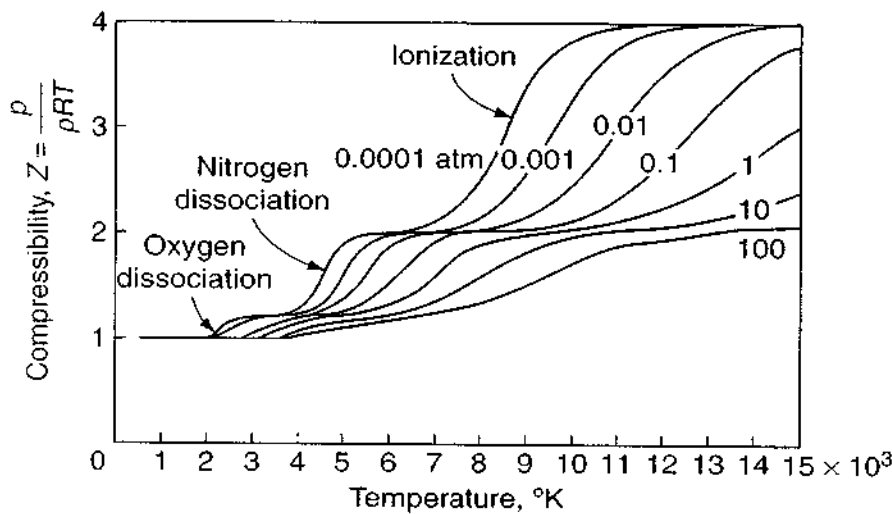
FIGURE 1-25
Calculated compressibility of air. [*After Hansen (1958).*]

suspicion for multiatom molecules, which may dissociate into smaller particles and raise the value of Z markedly. In air, for example, dissociation happens twice: at 2000 K, where $O_2 \rightarrow 2O$, and at 4000 K, where $N_2 \rightarrow 2N$. Figure 1-25 shows the compressibility factor of air as calculated by Hansen (1958). Note the first and second plateaus corresponding to O_2 and then N_2 dissociation. The effect is particularly strong at low pressure.

1-3.15   Other Properties of the Perfect Gas

As a direct consequence of the perfect-gas law [Eq. (1-73)], many useful and simple relations arise. The specific heats are constrained to be functions of temperature only:

$$c_p = c_p(T) \text{ only}$$

and

$$c_v = c_v(T) \text{ only} \tag{1-80}$$

Hence, from Eqs. (1-69), we have

$$de = c_v \, dT$$

$$dh = c_p \, dT \tag{1-81}$$

Further, it follows that

$$\gamma = \gamma(T) \text{ only}$$

$$c_p(T) = c_v(T) + R = \frac{\gamma(T)R}{\gamma(T) - 1} \tag{1-82}$$

$$c_v(T) = \frac{R}{\gamma(T) - 1}$$

Finally, from Eq. (1-72), the speed of sound takes the simple form

$$a^2_{\text{perfect gas}} = \gamma RT \tag{1-83}$$

Because of reasonable accuracy and delightful simplicity, the perfect-gas relations are understandably popular in viscous-flow analysis. We make liberal use of the perfect-gas law in Chap. 7.

As shown in Fig. 1-22, the specific-heat ratio γ tends to decrease with temperature. Since all these gases are reasonably perfect, it follows from Eqs. (1-82)
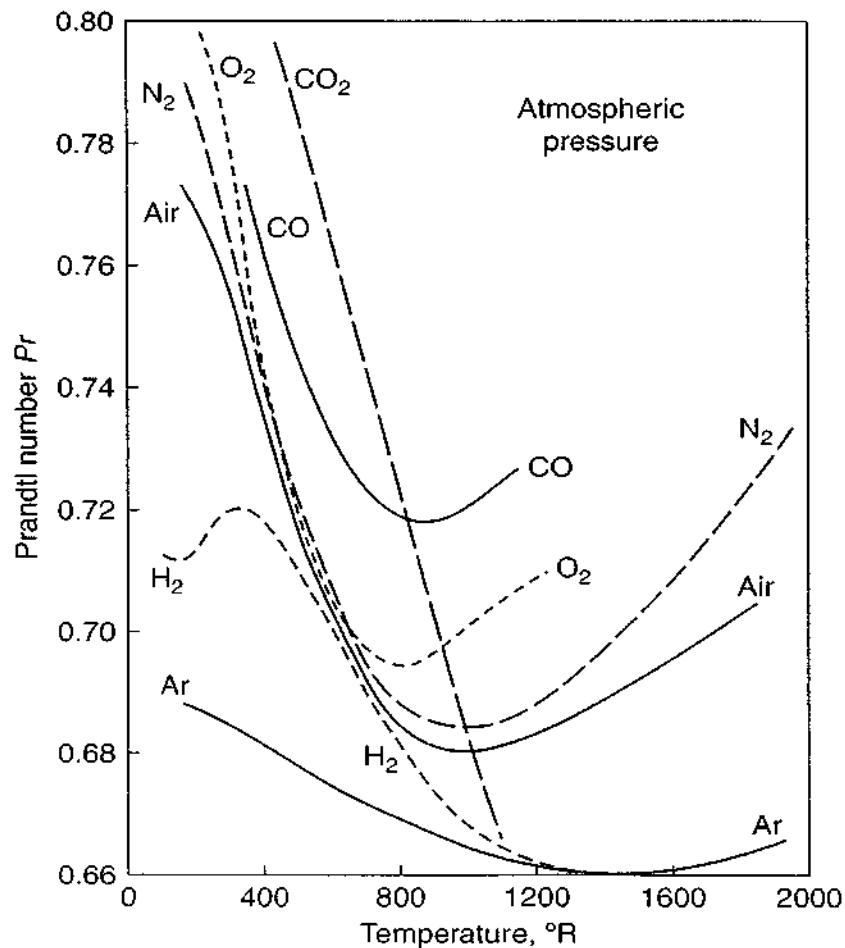
FIGURE 1-26
Prandtl number vs. temperature for seven gases. [*Data from Hilsenrath et al. (1955).*]

that c_p and c_v must increase with temperature. Since R is known from Eq. (1-75), Fig. 1-22 may be used to calculate c_p and c_v to good accuracy.

Finally, Fig. 1-26 shows the Prandtl number, $Pr = \mu c_p / k$, for various common gases. Note by comparison with Fig. 1-22 that Eucken's formula, Eq. (1-43), is only a fair approximation.

1-3.16 Bulk Modulus

In flow problems which involve sound-wave propagation, it is useful to have a thermodynamic property which expresses the change of density with increasing pressure. This property is the *bulk modulus K*:

$$K = \rho \left(\frac{\partial p}{\partial \rho} \right)_T \tag{1-84}$$

From Eq. (1-72), then, we see that the speed of sound can be written in terms of K:

$$a^2 = \frac{\gamma K}{\rho} \tag{1-85}$$

where γ may be taken as 1.0 for liquids and solids.[*] For a perfect gas, the reader may verify that $K = p$ itself. For liquids, however, K is fairly constant, varying slightly with pressure and temperature. For water, a good average value is $K = 2.2E9$ Pa. Taking $\gamma = 1.0$ and an average water density of 998 kg/m^3, we calculate the speed of sound in water to be approximately 1480 m/s.

1-3.17 Coefficient of Thermal Expansion

There is a subset of flow problems, called *natural convection*, where the flow pattern is due to buoyant forces caused by temperature differences. Such buoyant forces are proportional to the coefficient of thermal expansion β, defined as

$$\beta = -\frac{1}{\rho} \left(\frac{\partial \rho}{\partial T} \right)_p \tag{1-86}$$

For a perfect gas, the reader may show that $\beta = 1/T$. For a liquid, β is usually smaller than $1/T$ and may even be negative (the celebrated inversion of water near the freezing point). For imperfect gases, β can be considerably larger than $1/T$ near the saturation line, particularly at high pressures. This is illustrated in Fig. 1-27 for steam. We see that steam is well approximated by the perfect-gas result $\beta T = 1$ at low pressures and high temperatures.

---

[*] A solid has *two* sound speeds: $(K/\rho)^{1/2}$ is the dilatation, or longitudinal-wave, speed, and $(G/\rho)^{1/2}$ is the rotational, or shear-wave, speed. Fluids have only one sound speed.
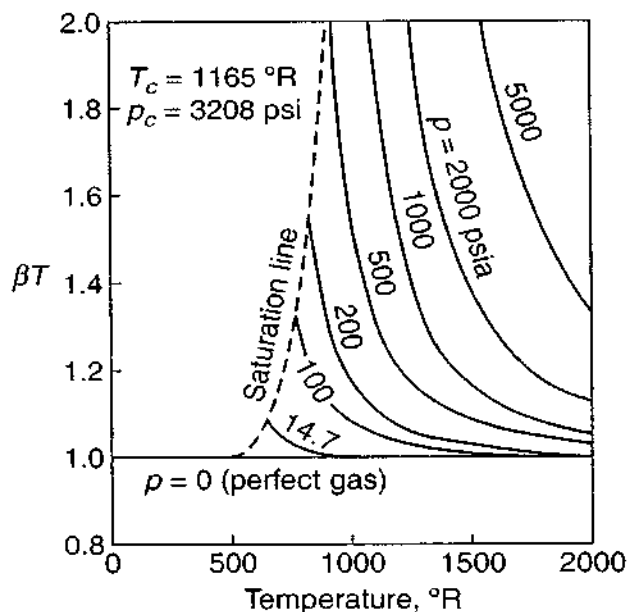
FIGURE 1-27

Thermal-expansion coefficient for steam.

The quantity β is also useful in estimating the dependence of enthalpy on pressure, from the thermodynamic relation

$$dh = c_p \, dT + (1 - \beta T)\frac{dp}{\rho} \tag{1-87}$$

where we remark that of course T must be absolute temperature. For the perfect gas, the second term vanishes, so that $h = h(T)$ only. Figure 1-27 shows that imperfect gases like steam also often fit this approximation $dh \approx c_p \, dT$.

Table 1-4 gives measured values of the bulk modulus K and the thermal-expansion coefficient β for water at saturation pressures.

TABLE 1-4

Bulk modulus K and expansion coefficient β for water at saturation conditions

T, K	p_{sat}, kPa	βT	K, MPa
273	0.61	−0.019	2,062
293	2.34	0.057	2,230
313	7.38	0.119	2,304
333	19.92	0.176	2,301
353	47.35	0.230	2,235
373	101.3	0.281	2,120
423	461	0.447	1,692
473	1,580	0.637	1,190
523	3,970	0.985	716
573	8,560	1.80	342
623	16,500	4.8	82
647[*]	22,090[*]	∞	0

[*]Critical point.

1-4 BOUNDARY CONDITIONS FOR VISCOUS-FLOW PROBLEMS

The equations of motion to be discussed in Chap. 2 will require mathematically tenable and physically realistic boundary conditions. It is of interest here to study the underlying physical mechanisms of the boundary approximations commonly used. For fluid flow, there are five types of boundaries considered:

1. A solid surface (which may be porous)
2. A free liquid surface
3. A liquid–vapor interface
4. A liquid–liquid interface
5. An inlet or exit section

Cases 2 and 3 are related in the sense that a free liquid surface is a special case of the liquid–vapor interface where the vapor causes a negligible interaction. Let us take up these cases in order.

1-4.1 Conditions at a Solid Surface: Microflow Slip in Liquids

Wall boundary conditions depend upon whether the fluid is a liquid or a gas. For *macroflows*, system dimensions are large compared to molecular spacing, so that both liquid and gas particles contacting the wall must essentially be in equilibrium with the solid. At a solid surface, the fluid will assume the velocity of the wall (the *no-slip* condition) and the temperature of the wall (the *no-temperature-jump* condition):

$$\mathbf{V}_{\text{fluid}} = \mathbf{V}_{\text{sol}}$$
$$T_{\text{fluid}} = T_{\text{sol}} \tag{1-88}$$

We shall use Eqs. (1-88) throughout this text for newtonian liquids. However, certain liquid/solid combinations are known to *slip* under small-scale *microflow* conditions. The subject is somewhat controversial and is reviewed in the monograph edited by Gad-el-Hak (2001). Some liquid microflows studies show slip and others do not.

One way to characterize slip in liquids is the *slip length* L_{slip} relating slip velocity to the local velocity gradient, a model first suggested by Navier himself:

$$u_{\text{wall}} = L_{\text{slip}} \left(\frac{\partial u}{\partial n} \right)_{\text{wall}} \tag{1-89}$$

The slip length depends upon the liquid, the geometry, and the shear rate. Tretheway and Meinhart (2002) test water flowing in a 30 μm width microchannel coated with hydrophobic octadecyltrichlorosilane (OTS). They measure $L_{\text{slip}} \approx 1$ μm and a wall-slip velocity equal to 10 percent of the centerline velocity. Choi et al. (2003), studying

hydrophilic and hydrophobic coated $1-2$ μm width microchannels, report $L_{slip} \approx 5-35$ nm, increasing with shear rate. Lin and Schowalter (1989) measure both slip and stick-slip behavior when high molecular weight polybutadienes flow through a capillary. Brutin and Tadrist (2003) report an unexpected wall friction increase when water flows through fused silica microtubes. They hypothesize a fluid ionic coupling with the silica surface. Denn (2001) reviews the extrusion of polymer melts and reports slip-flow conditions. A recent conference, CECAM (2004), is entirely devoted to experimental measurements of microfluidic interfaces.

To the writer's knowledge, there is no fundamental theory yet that can predict the slip of liquids flowing past solid walls. This is not the case for gases.

1-4.2 Kinetic Theory for Slip Velocity in Gases

If the fluid is a gas, Eqs. (1-88) will fail when the mean free path ℓ is comparable to the length-scale L of the flow. The ratio of these two lengths is called the Knudsen number, Kn:

$$Kn = \frac{\ell}{L} \tag{1-90}$$

Thus, if $Kn \ll 1$, there is negligible slip. If $Kn = \mathcal{O}(0.1)$, there is slip. If $Kn = \mathcal{O}(1)$ or greater, the flow is molecular and slip is an inadequate concept. There are two ways for the Knudsen number to dominate: (1) if ℓ is very large, that is, a very rarefied gas, Cercignani (2000); and (2) if L is very small, as occurs in micro- and nanoflows, Karniadakis and Bestok (2001).

Consider gas molecules as they strike and reflect from a solid wall, as in Fig. 1-28. If the wall is perfectly smooth, the molecules would impinge and reflect at the same angle θ, similar to light rays from a mirror. This is *specular reflection*, where molecules conserve their tangential momentum and exert no wall shear. In this case, there is perfect slip flow at the wall.

On a molecular scale, however, even the most highly polished wall appears rough. It is more likely that the impinging molecules view the wall as rough and reflect at random angles uncorrelated with their entry angle. This is termed *diffuse*
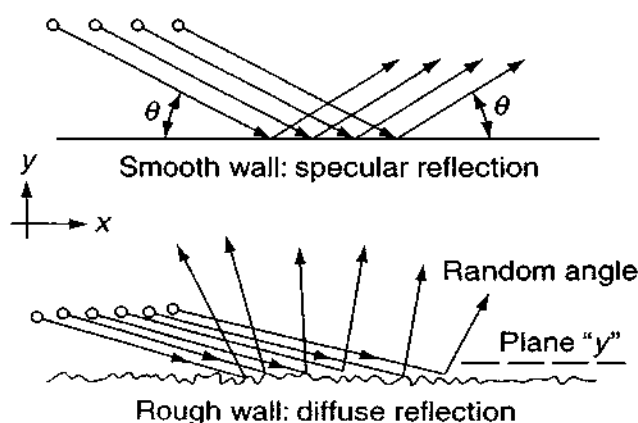
FIGURE 1-28
Specular and diffuse reflection of particles.

reflection and is shown in the lower half of Fig. 1-28. Equilibrium across a plane y near the wall requires that the loss of tangential momentum be balanced by a finite slip velocity u_w to transmit shear to the wall. As postulated by Navier in 1827, the slip velocity is proportional to the wall shear:

$$u_w \approx \alpha \tau_w$$

where α is a constant. Later, Maxwell in 1879 showed with kinetic theory that $\alpha \approx \ell/\mu$, or

$$u_w \approx \ell \left(\frac{\partial u}{\partial y}\right)_w \tag{1-91}$$

where ℓ is the mean free path of the gas. See, for example, Chap. 8 of the text by Kennard (1938). One can approximate the fluid away from the wall as a newtonian continuum. If we assume that a fraction f of the molecules is reflected diffusely, the slip velocity becomes

$$u_w \approx \left(\frac{2-f}{f}\right)\ell \left(\frac{\partial u}{\partial y}\right)_w \tag{1-92}$$

However, this correction seems superfluous, as a recent review by Sharipov and Seleznev (1998) indicates that the simpler Eq. (1-91) is quite accurate for single-component gases. Further, the recent theory of Sharipov and Kalempa (2003), based upon the Boltzmann equation, shows that Eq. (1-91) is only a few percent low for a wide variety of gas mixtures.

Is slip important in boundary-layer flows? When we substitute for ℓ from Eq. (1-32) and for $(\partial u/\partial y)$ from Eq. (1-91), viscosity cancels and the slip velocity becomes

$$u_w = \frac{3}{2}\frac{\tau_w}{\rho a} \tag{1-93}$$

We can then compare the slip velocity to freestream velocity U by dividing and rearranging:

$$\frac{u_w}{U} = \frac{3}{4}\frac{U}{a}\frac{2\tau_w}{\rho U^2} = 0.75\, Ma\, C_f \tag{1-94}$$

where $Ma = U/a$ is the Mach number of the freestream and C_f is called the *skin friction coefficient* of the flow. In turbulent flow, C_f is no larger than 0.005 and decreases with Mach number. In laminar flow, C_f increases as the Reynolds number decreases and can be quite large. Thus we conclude:

Boundary layers: Turbulent gas flow: no-slip

Laminar gas flow: possible slip at low $\qquad$ (1-95)
Re_L and high Ma

For further study of micro- and nanoflows and rarefied gases, see the monographs by Karniadakis and Bestok (2001) and Cercignani (2000). For most gas flow analyses in this text, we will use the standard no-slip condition, Eqs. (1-88).

For a new method of computer calculation of molecular flows, formulated by following and averaging thousands of individual particles, see the text by Bird (1994). This type of calculation is now called the direct simulation Monte Carlo method (DSMC).

1-4.3 Kinetic Theory for Wall-Temperature Jump

The temperature condition in Eq. (1-88) will also fail for a gas flow if the mean free path is large compared to flow dimensions. This effect is called *temperature jump* and is analogous to velocity slip. The kinetic-theory expression for the jump $T_{gas} - T_w$ in a gas flow was given by Smoluchowski (1898):

$$T_{gas} - T_w \approx \left(\frac{2}{\alpha} - 1\right)\frac{2\gamma}{\gamma + 1}\frac{\ell k}{\mu c_p}\left(\frac{dT}{dy}\right)_w \tag{1-96}$$

where α is the so-called thermal-accommodation coefficient, defined as the fraction of impinging molecules which becomes accommodated to the temperature of the wall. Clearly α is analogous to the diffuse-reflection coefficient f in Eq. (1-92). Experiments have shown that α is also fairly close to unity. With $\alpha = 1.0$, we can again substitute for ℓ from Eq. (1-32) and for dT/dy from Eq. (1-37) to obtain

$$T_{gas} - T_w \approx \frac{3\gamma}{\gamma + 1}\frac{\mu k}{\rho a \mu c_p}\frac{q_w}{k} \tag{1-97}$$

Eliminating μ and k, we divide by the temperature difference $T_r - T_w$ which controls the wall heat transfer (see Sec. 7-3) and rearrange:

$$\frac{T_{gas} - T_w}{T_r - T_w} \approx \frac{3\gamma}{\gamma + 1}\frac{U}{a}\frac{q_w}{\rho c_p U(T_r - T_w)} = \frac{3\gamma}{\gamma + 1}MaC_h \tag{1-98}$$

where C_h is the so-called Stanton number, or wall heat-transfer coefficient of the flow. It will be shown in Chap. 4 that in boundary-layer flows, the Stanton number is approximately one-half the friction coefficient, an effect which is called the *Reynolds analogy*:

$$C_h \approx \tfrac{1}{2}C_f \tag{1-99}$$

If finally we combine Eqs. (1-98) and (1-99) and take $\gamma = 1.4$ (air), we find that the temperature jump, expressed as a fraction of the driving temperature difference $T_r - T_w$, becomes

$$\frac{T_{gas} - T_w}{T_r - T_w} \approx 0.87 MaC_f \tag{1-100}$$

which is nearly identical to the slip relation, Eq. (1-94). Thus the same remarks as before apply here. Temperature jump in turbulent flow is entirely negligible, and the

jump in laminar flow is also extremely small except at low Reynolds number and high Mach number. It is customary, then, to adopt the no-slip and no-temperature-jump conditions in routine analysis of viscous gas-flow problems:

$$\mathbf{V}_{gas} \approx \mathbf{V}_w$$

$$T_{gas} \approx T_w \tag{1-101}$$

In many cases, of course, the coordinate system is such that the wall is stationary, so that the velocity condition is simply $\mathbf{V}_{fluid} = 0$.

1-4.4 Conditions at a Permeable Wall

In the event that the wall is porous and can permit fluid to pass through, the no-slip condition is relaxed on the velocity component normal to the wall. The proper conditions are complicated by the type of porosity of the wall, but, in general, we assume

$$V_{tangential} = 0 \quad \text{no slip}$$

$$V_{normal} \neq 0 \quad \text{flow through wall} \tag{1-102}$$

The temperature condition is also complicated by a porous wall. For wall *suction*, where the fluid leaves the main flow and passes into the wall, it is sufficiently accurate to assume

$$T_{fluid} = T_w \quad \text{suction} \tag{1-103}$$

For *injection* through a porous wall into the main stream (sometimes called *transpiration*), the injected fluid may be, say, a coolant at a temperature considerably different from the wall, and one needs to consider an energy balance at the wall. A good approximation for coolant injection is to use the boundary condition proposed by Roberts [in Truitt (1960, Chap. 11)]:

Injection: $$k \frac{dT}{dy}\bigg|_w \approx \rho_w V_n c_p (T_w - T_{coolant}) \tag{1-104}$$

where $\rho_w V_n$ is the mass flow of coolant per unit area through the wall. The actual numerical value of V_n depends largely upon the pressure drop across the porous wall. In general, although a few simple porous-wall solutions will be given in this text, the flow characteristics of porous media are a self-contained specialized subject of fluid mechanics. For more information, consult such texts on porous media as Bear (2000) or Crolet (2000).

1-4.5 Conditions at a Free Liquid Surface

There are many flow problems where the liquid fluid ends, not at a solid wall, but at an open or free surface exposed to an atmosphere of either gas or vapor. We distinguish between two cases: (1) the ideal or classic free surface that exerts only a known pressure on the liquid boundary and (2) a more complicated case where the atmosphere exerts not only pressure but also shear, heat flux, and mass flux at the
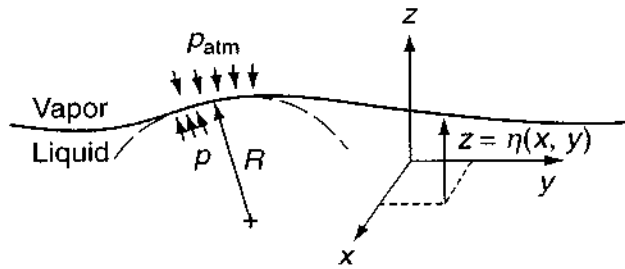
FIGURE 1-29
Conditions at an ideal free surface.

surface. This latter, more involved surface is more properly termed a liquid–vapor interface, the ocean surface being a splendid example.

The classic free surface is sketched in Fig. 1-29. Let us assume that the xy plane is more or less parallel to the free surface, so that the actual deflected shape of the surface can be denoted by $z = \eta(x, y)$.

The two required conditions for this surface are (1) the fluid particles at the surface must remain attached (kinematic condition) and (2) the liquid and the atmospheric pressure must balance except for surface-tension effects. The kinematic condition is specified mathematically by requiring the particle's upward velocity to equal the motion of the free surface:

$$w(x, y, \eta) = \frac{D\eta}{Dt} = \frac{\partial \eta}{\partial t} + u\frac{\partial \eta}{\partial x} + v\frac{\partial \eta}{\partial y} \tag{1-105}$$

The pressure equilibrium is expressed by

$$p(x, y, \eta) = p_a - \mathcal{T}\left(\frac{1}{R_x} + \frac{1}{R_y}\right) \tag{1-106}$$

where R_x and R_y are the radii of curvature of the surface and where $\mathcal{T}$ is the coefficient of surface tension of the interface. For a two-dimensional surface deflection $\eta = \eta(x)$ only, Eq. (1-106) becomes

$$p(x, \eta) = p_a - \frac{\mathcal{T}d^2\eta/dx^2}{[1 + (d\eta/dx)^2]^{3/2}} \tag{1-107}$$

We see from this relation that, when the interface smiles (concave upward, positive curvature), $p < p_a$, while a frowning interface (concave downward) results in $p > p_a$. Equations (1-105) and (1-106) are complex non-linear conditions, but they can be evaluated by numerical computer modeling.

In the range 0 to 100°C, a clean air–water interface has a nearly linear variation of surface tension with temperature:

$$\mathcal{T}\left(\frac{N}{m}\right) \approx 0.076 - 0.00017T \,(°C) \tag{1-108}$$

with accuracy of ±1 percent. Measured values of air–water surface tension are given in Table 1-5 for temperatures up to the critical point. These are ideal data for a very clean interface. Under field conditions, $\mathcal{T}$ can vary greatly due to the presence of surface contaminants or slicks.

TABLE 1-5
Surface-tension coefficient for an
air–water interface

T, °C	$\mathcal{T}$, N/m	T, °C	$\mathcal{T}$, N/m
0	0.0757	200	0.0377
20	0.0727	220	0.0331
40	0.0696	240	0.0284
60	0.0662	260	0.0237
80	0.0627	280	0.0190
100	0.0589	300	0.0144
120	0.0550	320	0.0099
140	0.0509	340	0.0056
160	0.0466	360	0.0019
180	0.0422	374*	0.0*

*Critical point.

In large-scale problems, such as open-channel or river flow, the free surface deforms only slightly and surface-tension effects are negligible. Equations (1-105) and (1-106) then simplify to

$$w \approx \frac{\partial \eta}{\partial t} \qquad p \approx p_a \tag{1-109}$$

These are obviously very attractive linearized conditions.

Note: The present discussion concerns the deformation of an interface by *uniform* surface tension. If the surface tension varies along the interface, due, for example, to a temperature gradient, a flow called *Marangoni convection* will be induced from the hot surface toward the cold surface. This condition is beyond the scope of the present text. For an example of Marangoni flow analysis, see the paper by Sasmal and Hochstein (1994) or the reviews by Ostrach (1982) and Davis (1987).

1-4.6 Conditions at a Liquid–Vapor or Liquid–Liquid Interface

The term *free surface* means that the gas lying over the liquid has no effect except to impose pressure on the interface. Heat transfer and shear effects are negligible. In a true liquid–vapor or liquid–liquid interface, the upper fluid is strongly coupled and exerts kinematic, stress, and energy constraints on the lower fluid. The motions of the two fluids are solved simultaneously and must match in certain ways at the interface.

Since an interface has vanishing mass, it cannot store momentum or thermal energy. Therefore the total velocity, shear stress, and temperature must be continuous across the interface. If "1" and "2" denote the upper and lower fluid, respectively, then, at a true fluid–fluid interface,

$$\mathbf{V}_1 = \mathbf{V}_2 \qquad \tau_1 = \tau_2 \qquad T_1 = T_2 \tag{1-110}$$

The normal velocities match, $V_{n1} = V_{n2}$, and each can, if desired, be expressed in terms of the interface motion $\eta(x, y, t)$ as in Eq. (1-105). The tangential velocities also match, $V_{t1} = V_{t2}$, which is the equivalent of the no-slip condition, Eq. (1-101). The pressures satisfy Eq. (1-106) with $p_2 = p$ and $p_1 = p_a$ and do not match unless surface tension or interface curvature is negligible.

Although velocities and temperatures are continuous across the interface, their slopes generally do not match because of differing transport coefficients, that is,

$$\tau_1 = \mu_1 \frac{\partial V_{t1}}{\partial n} = \tau_2 = \mu_2 \frac{\partial V_{t2}}{\partial n}$$

$$q_1 = -k_1 \frac{\partial T_1}{\partial n} = q_2 = -k_2 \frac{\partial T_2}{\partial n} \tag{1-111}$$

where n is the coordinate normal to the interface. The slopes are not equal if $\mu_1 \neq \mu_2$ or $k_1 \neq k_2$. This situation is illustrated in Fig. 1-30 and is typical of momentum and energy interactions between dissimilar fluids.

Since k and μ for a vapor are usually much smaller than for a liquid, we can often approximate liquid conditions at the interface as

$$\left. \frac{\partial V_t}{\partial n} \right|_{\text{liq}} \approx 0 \qquad \left. \frac{\partial T}{\partial n} \right|_{\text{liq}} \approx 0 \tag{1-112}$$

Finally, if there is evaporation, condensation, or diffusion at the interface, the mass flows must also balance, $\dot{m}_1 = \dot{m}_2$. For diffusion,

$$D_1 \frac{\partial C_1}{\partial n} = D_2 \frac{\partial C_2}{\partial n} \tag{1-113}$$

This condition is of course analogous to Eqs. (1-111).
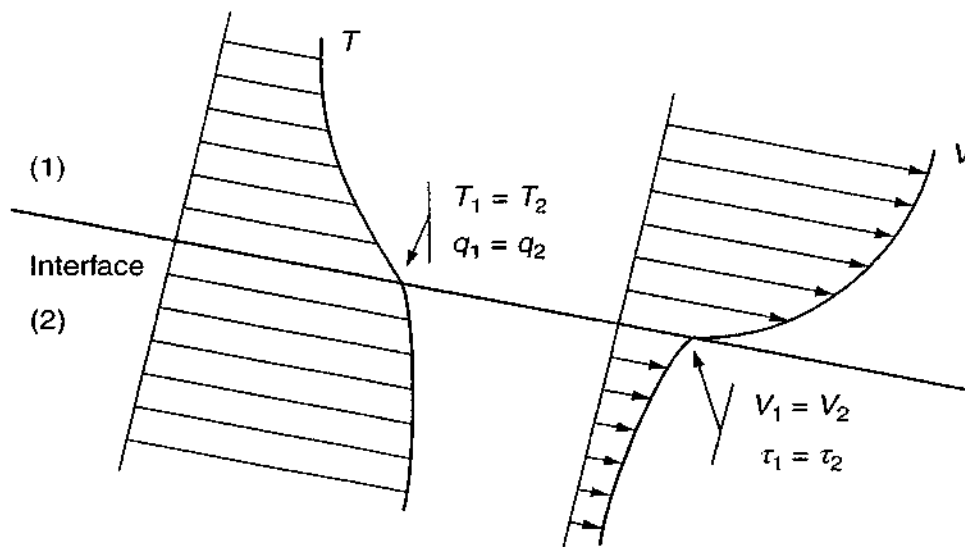
FIGURE 1-30

Conditions at an actual fluid interface. Velocities and temperatures match, but their slopes do not because of differing k and μ. Pressures also match except for the surface-tension effect of Eq. (1-106).

1-4.7 Conditions at a Deformable Fluid–Solid Interface

In most of the problems of this text, we shall take a solid boundary to be a rigid interface which merely imposes no-slip and no-temperature-jump conditions on the fluid. The dynamics and thermodynamics of the solid are neglected. However, there is a growing field of research in which the solid is coupled to the fluid through deformable and dynamic interactions. In this case, we must match the velocity, stress, temperature, and heat transfer across the interface, and the equations of motion of fluid and solid are to be solved simultaneously. Material-behavior relations analogous to Eqs. (1-111) must be used—perhaps the fluid is newtonian and the solid satisfies Hooke's law. For details, see the texts by Blevins (1977) or Au-Yang (2001).

1-4.8 Inlet and Exit Boundary Conditions

In many viscous-flow problems, it is convenient to limit the analysis to a finite region through which the flow passes. In the pipe-flow problem of Fig. 1-11, for example, we would like to limit our analysis to the short length of pipe shown.

Both finite and infinite regions require known property conditions at all boundaries. In pipe flow, Fig. 1-11, we specify no-slip and no-temperature-jump at the pipe walls. An alternate temperature condition would be known heat flux, $q_w = -k(\partial T/\partial n)_w$, which specifies the normal temperature gradient. In this latter case, the wall temperature would be found from the solution. At the pipe inlet, we would specify the distributions of V, T, and p. Often the inlet pressure is assumed uniform as a simplification. At the pipe exit, we specify V and T. No exit condition is required upon p, which is then found from the solution. As we shall see, pressure occurs only as first derivatives in the equations of motion (Chap. 2); thus only one pressure condition is needed. We can disregard temperature conditions if the flow is assumed isothermal.

For the infinite-region example of flow about a cylinder (Fig. 1-6), we specify no-slip and no-temperature-jump at the cylinder walls. At the "inlet," or approach flow, we would specify the distributions of V, T, and p. Far downstream, we specify V and T, which is very difficult, because the wake of the body will cause nonuniformity and possible unsteadiness in V and T. We would not know, in advance, the exact velocity and temperature far downstream, but there are several useful downstream approximations that lead to excellent CFD simulations of flow past immersed bodies. Pressure downstream will be calculated and need not be specified.

1-4.9 Résumé of Fluid-Flow Boundary Conditions

We have discussed the physical conditions which must hold at three different types of fluid-flow boundaries: (1) a fluid–solid interface, (2) a fluid–fluid interface, and (3) the inlet and exit of a flow. These various types of conditions are sketched in
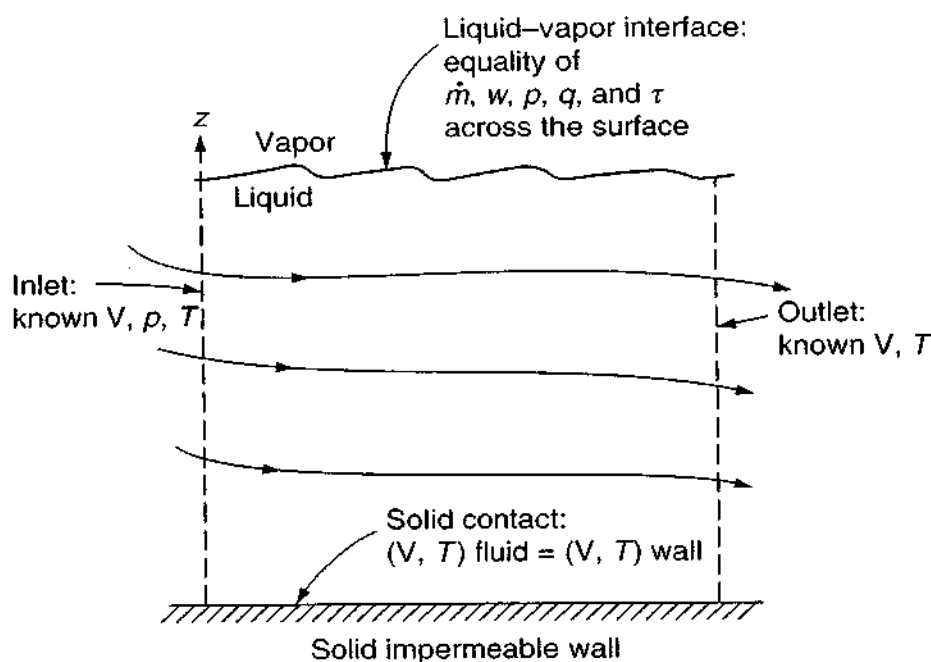
FIGURE 1-31
Various boundary conditions in fluid flow.

Fig. 1-31. The general results are that, for the majority of viscous-flow analyses, we must have the following information at the boundaries:

1. No slip or temperature jump at a fluid–solid interface:

$$\mathbf{V}_{\text{fluid}} = \mathbf{V}_{\text{sol}} \qquad T_{\text{fluid}} = T_{\text{sol}} \qquad (1\text{-}101a)$$

Note that there is no condition on p unless the wall is permeable.

2. Equality of velocity, momentum flux, heat flux, and mass flux at a liquid–fluid interface (neglecting surface tension):

$$(\mathbf{V}, p, \tau, q, \dot{m})_{\text{fluid above}} = (\mathbf{V}, p, \tau, q, \dot{m})_{\text{liq below}} \qquad (1\text{-}114)$$

If the fluid above is a gas with negligible interaction, the conditions on τ, q, and $\dot{m}$ may be ignored.

3. Known values of $\mathbf{V}$, p, and T at every point on an inlet section of the flow. Also, unless simplifying approximations are made, $\mathbf{V}$, and T must be known on any exit section.

SUMMARY

This chapter has reviewed the introductory concepts of fluid motion with which the reader should already be conversant. A brief history and some sample viscous-flow problems were outlined, followed by an extensive discussion of the different quantities which distinguish a fluid: (1) the kinematic properties, (2) the transport properties, and (3) the thermodynamic properties. The chapter closes with a detailed look at the various boundary conditions relevant to viscous-fluid flow.

PROBLEMS

1-1. A sphere 1.4 cm in diameter is placed in a freestream of 18 m/s at 20°C and 1 atm. Compute the diameter Reynolds number of the sphere if the fluid is (*a*) air, (*b*) water, (*c*) hydrogen.

1-2. A telephone wire 8 mm in diameter is subjected to a crossflow wind and begins to shed vortices. From Fig. 1-8, what wind velocity (in m/s) will cause the wire to "sing" at middle C (256 Hz)?

1-3. If the wire in Prob. 1-2 is subjected to a crossflow wind of 12 m/s, use Fig. 1-9 to estimate its drag force (in N/m).

1-4. For oil flow in a pipe far downstream of the entrance (Figs. 1-10 and 1-11), the axial velocity profile is a function of r only and is given by $u = (C/\mu)(R^2 - r^2)$, where C is a constant and R is the pipe radius. Suppose the pipe is 1 cm in diameter and $u_{max} = 30$ m/s. Compute the wall shear stress (in Pa) if $\mu = 0.3$ kg/(m·s).

1-5. A tornado may be simulated as a two-part circulating flow in cylindrical coordinates, with $v_r = v_z = 0$,

$$v_\theta = \omega r \quad \text{if } r \leq R \qquad \text{and} \qquad v_\theta = \omega R^2/r \quad \text{if } r \geq R$$

Determine (*a*) the vorticity and (*b*) the strain rates in each part of the flow.

1-6. A plane unsteady viscous flow is given in polar coordinates by

$$v_r = 0 \qquad v_\theta = \frac{C}{r}\left[1 - \exp\left(-\frac{r^2}{4\nu t}\right)\right]$$

where C is a constant and ν is the kinematic viscosity. Compute the vorticity $\omega_z(r, t)$ and sketch an array of representative velocity and vorticity profiles for various times.

1-7. A two-dimensional unsteady flow has the velocity components:

$$u = \frac{x}{1 + t} \qquad v = \frac{y}{1 + 2t}$$

Find the equation of the streamlines of this flow which pass through the point (x_0, y_0) at time $t = 0$.

1-8. Using Eq. (1-2) for inviscid flow past a cylinder, consider the flow along the streamline approaching the forward stagnation point $(r, \theta) = (R, \pi)$. Compute (*a*) the distribution of strain rates ϵ_{rr} and $\epsilon_{r\theta}$ along this streamline and (*b*) the time required for a particle to move from the point $(2R, \pi)$ to the stagnation point.

1-9. A commonly used equation of state for water is approximately independent of temperature:

$$\frac{p}{p_0} \approx (A + 1)\left(\frac{\rho}{\rho_0}\right)^n - A$$

where $A \approx 3000$, $n \approx 7$, $p_0 = 1$ atm, and $\rho_0 = 998$ kg/m³. From this formula, compute (*a*) the pressure (in atm) required to double the density of water, (*b*) the bulk modulus of water at 1 atm, and (*c*) the speed of sound in water at 1 atm.

1-10. As shown in Fig. P1-10, a 3 × 3-ft plate slides down a long 30° incline on which there is a film of oil 0.005 in. thick with viscosity $\mu = 0.0005$ slug/(ft·s). Assuming that

the plate does not deform the oil film, estimate (*a*) the terminal sliding velocity (in ft/s) and (*b*) the time required for the plate to accelerate from rest to 99 percent of the terminal velocity.
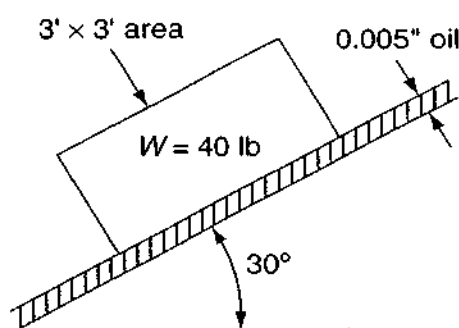
FIGURE P1-10

1-11. Estimate the viscosity of nitrogen at 86 MPa and 49°C and compare with the measured value of 45 μPa · s.

1-12. Estimate the thermal conductivity of helium at 420°C and 1 atm and compare with the measured value of 0.28 W/(m · K).

1-13. It is desired to form a gas mixture of 23% CO_2, 14% O_2, and 63% N_2 at 1 atm and 20°C. The constituent properties are as follows:

Constituent	Mole fraction	μ, Pa · s	k, W/(m · K)
CO_2	0.23	1.37E−5	0.0146
O_2	0.14	1.92E−5	0.0244
N_2	0.63	1.66E−5	0.0242

Estimate the viscosity and thermal conductivity of this mixture.

1-14. Some measured values for the viscosity of ammonia gas are as follows:

T, K	300	400	500	600	700	800
μ, Pa · s	1.03E−5	1.39E−5	1.76E−5	2.14E−5	2.51E−5	2.88E−5

Fit these data, in the least-square-error sense, to the power law, Eq. (1-35), and the Sutherland law, Eq. (1-36).

1-15. Analyze the flow between two plates of Fig. 1-15 by assuming the fluid is a de Waele power-law fluid as in Eq. (1-31*a*). Compute (*a*) the velocity profile $u(y)$ with the power n as a parameter and (*b*) the velocity at the midpoint $h/2$ for n = 0.5, 1.0, and 2.0.

Answer: (*b*) $u = V/2$ for all cases

1-16. Repeat the analysis of the velocity profile between two plates (Fig. 1-15) for a newtonian fluid but allow for a slip velocity $\delta u \approx \ell(du/dy)$ at both walls. Compute the shear stress at both walls. [$\tau_w = \mu V/(h + 2\ell)$ at both walls.]

1-17. By considering the equilibrium of forces on the element shown in Fig. P1-17, derive Eq. (1-106), which expresses the pressure jump across a curved surface due to surface tension.
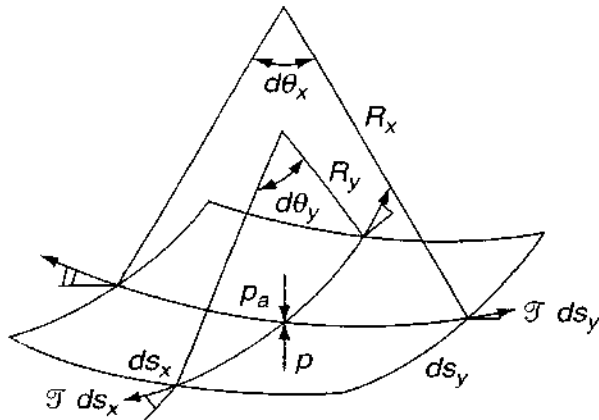
FIGURE P1-17

1-18. Two spherical bubbles of radii R_1 and R_2, respectively, containing air, coalesce into a single bubble of radius R_3. If the ambient air pressure is p_0 and the merging process is isothermal, derive a formula for relating R_3 to $(p_0, R_1, R_2, \mathcal{T})$.

1-19. In Prob. 1-1, if the temperature, sphere size, and velocity remain the same for airflow, at what air pressure will the Reynolds number Re_D be equal to 10,000?

1-20. A solid cylinder of mass m, radius R, and length L falls concentrically through a vertical tube of radius $R + \Delta R$, where $\Delta R \ll R$. The tube is filled with gas of viscosity μ and mean free path ℓ. Neglect fluid forces on the front and back faces of the cylinder and consider only shear stress in the annular region, assuming a linear velocity profile. Find an analytic expression for the terminal velocity of fall, V, of the cylinder (a) for no slip; (b) with slip, Eq. (1-91).

1-21. Oxygen at 20°C and approximately 1200 Pa absolute flows through a 35 μm diameter smooth capillary tube at an average velocity of 10 cm/s. Estimate the Knudsen number of the flow and whether slip flow will be important.

1-22. In Fig. P1-22 a disk rotates steadily inside a disk-shaped container filled with oil of viscosity μ. Assume linear velocity profiles with no slip and neglect stress on the outer edges of the disk. Find a formula for the torque M required to drive the disk.
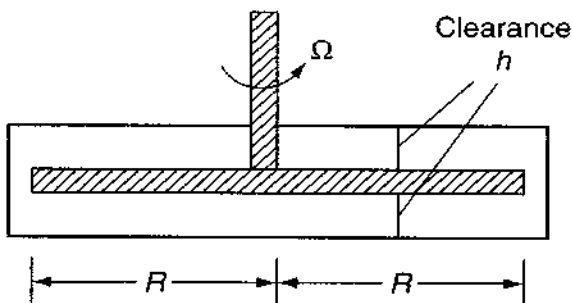
FIGURE P1-22

1-23. Show, from Eq. (1-86), that the coefficient of thermal expansion of a perfect gas is given by $\beta = 1/T$. Use this approximation to estimate β of ammonia gas (NH_3) at 20°C and 1 atm and compare with the accepted value from a data reference.

1-24. The *rotating-cylinder viscometer* in Fig. P1-24 shears the fluid in a narrow clearance Δr, as shown. Assuming a linear velocity distribution in the gaps, if the driving torque M is measured, find an expression for μ by (a) neglecting, and (b) including the bottom friction.
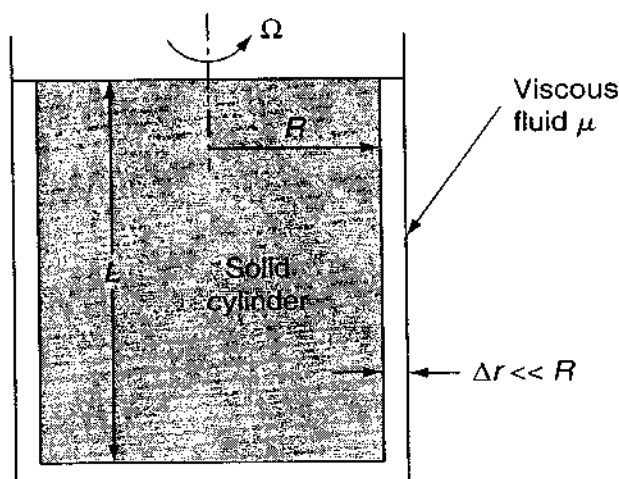
FIGURE P1-24

1-25. Consider 1 m^3 of a fluid at 20°C and 1 atm. For an isothermal process, calculate the final density and the energy, in joules, required to compress the fluid until the pressure is 10 atm, for (a) air and (b) water. Discuss the difference in results.

1-26. Equal layers of two immiscible fluids are being sheared between a moving and a fixed plate, as in Fig. P1-26. Assuming linear velocity profiles, find an expression for the interface velocity U as a function of V, μ_1, and μ_2.
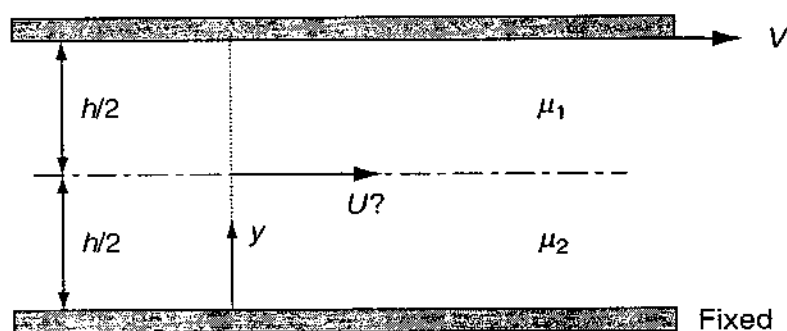
FIGURE P1-26

1-27. Use the inviscid-flow solution of flow past a cylinder, Eqs. (1-3), to (a) find the location and value of the maximum fluid acceleration along the cylinder surface. Is your result valid for gases and liquids? (b) Apply your formula for a_{max} to airflow at 10 m/s past a cylinder of diameter 1 cm and express your result as a ratio compared to the acceleration of gravity. Discuss what your result implies about the ability of fluids to withstand acceleration.

CHAPTER
2

FUNDAMENTAL EQUATIONS OF COMPRESSIBLE VISCOUS FLOW

2-1 INTRODUCTION

The equations of viscous flow have been known for more than 100 years. In their complete form, these equations are very difficult to solve, even on modern digital computers. In fact, at high Reynolds numbers (turbulent flow), the equations are, in effect, *impossible* to solve with present mathematical techniques because the boundary conditions become randomly time-dependent. Nevertheless, it is very instructive to derive and discuss these fundamental equations because they give many insights, yield several particular solutions, and can be examined for modeling laws. Also, these exact equations can then be simplified, using Prandtl's boundary-layer approximations. The resulting simpler system is very practical and yields many fruitful engineering solutions.

2-2 CLASSIFICATION OF THE FUNDAMENTAL EQUATIONS

The basic equations considered here are the three laws of conservation for physical systems:

1. Conservation of mass (continuity)
2. Conservation of momentum (Newton's second law)
3. Conservation of energy (first law of thermodynamics)

The three unknowns that must be obtained simultaneously from these three basic equations are the velocity V, the thermodynamic pressure p, and the absolute temperature T. We consider p and T to be the two required independent thermodynamic variables. However, the final forms of the conservation equations also contain four other thermodynamic variables: the density ρ, the enthalpy h (or the internal energy e), and the two transport properties μ and k. Using our tacit assumption of local thermodynamic equilibrium, the latter four properties are uniquely determined by the values of p and T. Thus the system is completed by assuming knowledge of four state relations

$$\rho = \rho(p, T) \qquad h = h(p, T)$$
$$\mu = \mu(p, T) \qquad k = k(p, T)$$

(2-1)

which can be in the form of tables or charts or semitheoretical formulas from kinetic theory. Many useful analyses simply assume that ρ, μ, and k are constant and that h is proportional to T ($h = c_p T$).

Finally, to specify a particular problem completely, we must have known conditions (of various types) for V, p, and T at *every* point of the boundary of the flow regime.

The preceding considerations apply to a fluid of assumed uniform, homogeneous composition, i.e., diffusion and chemical reactions are not considered. Multicomponent reacting fluids must consider at least two extra basic relations:

4. Conservation of species

5. Laws of chemical reaction

plus additional auxiliary relations such as knowledge of the diffusion coefficient $D = D(p, T)$, chemical-equilibrium constants, reaction rates, and heats of formation. This text does not consider reacting boundary-layer flows [see Kee et al. (2003)].

Finally, even more relations are necessary if one considers the flow to be influenced by electromagnetic effects. This is the subject of the field of *magnetohydrodynamics*. Such effects are not considered in the present text.

Let us now derive the three basic equations of a single-component fluid, bearing in mind that the results will also apply to uniform nonreacting mixtures, such as air or liquid solutions.*

2-3 CONSERVATION OF MASS: THE EQUATION OF CONTINUITY

As mentioned in the discussion of Eq. (1-5), all three of the conservation laws are Lagrangian in nature, i.e., they apply to fixed systems (particles). Thus, in the

---

*Note, however, that air flowing at very high temperatures will undergo spontaneous diffusion and chemical reactions, as will many other mixtures. Even single-component fluids, such as oxygen, will dissociate into atomic oxygen at high temperatures.

Eulerian system appropriate to fluid flow, our three laws must utilize the particle derivative

$$\frac{D}{Dt} = \frac{\partial}{\partial t} + (\mathbf{V} \cdot \nabla) \tag{1-8}$$

which is a formidable expression. In Lagrangian terms, the law of conservation of mass is surpassingly simple:

$$m = \rho \mathcal{V} = \text{const} \tag{2-2}$$

where $\mathcal{V}$ is the volume of a particle. In Eulerian terms, this is equivalent to

$$\frac{Dm}{Dt} = \frac{D}{Dt}(\rho \mathcal{V}) = 0 = \rho \frac{D\mathcal{V}}{Dt} + \mathcal{V}\frac{D\rho}{Dt} \tag{2-3}$$

We can relate $D\mathcal{V}/Dt$ to the fluid velocity by noticing that the total dilatation or normal-strain rate is equal to the rate of volume increase of a particle per unit volume:

$$\epsilon_{xx} + \epsilon_{yy} + \epsilon_{zz} = \frac{1}{\mathcal{V}}\frac{D\mathcal{V}}{Dt} \tag{2-4}$$

Further, we can substitute for the strain rates from our kinematic relations, Eqs. (1-21):

$$\begin{aligned}
\epsilon_{xx} + \epsilon_{yy} + \epsilon_{zz} &= \frac{\partial u}{\partial x} + \frac{\partial v}{\partial y} + \frac{\partial w}{\partial z} \\
&= \text{div } \mathbf{V} = \nabla \cdot \mathbf{V}
\end{aligned} \tag{2-5}$$

Combining Eqs. (2-3) to (2-5) to eliminate $\mathcal{V}$, we obtain the equation of continuity for fluids in its most common general form:

$$\frac{D\rho}{Dt} + \rho \text{ div } \mathbf{V} = 0 \qquad \text{or} \qquad \frac{\partial \rho}{\partial t} + \text{div } \rho \mathbf{V} = 0 \tag{2-6}$$

If the density is constant (incompressible flow), Eq. (2-6) reduces to the simpler condition of velocity solenoidality:

$$\text{div } \mathbf{V} = 0 \tag{2-7}$$

which is equivalent to requiring particles of constant volume.[†]

2-3.1   A Useful Strategy: The Stream Function

If the continuity Eq. (2-6) reduces to only two nonzero terms, it can be satisfied identically, and therefore replaced, by the so-called *stream function* ψ. The idea dates back to the French mathematician J. L. Lagrange in 1755. The Cartesian

---

[†] But not necessarily constant *shape*, i.e., the element may undergo normal strains of opposite sign plus shear strains of any sign.

incompressible-flow stream function is treated in detail in Sec. 2-11. Here we illustrate with two-dimensional steady compressible flow in the xy plane, for which the continuity equation reduces to

$$\frac{\partial}{\partial x}(\rho u) + \frac{\partial}{\partial y}(\rho v) = 0 \qquad (2\text{-}8)$$

If we now define the stream function ψ such that

$$\rho u = \frac{\partial \psi}{\partial y} \qquad \text{and} \qquad \rho v = -\frac{\partial \psi}{\partial x} \qquad (2\text{-}9)$$

we see by direct substitution that Eq. (2-8) is satisfied identically, assuming of course that ψ is continuous to second-order derivatives. Thus the continuity equation can be discarded and the number of dependent variables reduced by one, the penalty being that the remaining velocity derivatives are increased by one order.

The stream function is not only useful but has physical significance:

$$d\psi = \frac{\partial \psi}{\partial x}\,dx + \frac{\partial \psi}{\partial y}\,dy = -\rho v\,dx + \rho u\,dy$$
$$= \rho \mathbf{V}\cdot d\mathbf{A} = d\dot{m} \qquad (2\text{-}10)$$

which means that lines of constant ψ ($d\psi = 0$) are lines across which there is no mass flow ($d\dot{m} = 0$), that is, they are streamlines of the flow. Also, the difference between the values of ψ of any two streamlines is numerically equal to the mass flow between those streamlines.

2-4   CONSERVATION OF MOMENTUM: THE NAVIER–STOKES EQUATIONS

This relation, commonly known as Newton's second law, expresses a proportionality between applied force and the resulting acceleration of a particle of mass m:

$$\mathbf{F} = m\mathbf{a} \qquad (2\text{-}11)$$

If the system is a fluid particle, it is convenient to divide Eq. (2-11) by the volume of the particle, so that we work with density instead of mass. It is also traditional to reverse the terms and place the acceleration on the left-hand side. Hence we write

$$\rho \frac{D\mathbf{V}}{Dt} = \mathbf{f} = \mathbf{f}_{\text{body}} + \mathbf{f}_{\text{surface}} \qquad (2\text{-}12)$$

where $\mathbf{f}$ is the applied force per unit volume on the fluid particle. Note that in our chosen Eulerian system, the acceleration is the rather complicated particle derivative from Eq. (1-9). We have divided $\mathbf{f}$ into two types: surface forces and body forces.

The so-called body forces are those that apply to the entire mass of the fluid element. Such forces are usually due to external fields such as gravity or an applied

τ_{ij} = stress in the j direction on a face normal to the i axis
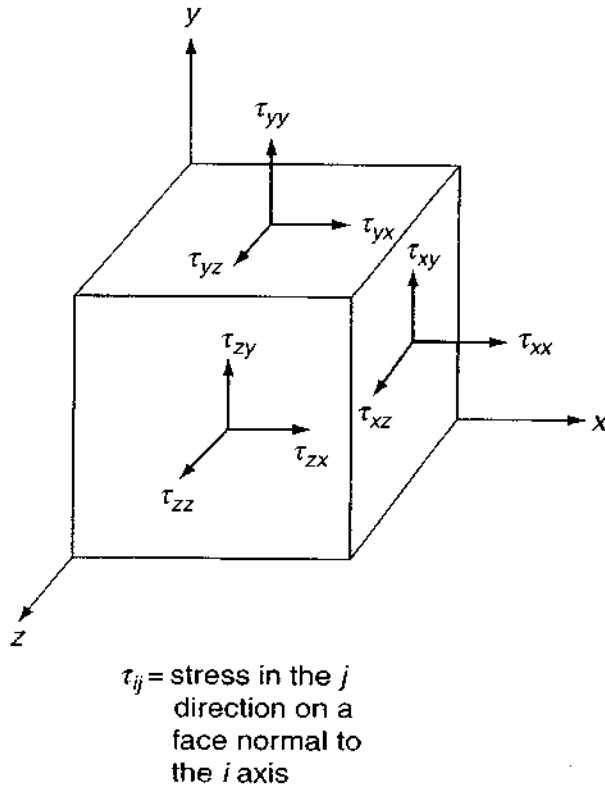
FIGURE 2-1
Notation for stresses.

electromagnetic potential. We ignore magnetohydrodynamic effects here and consider only the gravitational body force, which on our unit volume basis is

$$\mathbf{f}_{body} = \rho \mathbf{g} \tag{2-13}$$

where $\mathbf{g}$ is the vector acceleration of gravity.

The surface forces are those applied by external stresses on the sides of the element. The quantity stress τ_{ij} is a tensor, just as the strain rate ϵ_{ij} was in Sec. 1-3. The sign convention for stress components on a Cartesian element is shown in Fig. 2-1, where all stresses are positive. The stress tensor can be written as

$$\tau_{ij} = \begin{pmatrix} \tau_{xx} & \tau_{xy} & \tau_{xz} \\ \tau_{yx} & \tau_{yy} & \tau_{yz} \\ \tau_{zx} & \tau_{zy} & \tau_{zz} \end{pmatrix} \tag{2-14}$$

by analogy with ϵ_{ij} in Eq. (1-22). Like strain rate, τ_{ij} forms a symmetric tensor; that is, $\tau_{ij} = \tau_{ji}$. This symmetry is required to satisfy equilibrium of moments about the three axes of the element.[*]

The positions of the τ's in the array of Eq. (2-14) are not arbitrary; the rows correspond to applied force in each coordinate direction. Considering the

---

[*]Here we assume the absence of concentrated couple stresses.

front faces of the element in Fig. 2-1, the total force in each direction due to stress is

$$dF_x = \tau_{xx}\, dy\, dz + \tau_{yx}\, dx\, dz + \tau_{zx}\, dx\, dy$$

$$dF_y = \tau_{xy}\, dy\, dz + \tau_{yy}\, dx\, dz + \tau_{zy}\, dx\, dy \qquad (2\text{-}15)$$

$$dF_z = \tau_{xz}\, dy\, dz + \tau_{yz}\, dx\, dz + \tau_{zz}\, dx\, dy$$

preserving the positions in the array. For an element in equilibrium, these forces would be balanced by equal and opposite forces on the back faces of the element. If the element is accelerating, however, the front- and back-face stresses will be different by differential amounts. For example,

$$\tau_{xx,\,\text{front}} = \tau_{xx,\,\text{back}} + \frac{\partial \tau_{xx}}{\partial x}\, dx \qquad (2\text{-}16)$$

Hence the *net* force on the element in the x direction, for example, will be due to three derivative terms:

$$dF_{x,\,\text{net}} = \left(\frac{\partial \tau_{xx}}{\partial x}\, dx\right) dy\, dz + \left(\frac{\partial \tau_{yx}}{\partial y}\, dy\right) dx\, dz + \left(\frac{\partial \tau_{zx}}{\partial z}\, dz\right) dx\, dy$$

or, on a unit volume basis, dividing by $dx\, dy\, dz$, since $\tau_{ij} = \tau_{ji}$,

$$f_x = \frac{\partial \tau_{xx}}{\partial x} + \frac{\partial \tau_{xy}}{\partial y} + \frac{\partial \tau_{xz}}{\partial z} \qquad (2\text{-}17)$$

which we note is equivalent to taking the divergence of the vector $(\tau_{xx}, \tau_{xy}, \tau_{xz})$, the upper row of the stress tensor. Similarly, f_y and f_z are the divergences of the second and third row of τ_{ij}. Thus the total vector surface force is

$$\mathbf{f}_{\text{sur}} = \nabla \cdot \tau_{ij} = \frac{\partial \tau_{ij}}{\partial x_j} \qquad (2\text{-}18)$$

where the divergence of τ_{ij} is to be interpreted in the tensor sense, so that the result is a vector.

Newton's law, Eq. (2-12), now becomes

$$\rho \frac{D\mathbf{V}}{Dt} = \rho \mathbf{g} + \nabla \cdot \tau_{ij} \qquad (2\text{-}19)$$

and it remains only to express τ_{ij} in terms of the velocity $\mathbf{V}$. This is done by relating τ_{ij} to ϵ_{ij} through the assumption of some viscous deformation-rate law, e.g., the newtonian fluid.

2-4.1 The Fluid at Rest: Hydrostatics

From the definition of a fluid, Sec. 1-3, viscous stresses vanish if the fluid is at rest. The velocity and shear stresses are zero, and the normal stresses become equal to

the hydrostatic pressure. Equation (2-19) reduces to the hydrostatic equation if $V = 0$:

$$\tau_{xx} = \tau_{yy} = \tau_{zz} = -p$$

$$\tau_{ij} = 0 \quad \text{for } i \neq j \tag{2-20}$$

$$\nabla p = \rho \mathbf{g}$$

If we take the z coordinate as *up* and assume ρ and g are constant, the pressure varies linearly with z, $\delta p = -\rho g \, \delta z$. Pressure increases downward, proportional to the specific weight of the fluid. Recall that *hydrostatics* is treated extensively in undergraduate texts, e.g., White (2003). We must ensure here that our dynamic momentum equation reduces to Eq. (2-20) when $V = 0$.

2-4.2   Deformation Law for a Newtonian Fluid

By analogy with Hookean elasticity, the simplest assumption for the variation of viscous stress with strain rate is a linear law. These considerations were first made by Stokes (1845), and, as far as we know, the resulting deformation law is satisfied by all gases and most common fluids. Stokes' three postulates are

1. The fluid is continuous, and its stress tensor τ_{ij} is at most a linear function of the strain rates ϵ_{ij}.
2. The fluid is isotropic, i.e., its properties are independent of direction, and therefore the deformation law is independent of the coordinate axes in which it is expressed.
3. When the strain rates are zero, the deformation law must reduce to the hydrostatic pressure condition, $\tau_{ij} = -p\delta_{ij}$, where δ_{ij} is the Kronecker delta function ($\delta_{ij} = 1$ if $i = j$ and $\delta_{ij} = 0$ if $i \neq j$).

Note that the isotropic condition 2 requires that the principal stress axes be identical with the principal strain-rate axes. This makes the principal axes a convenient place to begin the deformation-law derivation. Let x_1, y_1, and z_1 be the principal axes, where the shear stresses and shear strain rates vanish [see Eq. (1-24)]. With these axes, the deformation law could involve at most three linear coefficients, C_1, C_2, C_3. For example,

$$\tau_{11} = -p + C_1\epsilon_{11} + C_2\epsilon_{22} + C_3\epsilon_{33} \tag{2-21}$$

The term $-p$ is added to satisfy the hydrostatic condition (condition 3 above). But the isotropic condition 2 requires that the crossflow effect of ϵ_{22} and ϵ_{33} be identical, i.e., that $C_2 = C_3$. Therefore, there are really only *two* independent linear coefficients in an anisotropic newtonian fluid. We can rewrite Eq. (2-21) in the simpler form

$$\tau_{11} = -p + K\epsilon_{11} + C_2(\epsilon_{11} + \epsilon_{22} + \epsilon_{33}) \tag{2-22}$$

where $K = C_1 - C_2$, for convenience. Note also that $\epsilon_{11} + \epsilon_{22} + \epsilon_{33}$ equals div V from Eq. (2-5).

Now let us transform Eq. (2-22) to some arbitrary axes x, y, z, where shear stresses are *not* zero, and thereby find an expression for the general deformation law. With respect to the principal axes x_1, y_1, z_1, let the x axis have direction cosines l_1, m_1, n_1, let the y axis have l_2, m_2, n_2, and let the z axis have l_3, m_3, n_3. Remember also that, for example, $l_1^2 + m_1^2 + n_1^2 = 1.0$ for any set of direction cosines. Then the transformation rule between a normal stress or strain rate in the new system and the principal stresses or strain rates is given by, for example,

$$\tau_{xx} = \tau_{11}l_1^2 + \tau_{22}m_1^2 + \tau_{33}n_1^2$$
$$\epsilon_{xx} = \epsilon_{11}l_1^2 + \epsilon_{22}m_1^2 + \epsilon_{33}n_1^2$$

$$(2\text{-}23)$$

Similarly, the shear stresses (strain rates) are related to the principal stresses (strain rates) by the following transformation law:

$$\tau_{xy} = \tau_{11}l_1l_2 + \tau_{22}m_1m_2 + \tau_{33}n_1n_2$$
$$\epsilon_{xy} = \epsilon_{11}l_1l_2 + \epsilon_{22}m_1m_2 + \epsilon_{33}n_1n_2$$

$$(2\text{-}24)$$

We can now eliminate τ_{11}, ϵ_{11}, τ_{22}, etc., from Eq. (2-23) by using the principal-axis deformation law, Eq. (2-22), and the fact that $l^2 + m^2 + n^2 = 1.0$. The result is

$$\tau_{xx} = -p + K\epsilon_{xx} + C_2 \operatorname{div} \mathbf{V} \qquad (2\text{-}25)$$

with exactly similar expressions for τ_{yy} and τ_{zz}. Similarly, we can eliminate τ_{11}, ϵ_{11}, etc., from Eqs. (2-24) to give

$$\tau_{xy} = K\epsilon_{xy} \qquad (2\text{-}26)$$

and exactly analogous expressions for τ_{xz} and τ_{yz}. Note that the direction cosines have all politely vanished. Equations (2-25) and (2-26) are, in effect, the desired general deformation law. By comparing Eq. (2-26) and Eq. (1-30) for shear flow between parallel plates, we see that the linear coefficient K is equal to twice the ordinary coefficient of viscosity, $K = 2\mu$. The coefficient C_2 is new and independent of μ and may be called the *second coefficient of viscosity*. In linear elasticity, C_2 is called Lamé's constant and is given the symbol λ, which we adopt here also. Since λ is associated *only* with volume expansion, it is customary to call it the *coefficient of bulk viscosity* λ.

Equations (2-25) and (2-26) can be combined, using the initial notation, and rewritten into a single general deformation law for a newtonian (linear) viscous fluid:

$$\tau_{ij} = -p\delta_{ij} + \mu\left(\frac{\partial u_i}{\partial x_j} + \frac{\partial u_j}{\partial x_i}\right) + \delta_{ij}\lambda \operatorname{div} \mathbf{V} \qquad (2\text{-}27)$$

where we have written ϵ_{ij} in terms of the velocity gradients from Eq. (1-26). As mentioned, this deformation law was first given by Stokes (1845). In deriving it, we have assumed knowledge of the geometric rules for coordinate transformation of stresses and strain rates. The interested reader may wish to obtain further details from textbooks on continuum mechanics, e.g., Lai et al. (1995), Malvern (1997), or Talpaert (2003).

2-4.3   Thermodynamic Pressure versus Mechanical Pressure

Stokes (1845) pointed out an interesting consequence of Eq. (2-27). By analogy with the strain relation [Eqs. (1-25)], the sum of the three normal stresses $\tau_{xx} + \tau_{yy} + \tau_{zz}$ is a tensor invariant. Define the *mechanical pressure* $\bar{p}$ as the negative one-third of this sum, i.e., the average compression stress on the element. Then, by summing Eq. (2-27), we obtain

$$\bar{p} = -\tfrac{1}{3}(\tau_{xx} + \tau_{yy} + \tau_{zz}) = p - \left(\lambda + \tfrac{2}{3}\mu\right) \operatorname{div} \mathbf{V} \qquad (2\text{-}28)$$

Thus the mean pressure in a deforming viscous fluid is *not* equal to the thermodynamic property called pressure. This distinction is rarely important, since div $\mathbf{V}$ is usually very small in typical flow problems, but the exact meaning of Eq. (2-28) has been a controversial subject for more than a century. Stokes himself simply resolved the issue by an assumption:

Stokes' hypothesis (1845): $\qquad \lambda + \tfrac{2}{3}\mu = 0$

This simply assumes away the problem; it is essentially what we do in this book. However, the available experimental evidence from the measurement of sound-wave attenuation, as reviewed by Karim and Rosenhead (1952), indicates that λ for most liquids is actually positive, rather than $-2\mu/3$, and often is much larger than μ. The experiments themselves are a matter of some controversy [Truesdell (1954)].

A second type of assumption will also make $\bar{p}$ equal to p:

Incompressible flow: $\qquad \operatorname{div} \mathbf{V} = 0$

Again this merely assumes away the problem. The bulk viscosity cannot affect a truly incompressible fluid, but in fact it *does* affect certain phenomena occurring in *nearly* incompressible fluids, e.g., sound absorption in liquids. Meanwhile, if div $\mathbf{V} \neq 0$, that is, compressible flow, we may still be able to avoid the problem if viscous normal stresses are negligible. This is the case in *boundary-layer flows* of compressible fluids, for which only the *first* coefficient of viscosity μ is important. However, the normal shock wave is a case where the coefficient λ cannot be neglected. The second case (only two cases are known to this author) is the previously mentioned problem of sound-wave absorption and attenuation.

It appears, then, that the second viscosity coefficient is still a controversial quantity. In fact, λ may not even be a thermodynamic property, since it is apparently frequency-dependent. Fortunately, the disputed term, λ div $\mathbf{V}$, is almost always so very small that it is entirely proper simply to ignore the effect of λ altogether. An interesting discussion of second viscosity is in Landau and Lifshitz (1959, Sec. 78). For further reading, see Panton (1996).

2-4.4   The Navier–Stokes Equations

The desired momentum equation for a general linear (newtonian) viscous fluid is now obtained by substituting the stress relations, Eq. (2-27), into Newton's law

[Eq. (2-19)]. The result is the famous equation of motion which bears the names of Navier (1823) and Stokes (1845). In scalar form, we obtain

$$\rho \frac{Du}{Dt} = \rho g_x - \frac{\partial p}{\partial x} + \frac{\partial}{\partial x}\left(2\mu \frac{\partial u}{\partial x} + \lambda \operatorname{div} \mathbf{V}\right) + \frac{\partial}{\partial y}\left[\mu\left(\frac{\partial u}{\partial y} + \frac{\partial v}{\partial x}\right)\right]$$
$$+ \frac{\partial}{\partial z}\left[\mu\left(\frac{\partial w}{\partial x} + \frac{\partial u}{\partial z}\right)\right]$$

$$\rho \frac{Dv}{Dt} = \rho g_y - \frac{\partial p}{\partial y} + \frac{\partial}{\partial x}\left[\mu\left(\frac{\partial v}{\partial x} + \frac{\partial u}{\partial y}\right)\right] + \frac{\partial}{\partial y}\left(2\mu \frac{\partial v}{\partial y} + \lambda \operatorname{div} \mathbf{V}\right)$$
$$+ \frac{\partial}{\partial z}\left[\mu\left(\frac{\partial v}{\partial z} + \frac{\partial w}{\partial y}\right)\right] \qquad (2\text{-}29a)$$

$$\rho \frac{Dw}{Dt} = \rho g_z - \frac{\partial p}{\partial z} + \frac{\partial}{\partial x}\left[\mu\left(\frac{\partial w}{\partial x} + \frac{\partial u}{\partial z}\right)\right] + \frac{\partial}{\partial y}\left[\mu\left(\frac{\partial v}{\partial z} + \frac{\partial w}{\partial y}\right)\right]$$
$$+ \frac{\partial}{\partial z}\left(2\mu \frac{\partial w}{\partial z} + \lambda \operatorname{div} \mathbf{V}\right)$$

These are the Navier–Stokes equations, fundamental to the subject of viscous-fluid flow. Considerable economy is achieved by rewriting them as a single vector equation, using the indicial notation:

$$\rho \frac{D\mathbf{V}}{Dt} = \rho \mathbf{g} - \nabla p + \frac{\partial}{\partial x_j}\left[\mu\left(\frac{\partial v_i}{\partial x_j} + \frac{\partial v_j}{\partial x_i}\right) + \delta_{ij}\lambda \operatorname{div} \mathbf{V}\right] \qquad (2\text{-}29b)$$

2-4.5 Incompressible Flow: Thermal Decoupling

If the fluid is assumed to be of constant density, div $\mathbf{V}$ vanishes due to the continuity Eq. (2-7) and the vexing coefficient λ disappears from Newton's law. Equations (2-29) are not greatly simplified, though, if the first viscosity μ is allowed to vary with temperature and pressure (and hence with position). If, however, we assume that μ is constant, many terms vanish, leaving us with a much simpler Navier–Stokes equation for *constant viscosity and density*:

$$\rho \frac{D\mathbf{V}}{Dt} = \rho \mathbf{g} - \nabla p + \mu \nabla^2 \mathbf{V} \qquad (2\text{-}30)$$

Most of the problems and solutions in this text are for incompressible flow, Eqs. (2-7) and (2-30). Note that, if ρ and μ are constant, these equations are entirely *uncoupled* from temperature. One may solve continuity and momentum for velocity and pressure and then later, if one desires, solve for temperature from the *energy equation* of Sec. 2-5. This approximation often divides textbooks into "fluid mechanics" and, later, "heat transfer." However, the present text will maintain some heat-transfer discussions throughout.

2-4.6 Inviscid Flow: The Euler and Bernoulli Equations

If we further assume that viscous terms are negligible, Eq. (2-30) reduces to

$$\rho \frac{D\mathbf{V}}{Dt} \approx \rho \mathbf{g} - \nabla p \tag{2-30a}$$

This is called *Euler's equation* (derived by Leonhard Euler in 1755) for inviscid flow. It is first order in $\mathbf{V}$ and p and thus rather simpler than the second-order Navier–Stokes Eq. (2-30). At a fixed wall, the no-slip condition must be *dropped*, and tangential velocity is allowed to slip. Much research has been reported for Euler's equation: analytical (Currie 1993), numerical (Tannehill et al. 1997), and mathematical theorems (Kreiss and Lorenz 1989). As covered in undergraduate texts, for example, White (2003), Euler's equation for steady, incompressible, frictionless flow may be integrated along a streamline between any points 1 and 2 to yield

$$\left(p + \tfrac{1}{2}\rho V^2 + \rho gz\right)_1 \approx \left(p + \tfrac{1}{2}\rho V^2 + \rho gz\right)_2 \tag{2-30b}$$

where z is up, that is, opposite gravity. This is *Bernoulli's equation* for steady frictionless flow. Though approximate, since all fluids are viscous, it has many applications in aeronautics and hydrodynamics and serves as an outer boundary matching condition in boundary-layer theory (Chap. 4). The unsteady form of Bernoulli's equation will be given in Sec. 2-10.

2-5 THE ENERGY EQUATION (FIRST LAW OF THERMODYNAMICS)

The first law of thermodynamics for a system is a statement of the fact that the sum of the work and heat added to the system will result in an increase in the energy of the system:

$$dE_t = dQ + dW \tag{2-31}$$

where Q = heat added
W = work done on system

The quantity E_t denotes the total energy of the system; hence, in a moving system, such as a flowing fluid particle, E_t will include not only internal energy but also kinetic and potential energy. Thus, for a fluid particle, the energy per unit volume is

$$E_t = \rho\left(e + \tfrac{1}{2}V^2 - \mathbf{g} \cdot \mathbf{r}\right) \tag{2-32}$$

where e = internal energy per unit mass
$\mathbf{r}$ = displacement of particle

Just as in conservation of mass and momentum, the energy equation for a fluid is conveniently written as a time rate of change, following the particle. Thus

Heat flow per
unit area:

$q_x = -k\dfrac{\partial T}{\partial x}$

$q_x + \dfrac{\partial q_x}{\partial x}\, dx$

dx

w_x

$w_x + \dfrac{\partial w_x}{\partial x}\, dx$
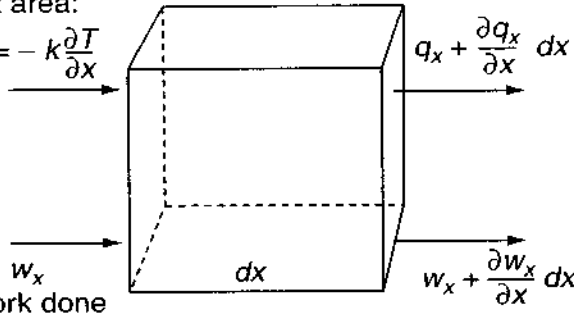
Work done
per unit area:

$w_x = -(u\tau_{xx} + v\tau_{xy} + w\tau_{xz})$

FIGURE 2-2
Heat and work exchange on the left and right sides of
an element.

Eq. (2-31) becomes

$$\frac{DE_t}{Dt} = \frac{DQ}{Dt} + \frac{DW}{Dt} \tag{2-33}$$

From Eq. (2-32), we have

$$\frac{DE_t}{Dt} = \rho\left(\frac{De}{Dt} + V\frac{DV}{Dt} - \mathbf{g}\cdot\mathbf{V}\right) \tag{2-34}$$

It remains to express Q and W in terms of fluid properties.

It is assumed that the heat transfer Q to the element is given by Fourier's law. From Eq. (1-37), the vector heat flow per unit area is

$$\mathbf{q} = -k\nabla T \tag{1-37}$$

Referring to Fig. 2-2, the heat flow into the left face of the element is

$$q_x\, dy\, dz$$

while the heat flow out of the right face is

$$\left(q_x + \frac{\partial q_x}{\partial x}\, dx\right) dy\, dz$$

A similar situation holds for the upper and lower faces, involving q_y, and the front and rear faces, involving q_z. In each case, the net heat flow is out of the element. Hence the net heat transferred *to* the element is

$$-\left(\frac{\partial q_x}{\partial x} + \frac{\partial q_y}{\partial y} + \frac{\partial q_z}{\partial z}\right) dx\, dy\, dz$$

Dividing by the element volume $dx\, dy\, dz$, we have the desired expression for the heat-transfer term neglecting internal heat generation:

$$\frac{DQ}{Dt} = -\text{div } \mathbf{q} = +\text{div}(k\,\nabla T) \tag{2-35}$$

Referring again to Fig. 2-2, the rate of work done to the element per unit area on the left face is

$$w_x = -(u\tau_{xx} + v\tau_{xy} + w\tau_{xz})$$

and the rate of work done by the right-face stresses is

$$-w_x - \frac{\partial w_x}{\partial x}\, dx \qquad \text{per unit area}$$

Again the other faces are similar. In just the same fashion as the heat transfer, then, the net rate of work done on the element is

$$\frac{DW}{Dt} = -\text{div } \mathbf{w} = \frac{\partial}{\partial x}(u\tau_{xx} + v\tau_{xy} + w\tau_{xz})$$

$$+ \frac{\partial}{\partial y}(u\tau_{yx} + v\tau_{yy} + w\tau_{yz})$$

$$+ \frac{\partial}{\partial z}(u\tau_{zx} + v\tau_{zy} + w\tau_{zz}) \qquad (2\text{-}36)$$

Using the indicial notation, this becomes, very simply,

$$\frac{DW}{Dt} = \nabla \cdot (\mathbf{V} \cdot \tau_{ij}) \qquad (2\text{-}37)$$

This expression can be decomposed in very convenient fashion into

$$\nabla \cdot (\mathbf{V} \cdot \tau_{ij}) = \mathbf{V} \cdot (\nabla \cdot \tau_{ij}) + \tau_{ij}\frac{\partial u_i}{\partial x_j} \qquad (2\text{-}38)$$

the first term of which is directly related to the momentum equation

$$\nabla \cdot \tau_{ij} = \rho\left(\frac{D\mathbf{V}}{Dt} - \mathbf{g}\right) \qquad (2\text{-}19)$$

Hence

$$\mathbf{V} \cdot (\nabla \cdot \tau_{ij}) = \rho\left(V\frac{D\mathbf{V}}{Dt} - \mathbf{g} \cdot \mathbf{V}\right) \qquad (2\text{-}39)$$

which are exactly the kinetic- and potential-energy terms in Eq. (2-34). Thus the kinetic and potential energy vanish when we substitute for E_t, Q, and W in Eq. (2-33) from Eqs. (2-34), (2-35), and (2-38):

$$\rho\frac{De}{Dt} = \text{div}(k\,\nabla T) + \tau_{ij}\frac{\partial u_i}{\partial x_j} \qquad (2\text{-}40)$$

This is a widely used form of the first law of thermodynamics for fluid motion. If we split the stress tensor into pressure and viscous terms, using Eq. (2-27), we have

$$\tau_{ij}\frac{\partial u_i}{\partial x_j} = \tau'_{ij}\frac{\partial u_i}{\partial x_j} - p\,\text{div }\mathbf{V} \qquad (2\text{-}41)$$

From the equation of continuity, Eq. (2-6), we have

$$p \, \text{div } \mathbf{V} = -\frac{p}{\rho}\frac{D\rho}{Dt} = \rho\frac{D}{Dt}\left(\frac{p}{\rho}\right) - \frac{Dp}{Dt} \qquad (2\text{-}42)$$

Combining Eqs. (2-40) to (2-42) gives

$$\rho\frac{D}{Dt}\left(e + \frac{p}{\rho}\right) = \frac{Dp}{Dt} + \text{div}(k\,\nabla T) + \tau'_{ij}\frac{\partial u_i}{\partial x_j} \qquad (2\text{-}43)$$

The advantage of this rearrangement, if any, is that an old friend crops up, the fluid enthalpy:

$$h = e + \frac{p}{\rho} \qquad (2\text{-}44)$$

Generally, enthalpy will be a more useful function than internal energy, particularly in boundary-layer flows. Also, the pressure term Dp/Dt may often be neglected in Eq. (2-43), while the related term $p\,\text{div } \mathbf{V}$ in Eq. (2-40) will be nonnegligible for the same flow.

The last term in Eq. (2-43), involving viscous stresses, is customarily called the *dissipation function* Φ:

$$\Phi = \tau'_{ij}\frac{\partial u_i}{\partial x_j} \qquad (2\text{-}45)$$

The term Φ is always positive definite, in accordance with the second law of thermodynamics, since viscosity cannot add energy to the system. For a newtonian fluid, using τ' from Eq. (2-27), we obtain

$$\Phi = \mu\left[2\left(\frac{\partial u}{\partial x}\right)^2 + 2\left(\frac{\partial v}{\partial y}\right)^2 + 2\left(\frac{\partial w}{\partial z}\right)^2 + \left(\frac{\partial v}{\partial x} + \frac{\partial u}{\partial y}\right)^2\right.$$
$$\left. + \left(\frac{\partial w}{\partial y} + \frac{\partial v}{\partial z}\right)^2 + \left(\frac{\partial u}{\partial z} + \frac{\partial w}{\partial x}\right)^2\right] + \lambda\left(\frac{\partial u}{\partial x} + \frac{\partial v}{\partial y} + \frac{\partial w}{\partial z}\right)^2 \qquad (2\text{-}46)$$

which is always positive since all the terms are quadratic. On the other hand, λ may actually be negative, e.g., Stokes' hypothesis, $\lambda = -\frac{2}{3}\mu$. It is an interesting exercise, using Eq. (2-46), to prove that the correct conditions in which Φ may not be negative are

$$\mu \geq 0 \qquad 3\lambda + 2\mu \geq 0 \qquad (2\text{-}47)$$

Using this short notation, the energy relation Eq. (2-43) takes the final form

$$\rho\frac{Dh}{Dt} = \frac{Dp}{Dt} + \text{div}(k\,\nabla T) + \Phi \qquad (2\text{-}48)$$

where Φ is given by Eq. (2-46).

2-5.1 The Incompressible-Flow Approximation

From the thermodynamic identity (1-87), we can rewrite Eq. (2-48) as

$$\rho c_p \frac{DT}{Dt} = \beta T \frac{Dp}{Dt} + \text{div}(k\,\nabla T) + \Phi \tag{2-49}$$

Now, if flow velocity scale U becomes smaller, while heat transfer remains important, the fluid kinetic energy U^2 will eventually become much smaller than the enthalpy change $c_p\,\Delta T$. Since both Dp/Dt and Φ are of order U^2, the limit of low-velocity or *incompressible* flow will be

$$\rho c_p \frac{DT}{Dt} \approx \text{div}(k\,\nabla T) \tag{2-50}$$

If we further assume constant thermal conductivity, we obtain the more familiar incompressible heat-convection equation:

$$\rho c_p \frac{DT}{Dt} \approx k\,\nabla^2 T \tag{2-51}$$

Note that the correct specific heat is c_p, not c_v, even in the incompressible-flow limit of near-zero Mach number. A very good discussion of this point is given in Panton (1996, Sec. 10.9).

2-5.2 Summary of the Basic Equations

Summarizing, the three basic laws of conservation of mass, momentum, and energy have been adapted for use in fluid motion. They are, respectively,

$$\frac{\partial \rho}{\partial t} + \text{div}\,\rho\mathbf{V} = 0 \tag{2-6}$$

$$\rho \frac{D\mathbf{V}}{Dt} = \rho\mathbf{g} + \nabla\cdot\tau'_{ij} - \nabla p \tag{2-19a}$$

$$\rho \frac{Dh}{Dt} = \frac{Dp}{Dt} + \text{div}(k\,\nabla T) + \tau'_{ij}\frac{\partial u_i}{\partial x_j} \tag{2-48a}$$

where, for a linear (newtonian) fluid, the viscous stresses are

$$\tau'_{ij} = \mu\left(\frac{\partial u_i}{\partial x_j} + \frac{\partial u_j}{\partial x_i}\right) + \delta_{ij}\lambda\,\text{div}\,\mathbf{V} \tag{2-27}$$

As mentioned in the beginning of this chapter, Eqs. (2-6), (2-19), and (2-48) involve seven variables, of which three are assumed to be primary: p, $\mathbf{V}$, and T (say). The remaining four variables are assumed known from auxiliary relations and data of the form

$$\rho = \rho(p, T) \qquad \mu = \mu(p, T)$$
$$h = h(p, T) \qquad k = k(p, T) \tag{2-1}$$

Finally, we note that these relations are fairly general and involve only a few restrictive assumptions: (1) the fluid forms a (mathematical) continuum, (2) the particles are essentially in thermodynamic equilibrium, (3) the only effective body forces are due to gravity, (4) the heat conduction follows Fourier's law, and (5) there are no internal heat sources.

2-6   BOUNDARY CONDITIONS FOR VISCOUS HEAT-CONDUCTING FLOW

The various types of boundary conditions have been discussed in detail in Sec. 1-4 for the three different basic boundaries: (1) a fluid–solid interface, (2) a fluid–fluid interface, and (3) an inlet or exit section. A sketch was given in Fig. 1-31. In their full generality, the conditions in Sec. 1-4 can be quite complex and non-linear, necessitating digital-computer treatment. Thus the bulk of our analytical solutions in this text will be confined to simple but realistic approximations:

1. At a fluid–solid interface, there must be no slip

$$V_{\text{fluid}} = V_{\text{sol}} \tag{2-52}$$

and either no temperature jump (when the wall temperature is known)

$$T_{\text{fluid}} = T_{\text{sol}} \tag{2-53}$$

or equality of heat flux (when the solid heat flux is known)

$$\left(k \frac{\partial T}{\partial n} \right)_{\text{fluid}} = q \qquad \text{from solid to fluid} \tag{2-54}$$

2. At the interface between a liquid and a gaseous atmosphere, there must be kinematic equivalence

$$V_{n,\,\text{liq}} \approx \frac{\partial \eta}{\partial t} \tag{2-55}$$

where η is the surface coordinate, and there must be equality of normal momentum flux

$$p_{\text{liq}} \approx p_{\text{atm}} \tag{2-56}$$

We must also have equality of tangential momentum flux and heat flux, which leads to the approximations

$$\frac{\partial V}{\partial n}\bigg|_{\text{liq}} = \frac{\partial T}{\partial n}\bigg|_{\text{liq}} \approx 0 \tag{2-57}$$

when the atmosphere has negligibly small transport coefficients. Also, in some problems, such as the analysis of confused, stormy seas, we need to know the moisture evaporation rate $\dot{m}$ at the interface.

3. At any inlet section of the flow, we need the three quantities V, p, and T at every point on the boundary. At the exit section, we generally need to know V and T,

but not the pressure p, as you recall from the discussion of Fig. 1-31. Exit conditions are difficult because of the formation of wakes and other a priori unknown outflow behavior. One approximation is to let the streamwise flow gradients vanish far downstream of the flow field of interest.

Note: If the pressure can be eliminated, as, for example, with the vorticity/stream-function approach to be discussed in Sec. 2-11, then there is no need to impose a pressure boundary condition. The new computer-oriented *vortex methods*, explained in the monograph by Cottet and Koumoutsakos (1999), do not compute the pressure at all.

2-7   ORTHOGONAL COORDINATE SYSTEMS

Most of the previous discussion has been illustrated by Cartesian coordinates, and only lip service has been paid to other important orthogonal systems. The basic equations of motion, Eqs. (2-6), (2-19), and (2-48) are, of course, valid for any coordinate system when written in tensor form; the problem for non-Cartesian systems is to derive the correct formula for the gradient vector ∇ plus the related expressions for divergence and curl. A straightforward procedure is to use the metric *stretching factors* h_i to relate the new curvilinear coordinates to a Cartesian system, as discussed in standard mathematical references, e.g., Pipes (1958). Let the general curvilinear system (x_1, x_2, x_3) be related to a Cartesian system (x, y, z) so that the element of arc length ds is given by

$$
\begin{aligned}
(ds)^2 &= (dx)^2 + (dy)^2 + (dz)^2 \\
&= (h_1\, dx_1)^2 + (h_2\, dx_2)^2 + (h_3\, dx_3)^2
\end{aligned}
\tag{2-58}
$$

which defines the factors h_i. Note that h_i in general will be functions of the new coordinates x_i. Then, in the new system, the components of the gradient of a scalar ϕ are

$$
\frac{1}{h_1}\frac{\partial\phi}{\partial x_1} \qquad \frac{1}{h_2}\frac{\partial\phi}{\partial x_2} \qquad \frac{1}{h_3}\frac{\partial\phi}{\partial x_3}
\tag{2-59}
$$

The divergence of any vector $\mathbf{A} = (A_1, A_2, A_3)$ is given by

$$
\operatorname{div} \mathbf{A} = \frac{1}{h_1 h_2 h_3}\left[\frac{\partial}{\partial x_1}(h_2 h_3 A_1) + \frac{\partial}{\partial x_2}(h_3 h_1 A_2) + \frac{\partial}{\partial x_3}(h_1 h_2 A_3)\right]
\tag{2-60}
$$

and the components of the vector $\mathbf{B} = \operatorname{curl} \mathbf{A}$ are given by

$$
B_1 = \frac{1}{h_2 h_3}\left[\frac{\partial}{\partial x_2}(h_3 A_3) - \frac{\partial}{\partial x_3}(h_2 A_2)\right]
\tag{2-61}
$$

with exactly similar expressions for B_2 and B_3. Equations (2-59) to (2-61) are sufficient to derive the equations of motion in the new coordinate system x_i. We illustrate with the two classic (and probably most important) systems, cylindrical and spherical.

2-7.1 Cartesian Coordinates

Just to review our previous results, let $x_i = (x, y, z)$, from which $h_i = (1, 1, 1)$. If $V = (u, v, w)$, the vector operations are

$$\nabla\phi = \left(\frac{\partial\phi}{\partial x}, \frac{\partial\phi}{\partial y}, \frac{\partial\phi}{\partial z}\right)$$

$$\text{div } V = \frac{\partial u}{\partial x} + \frac{\partial v}{\partial y} + \frac{\partial w}{\partial z}$$

$$\text{curl } V = \left(\frac{\partial w}{\partial y} - \frac{\partial v}{\partial z}, \frac{\partial u}{\partial z} - \frac{\partial w}{\partial x}, \frac{\partial v}{\partial x} - \frac{\partial u}{\partial y}\right) \tag{2-62}$$

$$V \cdot \nabla = u\frac{\partial}{\partial x} + v\frac{\partial}{\partial y} + w\frac{\partial}{\partial z}$$

$$\nabla^2\phi = \frac{\partial^2\phi}{\partial x^2} + \frac{\partial^2\phi}{\partial y^2} + \frac{\partial^2\phi}{\partial z^2}$$

2-7.2 Cylindrical Polar Coordinates

These coordinates (r, θ, z) are related to the Cartesian system (x, y, z) by

$$x = r\cos\theta \qquad y = r\sin\theta \qquad z = z \tag{2-63}$$

from which we find that $h_1 = 1, h_2 = r$, and $h_3 = 1$. Let the cylindrical polar velocity components be (v_r, v_θ, v_z). Then the new vector relations are

$$\nabla\phi = \left(\frac{\partial\phi}{\partial r}, \frac{1}{r}\frac{\partial\phi}{\partial\theta}, \frac{\partial\phi}{\partial z}\right)$$

$$\nabla \cdot V = \frac{1}{r}\frac{\partial}{\partial r}(rv_r) + \frac{1}{r}\frac{\partial v_\theta}{\partial\theta} + \frac{\partial v_z}{\partial z}$$

$$V \cdot \nabla = v_r\frac{\partial}{\partial r} + \frac{v_\theta}{r}\frac{\partial}{\partial\theta} + v_z\frac{\partial}{\partial z} \tag{2-64}$$

$$\nabla^2\phi = \frac{1}{r}\frac{\partial}{\partial r}\left(r\frac{\partial\phi}{\partial r}\right) + \frac{1}{r^2}\frac{\partial^2\phi}{\partial\theta^2} + \frac{\partial^2\phi}{\partial z^2}$$

2-7.3 Spherical Polar Coordinates

The spherical polar coordinates (r, θ, λ) are defined by the relations

$$x = r\sin\theta\cos\lambda \qquad y = r\sin\theta\sin\lambda \qquad z = r\cos\theta \tag{2-65}$$

from which we find that $h_1 = 1, h_2 = r$, and $h_3 = r\sin\theta$. Let the velocity

components be $\mathbf{V} = (v_r, v_\theta, v_\lambda)$. Then the desired new vector relations are

$$\nabla\phi = \left(\frac{\partial\phi}{\partial r}, \frac{1}{r}\frac{\partial\phi}{\partial\theta}, \frac{1}{r\sin\theta}\frac{\partial\phi}{\partial\lambda}\right)$$

$$\text{div }\mathbf{V} = \frac{1}{r^2}\frac{\partial}{\partial r}(r^2 v_r) + \frac{1}{r\sin\theta}\frac{\partial}{\partial\theta}(v_\theta\sin\theta) + \frac{1}{r\sin\theta}\frac{\partial v_\lambda}{\partial\lambda} \qquad (2\text{-}66)$$

$$\mathbf{V}\cdot\nabla = v_r\frac{\partial}{\partial r} + \frac{v_\theta}{r}\frac{\partial}{\partial\theta} + \frac{v_\lambda}{r\sin\theta}\frac{\partial}{\partial\lambda}$$

$$\nabla^2\phi = \frac{1}{r^2}\frac{\partial}{\partial r}\left(r^2\frac{\partial\phi}{\partial r}\right) + \frac{1}{r^2\sin\theta}\frac{\partial}{\partial\theta}\left(\sin\theta\frac{\partial\phi}{\partial\theta}\right) + \frac{1}{r^2\sin^2\theta}\frac{\partial^2\phi}{\partial\lambda^2}$$

It is seen that the terms in non-Cartesian systems are somewhat more complicated in form but relatively straightforward. The complete equations of motion in cylindrical and spherical coordinates [the special-case forms of Eqs. (2-6), (2-19), and (2-48)] are given in App. B.

2-8 MATHEMATICAL CHARACTER OF THE BASIC EQUATIONS

The character of the basic relations, Eqs. (2-6), (2-19), and (2-48), is extremely complex. There are at least two factors that hinder our analysis: (1) the equations are coupled in the three variables $\mathbf{V}$, p, and T, and (2) each equation contains one or more non-linearities. Are these equations of the boundary-value type or are they wavelike in nature? The answer is that they contain mixtures of both boundary-value and wavelike characteristics.

The general theory concerning the character of partial differential equations has developed from the study of the interesting but rather specialized quasi-linear second-order equation studied in, for example, Kreyszig (1999):

$$A\frac{\partial^2\phi}{\partial x^2} + B\frac{\partial^2\phi}{\partial x\,\partial y} + C\frac{\partial^2\phi}{\partial y^2} = D \qquad (2\text{-}67)$$

where the coefficients A, B, C, and D may be non-linear functions of x, y, ϕ, $\partial\phi/\partial x$, and $\partial\phi/\partial y$ but not of the second derivatives of ϕ (hence the term quasi-linear in the second derivatives). By developing an analytic continuation of these second derivatives, it is found that the character of Eq. (2-67) changes radically, depending upon the sign of the *discriminant* function $B^2 - 4AC$. In particular,

$$\text{If } B^2 - 4AC \begin{cases} < 0 & \text{the equation is } elliptical \\ = 0 & \text{the equation is } parabolic \\ > 0 & \text{the equation is } hyperbolic \end{cases} \qquad (2\text{-}68)$$

The names elliptical, parabolic, and hyperbolic mean little by themselves, having arisen by analogy with the conic sections of analytic geometry. However,

like the conic sections, these names denote a vastly different character for Eq. (2-67):

1. If the equation is *elliptical*, it can be solved only by specifying the boundary conditions on a *complete contour enclosing the region*; it is a boundary-value problem.
2. If the equation is *parabolic*, boundary conditions must be *closed in one direction* but remain *open at one end* of the other direction; it is a mixed initial- and boundary-value problem.
3. If the equation is *hyperbolic*, it can be solved in a given region by specifying conditions at only *one portion* of the boundary, the other boundaries remaining *open*; it is an initial-value problem.

Many of the partial differential equations of mathematical physics can be classified with reference to Eq. (2-67); for example,

Laplace equation: $\dfrac{\partial^2 \phi}{\partial x^2} + \dfrac{\partial^2 \phi}{\partial y^2} = 0$ elliptical

Heat-conduction equation: $\dfrac{\partial^2 \phi}{\partial x^2} - \dfrac{\partial \phi}{\partial y} = 0$ parabolic   (2-69)

Wave equation: $\dfrac{\partial^2 \phi}{\partial x^2} - \dfrac{\partial^2 \phi}{\partial y^2} = 0$ hyperbolic

For further examples and discussion of these partial-differential-equation classifications, see Chap. 21 of the text by Kreyszig (1999). Certain special cases of fluid flow, such as two-dimensional inviscid flow, do fit the form of Eq. (2-67). But the full viscous-flow equations, (2-6), (2-19), and (2-48), are too complicated and display a variable mixture of elliptic, parabolic, and hyperbolic behavior. The monograph by Kreiss and Lorenz (1989) develops a variety of mathematical properties and theorems for the Navier–Stokes equations.

It is instructive now to consider the special case of *diffusion*.

2-8.1 Low-Speed Diffusion: The Prandtl Number

Consider a newtonian fluid at low speed with constant ρ, μ, and k. Let the streamwise changes be small, that is, neglect the convective derivatives compared to local changes. Then the momentum and energy equations reduce to

Momentum: $\rho \dfrac{\partial \mathbf{V}}{\partial t} \approx \rho \mathbf{g} - \nabla p + \mu \nabla^2 \mathbf{V}$ (2-70)

Energy: $\rho c_p \dfrac{\partial T}{\partial t} \approx k \nabla^2 T$ (2-71)

We recognize Eq. (2-71) as a multidimensional form of the heat-conduction equation (2-69). The temperature has elliptic boundary-value behavior in space (x, y, z)

and parabolic "marching" behavior in time. We only need an initial condition $T(x, y, z, 0)$ to get started and can "march" forward in time indefinitely if we know boundary values on T at all times.

The behavior of Eq. (2-70) is not so obvious. But we can eliminate $\mathbf{V}$ by taking the divergence of the entire equation, noting that $\text{div}(\mathbf{V}) = 0$ for constant density. The result is

$$\nabla^2 p = 0 \tag{2-72}$$

Thus, for these simplifications, the pressure shows elliptic behavior from Eq. (2-69). Finally, the pressure itself could be eliminated by taking the curl of Eq. (2-70), with the result

$$\frac{\partial \boldsymbol{\omega}}{\partial t} = \frac{\mu}{\rho} \nabla^2 \boldsymbol{\omega},$$

where

$$\boldsymbol{\omega} = \text{curl } \mathbf{V} = \text{fluid vorticity} \tag{2-73}$$

This relation, like Eq. (2-71), is also the heat-conduction equation with diffusivity coefficients that are purely fluid properties:

$$\nu = \frac{\mu}{\rho} = \text{viscous } \textit{diffusivity}$$

$$\alpha = \frac{k}{\rho c_p} = \text{thermal } \textit{diffusivity} \tag{2-74}$$

The coefficient ν is also called the *kinematic viscosity* because it has no mass units. The units of both coefficients are m^2/s, exactly the same as the *mass diffusivity D* from Eq. (1-45). Their ratios are important dimensionless fluid-property groups that give a measure of relative rates of diffusion:

Prandtl number: $Pr = \dfrac{\nu}{\alpha} = \dfrac{\text{viscous diffusion rate}}{\text{thermal diffusion rate}}$

Schmidt number: $Sc = \dfrac{\nu}{D} = \dfrac{\text{viscous diffusion rate}}{\text{mass diffusion rate}}$ (2-75)

Lewis number: $Le = \dfrac{D}{\alpha} = \dfrac{\text{mass diffusion rate}}{\text{thermal diffusion rate}}$

Note the identity $Pr = ScLe$. Since mass diffusion is not emphasized here, consider viscous and thermal effects. Table 2-1 gives values of the Prandtl number for various fluids at 20°C. It shows that liquid metals have small Prandtl number, gases are slightly less than unity, light liquids somewhat higher than unity, and oils have very large Pr. Thus there are dramatic differences among the fluids in their relative spreading of viscous and thermal effects.

Figure 2-3 shows low-speed viscous flow past a hot wall as an example. The sketches illustrate low Reynolds number or laminar-flow effects. High Reynolds number, or turbulent, flows agree qualitatively with Fig. 2-3, but the profile differences are not so broadly obvious.

TABLE 2-1
Prandtl number of various fluids at 20°C

Fluid	Prandtl number Pr	Fluid	Prandtl number Pr
Mercury	0.024	Benzene	7.4
Helium	0.70	Carbon tetrachloride	7.9
Air	0.72	Ethyl alcohol	16
Liquid ammonia	2.0	SAE 30 oil	3500
Freon-12	3.7	Castor oil	10,000
Methyl alcohol	6.8	Glycerin	12,000
Water	7.0		

A quantitative formula for the relative spreading is obtained by remembering that the two diffusion equations

$$\frac{\partial T}{\partial t} = \alpha \, \nabla^2 T \tag{2-76}$$

$$\frac{\partial \omega}{\partial t} = \nu \, \nabla^2 \omega \tag{2-77}$$

can be made independent of the constants α and ν by defining new spatial variables: $x_i/\sqrt{\alpha}$ for the T equation and $x_i/\sqrt{\nu}$ for the ω equation. The equations then have unit diffusion constants and hence both show unit spreading. For any given time, then, the thermal spreading distance L_T and the viscous spreading length L_V must be related by

$$\frac{L_T}{\sqrt{\alpha}} = \frac{L_V}{\sqrt{\nu}}$$

or

$$\frac{L_V}{L_T} \approx \sqrt{Pr} \tag{2-78}$$

Equation (2-78) is a good approximation for all laminar boundary-layer flows, even at high speeds.

Liquid metals: $Pr \ll 1$ Gases: $Pr = 0.7$ Water: $2.0 \le Pr \le 7$ Oils: $Pr \gg 1$
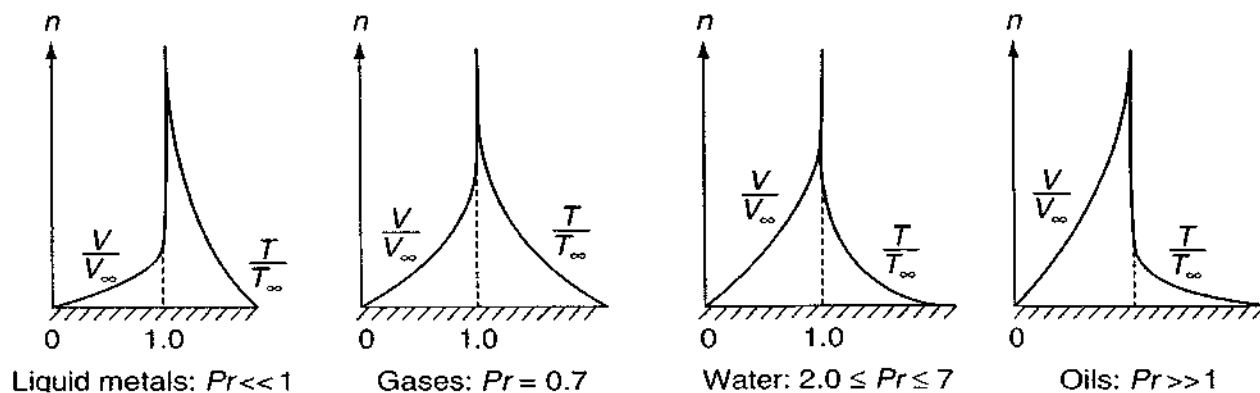
FIGURE 2-3
Prandtl number effects on viscous and thermal diffusion. (Hot wall shown for convenience.)

2-9 DIMENSIONLESS PARAMETERS IN VISCOUS FLOW

Since our basic equations of motion are extremely difficult to analyze in general, we should cast them in their most efficient form, thereby increasing the usefulness of whatever solutions we find. This is accomplished by nondimensionalizing the equations and boundary conditions.

For simplicity, assume constant c_p and c_v, approximately true for all gases, and also neglect the second coefficient of viscosity, λ, which is seldom needed. Then our four variables, p, ρ, $\mathbf{V}$, and T, will depend upon space and time and eight parameters that occur in the basic equations and boundary conditions:

$$\mathbf{V} \text{ or } p \text{ or } \rho \text{ or } T = f(x_i, t, \mu, k, g, c_p, T_w, q_w, \ell, \mathcal{T}) \tag{2-79}$$

The eight parameters, μ through $\mathcal{T}$, are assumed to be known from data or thermodynamic state relations. Let g be constant. Now select *constant* reference properties appropriate to the flow:

1. Reference velocity U (the freestream velocity)
2. Reference length L (the writer suggests body length for external flows or duct diameter for internal flows) $\qquad$ (2-80)
3. Freestream properties p_0, ρ_0, T_0, μ_0, k_0

Steady viscous flows have no characteristic time of their own, so select particle residence time L/U as a reference time. (If the flow oscillates with frequency ω, one might select ω^{-1} as a reference time). Now define dimensionless variables and denote them by an asterisk.

$$x_i^* = \frac{x_i}{L} \qquad t^* = \frac{tU}{L} \qquad \mathbf{V}^* = \frac{\mathbf{V}}{U} \qquad p^* = \frac{p - p_0}{\rho U^2} \qquad \Phi^* = \frac{L^2}{\mu_0 U^2}\Phi$$

$$\rho^* = \frac{\rho}{\rho_0} \qquad T^* = \frac{T - T_0}{T_w - T_0} \qquad \mu^* = \frac{\mu}{\mu_0} \qquad k^* = \frac{k}{k_0} \qquad \nabla^* = L\nabla \tag{2-81}$$

2-9.1 Nondimensionalizing the Basic Equations

Substitute the above variables from (2-81) into our basic equations (2-6), (2-19), and (2-48). Collect terms and divide out dimensional constants so that all remaining terms are dimensionless. The final results are our nondimensional equations of motion:

Continuity: $\qquad\qquad \dfrac{\partial \rho^*}{\partial t^*} + \nabla \cdot (\rho^* \mathbf{V}^*) = 0$

Navier–Stokes: $\rho^* \dfrac{D\mathbf{V}^*}{Dt^*} = \dfrac{1}{Fr}\rho^* - \nabla^* p^* + \dfrac{1}{Re}\nabla^* \cdot \left[\mu^*\left(\dfrac{\partial u_i^*}{\partial x_j^*} + \dfrac{\partial u_j^*}{\partial x_i^*}\right)\right]$ (2-82)

Energy: $\qquad\qquad \rho^* \dfrac{DT^*}{Dt^*} = Ec\dfrac{Dp^*}{Dt^*} + \dfrac{1}{RePr}\nabla^* \cdot (k^* \nabla^* T^*) + \dfrac{Ec}{Re}\Phi^*$

We see that continuity is devoid of parameters, while Navier–Stokes contains two:

Reynolds number:
$$Re = \frac{\rho_0 UL}{\mu_0}$$

Froude number:
$$Fr = \frac{U^2}{gL} \tag{2-83}$$

The Reynolds number is the most important dimensionless group in fluid mechanics. Almost all viscous-flow phenomena depend upon the Reynolds number. The Froude number is important only if there is a free surface in the flow.

The dimensionless energy equation also contains the Reynolds number, plus two additional parameters:

Prandtl number:
$$Pr = \frac{\mu_0 c_p}{k_0}$$

Eckert number:
$$Ec = \frac{U^2}{c_p T_0} \tag{2-84}$$

For a perfect gas, the more familiar *Mach* number, $Ma = U/a_0$, can replace the Eckert number:

$$Ec = \frac{U^2}{c_p T_0} = \frac{U^2}{[\gamma R/(\gamma - 1)]T_0} = (\gamma - 1)\frac{U^2}{\gamma R T_0}$$

$$= (\gamma - 1)\frac{U^2}{a_0^2} = (\gamma - 1)Ma^2 \tag{2-85}$$

The Prandtl number is always important in convective heat-transfer problems. In high-speed flows, Re, Pr, γ, and Ma are all important (Chap. 7), but at low speeds ($Ma < 0.3$), the Eckert/Mach number terms are often negligible and the energy equation reduces to Eq. (2-51). The product $RePr$ in the conduction term is often called the *Peclet* number, Pe.

An important point, sometimes neglected in elementary approaches, is that the variables ρ, μ, and k must be specified as thermodynamic functions for the particular fluid studied:

$$\rho^*, \mu^*, k^* = f(p^*, T^*)$$

Thus, if different fluids are being compared, Re, Pr, and Ec might not be sufficient if there are large temperature variations. As seen in Chap. 1, gases and liquids have quite different temperature-dependent ρ, μ, and k. Temperature corrections might be needed.

2-9.2   Momentum with Free Convection

In free or "natural" convection, there is no freestream U. The flow is driven by gravity acting on slight density changes. Pressure is nearly constant, and the density can

be modeled as

$$\rho \approx \rho_0[1 - \beta(T - T_0)]$$

where

$$\beta = -\frac{1}{\rho}\left(\frac{\partial \rho}{\partial T}\right)_p \tag{2-86}$$

The parameter U is replaced by the velocity grouping $[\mu/(\rho_0 L)]$. The reader is invited (as a problem exercise) to nondimensionalize the Navier–Stokes equation again and find a new parameter characteristic of free convection:

Grashof number:
$$Gr = \frac{g\beta\rho_0^2 L^3(T_w - T_0)}{\mu_0^2} \tag{2-87}$$

As we shall see in Sec. 4-13, Gr and Pr correlate heat-transfer results in free convection.

2-9.3 Nondimensionalizing the Boundary Conditions

Just analyzing the basic equations is not enough. The boundary conditions also contain important dimensionless parameters. In the freestream, where $V = U$ and $T = T_0$, the conditions simply become $V^* = 1$ and $T^* = 0$. If, then, we substitute the same variables from Eqs. (2-81) into the boundary conditions at a fixed wall in Sec. 2-6, we obtain

$$\mathbf{V}_w^* = 0 \qquad T_w^* = 1 \quad \text{or} \quad \left(k^* \frac{\partial T^*}{\partial n^*}\right)_w = \frac{q_w L}{k_0(T_w - T_0)} = Nu \tag{2-88}$$

So the temperature conditions specify either a unit temperature ratio or a dimensionless wall heat transfer that is called the *Nusselt* number, Nu. The computed results at the wall will then be the opposite: either a Nusselt number or a (nonunit) temperature ratio.

If there is slip or temperature jump at the wall, Eqs. (1-91) and (1-96) become

$$u_w^* = Kn\left(\frac{\partial u^*}{\partial n^*}\right)_w$$

and

$$T_w^* = 1 + \frac{2\gamma}{Pr(\gamma + 1)} Kn\left(\frac{\partial T^*}{\partial n^*}\right)_w \tag{2-89}$$

Slip conditions introduce the Knudsen number, $Kn = \ell/L$, and the specific-heat ratio, $\gamma = c_p/c_v$.

Finally, at an interface where surface tension is important, Eq. (1-106) for interfacial pressure becomes

$$p_{\text{interface}}^* = Ca + \frac{1}{Fr}\eta^* - \frac{1}{We}\left(\frac{1}{R_x^*} + \frac{1}{R_y^*}\right) \tag{2-90}$$

This equation introduces our three final dimensionless groups:

Cavitation number:
$$Ca = \frac{p_a - p_0}{\rho U^2}$$

Froude number:
$$Fr = \frac{U^2}{gL} \qquad (2\text{-}91)$$

Weber number:
$$We = \frac{\rho_0 U^2 L}{\mathcal{G}}$$

The Froude number is the most important of the three. It is fundamental to all free-surface flows and can never be neglected. The Weber number is important only if it is small, of $O(10)$ or less, which is usually due to a small length scale L. The cavitation number is appropriate if the pressure p_0 is interpreted as the *vapor pressure* of the liquid, p_v. If $Ca \ll 1$, the liquid might vaporize (cavitate) when the local pressure drops below p_v. For further details, see the text by Brennen (1995).

To summarize, the following parameters are important for any particular flow:

1. All viscous flows: Reynolds number
2. Variable-temperature problems: Prandtl and Eckert (or Mach) numbers
3. Flow with free convection: Grashof and Prandtl numbers
4. Wall heat transfer: temperature ratio or Nusselt number
5. Slip flow: Knudsen number and specific-heat ratio
6. Free-surface conditions: Froude number (always); Weber number (sometimes), and cavitation number (sometimes)

It is interesting to note that, in spite of our care, we have missed two parameters which become important at higher Reynolds numbers, where the flow becomes turbulent (a mean flow plus a superimposed random unsteadiness). These two parameters, which occur in Chaps. 5 to 7, are the degree of surface roughness (a departure from geometric similarity) and the amount of turbulence (percentage of random fluctuation) in the reference velocity U (called freestream turbulence). Reference to these two effects was made in the discussion of the drag of a cylinder in Fig. 1-10. To the novice, these parameters express unexpected effects—timely reminders that fluid mechanics is a difficult subject, containing many hidden surprises to confound or delight the would-be analyst.

2-10 VORTICITY CONSIDERATIONS IN INCOMPRESSIBLE VISCOUS FLOW

As discussed in Chap. 1, the vorticity vector $\boldsymbol{\omega} = \text{curl } \mathbf{V}$ is a measure of rotational effects, being equal to twice the local angular velocity of a fluid element. While vorticity is not a primary variable in flow analysis, the velocity itself being far more useful and significant, it is still extremely instructive to examine the impact of the vorticity vector on the Navier–Stokes Eq. (2-29). To keep the lesson from being lost in a

maze of algebra, let us assume constant ρ and μ, so that Eq. (2-30) applies. Also let $\mathbf{g} = -g\mathbf{k}$, again for simplicity. Then the Navier–Stokes equation becomes

$$\rho \frac{D\mathbf{V}}{Dt} = -\nabla p - \rho g \, \mathbf{k} + \mu \nabla^2 \mathbf{V} \tag{2-92}$$

Introduce vorticity into both the acceleration and the viscous terms, using the two vector identities,

$$(\mathbf{V} \cdot \nabla)\mathbf{V} = \nabla \frac{V^2}{2} - \mathbf{V} \times \boldsymbol{\omega} \tag{1-10}$$

$$\nabla^2 \mathbf{V} = \nabla(\text{div } \mathbf{V}) - \text{curl } \boldsymbol{\omega} \tag{2-93}$$

and remember that div $\mathbf{V} = 0$ if ρ is constant. Equation (2-92) then becomes

$$\rho \frac{\partial \mathbf{V}}{\partial t} + \nabla\left(p + \tfrac{1}{2}\rho V^2 + \rho gz\right) = \rho \mathbf{V} \times \boldsymbol{\omega} - \mu \text{ curl } \boldsymbol{\omega} \tag{2-94}$$

Equation (2-94) is most illuminating. The left-hand side is the sum of the classic Euler terms of inviscid flow. The right-hand side vanishes if the vorticity is zero, regardless of the value of the viscosity. Thus, if $\boldsymbol{\omega} = 0$ identically, which is the classic assumption of irrotational flow, the velocity vector must by definition be a potential function, $\mathbf{V} = \nabla\phi$, where ϕ is the velocity potential, and Eq. (2-94) becomes the celebrated Bernoulli equation for unsteady incompressible flow:

$$\rho \frac{\partial \phi}{\partial t} + p + \tfrac{1}{2}\rho V^2 + \rho gz = \text{const} \tag{2-95}$$

It follows that Bernoulli's equation is valid even for *viscous* fluids if the flow is irrotational. Put another way, Eq. (2-94) shows that every potential-flow solution of classical hydrodynamics is in fact an exact solution of the full Navier–Stokes equations. The difficulty is, of course, that potential flows do not and cannot satisfy the no-slip condition at a solid wall, which requires both the normal and tangential velocities to vanish. This is because the assumption of irrotationality eliminates the second-order velocity derivatives from Eq. (2-92), leaving only first-order derivatives, so that only *one* velocity condition can be satisfied at a solid wall. In potential flow, then, we require only the normal velocity to vanish at a wall and put no restriction on the tangential velocity, which commonly slips at the wall. It would appear at this point that potential solutions are no aid in viscous analysis, but in fact at high Reynolds numbers, viscous flow past a solid body is primarily potential flow everywhere except close to the body, where the velocity drops off sharply through a thin viscous boundary layer to satisfy the no-slip condition. In many cases, the boundary layer is so thin that it does not really disturb the outer potential flow, which can be calculated by the methods of classical hydrodynamics described, for example, in the texts by Milne-Thomson (1968) or Robertson (1965). This was the case in Fig. 1-1a. It behooves the reader, therefore, to master potential-flow analysis as a natural introduction to the study of viscous flow.

We can ascertain when irrotational flow occurs by deriving an expression for the rate of change of vorticity. One form is obtained by taking the curl of Eq. (2-94), with the result

$$\frac{D\omega}{Dt} = (\omega \cdot \nabla)V + \nu\nabla^2\omega \tag{2-96}$$

which is the famous Helmholtz equation of hydrodynamics, usually written without the second term involving the kinematic viscosity. The first term on the right arises from the convective derivative and is called the *vortex-stretching term*; this term was zero in the special case of Eq. (2-77). The second term is obviously a viscous-diffusion term; if it is neglected (the ideal fluid), Eq. (2-96) leads to Helmholtz' theorem that the strength of a vortex remains constant and also to Lagrange's theorem that $\omega = 0$ for all time if it is zero everywhere at $t = 0$. Still a third result of neglecting the viscous term is Kelvin's theorem that the circulation about any closed path moving with the fluid is a constant. All three theorems are valid and useful in the inviscid approximation, but all three fail when the viscosity is not zero because the second term in Eq. (2-96) is constrained by the no-slip condition not to vanish near solid walls. Thus, in all viscous flows, vorticity is generally present, being generated by relative motion near solid walls. If the Reynolds number is large, the vorticity is swept down stream and remains close to the wall. A boundary layer is formed, outside of which the vorticity may be taken as zero. If the flow is between two walls, as in duct flow, the two boundary layers will meet and fill the duct with vorticity, as in Fig. 1-11, so that the potential-flow model is generally not valid in duct flow.

2-11 TWO-DIMENSIONAL CONSIDERATIONS: THE STREAM FUNCTION

In Eq. (2-9) we noted that the stream function is an exact solution of the continuity equation when only two independent spatial variables are involved in the flow. For maximum benefit, let us examine the simple case of constant μ and ρ and two-dimensional flow in the xy plane, i.e., a flow with only the two velocity components $u(x, y, t)$ and $v(x, y, t)$. The equations of motion then are the continuity equation and the two components of the Navier–Stokes equations:

$$\frac{\partial u}{\partial x} + \frac{\partial v}{\partial y} = 0 \tag{2-97}$$

$$\frac{\partial u}{\partial t} + u\frac{\partial u}{\partial x} + v\frac{\partial u}{\partial y} = g_x - \frac{1}{\rho}\frac{\partial p}{\partial x} + \nu\left(\frac{\partial^2 u}{\partial x^2} + \frac{\partial^2 u}{\partial y^2}\right) \tag{2-98}$$

$$\frac{\partial v}{\partial t} + u\frac{\partial v}{\partial x} + v\frac{\partial v}{\partial y} = g_y - \frac{1}{\rho}\frac{\partial p}{\partial y} + \nu\left(\frac{\partial^2 v}{\partial x^2} + \frac{\partial^2 v}{\partial y^2}\right) \tag{2-99}$$

to be solved for the three dependent variables u, v, and p. Note that the momentum equation has been uncoupled from the energy equation by the assumption of constant μ and ρ, so that $T(x, y, t)$ can be solved later from Eq. (2-50) if desired.

Lest the reader think that the system, Eqs. (2-97) to (2-99), has been so oversimplified that it is not worth making a fuss over, the remark that this system has borne the brunt of much of the theoretical work on viscous flow to this date.

By analogy with Eq. (2-9), Eq. (2-97) yields immediately to a stream function $\psi(x, y, t)$ defined by

$$u = \frac{\partial \psi}{\partial y} \qquad v = -\frac{\partial \psi}{\partial x} \tag{2-100}$$

where ψ now takes on the meaning of volume flow rather than mass flow, since the density is missing in the definition. Meanwhile, the pressure and gravity can be eliminated from Eqs. (2-98) and (2-99) by cross-differentiation, i.e., taking the curl of the two-dimensional vector momentum equaiton. The result is

$$\frac{\partial \omega_z}{\partial t} + u \frac{\partial \omega_z}{\partial x} + v \frac{\partial \omega_z}{\partial y} = \nu \left(\frac{\partial^2 \omega_z}{\partial x^2} + \frac{\partial^2 \omega_z}{\partial y^2} \right) \tag{2-101}$$

where

$$\omega_z = \left(\frac{\partial v}{\partial x} - \frac{\partial u}{\partial y} \right) \tag{1-13}$$

Since $\mathbf{V} = \mathbf{V}(x, y, t)$ only, the vorticity has only the single nonvanishing component ω_z. By comparison with the more general vorticity transport relation, Eq. (2-97), we see that the vortex-stretching term $(\boldsymbol{\omega} \cdot \nabla)\mathbf{V}$ has vanished identically because, for this special case of flow in the xy plane, the vorticity vector $\boldsymbol{\omega}$ is perpendicular to the gradient of $\mathbf{V}$. Combining Eqs. (2-100) and (1-13), we have the intriguing relation

$$\omega_z = -\nabla^2 \psi \tag{2-102}$$

so that Eq. (2-101) can be rewritten as a fourth-order partial differential equation with the stream function as the only variable:

$$\frac{\partial}{\partial t} (\nabla^2 \psi) + \frac{\partial \psi}{\partial y} \frac{\partial}{\partial x} (\nabla^2 \psi) - \frac{\partial \psi}{\partial x} \frac{\partial}{\partial y} (\nabla^2 \psi) = \nu \nabla^4 \psi \tag{2-103}$$

The boundary conditions would be in terms of the first derivatives of ψ, from Eq. (2-100). For example, in the flow of a uniform stream in the x direction past a solid body, the conditions would be

At infinity: $\qquad \dfrac{\partial \psi}{\partial x} = 0 \qquad \dfrac{\partial \psi}{\partial y} = U_\infty$

$$\tag{2-104}$$

At the body (no slip): $\qquad \dfrac{\partial \psi}{\partial x} = 0 = \dfrac{\partial \psi}{\partial y}$

This *stream-function vorticity* approach is an alternative to the direct or "primitive" variable approach of solving for (u, v, p) in Eqs. (2-97) to (2-99). Equations (2-103) and (2-104) are convenient to numerical analysis and were used in the first (hand-calculated) CFD solution, Thom (1933), known to this writer.

2-11.1 Creeping Flow: $Re \ll 1$

If the viscosity is very large, the Reynolds number UL/ν is very small, $Re \ll 1$, and the right-hand side of Eq. (2-103) dominates. We are left with a linear fourth-order equation:

$$Re \ll 1: \qquad\qquad \nabla^4 \psi = 0 \qquad\qquad (2\text{-}105)$$

This is the two-dimensional *biharmonic* equation for "creeping flow." Many solutions are known from elasticity, Timoshenko and Goodier (1970), which can be adapted to creeping flow. A wide variety of low Reynolds number flows are treated in the monographs by Langlois (1964) and by Happel and Brenner (1983). We shall briefly treat this subject in Sec. 3-9.

2-12 NONINERTIAL COORDINATE SYSTEMS

By far the majority of flow problems are attacked in a fixed, or inertial, coordinate system. Cases do arise, though, such as the flow over rotating turbine blades or the geophysical boundary layer on a rotating earth, where we may wish to use noninertial coordinates moving with the accelerating system. Then we must modify Newton's law, Eq. (2-11), which is valid only if **a** is the absolute acceleration of the particle relative to inertial coordinates.

Suppose that (X, Y, Z) are in an inertial frame and that our chosen coordinates (x, y, z) are translating and rotating relative to that frame. Let **R** and Ω be the displacement and angular velocity vector of the (x, y, z) system relative to (X, Y, Z). Then, by straightforward vector calculus [see Greenwood (1988, pp. 49ff.)], we can relate the absolute acceleration **a** of a particle to its displacement **r** and velocity **V** relative to the moving system:

$$\mathbf{a} = \frac{d^2\mathbf{R}}{dt^2} + \frac{d\Omega}{dt} \times \mathbf{r} + \Omega \times (\Omega \times \mathbf{r}) + \frac{d\mathbf{V}}{dt} + 2\Omega \times \mathbf{V} \qquad (2\text{-}106)$$

Thus, if **V** is a noninertial velocity vector, the entire formidable right-hand side of Eq. (2-106) must replace the derivative $D\mathbf{V}/Dt$ in Eq. (2-12) or (2-19). However, we would be expected to know the functions $\mathbf{R}(t)$ and $\Omega(t)$ which relate the two systems, so that in a sense we are merely adding known inhomogeneities to the problem.

2-12.1 Geophysical Flows: The Rossby Number

A classic example of a noninertial system is the use of earth-fixed coordinates to calculate large-scale (geophysical) motions, where the earth's rotation cannot be neglected. In this case, the first three terms of Eq. (2-106) can be neglected, for three different reasons: (1) the first term is the earth's acceleration relative to the fixed stars and is surely almost zero; (2) the second term vanishes because $d\Omega/dt$ is nearly zero for the earth; and (3) the third term is nothing more than the earth's

centripetal acceleration, which essentially accounts for the variation of the gravity vector **g** with latitude. Thus, for geophysical flows,

$$\mathbf{a} \approx \frac{d\mathbf{V}}{dt} + 2\mathbf{\Omega} \times \mathbf{V} \qquad (2\text{-}107)$$

the second term of which is called the *Coriolis acceleration*, named after the French mathematician G. Coriolis, who was the first, in 1835, to study this phenomenon. If, as before, we use U and L to nondimensionalize this expression, we obtain

$$\mathbf{a}^* \approx \frac{d\mathbf{V}^*}{dt^*} + \frac{1}{Ro}(2\mathbf{\Omega}^* \times \mathbf{V}^*) \qquad (2\text{-}108)$$

where $Ro = U/\Omega L$ is the dimensionless Rossby number. It follows that the Coriolis term can be neglected if Ro is large, which will be true if the motion scale L is small compared to the earth's radius. We shall study a geophysical viscous flow (Ekman flow) in Chap. 3.

2-13   CONTROL-VOLUME FORMULATIONS

The expressions so far in this chapter have all been differential relations: fluid flow in the small, so to speak. We shall also have use for integral relations to calculate the gross fluxes of mass, momentum, and energy passing through a finite region of the flow. This is the control-volume approach now widely used in fluid mechanics [see White (2003), Chap. 3]. We shall content ourselves here with a fixed control volume; the text by Hansen (1967) treats moving and deformable control volumes.

Let the closed solid curve in Fig. 2-4 represent a finite region (control volume) through which a fluid flow passes. At any instant t, the region is filled by an aggregate of fluid particles which we shall call the *system*, i.e., a quantity of known identity. We wish to calculate the rate of change dB/dt of any gross property B (mass, kinetic energy, enthalpy, etc.) of the system at that instant t. We do this by a limiting process: At time $t + \Delta t$, the system has passed on slightly to the right, as indicated by the dotted lines in Fig. 2-4 and suggested by the streamline arrows.
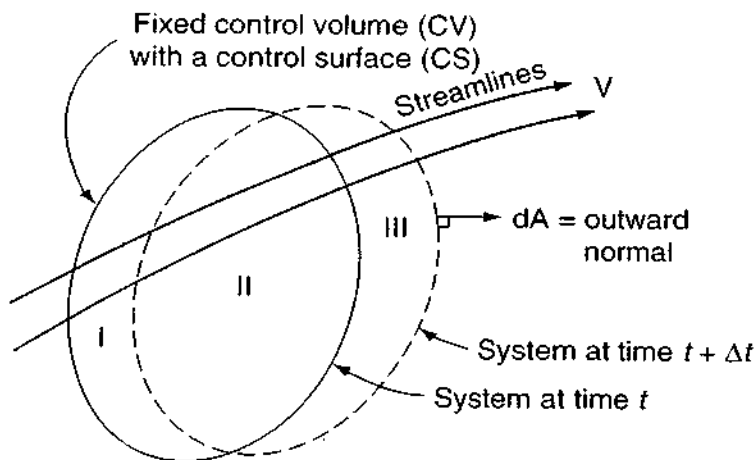
FIGURE 2-4
Sketch of a control volume.

The slight motion has outlined three regions, I, II, and III, as marked on the figure. The limit we are looking for is

$$\frac{dB}{dt} \text{ (system at } t) = \lim_{\Delta t \to 0} \frac{(B_{II} + \Delta B_{III})_{t+\Delta t} - (\Delta B_{I} + B_{II})_t}{\Delta t}$$

$$= \lim_{\Delta t \to 0} \left[\frac{(B_{II})_{t+\Delta t} - (B_{II})_t}{\Delta t} + \frac{\Delta B_{III}}{\Delta t} - \frac{\Delta B_{I}}{\Delta t} \right] \quad (2\text{-}109)$$

As shown in undergraduate texts, such as White (2003), Sec. 3.2, the region II terms in the brackets become the rate of change of B within the control volume. The region III term is the outflow of B, and the region I term is the inflow of B into the control volume. By the device of defining the area vector $d\mathbf{A}$ as having the direction of the *outward* normal to the control surface (see Fig. 2-4), we can account for outflow and inflow with a single dot product. The final limit is

$$\frac{dB}{dt} = \frac{d}{dt} \int_{CV} \frac{dB}{dm} \rho \, d(vol) + \int_{CS} \frac{dB}{dm} \rho \mathbf{V} \cdot d\mathbf{A} \quad (2\text{-}110)$$

This general relation is often called the *Reynolds transport theorem*. We can apply this formulation to any property B. Here we select mass, momentum, and energy.

2-13.1 Conservation of Mass

The relevant property is $B = $ mass m, and $dm/dm = 1$. Equation (2-110) becomes

$$\frac{dm}{dt} = 0 = \frac{d}{dt} \int_{CV} \rho \, d(vol) + \int_{CS} \rho \mathbf{V} \cdot d\mathbf{A} \quad (2\text{-}111)$$

This relation must be true for any fixed control volume and will be very useful in boundary-layer theory, Chap. 4. As an exercise, one can show, using Gauss' theorem, that Eq. (2-111) is identical to the differential equation of continuity, Eq. (2-6).

2-13.2 Conservation of Linear Momentum

The relevant property is $B = $ linear momentum $m\mathbf{V}$, and $d(m\mathbf{V})/dm = \mathbf{V}$ itself. Equation (2-110) becomes equal to the total force $\mathbf{F}$ acting on the system passing through the control volume:

$$\mathbf{F} = \frac{d}{dt}(m\mathbf{V}) = \frac{d}{dt} \int_{CV} \mathbf{V} \rho \, d(vol) + \int_{CS} \mathbf{V}(\rho \mathbf{V} \cdot d\mathbf{A}) \quad (2\text{-}112)$$

It is emphasized that this relation holds only for an inertial control volume. The force $\mathbf{F}$ includes both surface forces on the control surface and body forces on the mass within. Equation (2-112) was first applied to viscous boundary layers by Kármán (1921).

2-13.3 Conservation of Energy

The relevant property is B = total energy E, and we denote $dE/dm = e_t$. Recall the first law of thermodynamics, Eq. (1-59), $dE = dQ + dW$. Equation (2-110) becomes

$$\frac{dE}{dt} = \frac{dQ}{dt} + \frac{dW}{dt} = \frac{d}{dt}\int_{CV} e_t\, \rho\, d(vol) + \int_{CS} e_t\, \rho \mathbf{V} \cdot d\mathbf{A} \qquad (2\text{-}113)$$

where

$$e_t = \frac{dE}{dm} = e + \tfrac{1}{2} V^2 - \mathbf{g} \cdot \mathbf{r}$$

The work term dW includes work on the boundaries of normal and shear stresses plus any shaft work added to the system:

$$W = W_{\text{normal stress}} + W_{\text{shear stress}} + W_{\text{shaft}} \qquad (2\text{-}114)$$

Equation (2-113) may be applied to boundary layers to determine the heat transfer.

2-13.4 The Steady-Flow Energy Equation

An important special case of Eq. (2-113) occurs in steady flow when the control volume consists of fixed solid walls plus a simple one-dimensional inlet and outlet, as shown in Fig. 2-5. The work of boundary forces is zero at the fixed walls because of the no-slip condition. Further, if the inlet and outlet flows are approximately uniform and parallel, we may reasonably neglect viscous normal stresses there, so that the only important boundary work is due to pressure forces at inlet and outlet. The term d/dt vanishes for steady flow, and Eq. (2-113) reduces to

$$\frac{dQ}{dt} + \frac{dW_{\text{shaft}}}{dt} - \iint_{CS} p\mathbf{V} \cdot d\mathbf{A} = \iint_{CS} e_t\, \rho \mathbf{V} \cdot d\mathbf{A} \qquad (2\text{-}115)$$

But the only contributions to $\mathbf{V} \cdot d\mathbf{A}$ are $-V_1 A_1$ and $+V_2 A_2$ at the inlet and outlet, respectively. Thus we can carry out the integration to yield two terms

$$\frac{dQ}{dt} + \frac{dW_s}{dt} = \left(\frac{p}{\rho} + e + \tfrac{1}{2}V^2 + gz\right)_2 \rho_2 A_2 V_2$$

$$-\left(\frac{p}{\rho} + e + \tfrac{1}{2}V^2 + gz\right)_1 \rho_1 A_1 V_1 \qquad (2\text{-}116)$$

ρ_1, V_1, A_1 dQ dW_{shaft} dW_{shear} = 0 at walls and normal ρ_2, V_2, A_2 Fixed casing
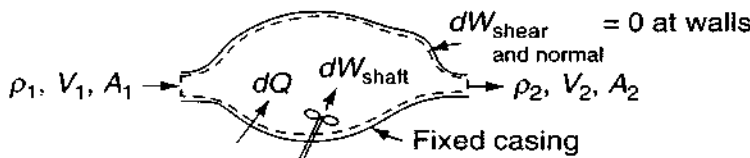
FIGURE 2-5

Sketch for the one-dimensional steady-flow energy equation.

where we have introduced $(-\mathbf{g} \cdot \mathbf{r}) = +gz$, implying as before the choice of the gravity direction $\mathbf{g} = -g\mathbf{k}$. For steady flow, $\rho_1 A_1 V_1 = \rho_2 A_2 V_2$ equals the mass flow rate dm/dt through the control volume. Also, the quantity $p/\rho + e$ is the fluid enthalpy h. We divide through by dm/dt to achieve the familiar form

$$\frac{dQ}{dm} + \frac{dW_s}{dm} = \left(h + \tfrac{1}{2}V^2 + gz \right)_2 - \left(h + \tfrac{1}{2}V^2 + gz \right)_1 \qquad (2\text{-}117)$$

which we recognize as the so-called steady-flow energy equation, stating that the change in total enthalpy $h + \tfrac{1}{2}V^2 + gz$ equals the sum of the heat and shaft-work addition per unit mass. The formula does not hold in boundary-layer theory unless we are careful to define our control volume to match Fig. 2-5 conditions.

SUMMARY

It is the role of this chapter to derive and discuss the basic equations of viscous fluid flow: conservations of mass, momentum, and energy plus the auxiliary state relations. The various boundary conditions and coordinate systems are discussed, and dimensionless parameters are derived and related to particular classes of flow. Stream-function and vorticity approaches are discussed, and the basic relations are also derived in integral form for finite control volumes. It is the purpose of the remainder of this text to attack these equations as best we can for particular classes of viscous flow.

PROBLEMS

2-1. By consideration of the cylindrical elemental control volume shown in Fig. P2-1, use the conservation of mass to derive the continuity equation in cylindrical coordinates [App. B, Eq. (B-3)].
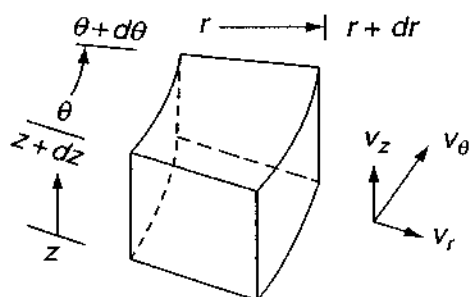
FIGURE P2-1

2-2. Simplify the equation of continuity in cylindrical coordinates (r, θ, z) to the case of steady compressible flow in polar coordinates $(\partial/\partial z = 0)$ and derive a stream function for this case.

2-3. Simplify the equation of continuity in cylindrical coordinates to the case of steady compressible flow in axisymmetric coordinates $(\partial/\partial\theta = 0)$ and derive a stream function for this case.

Answer: $\partial\psi/\partial r = \rho r v_z;\ \partial\psi/\partial z = -\rho r v_r$

2-4. For steady incompressible flow with negligible viscosity, show that the Navier–Stokes relation [Eq. (2-30)] reduces to the condition that $p/\rho + |V|^2/2 + gh$ is constant along a streamline of the flow, where h denotes the height of the fluid particle above a horizontal datum. This is the weaker form of the so-called Bernoulli relation.

2-5. Show that for incompressible steady flow with negligible viscosity and thermal conductivity, the energy Eq. (2-40) reduces to the condition that $e + p/\rho + |V|^2/2 + gh$ is constant along a streamline of the flow. This is the stronger form of Bernoulli's relation.

2-6. Consider the proposed incompressible axisymmetric flow field $v_z = C(R^2 - r^2)$, $v_r = 0$ in the region $0 \le z \le L, 0 \le r \le R$, where C is a constant. (a) Determine if this is an exact solution of the Navier–Stokes equation. (b) What might it represent? (c) If an axisymmetric stream function $\psi(r, z)$ exists for this flow, find its form.

2-7. Investigate the two-dimensional stream function $\psi = Cxy$, with C a constant, to determine whether it can represent (a) a realistic incompressible frictionless flow and (b) a realistic incompressible viscous flow. Sketch some streamlines of the flow.

2-8. Investigate a proposed plane stream function for isothermal incompressible flow: $\psi = C(x^2 y - y^3/3)$, where C is a constant. Determine whether this flow is an exact solution for constant μ and, if so, find the pressure distribution $p(x, y)$ and plot a few representative streamlines.

2-9. Consider the following incompressible plane unsteady flow:

$$v_r = 0 \qquad v_\theta = \frac{C}{r}\left[1 - \exp\left(-\frac{r^2}{4t\nu}\right)\right]$$

where C and ν are constant and gravity is neglected. Is this an exact solution of the continuity and Navier–Stokes equations? If so, plot some velocity profiles for representative times. Is there any vorticity in the flow? If so, plot some vorticity profiles.

2-10. Using the expression for dissipation Φ from Eq. (2-46), prove the inequalities about μ and λ given by Eq. (2-47).

2-11. The differential equation for irrotational plane compressible gas flow [Shapiro (1954), Chap. 9] is

$$\frac{\partial^2\phi}{\partial t^2} + \frac{\partial}{\partial t}(u^2 + v^2) + (u^2 - a^2)\frac{\partial^2\phi}{\partial x^2} + (v^2 - a^2)\frac{\partial^2\phi}{\partial y^2} + 2uv\frac{\partial^2\phi}{\partial x\,\partial y} = 0$$

where ϕ is the velocity potential and a the (variable) speed of sound in the gas. In the spirit of Sec. 2-9.1, nondimensionalize this equation and define any parameters which appear.

2-12. In flow at moderate to high Reynolds numbers, pressure changes scale with $(\rho_0 U_0^2)$, as in Eq. (2-83). In very viscous (low Reynolds number) flow, pressure scales as

$(\mu U_0/L)$. Make this change in Eqs. (2-83) and repeat the nondimensionalization of the Navier–Stokes equation. Define any parameters which arise and show what happens if the Reynolds number is very small.

2-13. The equations of motion for free convection near a hot vertical plate for incompressible flow with constant properties are

$$\frac{\partial u}{\partial x} + \frac{\partial v}{\partial y} = 0$$

$$u\frac{\partial u}{\partial x} + v\frac{\partial u}{\partial y} = g\beta(T - T_1) + \nu\left(\frac{\partial^2 u}{\partial x^2} + \frac{\partial^2 u}{\partial y^2}\right)$$

$$\rho c_p\left(u\frac{\partial T}{\partial x} + v\frac{\partial T}{\partial y}\right) = k\left(\frac{\partial^2 T}{\partial x^2} + \frac{\partial^2 T}{\partial y^2}\right)$$

Introduce the dimensionless variables

$$u^* = \frac{uL}{\nu} \qquad v^* = \frac{vL}{\nu} \qquad x^* = \frac{x}{L} \qquad y^* = \frac{y}{L} \qquad T^* = \frac{T - T_1}{T_0 - T_1}$$

where L is the length of the plate. Use these variables to nondimensionalize the free convection equations and define any parameters which arise.

2-14. For laminar flow in the entrance to a pipe, as shown in Fig. P2-14, the entrance flow is uniform, $u = U_0$, and the flow downstream is parabolic in profile, $u(r) = C(r_0^2 - r^2)$. Using the integral relations of Sec. 2-13, show that the viscous drag exerted on the pipe walls between 0 and x is given by

$$\text{Drag} = \pi r_0^2\left(p_0 - p_x - \tfrac{1}{3}\rho U_0^2\right)$$
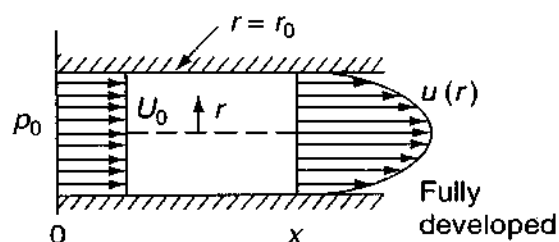
FIGURE P2-14

2-15. To illustrate "boundary-layer" behavior, i.e., the effect of the no-slip condition for large Reynolds numbers, Prandtl in a 1932 lecture proposed the following model (linear) differential equation:

$$\epsilon\frac{d^2u}{dy^2} + \frac{du}{dy} + u = 0 \qquad \epsilon \ll 1$$

where ϵ mimics the small viscosity of the fluid. The boundary conditions are (1) $u(0) = 2$, and (2) u remains bounded as y becomes large. Solve this equation for these conditions and plot the profile $u(y)$ in the range $0 < y < 2$ for $\epsilon = 0, 0.01$, and 0.1. Comment on the results. Is the plot for $\epsilon = 0$ the same as that obtained by setting $\epsilon = 0$ in the original differential equation and then solving?

2-16. Consider the plane, incompressible, Cartesian stream function in the region $0 \leq y \leq \infty$:

$$\psi = ax + by + \frac{b}{c} e^{-cy}$$

where (a, b, c) are positive constants. (a) Determine if this is an exact solution to the continuity and Navier–Stokes equations if gravity and pressure gradient are neglected. (b) What are the dimensions of (a, b, c)? (c) If $y = 0$ represents a wall, does the no-slip condition hold there? (d) Is there any vorticity in the flow field? If so, what is its form?

2-17. Use Eq. (2-86) for density in the gravity term of the Navier–Stokes equation (2-29b), let $\rho \approx \rho_0$ in the acceleration term, and let $\mu = $ constant. For free convection, with U replaced by $\mu/(\rho_0 L)$, nondimensionalize Navier–Stokes and show that the Grashof number appears.

2-18. Flow through a well-designed contraction or nozzle is nearly frictionless, as shown, for example, in White (2003), Sec. 6.12. Suppose that water at 20°C flows through a horizontal nozzle at a weight flow of 50 N/s. If entrance and exit diameters are 8 cm and 3 cm, respectively, and the exit pressure is 1 atm, estimate the entrance pressure from Bernoulli's equation.

2-19. Show, using Gauss' theorem [Kreyszig (1999), Sec. 9.8] that the control-volume mass relation, Eq. (2-111), leads directly to the partial differential equation of continuity, Eq. (2-6).

2-20. In discussing incompressible flow with constant μ, Eq. (2-30), we cavalierly said, "many terms vanish" from Eq. (2-29a). Be less cavalier and show that the many viscous terms in Eqs. (2-29a) do indeed reduce to the single vector term $\mu \nabla^2 V$, in three dimensions.

2-21. In deriving the basic equations of motion in this chapter, we skipped over the partial differential equation of *angular momentum*. Did we forget? Do some reading, perhaps in Lai et al. (1995) or Malvern (1997), and explain the significance of the angular momentum equation.

CHAPTER
3

SOLUTIONS
OF THE
NEWTONIAN
VISCOUS-FLOW
EQUATIONS

3-1   INTRODUCTION AND CLASSIFICATION
OF SOLUTIONS

The equations of continuity, momentum, and energy, derived in Chap. 2, are a formidable system of non-linear partial differential equations. No general analytical method exists, and no general existence or uniqueness theorems exist. For example, no exact solution is known for the thin airfoil problem of Fig. 1-1a, and certainly not for the stalled airfoil of Fig. 1-1b. However, the boundary-layer techniques of Chaps. 4 and 6 will be a good approximate tool for many problems. Meanwhile, for *laminar* flows, where no fine-scale turbulent fluctuations occur, computational fluid dynamics (CFD) is quite accurate, if rather specific, for a variety of flows and geometries. See, for example, Orszag et al. (1991), Chung (2002), Lomax et al. (2001), or Tannehill et al. (1997). For turbulent flow (Chap. 6), except for *direct numerical simulation* (DNS) at low Reynolds numbers, we must resort either to empirical correlations or use approximate CFD models that are reliable only for a limited subset of flow patterns.

In accumulating exact solutions, then, we are poor but not destitute. Over the past 150 years, a considerable number[†] of exact but particular solutions have been

---

[†]There are about 80 different cases, depending upon how one counts them. A large number are given by Berker (1963). See also Rogers (1992) and Profilo et al. (1998).

found which satisfy the complete equations for some special geometry. This chapter will outline some of these particular solutions, many of which are very illuminating about viscous-flow phenomena.

As we might expect, almost all the known particular solutions are for incompressible newtonian flow with constant transport properties, for which the basic equations [(2-6), (2-19), and (2-48)] reduce to

Continuity:
$$\text{div}\mathbf{V} = 0 \qquad (3\text{-}1)$$

Momentum:
$$\rho \frac{D\mathbf{V}}{Dt} = -\nabla\hat{p} + \mu\nabla^2\mathbf{V} \qquad (3\text{-}2)$$

Energy:
$$\rho c_p \frac{DT}{Dt} = k\nabla^2 T + \Phi \qquad (3\text{-}3)$$

where Φ denotes the dissipation function from Eq. (2-46) and $\hat{p}$ is the total hydrostatic pressure, i.e., it includes the gravity term for convenience:

or
$$\nabla\hat{p} = \nabla p - \rho\mathbf{g}$$
$$\hat{p} = p + \rho g z \qquad (3\text{-}2a)$$

where z is the vertical coordinate. The three unknowns in Eqs. (3-1) to (3-3) are $\mathbf{V}$, $\hat{p}$, and T. Note an important fact, mentioned earlier: Since we assume that μ is constant, Eqs. (3-1) and (3-2) are uncoupled from temperature and thus can be solved for $\mathbf{V}$ and $\hat{p}$ independently of T, after which T can be solved from Eq. (3-3). Note also that T itself is *not* independent of $\hat{p}$ or $\mathbf{V}$, since the velocity, which may be pressure-dependent, enters Eq. (3-3) through the terms Φ and $DT/Dt = \partial T/\partial t + \mathbf{V}\cdot\nabla T$. Because of this uncoupling of temperature in incompressible flows, many texts simply ignore the energy equation, but we consider T here to be very important, both practically and pedagogically.

Basically, there are two types of exact solutions of Eq. (3-2):

1. Linear solutions, where the convective acceleration $\mathbf{V}\cdot\nabla$ vanishes
2. Non-linear solutions, where $\mathbf{V}\cdot\nabla$ does not vanish

It is also possible to classify solutions by the type or geometry of flow involved:

1. Couette (wall-driven) steady flows
2. Poiseuille (pressure-driven) steady duct flows
3. Unsteady duct flows
4. Unsteady flows with moving boundaries
5. Duct flows with suction and injection
6. Wind-driven (Ekman) flows
7. Similarity solutions (rotating disk, stagnation flows, etc.)

These are the topics of the next seven sections of this chapter, after which we conclude with the creeping-flow approximation (Sec. 3-9) and digital computer solutions (Sec. 3-10).

Although a general solution is unattainable, particular exact solutions of Navier–Stokes are still being found. Here are some recent examples: a porous channel with moving walls, Dauenhauer and Majdalani (2003); oscillating flow in a rectangular duct, Tsangaris and Vlachakis (2003); chaotic flow in cylindrical tubes, Blyth et al. (2003); generalized Beltrami flows, Wang (1990); an unsteady stretching surface, Smith (1994); free shear layers, Varley and Seymour (1994); and two interacting vortices, Agullo and Verga (1997). For further study of laminar viscous flows, see the monographs by Constantinescu (1995), Ockendon and Ockendon (1995), and Papanastasiou et al. (1999).

3-2   COUETTE FLOWS DUE TO MOVING SURFACES

These flows are named in honor of M. Couette (1890), who performed experiments on the flow between a fixed and moving concentric cylinder. We consider several examples.

3-2.1   Steady Flow between a Fixed and a Moving Plate

In Fig. 3-1, two infinite plates are $2h$ apart, and the upper plate moves at speed U relative to the lower. The pressure $\hat{p}$ is assumed constant. The upper plate is held at temperature T_1 and the lower plate at T_0. These boundary conditions are independent of x or z ("infinite plates"); hence it follows that $u = u(y)$ and $T = T(y)$. Equations (3-1) to (3-3) reduce to

Continuity: $\quad\quad\quad\quad\quad \dfrac{\partial u}{\partial x} = 0$

Momentum: $\quad\quad\quad\quad 0 = \mu \dfrac{d^2 u}{dy^2}$ $\quad\quad\quad\quad\quad\quad\quad$ (3-4)

Energy: $\quad\quad\quad\quad\quad 0 = k \dfrac{d^2 T}{dy^2} + \mu \left(\dfrac{du}{dy}\right)^2$ $\quad\quad\quad\quad$ (3-5)
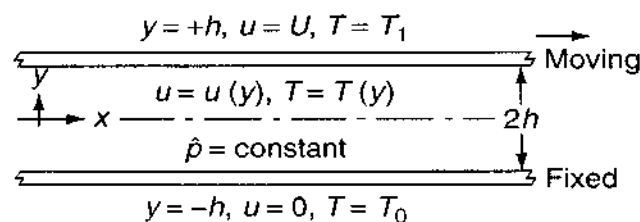
FIGURE 3-1
Couette flow between parallel plates.
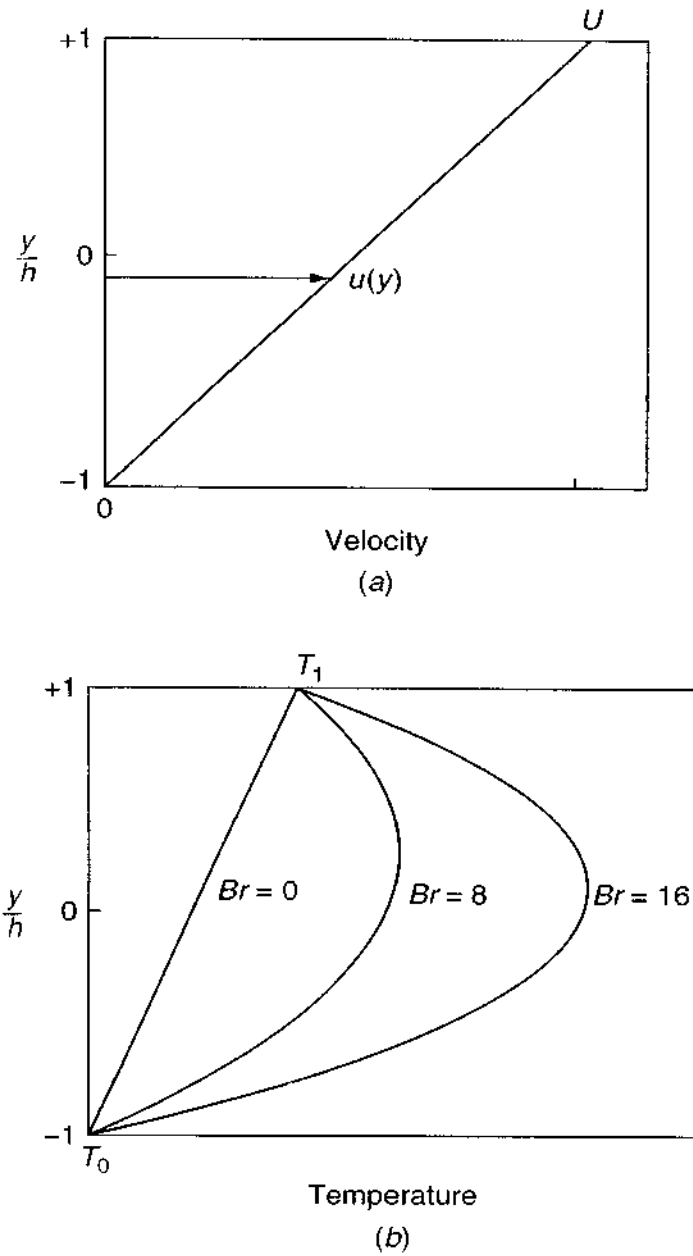
FIGURE 3-2

Couette flow between a fixed and a moving plate: (*a*) the velocity profile; (*b*) temperature profiles for various Brinkman numbers.

where continuity merely verifies our assumption that $u = u(y)$ only. Equation (3-4) can be integrated twice to obtain

$$u = C_1 y + C_2$$

The boundary conditions are no slip, $u(-h) = 0$ and $u(+h) = U$, whence $C_1 = U/2h$ and $C_2 = U/2$. Then the velocity distribution is

$$u = \frac{U}{2}\left(1 + \frac{y}{h}\right) \tag{3-6}$$

This is plotted in Fig. 3-2*a* and is seen to be a straight line connecting the no-slip condition at each plate. We term this plot a *velocity profile* and commonly sketch in line segments with arrows, as shown, to indicate motion. Since $\mu = $ const and we have neglected buoyancy, this profile is independent of the temperature distribution.

The shear stress at any point in the flow follows from the viscosity law:

$$\tau = \mu\left(\frac{\partial u}{\partial y} + \frac{\partial v}{\partial x}\right) = \mu\frac{du}{dy} = \frac{\mu U}{2h} = \text{const} \tag{3-7}$$

Thus for this simple flow, the shear stress is constant throughout the fluid, as is the strain rate—even a nonnewtonian fluid would maintain a linear velocity profile.

The dimensionless shear stress is usually defined in engineering flows as the *friction coefficient*,

$$C_f = \frac{\tau}{\frac{1}{2}\rho U^2} = \frac{\mu}{\rho U h} = \frac{1}{Re_h} \tag{3-8}$$

Thus the Reynolds number $Re_h = \rho U h/\mu$ arises naturally when the shear stress is nondimensionalized. Or perhaps *unnaturally* is more appropriate: Churchill (1988) points out that the Reynolds number is unsuitable for this nonaccelerating flow, since density does not play a part. He suggests that one should instead use the *Poiseuille number*,

$$Po = C_f Re_h = \frac{2h\tau}{\mu U} = 1 \tag{3-9}$$

Clearly a unit Poiseuille number is more convenient than a varying friction coefficient.

With $du/dy = U/2h$ known from Eq. (3-6), we may substitute into Eq. (3-5) and integrate twice to obtain the temperature distribution:

$$T = -\frac{\mu U^2}{4kh^2}\frac{y^2}{2} + C_3 y + C_4 \tag{3-10}$$

The no-temperature-jump conditions require $T(-h) = T_0$ and $T(+h) = T_1$, whence C_3 and C_4 can be evaluated. The final solution is

$$T = \left(\frac{T_1 + T_0}{2} + \frac{T_1 - T_0}{2}\frac{y}{h}\right) + \frac{\mu U^2}{8k}\left(1 - \frac{y^2}{h^2}\right) \tag{3-11}$$

The first term in parentheses represents the straight-line distribution which would arise due to pure conduction in the fluid. The second (parabolic) term is the temperature rise due to *viscous dissipation* in the fluid. The temperatures $T(y)$ from Eq. (3-11) are plotted in Fig. 3-2b. If T is nondimensionalized by $(T_1 - T_0)$, a dimensionless dissipation parameter arises naturally, the *Brinkman number*:

$$Br = \frac{\mu U^2}{k(T_1 - T_0)} = \frac{\mu c_p}{k}\frac{U^2}{c_p(T_1 - T_0)} = PrEc \tag{3-12}$$

From Fig. 3-2b, a Brinkman number of order unity or greater means that the temperature rise due to dissipation is significant. Qualitatively, it represents the ratio of dissipation effects to fluid conduction effects.

For low-speed flows, only the most viscous fluids (oils) have significant Brinkman numbers. For example, take $U = 10$ m/s and $(T_1 - T_0) = 10°C$ and compare the following numerical values for four fluids:

Fluid	$\mu(kg/m \cdot s)$	$k(W/m \cdot °C)$	Brinkman number
Air	1.8E–5	0.26	0.0007
Water	1.0E–3	0.60	0.017
Mercury	1.54E–3	8.7	0.0018
SAE 30 oil	0.29	0.145	20.0

Thus, except for heavy oils, we commonly neglect dissipation effects in low-speed flow temperature analyses.

To complete this lengthy initial-case discussion, we compute the rate of heat transfer at the walls:

$$q_w = \left| k\frac{\partial T}{\partial y}\right|_{\pm h} = \frac{k}{2h}(T_1 - T_0) \pm \frac{\mu U^2}{4h} \tag{3-13}$$

where the ($\pm$) refers to lower and upper surface, respectively. The first term on the right represents pure conduction through the fluid.

Since many convection analyses result in q_w being proportional to ΔT, it is customary to refer to their ratio as a *heat-transfer coefficient*:

$$\zeta = \frac{q_w}{T_1 - T_0} \tag{3-14}$$

One then nondimensionalizes ζ either as the Stanton number from Eq. (1-98) or, alternately, as the *Nusselt number*:

$$Nu_L = \frac{\zeta L}{k} = C_h Re_L Pr \tag{3-15}$$

where L is the characteristic length of the flow geometry. Here we select L as the plate separation distance ($2h$) and compute, from Eq. (3-13),

$$Nu_{2h} = \frac{2h\zeta}{k} = 1 \pm \frac{Br}{2} \tag{3-16}$$

where again the ($+$) means the lower surface. If $Br > 2$, both the upper and lower surfaces must be cooled to maintain their temperatures. Note that, since $Nu \approx 1$ for pure conduction, the numerical value of Nu represents the ratio of convective heat transfer to conduction for the same value of ΔT.

3-2.2 Axially Moving Concentric Cylinders

Consider two long concentric cylinders with a viscous fluid between them, as in Fig. 3-3. Let either the inner ($r = r_0$) cylinder move axially at $u = U_0$ or the outer ($r = r_1$) cylinder move at $u = U_1$, as shown. Let the pressure and temperature be constant for this example. The no-slip condition will set the fluid into steady motion $u(r)$, and u_θ and u_r will be zero. The equations of motion in cylindrical coordinates
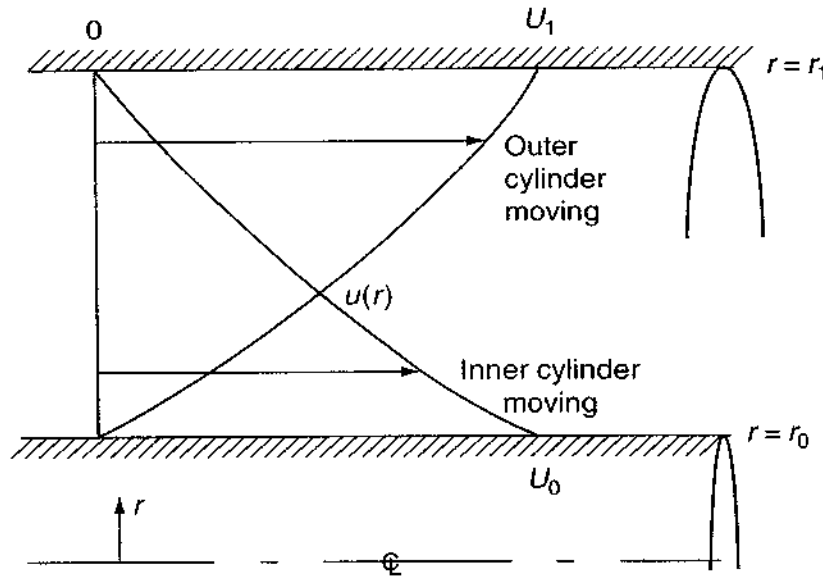
FIGURE 3-3

Axial annular Couette flow between concentric moving cylinders. The velocity distributions are plotted from Eqs. (3-18) and (3-19).

are given in App. B. Continuity is satisfied identically if $u = u(r)$, and the axial momentum equation reduces to

$$\nabla^2(u) = \frac{1}{r}\frac{\partial}{\partial r}\left(r\frac{\partial u}{\partial r}\right) = 0 \tag{3-17}$$

which is, like the previous example, independent of fluid properties. The solution has the form

$$u = C_1 \ln(r) + C_2$$

If the inner cylinder moves, the no-slip conditions are $u(r_0) = U_0$ and $u(r_1) = 0$, whence $C_1 = U_0/\ln(r_0/r_1)$ and $C_2 = -C_1\ln(r_1)$. The solution is

$$u = U_0\frac{\ln(r_1/r)}{\ln(r_1/r_0)}$$

$$\tau = \frac{-\mu U_0}{r\ln(r_1/r_0)} \tag{3-18}$$

Similarly, if, instead, the outer cylinder is moving, the boundary conditions are $u(r_0) = 0$ and $u(r_1) = U_1$, and the solution is

$$u = U_1\frac{\ln(r/r_0)}{\ln(r_1/r_0)}$$

$$\tau = \frac{\mu U_1}{r\ln(r_1/r_0)} \tag{3-19}$$

These two velocity distributions are sketched in Fig. 3-3; they are exactly analogous to temperature distributions $T(r)$ in pure conduction through the fluid. Note the

difference in curvature for the two cases: If the inner cylinder moves, $u(r)$ is concave, whereas it is convex if the outer cylinder moves.

The temperature distribution is given as a problem exercise, as is the question of what happens if both cylinders move at once.

3-2.3 Flow between Rotating Concentric Cylinders

Consider the steady flow maintained between two concentric cylinders by steady angular velocity of one or both cylinders. Let the inner cylinder have radius r_0, angular velocity ω_0, and temperature T_0, and the outer cylinder has r_1, ω_1, and T_1, respectively. The geometry is such that the only nonzero velocity component is u_θ and the variables u_θ, T, and p must be functions only of radius r. The equations of motion in polar coordinates [Eq. (2-64)] reduce to

Continuity:
$$\frac{\partial u}{\partial \theta} = 0$$

r momentum:
$$\frac{dp}{dr} = \frac{\rho u_\theta^2}{r} \tag{3-20}$$

θ momentum:
$$\frac{d^2 u_\theta}{dr^2} + \frac{d}{dr}\left(\frac{u_\theta}{r}\right) = 0$$

Energy:
$$0 = \frac{k}{r}\frac{d}{dr}\left(r\frac{dT}{dr}\right) + \mu\left(\frac{du_\theta}{dr} - \frac{u_\theta}{r}\right)^2$$

with boundary conditions at each cylinder.

At $r = r_0$: $u_\theta = r_0\omega_0$ $T = T_0$ $p = p_0$
At $r = r_1$: $u_\theta = r_1\omega_1$ $T = T_1$ \hfill (3-21)

The solution to the θ-momentum equation has the form

$$u_\theta = C_1 r + \frac{C_2}{r}$$

i.e., the sum of a solid-body rotation and a "potential" vortex whose Laplacian is zero. We may find C_1 and C_2 from the boundary conditions Eq. (3-21) and write the solution as the sum of inner and outer driven flows:

$$u_\theta = r_0\omega_0\frac{r_1/r - r/r_1}{r_1/r_0 - r_0/r_1} + r_1\omega_1\frac{r/r_0 - r_0/r}{r_1/r_0 - r_0/r_1} \tag{3-22}$$

If this velocity distribution is substituted into the energy equation in Eq. (3-20), the temperature distribution may be found as follows:

$$\frac{T - T_0}{T_1 - T_0} = PrEc\,\frac{r_1^4}{(r_1^2 - r_0^2)^2}\left[\left(1 - \frac{r_0^2}{r^2}\right) - \left(1 - \frac{r_0^2}{r_1^2}\right)\frac{\ln(r/r_0)}{\ln(r_1/r_0)}\right] + \frac{\ln(r/r_0)}{\ln(r_1/r_0)}$$

$$\tag{3-23}$$

where $PrEc = \mu r_0^2 \omega_0^2 / k(T_1 - T_0)$ is the Brinkman number expressing the temperature rise due to dissipation. If $PrEc = 0$, T reduces to the simple heat-conduction solution. The evaluation of the pressure $p(r)$ is left as an exercise.

Some special cases are of interest. In the limit as the inner cylinder vanishes $(r_0, \omega_0 = 0)$, we obtain from Eq. (3-22):

$$u_\theta = \omega_1 r = \text{const} \qquad (3\text{-}24)$$

i.e., steady outer rotation of a tube filled with fluid induces solid-body rotation.

In the limit as the outer cylinder becomes very large and remains fixed $(\omega_1 = 0, r_1 \to \infty)$, we obtain

$$u_\theta = \frac{r_0^2 \omega_0}{r} \qquad (3\text{-}25)$$

This is a *potential vortex*, driven by the rotating cylinder with the no-slip condition. As anyone who paddles a canoe knows, a vortex, if not maintained by a driving moment, will decay. Two examples of decaying vortex distributions are given as end-of-chapter Probs. 3-14 and 3-22.

Figure 3-4a shows velocity distributions for various (r_1/r_0), when only the inner cylinder is rotating. Figure 3-4b shows the temperature distributions for the single case $r_1/r_0 = 5$ from Fig. 3-4a.

Another interesting special case is that of very small clearance between the cylinders, $r_1 - r_0 \ll r_0$. Again let the outer cylinder remain stationary. Equation (3-22) becomes, in the limit,

Small clearance:
$$\frac{u_\theta}{r_0 \omega_0} \approx 1 - \frac{r - r_0}{r_1 - r_0} \qquad (3\text{-}26)$$

which is a linear Couette flow between effectively parallel plates, as in Fig. 3-1. In Fig. 3-4a, the approach to linearity is already being hinted at for $r_1/r_0 = 2$. The
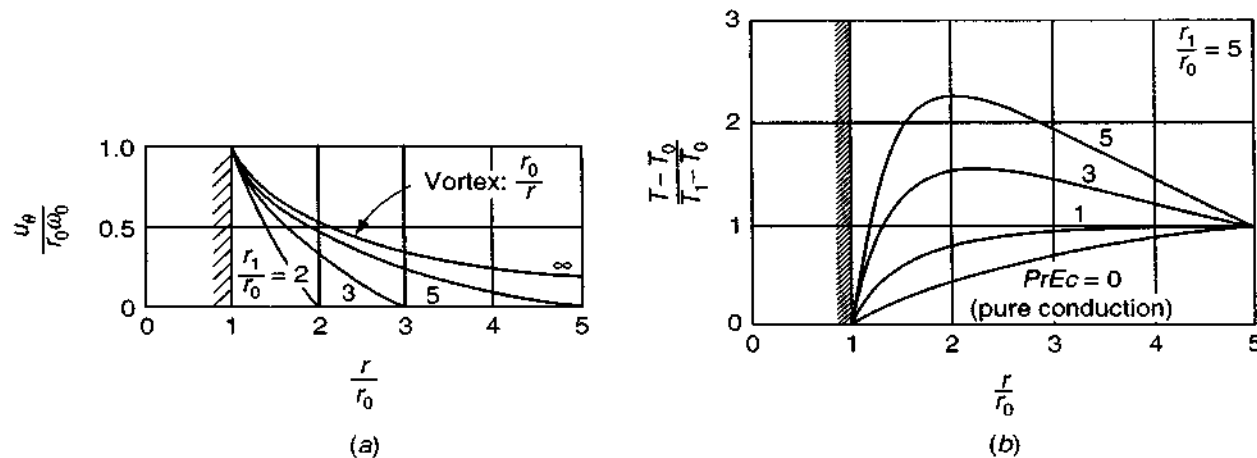
FIGURE 3-4
Velocity and temperature distributions between a stationary outer and a rotating inner cylinder, Eqs. (3-22) and (3-23): (a) velocity distribution; (b) temperature distribution for $r_1/r_0 = 5$.

velocity gradient is high, and hence a wide variety of shear stresses can be generated in a small-clearance apparatus.

Of interest in viscometry is the moment or torque exerted by the cylinders upon each other. This moment is independent of r and has the value (per unit depth of cylinder) of

$$M = 4\pi\mu \, \frac{r_1^2 r_0^2}{r_1^2 - r_0^2} \, (\omega_1 - \omega_0) \tag{3-27}$$

By knowing the geometry and measuring M at either cylinder, one can calculate the viscosity of the fluid, as first suggested by Couette (1890). This is still a popular method in viscometry.

3-2.4 Stability of Couette Flows

All of the solutions in this section are exact steady-flow solutions of the Navier–Stokes equations. They are called *laminar* flows and have a smooth-streamline character. It is known that all laminar flows become *unstable* at a finite value of some critical parameter, usually the Reynolds number. A different type of flow then ensues, sometimes still laminar or, more often, an entirely new fluctuating flow regime called *turbulent*.

The laminar straight-line profile of flow between plates, Fig. 3-2a, is valid only up to $Re_h = Uh/\nu \approx 1500$. Above this value, the pattern changes into a randomly fluctuating flow whose time-mean S-shaped profile is shown in Fig. 3-5. This shape, sketched from data given by Reichardt (1956), varies slightly with the Reynolds number and increases the wall shear (and heat-transfer rate) by two orders of magnitude. We will discuss these effects in detail in Chaps. 5 and 6.
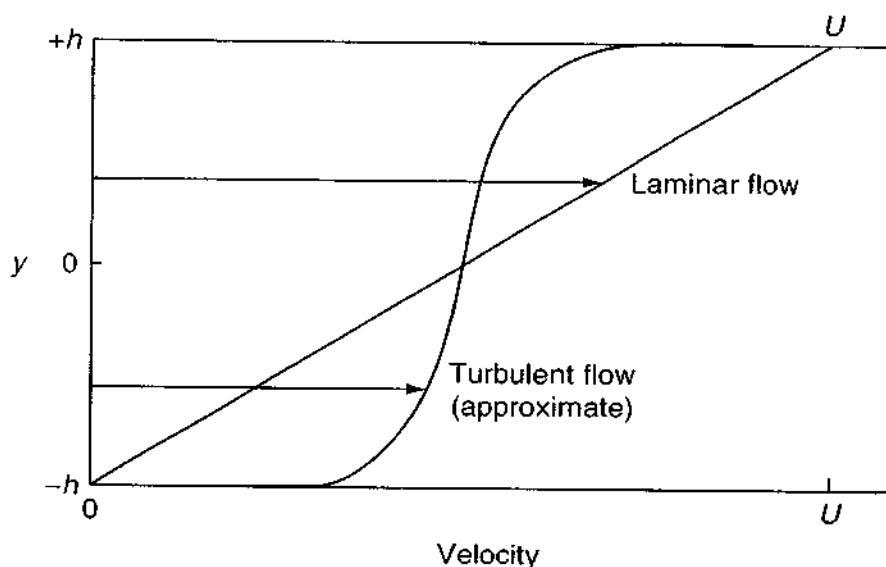
FIGURE 3-5

Instability of Couette flow between parallel plates: The straight-line laminar profile of Eq. (3-6) is valid only up to $Re_h = Uh/\nu = 1500$. [*Reichardt (1956)*.]

The axial annular flows of Fig. 3-3 are also unstable. Experiments by Polderman et al. (1986), with the inner cylinder moving, show fully turbulent flow at a clearance Reynolds number $Re_c = U_0(r_1 - r_0)/\nu \geq 7000$. The probable point of "transition" from laminar to turbulent flow, not reported, is about $Re_c \approx 2000$.

Although early work [Rayleigh (1916)] indicated that the rotating inner cylinder flows of Fig. 3-4a are unstable for all rotation rates, a classic paper by Taylor (1923) showed that the laminar profiles are valid until a critical rotation rate. For small clearance, $(r_1 - r_0) \ll r_0$, the critical value for instability is given by the *Taylor number*:

$$Ta = r_0(r_1 - r_0)^3 \frac{\omega_0^2}{\nu^2} \approx 1700$$

Above this value, the pattern changes into strikingly different three-dimensional laminar flow consisting of counterrotating pairs of toroidal vortices—see Fig. 5-22a.

All laminar flows are subject to instability. Therefore, all the exact solutions in this chapter are, in principle, valid only for a certain finite range of their governing parameter, e.g., the Reynolds number.

3-3 POISEUILLE FLOW THROUGH DUCTS

Whereas Couette flows are driven by moving walls, Poiseuille flows are generated by pressure gradients, with application primarily to ducts. They are named after J. L. M. Poiseuille (1840), as a French physician who experimented with low-speed flow in tubes.

Consider a straight duct of arbitrary but constant shape, as illustrated in Fig. 3-6. There will be an *entrance effect*, i.e., a thin initial shear layer and core acceleration as depicted in Fig. 1-10. The shear layers grow and meet, and the core disappears within a fairly short entrance length L_e. Shah and London (1978) show that, regardless of duct shape, the entrance length can be correlated for laminar flow
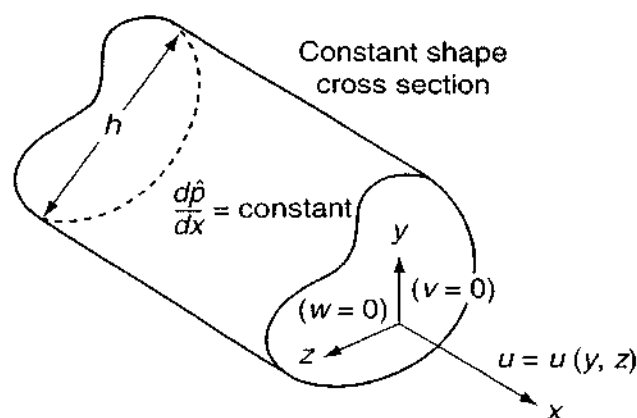
FIGURE 3-6
Fully developed duct flow.

in the form

$$\frac{L_e}{D_h} \approx C_1 + C_2 Re_{D_h} \tag{3-28}$$

where $C_1 \approx 0.5$, $C_2 \approx 0.05$, and D_h is a suitable "diameter" scale for the duct. Since transition to turbulence occurs at about $Re \approx 2000$, L_e is thus limited to, at most, 100 diameters.

For $x > L_e$, the velocity becomes purely axial and varies only with the lateral coordinates, that is, $v = w = 0$ and $u = u(y, z)$. The flow is then called *fully developed*, as depicted in Fig. 3-6. For fully developed flow, the continuity and momentum equations for incompressible flow, Eqs. (3-1) and (3-2) reduce to

Continuity:
$$\frac{\partial \mu}{\partial x} = 0$$

Momentum:
$$0 = -\frac{\partial \hat{p}}{\partial x} + \mu \left(\frac{\partial^2 u}{\partial y^2} + \frac{\partial^2 u}{\partial z^2} \right) \tag{3-29}$$

$$0 = -\frac{\partial \hat{p}}{\partial y} = -\frac{\partial \hat{p}}{\partial z}$$

These indicate that the total pressure $\hat{p}$ is a function only of x for this fully developed flow. Further, since u does not vary with x, it follows from the x-momentum equation that the gradient $d\hat{p}/dx$ must only be a (negative) constant. Then the basic equation of fully developed duct flow is

$$\frac{\partial^2 u}{\partial y^2} + \frac{\partial^2 u}{\partial z^2} = \frac{1}{\mu} \frac{d\hat{p}}{dx} = \text{const} \tag{3-30}$$

subject only to the no-slip condition $u_w = 0$ everywhere on the duct surface. This is the classic Poisson equation and is equivalent to the torsional stress problem in elasticity [see, e.g., Timoshenko and Goodier (1970)] for a simply connected cross section.[*] Thus there are many known solutions for different duct shapes, especially well summarized by Berker (1963). Shah and London (1978) tabulate and chart both the laminar friction and heat-transfer characteristics of many different shapes. If new shapes arise, Eq. (3-30) is easily solved by complex-variable or numerical techniques.

Note that, like the Couette flow problems of the previous section, the acceleration terms vanish here, taking the density with them. These flows then are creeping flows in the sense that they are independent of density, even though the Reynolds number need not be small, as was required in Sec. 2-11. The Reynolds number is not even a required parameter (except to specify the stability limits),

---

[*] The duct problem is more restrictive for a multiply connected section than the torsion problem, which does not require that u vanish on the surfaces of the inner holes in the cross section.

but it is usually introduced artificially anyway. There is no characteristic velocity U and no axial length scale L either, since we are supposedly far from the entrance or exit. The proper scaling of Eq. (3-30) should include μ, $d\hat{p}/dx$, and some characteristic duct width h, as suggested in Fig. 3-6. Thus the dimensionless variables are

$$y^* = \frac{y}{h} \qquad z^* = \frac{z}{h} \qquad u^* = \frac{\mu u}{h^2(-d\hat{p}/dx)} \tag{3-31}$$

where the negative pressure gradient is needed to make u^* a positive quantity. In terms of these variables, Eq. (3-30) becomes

$$\nabla^{*2}(u^*) = -1 \tag{3-32}$$

subject to $u^* = 0$ at all points on the boundary of the duct cross section.

3-3.1   The Circular Pipe: Hagen–Poiseuille Flow

The circular pipe is perhaps our most celebrated viscous flow, first studied by Hagen (1839) and Poiseuille (1840). The single variable is $r^* = r/r_0$, where r_0 is the pipe radius. The Laplacian operator reduces to

$$\nabla^2 = \frac{1}{r}\frac{d}{dr}\left(r\frac{d}{dr}\right)$$

and the solution of Eq. (3-32) is

$$u^* = -\tfrac{1}{4}r^{*2} + C_1 \ln r^* + C_2 \tag{3-33}$$

Since the velocity cannot be infinite at the centerline, on physical grounds, we reject the logarithm term and set $C_1 = 0$. The no-slip condition is satisfied by setting $C_2 = +\tfrac{1}{4}$. The pipe-flow solution is thus

$$u = \frac{-d\hat{p}/dx}{4\mu}(r_0^2 - r^2) \tag{3-34}$$

Thus the velocity distribution in fully developed laminar pipe flow is a paraboloid of revolution about the centerline (the *Poiseuille paraboloid*). The total volume rate of flow Q is of interest, as defined for any duct by

$$Q = \int_{\text{section}} u \, dA$$

where the element of area is $2\pi r \, dr$ for this pipe case. The integration is simple and yields

$$Q_{\text{pipe}} = \frac{\pi r_0^4}{8\mu}\left(-\frac{d\hat{p}}{dx}\right) \tag{3-35}$$

The mean velocity is defined by $\bar{u} = Q/A$ and gives, in this case

$$\bar{u} = \frac{r_0^2(-d\hat{p}/dx)}{8\mu} = \frac{1}{2} u_{max} \qquad (3\text{-}36)$$

Finally, the wall shear stress is constant and is given by

$$\tau_w = \mu\left(-\frac{du}{dr}\right)_w = \frac{1}{2} r_0\left(-\frac{d\hat{p}}{dx}\right) = \frac{4\mu\bar{u}}{r_0} \qquad (3\text{-}37)$$

Even though τ_w is proportional to mean velocity (laminar flow), it is customary, anticipating turbulent flow, to nondimensionalize wall shear with the pipe *dynamic pressure*, $\rho\bar{u}^2/2$, by analogy with Eq. (3-8). Two different friction factor definitions are in common use in the literature:

$$\lambda = \frac{8\tau_w}{\rho\bar{u}^2} = \text{Darcy friction factor}$$

$$C_f = \frac{2\tau_w}{\rho\bar{u}^2} = \frac{1}{4}\lambda = \text{Fanning friction factor, or skin-friction coefficient} \qquad (3\text{-}38)$$

By substituting into Eqs. (3-38), we obtain the classic relations

$$\lambda = \frac{64}{Re_D}$$

$$C_f = \frac{16}{Re_D} \qquad (3\text{-}39)$$
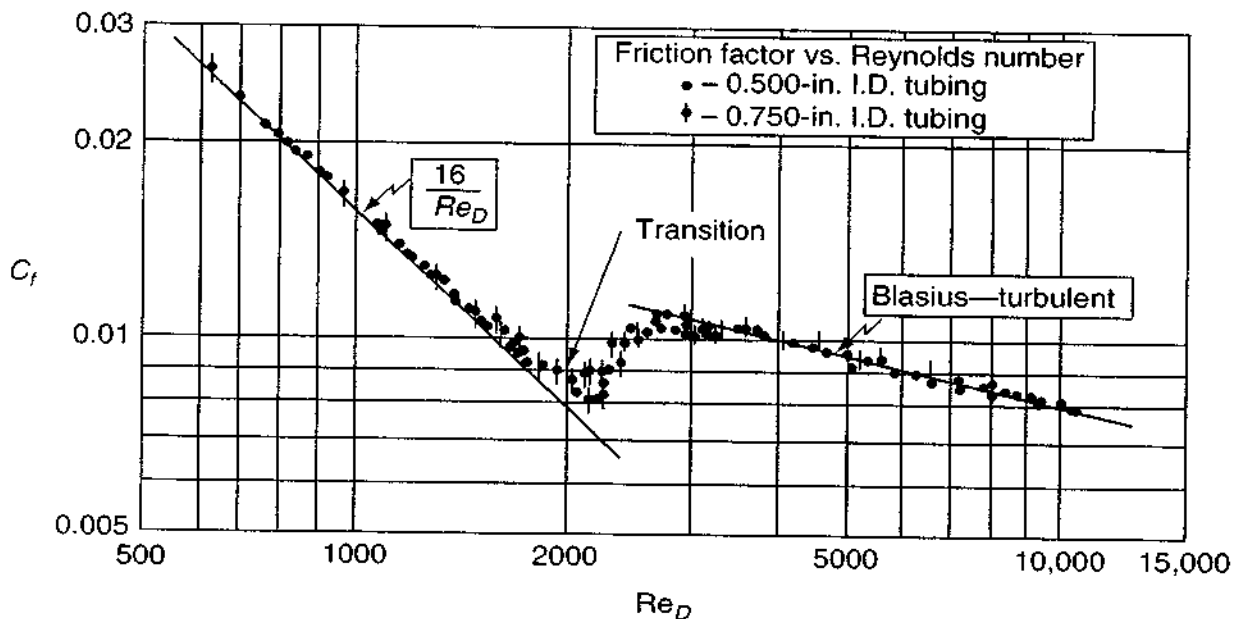
FIGURE 3-7

Comparison of theory and experiment for the friction factor of air flowing in small-bore tubles. [*After Senecal and Rothfus (1953).*]

As with Couette flow, Eq. (3-9), the Poiseuille number makes a lot more sense in laminar tube flow, being a pure constant:

$$Po = C_f Re_D = \frac{2\tau_w D}{\mu \bar{u}} = 16$$

This classic laminar-flow solution is in good agreement with experiment, as shown in Fig. 3-7, from the data of Senecal and Rothfus (1953). The flow undergoes transition to turbulence at approximately $Re_D \approx 2000$, a value which can be raised somewhat by taking care to eliminate flow disturbances. Above $Re_D \approx 3000$, the pipe flow is fully turbulent. The curve labeled "Blasius" is a curve fit to turbulent-flow data, $C_f \approx 0.0791/Re_D^{1/4}$, by Prandtl's student H. Blasius (1913)—one of the first demonstrations of the power of dimensional analysis.

3-3.1.1   MICROFLOWS: TUBE FLOW OF GASES WITH SLIP. The classical Poiseuille flow, Eq. (3-34), is for no-slip conditions at the walls. If the Knudsen number, $Kn = \ell/D$, is not small, due to either small D or large ℓ, slip will occur at the walls, and the flow rate and velocity will increase for a given pressure gradient. In Eq. (3-33), C_1 will still be zero, but C_2 must satisfy the slip condition of Eq. (1-91): $u_w = \ell(\partial u/\partial r)$ at $r = r_0$. When the new value of C_2 is found, the velocity and flow rate become

$$u = \frac{-d\hat{p}/dx}{4\mu}\left(r_0^2 - r^2 + 2\ell r_0\right)$$

$$Q = \frac{\pi r_0^4}{8\mu}\left(-\frac{d\hat{p}}{dx}\right)\left(1 + 8\frac{\ell}{D}\right) \tag{3-40}$$

Thus the flow rate is increased over the no-slip case by the fraction $8\ell/D = 8Kn$. If we require, for example, that the slip flow-rate effect be less than 2 percent, then Kn must be less than 0.0025. This is why we stated in Sec. 1-4.2 that $Kn = \mathcal{O}(0.1)$ is not small enough, slip would occur. The complete derivation of Eqs. (3-40) is given as an end-of-chapter problem.

Equations (3-40) are applicable to gases. For *liquid* slip flows, as a first approximation, one could replace the mean free path ℓ by the slip length L_{slip} defined in Eq. (1-89). For further reading on microchannel flows, see the monograph by Karniadakis and Bestok (2001).

3-3.2   Combined Couette–Poiseuille Flow Between Plates

Return now to our first Couette flow example, Fig. 3-1, and impose a constant pressure gradient $(d\hat{p}/dx)$ on the flow in addition to the moving upper wall. We now

solve the differential equation

$$\mu \frac{d^2u}{dy^2} = \frac{d\hat{p}}{dx} = \text{const} \tag{3-41}$$

subject to the no-slip condition $u(-h) = 0$. The solution is

$$\frac{u}{U} = \frac{1}{2}\left(1 + \frac{y}{h}\right) + P\left(1 - \frac{y^2}{h^2}\right) \quad P = \left(-\frac{dp}{dx}\right)\frac{h^2}{2\mu U} \tag{3-42}$$

This relation is a superposition, possible because the non-linear convective acceleration is zero, of Couette wall-driven flow (the first term) and Poiseuille pressure-driven flow (the second term). It is plotted in Fig. 3-8 for various values of the dimensionless pressure gradient P. Of particular interest is the dashed line, $P = -\frac{1}{4}$, for which the shear stress $\mu(\partial u/\partial y)$ at the lower wall is zero. For $P < -\frac{1}{4}$ there is *backflow* at the lower wall, an indication of "flow separation" in unbounded shear layers (Chap. 4). In terms of the "thickness" $(2h)$ of the shear layer, we may write the separation criterion $P = -\frac{1}{4}$ in the form

$$\frac{dp}{dx}\frac{(2h)^2}{\mu U} = 2 \tag{3-43}$$

This is identical in form to the laminar-boundary-layer separation estimates to be discussed in Chap. 4, except that the constant "2" is too small.
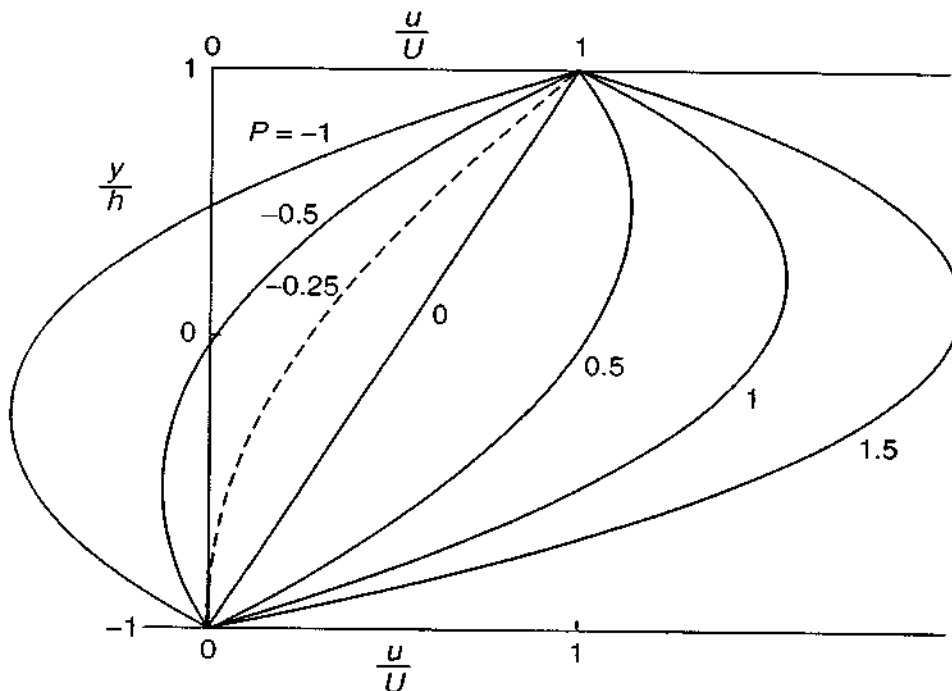
FIGURE 3-8

Combined Couette–Poiseuille flow between parallel plates, from Eq. (3-42). Backflow or "flow separation" occurs if $P < -\frac{1}{4}$.

If $U = 0$ (fixed walls), Eq. (3-42) reduces to pure Poiseuille flow between parallel plates:

$$u = u_{max}\left(1 - \frac{y^2}{h^2}\right)$$

$$u_{max} = \left(-\frac{dp}{dx}\right)\frac{h^2}{2\mu}$$

(3-44)

This is similar to laminar pipe flow, Eq. (3-34). The flow rate per unit depth is

$$Q = \int_{-h}^{+h} u\, dy = \frac{4}{3} h u_{max}$$

or   (3-45)

$$\bar{u} = \frac{Q}{2h} = \frac{2}{3} u_{max}$$

The wall shear stress is $\tau_w = 3\mu\bar{u}/h$ or, in dimensionless form,

$$C_f = \frac{6\mu}{\rho\bar{u}h}$$

or   (3-46)

$$Po = C_f Re_h = 6$$

Thus, except for differences in numerical constants, Poiseuille flow between plates is identical in form to laminar pipe flow.

3-3.3 Noncircular Ducts

Since Eq. (3-32) for fully developed duct flow is equivalent to a classic Dirichlet problem, it is not surprising that an enormous number of exact solutions are known

| Circle | Rectangle | Ellipse | Concentric annulus |
| Eq. (3-34) | Eq. (3-48) | Eq. (3-47) | Eq. (3-51) |

| Half moon | Circular sector | Eccentric annulus | Equilateral triangle | Limaçon |
| Berker (1963) | Eq. (3-50) | Eq. (3-52) | Eq. (3-49) | Berker (1963) |
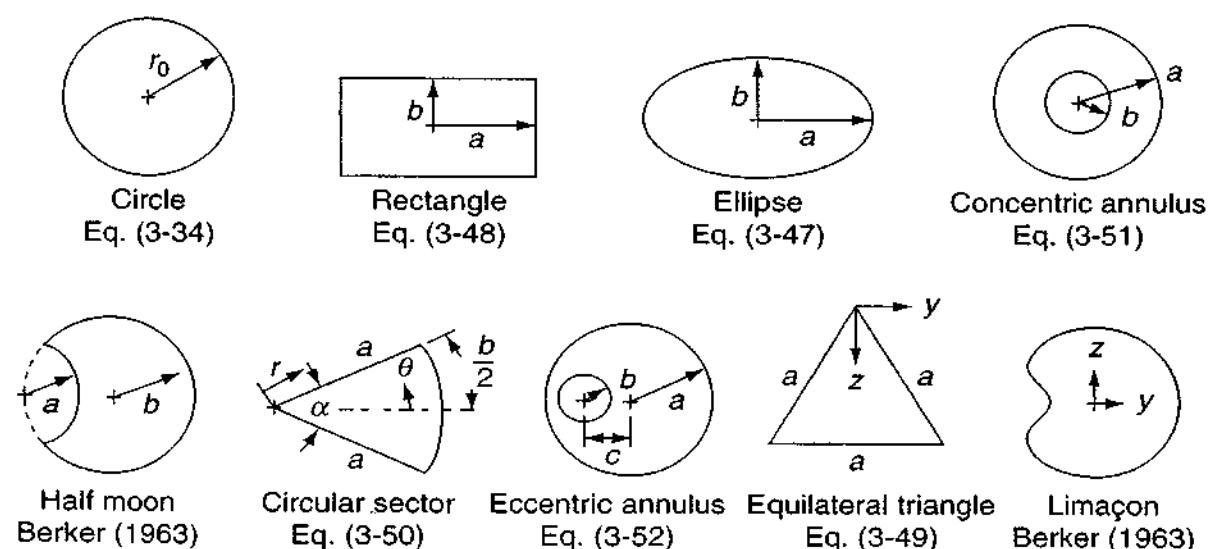
FIGURE 3-9

Some cross sections for which fully developed flow solutions are known; for still more, consult Berker (1963, pp. 67ff.) or Shah and London (1978).

for noncircular shapes, as reviewed by Berker (1963). Some of these shapes are shown in Fig. 3-9. Each solution is fascinating, but our mathematical ardor should be dampened somewhat by the practical fact that limaçon-shaped ducts, for example, are not commercially available at present. Nevertheless we list a few of these solutions because they lead to a valuable approximate principle, the *hydraulic radius*.

Elliptical section: $y^2/a^2 + z^2/b^2 \leq 1$:

$$u(y, z) = \frac{1}{2\mu}\left(-\frac{d\hat{p}}{dx}\right)\frac{a^2b^2}{a^2 + b^2}\left(1 - \frac{y^2}{a^2} - \frac{z^2}{b^2}\right)$$

$$Q = \frac{\pi}{4\mu}\left(-\frac{d\hat{p}}{dx}\right)\frac{a^3b^3}{a^2 + b^2}$$

(3-47)

Rectangular section: $-a \leq y \leq a, -b \leq z \leq b$:

$$u(y, z) = \frac{16a^2}{\mu\pi^3}\left(-\frac{d\hat{p}}{dx}\right)\sum_{i=1,3,5,\ldots}^{\infty}(-1)^{(i-1)/2}\left[1 - \frac{\cosh(i\pi z/2a)}{\cosh(i\pi b/2a)}\right]$$

$$\times \frac{\cos(i\pi y/2a)}{i^3}$$

(3-48)

$$Q = \frac{4ba^3}{3\mu}\left(-\frac{d\hat{p}}{dx}\right)\left[1 - \frac{192a}{\pi^5 b}\sum_{i=1,3,5,\ldots}^{\infty}\frac{\tanh(i\pi b/2a)}{i^5}\right]$$

Equilateral triangle of side a: coordinates in Fig. 3-9:

$$u(y, z) = \frac{-d\hat{p}/dx}{2\sqrt{3}\,a\mu}\left(z - \frac{1}{2}a\sqrt{3}\right)(3y^2 - z^2)$$

$$Q = \frac{a^4\sqrt{3}}{320\mu}\left(-\frac{d\hat{p}}{dx}\right)$$

(3-49)

Circular sector: $-\frac{1}{2}\alpha \leq \theta \leq +\frac{1}{2}\alpha, 0 \leq r \leq a$:

$$u(r, \theta) = \frac{d\hat{p}/dx}{4\mu}\left[r^2\left(1 - \frac{\cos 2\theta}{\cos \alpha}\right) - \frac{16a^2\alpha^2}{\pi^3}\right.$$

$$\left.\times \sum_{i=1,3,5,\ldots}^{\infty}(-1)^{(i+1)/2}\left(\frac{r}{a}\right)^i\frac{\cos(i\pi\theta/\alpha)}{i(i + 2\alpha/\pi)(i - 2\alpha/\pi)}\right]$$

$$Q = \frac{a^4}{4\mu}\left(-\frac{d\hat{p}}{dx}\right)$$

(3-50)

$$\times \left[\frac{\tan \alpha - \alpha}{4} - \frac{32\alpha^4}{\pi^5}\sum_{i=1,3,5,\ldots}^{\infty}\frac{1}{i^2(i + 2\alpha/\pi)^2(i - 2\alpha/\pi)}\right]$$

Concentric circular annulus: $b \leq r \leq a$:

$$u(r) = \frac{-d\hat{p}/dx}{4\mu}\left[a^2 - r^2 + (a^2 - b^2)\frac{\ln(a/r)}{\ln(b/a)}\right]$$

$$Q = \frac{\pi}{8\mu}\left(-\frac{d\hat{p}}{dx}\right)\left[a^4 - b^4 - \frac{(a^2 - b^2)^2}{\ln(a/b)}\right] \tag{3-51}$$

This is but a sample of the wealth of solutions available. The formula for a concentric annulus is important in viscometry, with a measured Q being used to calculate μ. To increase the pressure drop, the clearance $(a - b)$ is held small, in which case Eq. (3-51) for Q becomes the difference between two nearly equal numbers. However, if we expand the bracketed term [ ] in a series, the result is

$$(a^4 - b^4) - \frac{(a^2 - b^2)^2}{\ln(a/b)} = \frac{4}{3}b(a - b)^3 + \frac{2}{3}(a - b)^4 + \cdots + \mathcal{O}(a - b)^5$$

so that Q for small clearance is seen to be cubic in $(a - b)$.

The eccentric annulus in Fig. 3-9 has practical applications, for example, when a needle valve becomes misaligned. The solution was given by Piercy et al. (1933), using an elegant complex-variable method which transformed the geometry to a concentric annulus, for which the solution was already known, Eq. (3-51). We reproduce here only their expression for volume rate of flow:

$$Q = \frac{\pi}{8\mu}\left(-\frac{d\hat{p}}{dx}\right)\left[a^4 - b^4 - \frac{4c^2M^2}{\beta - \alpha} - 8c^2M^2\sum_{n=1}^{\infty}\frac{ne^{-n(\beta+\alpha)}}{\sinh(n\beta - n\alpha)}\right] \tag{3-52}$$

where
$$M = (F^2 - a^2)^{1/2} \qquad F = \frac{a^2 - b^2 + c^2}{2c}$$

$$\alpha = \frac{1}{2}\ln\frac{F + M}{F - M} \qquad \beta = \frac{1}{2}\ln\frac{F - c + M}{F - c - M}$$

Flow rates computed from this formula are compared in Fig. 3-10 to the concentric result $Q_{c=0}$ from Eq. (3-51). It is seen that eccentricity substantially increases the flow rate, the maximum ratio of $Q/Q_{c=0}$ being 2.5 for a narrow annulus of maximum eccentricity. The curve for $b/a = 1$ can be derived from lubrication theory:

Narrow annulus:
$$\frac{Q}{Q_{c=0}} = 1 + \frac{3}{2}\left(\frac{c}{a - b}\right)^2 \tag{3-53}$$

The reason for the increase in Q is that the fluid tends to bulge through the wider side. This is illustrated for one case in Fig. 3-11, where the wide side develops a set of closed high-velocity streamlines. This effect is well known to piping engineers, who have long noted the drastic leakage that occurs when a nearly closed valve binds to one side.
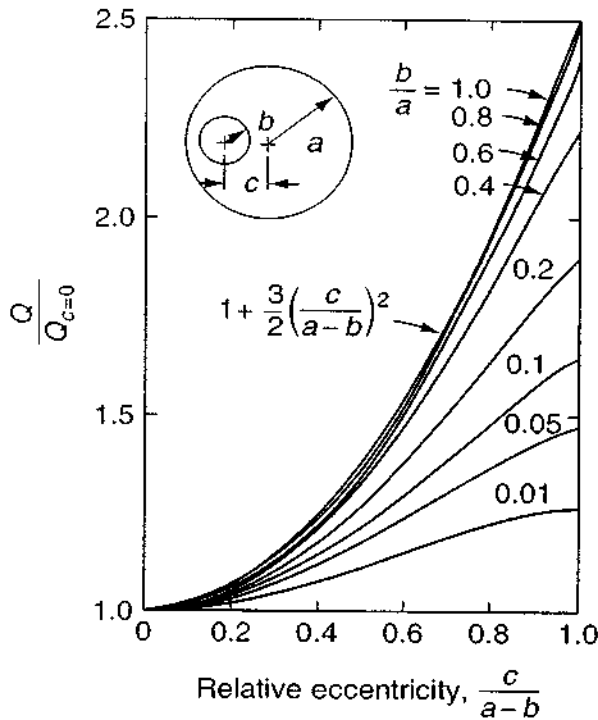
FIGURE 3-10

Volume flow through an eccentric annulus as a function of eccentricity, Eq. (3-52).
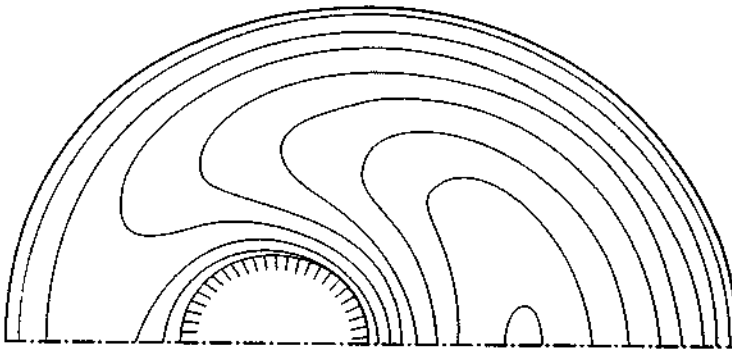
FIGURE 3-11

Constant-velocity lines for an eccentric annulus, $b/a = c/a = \frac{1}{4}$. [*After Piercy et al. (1933)*.]

3-3.4 The Concept of Hydraulic Diameter

The definition of λ proposed in Eq. (3-39) fails for a noncircular duct since τ_w varies around the perimeter. For example, in the equilateral-triangle duct, Eq. (3-49), τ_w is zero in the corners and a maximum at the midpoints of the sides. The remedy, at least partially, is to define a mean wall shear stress

$$\overline{\tau}_w = \frac{1}{P}\int_0^P \tau_w \, ds$$

where ds = element of arc length
$\quad\quad P$ = perimeter of section

It we isolate a slug of fluid passing through the duct as in Fig. 3-12 and note that there is no net momentum flux due to the fully developed flow, we can equate the
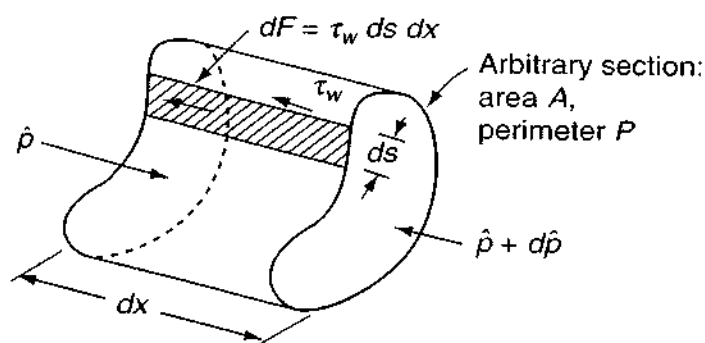
FIGURE 3-12
Force equilibrium in fully developed arbitrary duct flow.

net pressure and wall shear force on the fluid as follows:

$$dx \int_0^P \tau_w \, ds = -A \, d\hat{p}$$

or, from the definition of mean shear, we have

$$\bar{\tau}_w = \frac{A}{P}\left(-\frac{d\hat{p}}{dx}\right) \tag{3-54}$$

which is entirely analogous to Eq. (3-38) for a circular duct. The quantity A/P is a length and equals $r_0/2$ if the duct is circular. For a noncircular duct, then, we set $A/P = D_h/4$, where D_h is called the *hydraulic diameter* of the cross section:

$$D_h = \frac{4A}{P} = \frac{4 \times \text{area}}{\text{wetted perimeter}} \tag{3-55}$$

For a cross section with multiple surfaces, P must include all wetted walls. For example, for the concentric annulus in Fig. 3-9, we have

$$D_h(\text{annulus}) = \frac{4\pi(a^2 - b^2)}{2\pi a + 2\pi b} = 2(a - b) \tag{3-56}$$

or twice the clearance. By dimensional reasoning for laminar fully developed flow, we are guaranteed that the friction factor of a noncircular duct will vary inversely with a Reynolds number based on hydraulic diameter:

$$C_f = \frac{\lambda}{4} = \frac{\text{const}}{Re_{D_h}} \qquad Re_{D_h} = \frac{\rho \bar{u} D_h}{\mu} \tag{3-57}$$

In other words, the Poiseuille number $Po = C_f Re$ remains constant for a noncircular duct. However—and this is the critical flaw—the constant usually does *not* equal 16 as it did for a circular pipe.

Using our many exact solutions from Eqs. (3-47) to (3-51), we may compute the value of $Po = C_f Re_{D_h}$ and plot them versus section slenderness ratio b/a in Fig. 3-13. We see that some are higher and some are lower than the nominal circle value of 16, and the error can be as high as 50 percent. For laminar flow, then, one should use the exact values of Po from Fig. 3-13 or the exact formulas given here or in Shah and London (1978).
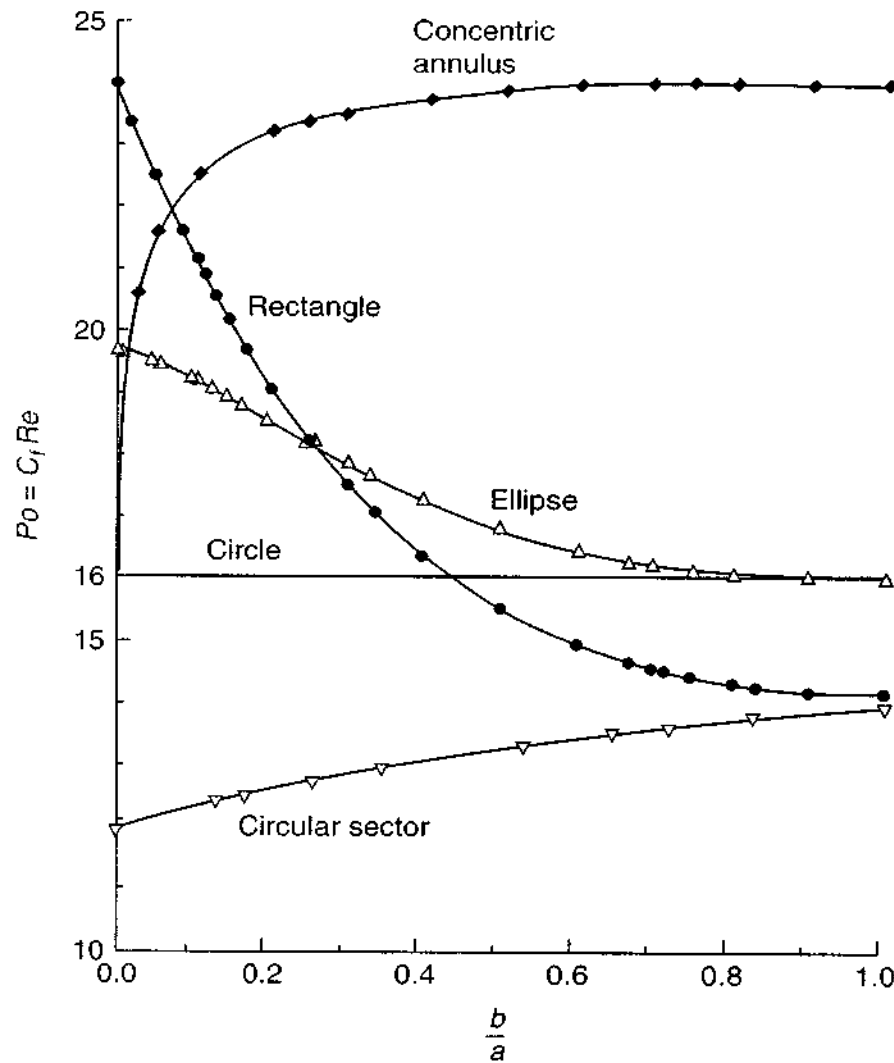
FIGURE 3-13

Comparison of Poiseuille numbers for various duct cross sections when the Reynolds number is scaled by the hydraulic diameter. [*Numerical data taken from Shah and London (1978).*]

We note for completeness that the equilateral triangle, Eq. (3-49), has a hydraulic diameter $D_h = a/\sqrt{3}$ and $C_f Re = 13.333$, or 17 percent low.

Especially vexing is the fact that the hydraulic diameter concept is insensitive to core eccentricity. The eccentric annulus in Fig. 3-10 has the same value $D_h = 2(a - b)$ regardless of the value of c, yet its flow rate may vary by over 100 percent depending upon c. Exact solutions are definitely needed.

The exact Poiseuille numbers in Fig. 3-13 are in very good agreement with the following laminar-flow experiments:

1. Rectangular and triangular ducts: Eckert and Irvine (1957)
2. Concentric annulus: Walker et al. (1957)

This is to be expected since, as far as we know, the Navier–Stokes equations are fundamentally correct for the common fluids and therefore should agree "exactly" with an accurate experiment.

Figure 3-13 has a surprising—and very relevant—use in an empirical method of determining the friction factor for *turbulent* flow in noncircular ducts for which the laminar solution is known—see Chap. 6.

3-3.5   Temperature Distribution in Fully Developed Duct Flow

The assumption of constant viscosity uncoupled the energy and momentum equations if natural convection was neglected, and we have solved for the velocity distribution in several ducts. With $u(y, z)$ known, Eq. (3-3) can be solved for T, which may be a function of (x, y, z), if the boundary conditions change with x. Equation (3-3) is linear in T, making it possible to examine some separate effects and add them together later, if desired. First let us look at the effect of viscous dissipation, assuming constant T_w. For the pipe case, T then equals $T(r)$ only, and Eq. (3-3) becomes

$$\frac{k}{r}\frac{d}{dr}\left(r\frac{dT}{dr}\right) = -\mu\left(\frac{du}{dr}\right)^2 = -\frac{16\mu\bar{u}^2 r^2}{r_0^4} \tag{3-58}$$

where we have introduced $u(r)$ from Eq. (3-34). Double integration leads to a logarithmic term which we discard to avoid a singularity at $r = 0$. Putting $T = T_w$ at $r = r_0$, we obtain

$$T = T_w + \frac{\mu\bar{u}^2}{k}\left(1 - \frac{r^4}{r_0^4}\right) \tag{3-59}$$

which is similar to Eq. (3-11) for flow between parallel plates. The maximum temperature rise $\mu\bar{u}^2/k$, at $\bar{u} = 100$ ft/s, is about $1°F$ for air and $3°F$ for water. Thus dissipation is usually neglected except for oils, where the viscosity is large, or in gas dynamics, where velocities are high (Chap. 7). The wall heat transfer is $q_w = k(dT/dr)$ at $r = r_0$, or $q_w = 4k(T_w - T_0)/r_0$, showing that the wall is being cooled to maintain constant T_w. The Nusselt number at the wall can be defined in the manner of Eq. (3-15), with L taken as the pipe diameter. Thus

$$Nu = \frac{q_w(2r_0)}{k(T_w - T_0)} = 8 \qquad \text{for viscous dissipation} \tag{3-60}$$

This is a substantial number, but, as noted, the driving temperature difference $T_w - T_0$ is usually very small.

3-3.6   Asymptotic Uniform Heat-Flux Approximation

Before attacking the thermal-entrance problem of a sudden change in wall temperature, consider the conditions far downstream of such an entrance. The temperature varies with x, but the deviation $T_w - T$ is nearly independent of x, and q_w is nearly

constant. Thus we specify

$$\frac{\partial}{\partial x}(T_w - T) = 0$$

$$\frac{q_w}{k} = \frac{\partial T}{\partial r} = \text{const} \tag{3-61}$$

Taken together, these require that the axial gradient be independent of r:

$$\frac{\partial T}{\partial x} = \frac{\partial T_w}{\partial x} = \text{const independent of } r \tag{3-62}$$

When we neglect (or separate out) dissipation, Eq. (3-3) becomes

$$\rho c_p u \frac{\partial T}{\partial x} = (\text{const}) \, u = \frac{k}{r} \frac{\partial}{\partial r}\left(r \frac{\partial T}{\partial r}\right) \tag{3-63}$$

which can be integrated twice; again we discard a logarithmic term. With $T = T_w$ at $r = r_0$, we obtain

$$T_w - T = \frac{c_p \bar{u} r_0^2}{8k} \frac{\partial T_w}{\partial x}\left(3 - \frac{4r^2}{r_0^2} + \frac{r^4}{r_0^4}\right) \tag{3-64}$$

from which we can calculate the Nusselt number. However, from a practical standpoint, Nu should not be based upon $T_w - T_0$ but upon a mean difference $T_w - T_m$, where T_m is the *cup-mixing temperature* of the fluid, computed by averaging T over the mass distribution of fluid in the pipe. Define

$$T_m = \frac{\int T \, dm}{\int dm} = \frac{\int_0^{r_0} T \rho u \, dA}{\int_0^{r_0} \rho u \, dA} \tag{3-65}$$

where $dA = 2\pi r \, dr$ for this case. For incompressible flow, the density cancels out. Using u from Eq. (3-34) for Poiseuille flow and T from Eq. (3-64), we obtain

$$T_w - T_m = \frac{11}{18}\left(\frac{3\rho c_p \bar{u} r_0^2}{8k} \frac{\partial T_w}{\partial x}\right) = \frac{11}{18}(T_w - T_0) \tag{3-66}$$

It is this temperature difference upon which engineers base the dimensionless wall heat-transfer, or Nusselt, number

$$Nu_m = \frac{q_w 2r_0}{k(T_w - T_m)} = \frac{48}{11} = 4.36 \qquad \text{asymptotic uniform heat flux} \tag{3-67}$$

A similar but algebraically more complicated solution for asymptotic constant wall temperature gives

$$Nu_m = 3.66 \tag{3-68}$$

as will be shown in the next section. These asymptotic values are more sensitive to duct cross section than to wall conditions. Calculations for other duct shapes (rectangular, triangular, etc.) are given by Shah and London (1978).
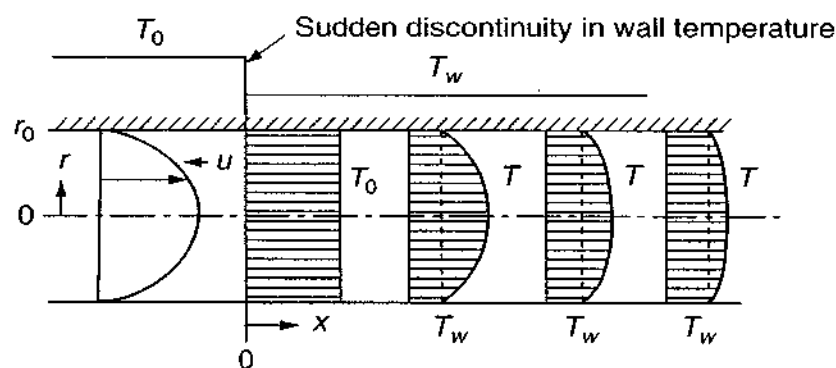
FIGURE 3-14
A thermal-entrance problem.

3-3.7 Thermal Entrance: The Graetz Problem

Now consider the problem of developing temperature profiles $T(x, r)$ in a pipe, due to a sudden change in wall temperature (Fig. 3-14). We neglect dissipation *and* axial heat conduction, for which Eq. (3-3) reduces to

$$u \frac{\partial T}{\partial x} \approx \frac{\alpha}{r} \frac{\partial}{\partial r}\left(r \frac{\partial T}{\partial r}\right) \tag{3-69}$$

where $\alpha = k/\rho c_p$ is the thermal diffusivity of the fluid. The velocity distribution $u(x, r)$ is assumed known in this equation and might be one of three types:

1. $u = \bar{u} = $ const, or slug flow: appropriate for low Prandtl number fluids (liquid metals), where T develops much faster than u
2. $u = 2\bar{u}(1 - r^2/r_0^2)$, or Poiseuille flow: appropriate for high Prandtl number fluids (oils) or when the thermal entrance is far downstream of the duct entrance
3. Developing u profiles (Sec. 4-9): suitable for any Prandtl number when the velocity and temperature entrance are at the same position

The thermal-entrance problem with a sudden change in wall temperature is illustrated in Fig. 3-14. The solution was given as an infinite series by Graetz (1883) for slug flow and another series in 1885 for Poiseuille flow. Further details and other geometries are given in the texts by Shah and London (1978) or by Kays and Crawford (1993).

With reference to Fig. 3-14, the proper boundary conditions on $T(x, r)$ for Eq. (3-69) are

$$T(0, r) = T_0; \qquad T(r_0, x) = T_w \tag{3-70}$$

Let us outline Graetz' solution for Poiseuille flow (case 2). Define dimensionless variables:

$$T^* = \frac{T_w - T}{T_w - T_0} \qquad r^* = \frac{r}{r_0} \qquad x^* = \frac{x}{d_0 \, RePr} \tag{3-71}$$

where $Re = \bar{u} d_0 / \nu$ is the diameter Reynolds number and Pr is the Prandtl number, or $RePr = \rho c_p \bar{u} d_0 / k$ is the Peclet number, named after the French physicist

J. C. E. Peclet. The variables in Eq. (3-71) convert Eqs. (3-69) and (3-70) to

$$\frac{\partial T^*}{\partial x^*} = \frac{2}{r^*(1 - r^{*2})} \frac{\partial}{\partial r^*}\left(r^*\frac{\partial T^*}{\partial r^*}\right) \quad \begin{array}{l} T^*(r^*, 0) = 1 \\ T^*(1, x^*) = 0 \end{array} \tag{3-72}$$

Note that Eqs. (3-72) are entirely independent of parameters because of our choice of variables (T^*, r^*, x^*). It is clear that the variables are separable, so that a product solution will work. Let

$$T^*(r^*, x^*) = f(r^*) g(x^*) \tag{3-73}$$

be a particular solution and substitute into Eq. (3-72). We obtain

$$\frac{g'}{2g} = \frac{r^*f'' + f'}{r^*(1 - r^{*2})f} = -\lambda^2 = \text{const} \tag{3-74}$$

The g function clearly has the solution $g = C \exp(-2\lambda^2 x^*)$, whereas the equation for f is somewhat less familiar. To make the product solution $T = fg$ satisfy the condition $T^*(r^*, 0) = 1$ for all r^*, we take advantage of linearity and superimpose many such solutions, so that the proper formulation is, finally,

$$T^*(r^*, x^*) = \sum_{n=0}^{\infty} C_n f_n(r^*) e^{-2\lambda_n^2 x^*} \tag{3-75}$$

where the functions f_n are characteristic solutions of Eq. (3-74):

$$r^*f_n'' + f_n' + \lambda_n^2 r^*(1 - r^{*2}) f_n = 0 \tag{3-76}$$

We take $f_n(0) = 1$ for simplicity and force $f_n(1) = 0$ to satisfy the wall-temperature condition $T^*(1, x^*) = 0$ from Eq. (3-72). Then the solution is complete if the other (initial) condition from Eq. (3-72) is satisfied:

$$T^*(r^*, 0) = 1 = \sum_{n=0}^{\infty} C_n f_n(r^*) \tag{3-77}$$

Graetz showed that the eigenfunctions f_n are orthogonal over the interval 0 to 1 with respect to the weighting function $r^*(1 - r^{*2})$. Thus, if one multiplies Eq. (3-77) by $r^*(1 - r^{*2})f_m$ and integrates from 0 to 1, the constants may be found as follows:

$$C_n = \frac{\int_0^1 r^*(1 - r^{*2}) f_n \, dr^*}{\int_0^1 r^*(1 - r^{*2}) f_n^2 \, dr^*} \tag{3-78}$$

The first 10 values are tabulated in Table 3-1. We remark that Eq. (3-76), with its two conditions $f_n(0) = 1$ and $f_n(1) = 0$, is an eigenvalue problem and can be satisfied only for certain discrete values of λ_n, the *eigenvalues* of the Graetz functions f_n. Table 3-1 gives the first 10 eigenvalues and their associated constants. These are sufficient to calculate Nusselt numbers for almost any given wall conditions, even an arbitrary distribution of T_w^*.

TABLE 3-1
Important constants in the Graetz problem

n	λ_n	C_n	$-C_n f'_n(1)$
0	2.7043644	+1.46622	1.49758
1	6.679032	−0.802476	1.08848
2	10.67338	+0.587094	0.92576
3	14.67108	−0.474897	0.83036
4	18.66987	+0.404402	0.76474
5	22.67	−0.35535	0.71571
6	26.67	+0.31886	0.67798
7	30.67	−0.29049	0.64711
8	34.67	+0.26769	0.62119
9	38.67	−0.24890	0.59900

For large n, Sellars et al. (1956) give the following approximations:

$$\lambda_n \approx 4n + \tfrac{8}{3}$$

$$C_n \approx (-1)^n \frac{2\Gamma\left(\tfrac{2}{3}\right)6^{2/3}}{\pi\lambda_n^{2/3}} = \frac{(-1)^n(2.8461)}{\lambda_n^{2/3}} \tag{3-79}$$

$$-C_n f'_n(1) \approx \frac{4\left(\tfrac{4}{3}\right)^{1/6}\Gamma\left(\tfrac{2}{3}\right)}{\pi\lambda_n^{1/3}\Gamma\left(\tfrac{4}{3}\right)} = \frac{2.0256}{\lambda_n^{1/3}}$$

These formulas have been used to compute the last five rows of Table 3-1 with an error of less than 0.15 percent.

To calculate the Nusselt number at the wall, we need the cup-mixing temperature, which we obtain by combining Eqs. (3-65) and (3-77):

$$T_m^* = 4\int_0^1 T^*(1 - r^{*2})r^* \, dr^* \tag{3-80}$$

Introducing T^* from Eq. (3-77), we obtain

$$Nu_x = \frac{2r_0 q_w}{k(T_w - T_m)} = \frac{\sum C_n f'_n(1)\exp(-2\lambda_n^2 x^*)}{2\sum C_n \lambda_n^{-2} f'_n(1)\exp(-2\lambda_n^2 x^*)} \tag{3-81}$$

which converges well except at very small x^*. For large x^* (> 0.05), the first term of the series is dominant, giving the asymptotic result

$$Nu_x(x^* > 0.05) \approx \frac{\lambda_0^2}{2} = 3.66 \tag{3-82}$$

which is the thermally fully developed result already mentioned in Eq. (3-68). For small x^*, the results fit the approximation

$$Nu_x \approx 1.076x^{*-1/3} - 1.064 \tag{3-83}$$

with an error no more than 1 percent for $x^* < 0.0004$.

3-3.8   Mean Nusselt Number

The total heat transferred to (or from) the wall is a useful quantity, since it equals the heat lost (or gained) by the fluid over the total length L of the tube. We define a mean wall heat flux per unit area

$$\bar{q}_w = \frac{1}{A_w} \int q_w \, dA_w = \frac{1}{L} \int_0^L q_w \, dx \tag{3-84}$$

This mean heat flux must exactly balance the enthalpy change of the fluid between $x = 0$ and $x = L$:

$$\bar{q}_w A_w = \rho \bar{u} c_p (\pi r_0^2)[T_m(L) - T_0] \tag{3-85}$$

so that $T_m(L)$ at the exit can be calculated from the mass flow rate in the tube. The dimensionless from $\bar{q}_w$ is called the mean Nusselt number:

$$Nu_m = \frac{2 r_0 \bar{q}_w}{k \Delta T} \tag{3-86}$$

and if T_w is variable, the choice of a suitable temperature difference ΔT is somewhat arbitrary. The reader may verify as an exercise that if one chooses the logarithmic mean-temperature difference,

$$\Delta T_{\ln} = \frac{[T_w(0) - T_m(0)] - [T_w(L) - T_m(L)]}{\ln\{[T_w(0) - T_m(0)]/[T_w(L) - T_m(L)]\}} \tag{3-87}$$

then Nu_m is simply the average value of Nu_x in the tube between 0 and L:

$$Nu_m(\text{log mean}) = \frac{2 r_0 \bar{q}_w}{k \Delta T_{\ln}} = \frac{1}{L} \int_0^L Nu_x \, dx \tag{3-88}$$

For the present Graetz problem (large Prandtl number), we can evaluate Nu_m by using the differential form of Eq. (3-85):

$$q_w 2 \pi r_0 \, dx = \rho \bar{u} \pi r_0^2 c_p \, dT_m$$

or

$$4 Nu_x \, dx^* = -dT_m^*/T_m^* \tag{3-89}$$

We can integrate this from $x^* = 0$, $T_m^* = 1$ to $x^* = L^*$, $T_m^* = T_m^*(L)$, with a starkly simple result:

$$Nu_m = \frac{-1}{4L^*} \ln T_m^*(L) \tag{3-90}$$

This is a general result for constant wall temperature. By carrying out the integration of Eq. (3-80), we find that

$$T_m^*(x^*) = \sum_{n=0}^{\infty} 4 C_n f_n'(1) \lambda_n^{-2} \exp(-2\lambda_n^2 x^*) \tag{3-91}$$

for Poiseuille flow.
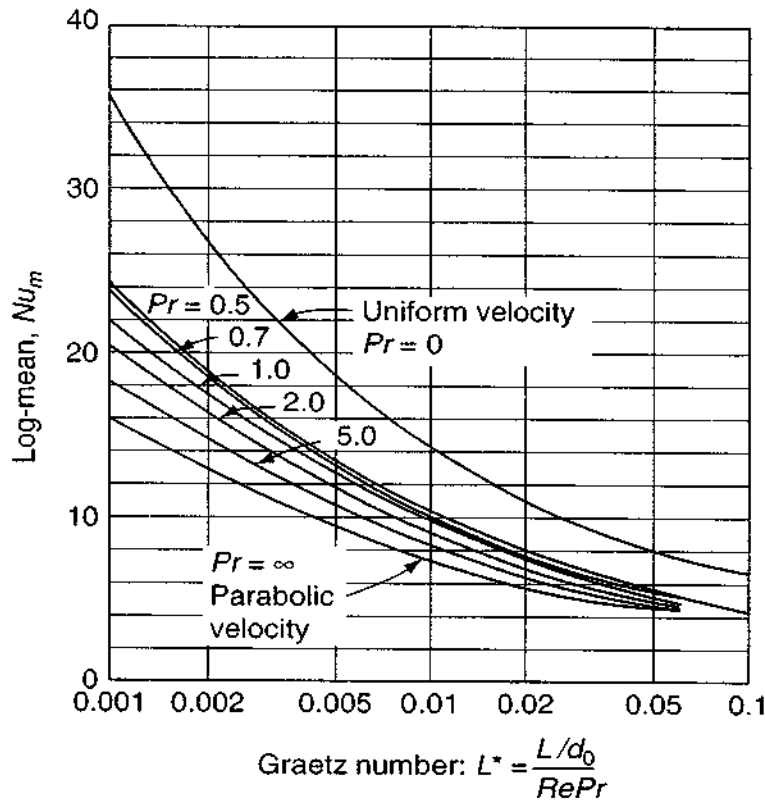
FIGURE 3-15

Finite-difference calculations for the log-mean Nusselt number in laminar pipe flow with developing velocity profiles. [*After Goldberg (1958).*]

Figure 3-15 shows the computations of Goldberg (1958) for a mean Nusselt number with velocity and temperature effects which are assumed to start at the same point, $x = 0$. The upper curve is for slug flow (type 1), valid for $Pr \ll 1$, that is, liquid metals. The lowest curve is for Poiseuille flow (type 2) for $Pr \gg 1$ (oils) and is computed from Eqs. (3-90) and (3-91). The intermediate curves are for type 3, where velocity and temperature develop together. Note that the abscissa is the *Graetz number*, $L^* = x^*(L)$, being based on diameter rather than r_0. The slug-flow curve ($Pr = 0$) is unique in that the parabolic velocity never develops and the limiting value of Nu_m is 5.78 at large L^* [Graetz (1883)].

All of the curves for finite Pr in Fig. 3-15 approach $Nu_m = 3.66$ at large L^*. We are reasonably close to this limit when $L^* \approx 0.05$. Thus we may define the *thermal-entrance length* in pipe flow as

$$L_{e, \text{thermal}} \approx 0.05 d_0 Re_D Pr \qquad (3\text{-}92)$$

This is in the same sprit as the velocity-entrance-length formula proposed in Eq. (3-28).

The Graetz problem, especially for oil flow, $Pr \gg 1$, has many practical applications. For computation, one may curve-fit the lower curve in Fig. 3-15 to a type of formula proposed by Hausen (1943)

$$Nu_m(Pr \gg 1) \approx 3.66 + \frac{0.075/L^*}{1 + 0.05/L^{*2/3}} \qquad (3\text{-}93)$$

where $L^* = (L/d_0)/(Re_D Pr)$. The error of this approximation is ± 5 percent.

Finally, we remark that the present analysis assumes constant fluid transport properties, whereas both liquids and gases have significant variations in μ and k with temperature. A first-order correction for this effect would be to evaluate fluid properties at the "film" temperature $(T_w + T_m)/2$. If the wall and fluid temperatures differ by more than 20°C, one should further correct the previous formulas for variable properties. Chapter 15 of the text by Kays and Crawford (1993) is a detailed discussion of these correction factors.

3-4   UNSTEADY DUCT FLOWS

Some interesting problems of unsteady duct flow can be worked out by retaining the fully developed flow assumption, and we give two examples here for circular pipe flow, with the same principle applying to other shapes. If we assume that the pipe axial velocity $u = u(r, t)$ only, with $v = w = 0$, then the continuity equation is identically satisfied and the momentum equation becomes

$$\rho \frac{\partial u}{\partial t} = -\frac{d\hat{p}}{dx} + \mu \left(\frac{\partial^2 u}{\partial r^2} + \frac{1}{r} \frac{\partial u}{\partial r} \right) \tag{3-94}$$

which is identical to the linear heat-conduction equation with a source term. The pressure gradient can vary only with time and thus represents a uniformly distributed heat source. Let us discuss two cases.

3-4.1   Starting Flow in a Circular Pipe

Suppose that the fluid in a long pipe is at rest at $t = 0$, at which time a sudden, uniform, and constant pressure gradient $d\hat{p}/dx$ is applied. An axial flow will commence which gradually approaches the steady Poiseuille flow

$$u = u_{\text{max}}(1 - r^{*2})$$

where $r^* = r/r_0$. This problem was solved by Szymanski (1932). The boundary conditions are

Initial condition: $u(r, 0) = 0$

No-slip condition: $u(r_0, t) = 0$ (3-95)

The variables will separate in Eq. (3-94) if we subtract the steady Poiseuille flow and work with the *deviation* of u from the Poiseuille paraboloid. This removes the inhomogeneity $d\hat{p}/dx$, and the solution of Eq. (3-94) is then of the form $u = J_0(\lambda r^*)\, e^{-\lambda^2 t^*}$, where J_0 denotes the Bessel function of the first kind. The no-slip condition requires $J_0(\lambda_n)$ to vanish for each value of the separation constant, i.e., the λ_n are the roots of the Bessel function. These are tabulated in Table 3-2. Since the J_0 function is not a paraboloid, we must sum the functions $J_0(\lambda_n r^*)$ to obtain a negative paraboloid and thus satisfy the initial condition of the fluid at rest. The coefficients are obtained from the usual theory of orthogonal functions, and the final

TABLE 3-2

First ten roots of the Bessel function $J_0^\dagger$

n	λ_n	$J_1(\lambda_n)$
1	2.4048	0.5191
2	5.5201	−0.3403
3	8.6537	0.2715
4	11.7915	−0.2325
5	14.9309	0.2065
6	18.0711	−0.1877
7	21.2116	0.1733
8	24.3525	−0.1617
9	27.4935	0.1522
10	30.6346	−0.1442

† For $n > 10$:

$$\lambda_n = \frac{(4n-1)\pi}{4} \qquad J_1(\lambda_n) \approx (-1)^{n+1}\left(\frac{2}{\pi\lambda_n}\right)^{1/2}$$

solution for this pipe starting-flow problem is

$$\frac{u}{u_{max}} = (1 - r^{*2}) - \sum_{n=1}^{\infty} \frac{8J_0(\lambda_n r^*)}{\lambda_n^3 J_1(\lambda_n)} \exp\left(-\lambda_n^2 \frac{vt}{r_0^2}\right) \qquad (3\text{-}96)$$

where $u_{max} = (-d\hat{p}/dx)r_0^2/4\mu$ from Eq. (3-37). Numerical results are plotted in Fig. 3-16 for various values of the dimensionless time vt/r_0^2. Two points are of particular interest: (1) initially a sort of boundary-layer effect occurs, where the central core of fluid accelerates uniformly (potential flow) but the wall region is retarded by friction; and (2) the flow is essentially the Poiseuille paraboloid when $t^* \approx 0.75$, giving us an estimate of how rapidly laminar tube flow responds to sudden change. Flows with small diameter and large viscosity will develop rapidly. Consider a 1 cm diameter tube. For air, $v = 1.5E{-}5$ m²/s, the value $t^* = 0.75$ translates to $t = 1.25$ s. For SAE 30 oil under the same conditions,
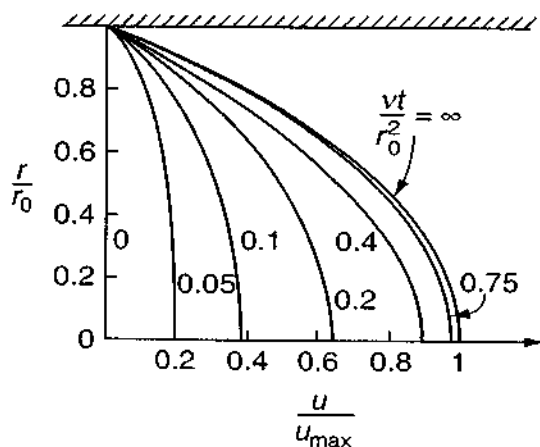
FIGURE 3-16

Instantaneous velocity profiles for starting flow in a pipe, Eq. (3-96). [After Szymanski (1932).]

Poiseuille flow will develop in 0.06 s. Thus, in laminar small-bore pipe flows under varying pressure gradients, it is common to use a quasi-steady Poiseuille flow approximation.

Lefebvre and White (1989, 1991) have reproduced this flow experimentally for large tubes ($D = 5$ and 9 cm) and short times ($t^* < 0.01$). The measured velocity profiles are in good agreement with the Szymanski solution Eq. (3-96), and the laminar-flow state, stabilized by the acceleration, persists up to surprisingly high Reynolds numbers, $Re_D > 10^5$.

3-4.2 Pipe Flow Due to an Oscillating Pressure Gradient

As a second example, consider the solution of Eq. (3-94) if the pressure gradient varies sinusoidally with time:

$$\frac{d\hat{p}}{dx} = -\rho K e^{i\omega t}$$

where
$$e^{i\omega t} = \cos \omega t + i \sin \omega t \qquad (3\text{-}97)$$

$$i = \sqrt{-1}$$

We use the no-slip condition and look for a long-term steady oscillation, neglecting the transient, or start-up, of the flow. This is a classic problem in mathematical physics and leads to a Bessel function with imaginary arguments:

$$u = \frac{K}{i\omega} e^{i\omega t} \left[1 - \frac{J_0(r\sqrt{-i\omega/\nu})}{J_0(r_0\sqrt{-i\omega/\nu})} \right] \qquad (3\text{-}98)$$

which is neat but rather difficult to evaluate numerically. Equation (3-98) was first given by Sexl (1930), and further numerical calculations are given by Uchida (1956). Without bothering with exact calculations, we can show the general effect with the two overlapping series approximations

Small $z < 2$:
$$J_0(z) \approx 1 - \frac{z^2}{4} + \frac{z^4}{64} - \cdots$$

$$(3\text{-}99)$$

Large $z > 2$:
$$J_0(z) \approx \sqrt{\frac{2}{\pi z}} \cos\left(z - \frac{\pi}{4}\right)$$

Equation (3-98) shows that the proper dimensionless variables are

$$r^* = \frac{r}{r_0} \qquad \omega^* = \frac{\omega r_0^2}{\nu} \qquad u^* = \frac{u}{u_{max}} \qquad (3\text{-}100)$$

where $u_{max} = Kr_0/4\nu$ is the centerline velocity for steady Poiseuille flow with a pressure gradient $-\rho K$. The quantity ω^* is sometimes called the *kinetic Reynolds number* and is a measure of viscous effects in oscillating flow. Similar to the static

Reynolds number, oscillating flows may become turbulent when ω^* exceeds approximately 2000.

By combining Eqs. (3-98) and (3-99), we obtain two series approximations for the velocity, which is the real part of the solution:

Small $\omega^* < 4$:

$$\frac{u}{u_{\max}} \approx (1 - r^{*2}) \cos \omega t + \frac{\omega^*}{16} (r^{*4} + 4r^{*2} - 5) \sin \omega t + \mathcal{O}(\omega^{*2}) \quad (3\text{-}101)$$

Large $\omega^* > 4$:

$$\frac{u}{u_{\max}} \approx \frac{4}{\omega^*} \left[\sin \omega t - \frac{e^{-B}}{\sqrt{r^*}} \sin (\omega t - B) \right] + \mathcal{O}(\omega^{*-2}) \quad (3\text{-}102)$$

where

$$B = (1 - r^*)\sqrt{\frac{\omega^*}{2}}$$

Remembering that dp/dx is proportional to $\cos \omega t$, we see that for very small ω^*, the velocity is nearly a quasi-static Poiseuille flow in phase with the slowly varying pressure gradient; the second term in Eq. (3-101) adds a lagging component which reduces the velocity at the centerline. At large ω^*, from Eq. (3-102), the flow approximately lags the pressure gradient by 90°, and again the centerline velocity is less than $u_{\max}$. However, near the wall, there is a region of high-velocity flow, as can be seen be averaging Eq. (3-102) over one cycle to obtain the mean square velocity $\overline{u^2}(r^*)$. We obtain

$$\frac{\overline{u^2}}{K^2/2\omega^2} = 1 - \frac{2}{\sqrt{r^*}} e^{-B} \cos B + \frac{e^{-2B}}{r^*} \quad (3\text{-}103)$$

This relation is plotted in Fig. 3-17 for two values of ω^*. There is an overshoot in mean velocity near the wall, which occurs when $\cos B + \sin B \approx e^{-B}$, or $B \approx 2.284$.
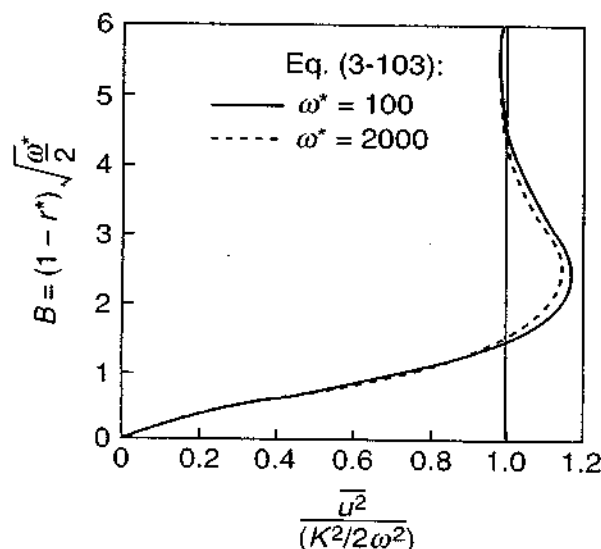
FIGURE 3-17
The near-wall velocity overshoot (Richardson's annular effect) due to an oscillating pressure gradient.

This effect is characteristic of oscillating duct flows and was first noted by Richardson and Tyler (1929) in a tube-flow experiment. The overshoot, now called *Richardson's annular effect*, was then verified theoretically through Eq. (3-102) by Sexl (1930). For a further discussion of these problems, the reader is referred to Uchida (1956) and the general review article by Rott (1964). A solution for oscillating flow in a rectangular duct is given by Tsangaris and Vlachakis (2003).

3-5 UNSTEADY FLOWS WITH MOVING BOUNDARIES

A variety of solutions are known for laminar flow with moving boundaries, some of which illustrate boundary-layer behavior. Again we make the parallel-flow assumption of $u = u(y, z, t)$, $v = 0$, $w = 0$, so that the momentum equation (3-2) becomes

$$\frac{\partial u}{\partial t} = -\frac{1}{\rho}\frac{d\hat{p}}{dx} + \nu\left(\frac{\partial^2 u}{\partial y^2} + \frac{\partial^2 u}{\partial z^2}\right) \tag{3-104}$$

The pressure gradient can only be a function of time for this flow and hence can be absorbed into the velocity by a change of variables. Define

$$u' = u + \int \frac{1}{\rho}\frac{d\hat{p}}{dx}\,dt$$

Then

$$\frac{\partial u'}{\partial t} = \nu\left(\frac{\partial^2 u'}{\partial y^2} + \frac{\partial^2 u'}{\partial z^2}\right) \tag{3-105}$$

Equation (3-105) is the homogeneous heat-conduction equation, for which a wealth of unsteady solutions are known [see, e.g., Carslaw and Jaeger (1959)]. One of these corresponds to the motion of a fluid above an infinite plane which is moved arbitrarily. Let the plane be at $y = 0$, so that $u = u(y, t)$. The boundary conditions are no slip at the plane and no initial motion of the fluid:

$$u(0, t) = U(t) \qquad \text{for } t > 0$$
$$u(y, 0) = 0 \qquad \text{for } y > 0 \tag{3-106}$$

No matter how complex $U(t)$ is, the solution can be obtained from superposition of the indicial, or step-function, solution, as shown by Watson (1958). We confine ourselves to two cases:

1. Sudden acceleration of the plane to constant U_0
2. Steady oscillation of the plane at $U \cos \omega t$

Case 1 is analogous to a conducting solid whose bottom plane is suddenly changed to a different temperature. The solution is well known to be the complementary

error function or probability integral

$$\frac{u}{U_0} = 1 - \text{erf}\left(\frac{y}{2\sqrt{\nu t}}\right) = \text{erfc}\left(\frac{y}{2\sqrt{\nu t}}\right) \tag{3-107}$$

where

$$\text{erf}(\beta) = \frac{2}{\sqrt{\pi}}\int_0^\beta e^{-x^2}\,dx$$

Note that the independent variables y and t have been combined into a single dimensionless *similarity variable*, $\eta = y/[2\sqrt{\nu t}]$. Equation (3-105) becomes an ordinary differential equation for a variable $u'/U_0 = f(\eta)$. More discussion of similarity theory is given in Sec. 3-8.

Values of the complementary error function are tabulated in Table 3-3.

The solution can be reversed so that the fluid is moving at uniform speed U_0 and the plate is suddenly decelerated to zero velocity. In this case,

Suddenly stopped plate: $\qquad u = U_0\,\text{erf}\left(\frac{y}{2\sqrt{\nu t}}\right) \tag{3-108}$

These two complementary solutions are shown in Fig. 3-18. The suddenly started plate from Eq. (3-107) is shown in Fig. 3-18a; the suddenly stopped plate from Eq. (3-108) is shown in Fig. 3-18b. The units of y are arbitrary, and the curves (a) and (b) are of course mirror images.

In either (a) or (b) in Fig. 3-18, the plate's effect diffuses into the fluid at a rate proportional to the square root of the kinematic viscosity. It is customary to define the shear layer *thickness* as the point where the wall effect on the fluid has

TABLE 3-3

Numerical values of the complementary error function

β	erfc(β)	β	erfc(β)
0	1.0	1.1	0.11980
0.05	0.94363	1.2	0.08969
0.1	0.88754	1.3	0.06599
0.15	0.83200	1.4	0.04772
0.2	0.77730	1.5	0.03390
0.25	0.72367	1.6	0.02365
0.3	0.67137	1.7	0.01621
0.35	0.62062	1.8	0.01091
0.4	0.57161	1.9	0.00721
0.5	0.47950	2.0	0.00468
0.6	0.39615	2.5	0.000407
0.7	0.32220	3.0	0.0000221
0.8	0.25790	3.5	0.00000074
0.9	0.20309	4.0	0.00000001
1.0	0.15730	∞	0.0

(a)

(b)
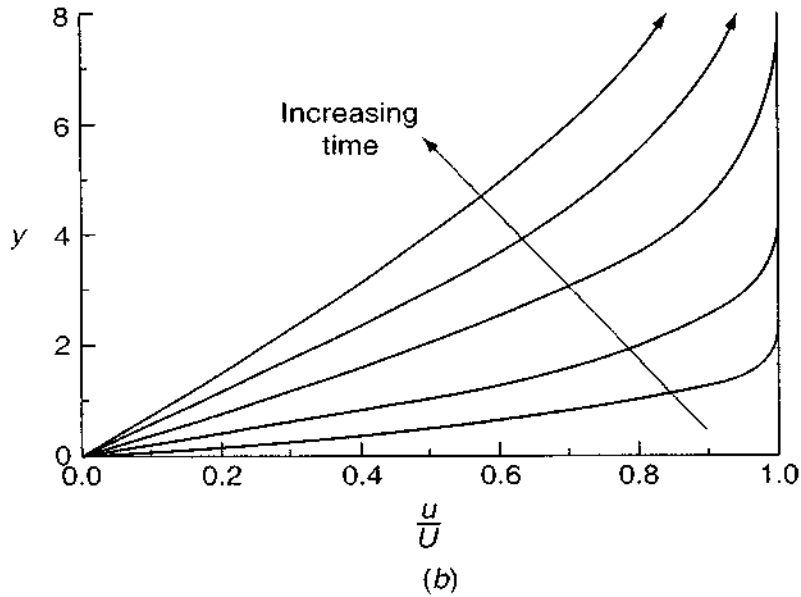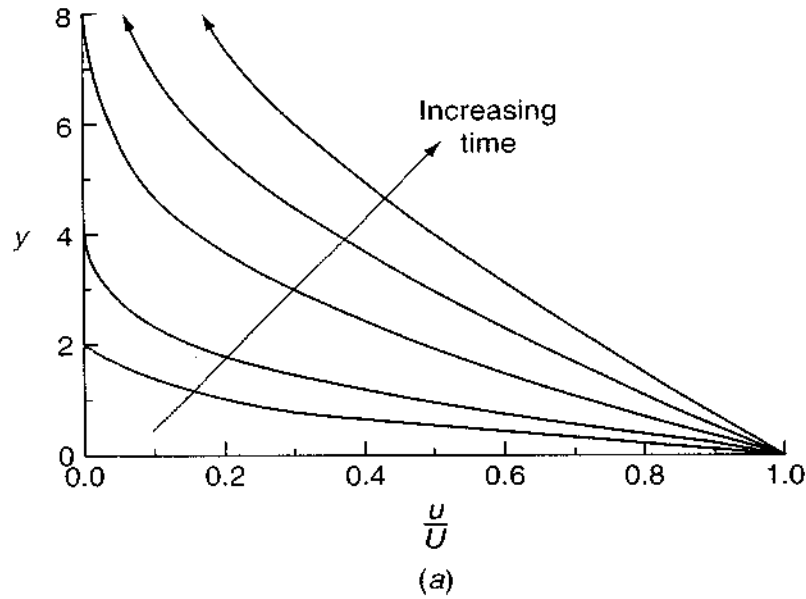
FIGURE 3-18
Stokes' first problem: (a) flow above a suddenly started plate; (b) streaming flow above a suddenly stopped plate.

dropped to 1 percent: in (a), where $u/U_0 = 0.01$; in (b), where $u/U_0 = 0.99$. These both correspond to $\mathrm{erfc}(\beta) = 0.01$, or $\beta \approx 1.82$. Then the shear layer thickness in these flows is, approximately,

$$\delta \approx 3.64\sqrt{\nu t} \qquad (3\text{-}109)$$

For example, for air at 20°C with $\nu = 1.5\mathrm{E}{-}5 \ \mathrm{m^2/s}$, $\delta \approx 11$ cm after 1 min.

3-5.1   Fluid Oscillation above an Infinite Plate

Case 2, with an oscillating wall (or stream), is often called Stokes' second problem, after a celebrated paper by Stokes (1851). Consider first the oscillating wall, with $u(0, t) = U_0 \cos \omega t$, and the fluid in the far field at rest: $u(\infty, t) = 0$. The steadily

(a)

(b)
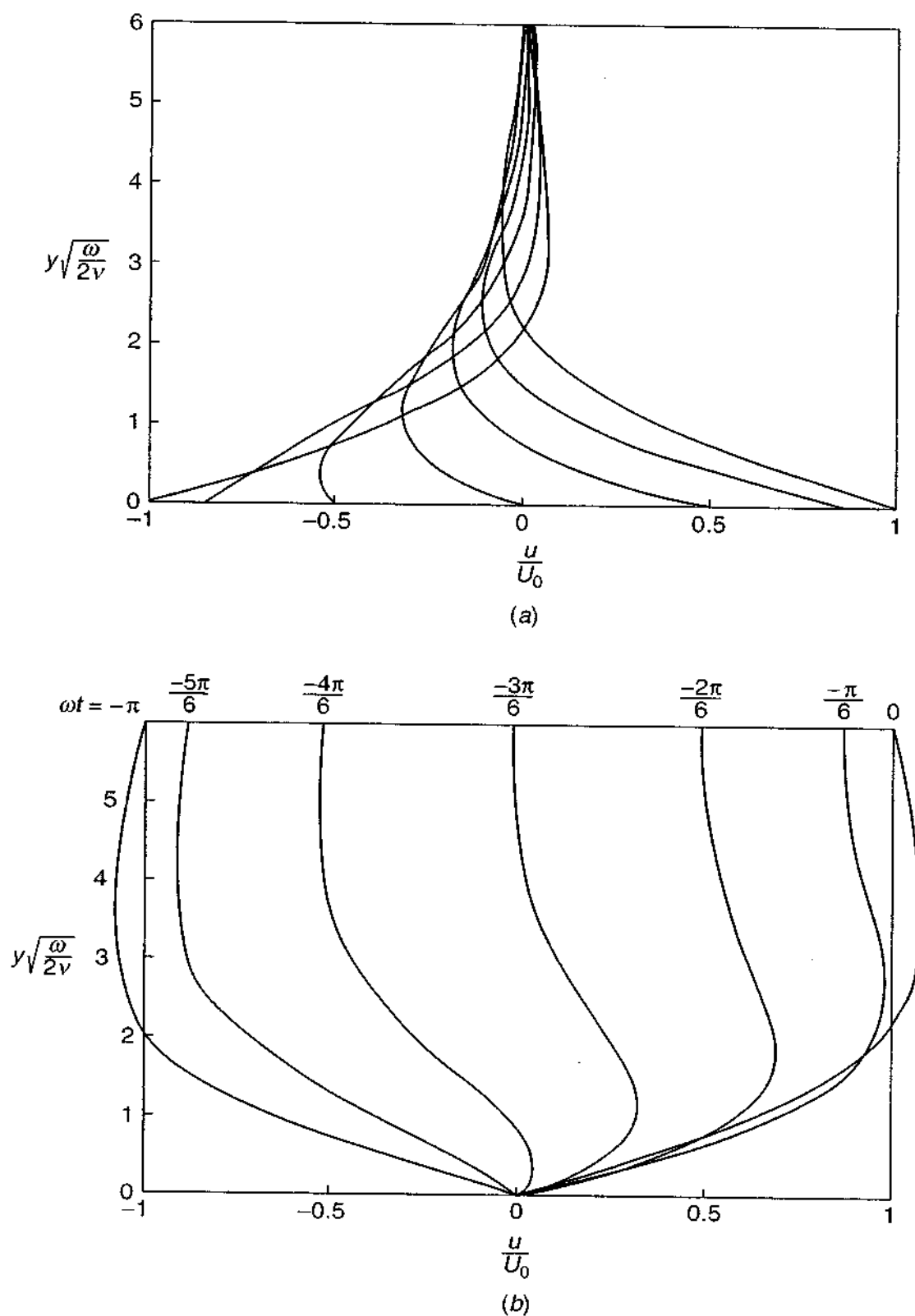
FIGURE 3-19

Stokes' second problem: (a) flow above an oscillating infinite plate, Eq. (3-111); (b) an oscillating stream above a fixed plate, Eq. (3-112). Velocity profiles shown for 30° increments over a half period.

oscillating solution to Eq. (3-105) must be of the form $u(y, t) = f(y)e^{i\omega t}$, where $i = \sqrt{-1}$. Substitution in Eq. (3-105) gives the ordinary differential equation

$$\frac{d^2 f}{dy^2} - \frac{i\omega}{\nu} f = 0 \tag{3-110}$$

and the solution is of the form $f = \exp[-y\sqrt{i\omega/\nu}]$. We may separate u into real and imaginary parts. If the wall is oscillating, the final result is

$$u_1 = U_0 \exp(-\eta) \cos(\omega t - \eta)$$
$$\eta = y\sqrt{\frac{\omega}{2\nu}} \tag{3-111}$$

If, instead, the stream is oscillating, $u(\infty, 0) = U_0 \cos \omega t$, and the wall is still, $u(0, t) = 0$, the solution is

$$u_2 = U_0 \cos \omega t - u_1 \tag{3-112}$$

where u_1 is given by Eq. (3-111).

The instantaneous velocity profiles for the oscillating wall or stream are shown in Fig. 3-19a and b, respectively. The curves differ in time by 30° during the half-cycle of sweep, from left to right, of the driving oscillation. In Fig. 3-19a, the waves created in the fluid by the moving wall lag behind in phase and damp out as y increases. The thickness δ of the oscillating layer can again be defined where $u/U_0 = 0.01$, that is, where $e^{-\eta} = 0.01$ or $\eta = 4.6$. Solving for y, we have

$$\delta \approx 6.5\sqrt{\frac{\nu}{\omega}} \tag{3-113}$$

Again we have the characteristic laminar-flow dependence upon $\sqrt{\nu}$. For air at 20°C with a plate frequency of 1 Hz ($\omega = 2\pi$ rad/s), we compute $\delta \approx 1$ cm. The wall shear stress at the oscillating plate is given by

$$\tau_w = \mu \left(\frac{\partial u}{\partial y}\right)_\omega = U_0 \sqrt{\rho \omega \mu} \sin\left(\omega t - \frac{\pi}{4}\right) \tag{3-114}$$

and thus the maximum shear lags the maximum velocity by 135°.

The case of the fixed wall, Fig. 3-19b, is rather different. The low-momentum fluid near the wall actually leads in phase, and we see the "Richardson" type of velocity overshoot (Fig. 3-17) at both ends of the cycle.

3-5.2   Unsteady Flow between Two Infinite Plates

Recall the linear Couette flow between a fixed and a moving plate from Eq. (3-6) and Fig. 3-2a. Let us analyze the start-up of this flow from rest. Since the coordinate system of Fig. 3-2a is somewhat awkward, we will switch to the geometry shown in
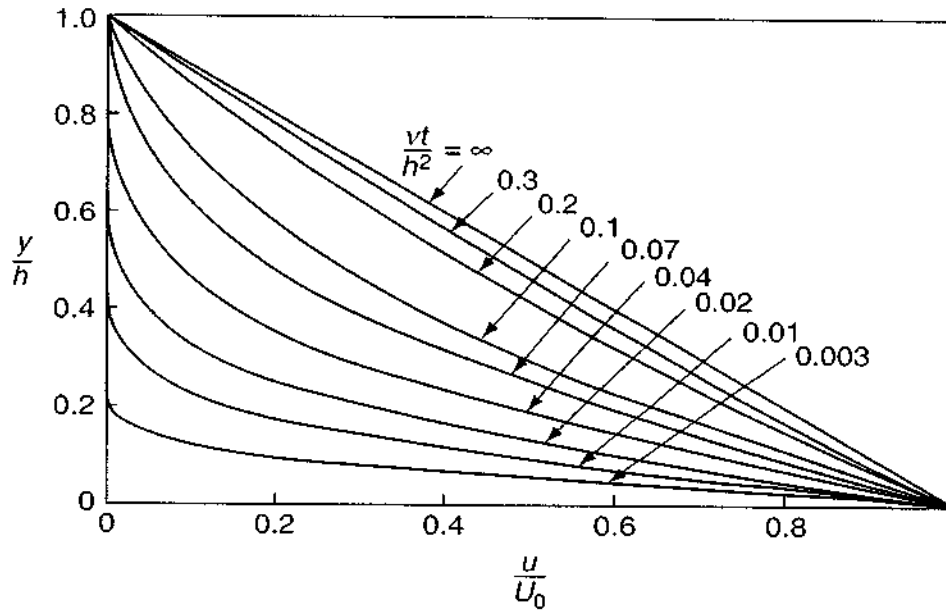
FIGURE 3-20
The development of plane Couette flow due to a suddenly accelerated lower wall, Eq. (3-119).

Fig. 3-20: The upper plate ($y = h$) is fixed; at time $t = 0$, the lower plate ($y = 0$) begins to move at uniform velocity U_0. In this system, the final steady flow is $u = U_0(1 - y/h)$. It is convenient to work with the *difference* between u and its final steady-flow value, i.e., define

$$u_1 = u - U_0\left(1 - \frac{y}{h}\right) \tag{3-115}$$

If we adopt the dimensionless variables $u_1^* = u_1/U_0$, $y^* = y/h$, and $t^* = \nu t/h^2$, the basic differential equation (3-105) becomes

$$\frac{\partial u_1^*}{\partial t^*} = \frac{\partial^2 u_1^*}{\partial y^{*2}} \tag{3-116}$$

subject to

$$u_1^*(0, t^*) = u_1^*(1, t^*) = 0$$

$$u_1^*(y^*, 0) = -1 + y^*$$

Equation (3-116) yields to a separation of variables $u_1^* = f(y^*)g(t^*)$, and substitution and separation give

$$\frac{g'}{g} = \frac{f''}{f} = -\lambda^2$$

or

$$\tag{3-117}$$

$$g = C\exp(-\lambda^2 t^*) \qquad f = A\sin(\lambda y^*) + B\cos(\lambda y^*)$$

where (A, B, C) are constants. To satisfy $u_1^*(0, t^*) = 0$, we must have $B = 0$. To satisfy $u_1^*(1, t^*) = 0$ with $A \neq 0$, it must be that $\lambda = n\pi$, where n is an integer.

Since no single sine wave will satisfy the initial condition, we form a Fourier sine series to require that $u_1^*(y^*, 0) = \sum A_n \sin(n\pi y^*) = -1 + y^*$. The standard Fourier orthogonality condition [Kreyszig (1999)] yields

$$A_n = \int_{-1}^{+1} (-1 + y^*) \sin(n\pi y^*) \, dy^* = -\frac{2}{n\pi} \qquad (3\text{-}118)$$

The final solution for Couette flow start-up is thus

$$\frac{u}{U_0} = \left(1 - \frac{y}{h}\right) - \frac{2}{\pi} \sum_{n=1}^{\infty} \frac{1}{n} \exp(-n^2\pi^2 t^*) \sin\frac{n\pi y}{h} \qquad (3\text{-}119)$$

Velocity profiles plotted from this expression are shown in Fig. 3-20. The linear asymptote is approached at $t^* \approx 0.3$; for air at 20°C, this corresponds to $t = 2$ s if $h = 1$ cm.

In taking leave of these sections on steady and unsteady Couette and Poiseuille flows, we should note that other relatively straightforward one-coordinate solutions exist for the Navier–Stokes equations. An excellent summary is given in the review article by Berker (1963). Some of these solutions will be given as problem assignments:

1. Steady Couette flow where the moving wall suddenly stops
2. Unsteady Couette flow between a fixed and an oscillating plate
3. Radial outflow from a porous cylinder, Prob. 3-24.
4. Radial outflow between two circular plates, Probs. 3-23 and 3-36.
5. Combined Poiseuille and Couette flow in a tube or annulus, Prob. 3-11.
6. Gravity-driven thin fluid films, Probs. 3-15 to 3-18.
7. Decay of a line Oseen–Lamb vortex, Prob. 3-14.
8. The Taylor vortex profile, Prob. 3-22.

In the next three sections we will outline some more complex solutions, usually involving two- or three-dimensional flows.

3-6 ASYMPTOTIC SUCTION FLOWS

All the solutions discussed so far in this chapter have had vanishing convective acceleration, i.e., no non linear terms in the momentum equation. We now consider the case of simple but nonvanishing convection, i.e., flows with uniform suction (or injection) at the wall.

3-6.1 Uniform Suction on a Plane

Consider steady flow at velocity U (at $y = \infty$) past an infinite plane ($y = 0$). Let the plate be porous, and allow a normal velocity through the wall, so that $u = 0$ but

$v = v_w \neq 0$. The continuity equation for two-dimensional incompressible flow is satisfied if $u = u(y)$ and $v = v_w = $ const. The momentum equation then becomes

$$\rho v_w \frac{du}{dy} = \mu \frac{d^2u}{dy^2} \tag{3-120}$$

subject to $u = 0$ at $y = 0$. Since v_w is constant, the convective acceleration is linear, and the solution is readily obtained:

$$u = U(1 - e^{yv_w/\nu}) \tag{3-121}$$

Physically, v_w must be negative (wall suction), otherwise u would be unbounded at large y. As usual, define the boundary-layer thickness to be the point where $u = 0.99U$. This gives

$$\delta = -4.6 \frac{\nu}{v_w} \tag{3-122}$$

This thickness is constant, independent of y or U, because the convection toward the wall exactly balances the tendency of the shear layer to grow due to viscous diffusion. For air at 20°C, if $v_w = -1$ cm/s, $\delta \approx 7$ mm. For a plate with a leading edge ($x = 0$), a laminar shear layer would grow and approach this constant value at a distance estimated by Iglisch (1944) to be $x \approx 4\nu U/v_w^2$ (see Sec. 4.4). For air at 20°C with $U = 10$ m/s and $v_w = -1$ cm/s, this corresponds to a length $x \approx 6$ m.

3-6.2 Flow between Plates with Bottom Injection and Top Suction

Now consider the flow between two porous plates at $y = +h$ and $y = -h$, respectively, similar to Fig. 3-1. Let the main flow be generated by a constant pressure gradient $-d\hat{p}/dx$. Let the porous walls be such that a uniform vertical crossflow is generated:

$$v = v_w = \text{const} \tag{3-123}$$

Then the equation of continuity with $w = 0$ requires, as before, that $u = u(y)$ only. The momentum Eq. (3-2) reduces to

$$\rho v_w \frac{du}{dy} = -\frac{d\hat{p}}{dx} + \mu \frac{d^2u}{dy^2} \tag{3-124}$$

Since v_w is constant, the equation is linear. We retain the no-slip condition for the main flow:

$$u(+h) = u(-h) = 0 \tag{3-125}$$

Positive v_w corresponds to injection at the bottom plate and suction at the top plate (Fig. 3-21). The solution can be written in dimensionless form and contains the *wall*
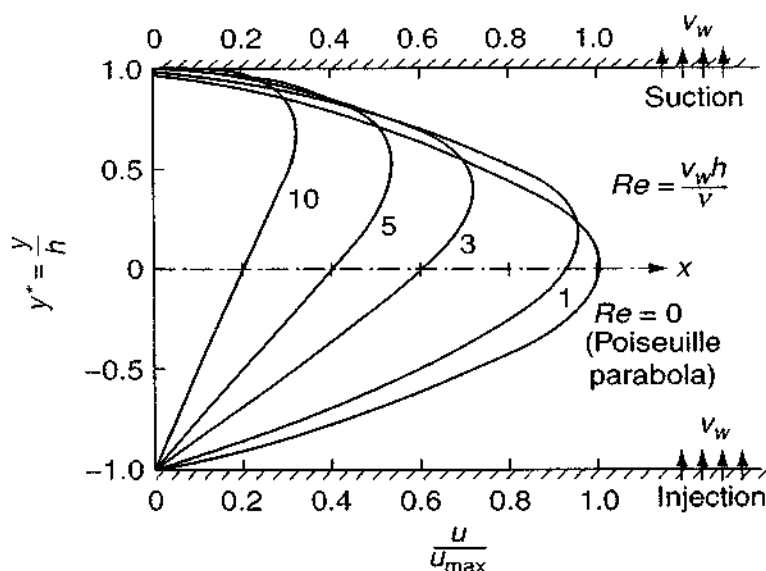
FIGURE 3-21
Velocity profiles for flow between parallel plates with equal and opposite porous walls, Eq. (3-126).

Reynolds number $Re = v_w h/\nu$ *as a parameter:*

$$\frac{u}{u_{max}} = \frac{2}{Re}\left(\frac{y}{h} - 1 + \frac{e^{Re} - e^{Re\,y/h}}{\sinh Re}\right) \tag{3-126}$$

where $u_{max} = h^2(-d\hat{p}/dx)/2\mu$ is the centerline velocity for imporous or Poiseuille flow, Eq. (3-42). For very small Re, the last term in the parentheses can be expanded in a power series, and the Poiseuille solution $1 - y^2/h^2$ is reclaimed. For very large Re, the same last term in the parentheses has the approximate value 2.0 except very near $y = +h$, so that

$$\frac{u}{u_{max}} \approx \frac{2(1 + y/h)}{Re}$$

a straight-line variation that suddenly drops off to zero at the upper wall. Some velocity profiles that illustrate these conditions are shown in Fig. 3-21, plotted from Eq. (3-126). Note that the average velocity is decreasing as Re increases, i.e., the friction factor increases as we apply more crossflow through the walls.

Similar analyses can be made with other geometries by imposing a known crossflow field, e.g., between rotating porous cylinders. The flow outside a single rotating cylinder with wall suction is given as a problem assignment; the character of this flow changes when the suction velocity v_w exceeds $2\nu/r_0$, where r_0 is the cylinder radius.

3-6.3 Non-Linear Effects: Flow in Porous Ducts

The previous examples in this section were linear because of the assumption of constant crossflow velocity. If we impose more realistic boundary conditions, e.g., suction at both walls, then the net mass flow will change with x, and at the very least we must have $u = u(x, y)$ and $v = v(y)$ to satisfy the continuity relation. This

means that both of the axial convective-acceleration terms $u\,\partial u/\partial x$ and $v\,\partial u/\partial y$ will be products of variables and thus non-linear. The solutions may be vexed with both existence and nonuniqueness problems, and it is instructive to consider an example.

Let the duct be uniformly porous, i.e., the wall velocity v_w is a constant, independent of x. Then the average velocity $\bar{u}$ in the duct will vary linearly with x because of the mass flow through the walls. The two most studied geometries are the circular tube and channel flow between parallel plates. In practice, there must always be an entrance region, and, since the mean velocity continually varies, it is a controversial question as to whether a "fully developed" condition can be achieved.

For the present example, let us consider channel flow between uniformly porous parallel plates, with the geometry of Fig. 3-1. We assume, without proof, that we are far downstream of the entrance and that the boundary conditions

$$\text{At } y = +h: \qquad u = 0 \qquad v = +v_w$$

$$\text{At } y = -h: \qquad u = 0 \qquad v = -v_w \tag{3-127}$$

i.e., both walls have either equal suction ($v_w > 0$) or equal injection ($v_w < 0$). Let $\bar{u}(0)$ denote the average axial velocity at an initial section ($x = 0$). Then it is clear from a gross mass balance that $\bar{u}(x)$ will differ from $\bar{u}(0)$ by the amount $v_w x/h$. This observation led Berman (1953) to formulate the following relation for the stream function in the channel:

$$\psi(x, y) = (h\bar{u}(0) - v_w x)f(y^*) \tag{3-128}$$

where $y^* = y/h$ and f is a dimensionless function to be determined. The velocity components follow immediately from the definition of ψ:

$$u(x, y^*) = \frac{\partial \psi}{\partial y} = \left[\bar{u}(0) - \frac{v_w x}{h}\right]f'(y^*) = \bar{u}(x)f'(y^*)$$

$$v(x, y^*) = -\frac{\partial \psi}{\partial y} = v_w f(y^*) = v(y) \text{ only} \tag{3-129}$$

Thus the function f and its derivative f' represent the shape of the velocity profiles; these are independent of x, and the flow is thus termed *similar*; see Secs. 3-8 and 4-3 for further examples. The stream function must now be made to satisfy the momentum (Navier–Stokes) Eq. (3-2) for steady flow:

$$u\frac{\partial u}{\partial x} + v\frac{\partial u}{\partial y} = -\frac{1}{\rho}\frac{\partial p}{\partial x} + \nu\left(\frac{\partial^2 u}{\partial x^2} + \frac{\partial^2 u}{\partial y^2}\right)$$

$$u\frac{\partial v}{\partial x} + v\frac{\partial v}{\partial y} = -\frac{1}{\rho}\frac{\partial p}{\partial y} + \nu\left(\frac{\partial^2 v}{\partial x^2} + \frac{\partial^2 v}{\partial y^2}\right) \tag{3-130}$$

If we substitute u and v from (3-129) into (3-130), we find by cross-differentiation that

$$\frac{\partial^2 p}{\partial x\,\partial y} = 0 \tag{3-131}$$

showing that, unlike that for nonporous duct flow, the pressure gradient is *not* constant. When Eqs. (3-130) and (3-131) are combined, the result is a single fourth-order ordinary non-linear differential equation for $f(y^*)$:

$$f'''' + Re(f'f'' - ff''') = 0 \qquad (3\text{-}132)$$

where $Re = v_w h/\nu$ is the wall Reynolds number and primes denote differentiation with respect to y^*. The boundary conditions are converted from (3-127):

$$\begin{array}{ll} f'(1) = 0 & f(1) = 1 \\ f'(-1) = 0 & f(-1) = -1 \end{array} \qquad (3\text{-}133)$$

These show that $f(y^*)$ is antisymmetric about $y^* = 0$, so that at the centerline, $v = 0$ and $\partial u/\partial y = 0$, or $f(0) = f''(0) = 0$. Equation (3-132) has no known analytic closed-form solution, but it can be integrated once:

$$f''' + Re(f'^2 - ff'') = k\,(Re) = \text{const} \qquad (3\text{-}134)$$

Further progress requires some other technique, e.g.,

1. A perturbation solution: Berman (1953)
2. A numerical solution: Eckert et al. (1957)
3. A power-series solution: White (1959)

These are general techniques, and we shall have occasion later to use all three of them in analyzing problems for which the exact solution is not known. One should also look for special cases, and three of these have been found for Eq. (3-132) which satisfy conditions (3-133):

$Re = 0$ (Poiseuille flow):

$$f = \tfrac{3}{2}y^* - \tfrac{1}{2}y^{*3} \qquad f' = \tfrac{3}{2}(1 - y^{*2}) \qquad (3\text{-}135)$$

$Re = +\infty$ (infinite suction):

$$f = y^* \qquad f' = 1 \qquad \text{slug flow} \qquad (3\text{-}136)$$

$Re = -\infty$ (infinite injection):

$$f = \sin\frac{\pi y^*}{2} \qquad f' = \frac{\pi}{2}\cos\frac{\pi y^*}{2} \qquad (3\text{-}137)$$

For other Raynolds numbers, one could use, e.g., the Runge–Kutta program in App. C to solve Eq. (3-132) numerically. Two initial conditions are unknown, i.e., if one started at $y^* = -1$, $f''(-1)$ and $f'''(-1)$ would have to be guessed and the solution double-interated until $f(1) = 1$ and $f'(1) = 0$. The most complete sets of profiles in the literature are given by White et al. (1958), and are shown in Fig. 3-22. The shapes change smoothly with Reynolds numbers over the full range $-\infty < Re < +\infty$ and show no odd or unstable behavior. Suction tends to draw the profile toward the wall, as it did in Fig. 3-21.
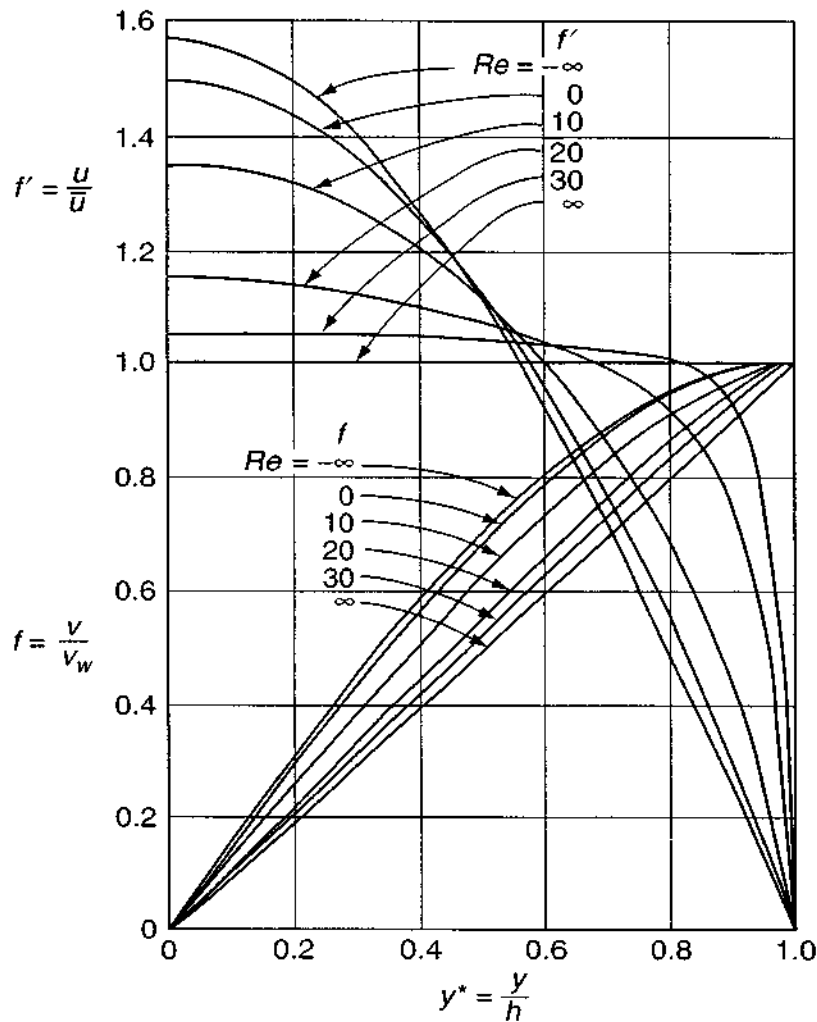
FIGURE 3.22
Similar velocity profiles for a symmetrically porous channel as a function of the wall Reynolds number $Re = v_w h/v$. [After White et al. (1958).]

The odd behavior shows up with uniformly porous *pipe*. White (1962a) gave an array of solutions for various values of $Re = v_w r_0/v$. The injection profiles ($Re < 0$) vary smoothly but are drawn *toward* the wall, which is physically unexpected. The suction solution ($Re > 0$) show the following pathological behavior:

1. Double solutions, one with backflow, for $0 < Re < 2.3$
2. No solutions whatever in the range $2.3 < Re < 9.1$
3. Multiple sets of double solutions for $Re > 9.1$

At the least, we learn that the Navier–Stokes equations, being non linear and complex, are subject to nonuniqueness and nonexistence difficulties. The previous results are so offbeat that we conclude that "fully developed" similar profiles probably do not occur in laminar porous pipe flow. An analysis by Weissberg (1959) for the special case $Re = 3$ (where no similar solutions have been found) shows that a Poiseuille parabolic entry flow does *not* develop into any kind of a similar profile downstream. One concludes that similar porous-pipe profiles, if they occur at all, are merely way stations along development of the flow into very complex and changing profiles.

3-7   WIND-DRIVEN FLOWS: THE EKMAN DRIFT

There are a number of problems where a liquid free surface is set into motion by a gas flowing over it, e.g., wind blowing over a pond. The shear stresses must match at the air–water interface. Let $(z = 0)$ be the interface, with $z > 0$ upward. Then the free-surface condition is

$$\tau_0 = \left(\mu \frac{\partial u}{\partial z} \right)_{\text{air}} = \left(\mu \frac{\partial u}{\partial z} \right)_{\text{water}} \tag{3-138}$$

where we have assumed wind and water flow in the x direction. Since $\mu_{\text{air}} \ll \mu_{\text{water}}$, it follows that the gradient $(\partial u / \partial z)$ in the water will be relatively small. Let us call this interface water-gradient $K = \tau_0 / \mu_{\text{water}}$.

3-7.1   Start-Up of Wind-Driven Surface Water

Consider water at rest which is suddenly subjected to a wind stress τ_0. Assuming an unsteady parallel laminar flow $u(z, t)$ and neglecting Coriolis acceleration, we must solve the linear differential equation:

$$\frac{\partial u}{\partial t} = \nu \frac{\partial^2 u}{\partial z^2} \tag{3-139}$$

subject to the boundary conditions

$$\frac{\partial u}{\partial z} (z = 0) = K \qquad u(z \rightarrow -\infty) = 0$$

and the initial condition

$$u(z, 0) = 0 \qquad z < 0$$

This is similar to Stokes' first problem, Eq. (3-107), except that the surface condition involves $(\partial u / \partial z)$ rather than u itself. The solution is

$$\frac{\partial u}{\partial z} = K \left[1 + \text{erf} \left(\frac{z}{2\sqrt{\nu t}} \right) \right]$$

or

$$\frac{u}{K} = z \left[1 + \text{erf} \left(\frac{z}{2\sqrt{\nu t}} \right) \right] + 2\sqrt{\frac{\nu t}{\pi}} \, e^{-z^2/4\nu t} \tag{3-140}$$

This laminar-flow solution predicts that the water-interface velocity $(z = 0)$ will grow rapidly, as $u_0 = 2K\sqrt{\nu t / \pi}$. We can try out some numerical values by using the estimate from the text by Roll (1965) of the wind stress for airflow over a water surface:

$$\tau_0 \approx 0.002 \rho_{\text{air}} (V_{\text{wind}} - u_0)^2 \tag{3-141}$$

If we assume a brisk wind speed of 6 m/s (about 12 knots) and an air–water interface at 20°C, we may compute from Eqs. (3-140) and (3-141) that $u_0 \approx 0.6$ m/s after

1 min and 2.3 m/s after 1 h. These water velocities are greatly overestimated: In an actual flow of this type, the surface-water flow would rise in about 1 h to a nearly constant velocity of 0.2 m/s, or about 3 percent of the wind speed. The main reason for the discrepancy is that both the air and water flows, in such a large-scale (high Reynolds number) motion, are turbulent. In turbulent flow, we must replace the fluid's molecular velocity μ by a turbulent-mixing or *eddy* viscosity, μ_t, which is much larger and scaled with flow parameters. We will see how to model turbulent flows in Chap. 6 and can return to this problem more realistically.

3-7.1   Coriolis Effects: The Ekman Spiral

In practical ocean flows, the wind-driven water moves at such low velocities that the Coriolis acceleration [Eq. (2-137)] is not negligible. The resulting flow is steady but accelerating, i.e., the unbalanced momentum flux is in the direction of the Coriolis acceleration. The oceanographer F. Nansen (1902) found that drifting ice in the Arctic deviated from the wind direction by 20 to 40° to the right, which he correctly concluded was due to the earth's rotation. Nansen's student, V. W. Ekman, gave the following analytic solution (1905), which laid the foundation for modern dynamic oceanography. Let (x, y) be the plane of the horizontal, and let the z axis be directed upward. For convenience, let the applied surface wind stress τ_0 be in the y direction. Then, for steady flow with negligible pressure gradients and the acceleration given by Eq. (2-125), a realistic flow solution is possible with the horizontal velocities u and v as functions of z only. The momentum Eq. (3-2) becomes

$$\nu \frac{d^2}{dz^2} (u + iv) - 2i\omega \sin \phi \, (u + iv) = 0 \qquad (3\text{-}142)$$

Where $i = \sqrt{-1}$
ϕ = latitude angle
ω = earth rotation rate

This has an exponential solution if ϕ is assumed constant, i.e., localized wind drift at a given latitude. The boundary conditions are a y-directed shear at the surface and negligible velocity at great depth:

At $z = 0$: $\qquad\qquad \dfrac{du}{dz} = 0 \qquad\qquad \dfrac{dv}{dz} = K = \dfrac{\tau_0}{\mu_{\text{water}}}$

At $z = -\infty$: $\qquad\qquad u = v = 0 \qquad\qquad\qquad\qquad\qquad (3\text{-}143)$

The proper solution to Eq. (3-142) is of the form $u + iv = C_1 e^{\beta z}$, and C_1 and β can be found from Eq. (3-143). The results can then be decomposed

$$u = V_0 \exp \frac{\pi z}{D} \cos\left(\frac{\pi z}{D} + 45°\right)$$

$$v = V_0 \exp \frac{\pi z}{D} \sin\left(\frac{\pi z}{D} + 45°\right) \qquad (3\text{-}144)$$

where V_0 is the surface-water speed and D is a vertical decay distance, often called the *penetration depth* of the wind:

$$V_0 = \frac{\tau_0/\rho}{\sqrt{2\omega\,\nu\,\sin\phi}} \qquad D = \pi\sqrt{\frac{\nu}{\omega\,\sin\phi}} \tag{3-145}$$

Equation (3-144) has several fascinating implications, particularly for engineers not used to Coriolis effects in fluid motion. First note that the surface-water velocities are $u = V_0\cos 45°$ and $v = V_0\sin 45°$, showing that the resultant surface-velocity vector is at a 45° angle to the right of the wind (in the Northern Hemisphere). As we move below the surface (negative z), the resultant current vector moves uniformly to the right and decreases exponentially in magnitude, forming a logarithmic spiral, as shown in Fig. 3-23, for equal-depth intervals. At $z = -3D/4$, the current is exactly opposite the wind and has a magnitude of only $V_0 e^{-3\pi/4} \approx 0.095 V_0$.

Another interesting feature is found by integrating the velocity distribution to find the net mass flux. For the x and y directions separately, this gives

$$\dot{m}_x = \int_0^{-\infty} u\,dz = \frac{\tau_0}{2\omega\sin\phi}$$

$$\dot{m}_y = \int_0^{-\infty} v\,dz = 0 \tag{3-146}$$

Thus the net mass transport of water is perpendicular to the wind direction and is independent of ν if τ_0 is assumed known. We can explain this by noting that this is the direction of the Coriolis acceleration, which is the only dynamic imbalance on the system.
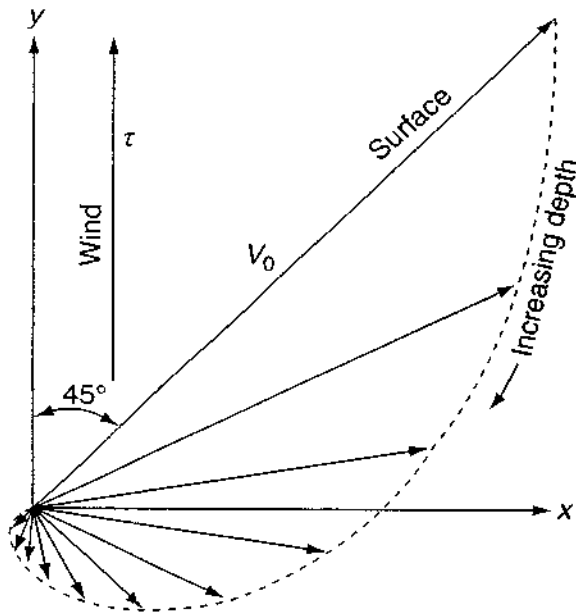

FIGURE 3-23
Wind-driven current vectors for depths of equal interval. The dashed line is a logarithmic spiral from Eq. (3-144). [*After Ekman (1905).*]

As in the previous wind-start-up example, a few numbers will dispel the idea that ocean currents are laminar. Again take $V_{wind} = 6$ m/s over a 20°C air–water interface at a latitude of 41°N (Rhode Island). Equations (3-145) predict that $V_0 = 2.7$ m/s, which is far too high, and $D = 45$ cm, which is ridiculously low. The difficulty again is that real ocean flows are turbulent. If we scale the flow with an "eddy" viscosity as discussed in Chap. 6, we obtain the realistic results $V_0 \approx 2$ cm/s and $D \approx 100$ m. Thus an actual wind-driven Ekman current is a slow transport in a wide upper layer of the ocean.

For further details on ocean current, wind-driven or otherwise, consult a textbook on physical oceanography, such as Defant (1961) or Knauss (1978).

3-8 SIMILARITY SOLUTIONS

We complete our description of exact incompressible-flow solutions of the Navier–Stokes equations by discussing three similar flows. A *similarity solution* is one in which the number of independent variables is reduced by at least one, usually by a coordinate transformation. The idea is analogous to dimensional analysis. Instead of *parameters*, like the Reynolds number, the *coordinates* themselves are collapsed into dimensionless groups that scale the velocities.

We have seen two similarity solutions already, without much emphasis. In Stokes' suddenly moved wall problem, Eq. (3-107), the independent variables y and t were combined into the single similarity variable $\eta = y/[2\sqrt{(\nu t)}]$. The solution was then found analytically. In the porous-duct problem, Eq. (3-128), x was broken out into a linear expression, leaving a similarity variable $f(y^*)$, where $y^* = y/h$. In both cases, partial differential equations, perhaps requiring computer modeling, were reduced to ordinary differential equations.

Similarity solutions generally require a semi-infinite or infinite spatial and temporal extent. If Stokes' suddenly moved wall were only L long or if the wall stopped after a finite time t_0, the similarity variable idea would be compromised.

The general theory of similarity in physical problems has been examined in several textbooks: from a physical emphasis by Sedov (1959) and Hansen (1964), and from the mathematical viewpoint by Ames (1965), Bluman and Cole (1974), Dresner (1983), and Sachdev (2000). The benefits of a similarity analysis are signal: The three examples given here reduce a set of partial differential equations, which may yield only to the all-out computer assault of Sec. 3-10, into ordinary differential equations, which we can handle with an elementary numerical method such as Runge–Kutta integration. These mathematical gains are accompanied by a loss in generality: Similarity solutions are, without exception, limited to certain geometries and certain boundary conditions. For example, in the porous-channel problem, the solution of Eq. (3-132) is invalid if v_w varies with x, and the inlet velocity profile $u(0, y)$ must have the same shape as the curves of Fig. 3-22.

Let us now discuss three examples of laminar similarity solutions: (1) flow near a stagnation point, (2) flow near an infinite rotating disc, and (3) flow in a wedge-shaped region.

Region of nonzero vorticity   0   Rigid boundary
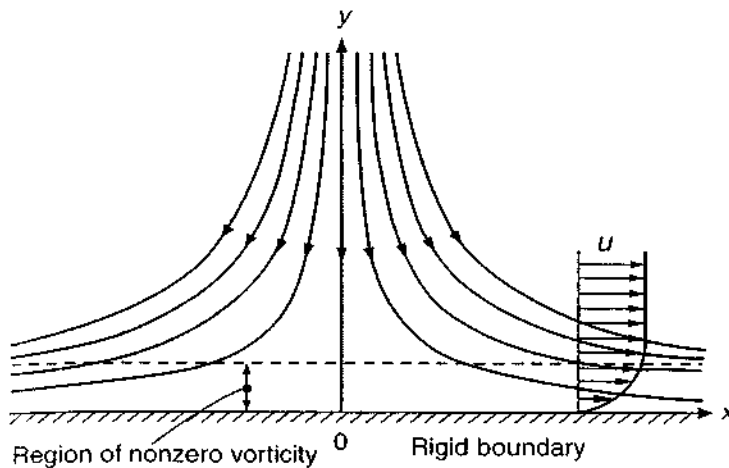
FIGURE 3-24
Stagnation-point flow.

3-8.1 Viscous Flow near a Stagnation Point

One of Prandtl's first students, Hiemenz (1911), discovered that stagnation-point flow can be analyzed exactly by the Navier–Stokes equations.[*] We piece together here several analyses in the literature: the two-dimensional velocity distribution by Hiemenz (1911) and the temperature distribution by Goldstein (1938), the axisymmetric velocity distribution by Homann (1936) and the temperature distribution by Sibulkin (1952).

The coordinate system is shown in Fig. 3-24. The origin is the stagnation point (where $u = v = 0$ in the frictionless solution), and y is the normal to the plane. For axisymmetric flow, x is to be interpreted as a radial coordinate. In order to satisfy the no-slip condition for $u(x, 0)$ along the wall, a viscous region must develop near the wall. It turns out that this shear layer has a constant thickness and has the effect of "displacing" the outer inviscid flow away from the wall. Let us first consider two-dimensional flow in detail and follow with a more cursory treatment of axisymmetric flow.

3-8.1.1 PLANE STAGNATION FLOW. For plane incompressible flow, the continuity Eq. (3-1) reduces to

$$\frac{\partial u}{\partial x} + \frac{\partial v}{\partial y} = 0$$

which can be satisfied by the plane stream function

$$u = \frac{\partial \psi}{\partial y} \qquad v = -\frac{\partial \psi}{\partial x} \tag{3-147}$$

---

[*]Stagnation flow also happens to be an exact solution to the simpler boundary-layer equations. It is, in fact, one of the similar solutions to be discussed in Sec. 4-3.

Note that stream functions are valid for both viscous and potential flow. Once $\psi(x, y)$ is defined, it must satisfy the two-dimensional momentum relations, Eq. (3-2):

$$u \frac{\partial u}{\partial x} + v \frac{\partial u}{\partial y} = -\frac{1}{\rho} \frac{\partial p}{\partial x} + \nu \left(\frac{\partial^2 u}{\partial x^2} + \frac{\partial^2 u}{\partial y^2} \right)$$

$$u \frac{\partial v}{\partial x} + v \frac{\partial v}{\partial y} = -\frac{1}{\rho} \frac{\partial p}{\partial y} + \nu \left(\frac{\partial^2 v}{\partial x^2} + \frac{\partial^2 v}{\partial y^2} \right) \tag{3-148}$$

Inviscid flow near a stagnation point of a body is described by the simple stream function

$$\psi = Bxy \qquad u = By \qquad v = -Bx$$

where B is a positive constant proportional to U_0/L, where U_0 is the stream velocity approaching the body and L a characteristic body length [see, e.g., White (2003, pp. 41–42)]. This flow slips at the wall, that is, $u \neq 0$ at $y = 0$. It must be modified to account for viscous effects.

Following Hiemenz (1911), we modify the stream function to vary with y so that the no-slip condition can be satisfied:

$$\psi_{\text{viscous}} = Bxf(y) \qquad u = \frac{\partial \psi}{\partial y} = Bx \frac{df}{dy} \qquad v = -\frac{\partial \psi}{\partial x} = -Bf$$

For no slip at the wall, we would require $f(0) = f'(0) = 0$. If we substitute this $\psi(x, y)$ into the y-momentum equation in Eq. (3-148), we find that the pressure gradient $\partial p/\partial y = fcn(y)$ only. Therefore, for this stream function,

$$\frac{\partial^2 p}{\partial x \, \partial y} = 0$$

By using this condition and the same stream function in the x-momentum relation of Eq. (3-148), we obtain the differential equation

$$f''' + \frac{B}{\nu} (ff'' - f'^2) = \text{const} = -\frac{B}{\nu} \tag{3-149}$$

The constant is evaluated by noticing that the form of ψ is such that, as y becomes large, f''' and f'' must vanish and f' must approach unity.

Equation (3-149) immediately tells us that Hiemenz achieved *similarity* with this stream function. The coordinate x has disappeared, leaving only a single similarity variable, y, and an ordinary differential equation. However, this equation should be nondimensionalized to eliminate the dimensional constants B and ν There is no body-length scale "L" for this flow. Rather, the proper length scale is $\sqrt{\nu/B}$, the velocity scale is $\sqrt{\nu B}$, and the appropriate dimensionless variables are

$$\eta = y\sqrt{\frac{B}{\nu}} \qquad \psi = xF(\eta)\sqrt{B\nu} \tag{3-150}$$

from which

$$u = BxF'(\eta) \qquad \text{and} \qquad v = -F(\eta)\sqrt{B\nu}$$

where the prime denotes differentiation with respect to η. Substitution in Eq. (3-149) gives a differential equation free of parameters:

$$F''' + FF'' + 1 - F'^2 = 0 \tag{3-151}$$

The boundary conditions are $u = v = 0$ at the wall ($\eta = 0$) and $u = Bx$ at a large distance from the wall:

$$F(0) = F'(0) = 0 \qquad F'(\infty) = 1 \tag{3-152}$$

Equation (3-151) contains two non-linearities, and no analytic solution has ever been found. Hiemenz (1911) performed numerical calculations by hand. It is no trouble nowadays to solve Eq. (3-151) on a personal computer using, say, the Subroutine RUNGE in App. C. We would let $Y(1) = F''$, $Y(2) = F'$, and $Y(3) = F$, and the proper FORTRAN relations for Eq. (3-151) would be

$$F(1) = Y(2) * Y(2) - 1 - Y(1) * Y(3)$$
$$F(2) = Y(1) \tag{3-153}$$
$$F(3) = Y(2)$$

As initial values at "X" = 0, we set $Y(2) = Y(3) = 0$ from the first two conditions of Eq. (3-152). The problem is to find the correct value of $Y(1) = F''_0$ which will cause $Y(2)$ to approach unity as η becomes very large. One must first address
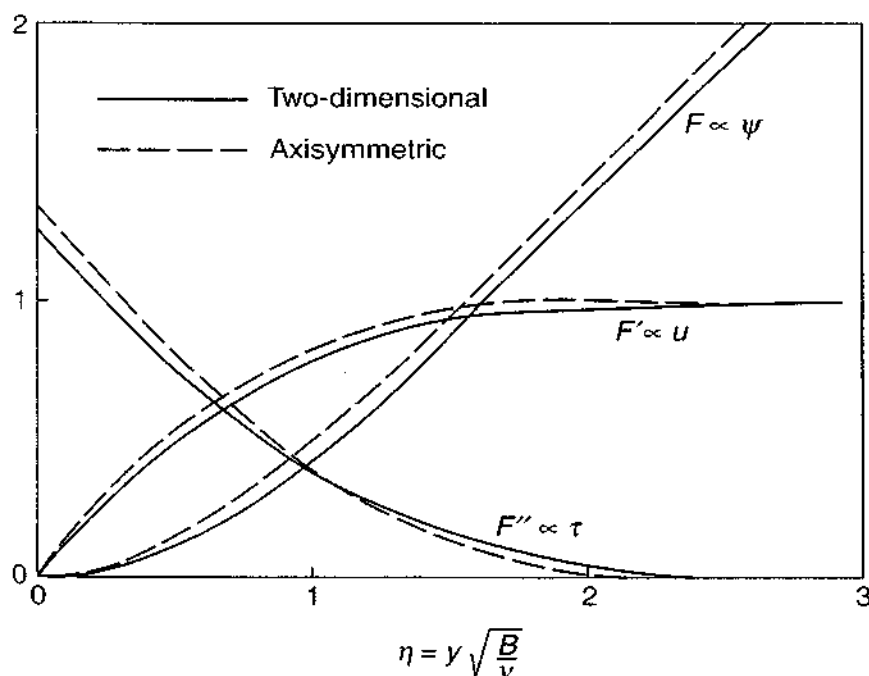
FIGURE 3-25
Numerical solutions of viscous stagnation flow for plane [Eq. (3-151)] and axisymmetric [Eq. (3-165)] conditions.

TABLE 3-4

Numerical solutions for stagnation flow

η	$F' = u/U$ Plane $F''(0) = 1.23259$ $\eta^* = 0.6479$	Axisymmetric $F''(0) = 1.31194$ $\eta^* = 0.5689$
0.1	0.11826	0.12619
0.2	0.22661	0.24239
0.3	0.32524	0.34863
0.4	0.41446	0.44499
0.5	0.49465	0.53160
0.6	0.56628	0.60871
0.7	0.62986	0.67663
0.8	0.68594	0.73577
0.9	0.73508	0.78666
1.0	0.77787	0.82987
1.1	0.81487	0.86608
1.2	0.84667	0.89598
1.3	0.87381	0.92032
1.4	0.89681	0.93983
1.5	0.91617	0.95522
1.6	0.93235	0.96718
1.7	0.94578	0.97631
1.8	0.95684	0.98316
1.9	0.96588	0.98822
2.0	0.97322	0.99190
2.2	0.98386	0.99635
2.4	0.99055	0.99847
2.6	0.99464	0.99940
2.8	0.99705	0.99979
3.0	0.99843	0.99993

the question, how large is "infinity"? One answer is, when F'' becomes very small, say, $< 10^{-5}$. The following would be a typical asymptotic analysis: In Eq. (3-151), as η becomes large, $F \approx a + \eta$ and $(1 - F'^2)$ approaches zero. Therefore, at large η, a conservative view of Eq. (3-151) is

$$\frac{F'''}{F''} \approx -\eta$$

or

$$F'' \approx e^{-\eta^2/2}$$

With this estimate, we are reasonably confident that $F'' < 10^{-5}$ if $\eta > 4.8 =$ "infinity." Finally, to ensure numerical accuracy of the fourth-order-accurate Runge–Kutta method, we choose a step size $\Delta\eta = 0.03$ so that $(\Delta\eta)^4 \leq 10^{-6}$.

Using these preliminaries, the numerical solution of Eq. (3-151) is readily obtained by making an array of guesses of $F_0'' \approx 0$ to 1.5.

The complete solution for viscous stagnation flow is shown in Fig. 3-25 and tabulated in Table 3-4. Also shown—and to be discussed next—is the solution for axisymmetric stagnation flow. Represented in Fig. 3-25 are the stream function F, the velocity profile F', and the shear stress F''. The correct value of F_0'' turned out to be 1.2326.

3-8.1.2 HARBINGERS OF BOUNDARY-LAYER BEHAVIOR. Stagnation flow, an exact solution of the Navier–Stokes equations, exhibits many characteristics of thin-shear-region or *boundary-layer* behavior. The no-slip condition creates a low-velocity region which merges smoothly with the outer inviscid flow along the wall. In boundary-layer theory, the outer flow is called the "freestream" velocity, $U(x)$:

Stagnation flow: $$U = u(x, \infty) = Bx \tag{3-154}$$

This type of accelerating freestream, whose pressure decreases in the flow direction, is called a *favorable* pressure gradient.

The thickness δ of this stagnation layer is defined as the point where $u/U = 0.99$, which occurs in Table 3-4 when $\eta \approx 2.4 = \delta\sqrt{B/\nu}$. Thus

$$\delta \approx 2.4\sqrt{\frac{\nu}{B}} \tag{3-155}$$

The boundary-layer thickness is constant in this case because the thinning due to stream acceleration exactly balances the thickening due to viscous diffusion. In Sec. 4-3, we will see that if $U = Cx^m$, the boundary layer will grow with x if $m < 1$ and will become thinner if $m > 1$.

In typical engineering applications, the stagnation boundary layer is quite thin. For example, let air at 20°C approach a 10 cm diameter cylinder at a speed $U_0 = 10$ m/s. Then $B = 4U_0/D = 400$ s^{-1} (see Sec. 7.3), and Eq. (3-155) predicts that $\delta \approx 0.46$ mm, or only 0.5 percent of the body diameter.

Another boundary-layer effect is displacement of the outer stream by the shear layer, as hinted at in Fig. 3-24. We define the *displacement thickness* δ^* as the distance the outer inviscid flow is pushed away from the wall by the retarded viscous layer. In terms of the stream function F, we find that

$$\lim_{\eta \to \infty} F(\eta) = \eta - \eta^*$$

where $\tag{3-156}$

$$\eta^* = \delta^*\sqrt{\frac{B}{\nu}} = 0.6479$$

as listed in Table 3-4. In stagnation flow, then, $\delta^* \approx 0.27\delta$.

The pressure distribution also exhibits boundary-layer behavior. With u and v known from Eqs. (3-150), we can return to the momentum equations (3-148) and

integrate for the pressure $p(x, y)$. The result is

$$p(0, 0) - p(x, \eta) = \tfrac{1}{2}\rho(BxF')^2 + \tfrac{1}{2}B\mu F^2 + B\mu F'$$

or

$$p(0, 0) - p(x, \eta) = \tfrac{1}{2}\rho(u^2 + v^2) + B\mu F' \tag{3-157}$$

Thus the pressure distribution is nearly the same as the frictionless Bernoulli equation except for the additional small term $B\mu F'$. It is instructive to calculate the pressure gradients in each direction:

$$\frac{\partial p}{\partial x} = -\rho B^2 x = -\rho U \frac{dU}{dx}$$

$$\frac{\partial p}{\partial y} = -\rho B\sqrt{B\nu}\,(FF + F'') = \mathcal{O}(\sqrt{\nu}) \tag{3-158}$$

Thus the gradient parallel to the wall satisfies Bernoulli's equation, whereas the gradient normal to the wall is negligibly small if the fluid viscosity is small. As we shall see in Chap. 4, these are two of the fundamental assumptions of boundary-layer theory.

Finally, the wall shear is also, yes, a type of boundary-layer relation. With u and v known, we readily compute

$$\tau_w = \mu\left(\frac{\partial u}{\partial y} + \frac{\partial v}{\partial x}\right)_{y=0} = \mu BxF_0''\sqrt{\frac{B}{\nu}} = UF_0''\sqrt{\mu\rho B} \tag{3-159}$$

In this flow, then, wall shear is proportional to freestream velocity. If we non-dimensionalize in the manner of Eq. (3-39), we obtain

$$C_f = \frac{2\tau_w}{\rho U^2} = \frac{2F_0''}{\sqrt{Re_x}} \qquad Re_x = \frac{Ux}{\nu} \tag{3-160}$$

This inverse variation of friction factor with the square root of the local Reynolds number is very common in laminar boundary layers.

3-8.1.3 AXISYMMETRIC STAGNATION FLOW.
In plane flow, the stagnation "point" is really a *line*, i.e., there is no variation in the z direction. In axisymmetric flow, stagnation is a true point, we interpret x in Fig. 3-24 as the cylindrical radius coordinate r, and y is the axial coordinate. The cylindrical stream function is defined differently (see App. B) using axisymmetric continuity:

$$u = -\frac{1}{x}\frac{\partial \psi}{\partial y} \qquad v = \frac{1}{x}\frac{\partial \psi}{\partial x} \tag{3-161}$$

Similarly, the x-(or radial) momentum equation is different:

$$u\frac{\partial u}{\partial x} + v\frac{\partial u}{\partial y} = -\frac{1}{\rho}\frac{\partial p}{\partial x} + \nu\left[\frac{1}{x}\frac{\partial}{\partial x}\left(x\frac{\partial u}{\partial x}\right) - \frac{u}{x^2} + \frac{\partial^2 u}{\partial y^2}\right] \tag{3-162}$$

The stream function for inviscid flow toward an axisymmetric stagnation point is given by

$$\psi = -Bx^2y$$

whence

$$u = Bx \quad \text{and} \quad v = -2By \tag{3-163}$$

Compare to the plane-flow case: Because of the circular geometry, with flow area increasing along the wall with x, an increase in u is balanced by twice as much of a decrease in v.

Following Hiemenz's analysis, Homann (1936) defined the appropriate dimensionless variables for axisymmetric flow:

$$\eta = y\sqrt{\frac{B}{\nu}} \quad \psi = -x^2F(\eta)\sqrt{B\nu} \tag{3-164}$$

from which

$$u = BxF'(\eta)$$

and

$$v = -2F(\eta)\sqrt{B\nu}$$

Compare with Eqs. (3-150). Substitution in the y-momentum equation again yielded $\partial^2p/\partial x\,\partial y = 0$, and then from Eq. (3-162), one obtains the basic axisymmetric differential equation:

$$F''' + 2FF'' + 1 - F'^2 = 0 \tag{3-165}$$

with, as before, $F(0) = F'(0) = 0$ and $F'(\infty) = 1$. Compare with Eq. (3-152). A numerical solution is found in the same manner as for plane flow, and the proper initial condition is $F_0'' = 1.31194$.

The axisymmetric solutions are also shown in Fig. 3-25 and tabulated in Table 3-4. They differ a little from plane flow, e.g., the displacement and boundary-layer thicknesses are slightly smaller and the wall shear stress slightly larger. Again there clearly is thin-shear-layer behavior.

3-8.1.4 STAGNATION-POINT TEMPERATURE DISTRIBUTIONS. Once the velocities are known from the previous analysis, the temperatures can be found from the energy equation. A similarity solution exists if the wall and stream temperatures, T_w and T_∞, are constant—a realistic approximation in typical stagnation heat-transfer problems.

The plane-flow solution was given by Goldstein (1938). The two-dimensional energy, Eq. (3-3), may be written as

$$\rho c_p\left(u\frac{\partial T}{\partial x} + v\frac{\partial T}{\partial y}\right) = k\left(\frac{\partial^2T}{\partial x^2} + \frac{\partial^2T}{\partial y^2}\right) + \Phi \tag{3-166}$$

where Φ is the dissipation function. Following Goldstein (1938), we define a dimensionless temperature Θ which is zero at the wall and unity at ∞:

$$\Theta(\eta) = \frac{T - T_w}{T_\infty - T_w} \qquad \eta = y\sqrt{\frac{B}{\nu}} \tag{3-167}$$

In other words, with constant T_w and T_∞, the fluid temperature $T = T(y)$ only. With u and v known from Eqs. (3-150), substitution in the energy Eq. (3-166) gives a second-order linear equation, with Φ neglected:

$$\frac{d^2\Theta}{d\eta^2} + PrF(\eta)\frac{d\Theta}{d\eta} = 0 \tag{3-168}$$

subject to $\Theta(0) = 0$ and $\Theta(\infty) = 1$. The stream function $F(\eta)$ is known from Fig. 3-25, and the Prandtl number $Pr = \mu c_p/k$ is assumed constant.

We suppress the temptation to attack Eq. (3-168) by Subroutine RUNGE in App. C, for it is linear and has an exact solution which the reader should verify as an exercise:

$$\Theta(\eta) = \frac{\int_0^\eta d\eta \, \exp\left(-Pr\int_0^\eta F\,ds\right)}{\int_0^\infty d\eta \, \exp\left(-Pr\int_0^\eta F\,ds\right)} \tag{3-169}$$

Figure 3-26 shows the temperature profiles from this relation for various Prandtl numbers. The region of large gradients in Θ may be termed the *thermal boundary layer* and, by analogy with the velocity shear layer thickness δ_u, its thickness δ_T is the point where $\Theta \approx 0.99$. A power law curve-fit to values computed from Fig. 3-26 gives the following:

$$\frac{\delta_u}{\delta_T} \approx Pr^{0.4} \tag{3-170}$$
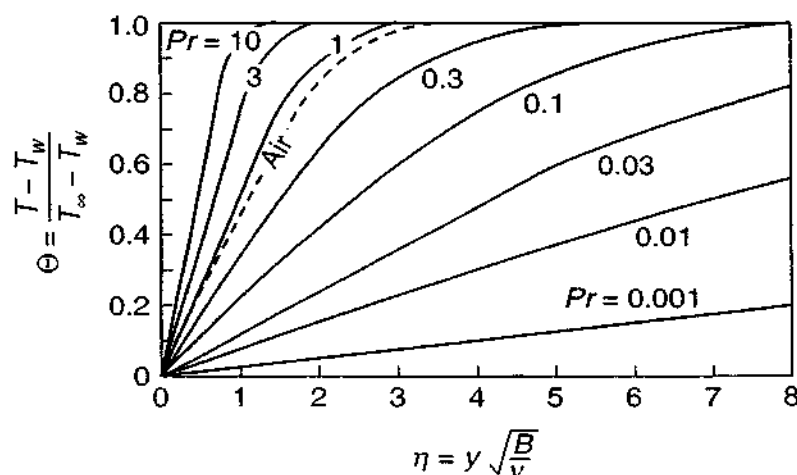
FIGURE 3-26

Stagnation-point temperature distributions for two-dimensional flow from Eq. (3-169).

Physically, the velocity boundary layer is thicker than the thermal boundary layer when $Pr > 1$, because viscous diffusion exceeds conduction effects. And the opposite is of course also true.

The heat transfer at the wall is computed from Fourier's law:

$$q_w = -k\frac{\partial T}{\partial y}\bigg|_{y=0} = -k(T_\infty - T_w)\, G(Pr)\sqrt{\frac{B}{\nu}} \qquad (3\text{-}171)$$

where G^{-1} is the denominator in Eq. (3-169):

$$\frac{1}{G(Pr)} = \int_0^\infty d\eta \, \exp\left(-Pr\int_0^\eta F\, ds\right) \qquad (3\text{-}172)$$

We may compute G simply by adding two FORTRAN statements to our earlier analysis, Eqs. (3-153):

$$F(4) = Y(3)$$

$$F(5) = EXP(-PR * Y(4))$$

The output $Y(5)$ from the subroutine equals $G(Pr)$. This effect of the Prandtl number on heat transfer is shown in Fig. 3-27. Some numerical values of G for both plane and axisymmetric flow follow:

Pr	G (plane flow)	G (axisymmetric)
0.01	0.076	0.106
0.1	0.220	0.301
1.0	0.570	0.762
10	1.339	1.752
100	2.986	3.870
1000	6.529	8.427

The axisymmetric values are about one-third higher. The log-log curves in Fig. 3-27 are nearly straight lines, so one can, if not too particular, fit them to a power law, at least near Prandtl number unity:

Plane flow: $\qquad\qquad G \approx 0.57 Pr^{0.4}$

$$\qquad\qquad\qquad\qquad\qquad\qquad\qquad\qquad\qquad (3\text{-}173)$$

Axisymmetric flow: $\qquad\qquad G \approx 0.762 Pr^{0.4}$

For axisymmetric flow, the energy equation has the form (App. B)

$$\rho c_p\left(u\frac{\partial T}{\partial x} + v\frac{\partial T}{\partial y}\right) = k\left[\frac{1}{x}\frac{\partial}{\partial x}\left(x\frac{\partial T}{\partial x}\right) + \frac{\partial^2 T}{\partial y^2}\right] \qquad (3\text{-}174)$$

The solution was given by Sibulkin (1952), using exactly the same similarity variable $\Theta(\eta)$ from Eq. (3-167). However, with u and v now given by the axisymmetric
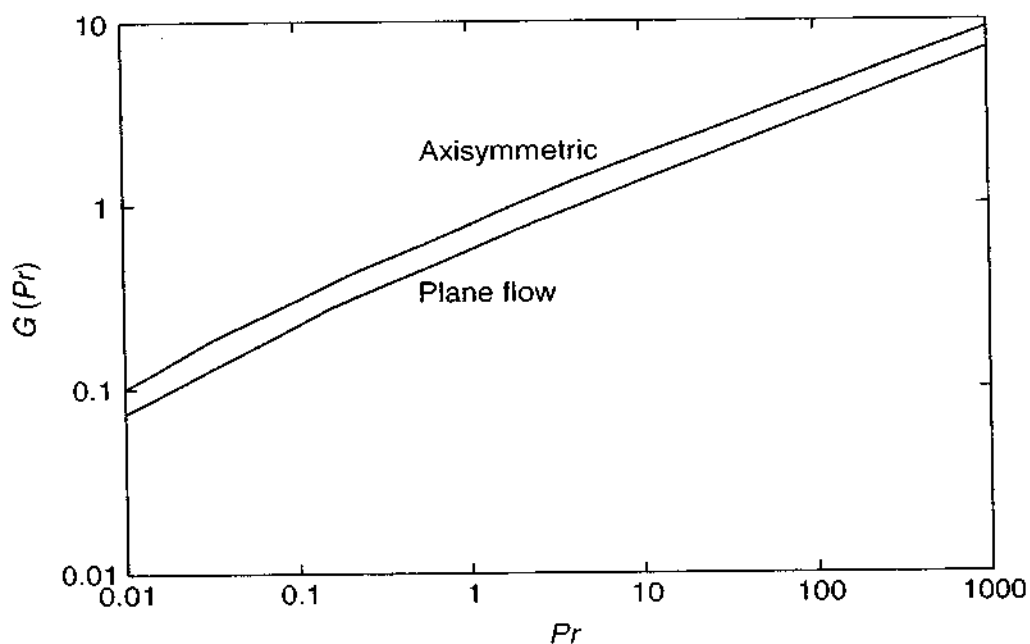
FIGURE 3-27
Variation of the heat-transfer parameter $G(Pr)$ for plane and axisymmetric stagnation flow.

forms Eq. (3-164), the equation for Θ becomes

$$\frac{d^2\Theta}{d\eta^2} + 2PrF\frac{d\Theta}{d\eta} = 0 \qquad (3\text{-}175)$$

The change is the factor "2" in the second term. The solutions for temperature distribution, Eq. (3-169), and heat-transfer parameter $G(Pr)$, Eq. (3-172), are valid for axisymmetric flow if the Prandtl number is replaced by "$2Pr$." Also, $F(\eta)$ must be taken from the axisymmetric stream function in Fig. 3-25.

The axisymmetric heat-transfer parameter $G(Pr)$ is also plotted in Fig. 3-27. Although Eq. (3-171) tells the whole story, namely, that q_w is constant independent of x, it is customary to nondimensionalize q_w as a local Nusselt number:

$$Nu_x = \frac{q_w x}{k(T_w - T_\infty)} = G(Pr)Re_x^{1/2} \qquad (3\text{-}176)$$

where $Re_x = Ux/\nu = Bx^2/\nu$ and $G(Pr)$ is given by Fig. 3-25 or the power-law approximations Eq. (3-173). As we shall see in Chap. 4, Eq. (3-176) has the typical form of laminar-boundary-layer heat-transfer relations, but in the present case, it is rather misleading because it contains a useless "x" on each side.

3-8.1.5 THE REYNOLDS ANALOGY. Osborne Reynolds (1874) postulated an approximation, now called the *Reynolds analogy*, for estimating heat transfer in shear layers. He found that, in pipe flow and "similar" boundary layers such as stagnation flow, the wall shear and heat-transfer rate are proportional:

$$\frac{|q_w|}{\tau_w} = \frac{|k(\partial T/\partial y)_w|}{\mu(\partial u/\partial y)_w} \approx \frac{k}{\mu}\left|\frac{dT}{du}\right|_w \qquad (3\text{-}177)$$

The analogy will not work unless u and T are similar in behavior, which is certainly true in stagnation flow from inspection of Figs. 3-25 and 3-26. Since T varies with Pr and u does not, the ratio above must vary with the Prandtl number. The appropriate way to nondimensionalize Eq. (3-177) is to compare the friction factor C_f to the Stanton number, $C_h = Nu/(RePr)$. Then, in general, the Reynolds analogy postulates that

$$\frac{C_h}{C_f} = fcn\left(Pr, \frac{x}{L}, \text{geometry}\right) \tag{3-178}$$

We may rewrite our stagnation-flow heat-transfer results, Eqs. (3-173) and (3-176), in terms of the Stanton number:

$$0.1 < Pr < 10: \quad C_h\sqrt{Re_x} \approx \begin{cases} 0.570Pr^{-0.6} & \text{(plane flow)} \\ 0.762Pr^{-0.6} & \text{(axisymmetric)} \end{cases} \tag{3-179}$$

Dividing this by the friction coefficient from Eq. (3-160), we obtain

$$\frac{C_h}{C_f} \approx \begin{cases} 0.23Pr^{-0.6} & \text{(plane flow)} \\ 0.29Pr^{-0.6} & \text{(axisymmetric)} \end{cases} \tag{3-180}$$

Thus, if C_f is known, C_h follows immediately. Comparable relations hold for turbulent shear flow over simple geometries, notably the flat plate. The draw back to Eq. (3-180) is that the constants (0.23, 0.29) vary markedly with pressure gradient (Sec. 4-3). Also, the Reynolds analogy fails to be accurate for (1) varying wall temperature and (2) nonsimilar flows.

This concludes our detailed study of stagnation flow, an exact solution to the Navier–Stokes equations. The results demonstrate a variety of boundary-layer phenomena: a thin viscous layer, a displacement thickness, a thin thermal layer, pressure varying with Bernoulli's relation in the outer layer, very small normal velocity near the wall, very small normal pressure gradient, the Reynolds analogy, and power-law Reynolds and Prandtl number effects. The only important effect missing is shear layer *separation* (Fig. 1.11), which cannot occur in stagnation flow because the freestream velocity increases with x ("favorable" pressure gradient, Fig. 4-5). Our third example in this section, Jeffery–Hamel wedge flow, will illustrate flow separation.

3-8.2 The Flow near an Infinite Rotating Disk

Consider the steady flow which results if the infinite plane $z = 0$ rotates at constant angular velocity ω about the axis $r = 0$ beneath a newtonian viscous fluid which would otherwise be at rest. The viscous drag of the rotating surface would set up a swirling flow toward the disk, as illustrated in Fig. 3-28. All three velocity components v_r, v_θ, and v_z would be involved—a genuine three-dimensional motion—but because of radial symmetry they would be independent of θ, as would the pressure p. It is required then to solve for these four variables as functions of r and z from
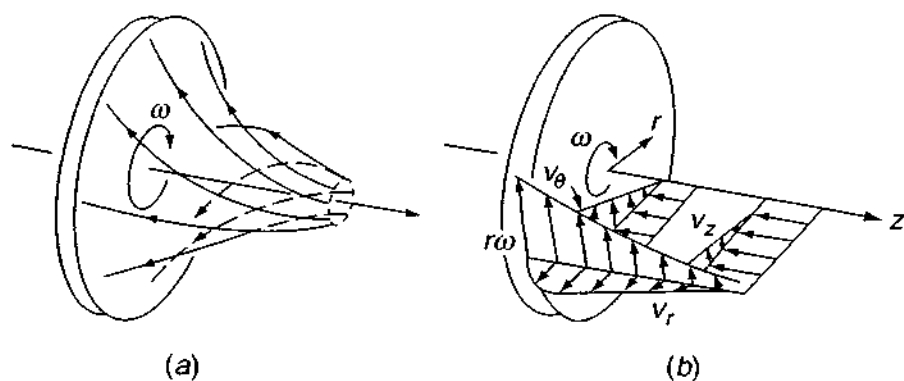
FIGURE 3-28
Laminar flow near a rotating disk: (a) streamlines; (b) velocity components.

the continuity equation and the momentum (Navier–Stokes) equations in the r, θ, and z directions:

$$\frac{1}{r}\frac{\partial}{\partial r}(rv_r) + \frac{\partial}{\partial z}(v_z) = 0$$

$$v_r\frac{\partial v_r}{\partial r} + v_z\frac{\partial v_r}{\partial z} - \frac{v_\theta^2}{r} = -\frac{1}{\rho}\frac{\partial p}{\partial r} + \nu\left(\frac{\partial^2 v_r}{\partial r^2} + \frac{1}{r}\frac{\partial v_r}{\partial r} + \frac{\partial^2 v_r}{\partial z^2} - \frac{v_r}{r^2}\right) \quad (3\text{-}181)$$

$$v_r\frac{\partial v_\theta}{\partial r} + v_z\frac{\partial v_\theta}{\partial z} + \frac{1}{r}v_rv_\theta = \nu\left(\frac{\partial^2 v_\theta}{\partial r^2} + \frac{1}{r}\frac{\partial v_\theta}{\partial r} + \frac{\partial^2 v_\theta}{\partial z^2} - \frac{v_\theta}{r^2}\right)$$

$$v_r\frac{\partial v_z}{\partial r} + v_z\frac{\partial v_z}{\partial z} = -\frac{1}{\rho}\frac{\partial p}{\partial z} + \nu\left(\frac{\partial^2 v_z}{\partial r^2} + \frac{1}{r}\frac{\partial v_z}{\partial r} + \frac{\partial^2 v_z}{\partial z^2}\right)$$

The boundary conditions are no slip at the wall and no viscous effect far from the wall (except an axial inflow):

$$\text{At } z = 0: \quad v_r = v_z = 0 \quad v_\theta = r\omega \quad p = \text{const} = 0$$

$$\text{As } z \to \infty: \quad v_r = v_\theta = \frac{\partial v_z}{\partial z} = 0 \quad (3\text{-}182)$$

This fully three-dimensional flow is often called "von Kármán's viscous pump" [Panton (1996)]. The rotating disk sets the near-wall fluid into circumferential motion v_θ. The flow would move in circular streamlines if the pressure increased radially to balance the inward centripetal acceleration. But, in fact, $p = p(z)$ only, and the radial imbalance causes an outward radial flow, $v_r > 0$ (Fig. 3-28a). This outward mass flow is balanced by an inward axial flow toward the disk, $v_z < 0$.

The solution to this problem was given in a remarkable paper by Kármán (1921), who considered not only the rotating disk but also all manner of laminar and turbulent shear flows. Kármán—whose autobiography (1964) is highly recommended by this writer—found a similarity solution by deducing that

v_r/r, v_θ/r, v_z, and p are all functions of z only. This reduces the problem to four coupled ordinary differential equations in the single variable z. Since the only parameters in the problem are ω and ν, it is easy to see that the correct dimensionless variable must be $z^* = z\sqrt{\omega/\nu}$. Following Kármán (1921), then, we propose the new dimensionless variables F, G, H, and P:

$$v_r = r\omega F(z^*)$$
$$v_\theta = r\omega G(z^*)$$
$$v_z = \sqrt{\omega\nu} H(z^*) \qquad (3\text{-}183)$$
$$p = \rho\omega\nu P(z^*)$$

We can substitute these variables into Eqs. (3-181) and obtain the following set of non-linear ordinary coupled differential equations:

$$H' = -2F$$
$$F'' = -G^2 + F^2 + F'H$$
$$G'' = 2FG + HG' \qquad (3\text{-}184)$$
$$P' = 2FH - 2F'$$

where primes denote differentiation with respect to z^*. The boundary conditions from (3-182) now become

$$F(0) = H(0) = P(0) = 0$$
$$G(0) = 1 \qquad (3\text{-}185)$$
$$F(\infty) = G(\infty) = 0$$

Note that P is uncoupled: We can solve the first three of Eq. (3-184) for F, G, and H and then solve for P from the fourth equation.

Kármán used this flow to illustrate his celebrated momentum-integral relation (Sec. 4-5) derived in the same 1921 paper. Cochran (1934) improved the accuracy with matched inner and outer expansions. Rogers and Lance (1960) gave very accurate numerical solutions. The system Eq. (3-184) is easily solved by Subroutine RUNGE in App. C: Define six variables: $Y_1 = H$, $Y_2 = F'$, $Y_3 = F$, $Y_4 = G'$, $Y_5 = G$, and $Y_6 = P$. Equations (3-184) are then simulated on a digital computer by the six FORTRAN statements

$$F(1) = -2. * Y(3)$$
$$F(2) = -Y(5) * Y(5) + Y(3) * Y(3) + Y(2) * Y(1)$$
$$F(3) = Y(2)$$
$$F(4) = 2. * Y(3) * Y(5) + Y(1) * Y(4) \qquad (3\text{-}186)$$
$$F(5) = Y(4)$$
$$F(6) = 2. * Y(3) * Y(1) - 2. * Y(2)$$

$$z = z\sqrt{\frac{\omega}{\nu}}$$
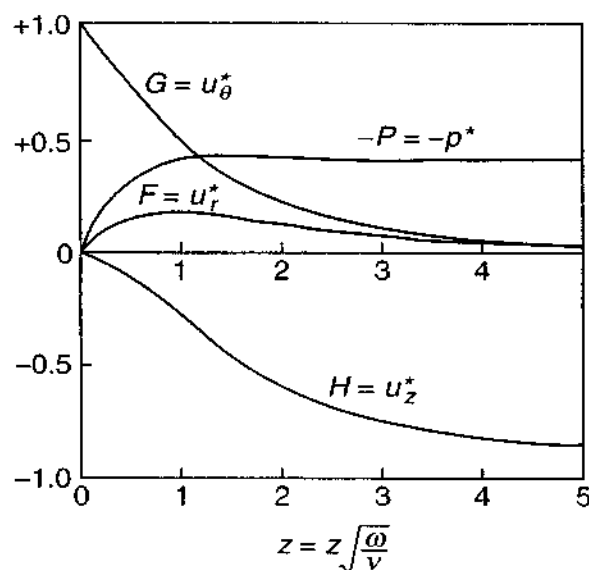
FIGURE 3-29
Numerical solutions of Eqs. (3-184) for the infinite rotating disk.

The reader should compare these statements with Eqs. (3-184). The known initial conditions from Eqs. (3-185) are $Y_1(0) = Y_3(0) = Y_6(0) = 0$ and $Y_5(0) = 1$. The unknown conditions are $F_0' = Y_2(0)$ and $G_0' = Y_4(0)$, which must be chosen to make Y_3 and Y_5 vanish at large η. An appropriate step size in $\Delta\eta \le 0.1$ and "infinity" is reached at about $\eta \approx 10$. The correct initial conditions are found to be $F_0' = 0.5102$ and $G_0' = -0.6159$, and the complete numerical solutions are shown in Fig. 3-29 and Table 3-5.

We may define the thickness δ as the point where the circumferential velocity v_θ drops to 1 percent of its wall value, or $G \approx 0.01$, which occurs at about $\eta \approx 5.4$. Then the layer thickness is

$$\delta \approx 5.4\sqrt{\frac{\nu}{\omega}} \tag{3-187}$$

For a disk rotating at 1000 rpm (105 rad/s) in air at 20°C, this relation predicts a (laminar) shear layer thickness of approximately 2 mm.

The asymptotic value $H(\infty) = -0.8838$, which means that the disk draws fluid toward it at the rate

$$v_z(\infty) = -0.8838\sqrt{\omega\nu} \tag{3-188}$$

Thus the disk's pumping action increases with both viscosity and rotation rate. For the above numerical example (1000 rpm in air), this streaming velocity would be 3.5 cm/s toward the disk.

The circumferential wall shear stress on the disk is

$$\tau_{z\theta} = \mu \left.\frac{\partial u_\theta}{\partial z}\right|_{z=0} = \rho r G_0' \sqrt{\nu\omega^3} \tag{3-189}$$

TABLE 3-5
Numerical solution for the rotating disk

z^*	F	F'	G	G'	H	$-P$
0.0	0.0	0.51023	1.0000	−0.61592	0.0	0.0
0.1	0.0462	0.4163	0.9386	−0.6112	−0.0048	0.0924
0.2	0.0836	0.3338	0.8780	−0.5987	−0.0179	0.1674
0.3	0.1133	0.2620	0.8190	−0.5803	−0.0377	0.2274
0.4	0.1364	0.1999	0.7621	−0.5577	−0.0628	0.2747
0.5	0.1536	0.1467	0.7075	−0.5321	−0.0919	0.3115
0.6	0.1660	0.1015	0.6557	−0.5047	−0.1239	0.3396
0.7	0.1742	0.0635	0.6067	−0.4763	−0.1580	0.3608
0.8	0.1789	0.0317	0.5605	−0.4476	−0.1933	0.3764
0.9	0.1807	0.0056	0.5171	−0.4191	−0.2293	0.3877
1.0	0.1801	−0.0157	0.4766	−0.3911	−0.2655	0.3955
1.2	0.1737	−0.0461	0.4037	−0.3381	−0.3364	0.4040
1.4	0.1625	−0.0640	0.3411	−0.2898	−0.4038	0.4066
1.6	0.1487	−0.0728	0.2875	−0.2470	−0.4661	0.4061
1.8	0.1338	−0.0754	0.2419	−0.2095	−0.5226	0.4042
2.0	0.1188	−0.0739	0.2034	−0.1771	−0.5732	0.4019
2.2	0.1044	−0.0698	0.1708	−0.1494	−0.6178	0.3997
2.4	0.0910	−0.0643	0.1433	−0.1258	−0.6568	0.3977
2.6	0.0788	−0.0580	0.1202	−0.1057	−0.6907	0.3961
2.8	0.0678	−0.0517	0.1008	−0.0888	−0.7200	0.3948
3.0	0.0581	−0.0455	0.0845	−0.0746	−0.7452	0.3938
3.2	0.0496	−0.0397	0.0709	−0.0625	−0.7666	0.3930
3.4	0.0422	−0.0344	0.0594	−0.0525	−0.7850	0.3924
3.6	0.0358	−0.0296	0.0498	−0.0440	−0.8005	0.3920
3.8	0.0303	−0.0254	0.0417	−0.0369	−0.8137	0.3917
4.0	0.0256	−0.0217	0.0349	−0.0309	−0.8249	0.3914
4.5	0.0167	−0.0144	0.0225	−0.0199	−0.8457	0.3911
5.0	0.0108	−0.0095	0.0144	−0.0128	−0.8594	0.3910
5.5	0.0070	−0.0062	0.0093	−0.0082	−0.8682	0.3910
6.0	0.0045	−0.0040	0.0059	−0.0053	−0.8739	0.3909
7.0	0.0018	−0.0017	0.0024	−0.0022	−0.8799	0.3909
8.0	0.0007	−0.0007	0.0010	−0.0009	−0.8824	0.3908
9.0	0.0002	−0.0003	0.0004	−0.0004	−0.8834	0.3908
10.0	0.0001	−0.0001	0.0001	−0.0001	−0.8838	0.3907
∞	0.0	−0.0	0.0	−0.0	−0.8838	0.3906

where $G'_0 = -0.6159$ from Table 3-5. We use this result with a radial strip integration to find the total torque required to turn a disk of radius r_0:

$$M = \int_0^{r_0} \tau_{z\theta}\, r\, (2\pi r\, dr) = \frac{\pi}{2}\, \rho r_0^4\, G'_0 \sqrt{\nu \omega^3} \qquad (3\text{-}190)$$
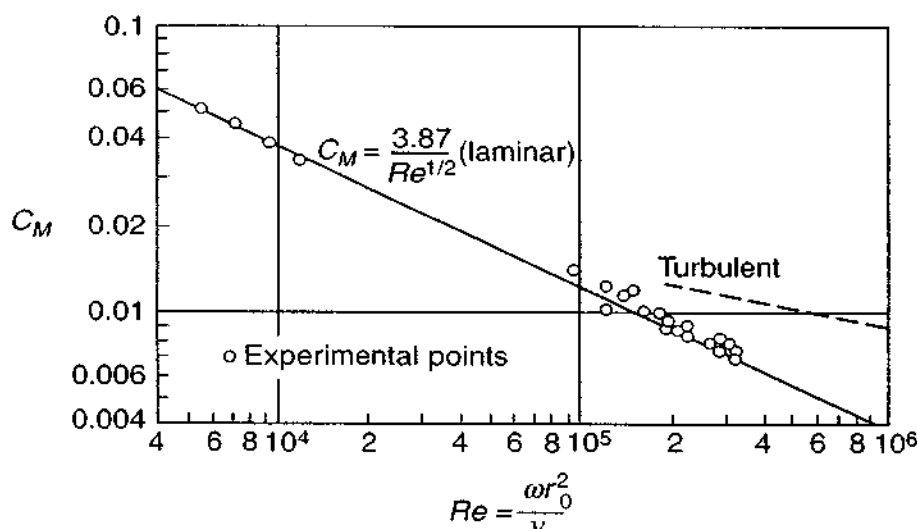
FIGURE 3-30

Theoretical and experimental torque coefficient for a rotating disk. [*Data from Theodorsen and Regier (1944)*.]

Thus the required (laminar) moment increases as the fourth power of the disk radius. For our running example, 1000 rpm in air, if the disk radius is 10 cm, this torque is only 0.0005 N · m. A dimensionless torque coefficient can be defined for a disk wetted on both sides:

$$C_M = \frac{-2M}{\frac{1}{2}\rho\omega^2 r_0^5} \approx \frac{3.87}{\sqrt{Re}}$$

$$Re = \frac{\omega r_0^2}{\nu}$$

(3-191)

Again we have the characteristic inverse variation with the square root of the Reynolds number. Equation (3-191) is compared in Fig. 3-30 with the data of Theodorsen and Regier (1944). The agreement is good, but for $Re > 300,000$, the flow becomes turbulent and follows the dashed line.

The expected instability of laminar rotating-disk flow was clearly shown in the experiments of Kobayashi et al. (1980). They rotated a 40 cm diameter black aluminum disk in air at 1300 to 1900 rpm and visualized the flow with white titanium tetrachloride gas. A photograph of the flow is shown in Fig. 3-31. Instability is observed at $Re = \omega r^2/\nu \approx 8.8 \times 10^4$ and from 30 to 34 spiral laminar vortices from spreading out at an angle of 10 to 15°. Then, at $Re \approx 3.2 \times 10^5$, turbulence ensues.

Many other papers have been written about various flow problems associated with one or more circular disks. Of particular interest is rotating *flow* next to a fixed disk, first considered by Bödewadt (1940) and later by Rogers and Lance (1960). The picture is essentially reversed from Fig. 3-28. The rotating outer flow sets up a radial pressure gradient which, when acting on the low-velocity fluid near the disk, causes an *inward* radial flow, called "secondary" flow. This inward flow is balanced
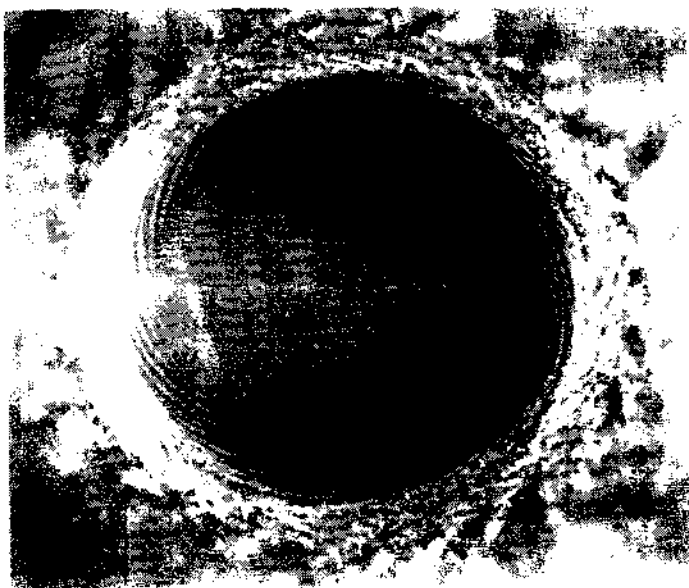
FIGURE 3-31
Flow pattern on a disk rotating in air at 1800 rpm. Laminar flow becomes unstable at $r = 8$ cm, laminar spiral vortices form at $r = 12$ cm, and transition to turbulence is at $r = 16$ cm. [*After Kobayashi et al. (1980).*]

by axial flow *away* from the disk. Secondary inward wall flow is familiar to anyone who stirs tea made with loose leaves.

3-8.3 Jeffery–Hamel Flow in a Wedge-Shaped Region

Our third and final example of an exact similarity solution is the radial flow caused by a line source or sink, first discussed by Jeffery (1915) and independently by Hamel (1917). Many subsequent analyses have been made for this flow, and we mention especially Rosenhead (1940) and Millsaps and Pohlhausen (1953).

As shown in Fig. 3-32, we consider the flow in polar coordinates (r, θ), generated by a source (or sink) at the origin and boundary by solid walls at $\theta = \pm\alpha$, as shown. Assume that the flow is purely radial, $u_\theta = 0$. Then, from the continuity equation in polar coordinates (App. B),

$$\frac{1}{r}\frac{\partial}{\partial r}(ru_r) = 0$$

or

$$ru_r = fcn(\theta)$$

(3-192)

We expect that u_r will have a local maximum, u_{max}, probably at $\theta = 0$. Then a convenient nondimensionalization for this problem is

$$\eta = \frac{\theta}{\alpha}$$
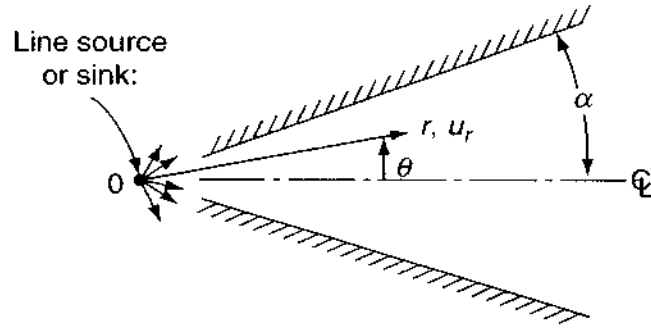
$$\frac{u_r}{u_{max}} = f(\eta)$$

(3-193)

FIGURE 3-32
Geometry of the Jeffery–Hamel flow.

The momentum equations in polar coordinates, for $u_\theta = 0$, are

$$u_r \frac{\partial u_r}{\partial r} = -\frac{1}{\rho} \frac{\partial p}{\partial r} + \nu \left(\frac{\partial^2 u_r}{\partial r^2} + \frac{1}{r} \frac{\partial u_r}{\partial r} - \frac{u_r}{r^2} + \frac{1}{r^2} \frac{\partial^2 u_r}{\partial \theta^2} \right)$$

$$0 = -\frac{1}{\rho r} \frac{\partial p}{\partial \theta} + \frac{2\nu}{r^2} \frac{\partial u_r}{\partial \theta}$$

$$(3\text{-}194)$$

We can eliminate pressure by cross-differentiation and introduce the variables η and $f(\eta)$. The result is a third-order non-linear differential equation for f:

$$f''' + 2Re\,\alpha f f' + 4\alpha^2 f' = 0 \qquad (3\text{-}195)$$

where $Re = u_{max} r \alpha / \nu$ is the characteristic Reynolds number of the flow. The boundary conditions are no slip at either wall and an assumed symmetric flow with a maximum at the centerline:

$$f(+1) = f(-1) = 0 \qquad f(0) = 1 \qquad (3\text{-}196)$$

We could replace the second condition with the symmetry requirement $f'(0) = 0$ and confine the analysis to the upper half of the wedge region.

Since Eq. (3-195) is non-linear, we are tempted immediately to call upon Subroutine RUNGE, just as we did with stagnation flow and the rotating disk. In fact, however, an analytic solution is possible. We integrate once to obtain

$$f'' + Re\,\alpha f^2 + 4\alpha^2 f = \text{const}$$

Multiply this by f' and integrate again, using $f(0) = 1$ and $f'(0) = 0$:

$$f'^2 = (1 - f)\left[\tfrac{2}{3} Re\,\alpha(f^2 + f) + 4\alpha^2 f + C \right]$$

which can be integrated again because the variables are separable:

$$\eta = \int_f^1 \frac{df}{\left\{ (1 - f)\left[\tfrac{2}{3} Re\,\alpha(f^2 + f) + 4\alpha^2 f + C \right] \right\}^{1/2}} \qquad (3\text{-}197)$$

where the boundary condition $f(0) = 1$ has been used again. As η approaches 1, the lower limit approaches zero, $f(1) = 0$, which specifies the constant C:

$$1 = \int_0^1 \frac{df}{\left\{(1 - f)\left[\frac{2}{3}Re\ \alpha(f^2 + f) + 4\alpha^2 f + C\right]\right\}^{1/2}} \tag{3-198}$$

Thus Eqs. (3-197) and (3-198) are the formal solution of the problem. The integral is an elliptical integral and can be evaluated from tables or by careful application of Subroutine RUNGE to avoid trouble as $(1 - f) \rightarrow 0$.

Rosenhead (1940) made a very extensive analysis of this flow and cited the following observations:

1. For any given α and Re, there are an infinite number of possible solutions, both symmetric and asymmetric, corresponding to multiple regions of inflow and outflow.
2. For a given α and a specified number of inflow and outflow regions, there is a critical Re above which this specified solution in impossible.
3. For $\pi/2 < \alpha < \pi$, a solution with pure outflow is impossible, and pure-inflow solutions are limited in certain respects.
4. For $\alpha < \pi/2$, pure inflow is always possible and tends at large Re to have boundary-layer behavior, whereas pure outflow is limited to certain small Re whose approximate range is $Re < 10.31/\alpha$.

Thus once again we encounter nonuniqueness of the Navier–Stokes equations, although here it is regular and predictable.

3.8.3.1   SOLUTION FOR SMALL WEDGE ANGLE α.

The most practical application of this flow is to large Re and small α. If both Re and α are small, we may neglect the second and third terms in Eq. (3-195) and integrate to

$$\alpha, Re\alpha \ll 1: \qquad f = \frac{u_r}{u_{max}} = 1 - \eta^2 \tag{3-199}$$

which is Poiseuille flow, Eq. (3-42), valid for either inflow or outflow.

Suppose instead that α is small but $Re\alpha$ is not. Then Eq. (3-198) reduces to

$$\left(\frac{2Re\ \alpha}{3}\right)^{1/2} = \int_0^1 \frac{df}{[(1 - f)(f^2 + f + K)]^{1/2}} \tag{3-200}$$

where $K = 3C/2Re\ \alpha$. Thus we can specify a range of values of K and carry out the integration to obtain $Re\alpha$, after which C follows from K. Values calculated in this manner are shown in Fig. 3-33. For negative Re (inflow), the values approach the straight line $C = -4\,Re\alpha/3$, which is a boundary-layer approximation first discovered by Pohlhausen (1921). For positive Re (outflow), C drops to zero at $Re\ \alpha \approx 10.31$; since $C = f'^2(1)$, this must be a point of zero wall shear stress, a separation point beyond which backflow will occur at the wall. After evaluating C
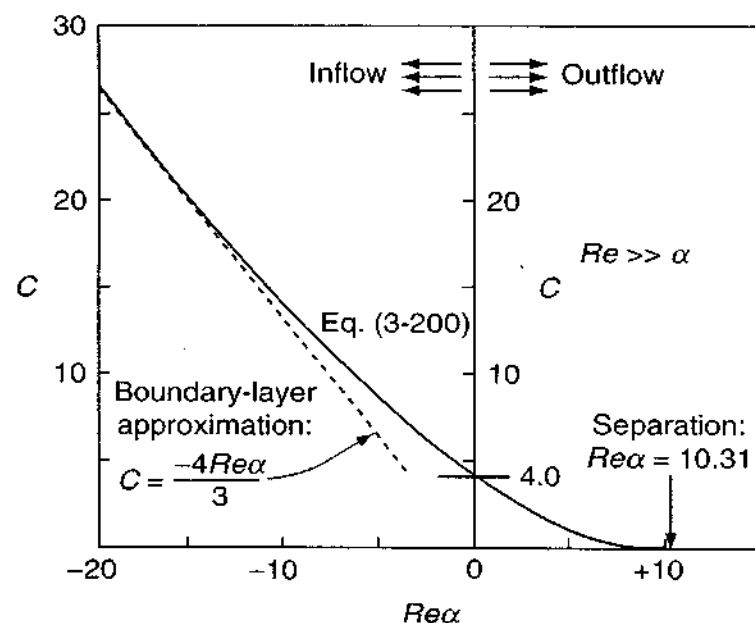
FIGURE 3-33
Values of the shear-stress constant C for wedge flow at large Reynolds numbers.

in this manner, Millsaps and Pohlhausen (1953) computed several velocity profiles from Eq. (3-197). Figure 3-34 shows an array of inflow ($Re < 0$) and outflow ($Re > 0$) profiles computed in the same manner. The inflow curves become flatter and more stable as Re increases and will be discussed again in Chap. 4.

The outflow profiles become S-shaped and have zero wall shear stress (the separation point) when $Re\,\alpha = 10.31$. If $Re\,\alpha > 10.31$, there is backflow at the wall. The difference in profile shape is the result of the change in sign of the
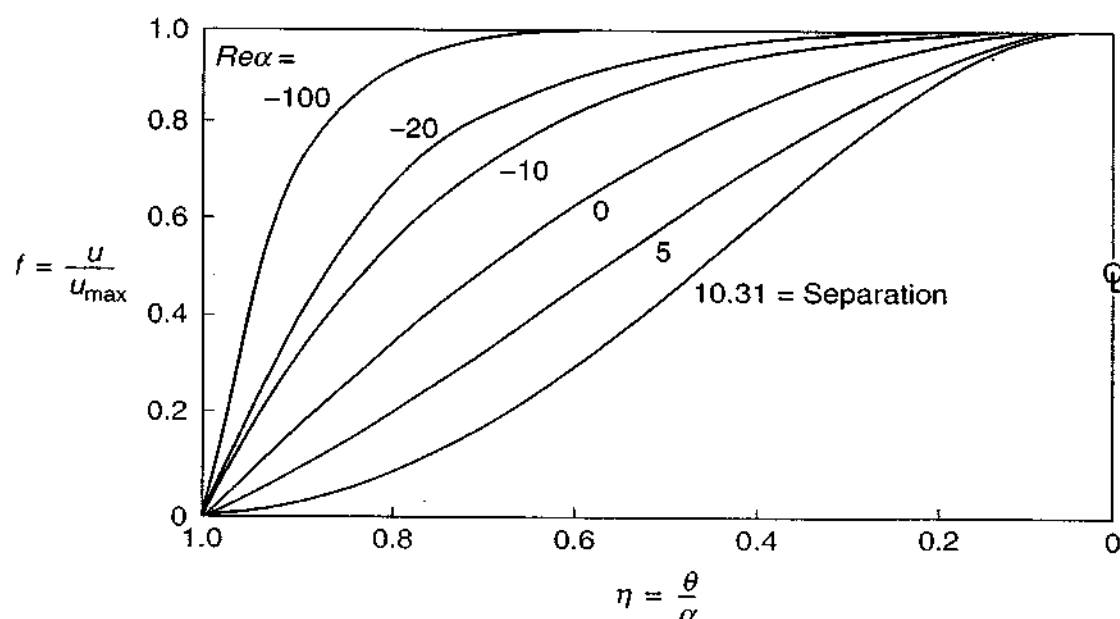
FIGURE 3-34
Velocity profiles for Jeffery–Hamel wedge flow at large $Re \gg \alpha$, from Eq. (3-197). [*Modified from the results of Millsaps and Pohlhausen (1953).*]

streamwise pressure gradient. For inflow, p decreases in the flow direction (favorable gradient) and there is no separation. For outflow, p increases downstream (adverse gradient), a point of inflection occurs in the profile, and separation is imminent.

A separation criterion can be found from the pressure gradient along the centerline, which from Eq. (3-194) is given by

$$\frac{\partial p}{\partial r}(r, 0) \approx \frac{\rho u_{max}^2}{r}$$

if $\alpha^2 \ll 1$. If we interpret $(r\alpha)$ as the thickness δ of the shear layer, the dimensionless form of the pressure gradient at separation would be

$$\frac{\delta^2}{\mu u_{max}} \frac{\partial p}{\partial r}(r, 0)_{separation} \approx (Re\, \alpha)_{separation} = 10.31 \tag{3-201}$$

This is much more realistic than the Couette–Poiseuille flow estimate given earlier as Eq. (3-43). In laminar boundary layers, this quantity is called the Kármán–Pohlhausen parameter, $\Lambda = \delta^2(dp/dx)/\mu U$, which at the point of separation takes on values between $+8$ and $+12$.

With the velocity profiles given from Fig. 3-34, Millsaps and Pohlhausen (1953) also solved for temperature profiles, assuming dissipation only—no hot or cold walls. For inflow, there is a region of very strong dissipation temperature rise near the wall.

This completes our study of similar solutions to the Navier–Stokes equations. Other cases are given in the problem exercises.

3-9 LOW REYNOLDS NUMBER: LINEARIZED CREEPING MOTION

All the problems we have looked at so far in this chapter have been exact solutions, valid for an arbitrary Reynolds number, at least until instability sets in and turbulence ensues. While interesting, these exact solutions lack generality. In particular, there is no known solution for the very practical problem of viscous flow past an immersed body at an arbitrary Reynolds number. Other than direct experiment, immersed-body problems are presently solvable only by three approaches: (1) digital-computer simulations, as in Sec. 3-10 to follow; (2) boundary-layer viscous/inviscid patching schemes, as in Chap. 4; and (3) the creeping-flow approximation, to be discussed now.

The basic assumption of creeping flow, developed by Stokes (1851) in a seminal paper, is that density (inertia) terms are negligible in the momentum equation. In such a flow, with stream velocity U and body length L, pressure cannot scale with the "dynamic" or inertia term ρU^2 but rather must depend upon a "viscous" scale $\mu U/L$. If we nondimensionalize the Navier–Stokes Eq. (3-2) with the variables

$$x^* = \frac{x}{L} \qquad V^* = \frac{V}{U} \qquad t^* = \frac{tU}{L} \qquad p^* = \frac{p - p_\infty}{\mu U/L}$$

then we obtain the following dimensionless momentum equation:

$$Re \frac{D\mathbf{V}^*}{Dt^*} = -\nabla^* p^* + \nabla^{*2}\mathbf{V}^* \tag{3-202}$$

where $Re = \rho UL/\mu$. We can therefore neglect inertia (the left-hand side) if the Reynolds number is small. This is the creeping-flow or *Stokes flow* assumption:

$$Re \ll 1: \qquad\qquad \nabla p \approx \mu \nabla^2 \mathbf{V} \tag{3-203}$$

to be combined with the incompressible continuity relation,

$$\nabla \cdot \mathbf{V} = 0 \tag{3-204}$$

Note that inertia is also negligible if there is no convective acceleration, such as in fully developed duct flow, Sec. 3-3. In such a case, the creeping-flow approximation holds with no restriction on the Reynolds number.

By taking the curl and then the gradient of Eq. (3-203), we obtain two additional useful relations:

$$\nabla^2 \omega = 0$$
$$\nabla^2 p = 0 \tag{3-205}$$

Thus both the vorticity and the pressure satisfy Laplace's equation in creeping flow.

In two-dimensional Stokes flow, $\omega = -\nabla^2\psi$, where $\psi(x, y)$ is the stream function. The vorticity equation (3-205) may be rewritten as

$$\text{Plane flow:} \qquad\qquad \nabla^4 \psi = 0 \tag{3-206}$$

This is the *biharmonic* equation, much studied in plane elasticity problems. Typical boundary conditions for an immersed-body problem would be no slip at the body surface and uniform velocity and pressure in the freestream.

All of Eqs. (3-203) to (3-206) are linear partial differential equations and thus yield many solutions in closed form. Numerical methods are also very effective, including the boundary-element technique [Beer (2001) and Wrobel (2002)]. Whole textbooks are written about creeping flow, notably Happel and Brenner (1983). The drawback, of course, is that the condition $Re \ll 1$ is very restrictive and usually applies only to low-velocity, small-scale, highly viscous flows. At least four types of creeping flow arise:

1. *Fully developed duct flow.* We have given several examples here in Sec. 3-3 and many more can be found in Berker (1963), Ladyzhenskaya (1969), and Shah and London (1978).
2. *Flow about immersed bodies.* Stokes flow is the foundation of small-particle dynamics and is treated in a text by Happel and Brenner (1983), including multiple-body interaction effects.
3. *Flow in narrow but variable passages.* First formulated by Reynolds (1886) and now known as *lubrication theory*, these flows are covered in general Stokes flow

books such as Langlois (1964) and also in specialized texts such as Khonsari and Booser (2001), Szeri (1998), and Pirro et al. (2001).

4. *Flow through porous media.* This topic began with a famous treatise by Darcy (1856) and is now the subject of specialized texts such as Bear (2000), Ingham and Pop (2002), and Ehlers and Bluhm (2002). Civil engineers have long applied porous-media theory to groundwater movement [see, e.g., Charbeneau (1999)].

The fundamental principles of creeping, or small-inertia flows, are beautifully demonstrated in a 33-min color video, "Low Reynolds Number Flows," available from Encyclopedia Britannica Education Corp. The video was prepared from a color film produced 40 years ago under the sponsorship of the National Science Foundation. It is a historical document because its narrator is Sir Geoffrey Taylor, whose collected works contain scores of important contributions to our knowledge of fluid mechanics.

Finally, we should not fail to mention the interesting flow-visualization device constructed by Hele-Shaw (1898), wherein the streamlines of creeping motion in a narrow passage with an obstacle are shown to be identical to the potential (inviscid) flow about that same obstacle. As analogies go, this is certainly an ironic one.

3-9.1 Creeping Flow about Immersed Bodies: Stokes Paradox

This subject began with a solution for sphere motion given by Stokes (1851). Many solutions exist for three-dimensional bodies, but plane flows are fraught with paradox. As pointed out by Stokes himself, it is impossible to find a steady two-dimensional solution which satisfies both Eq. (3-206) and the no-slip and freestream boundary conditions. Three-dimensional flows do not have this problem, but they are slightly unrealistic in that the inertia terms are not strictly negligible in the far field of the body [Oseen (1910)].

We can illustrate the Stokes paradox with a dimensional argument: If inertia (density) is truly negligible, the force on the body must depend only upon freestream velocity U, fluid viscosity μ, and body-length scale L:

Two-dimensional flow:

$$F' = \text{force per unit length} = f(U, \mu, L) \tag{3-207a}$$

Three-dimensional flow:

$$F = \text{total drag force} = f(U, \mu, L) \tag{3-207b}$$

Dimensional analysis of these relations leads to the force laws

Two-dimensional: $$\frac{F'}{\mu U} = \text{const} \tag{3-208a}$$

Three-dimensional: $$\frac{F}{\mu U L} = \text{const} \tag{3-208b}$$

The second of these is quite realistic and verified by numerous experiments, but the first is physically in error, since it implies that the drag force is independent of the size L of the body, whether huge or tiny. It follows that there must *always* be a density effect in plane creeping motion:

Two-dimensional:

$$F' = f(\rho, U, \mu, L)$$

or

$$\frac{F'}{\mu U} = f\left(\frac{\rho U L}{\mu}\right)$$

(3-209)

The Reynolds number is always important, then. Mathematically, the Stokes paradox means that a plane creeping solution will produce a logarithmic singularity at infinity unless inertia terms are accounted for. Physically, we can infer that a body of infinite depth produces such a profound disturbance in a viscous flow that inertia effects are always important, no matter how slow the freestream speed. Langlois (1964) explains these difficulties very well.

To this writer's surprise, it turns out that the Stokes paradox is not so robust for nonnewtonian fluids. With a simple analysis for power-law fluids in two-dimensional flow past a cylinder, Eq. (1-31a), Tanner (1993) shows that the paradox holds only for $n = 1$ (newtonian fluid) and for $n > 1$ (dilatant or shear-thickening fluid). Both these cases, $n \geq 1$, have density (inertia) effects no matter how large the effective viscosity. However, for $n < 1$ (pseudoplastic or shear-thinning fluid), Tanner shows that the Stokes paradox vanishes and the creeping-flow cylinder drag is independent of the density.

3-9.2 Stokes' Solution for an Immersed Sphere

Consider creeping motion of a stream of speed U about a solid sphere of radius a (Fig. 3-35). It is convenient to use spherical polar coordinates (r, θ), with $\theta = 0$ in the direction of U. The velocity components u_r and u_θ are related to the Stokes stream function ψ by the relations

$$u_r = \frac{1}{r^2 \sin\theta}\frac{\partial\psi}{\partial\theta} \qquad u_\theta = -\frac{1}{r\sin\theta}\frac{\partial\psi}{\partial r}$$

(3-210)

These satisfy the continuity relation identically. The momentum equation then becomes

$$\left(\frac{\partial^2}{\partial r^2} + \frac{1}{r^2}\frac{\partial^2}{\partial\theta^2} - \frac{\cot\theta}{r^2}\frac{\partial}{\partial\theta}\right)^2 \psi = 0$$

(3-211)

Note that this is slightly more complicated than the biharmonic operator of
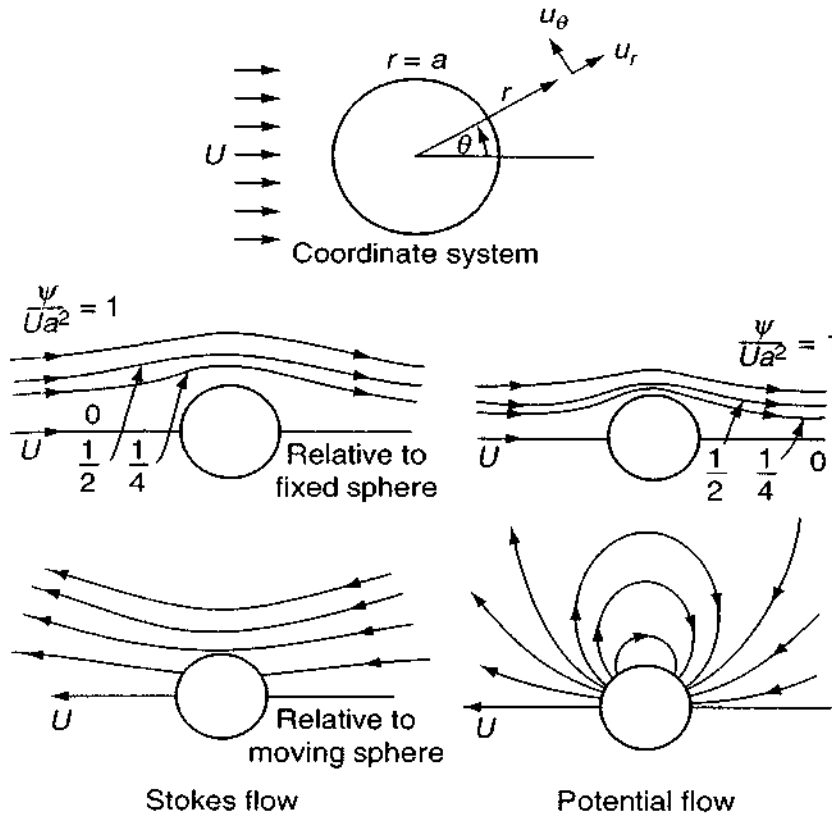
FIGURE 3-35
Comparison of creeping flow (*left*) and potential flow (*right*) past a sphere.

Eq. (3-206) because of the three-dimensional geometry. The boundary conditions are

At $r = a$:
$$\frac{\partial \psi}{\partial r} = \frac{\partial \psi}{\partial \theta} = 0$$

As $r \rightarrow \infty$:
$$\psi \rightarrow \tfrac{1}{2} U r^2 \sin^2 \theta + \text{const}$$

(3-212)

The problem appears formidable, but in fact it yields readily to a product solution $\psi(r, \theta) = f(r)g(\theta)$. With this broad hint, we substitute in Eq. (3-211), satisfy Eq. (3-212), and find the solution of Stokes (1851) for creeping motion past a sphere:

$$\psi = \frac{1}{4} U a^2 \sin^2 \theta \left(\frac{a}{r} - \frac{3r}{a} + \frac{2r^2}{a^2} \right)$$

(3-213)

The velocity components follow immediately from Eq. (3-210):

$$u_r = U \cos \theta \left(1 + \frac{a^3}{2r^3} - \frac{3a}{2r} \right)$$

$$u_\theta = U \sin \theta \left(-1 + \frac{a^3}{4r^3} + \frac{3a}{4r} \right)$$

(3-214)

Compared to the previous array of analyses in this chapter, this celebrated solution has several extraordinary properties:

1. The streamlines and velocities are entirely independent of the fluid viscosity. Upon reflection, we deduce that this is true of all creeping flows.
2. The streamlines possess perfect fore-and-aft symmetry: There is no wake of the type shown in Fig. 1-6. It is the role of the convective acceleration terms, here neglected, to provide the strong flow asymmetry typical of higher Reynolds number flows.
3. The local velocity is everywhere retarded from its freestream value: There is no faster region such as occurs in potential flow (Fig. 3-35) at the sphere shoulder (where $u_\theta = 1.5U$).
4. The effect of the sphere extends to enormous distances: At $r = 10a$, the velocities are still about 10 percent below their freestream values.

With u_r and u_θ known, the pressure is found by integrating the momentum relation, Eq. (3-203). The result is

$$p = p_\infty - \frac{3\mu a U}{2r^2} \cos \theta \qquad (3\text{-}215)$$

where p_∞ is the uniform freestream pressure. Thus the pressure deviation is proportional to μ and antisymmetric, being positive at the front and negative at the rear of the sphere. This creates a pressure drag on the sphere. There is also a surface shear stress which creates a drag force. The shear-stress distribution in the fluid is given by

$$\tau_{r\theta} = \mu \left(\frac{1}{r} \frac{\partial u_r}{\partial \theta} + \frac{\partial u_\theta}{\partial r} - \frac{u_\theta}{r} \right) = -\frac{\mu U \sin \theta}{r} \left(\frac{3a^3}{2r^3} \right) \qquad (3\text{-}216)$$

The total drag is found by integrating pressure and shear around the surface:

$$F = -\int_0^\pi \tau_{r\theta} \bigg|_{r=a} \sin \theta \, dA - \int_0^\pi p \bigg|_{r=a} \cos \theta \, dA$$

$$dA = 2\pi a^2 \sin \theta \, d\theta \qquad (3\text{-}217)$$

$$F = 4\pi\mu U a + 2\pi\mu U a = 6\pi\mu U a$$

This is the famous sphere-drag formula of Stokes (1851), consisting of two-thirds viscous force and one-third pressure force. The formula is strictly valid only for $Re \ll 1$ but agrees with experiment up to about $Re = 1$.

The proper drag coefficient should obviously be $F/\mu U a = 6\pi = \text{const}$, but everyone uses the inertia type of definition $C_D = 2F/\rho U^2(\text{area})$, which is nearly constant at high Reynolds numbers. Thus the sphere drag is written as

$$C_D = \frac{2F}{\rho U^2 \pi a^2} = \frac{24}{Re}$$

where

$$Re = \frac{2a\rho U}{\mu} \tag{3-218}$$

As noted earlier, this introduces a Reynolds number effect where none exists. The formula underpredicts the actual drag when, for $Re > 1$, an unsymmetrical wake forms and, for $Re > 20$, the flow separates from the rear surface, causing markedly increased pressure drag.

The Stokes flow streamlines from Eq. (3-213) are compared in Fig. 3-35 with the streamlines for inviscid (potential) flow past a sphere, for which the classical solution [e.g., White (2003)] is

$$\psi = \frac{1}{2} U r^2 \sin^2 \theta \left(1 - \frac{a^3}{r^3} \right) \tag{3-219}$$

When we compare streamlines past a fixed sphere, the two are superficially similar, except that the Stokes streamlines are displaced further by the body. However, the difference is striking when we compare (Fig. 3-35) streamlines for a sphere moving through a fixed fluid, which we calculate by subtracting the freestream function $\frac{1}{2}Ur^2 \sin^2 \theta$ from Eq. (3-213). The sphere moving in potential flow shows circulating streamlines, indicating that it is merely pushing fluid out of the way. By contrast, the creeping sphere seems to drag the entire surrounding fluid with it, and recirculation is absent.

3-9.3   Other Three-Dimensional Body Shapes

In principle, a Stokes flow analysis is possible for any three-dimensional body shape, providing that one has the necessary analytical skill. A number of interesting shapes are discussed in the texts by Happel and Brenner (1983) and Clift et al. (1978). Of particular interest is the drag of a circular disk:

Disk normal to the freestream: $F = 16\mu Ua$ (3-220a)

Disk parallel to the freestream: $F = \frac{32}{3}\mu Ua$ (3-220b)

Here a is the radius of the disk. It is interesting that the values differ only by -15 and -43 percent, respectively, from the drag of a sphere, in spite of the vastly different geometry and orientation. Thus we would expect the Stokes sphere law to be accurate for roughly spherical bodies, such as grains of sand or dust particles, and the estimate $F = 6\pi\mu Ua$ is often used in analysis of creeping motion of small particles.

Another shape of interest is the spheroid in Fig. 3-36a. The spheroid shown is *prolate, $a > b$*; it may also be *oblate, $a < b$*. The flow may either be tangential (U_t) or normal (U_n) to the axis of revolution. In either case, the drag force has the Stokes form

$$F = C\mu Ub \qquad C = \text{const}$$
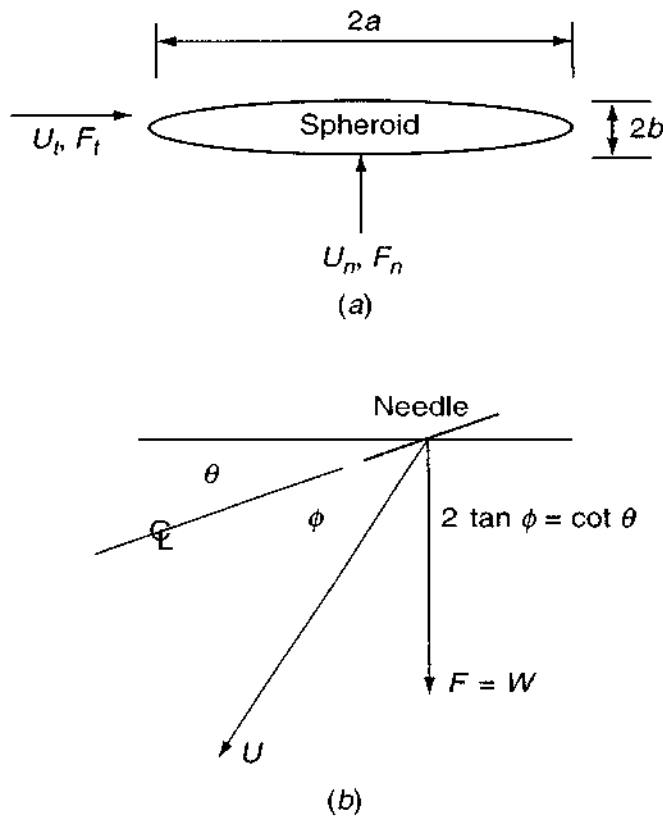
FIGURE 3-36
Forces on a body in creeping flow may be superimposed from tangential and normal components of the velocity vector: (a) ellipsoid geometry; (b) a nonhorizontal needle falls at an angle.

The exact solutions are rather lengthy and are given by Happel and Brenner (1983). Clift et al. (1978) give the following curve-fit formulas:

$$C_t \approx 6\pi \frac{4 + a/b}{5}$$

$$C_n \approx 6\pi \frac{3 + 2a/b}{5}$$

(3-221)

valid to ± 10 percent error in the range $0 < a/b < 5$. When $a \gg b$, the spheroid resembles a rod or needle, and the following asymptotic formulas apply:

$a \gg b$:

$$C_t \approx \frac{4\pi a/b}{\ln(2a/b) - 0.5}$$

$$C_n \approx 2C_t$$

(3-222)

The drag of a needle is twice as large for flow normal to its axis compared to flow along the axis.

The linearity of creeping motion means that normal and tangential flows may be superimposed without interaction. Suppose that the flow approaches the spheroid in Fig. 3-36a with velocity U at an angle α to its axis. Then one may break the velocity into components $U_n = U \sin \alpha$ and $U_t = U \cos \alpha$ and compute the force components $F_n = C_n \mu U_n b$ and $F_t = C_t \mu U_t b$. Then the total force on the body is the vector sum of F_n and F_t.

(a)

(b)
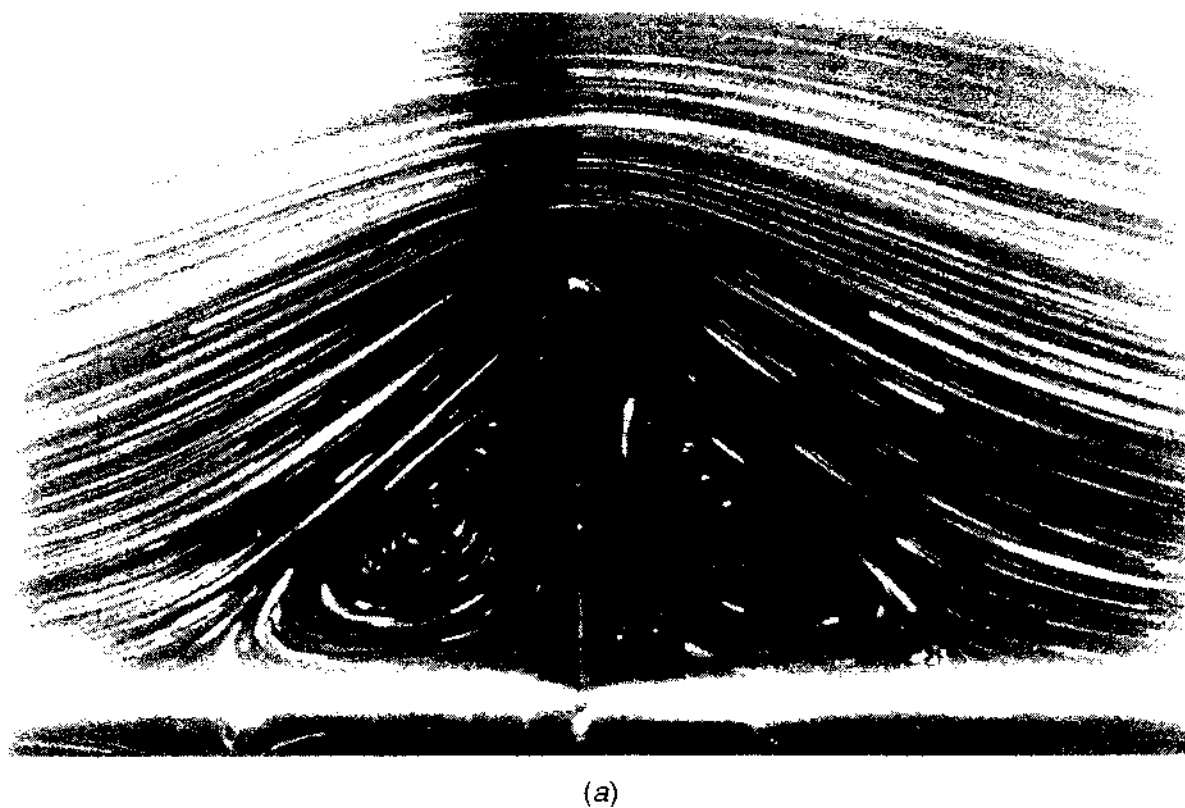
FIGURE 3-37
Separation occurs in creeping flow past sharp-cornered obstacles: (a) plane flow past a vertical fence at
$Re = 0.014$; (b) plane flow past a step at $Re = 0.01$ (in either direction). [*Experimental visualization by aluminum particles in glycerin by Taneda (1979).*]

When falling unsymmetrically, such bodies behave in an interesting way. Consider the needle in Fig. 3-36b, oriented with its axis at an angle θ to the horizontal. It must fall such that its total fluid force F is vertical to balance the body weight. Since $C_n = 2C_t$, it falls at angle ϕ with respect to its axis such that $F_n/F_t = 2 \sin \phi/\cos \phi = \tan (90° - \theta)$, or

Falling rod or needle: $\qquad\qquad 2 \tan \phi = \cot \theta$

This is illustrated in Fig. 3-36b. For example, if $\theta = 20°$, then $\phi = 54°$, or the needle moves along a direction $(20° + 54°)$ or $74°$ from the horizontal.

All of these forces are "in the ballpark" of the drag of a sphere of roughly the same size, i.e., shape effects do not vastly alter the drag. A remarkable theorem due to Hill and Power (1956) states that the Stokes drag of a body must be smaller than any circumscribed figure but larger than any inscribed figure. We can bound the drag of a particle of sand, for example, between inscribed and circumscribed spheres.

All of the immersed-body flows discussed have smooth streamlines near their surface with no separation. This is characteristic of rounded bodies in creeping flow. However, bodies with sharp corners or projecting appendages *do* show flow separation. Figure 3-37 illustrates two cases realized experimentally by Taneda (1979). In Fig. 3-37a, symmetric standing vortices form on either side of a plate or fence projecting into the flow. In Fig. 3-37b, a standing vortex forms in the corner region of a step in a wall; like all creeping flows, the direction of the flow may be *reversed* without any change in the pattern. Both parts of Fig. 3-37 are in good agreement with analytical solutions for the same cases.

3-9.3.1 CREEPING FLOWS ARE KINEMATICALLY REVERSIBLE. An important aspect of creeping flow is *reversibility*. Since the basic differential equation is linear, if a solution ψ is found, then its negative is also a solution. The streamlines can go either way. In Fig. 3-35 for Stokes flow, the arrows could be reversed with no penalty. This would change the signs of the viscosity-induced pressures and shear stresses, and the drag force would act to the left and still equal $6\pi\mu Ua$. If the body is symmetric, as in sphere flow, the fore-and-aft streamlines would be mirror images. Look ahead to another example in Fig. 3-50a for a perfectly symmetric, reversible creeping flow through an orifice.

Note that reversibility is also true of inviscid *potential flow*, which is itself governed by a linear relation, Laplace's Eq. (2-69), where ϕ denotes the velocity potential of the flow. Thus the arrows can also be reversed on the sphere potential flow in Fig. 3-35 and, in like manner, for the inviscid cylinder flow in Fig. 1-4.

3-9.4 Two-Dimensional Creeping Flow: Oseen's Improvement

As mentioned, the Stokes paradox is that a two-dimensional creeping flow cannot satisfy all boundary conditions without including inertia. Even three-dimensional flows are not rigorously valid in the far field. Oseen (1910) removed the paradox by

adding ad hoc linearized convective acceleration to the momentum equation:

$$\rho U \frac{\partial \mathbf{V}}{\partial x} \approx -\nabla p + \mu \nabla^2 \mathbf{V} \tag{3-223}$$

where U is the stream velocity acting in the x direction. Equation (3-223) is linear and can be solved for a variety of flows, as discussed in the texts by Oseen (1927) and Lamb (1932). For an immersed body, the solutions are unsymmetrical and show a wake but no separation. For sphere flow, the Oseen approximation adds an additional term to Eq. (3-218):

$$C_{D_{\text{sphere}}} = \frac{24}{Re}\left(1 + \frac{3}{16}Re + \cdots \right) \tag{3-224}$$

Other workers have used asymptotic analyses to add to this expression. As reviewed by Proudman and Pearson (1957), the next term in parentheses should be $[9Re^2 \,(\text{In } Re)/160]$, but this diverges greatly for $Re > 3$. The idea of using creeping flow to expand into the higher Reynolds number region has not been successful.

The Stokes paradox is not really a fundamental barrier. It is a failure of the lowest order theory to match flow conditions. Oseen's ad hoc idea is worthy, but the "paradox" has now been truly resolved by the newer asymptotic methods that develop systematic analyses of the governing equations. Asymptotic methods are beyond the scope of this text and may be studied in specialized monographs such as Cebeci and Cousteix (1998) and Nayfeh (2000).

Figure 3-38b compares the Stokes Eq. (3-218) and Oseen Eq. (3-224) theories with experimental data for the drag of a sphere. For $Re > 1$, neither expression is accurate and the data seem to lie in between. Since the sphere geometry is important in engineering, we offer the following curve-fit formula for the (laminar-flow) data:

$$C_{D_{\text{sphere}}} \approx \frac{24}{Re} + \frac{6}{1 + \sqrt{Re}} + 0.4 \qquad 0 \le Re \le 2 \times 10^5 \tag{3-225}$$

which is also plotted in Fig. 3-38b. The accuracy is ± 10 percent up to the "drag crisis," $Re_D \approx 250{,}000$, where the boundary layer on the sphere becomes turbulent, markedly thinning the wake and reducing the drag. The drag crisis occurs slightly earlier with rough surfaces or a fluctuating freestream.

The Oseen Eq. (3-223) can also be solved for various two-dimensional bodies. Of special interest is the drag on a flat plate of length L placed parallel to the stream from Lewis and Carrier (1949):

Plate: $$C_D = \frac{2F'}{\rho U^2 L} = \frac{4\pi}{Re_L[1 - \Gamma + \ln(16/Re_L)]} \tag{3-226}$$

where F' is the drag per unit depth and $\Gamma = 0.577216\ldots$ is Euler's constant. Note that the drag depends upon density no matter how small the Reynolds number.

The Oseen solution for the drag of a cylinder in crossflow is given by Tomotika and Aoi (1951):

Cylinder: $$C_D = \frac{2F'}{\rho U^2 D} = \frac{8\pi}{Re_D[0.5 - \Gamma + \ln(8/Re_D)]} \tag{3-227}$$
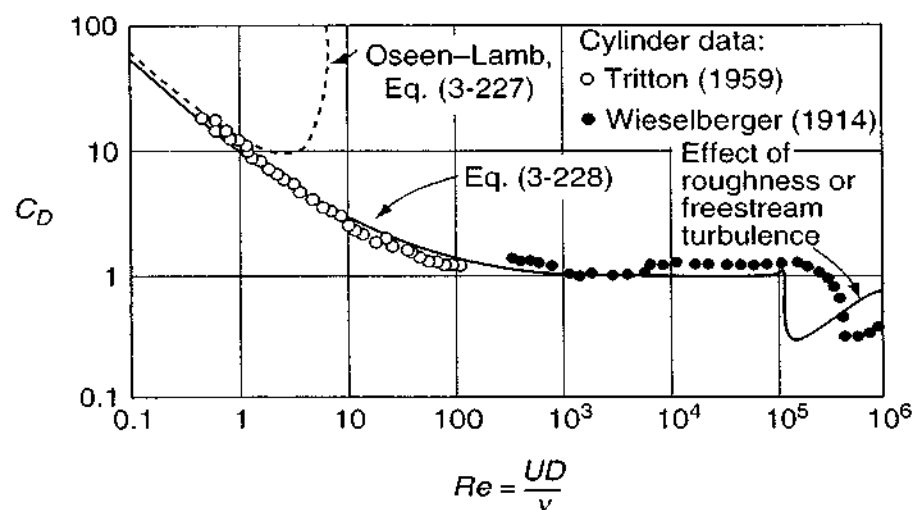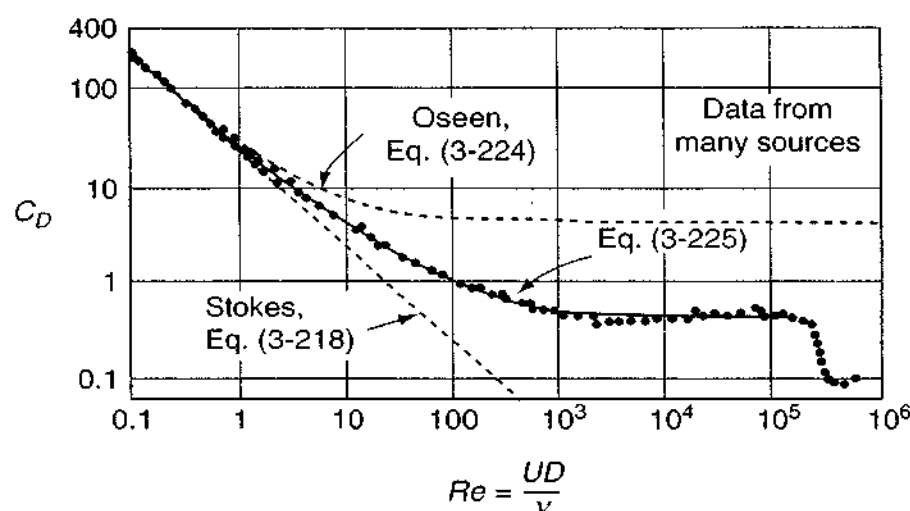
FIGURE 3-38

Comparison of experiment, theory, and empirical formulas for drag coefficients of a cylinder and a sphere (smooth walls): (a) cylinder; (b) sphere.

Figure 3-38a compares this expression with data for the drag of cylinders by Tritton (1959) and Wieselberger (1914). The formula fits up to about $Re \approx 1$ and then diverges. The author earlier offered the following simple curve-fit formula:

$$C_{D_{\text{cylinder}}} \approx 1 + \frac{10.0}{Re_D^{2/3}} \qquad (3\text{-}228)$$

which is in fair agreement up to the drag crisis, $Re \approx 250,000$. Sucker and Brauer (1975) offered a better curve-fit formula for the same data:

$$C_{D_{\text{cylinder}}} \approx 1.18 + \frac{6.8}{Re_D^{0.89}} + \frac{1.96}{Re_D^{1/2}} - \frac{0.0004 Re_D}{1 + 3.64\text{E}{-}7Re_D^2} \qquad (3\text{-}229)$$

valid with good accuracy for $10^{-4} < Re_D < 2 \times 10^5$. Textbooks which cover particle drag and motion are by Clift et al. (1978) and Sirignano (1999).
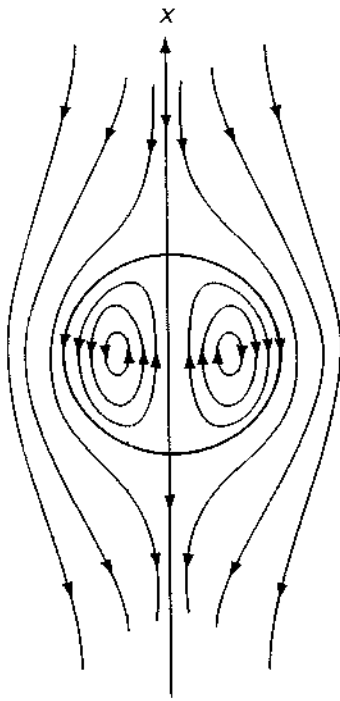
FIGURE 3-39
Streamlines for Stokes flow past a liquid droplet. See also Fig. 3-48.

3-9.5 Creeping Flow Past a Fluid Sphere

A large variety of creeping-motion solutions are given in the texts by Langlois (1964) and Happel and Brenner (1983). A particularly interesting solution is the flow past a spherical droplet of fluid. The outer stream has velocity U at infinity and viscosity μ_0, and the droplet has viscosity μ_i and a fixed interface. The boundary conditions at the droplet interface would be (1) zero radial velocities and (2) equality of surface shear and tangential velocity on either side of the interface. The solution was given by Rybczynski (1911) and independently by Hadamard (1911), and the drag force on a droplet is given by

$$F = 6\pi a \mu_0 U \frac{1 + 2\mu_0/3\mu_i}{1 + \mu_0/\mu_i} \tag{3-230}$$

For $\mu_i \gg \mu_0$, this simulates a solid sphere (Stokes solution), for which $F = 6\pi a \mu_0 U$. For $\mu_i \ll \mu_0$, this simulates a gas bubble in a liquid, for which $F = 4\pi a \mu_0 U$. A liquid droplet in another liquid would lie in between. Surface tension does not contribute to this drag force. Some streamlines of the flow are shown in Fig. 3-39. These patterns were verified in experiments by Spells (1952). For higher Reynolds numbers (>1.0), the flow changes character into a nearly irrotational outer flow about a droplet which distorts gradually into nonspherical, mushroom-like shapes.

3-9.6 Boundary-Element CFD
Creeping-Flow Solutions

Naturally most of our analytical creeping-flow solutions are for simple body shapes and walls. For more complex geometries, the boundary-element method (BEM)—see

Beer (2001) or Wrobel (2002)—is ideal because the creeping-flow equations are linear. Computations are compact and economical because no internal nodes are needed. One sums elemental biharmonic or Stokesian solutions to make the element strengths match the boundary conditions (no slip or streaming flow or a porous wall, etc.). Here are some recent examples of BEM creeping flows.

Trogdon and Farmer (1991) compute unsteady creeping flow through an orifice. Keh and Chen (2001) consider creeping flow of a droplet between plane walls. Vainshtein et al. (2002) study creeping flow near a permeable spheroid. Richardson and Power (1996) report BEM results for flow past two porous bodies of arbitrary shape. Roumeliotis and Fulford (2000) compute interactions between droplets. Lin and Han (1991) report a variety of BEM simulations: a rectangular cavity, a square bank, flow over a fence, and flow past a cylindrical arc. All these results are in good agreement with known experiments and theories. We conclude that any sensible creeping flow can be computed and analyzed with reliability and accuracy.

3-9.7 Heat Transfer in Creeping Motion

Temperature and heat transfer in Stokes flow can be computed from the linearized energy equation, including an Oseen term:

$$\rho c_p U \frac{\partial T}{\partial x} \approx k \nabla^2 T \tag{3-231}$$

where U is the (constant) freestream velocity. This relation is entirely uncoupled from the companion Stokes–Oseen velocity distribution. Typical boundary conditions would be known temperatures at the wall, T_w, and in the stream, T_∞. Nondimensionalization of Eq. (3-231) would yield a single parameter, the Peclet number $Pe = RePr = \rho c_p UL/k$. The mean Nusselt number would be defined as

$$Nu_m = \frac{\overline{q}_w L}{k(T_w - T_\infty)}$$

and would vary only with the Peclet number and the geometry.

The solution for flow past a sphere ($L = 2a$) was given by Tomotika et al. (1953):

$$Nu_{m,\,\text{sphere}} = 2.0 + 0.5 Pr Re + \mathcal{O}(Pr^2 Re^2) \ldots \tag{3-232}$$

The first term (2.0) is the Stokes theory, and the second term is the Oseen correction. When compared with sphere data in Fig. 3-40b, this formula is seen to be strictly qualitative. The curve-fit expression shown in the figure is the suggested formula

$$Nu_{m,\,\text{sphere}} \approx 2.0 + 0.3 Pr^{1/3} Re^{0.6} \tag{3-233}$$

which seems to agree with both liquid- and gas-flow data. If physical-property variations are important, it is suggested that μ, k, and c_p all be evaluated at the so-called film temperature $(T_w + T_\infty)/2$.
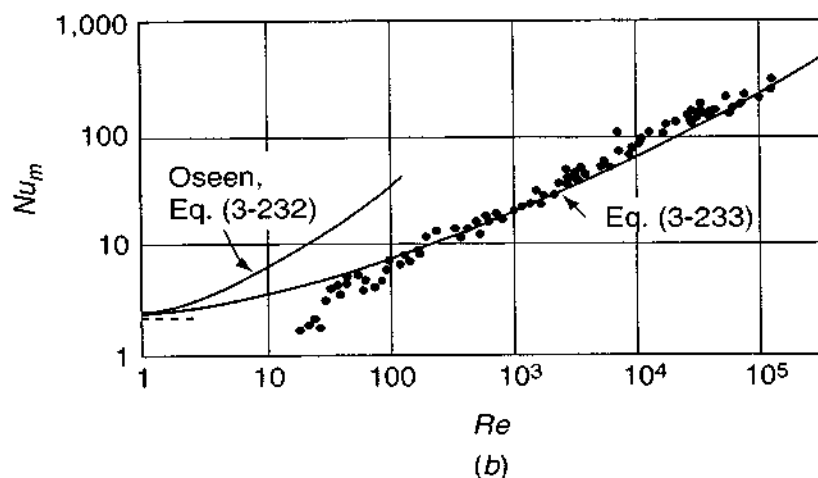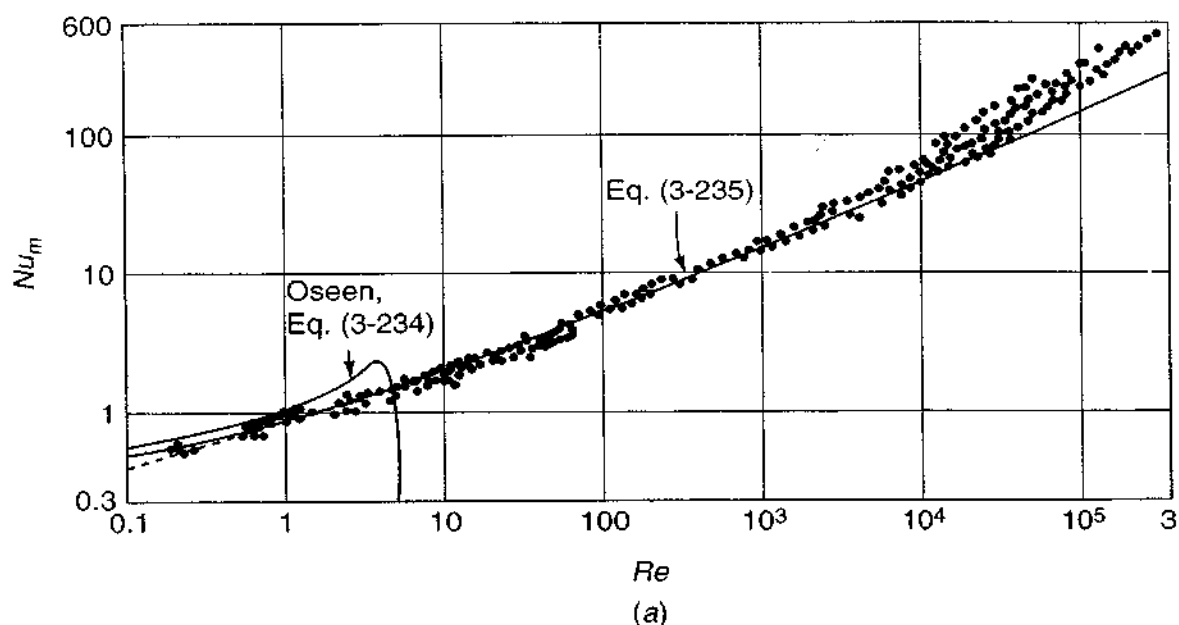
FIGURE 3-40
Comparison of theory and experiment for heat transfer from air to (*a*) cylinders and (*b*) spheres.

Tomotika et al. (1953) also obtained the Oseen solution for flow past a circular cylinder. The mean heat transfer ($L = 2a$) is given by

$$Nu_{m,\text{cylinder}} = B - \frac{Pr^2 Re^2}{12}(16 + B^2)$$

where

$$B = \frac{2}{\ln(8/PrRe) - \Gamma} \tag{3-234}$$

where $\Gamma = 0.577...$, as before. This formula is compared with cylinder data for airflow by Hilpert (1933) and is seen to be of very limited utility. A better formula was suggested by Kramers (1946) as a curve fit

$$Nu_{m,\text{cylinder}} \approx 0.42 Pr^{0.2} + 0.57 Pr^{1/3} Re_D^{1/2} \tag{3-235}$$

valid for $0.1 < Re_D < 10^4$. This formula follows *King's law*, $q_w = a + b\sqrt{U}$, predicted in an earlier study by L. V. King in 1914. It may be used to design the hot-wire anemometer, a fundamental instrument for the study of turbulence [see, e.g., Goldstein (1996)]. A fine wire mounted between two needles is the "cylinder in crossflow." If a current I is passed through the wire and the wire placed normal to a moving stream U, then I will be a measure of U. If the wire is held at constant temperature (constant resistance), Eq. (3-235) predicts a relation of the form $I^2 = a + bU^{1/2}$, where a and b are constants. Equation (3-235) could be used to compute a and b, but it is better to actually calibrate the hot wire in a stream of known velocity. The good agreement of Kramer's formula suggests that for air, with a typical wire diameter of 0.001 in., a hot-wire anemometer should be accurate in the velocity range suggested by Hinze (1975):

$$4.0 \leq U \leq 4.0 \times 10^6 \, \text{cm/s} \tag{3-236}$$

which is a vast span, certainly sufficient for most experimental purposes.

Note that the cylinder data in Fig. 3-40*a* fall above Kramer's formula Eq. (3-235) for $Re > 10^4$. This is attributed to noisiness or "freestream" turbulence in the oncoming stream approaching the cylinder. It is thought that the stream fluctuations trigger concave streamwise "Görtler vortices" (see Fig. 5-23) near the front of the body, increasing the nose heat transfer. Stream turbulence also hastens the onset of the drag crisis (Fig. 3-38*a*), causing increased (turbulent) heat transfer at the rear of the cylinder. This subject is discussed in detail in the monograph by Zukauskas and Ziukzda (1985).

We close this section by noting that the basic idea of Stokes or creeping flow is valid for $Re \ll 1$ but has not been successfully extended or modified into an accurate simulation of immersed-body flows when $Re > 1$. We will give a few more Stokes flow examples as problem exercises.

3-9.8 Lubrication Theory

The lubrication or friction reduction of two bodies in near contact is generally accomplished by a viscous fluid moving through a narrow but variable gap between the two bodies. One or both bodies may be moving. The theory was developed by Reynolds (1886).

An idealization of this problem is the slipper-pad bearing shown in Fig. 3-41. The bottom wall moves at velocity U and creates a Couette flow in the gap. Let us assume for the present that the upper block is fixed. The gap is very narrow, $h(x) \ll L$, and it decreases from h_0 in the entrance to h_L at the exit. The problem is to find the pressure and velocity distribution.

Assume in Fig. 3-41 that the flow is two-dimensional, that is, $\partial/\partial z = 0$ into the paper. Further assume Stokes flow, i.e., negligible inertia. This requires that $\rho u \, \partial u/\partial x \ll \mu \, \partial^2 u/\partial y^2$, or, approximately,

$$\rho U \frac{U}{L} \ll \mu \left(\frac{U}{h}\right)^2$$
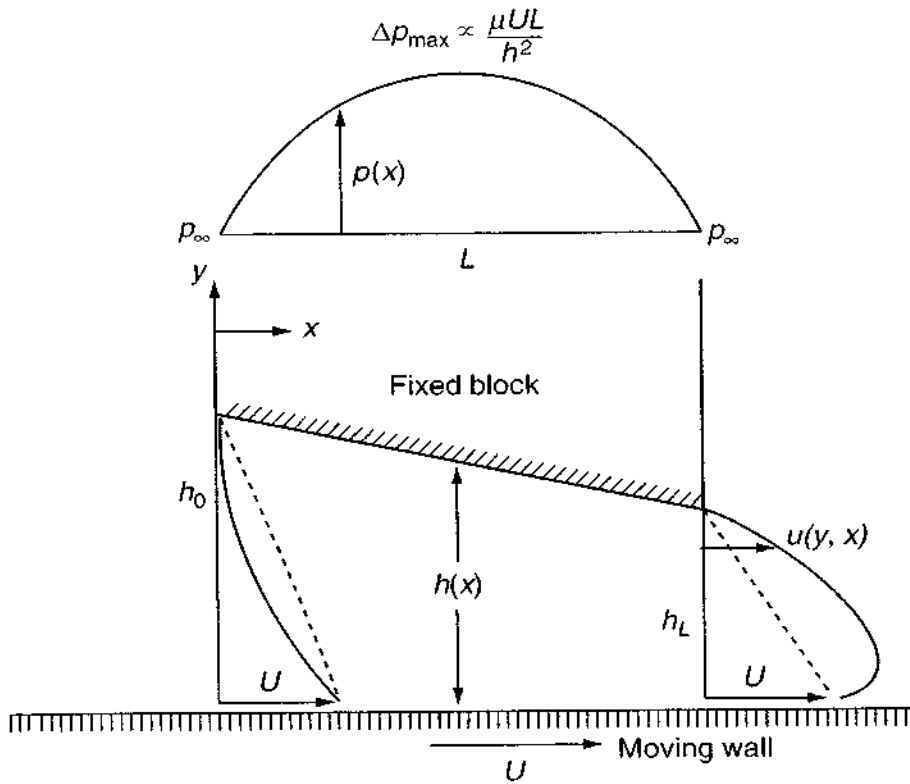
FIGURE 3-41

Low Reynolds number Couette flow in a varying gap: To maintain continuity, the gap pressure rises to a maximum and superimposes Poiseuille flow toward both ends of the gap.

or, finally,

$$\frac{\rho U L}{\mu} \frac{h^2}{L^2} \ll 1$$

Thus the Reynolds number Re_L can be large if the gap is very small. As a practical example, take $U = 10$ m/s, $L = 4$ cm, $h = 0.1$ mm, and SAE 50 lubricating oil, with $\nu \approx 7\text{E}{-}4$ m^2/s. Then $Re_L = 570$, but $Re_L h^2/L^2 = 0.004$. It is thus acceptable to neglect inertia in this case.

Now examine Fig. 3-41. The simple linear Couette flow profiles, shown as dashed lines at the entrance and exit, are impossible for this geometry because continuity is violated. The mass flow at the entrance would exceed the exit flow. To relieve this difficulty, high pressure develops in the gap and causes Poiseuille (parabolic) flow toward *both* ends of the gap, just sufficient to make the mass flow constant at every section x.

At any section in the gap, then, the local velocity profile is combined Couette–Poiseuille flow, from Eq. (3-42) modified for the new coordinates:

$$u = \frac{1}{2\mu} \frac{\partial p}{\partial x} y(y - h) + U\left(1 - \frac{y}{h}\right) \tag{3-237}$$

The correct distribution $p(x)$ is one which everywhere satisfies the continuity Eq. (3-1) for two-dimensional flow in the gap:

$$\int_0^h \frac{\partial u}{\partial x}\, dy = -\int_0^h \frac{\partial v}{\partial y}\, dy = -v(h) + v(0) \tag{3-238}$$

where in this particular case we are assuming that the vertical velocities $v(h)$ and $v(0)$ are zero at both walls.

Substituting for u from Eq. (3-237) and carrying out the integration in Eq. (3-238), we obtain a second-order differential equation for the pressure:

$$\frac{\partial}{\partial x}\left[h^3 \frac{\partial p}{\partial x}\right] = 6\mu U \frac{\partial h}{\partial x} \tag{3-239}$$

Here we assume U is constant and that the gap variation $h(x)$ is known. We then find $p(x)$ subject to the conditions $p(0) = p(L) = p_\infty$. Equation (3-42) is a simplified form of the Reynolds (1886) equation for lubrication. The development of Eq. (3-239) from Eqs. (3-237) and (3-238) is an excellent exercise, involving Leibnitz' rule, which we give as a problem assignment.

3-9.8.1 SOLUTION FOR A LINEARLY CONTRACTING GAP. Equation (3-239) may be integrated numerically for any gap variation $h(x)$. A closed-form solution is possible for a linear gap as in Fig. 3-41:

$$h = h_0 + (h_L - h_0)\frac{x}{L}$$

We may substitute in Eq. (3-239) and carry out the double integration. The algebra is quite laborious and we give only the final result:

$$\frac{p - p_\infty}{\mu U L / h_0^2} = \frac{6(x/L)(1 - x/L)(1 - h_L/h_0)}{(1 + h_L/h_0)[1 - (1 - h_L/h_0)x/L]^2} \tag{3-240}$$

This expression is plotted in Fig. 3-42 for various values of the gap contraction ratio h_L/h_0. When the contraction is only slight, the pressure distribution is nearly symmetric, with p_{max} at $x/L \approx 0.5$. As the degree of contraction increases, p_{max} increases and moves toward the exit plane. The maximum pressure rise is of the order of $(\mu U L / h_0^2)$ and can be amazingly high. For our previous example, SAE 50 oil with $U = 10$ m/s, $L = 4$ cm, and $h_0 = 0.1$ mm, we may compute that $(\mu U L / h_0^2) \approx 2.5\text{E}7$ Pa, or 250 atm. This provides a high force to the slipper block which can support a large load without the block touching the wall.

Recall that Stokes flows, being linear, are *reversible*. If we reverse the wall in Fig. 3-41 to move to the left, that is, $U < 0$, then the pressure change in Eq. (3-240) is *negative*. The fluid will not actually develop a large negative pressure but rather will cavitate and form a vapor void in the gap, as is well shown in the G. I. Taylor film "Low Reynolds Number Hydrodynamics" mentioned earlier on p. 167. Thus flow into an expanding narrow gap may not generally bear much load or provide good lubrication. This effect is unavoidable in a rotating journal bearing, where the gap contracts and then expands, and partial cavitation often occurs.
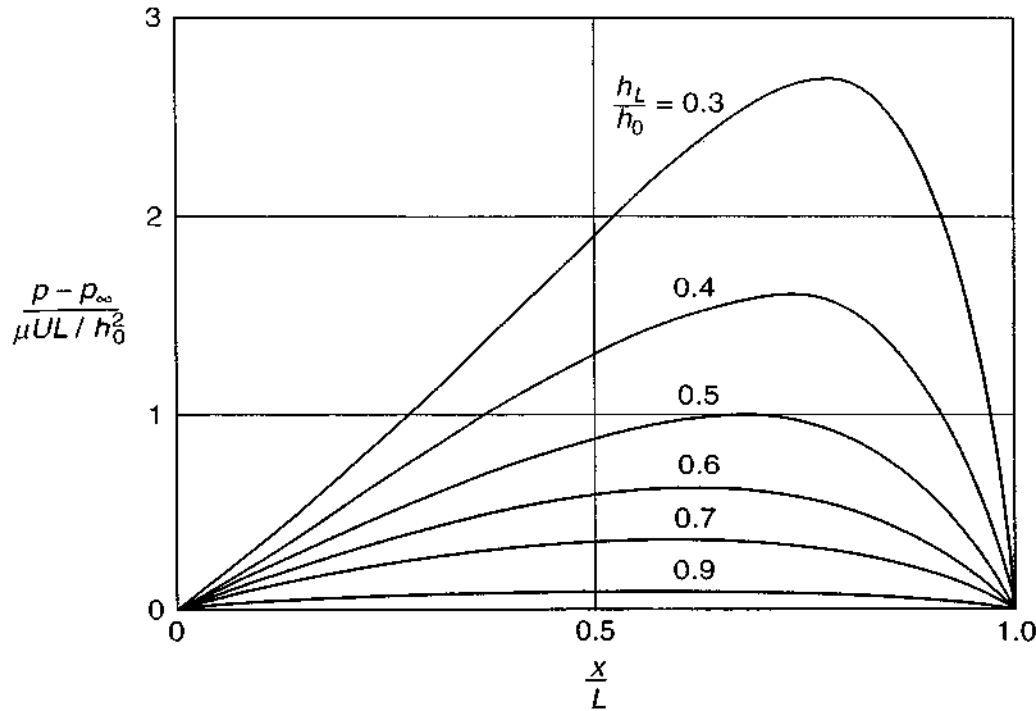
FIGURE 3-42
Pressure distribution in a two-dimensional linear-gap slipper-pad bearing, from Eq. (3-240).

3-9.8.2   THE GENERAL REYNOLDS EQUATION. In a general lubrication problem, both the upper and lower walls in Fig. 3-41 may be moving tangentially and normally, and the depth into the paper may be small, inducing a flow in the z direction. It is assumed there is no translation of the walls in the z direction. The complete derivation for this case is given, for example, in the text by Szeri (1998). The pressure now varies with both x and z and satisfies the following:

$$\frac{\partial}{\partial x}\left(h^3 \frac{\partial p}{\partial x}\right) + \frac{\partial}{\partial z}\left(h^3 \frac{\partial p}{\partial z}\right) = 6\mu \frac{\partial}{\partial x}[h\,\{U(0) + U(h)\}] + 12\mu[V(h) - V(0)]$$

$$(3\text{-}241)$$

where, in general, $h = h(x, z)$. This is the three-dimensional *Reynolds equation* for incompressible fluid lubrication. The pressure must be known on all four open sides of the gap.

3-10   COMPUTATIONAL FLUID DYNAMICS

This chapter has nearly exhausted the number of types of exact analytic solutions presently possible with viscous flows. The remainder of the text is primarily concerned with the boundary-layer (thin-shear) approximation. But there is still an important method of simulating viscous flows, often with nearly exact results: numerical analysis on a digital computer. One replaces the partial differential

equations of continuity, momentum, and energy by algebraic approximations applied at a finite number of discrete mesh points. Subject to certain restrictions on the Reynolds number, mesh spacing, and time increment, the results can be remarkably accurate, detailed, and useful. Three-dimensional flows can be modeled, and there is no need to assume boundary-layer (parabolic) behavior.

Laminar flows—the subject of the present chapter—are well adapted to near-exact simulation, subject only to limitations of computer size and speed and possible irregularities in the shape of the flow region. Turbulent flows (Chap. 6) can be computed accurately by direct simulation at very low (transitional) Reynolds numbers, but may be computed only approximately at high Reynolds numbers, using a variety of turbulence-modeling assumptions. The accuracy of turbulence models is variable at present, being only fair in reverse-flow or "recirculating" situations, but modeling and database improvements are being published regularly.

The algebraic simulation of a partial differential equation has taken two paths: (1) finite differences and (2) finite elements. The finite-difference technique [Lapidus and Pinder (1999)] constructs algebraic mesh-point models of the partial derivatives, whereas finite-element methods [Huebner et al. (2001)] model the functions themselves over regions between mesh points. Both schemes have been liberally applied to viscous flows, but finite differences are somewhat more popular, perhaps due to a feeling that finite elements, though pleasingly adaptable to irregular geometries, are somewhat slower and require more computer storage. However, a convincing argument in favor of finite elements is given in the text by Pironneau (1989). A special case of finite elements, called the boundary-element method, is applicable to linear viscous flows [Beer (2001) and Wrobel (2002)] and requires no mesh points whatsoever in the interior of the flow.

There is a third CFD option, *spectral methods*, now becoming popular. These methods approximate the desired solution by sophisticated trial functions that cover a wide region, not just one element as with FDM and FEM methods. Typical approximating functions are Fourier, Chebyshev, or Legendre series. The exact solution is usually approached by minimizing the errors with the *method of weighted residuals* (MWR). Spectral methods have been the topic of at least four recent monographs, Guo and Kuo (1998), Karniadakis and Sherwin (1999), Trefethen (2001), and Peyret (2002). These ideas may be applied to the full Navier–Stokes equations.

There is, finally, a fourth CFD option that does not model the Navier–Stokes equations, but rather models the flow itself. These are *vortex methods*, wherein both inviscid and viscous flows are simulated by summing hundreds, perhaps thousands, of elementary vortices to construct a model of a flow. Details are given in the texts by Cottet and Koumoutsakos (1999) and by Kamemoto and Tsutahara (2000).

3-10.1 Overview of the Literature

It would be an understatement to say that the literature on computational fluid dynamics has exploded. The emergence of the digital computer has provided an irresistible tool for numerical investigations. Although Prandtl and others had developed pencil-and-paper marching methods for (parabolic) boundary layers

prior to the computer era, very few workers had the patience, desire, or ability to attempt a hand computation of a fully elliptical viscous flow. One of these pioneers was Thom (1933), who calculated, by hand, a remarkably accurate solution of flow past a circular cylinder at $Re_D = 10$. The advent of the computer has created a new industry and a vast literature for numerical modeling.

The fluids engineering community is now blessed with a multitude of new monographs on computational fluid dynamics and/or heat transfer. Earlier classics, admired by this writer, were by Roache (1976), Patankar (1980), Peyret and Taylor (1983), Sod (1985), Jaluria and Torrance (1986), Minkowycz et al. (1988), Pironneau (1989), and Anderson (1995). Add to these a group of newer texts, in alphabetical order: Blazek (2001), Chung (2002), Ferziger and Peric (2001), Garg (1998), Hoffmann and Chiang (2000), Löhner (2001), Lomax et al. (2001), Tannehill et al. (1997), Versteeg and Malalasekera (1996), and Wesseling (2001). And there are more to come: Aref (2004), Caughey and Hafez (2004), Engquist and Rizzi (2004), and Morgan (2004). Some wider-ranging exact-solution studies are reported by Hamdan (1998), Profilo et al. (1998), and Bourchtein (2002). One should also understand the generation of numerical grids: Carey (1997), Thompson et al. (1998), and Miles and Farrashkhalvat (2003). The mathematics of numerical discretization is covered by Hirsch (1988). For readers new to numerical analysis, the general texts by Lucquin and Pironneau (1998) and Moin (2001) show how to handle basic numerical partial differential equations, including FORTRAN and BASIC codes and software. The present text cannot possibly compete with these monographs and will simply present a brief overview.

The traditional general fluid-flow and heat-transfer journals continue to publish numerical studies: *Journal of Fluid Mechanics, Journal of Fluids Engineering, Journal of Heat Transfer, Physics of Fluids, International Journal of Heat and Mass Transfer, Heat and Fluid Flow*, and the *AIAA Journal*. In addition, a number of numerically oriented, fluids-friendly journals have emerged, in alphabetical order: *Applied Mathematics and Computation, Applied Numerical Mathematics, Computational Mechanics, Computer Methods in Applied Mechanics and Engineering, Engineering Analysis with Boundary Elements, International Journal of Fluid Mechanics Research, International Journal for Numerical Methods in Engineering, International Journal for Numerical Methods in Fluids, Journal of Computational Physics, Numerical Heat Transfer (A) Applications* and *(B) Fundamentals, Numerical Methods in Heat Transfer, Numerical Methods for Partial Differential Equations*, and *SIAM Journal of Numerical Analysis*. One could use help in keeping up with such a burgeoning paper mass.

3-10.2 Finite-Difference Approximations

Finite differences simulate a partial derivative by an algebraic difference between discrete mesh points. Consider a two-dimensional flow property $Q(x, y)$, where Q could be velocity, pressure, temperature, etc. In numerical modeling, Q is computed only at a finite number of mesh points, usually equally spaced. A typical two-dimensional mesh is shown in Fig. 3-43. The spacings Δx and Δy need not be the
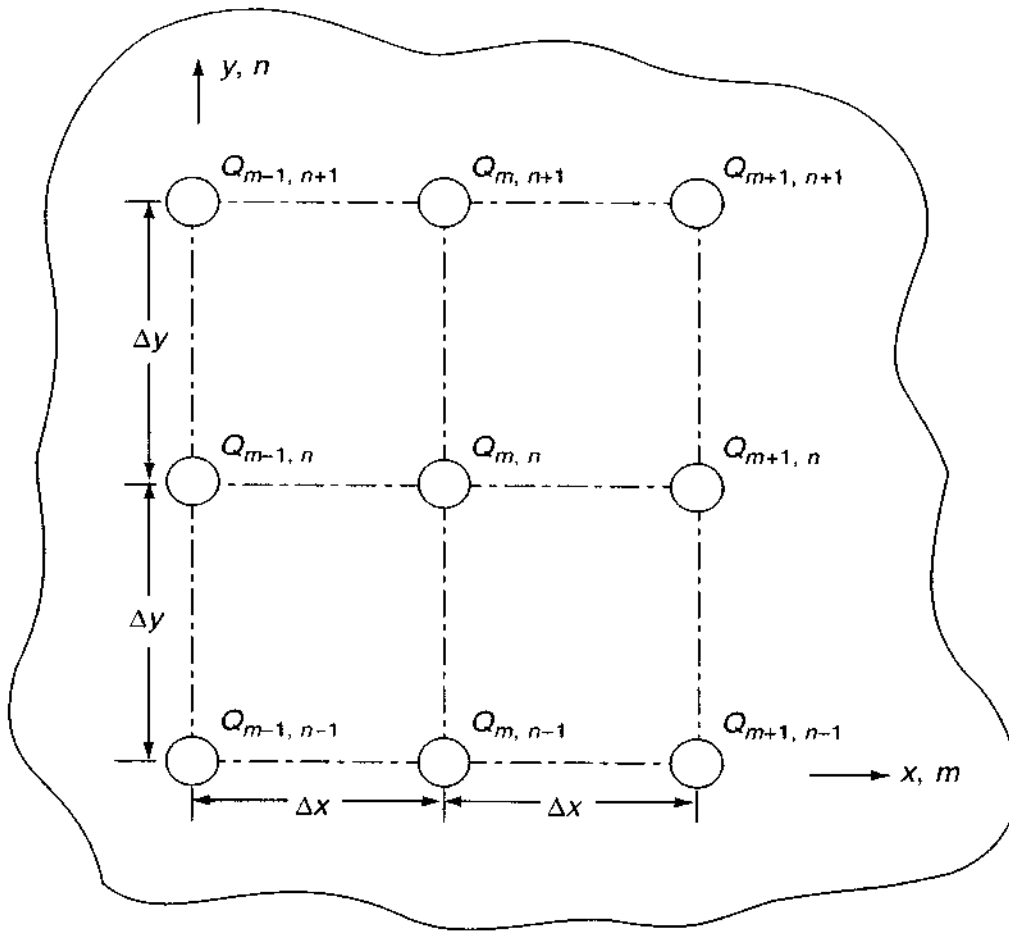
FIGURE 3-43

A typical rectangular finite-difference mesh, showing a discrete point property $Q_{m,n} = Q(x, y)$ surrounded by its eight neighbors.

same. To avoid a lot of parentheses, we adopt the subscript notation (m, n) shown for any particular location:

$$Q_{m,n} = Q(x, y) = Q(x_0 + m\Delta x, y_0 + n\Delta y)$$

The economy of description is immediately evident.

Partial derivatives are then approximated by using the mesh points in Fig. 3-43. For example, $(\partial Q/\partial x)$ at (x, y) may be simulated by a forward, backward, or central "difference":

$$\frac{\partial Q}{\partial x}(x, y) \approx \frac{Q_{m+1,n} - Q_{m,n}}{\Delta x} + \mathcal{O}(\Delta x) \qquad \text{forward}$$

$$\approx \frac{Q_{m,n} - Q_{m-1,n}}{\Delta x} + \mathcal{O}(\Delta x) \qquad \text{backward}$$

$$\approx \frac{Q_{m+1,n} - Q_{m-1,n}}{2\Delta x} + \mathcal{O}(\Delta x^2) \qquad \text{central} \qquad (3\text{-}242)$$

where $\mathcal{O}(\Delta x)$ means that the error in the approximation decreases linearly as the mesh spacing Δx decreases. Here the central difference is obviously more accurate, but it may lead to numerical problems in a full simulation. Similar approximations hold for $(\partial Q/\partial y)$ and $(\partial Q/\partial t)$.

By subtracting a backward from a forward difference in Eq. (3-242) and dividing by Δx, we simulate a second derivative:

$$\frac{\partial^2 Q}{\partial x^2}(x, y) \approx \frac{Q_{m+1, n} - 2Q_{m, n} + Q_{m-1, n}}{(\Delta x)^2} + \mathcal{O}(\Delta x^2) \qquad (3\text{-}243)$$

with an exactly analogous expression for $(\partial^2 Q/\partial y^2)$:

$$\frac{\partial^2 Q}{\partial y^2}(x, y) \approx \frac{Q_{m, n+1} - 2Q_{m, n} + Q_{m, n-1}}{(\Delta y)^2} + \mathcal{O}(\Delta y^2) \qquad (3\text{-}244)$$

Summing these two expressions gives a finite-difference approximation for the Laplacian of Q. For the common case of a square mesh, $\Delta x = \Delta y = h$,

$$\Delta^2 Q \approx \frac{Q_{m+1, n} + Q_{m-1, n} + Q_{m, n+1} + Q_{m, n-1} - 4Q_{m, n}}{h^2} + \mathcal{O}(h^2) \qquad (3\text{-}245)$$

The idea of this approximation is taken in at a glance by sketching what Milne (1953) calls a *stencil*, a term taken from the days when such computations were made by hand. Equation (3-245) is not unique. Here are three equivalent stencils for the Laplacian in a square mesh:

$$\nabla^2 \approx \frac{1}{h^2} \begin{array}{|c|c|c|} \hline & 1 & \\ \hline 1 & -4 & 1 \\ \hline & 1 & \\ \hline \end{array} \approx \frac{1}{2h^2} \begin{array}{|c|c|c|} \hline 1 & & 1 \\ \hline & -4 & \\ \hline 1 & & 1 \\ \hline \end{array} \approx \frac{1}{6h^2} \begin{array}{|c|c|c|} \hline 1 & 4 & 1 \\ \hline 4 & -20 & 4 \\ \hline 1 & 4 & 1 \\ \hline \end{array}$$

All have errors of $\mathcal{O}(h^2)$. The third stencil has a much smaller absolute error than the first two but is seldom used because of the extra computation needed and difficulties at the boundaries. The previous examples give an idea how finite-difference approximations are constructed. Texts on numerical methods give whole arrays of alternative difference models, e.g., Lucquin and Pironneau (1998), Moin (2001), or Lapidus and Pinder (1999).

3-10.3 Application to One-Dimensional Unsteady Laminar Flow

As an example of a finite-difference solution, consider one-dimensional unsteady flow with no pressure gradient, as discussed earlier in Sec. 3-5:

$$\frac{\partial u}{\partial t} = \nu \frac{\partial^2 u}{\partial y^2} \qquad (3\text{-}246)$$

subject to various boundary conditions such as the Stokes moving-wall problems of Fig. 3-18.

To include time in the notation, we use the superscript j as follows:

$$u_{m,n}^{j} = u(x, y, t) = u(x_0 + m\Delta x, y_0 + n\Delta y, t_0 + j\Delta t)$$

In the present case, Eq. (3-246), the m subscript is not needed. We adopt a forward difference for time and a central difference for the y derivative to model Eq. (3-246):

$$\frac{u_n^{j+1} - u_n^{j}}{\Delta t} \approx \nu \frac{u_{n+1}^{j} - 2u_n^{j} + u_{n-1}^{j}}{(\Delta y)^2}$$

The truncation error is $\mathcal{O}(\Delta t) + \mathcal{O}(\Delta y^2)$. Rearrange this to solve for the next nodal velocity at time $j + 1$:

$$u_n^{j+1} \approx \sigma(u_{n+1}^{j} + u_{n-1}^{j}) + (1 - 2\sigma)u_n^{j} \qquad (3\text{-}247)$$

where $\sigma = \nu\Delta t/(\Delta y)^2$ is a dimensionless mesh-size parameter. Since the right-hand side contains known (previous) values, this method is called *explicit*, i.e., the new value of u^{j+1} is computed immediately. However, there is a penalty for this algebraic ease: The coefficients of u^j must all be positive for numerical stability. Thus we are restricted to

$$\sigma \le \frac{1}{2}$$

or $\qquad\qquad\qquad\qquad\qquad\qquad\qquad\qquad\qquad\qquad\qquad\qquad\qquad (3\text{-}248)$

$$\Delta t \le \frac{\Delta y^2}{2\nu}$$

For a given mesh size Δy, then, the time step Δt is limited—sometimes severely—by Eq. (3-248). Given appropriate initial and boundary values for the mesh points, a complete numerical solution can be generated by repeated application of Eq. (3-247). For example, for Stokes' first problem, Fig. 3-18a, we would specify $u_{n>1} = 0$ at the initial time $j = 1$, plus $u_1 = U$ at the wall, and $u_{n_{max}} = 0$ for all j. We would limit Δt by Eq. (3-248) and continually check n_{max} to see that the solution has not diffused that far.

To avoid the limitation on time step, we may change the model so that the second derivative is evaluated at the *new* time step:

$$\frac{u_n^{j+1} - u_n^{j}}{\Delta t} \approx \nu \frac{u_{n+1}^{j+1} - 2u_n^{j+1} + u_{n-1}^{j+1}}{(\Delta y)^2}$$

We may rearrange this as follows:

$$-\sigma u_{n+1}^{j+1} + (1 + 2\sigma)u_n^{j+1} - \sigma u_{n-1}^{j+1} \approx u_n^{j} \qquad (3\text{-}249)$$

This an *implicit* method: When applied to each mesh point n, it results in a system of simultaneous algebraic equations. Since each equation contains only three unknowns centered around the diagonal of the coefficient matrix, the system may

be solved rapidly and easily by the tridiagonal matrix algorithm (TDMA), which will be described later in Sec. 4-7.2.1. There is no limitation, in this implicit method, on the time step, which can typically be an order of magnitude higher than that required by Eq. (3-248) and still achieve the same numerical accuracy.

Slight complications arise in these one-dimensional models if the equations are non-linear, i.e., contain convective-acceleration terms. We will illustrate both explicit and implicit non-linear models in Sec. 4-7 by applying them to the laminar boundary-layer equations.

More substantial complications arise if there are two dimensions or more. For example, suppose we wish to model the two-dimensional linear diffusion or heat-conduction equation,

$$\frac{\partial u}{\partial t} = \nu\left(\frac{\partial^2 u}{\partial x^2} + \frac{\partial^2 u}{\partial y^2}\right) \tag{3-250}$$

The explicit algorithm, to be given as a problem exercise, has the stability limitation

$$\frac{\nu \Delta t}{\Delta x^2} + \frac{\nu \Delta t}{\Delta y^2} \le \frac{1}{2} \tag{3-251}$$

This limitation is more restrictive than Eq. (3-248).

If we develop an implicit model for Eq. (3-250), there will be a system of equations each with five unknowns, corresponding to (m, n), $(m, n \pm 1)$, $(m \pm 1, n)$. Further, the matrix of coefficients is not pentadiagonal, i.e., there are nonzero terms far removed from the main diagonal. One must therefore contemplate lengthier schemes such as (1) iteration, (2) Gauss elimination, or (3) inversion of a sparse $N \times N$ matrix. In fact, what is often done is to split the procedure into two applications of the TDMA—one over a half time step in the x direction, then one over a second half time step in the y direction, each time using previous values for the additional two unknowns. This is the alternating-direction implicit (ADI) method developed by Peaceman and Rachford (1955). When applied to Eq. (3-250), the ADI model takes the form

Half-step 1:
$$\frac{u_{m,n}^{j+1/2} - u_{m,n}^{j}}{\frac{1}{2}\Delta t} \approx \nu(\delta_x^2 u_{m,n}^{j+1/2} + \delta_y^2 u_{m,n}^{j}) \tag{3-252}$$

Half-step 2:
$$\frac{u_{m,n}^{j+1} - u_{m,n}^{j+1/2}}{\frac{1}{2}\Delta t} \approx \nu(\delta_x^2 u_{m,n}^{j+1/2} + \delta_y^2 u_{m,n}^{j+1})$$

where δ^2 denotes the second partial derivative difference model from Eqs. (3-243) and (3-244). In half-step 1, the TDMA is used for the east–west neighbors $(m \pm 1)$, while half-step 2 sweeps the north–south neighbors $(n \pm 1)$. Further details of the ADI scheme are given by Ferziger (1998). There are also alternating-direction explicit (ADE) methods which half-step forward without using the TDMA [Tannehill et al. (1997)].

3-10.4 Modeling the Full Navier–Stokes Equations

The Navier–Stokes equations are non-linear, nonunique, and multidimensional, and solutions often contain very fine details of flow structure. To model them numerically requires considerably more sophistication than the one-dimensional explicit and implicit models discussed in Sec. 3-10.3. The last two decades have seen marked progress in creating "Navier–Stokes solvers," but three-dimensional complex-geometry flows remain challenging.

There is no single model in use. The handbook by Minkowycz et al. (1988) outlines, in detail, four different finite-difference models and two different finite-element models. Some of these—and related formulations—have been developed into commercial codes which a user can purchase, add boundary conditions, and get immediate results, especially for two-dimensional steady flows.

It is not the purpose—or hope—of this section to outline the latest advances at the frontiers of computational fluid dynamics. The reader is referred for this purpose to the review by Boris (1989), who discusses ideas beyond our scope: cellular automata, near-neighbor "atom" algorithms, adaptive gridding, spectral methods, and parallel processing for supercomputers. Here we choose only to give a brief overview of Navier–Stokes models.

3-10.4.1 ISSUES INVOLVED IN NAVIER–STOKES MODELING. There is considerable science, and not a little art, necessary to complete a successful Navier–Stokes computation for recirculating or "nonboundary-layer" flows, which have strong interactions between viscous and inviscid regions. Some of the issues involved are as follows:

1. *The coordinate-system viewpoint.* Most studies use the Eulerian or flow-field system. Unsteady flows, especially with material boundaries such as droplets or free surfaces, can benefit from a Lagrangian, or particle, formulation.

2. *The method of formulation.* The two main choices are finite differences (FDM) and finite elements (FEM)—usually developed and described independently. Workers rarely straddle both camps. The FDM formulation is localized by simple derivative approximations and leads to sparse matrices. The FEM method uses basis functions over a finite region and yields large, banded matrices. The FEM approach (not developed here) is very attractive for irregular geometries, but FDM methods are improving in this regard by the use of *boundary-fitted coordinates* [Thompson (1998)]. The two methods are compared by Pepper and Baker [Minkowycz et al. (1988, Chap. 13)].

3. *The method of discretization.* In FEM methods, the issue is the choice of basis function and the scheme for minimizing the integrated error. In FDM methods, the discretization may be accomplished either by (1) Taylor-series derivative truncations or by (2) control-volume (integral) techniques, the latter approach being a balance of physical terms popularized by Patankar (1980).

4. *The choice of dependent variables.* In two-dimensional flow, the stream function and vorticity can be convenient variables. In three dimensions, multiple stream functions are awkward, so the "primitive" variables of velocity and pressure are used.

5. *Grid selection.* The choice of grid is crucial to the performance of a numerical method. Plain, unadorned square meshes are rarely appropriate—grids should be finer in regions of high gradient. Poor gridding can result in instability or failure to converge. Grids can be generated in both two and three dimensions, using algebraic or differential transformations [Thompson et al. (1998)]. There are clustering techniques to pack grids into a high-gradient area. In unsteady flow, the gradients can move; hence the grids should be changeable or *adaptive*, using grid-speed algorithms to reduce the instantaneous numerical error [Tannehill et al. (1997, Sec. 10-7)].

6. *Simulation of boundary conditions.* Viscous flows depend strongly upon their boundary conditions, which should be modeled as accurately as possible. The effect of far-field boundary placement, such as "infinity," "upstream," or "downstream," must be carefully investigated. The mathematical requirements are discussed by Kreiss and Lorenz (1989).

7. *Solution techniques and numerical uncertainty.* Both explicit and implicit solutions are widely used in FDM methods. FEM methods, with large banded matrices coupled in space and time, are inherently implicit. Error estimates should be made for all numerical results. The availability of large and/or fast digital computers should eliminate untested single-fixed-grid computation. Since 1986, the *Journal of Fluids Engineering* will not accept any CFD articles unless their numerical accuracy is systematically tested by grid variation and far-field boundary placement.

3-10.4.2 THE STREAM FUNCTION-VORTICITY APPROACH.

For many years, most CFD papers studied two-dimensional incompressible viscous flows, for which the stream function ψ exists and the vorticity ω has only a single component:

$$u = \frac{\partial \psi}{\partial y} \qquad v = -\frac{\partial \psi}{\partial x} \qquad \omega = \frac{\partial v}{\partial x} - \frac{\partial u}{\partial y} \qquad (3\text{-}253)$$

The vorticity transport Eq. (2-114) may be written as

$$\frac{\partial \omega}{\partial t} + \frac{\partial \psi}{\partial y}\frac{\partial \omega}{\partial x} - \frac{\partial \psi}{\partial x}\frac{\partial \omega}{\partial y} = \nu\left(\frac{\partial^2 \omega}{\partial x^2} + \frac{\partial^2 \omega}{\partial y^2}\right) \qquad (3\text{-}254)$$

This equation is parabolic in time and elliptical in space and may be modeled in FDM just as was done in Sec. 3-10.3 for Eq. (3-246). Meanwhile, the stream function may be computed by rewriting Eq. (3-253) in the form

$$\frac{\partial^2 \psi}{\partial x^2} + \frac{\partial^2 \psi}{\partial y^2} = -\omega \qquad (3\text{-}255)$$

This is an elliptical (Poisson) equation for ψ and may be modeled in FDM similar to Laplace's equation in Eq. (3-245). Computations for nodal values of ψ and ω may be either explicit or implicit. Note that pressure is not present, having been eliminated in Eq. (3-254) by taking the curl of the Navier–Stokes equation.

Once the stream function is known everywhere, the pressure is computed from the following Poisson equation:

$$\Delta^2 p = 2\rho\left(\frac{\partial u}{\partial x}\frac{\partial v}{\partial y} - \frac{\partial u}{\partial y}\frac{\partial v}{\partial x}\right) = 2\rho\left[\frac{\partial^2\psi}{\partial x^2}\frac{\partial^2\psi}{\partial y^2} - \left(\frac{\partial^2\psi}{\partial x\,\partial y}\right)^2\right] \quad (3\text{-}256)$$

This equation is derived by differentiation of the x- and y-momentum equations and is given as a problem exercise. There are many finite-difference models for the mixed partial derivative [Tannehill et al. (1997, Table 3-2)], of which a popular form is

$$\frac{\partial^2\psi}{\partial x\,\partial y} \approx \frac{\psi_{m+1,n+1} - \psi_{m+1,n-1} - \psi_{m-1,n+1} + \psi_{m-1,n-1}}{4\Delta x\,\Delta y}$$

The computations must satisfy appropriate boundary conditions. In the far-field "freestream," one usually knows the values of ψ, ω, and p. At a wall with no slip, $u = v = 0$, we would satisfy

$$\psi_w = \text{const} \qquad \omega_w \approx \frac{2(\psi_w - \psi_{w+1})}{\Delta n^2} \qquad \left.\frac{\partial p}{\partial s}\right|_w = -\mu\left.\frac{\partial\omega}{\partial n}\right|_w \quad (3\text{-}257)$$

where s and n denote coordinates parallel and normal to the wall, respectively. In this manner, beginning with Thom (1933), almost all of the classical two-dimensional solutions in the literature were computed. Plane-flow (ψ, ω) modeling is still popular today.

3-10.4.3 THE PRIMITIVE-VARIABLE APPROACH. Presently, the most widely used CFD models of viscous flow use the direct or "primitive" variables (u, v, w, p, T). Consider, for simplicity, the two-dimensional, incompressible equations of motion with constant transport properties:

Continuity:
$$\frac{\partial u}{\partial x} + \frac{\partial v}{\partial y} = 0 \qquad (3\text{-}258a)$$

x momentum:
$$\frac{\partial u}{\partial t} + u\frac{\partial u}{\partial x} + v\frac{\partial u}{\partial y} = -\frac{1}{\rho}\frac{\partial p}{\partial x} + \nu\Delta^2 u \qquad (3\text{-}258b)$$

y momentum:
$$\frac{\partial v}{\partial t} + u\frac{\partial v}{\partial x} + v\frac{\partial v}{\partial y} = -\frac{1}{\rho}\frac{\partial p}{\partial y} + \nu\Delta^2 v \qquad (3\text{-}258c)$$

Energy:
$$\rho c_p\left(\frac{\partial T}{\partial t} + u\frac{\partial T}{\partial x} + v\frac{\partial T}{\partial y}\right) = k\Delta^2 T + \Phi \qquad (3\text{-}258d)$$

subject to suitable boundary conditions. The latter three have the same mathematical form—elliptical in space, parabolic in time, with non-linear convective terms—and may be modeled in a single generic manner [e.g., Patankar (1980)]. Thus the variables (u, v, T) are all computed in the same manner in a CFD model. The *odd* thing about the system Eq. (3-258) is that the fourth relation, continuity, does *not* define the fourth variable, pressure. We develop this oddity in the next section.

Each of Eqs. (3-258b) to (3-258d) consists of a time derivative, convective terms, a diffusion (Laplacian) term, and some remaining low-order terms which could be called "sources." For example, in Eq. (3-258b), the source term is the pressure gradient $(-\partial p/\partial x)/\rho$, and the equation could be modeled implicitly as

$$\frac{u_{m,n}^{j+1} - u_{m,n}^{j}}{\Delta t} + \text{convection}$$

$$\approx \text{source} + \nu\left(\frac{u_{m+1,n}^{j+1} + u_{m-1,n}^{j+1} + u_{m,n+1}^{j+1} + u_{m,n-1}^{j+1} - 4u_{m,n}^{j+1}}{\Delta x^2}\right)$$

where we have assumed a square mesh, $\Delta x = \Delta y$. For an explicit method, the superscripts on the right would be j, not $j + 1$.

At low Reynolds numbers, the convection terms could be modeled as central differences:

$$u\frac{\partial u}{\partial x} + v\frac{\partial u}{\partial y} \approx u_{m,n}^{j}\left(\frac{u_{m+1,n}^{j+1} - u_{m-1,n}^{j+1}}{2\Delta x}\right) + v_{m,n}^{j}\left(\frac{u_{m,n+1}^{j+1} - u_{m,n-1}^{j+1}}{2\Delta y}\right)$$

This expression causes increasing error as the Reynolds number increases. It is also physically wrong, implying that convection is equally dependent upon both upstream and downstream velocities. If we think of the "cell" surrounding point (m, n), its convection is *received* from upstream and *transmitted* to the next cell downstream.

The remedy to convection instability is simple and satisfying: Model convection only with the upstream contribution. For example,

$$u\frac{\partial u}{\partial x} = \frac{\partial}{\partial x}\left(\frac{u^2}{2}\right) \approx \frac{u_{m,n}^{j}(u_{m+1,n}^{j+1} + u_{m,n}^{j+1}) - u_{m-1,n}^{j}(u_{m,n}^{j+1} + u_{m-1,n}^{j+1})}{4\Delta x}$$

$$\text{if } u_{m,n}^{j} > 0$$

$$\approx \frac{u_{m+1,n}^{j}(u_{m+1,n}^{j+1} + u_{m,n}^{j+1}) - u_{m,n}^{j}(u_{m,n}^{j+1} + u_{m-1,n}^{j+1})}{4\Delta x}$$

$$\text{if } u_{m,n}^{j} < 0$$

This stabilizing procedure is called *upwind*, or donor-cell, differencing. Other upwind schemes are discussed by Tannehill et al. (1997). An interesting—and popular—alternative is given by Patankar (1980), who develops the equations of

motion in control-volume (integral) form and then finds an exact exponential solution for the convective terms. Exponential convection, or its power-law approximation, avoids the need to check the signs of the velocities but requires more execution time.

The pressure-gradient source terms in the momentum equation would normally be written as central differences. For example,

$$\frac{\partial p}{\partial x} \approx \frac{p_{m+1,n}^{j} - p_{m-1,n}^{j}}{2\Delta x} \qquad \frac{\partial p}{\partial y} \approx \frac{p_{m,n+1}^{j} - p_{m,n-1}^{j}}{2\Delta y}$$

However, this formulation leads to a vexing artifact: no net pressure force if the nodal pressures simply alternate. For example, the "checkerboard" pattern in Fig. 3-44, consisting of four sets of different pressure values alternating vertically and horizontally, contributes no net force to the momentum model. This pattern is obviously unrealistic and should be avoided. A similar paradox occurs in the continuity equations, i.e., central-difference models for $(\partial u/\partial x)$ and $(\partial v/\partial y)$ yield zero net fluxes on a checkboard pattern. Therefore Patankar (1980), in particular, recommends a staggered grid, with (u, v, p) evaluated at three different places in a cell. Such a grid leads to differences between *adjacent* grid points and thus avoids the possibility of checkerboarding.
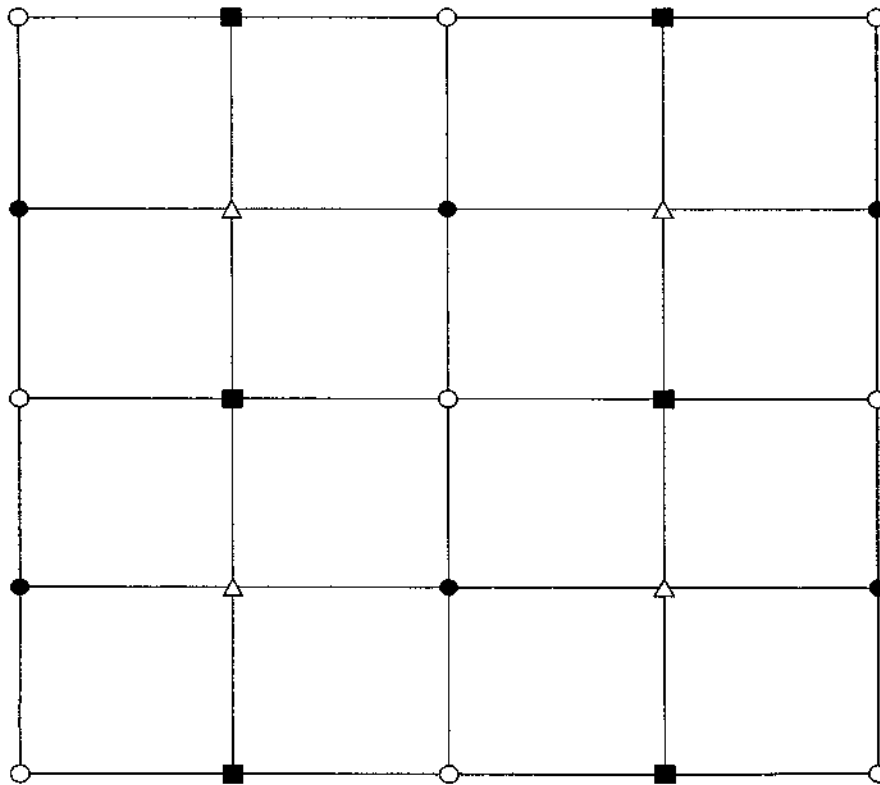

FIGURE 3-44

A checkerboard pressure pattern yields no net force yet is wildly unrealistic. Each symbol represents a different value of the pressure. Patankar (1980) recommends a staggered grid to eliminate this effect.

3-10.4.4   THE COMPUTATION OF FLUID PRESSURE. Suppose that temperature is not a variable (isothermal flow). Then an FDM for Eqs. (3-258b) and (3-258c) yields the "next" values of the velocities $u_{m,n}$ and $v_{m.n}$. It remains to compute the "next" pressure, $p_{m,n}$. Somewhat to our surprise, the remaining relation, (3-258a), does not even *contain* the fluid pressure. It concerns only velocities; yet it is fundamental and must also be satisfied.

In the stream function-vorticity formulation, the pressure is broken out and satisfies its own Poisson relation, Eq. (3-256). With primitive variables, however, it is appropriate to *construct* a pressure equation, either artificially or by manipulation.

For plane flow, Roache (1976) recommends use of Eq. (3-256)—which uses continuity in its derivation—to compute the pressure. To avoid occasional instability or long convergence time, this relation has been modified to include an *artificial compressibility*:

$$\Delta^2 p = \mu \Delta^2 B - \rho \left[\frac{\partial B}{\partial t} + \frac{\partial^2(u^2)}{\partial x^2} + \frac{\partial^2(v^2)}{\partial y^2} + 2\frac{\partial^2(uv)}{\partial x\,\partial y} \right] \qquad (3\text{-}259)$$

where $B = (\partial u/\partial x) + (\partial v/\partial y)$ is the *dilation* of the fluid and remains nonzero in the finite-difference approximation. Harlow and Welch (1965) demonstrate the stability of this type of computation. A similar relation is used for three-dimensional flow.

Other ideas for pressure computation are reviewed in the text by Tannehill et al. (1997). A popular method, called a "pressure-correction procedure," is given by Patankar (1980). The method presumes that initial guesses (u_0, v_0, p_0) are available, to be "corrected" by a convergent process to the actual (u, v, p):

$$u = u_0 + u' \qquad v = v_0 + v' \qquad p = p_0 + p'$$

After substitution in the momentum equations, the velocity corrections may be estimated by the relations

$$u' = -C\frac{\partial p'}{\partial x} \qquad v' = -C\frac{\partial p'}{\partial y} \qquad (3\text{-}260)$$

where C is a coefficient related to the element area and the convective-acceleration model. Meanwhile, substitution in the continuity relation yields the following "pressure-correction" equation:

$$\Delta^2 p' = \frac{1}{C}\left(\frac{\partial u_0}{\partial x} + \frac{\partial v_0}{\partial y} \right) \qquad (3\text{-}261)$$

As (u_0, v_0) approaches the correct velocity field (u, v), the right-hand side of Eq. (3-261) approaches zero; hence p' vanishes and p_0 is the desired pressure field.

Patankar (1980) calls this sequence the SIMPLE algorithm, meaning semi-implicit method for pressure-linked equations. The following steps constitute the algorithm:

1. Begin with the most recent pressure field p_0 as a guess.
2. Solve the discretized momentum equations for u_0 and v_0.
3. Solve for the corrections p' from a discretized Eq. (3-261).
4. Compute u' and v' from discretized Eqs. (3-260).
5. Correct the pressures and velocities everywhere.
6. Return to step 2 and repeat until converged.

In some cases, this procedure tends to overestimate the desired pressure correction, and convergence is slow. Patankar (1980) recommends an alternative SIMPLER algorithm, for SIMPLE-revised, which uses the pressure corrections only to change the velocity field. Pressures are then computed from a Poisson equation for total pressure. The SIMPLER method cuts computer time about one-third compared to SIMPLE.

There is no intrinsic difficulty in adding other variables (temperature, concentration, salinity) to a finite-difference model. These properties satisfy conservation laws of the same form as the Navier–Stokes equations and are modeled in the same manner.

3-10.4.5 SOME SUCCESSFUL COMPUTATIONS FROM THE LITERATURE. There have been thousands of publications in the literature of numerical analyses for various viscous flows. One of the earliest [Thom (1933)] hand-computed the still-popular problem of uniform crossflow past a circular cylinder. Figure 3-45 shows computer-generated streamlines and vorticity lines for $Re_D = 4$ [Keller and Takami (1966)] and for $Re_D = 40$ [Apelt (1961)].

The flow in Fig. 3-45a, for $Re_D = 4$, resembles an Oseen creeping-flow pattern, with slight asymmetry and streamlines slightly spread in the wake. At $Re_D = 40$, the asymmetry is striking, as vorticity lines are swept downstream by the strong convection. The Reynolds number can be thought of as the ratio of convection effects (ρU^2) to viscous effects $(\mu U/L)$. A standing eddy, whose size increases with Re, has formed behind the body. Even at $Re = 40$, the vorticity lines in front of the body have begun to concentrate in a narrow region, a portent of the "boundary layer" which becomes much thinner than the body at $Re = \mathcal{O}(1000)$. The calculations were performed by the stream function-vorticity $(\psi - \omega)$ formulation.

The standing eddy appears at about $Re = 7$ and grows linearly with Re to about $S/d = 2.5$ at $Re = 45$, as shown in Fig. 3-46 from the measurements of Taneda (1956). Above $Re = 60$, an unsteady Kármán vortex street forms, which can be suppressed up to $Re = 280$ by attaching a splitter plate aft of the cylinder [Grove et al. (1964)]. With a splitter plate, standing eddy growth continues to be linear, that is, $S/d \approx 0.065(Re - 7.0)$ up to $Re = 280$.

The computed wall shear stresses and surface pressures agree with experiments also, as does the total drag force. Figure 3-47 shows a compilation by Chang

(a)

(b)
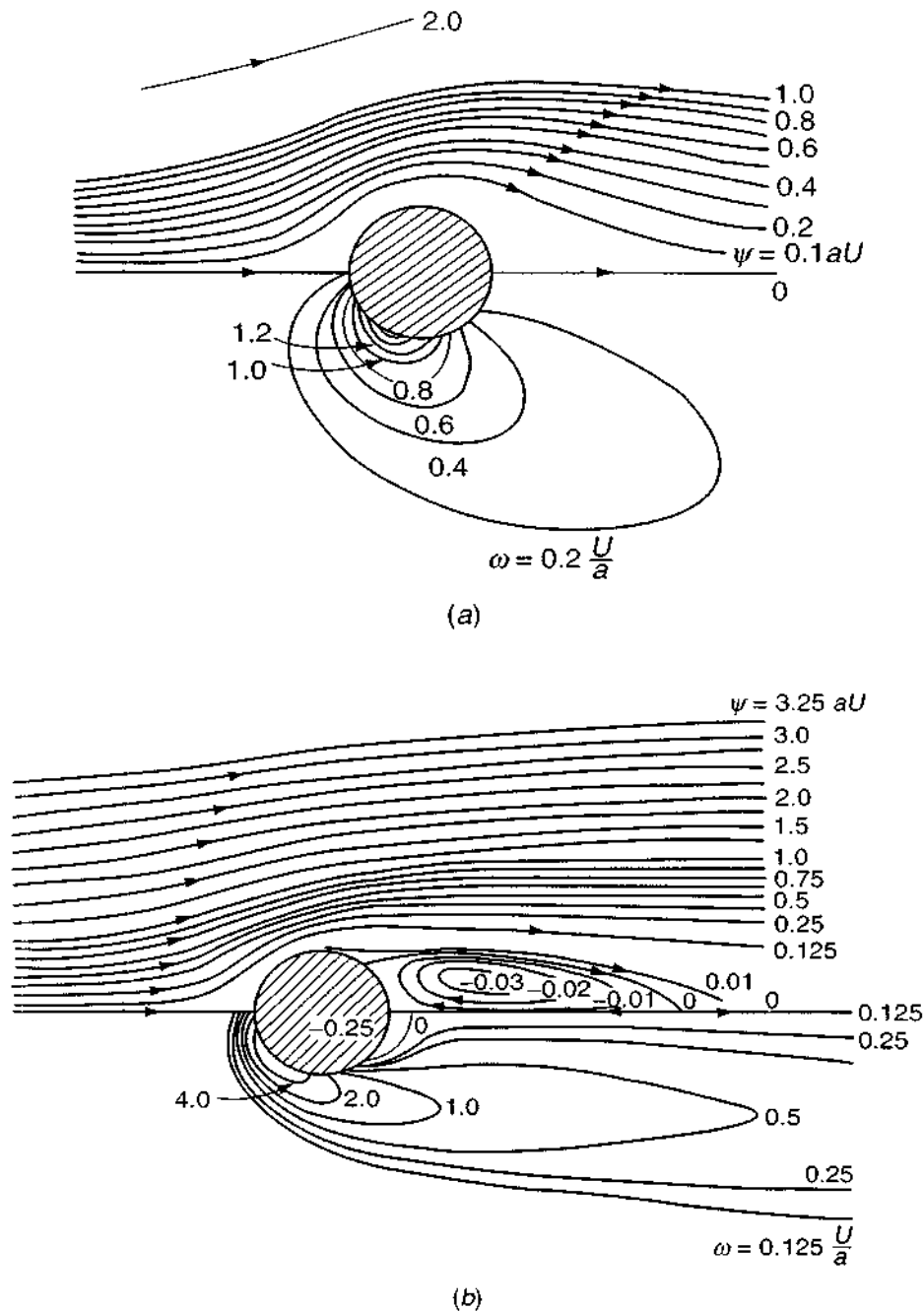
FIGURE 3-45

Numerical solutions for the flow past a circular cylinder: (a) streamlines (upper half) and lines of constant vorticity (lower half) in flow past a circular cylinder at $Re = 4$, calculated by Keller and Takami (1966); (b) streamlines (upper half) and lines of constant vorticity (lower half) in flow past a circular cylinder at $Re = 40$, calculated by Apelt (1961).

and Findlayson (1987) of numerical and experimental cylinder drag coefficients in the range $3 < Re < 100$. The results agree within experimental and numerical uncertainty. Our recommended curve fit, Eq. (3-229), is in fair agreement, being meant to fit well over a much wider range, $1E-4 < Re < 2E5$.

One can also compute the temperature field and heat transfer by adding a model of the energy equation to the CFD system. Chang and Findlayson (1987),
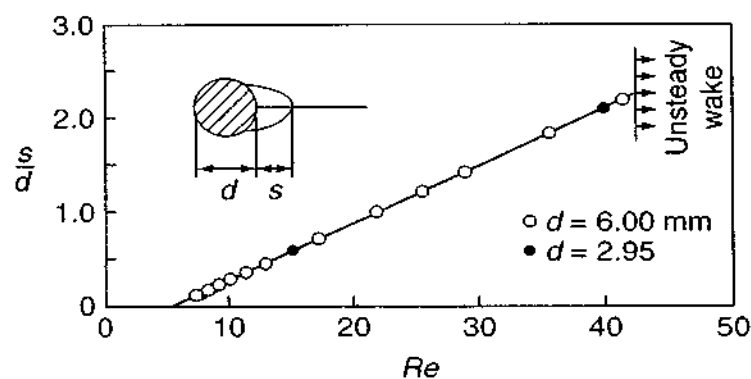
FIGURE 3-46
Observed lengths of the region of closed streamlines behind a circular cylinder. [*From Taneda (1956).*] Compare with Fig. 3-45.
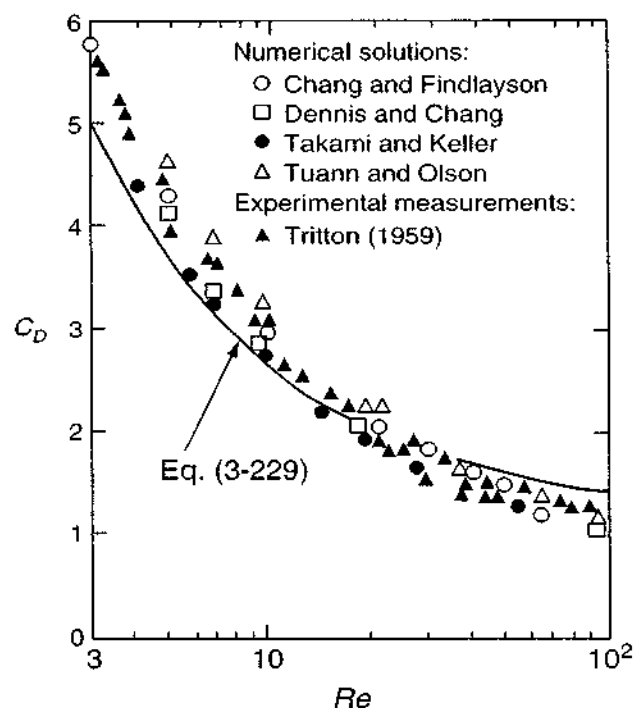
FIGURE 3-47
Comparison of experimental and numerical results for drag coefficient of a cylinder in crossflow. [*After Chang and Findlayson (1987).*]

for example, added heat transfer to their finite-element drag results in Fig. 3-47. Their numerical results, for $Re < 150$ and $0.01 \leq Pr \leq 1E4$, are in good agreement with our power-law correlation, Eq. (3-235).

3-10.4.6   FLOW PAST A LIQUID SPHERE. The related problem of flow past a solid sphere has been computed in many studies. The results are qualitatively similar to those of the cylinder in Fig. 3-46, with a standing eddy forming at $Re \approx 20$ and growing until $s/d \approx 1.1$ at $Re \approx 130$, above which the wake becomes unsteady.

A topic of current interest in multiphase flow of bubbles and droplets is flow past a *liquid* sphere of arbitrary viscosity ratio, $\lambda = \mu_{\text{inner}}/\mu_{\text{outer}}$. Analytically, only the creeping-flow solution of Rybczynski (1911) is known from Eq. (3-230). Numerical results, for $0.5 \leq Re \leq 1000$, were reported by Feng and Michaelides (2001) and summarized in the Freeman Scholar Lecture of Michaelides (2003). Their finite-difference method split the outer flow field into two matched layers and utilized 20,000 grid points. Figure 3-48 shows their computed streamlines and vorticity

(a)

(b)

(c)
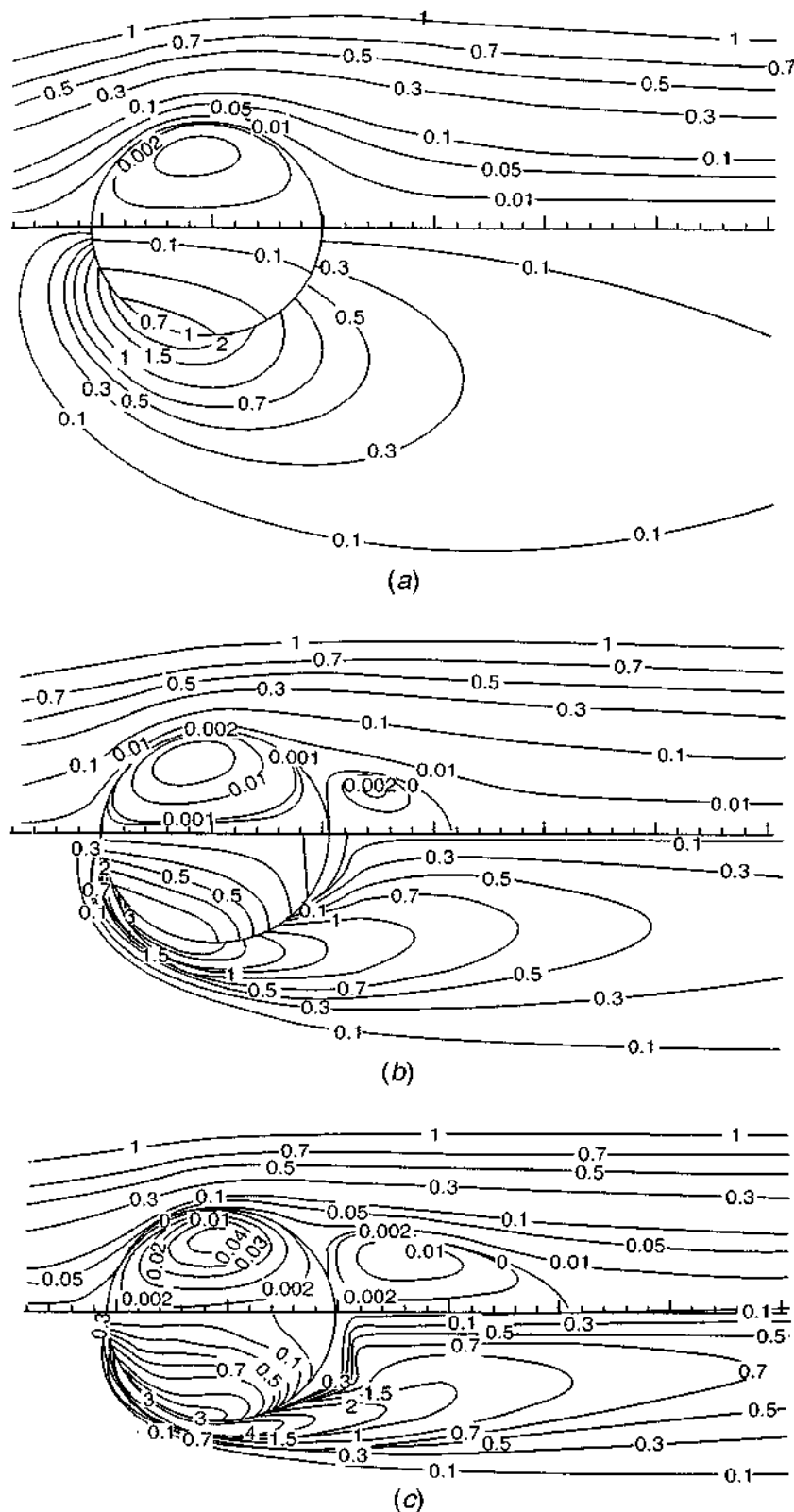
FIGURE 3-48

Streamlines (*upper half*) and vorticity contours (*lower half*) computed for flow past a liquid sphere, for $\lambda = \mu_{inner}/\mu_{outer} = 7$: (a) $Re_D = 10$; (b) $Re_D = 100$; (c) $Re_D = 500$. [*After Feng and Michaelides (2001), by permission of the American Society of Mechanical Engineers.*]

contours for three Reynolds numbers and an intermediate value $\lambda = 7$. The picture is similar to Fig. 3-45 for a cylinder. As Re increases, a standing eddy forms and lengthens, and the vorticity contours crowd together and are convected downstream.

Figure 3-49 shows the computed drag coefficients, based on outer fluid density, over the full viscosity range from $\lambda = 0$ (a bubble) to $\lambda = \infty$ (a solid sphere).
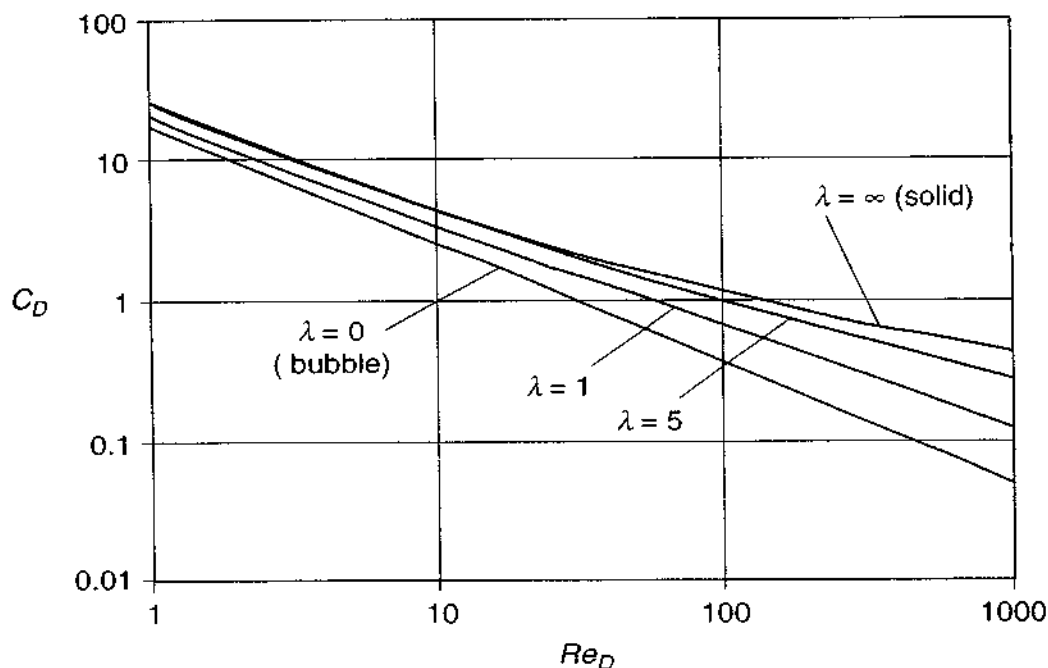
FIGURE 3-49

Drag coefficient of a liquid sphere for various values of the viscosity ratio $\lambda = \mu_{inner}/\mu_{outer}$. [*From calculations by Feng and Michaelides (2001), by permission of the American Society of Mechanical Engineers.*]

The bubble has a third less drag than a solid in the creeping-flow region, $C_D = 16/Re$, and at $Re = 1000$ has only one-ninth the drag of the solid. The solid curve in Fig. 3-49 has a simple and excellent curve fit

Solid sphere, $\lambda = \infty$, $Re \leq 1000$:

$$C_D \approx \frac{24}{Re}\left(1 + \frac{Re^{2/3}}{6}\right) \qquad (3\text{-}262)$$

as recommended by Feng and Michaelides (2001) for $Re \leq 1000$. Note, however, that this formula is *not* accurate for $Re > 1000$.

Let us summarize some facts about these two examples, CFD for a cylinder and a sphere. They are steady *laminar* flows, with no unsteady shedding. They use reasonable grid sizes and could be extended to shedding situations with good results, if the unsteady downstream boundary conditions are properly handled. Laminar-flow modeling can thus serve as a "numerical laboratory" for a wide variety of geometries. The same accuracy and reliability cannot yet be assured for turbulence modeling at higher Reynolds numbers.

3-10.4.7 FLOW THROUGH AN ORIFICE. Internal flows, such as ducts and channels, have well-defined geometries of confined size which correspondingly limit the number of necessary grid points. Figure 3-50 shows the streamlines and vorticity contours computed by Mills (1968) for laminar flow through a circular orifice whose diameter ($D_0 = a$) is 50 percent of the pipe size $D = 2a$. The orifice Reynolds number is $Re_0 = 4aU_{av}/\nu$ where $U_{av} = Q/A$ is the average velocity in the pipe.
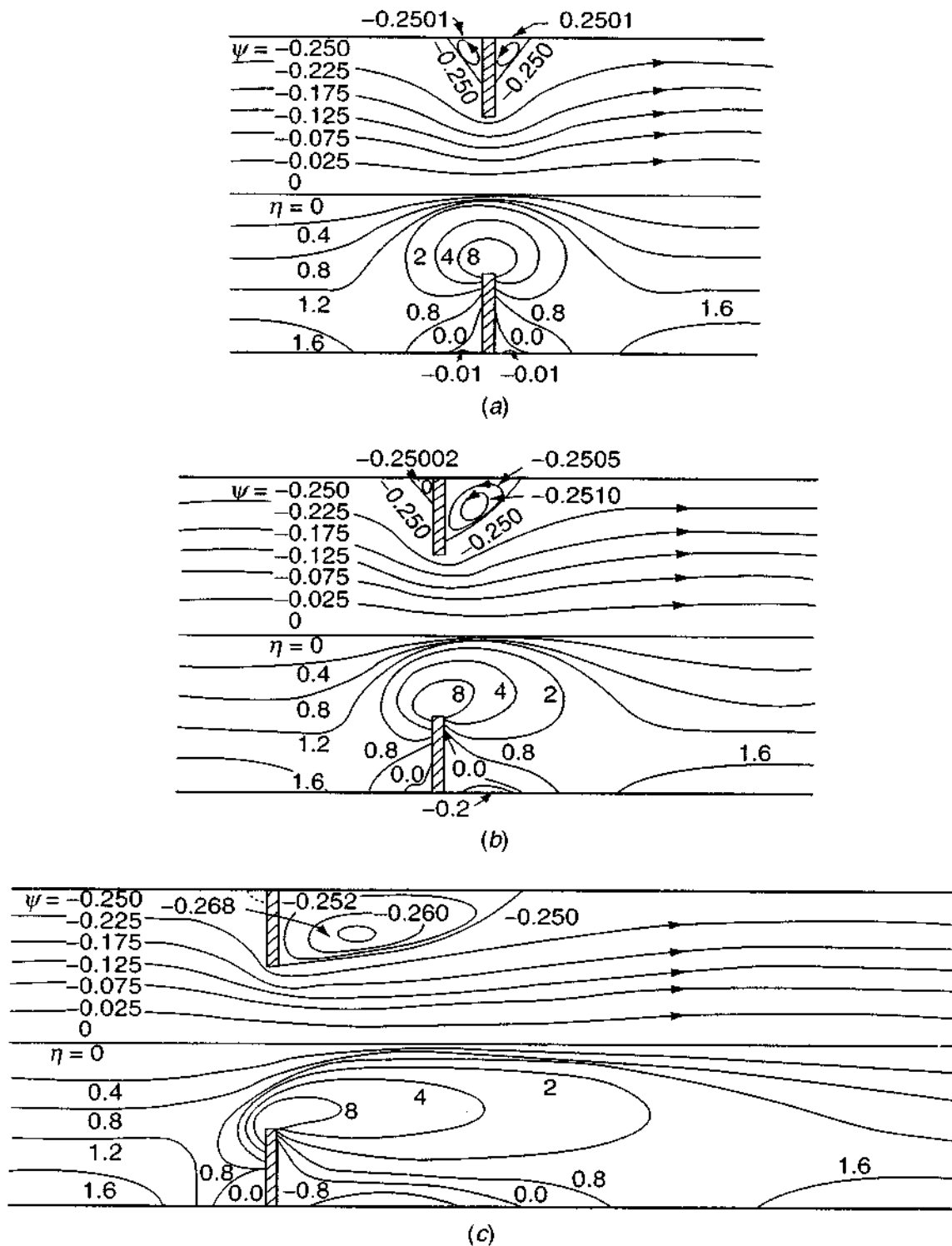
FIGURE 3-50

Numerical solutions for viscous flow through a circular orifice ($Re_0 = 4\,aU_{av}/\nu$). Streamlines and vorticity contours for (a) $Re_0 = 0$, $C_d = 0$; (b) $Re_0 = 10$, $C_d = 0.463$; (c) $Re_0 = 50$, $C_d = 0.690$.; [From Mills (1968).]

The flow pattern for creeping motion, $Re_0 = 0$, in Fig. 3-50a is perfectly symmetrical, with small standing eddies in the corners. Detailed examination would reveal that such separated-flow corners possess an infinity of nested eddies, each successive eddy being an order of magnitude smaller. At $Re_0 = 10$, Fig. 3-50b,

convection effects have caused a clear downstream asymmetry. In Fig. 3-50c, $Re_0 = 50$, the downstream eddy is elongated, and the flow through the orifice has the free-jet configuration characteristic of very high (laminar and turbulent) Reynolds numbers.

For the flows in Fig. 3-50, Mills (1968) computed the discharge coefficient, $C_d = Q/Q_{ideal}$, where Q_{ideal} is the flow rate computed for a one-dimensional inviscid approximation [White (2003, p. 416)]. For $Re_0 \leq 5$, $C_d \approx 0.15\sqrt{Re_0}$, and for $Re_0 > 5$, C_d rises slightly and levels off at the value of 0.7 expected for high Reynolds number thin-plate orifices. The computations are in excellent agreement with experiments.

As Re_0 increases beyond 50, orifice flow continues to resemble Fig. 3-50c, with discharge coefficients in the range of 0.6 to 0.7 expected for turbulent flow. One could continue the calculations with a turbulence model (Chap. 6). Since accurate discharge estimates are crucial for flowmeter applications, turbulent-flow correlations are provided, for example, by Scott et al. (1994) as a function of Re and $\beta = d_{orifice}/d_{pipe}$. Engineering formulas are provided in basic textbooks such as White (2003), Sec. 6.12. Recently a startling (to this writer) approach for orifice-data correlations was proposed by Morrison (2003), who replaced the Reynolds number with the *Euler* number, $Eu = 2\Delta p/(\rho U^2)$. This is quite a change from traditional practice.

3-10.4.8 CFD MODELING OF A MICROPUMP. There is now intense interest in microelectromechanical systems (MEMS), much of which involves flow at low Reynolds numbers in such systems. How can one pump a fluid through such tiny systems? Ordinary *rotodynamic* devices, such as compressors and centrifugal pumps, do not work at low Re. Positive-displacement pumps (PDPs) do work but involve complex fabrication and sealing problems. Sharatchandra et al. (1997) proposed, with testing and a CFD model, a simple rotating cylinder placed across a fluid between two plates. The cylinder picks up fluid due to the no-slip condition and drives it through the gap in the plates. Their CFD model was a finite-volume, two-dimensional computation using boundary-fitted coordinates and up to 8400 grid points.

Figure 3-51 shows the streamlines around their novel rotating-cylinder pump for $Re = 0.5$ as a function of the ratio s of plate spacing to cylinder diameter. The cylinder nearly touches the bottom plate. The quantity $\bar{u}$ is the dimensionless average velocity through the gap above the cylinder and is seen to be a maximum when $s \approx 1.5$. The gap is small, however, so the maximum volume flow occurs when $s \approx 2.0$. One can see in Fig. 3-51d that not much fluid is pumped when the gap is large. These CFD results are in good agreement with microflow experiments by the same group. For gas microflows, they investigated wall-slip effects and found no degradation in volume flow if the Knudsen number is less than 0.1. Finally, they investigated possible inertial effects (larger Reynolds number) and found no decrease in flow rate until $Re > 100$.

3-10.4.9 BOUNDARY-FITTING OF IRREGULAR GEOMETRIES. The CFD solutions illustrated in Figs. 3-45 to 3-51 have simple circular and/or rectangular geometries for which the equations of motion are well documented (App. B). If the

(a) $s = 1.25$ ($\bar{u} = 0.093$)

(b) $s = 1.5$ ($\bar{u} = 0.106$)

(c) $s = 2.5$ ($\bar{u} = 0.067$)

(d) $s = 3.5$ ($\bar{u} = 0.02$)
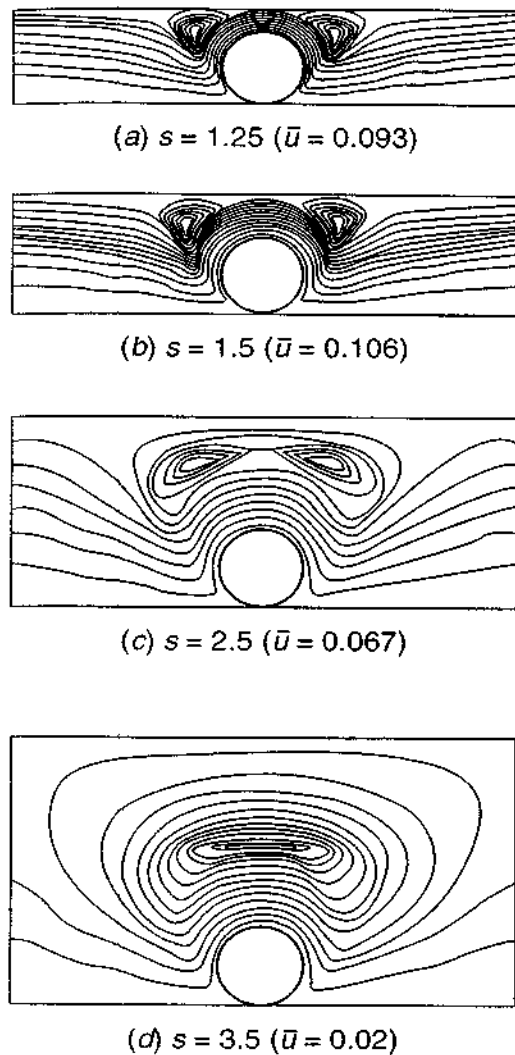
FIGURE 3-51
Streamlines computed for a rotating-cylinder micropump for $Re = 0.5$. Note the symmetry due to the low Reynolds number. The quantity s is the ratio of plate spacing to cylinder diameter, and $\bar{u}$ is the average velocity through the gap above the cylinder. [*After Sharatchandra et al. (1997), by permission of the American Society of Mechanical Engineers.*]

boundaries of the flow are irregular or asymmetrical, two approaches are suggested. Option 1 is to use a *finite-element* scheme, with triangular or quadrilateral elements that often fit irregular shapes very well. Details of the finite-element method are given in textbooks by, for example, Löhner (2001), Wrobel (2002), and Becker (2004), and commercial software is available.

Option 2 is to transform the coordinates and equations of motion to fit the irregular shapes. This is the method of *boundary-fitted coordinates*, popularized and now summarized by Thompson et al. (1998). First, one defines new (usually orthogonal) coordinates by solving the classical second-order partial differential equations that map the irregular region onto, say, a unit square. Numerical estimates of the coordinates' Jacobian are then used to transform the equations of motion so that conventional finite-difference schemes can be used on the unit square.

An example of a boundary-fitted solution is shown in Fig. 3-52, from Bramley and Sloan (1987). Laminar flow into a 45° half-angle Y branch is modeled by first defining orthogonal curvilinear coordinates for the region, using the method of Thompson et al. (1998). The resulting coordinates for the upper half of the flow
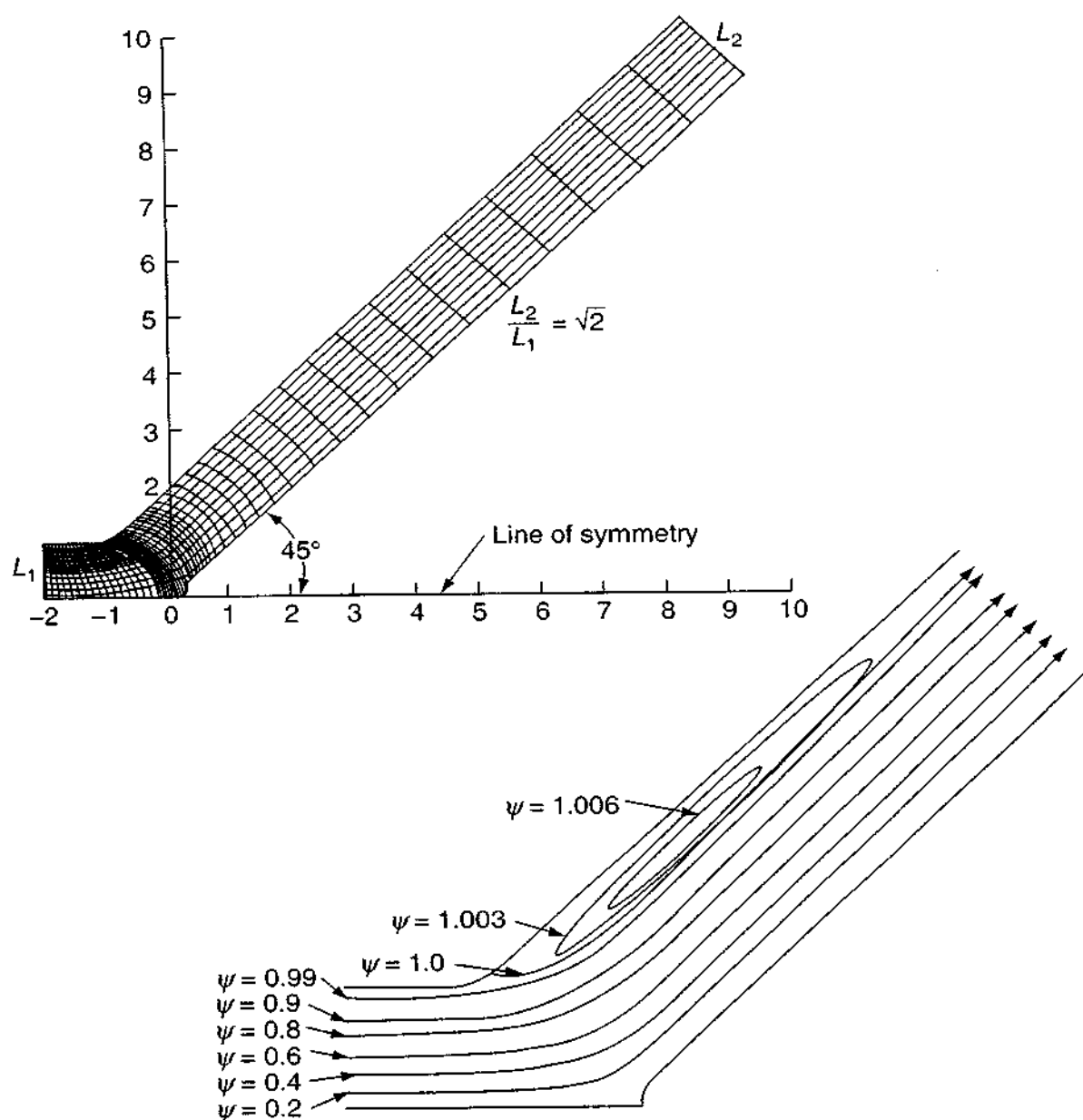
FIGURE 3-52
Computation of flow in a 45° Y branch: (*a*) boundary-fitted coordinates; (*b*) computed streamlines for $Re = 1000$. [*After Bramley and Sloan (1987).*]

are shown in Fig. 3-52*a*. The transformed Navier–Stokes equations are then solved for the flow pattern, shown in Fig. 3-52*b* for $Re = 1000$. An elongated separation bubble, similar to those in Fig. 3-51, is formed on the outside (suction) side of the Y. The bubble size increases with Re, but not linearly: It is 6.5 inlet half-widths long at $Re = 1000$, rising to 7.8 at $Re = 2000$ and is nearly independent of the half-angle of the Y in the range of 30 to 60°. Though we are confident that such laminar-flow results are accurate, the same computation for turbulent flow would be uncertain because empirical turbulence models are very sensitive to geometry and flow conditions.

SUMMARY

It has been the intent of the chapter to give a fairly complete survey of the various types of exact or near-exact solutions presently known for incompressible Navier–Stokes equations. Where appropriate, solutions have included not only the velocity but also temperature and pressure distributions, and dimensionless variables have been emphasized. The various types of solutions discussed were

1. Couette flows with steadily moving surfaces
2. Poiseuille flow through ducts
3. Unsteady duct flows
4. Unsteady flows with moving boundaries
5. Asymptotic suction flows
6. Wind-driven Ekman flows
7. Similarity solutions: stagnation flow, rotating disk, wedge flow
8. Low Reynolds number (creeping) flows
9. Lubrication theory
10. Computational fluid dynamics (CFD)

This list seems rather substantial until we reflect that none of these types possess any degree of arbitrariness except the computer solutions, which themselves are limited by mesh size and Reynolds number considerations. As the Reynolds number increases arbitrarily, laminar flows become unstable, and no method exists for exact analysis of such problems. In many flows, whether laminar or turbulent, the condition of high Reynolds number makes certain terms in the Navier–Stokes equations become negligible. What remains is a far more exploitable field of analysis: boundary-layer theory for laminar (Chap. 4), transitional (Chap. 5), turbulent (Chap. 6), and compressible (Chap. 7) flows. For nonboundary-layer flows, the use of computational fluid dynamics (CFD) for both laminar and turbulent flow is an increasingly powerful tool.

PROBLEMS

3-1. Reconsider the problem of Couette flow between parallel plates, Fig. 3-1, for a power-law nonnewtonian fluid, $\tau_{xy} = K(du/dy)^n$, where $n \neq 1$. Assuming constant pressure and temperature, solve for the velocity distribution $u(y)$ between the plates of (a) $n < 1$ and (b) $n > 1$, and compare with the newtonian solution, Eq. (3-6). Comment on the results.

3-2. Consider the axial Couette flow of Fig. 3-3 with both cylinders moving. Find the velocity distribution $u(r)$ and plot it for (a) $U_1 = U_0$, (b) $U_1 = -U_0$, and (c) $U_1 = 2U_0$. Comment on the results.

3-3. Consider the axial Couette flow of Fig. 3-3 with the inner cylinder moving at speed U_0 and the outer cylinder fixed. Solve for the temperature distribution $T(r)$ in the fluid if the inner and outer cylinder walls are at temperatures T_0 and T_1, respectively.

3-4. A long thin rod of radius R is pulled axially at speed U through an infinite expanse of still fluid. Solve the Navier–Stokes equation for the velocity distribution $u(r)$ in the fluid and comment on a possible paradox.

3-5. A circular cylinder of radius R is rotating at steady angular rate ω in an infinite fluid of constant ρ and μ. Assuming purely circular streamlines, find the velocity and pressure distribution in the fluid and compare with the flow field of an inviscid "potential" vortex.

3-6. Assuming that the velocity distribution between rotating concentric cylinders is known from Eq. (3-22), find the pressure distribution $p(r)$ if the pressure is p_0 at the inner cylinder.

3-7. An open U tube of radius r_0 filled with a length L of a viscous fluid is displaced from rest and oscillates with amplitude $X(t)$, as shown in Fig. P3-7. Show with a one-dimensional integral analysis that the governing equation for $X(t)$ is

$$\frac{d^2X}{dt^2} + \frac{C_f}{r_0}\left|\frac{dX}{dt}\right|\frac{dX}{dt} + \frac{2g}{L}X = 0$$

where C_f is the wall friction coefficient. Find the natural frequency of oscillation and the time to damp to one-half amplitude for an assumed Poiseuille-type friction factor, $C_f = 16\mu/[\rho\,|dX/dt|\,d_0]$.
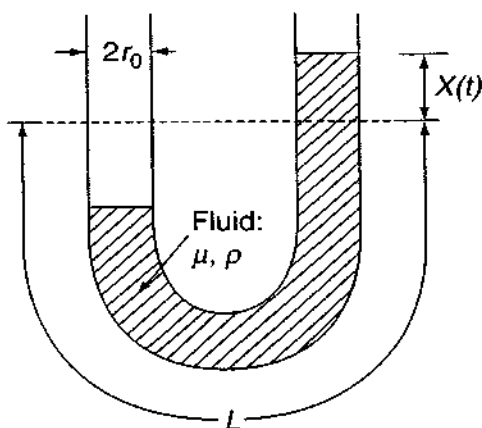
FIGURE P3-7

3-8. Air at 20°C and 1 atm is driven between two parallel plates 1 cm apart by an imposed pressure gradient (dp/dx) and by the upper plate moving at 20 cm/s. Find (a) the volume flow rate (in cm³/s per meter of width) if $dp/dx = -0.3$ Pa/m and (b) the value of (dp/dx) (in Pa/m) which causes the shear stress at the lower plate to be zero.

3-9. Derive the solution $u(y, z)$ for flow through an elliptical duct, Fig. 3-9, by solving Eq. (3-30). Begin with a guessed quadratic solution, $u = A + By^2 + Cz^2$, and work your way through to the exact solution.

3-10. Air at 20°C and approximately 1 atm flows at an average velocity of 1.7 m/s through a rectangular 1 × 4 cm duct. Estimate the pressure drop (in Pa/m) by (a) an exact calculation and (b) the hydraulic diameter approximation.

3-11. Consider a swirling motion superimposed upon a circular-duct flow by letting the velocity components take the form

$$v_r = 0 \qquad v_\theta = v_\theta(r, t) \qquad v_z = v_z(r)$$

Show that the axial flow v_z is unaffected by the swirl, so that an arbitrary v_θ can be added without changing the Poiseuille distribution.

3-12. It is desired to measure the viscosity of light lubricating oils ($\mu \approx 0.02$ to 0.1 Pa $\cdot$ s) by passing approximately 1 m³/h of fluid through an annulus of length 30 cm with inner and outer radii of 9 and 10 mm, respectively. Estimate the expected pressure drop through the device and an appropriate instrument for the pressure measurement.

3-13. Lubricating oil at 20°C [$\rho = 890$ kg/m³, $\mu = 0.8$ Pa $\cdot$ s, $k = 0.15$ W/(m $\cdot$ K), $c_p = 1800$ J/(kg $\cdot$ K)] is to be cooled by flowing at an average velocity of 2 m/s through a 3 cm diameter pipe whose walls are at 10°C. Estimate (*a*) the heat loss (in W/m²) at $x = 10$ cm and (*b*) the mean oil temperature at the pipe exit, $L = 2$ m. Comment on the results.

3-14. For plane polar coordinates with circular streamlines, show that the only nonzero vorticity component, $\omega = \omega_z(r)$, satisfies the equation

$$\frac{\partial \omega}{\partial t} = \nu\left(\frac{\partial^2 \omega}{\partial r^2} + \frac{1}{r}\frac{\partial \omega}{\partial r}\right)$$

Solve this equation for the decay of a line vortex initially concentrated at the origin with circulation Γ_0. Solve for $\omega(r, t)$ and show that

$$v_\theta = \frac{\Gamma_0}{2\pi r}\left[1 - \exp\left(-\frac{r^2}{4\nu t}\right)\right]$$

Sketch velocity profiles for a few representative times, including $t = 0$.

3-15. Consider a wide liquid film of constant thickness h flowing steadily due to gravity down an inclined plane at angle θ, as shown in Fig. P3-15. The atmosphere exerts constant pressure and negligible shear on the free surface. Show that the velocity distribution is given by

$$u = \frac{\rho g \sin \theta}{2\mu} y(2h - y)$$

and that the volume flow rate per unit width is $Q = \rho g h^3 \sin \theta / 3\mu$. Compare this result with flow between parallel plates, Eqs. (3-44) and (3-45).
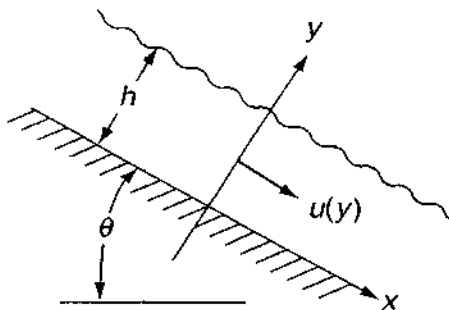
FIGURE P3-15

3-16. Consider a film of liquid draining at volume flow rate Q down the outside of a vertical rod of radius a, as shown in Fig. P3-16. Some distance down the rod, a fully developed region is reached where fluid shear balances gravity and the film thickness remains constant. Assuming incompressible laminar flow and negligible shear interaction with the atmosphere, find an expression for $v_z(r)$ and a relation between Q and film radius b.
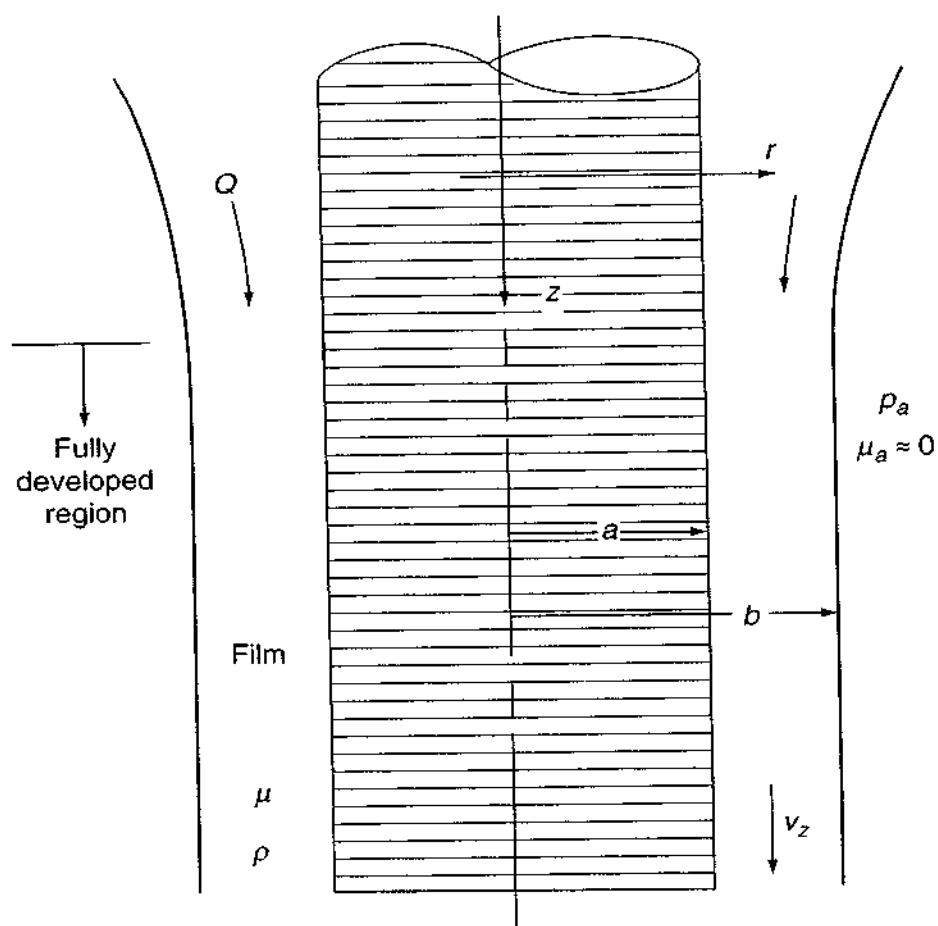
FIGURE P3-16

3-17. By extension of Prob. 3-15, consider a *double* layer of immiscible fluids 1 and 2, flowing steadily down an inclined plane, as in Fig. P3-17. The atmosphere exerts no shear stress on the surface and is at constant pressure. Find the laminar velocity distribution in the two layers.
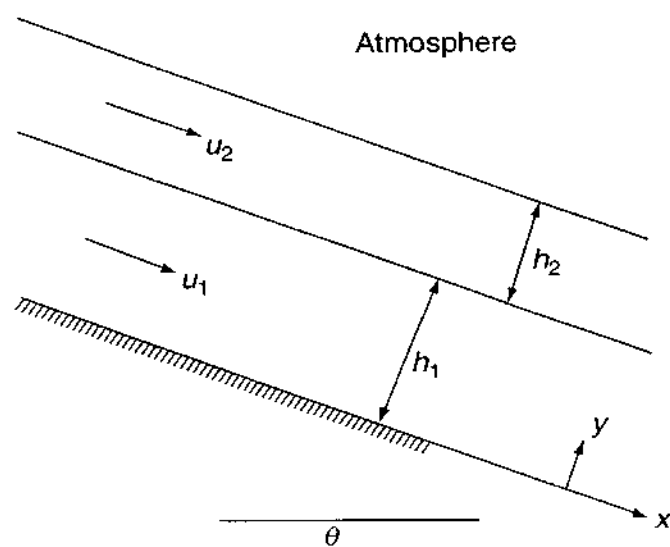
FIGURE P3-17

3-18. The surface of the draining liquid film in Prob. 3-15 will become wavy and unstable at a critical Reynolds number $Re^* = hu_{max}/\nu \approx \mathcal{O}(10)$ that depends upon slope θ, gravity g, density ρ, viscosity μ, and the surface tension $\mathcal{T}$. Rewrite this dependence in terms of two dimensionless parameters [Fulford (1964)]. For water at 20°C, what is the numerical value of the parameter which contains viscosity?

3-19. Derive Eq. (3-96) for start-up of flow in a circular pipe. Plot the instantaneous velocity profile for early times, $\nu t/r_0^2 = 0.005$ and 0.01.

3-20. Air at 20°C and 1 atm is at rest between two fixed parallel plates 2 cm apart. At time $t = 0$, the lower plate suddenly begins to move tangentially at 30 cm/s. Compute the air velocity in the center between plates after 2 s. When will the center velocity reach 14 cm/s?

3-21. A Couette pump consists of a rotating inner cylinder and a baffled entrance and exit, as shown in Fig. P3-21. Assuming zero circumferential pressure gradient and $(a - b) \ll a$, derive formulas for the volume flow and pumping power per unit depth. Illustrate for SAE 30 oil at 20°C, with $a = 10$ cm, $b = 9$ cm, and $\omega = 600$ rpm.

$r = a$

$r = b \approx a$

ω

ρ, μ
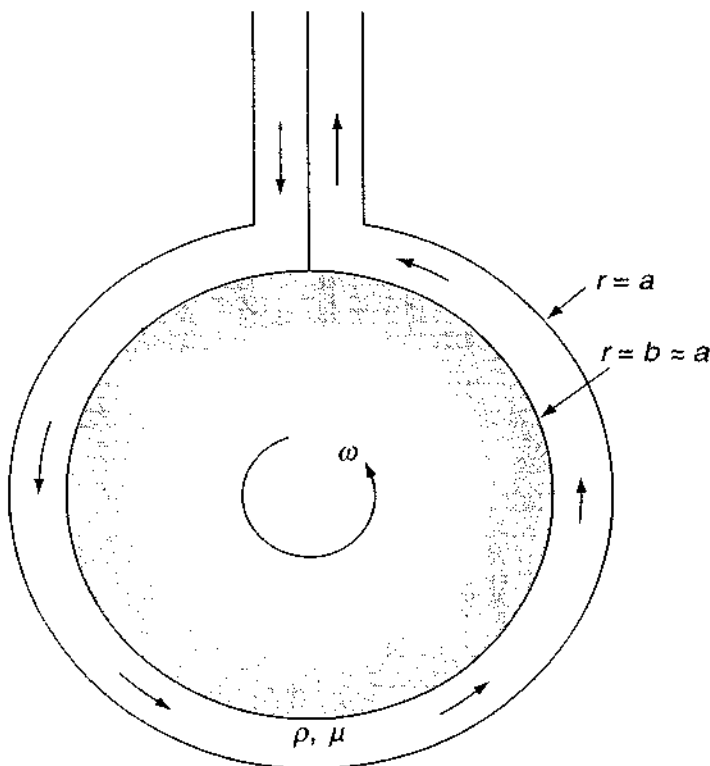
FIGURE P3-21

3-22. The Taylor vortex is defined by a purely circumferential flow

$$v_\theta = \text{const} \frac{r}{\nu t^2} \exp\left(-\frac{r^2}{\nu t}\right)$$

Determine whether this vortex is an exact solution of the incompressible Navier–Stokes equations with negligible gravity. Sketch a few instantaneous velocity profiles and compare to the Oseen vortex in Prob. 3-14.

3-23. Consider radial outflow between two parallel disks fed by symmetric entrance holes, as shown in Fig. P3-23. Assume that $v_z = v_\theta = 0$ and $v_r = f(r, z)$, with constant ρ and μ and $p = p(r)$ only. Neglect gravity and entrance effects at $r = 0$. Set up the appropriate differential equation and boundary conditions and solve as far as possible—numerical (e.g., Runge–Kutta) integration may be needed for a complete solution. Sketch the expected velocity profile shape.
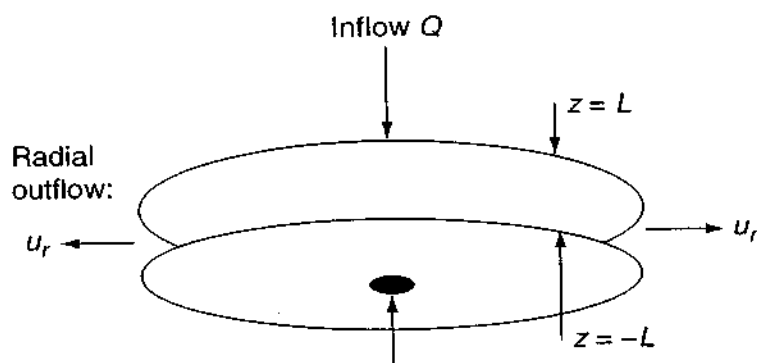
FIGURE P3-23

**3-24.** A long, uniformly porous cylinder of radius R exudes fluid at velocity U_0 into an unbounded fluid of constant ρ and μ. The pressure at the cylinder surface is p_0. Assuming purely radial outflow with negligible gravity, find the velocity and pressure distributions in the fluid.

3-25. Consider the problem of steady flow induced by a circular cylinder of radius r_0 rotating at surface vorticity ω_0 and having a wall-suction velocity $v_r(r = r_0) = -v_w = $ const. Set up the problem in polar coordinates assuming no circumferential variations $\partial/\partial\theta = 0$, and show that the vorticity in the fluid is given by

$$\omega = \frac{1}{r}\frac{\partial}{\partial r}(rv_\theta) = \omega_0\left(\frac{r_0}{r}\right)^{Re}$$

where $Re = r_0 v_w/\nu$ is the wall-suction Reynolds number of the cylinder. Integrate this relation to find the velocity distribution $v_\theta(r)$ in the fluid and show that the character of the solution is quite different for the three cases of the wall Reynolds number Re less than, equal to, or greater than 2.0.

3-26. Consider laminar flow in a uniformly porous tube, similar to the porous-channel problem, Eqs. (3-130). Let the similarity variable be $\zeta = (r/r_0)^2$ and find a suitable expression for the axisymmetric stream function $\psi(x, \zeta)$, similar to Eq. (3-128) for the channel. Then show that the differential equation equivalent to (3-132) is

$$2\zeta g'''' + 4g''' + Re(g'g'' - gg''') = 0 \qquad \text{[Yuan and Finkelstein (1956)]}$$

where $Re = v_w r_0/\nu$ and $g = g(\zeta)$ only. This equation has no known solutions in the range $2.305 \leq Re \leq 9.105$ [White (1962a)]. Establish the proper boundary conditions on the function $g(\zeta)$.

3-27. The practical difficulty with the Ekman spiral solution, Eq. (3-144), is that it assumes laminar flow whereas the real ocean is turbulent. One approximate remedy is to replace kinematic viscosity ν everywhere by a (constant) turbulent or

"eddy" viscosity correlated with wind shear and penetration depth using a suggestion by Clauser (1956):

$$\nu_{turb} \approx 0.04D\left(\frac{\tau_0}{\rho}\right)^{1/2}$$

Repeat our text example, $V_{wind} = 6$ m/s over a 20°C air-water interface of 41°N latitude. Compute penetration depth D and surface velocity V_0.

3-28. Repeat the analysis of the Ekman flow, Sec. 3-7.2, for shallow water, that is, apply the bottom boundary condition. Eq. (3-143), at $z = -h$. Find the velocity components and show that the surface velocity is no longer at a 45° angle to the wind but rather satisfies the equation as follows for the surface angle θ:

$$\tan\theta = \frac{\sinh(2\pi h/D) - \sin(2\pi h/D)}{\sinh(2\pi h/D) + \sin(2\pi h/D)} \qquad \text{[Ekman (1905)]}$$

Find the value of h/D for which $\theta = 20°$.

3-29. Air at 20°C and 1 atm flows at 1 m/s across a cylinder of diameter 2 cm and wall temperature 40°C. Using inviscid theory, Eq. (1-2), to establish the constant B, use the results of Sec. 3-8.1 to estimate (a) the shear layer thickness δ, (b) the wall shear stress, and (c) the heat-transfer rate q_w at the front stagnation point of the cylinder.

3-30. The opposite of von Kármán's rotating disk problem is Bödewadt's case [Rogers and Lance (1960)] of a fixed disk with a rotating outer stream, $v_\theta = r\omega$ as $z \to \infty$. Using the approach of Sec. 3-8.2, set up this problem and carry it out as far as possible, including numerical integration if a computer is available.

3-31. The rotating disk is sometimes called von Kármán's centrifugal pump, since it brings in fluid axially and throws it out radially. Consider one side of a 50 cm disk rotating at 1200 rpm in air at 20°C and 1 atm. Assuming laminar flow, compute (a) the flow rate, (b) the torque and power required, and (c) the maximum radial velocity at the disk edge.

3-32. Solve the Jeffery–Hamel wedge-flow relation, Eq. (3-195), for creeping flow, $Re = 0$ but $\alpha \neq 0$. Show that the proper solution is

$$f(\eta) = 1 + \frac{1}{2}\csc^2\alpha\left[\sin\left(\frac{\pi}{2} - 2\alpha\eta\right) - 1\right]$$

Show also that the constant $C = 4\alpha^2\cot^2\alpha$ and sketch a few profiles. Show that backflow always occurs for $\alpha > 90°$.

3-33. In spherical polar coordinates, when the variations $\partial/\partial\phi$ vanish, an incompressible stream function $\psi(r, \theta)$ can be defined such that

$$u_r = \frac{\partial\psi/\partial\theta}{r^2\sin\theta} \qquad u_\theta = -\frac{\partial\psi/\partial r}{r\sin\theta}$$

The particular stream function

$$\psi(r, \theta) = \frac{2\nu r\sin^2\theta}{1 + a - \cos\theta} \qquad a = \text{const}$$

is an exact solution of the Navier–Stokes equations and represents a round jet issuing from the origin. Sketch the streamlines in the upper two quadrants for a particular value of a between 0.001 and 0.1. (Various values could be distributed among a group.) Sketch the jet profile shape $u_r(1, \theta)$, and determine how the jet width δ (where $u_r = 0.01u_{max}$) and jet mass flow vary with r.

3-34. A sphere of specific gravity 7.8 is dropped into oil of specific gravity 0.88 and viscosity $\mu = 0.15$ Pa·s. Estimate the terminal velocity of the sphere if its diameter is (*a*) 0.1 mm, (*b*) 1 mm, and (*c*) 10 mm. Which of these is a creeping motion?

3-35. Verify Eq. (3-230) for the drag of a liquid droplet by repeating the Stokes problem with boundary conditions of zero radial velocity, equal tangential velocity, and equal shear stress at the droplet surface (assumed to be a perfect sphere, $r = a$).

3-36. Repeat the analysis of radial outflow between parallel disks, as in Prob. 3-23, for creeping flow, i.e., negligible inertia. Find the velocity and pressure distributions for this case.

3-37. Analyze the problem of creeping flow between parallel disks of radius R and separation distance L. The lower disk ($z = 0$) is fixed and the upper disk ($z = L$) rotates at angular rate ω. Assuming that $v_\theta = rf(z)$, reduce the problem as far as possible and solve for the velocities.

3-38. Set up the method of *separation of variables* for finding $u(y, z)$ for a rectangular duct, Fig. 3-9 and Eq. (3-48), by analyzing Eq. (3-30). First note that the separation will not work until one defines a new variable $U = u - F$, where $\nabla^2 F = (1/\mu)(dp/dx)$, so that $\nabla^2 U = 0$. Then separate U into x and y parts and find the form of each part. Show how an infinite series would be required to satisfy the boundary conditions, but do not determine the series coefficients.

3-39. Repeat the analysis of Sec. 3-9.7.1 for a parabolically varying gap:

$$h = h_L + (h_0 - h_L)\left(1 - \frac{x}{L}\right)^2$$

Nondimensionalize and solve for the pressure distribution similar to Eq. (3-240). Numerical integration may be required. Plot the resulting pressures for various h_L/h_0 and compare with Fig. 3-42.

3-40. Set up Stokes' first problem of the impulsively started plane wall, Fig. 3-18*a*, for solution by the explicit numerical method of Eq. (3-247). Plot some typical velocity profiles and compare quantitatively with the exact solution, Eq. (3-107).

3-41. Repeat Prob. 3-40 using the implicit method of Eq. (3-249).

3-42. Set up Stokes' second problem of the (long-term) oscillating wall, Fig. 3-19*a*, for solution by the explicit numerical method of Eq. (3-247). Let the initial transient die out. Plot some typical velocity profiles and compare quantitatively with the exact solution, Eq. (3-111).

3-43. Repeat Prob. 3-42 using the implicit method of Eq. (3-249).

3-44. Develop an explicit numerical algorithm for the two-dimensional unsteady viscous diffusion relation, Eq. (3-250). Determine the appropriate stability limits on time step and mesh sizes.

3-45. Develop an implicit numerical algorithm for the two-dimensional unsteady viscous diffusion relation, Eq. (3-250). Comment on a possible solution procedure and possible instability.

3-46. Derive the two-dimensional Poisson relation for pressure, Eq. (3-256), assuming unsteady incompressible flow.

3-47. The solutions $f_n(r)$ for Eq. (3-76) are called *Graetz functions*, but they are not tabulated. Set up a numerical solution of Eq. (3-76), perhaps using the Runge–Kutta subroutine of App. C, and solve iteratively for the first three functions f_{1-2-3} and their eigenvalues λ_{1-2-3}. Compare with Table 3-1, but no fair using the table for your initial guesses.

3-48. Explain the physical significance of each of the boundary conditions Eq. (3-257) and show how they are derived.

3-49. Set up a finite-difference model for fully elliptical flow in the entrance between parallel plates a distance h apart. At the entrance $(x = 0)$, assume uniform velocity U_0 and pressure p_0. Let the Reynolds number $U_0 h/\nu = 10$. Experiment with exit placement at $(x = 2h)$, using a square mesh, $\Delta x = \Delta y = h/10$. Modify the mesh size and exit position if necessary for convergence or accuracy. Solve (iteratively) for the interior nodal velocities and pressures and compare the results with Fig. 4-33 and Table 4-7.

3-50. Extend Prob. 1-21, where we found only the Knudsen number, $Kn \approx 0.17$, by using all the data given there. (*a*) Find the Reynolds number and see if it is less than 2000 (laminar flow). (*b*) Estimate the required pressure gradient in Pa/m. (*c*) Estimate the flow rate in mm^3/s.

3-51. Starting from the axial momentum equation, derive Eqs. (3-40) for slip flow in tubes.

3-52. For the geometry of Fig. 3-1, assume a constant pressure gradient with both walls fixed. Solve continuity and x momentum for laminar *slip flow* between the plates. Find the velocity distribution and the volume flow rate per unit depth. Does the Knudsen number appear?

3-53. Hadjiconstantinou (2003) has updated a second-order slip theory by Cercignani (2000) to give new numerical coefficients for the wall-slip velocity, to be compared with Eq. (1-91):

$$u_w \approx 1.11\ell \left.\frac{\partial u}{\partial y}\right|_w - 0.61\ell^2 \left.\frac{\partial^2 u}{\partial y^2}\right|_w$$

Repeat Prob. 3-52 with this formulation to solve continuity and x momentum for laminar *slip flow* between the plates. Find the velocity distribution and the volume flow rate per unit depth. Does the Knudsen number appear?

3-54. Carry out the steps that lead, for Stokes sphere flow, from Eq. (3-211) to (3-213) by assuming a product solution $\psi(r, \theta) = f(r)g(\theta)$, separating the variables, and solving for f and g.

3-55. Hill and Power (1956) proved that the creeping-flow (Stokes) drag of a solid object is greater than the drag of any inscribed shape but less than the drag of any circumscribed shape. Verify this result for the spheroid of Fig. 3-36 by comparing it to inscribed and circumscribed spheres. Do the relative drag forces differ markedly or by only a few percent?

3-56. The elemental creeping-flow solution $\psi = r \ln r \sin \theta$ is called an *Oseenlet*. Is this a solution for plane flow, Eq. (3-206), or axisymmetric flow, Eq. (3-211), or both? How might Oseenlets be used in analysis of more complex creeping flows?

3-57. Using a numerical method such as the Runge–Kutta subroutine of App. C, solve the axisymmetric stagnation flow Eq. (3-165) for the function $F(\eta)$. Use an iterative scheme to determine the proper value of $F''(0)$.

3-58. The rotating disk of Fig. 3-28 acts rather like a centrifugal pump. Consider a disk 60 cm in diameter, rotating at 120 rev/min in air at 20°C and 1 atm. Is the flow at the disk tip laminar, transitional, or turbulent? Using Kármán's theory of Sec. 3-8.2, estimate the volume flow of air, in cm^3/s, pumped outward by one side of the disk.

CHAPTER
4

LAMINAR BOUNDARY LAYERS

4-1 INTRODUCTION

Several of the exact solutions considered in Chap. 3—notably moving-boundary flows, stagnation flow, the rotating disk, convergent-wedge flow, and the flat plate with asymptotic suction—have hinted strongly at boundary-layer behavior. That is, at large Reynolds numbers, the effects of viscosity become increasingly confined to narrow regions near solid walls. The digital-computer solutions of Sec. 3-10 also showed this tendency at large Re to sweep the vorticity downstream and leave the flow far from the walls essentially irrotational. Physically, this means that the rate of downstream convection is much larger than the rate of transverse viscous diffusion. Consider a flow at speed U past a thin body of length L. The time a fluid particle spends near the body is approximately L/U, while the time required for viscous effects to spread across the streamlines is of order $\sqrt{\nu L/U^3}$. Then the viscous region will be thin if the diffusion time is much shorter than the residence time:

$$\sqrt{\frac{\nu L}{U^3}} \ll \frac{L}{U}$$

or   (4-1)

$$\sqrt{\frac{UL}{\nu}} = \sqrt{Re_L} \gg 1$$

Thus a *thin boundary layer* should exist if the flow Reynolds number Re_L is large. How large is difficult to specify and depends upon the geometry, the accuracy

desired, and whether the quantity L is a streamwise or a transverse length scale. The boundary layer is likely to be laminar at first and then, as Re_L increases, undergoes transition to turbulence. However, a thin layer is not ensured on the rear or lee side of bluff bodies. As we saw for spheres and cylinders in Chap. 3, at moderate Re, a standing eddy forms behind the body. At higher Re, the eddies are shed and a broad wake develops. The thin-boundary-layer approximations to be discussed here do not apply in "separated" regions such as occur behind bluff bodies. Boundary-layer theory can, however, estimate where the point of separation occurs on the body. Analytical studies of separated flow are difficult and rare, but there is considerable experimentation and numerical modeling.

Even though standard boundary-layer analysis is not applicable to (1) low Reynolds numbers or (2) flow separation, it is a very important subject, especially for understanding viscous flows. The present chapter is a reasonable survey of the traditional approach. Low Reynolds numbers and separated flows can yield to analysis by more advanced boundary-layer techniques. For further study, there are monographs entirely devoted to boundary-layer theory: Cebeci and Cousteix (1998), Schlichting and Gersten (2000), Schetz (1992), Oleinik and Samokhin (1999), plus the classical monograph by Rosenhead (1963).

4-1.1 Flat-Plate Integral Analysis

Following an idea first put forth by Kármán (1921), we may gain much insight and a remarkable amount of quantitative information about boundary layers by making a broad-brush momentum analysis of the flow of a viscous fluid at high Re past a flat plate. The proposed flow is sketched in Fig. 4-1. The sharp edge of the plate is at $(x, y) = (0, 0)$. The fluid will shear against the plate due to the no-slip condition and cause a frictional drag force D, and the velocity distribution $u(y)$ at any particular downstream position x will show a smooth drop-off to zero at the wall, as sketched in the figure. To satisfy conservation of mass, the streamlines will be deflected away from the plate—but not too much, we hope, so that the fluid pressure remains
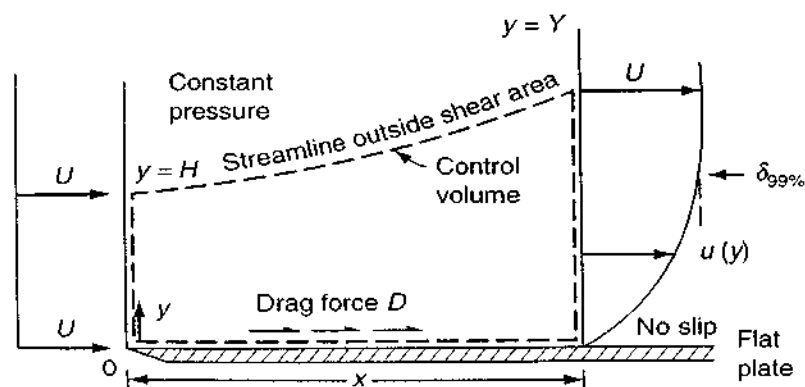

FIGURE 4-1
Definition of control volume for the analysis of flow past a flat plate.

approximately constant. We have labeled the shear-layer thickness as $\delta_{99\%}$; stream-lines outside this shear layer will deflect an amount δ^* (the displacement thickness) which depends only upon x. Thus the streamline in the figure moves outward from $y = H$ at $x = 0$ at $y = Y = H + \delta^*$ at $x = x_1$. Finally, we assume that the velocity just upstream of the sharp edge is uniform and parallel, $u = U = $ const; this would not be a good approximation at creeping-flow Reynolds numbers.

The control volume chosen for the analysis is enclosed by dashed lines in Fig. 4-1. This selection is not arbitrary but very clever. Since velocity distributions are known only at the inlet and exit, it is imperative that the other two sides on the control volume be streamlines, where no mass or momentum crosses. The lower side should be the wall itself; hence the drag force will be exposed. The upper side should be a streamline outside the shear layer, so that the viscous drag is zero along this line.

4-1.2 The Displacement Thickness

Conservation of mass for this control volume is obtained by applying Eq. (2-132) to this assumed steady flow:

$$\iint\limits_{CS} \rho \mathbf{V} \cdot d\mathbf{A} = 0 = \int_0^Y \rho u \, dy - \int_0^H \rho U \, dy \tag{4-2}$$

Assuming incompressible flow (constant density), this relation simplifies to

$$UH = \int_0^Y u \, dy = \int_0^Y (U + u - U) \, dy = UY + \int_0^Y (u - U) \, dy \tag{4-3}$$

Rearranging this and noting that $Y = H + \delta^*$, we can express the mass-flow relation in the following simple manner:

$$U(Y - H) = U\delta^* = \int_0^Y (U - u) \, dy$$

or $\tag{4-4}$

$$\delta^* = \int_0^{Y \to \infty} \left(1 - \frac{u}{U}\right) dy$$

Equation (4-4) is the formal definition of the boundary-layer displacement thickness δ^* and holds true for any incompressible flow, whether laminar or turbulent, constant or variable pressure, constant or variable temperature. In other words, to define δ^* is simply to state conservation of mass in steady flow. Note that since y variations are integrated away, δ^* is a function only of x. Its exact value depends upon the distribution $u(y)$.

4-1.3   Momentum Thickness as Related to Flat-Plate Drag

Conservation of x momentum results by applying Eq. (2-133) to our control volume:

$$\sum F_x = -D = \iint_{CS} u(\rho \mathbf{V} \cdot d\mathbf{A}) = \int_0^Y u(\rho u\, dy) - \int_0^H U(\rho U\, dy)$$

$$(4\text{-}5)$$

or

$$\text{Drag} = D = \rho U^2 H - \int_0^Y \rho u^2\, dy$$

Again assuming constant ρ and introducing

$$H = \int_0^Y \frac{u}{U}\, dy$$

from Eq. (4-3), we obtain, per unit depth into the paper,

$$\text{Drag} = \rho \int_0^Y u(U - u)\, dy$$

$$(4\text{-}6)$$

or

$$\frac{D}{\rho U^2} = \theta = \int_0^{Y \to \infty} \frac{u}{U}\left(1 - \frac{u}{U}\right) dy$$

Equation (4-6) is the defining relation for a second parameter, the momentum thickness θ, which, like δ^*, is clearly a function of x only. The definition holds true for any arbitrary incompressible boundary layer, but if we are not talking about flat-plate flow, θ is *not* equal to the drag divided by ρU^2. This means that momentum thickness, although interesting and useful in certain empirical correlations, is not as fundamental a quantity as δ^*.
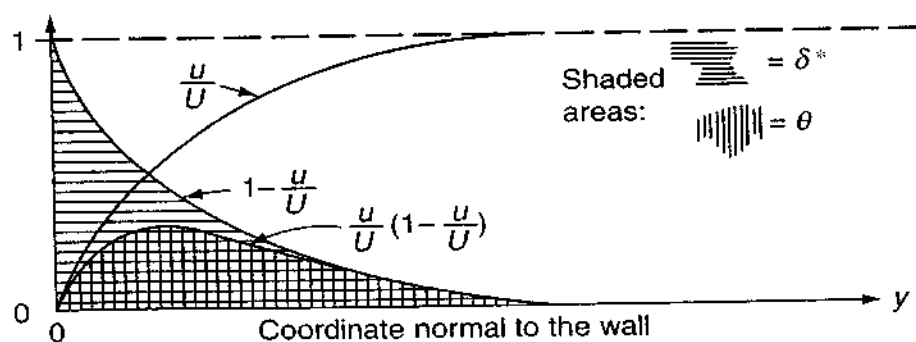

FIGURE 4-2
Momentum and displacement thicknesses.

The evaluation of δ^* and θ is illustrated graphically in Fig. 4-2. Clearly, δ^* is always the greater of the two. Their ratio, called the *shape factor*, is often used in boundary-layer analyses:

$$H = \frac{\delta^*}{\theta} > 1 \tag{4-7}$$

If $\tau_w(x)$ is the wall shear stress on the plate, the total drag per unit width on one side of a plate of length L is the integral of the wall shear forces:

$$D = \int_0^L \tau_w(x) \, dx \tag{4-8}$$

The wall shear and drag force may be nondimensionalized in the same manner as in Chap. 3:

Friction coefficient: $\qquad\qquad C_f(x) = \dfrac{\tau_w(x)}{\frac{1}{2}\rho U^2}$

$$\tag{4-9}$$

Drag coefficient: $\qquad\qquad C_D = \dfrac{D}{\frac{1}{2}\rho U^2 L}$

These are general definitions. For a flat plate, by comparison with Eqs. (4-6) and (4-8), these take the specialized form

$$C_{f,\,\text{plate}} = \frac{d}{dx}\,[xC_D(x)] = 2\frac{d\theta}{dx}$$

$$\tag{4-10}$$

$$C_{D,\,\text{plate}} = \frac{1}{L}\int_0^L C_f(x)\,dx = \frac{2\theta(L)}{L}$$

These formulas were derived by Kármán (1921) in his classic paper. They are valid for either laminar or turbulent flow. It is interesting that flat-plate friction and drag boil down entirely to the determination of the momentum thickness $\theta(x)$.

4-1.4 A Guessed Profile Yields Numerical Estimates

Assuming that the inlet profile is indeed a uniform velocity U, the previous relations are *exact* if one uses the correct profile $u(y)$. With the exact solution, though, we do not need integrals; we merely calculate the drag and wall shear and that is that. The beauty of Kármán's idea is that we can *guess* a reasonable form for $u(y)$ and get reasonable estimates because integration tends to wash out the positive and negative deviations of the assumed profile.

Let us therefore try a simple expression for $u(y)$ at the position x in Fig. 4-1. We will satisfy three physical conditions for the profile:

No slip at the wall: $\qquad\qquad\qquad u(0) = 0$

Smooth merging with the stream:

$$u(\delta) = U \qquad \frac{\partial u}{\partial y}\bigg|_{y=\delta} = 0$$

Other constraints will be discussed later. We can satisfy these three conditions for laminar flow with a second-order polynomial:

$$u \approx U\left(\frac{2y}{\delta} - \frac{y^2}{\delta^2}\right) \tag{4-11}$$

Now insert this approximation into Eqs. (4-4) and (4-6) to estimate

$$\delta^* \approx \frac{\delta}{3} \qquad \theta \approx \frac{2\delta}{15} \qquad H \approx \frac{5}{2} \tag{4-12}$$

This is not enough. We must also relate wall shear to the assumed shape $u(y)$, which we do, following Kármán (1921), by differentiating the profile relation, Eq. (4-11):

$$\tau_w = \mu \frac{\partial u}{\partial y}\bigg|_{y=0} \approx \frac{2\mu U}{\delta} \tag{4-13}$$

Substituting Eqs. (4-12) and (4-13) into the first of Eqs. (4-10), we obtain

$$C_f \approx \frac{2\mu U/\delta}{\frac{1}{2}\rho U^2} = 2\frac{d\theta}{dx} \approx 2\frac{d}{dx}\left(\frac{2\delta}{15}\right)$$

or

$$\delta \, d\delta \approx \frac{15\mu \, dx}{\rho U}$$

Integrate, assuming (for large Re) that the boundary layer begins at the leading edge, $\delta(0) = 0$. The result is

$$\delta^2 \approx \frac{30\mu x}{\rho U}$$

or

$$\frac{\delta}{x} \approx \frac{5.5}{\sqrt{Re_x}} \tag{4-14}$$

where $Re_x = \rho Ux/\mu$. This is only 10 percent higher than the exact solution for laminar flat-plate flow given by Blasius (1908).

By substituting δ from Eq. (4-14) into Eqs. (4-12) and (4-13), we obtain the additional flat-plate estimates

$$\frac{\delta^*}{x} \approx \frac{1.83}{\sqrt{Re_x}}$$

$$\frac{\theta}{x} = C_f \approx \frac{0.73}{\sqrt{Re_x}} \tag{4-15}$$

which are also within 10 percent of the exact solutions. Finally, by integration of $C_f(x)$ from Eq. (4-10), we obtain the drag coefficient:

$$C_D \approx \frac{1.46}{\sqrt{Re_L}} = 2C_f(L) \qquad (4\text{-}16)$$

As Kármán (1921) pointed out, these results are quite easily obtained compared to a full-blown attack on the continuity and momentum partial differential equations.

All of the previous integral momentum estimates for flat-plate flow are collected in the following table and compared with the exact solution due to Blasius (1908). The error is 10 percent, which is typical of integral theories. The advantage is that, by integrating across the shear layer in the y direction, we are left only with an *ordinary* differential equation to solve in the x direction for parameters such as $\delta(x)$.

Parameter	u from Eq. (4-11)	Exact from Blasius (1908)	Error, %
$\frac{\theta}{x}\sqrt{Re_x}$	0.73	0.664	+10
$\frac{\delta^*}{x}\sqrt{Re_x}$	1.83	1.721	+6
$\frac{\delta_{99\%}}{x}\sqrt{Re_x}$	5.5	5.0	+10
$C_f\sqrt{Re_x}$	0.73	0.664	+10
$C_D\sqrt{Re_L}$	1.46	1.328	+10

4-1.5 Some Insight into Boundary-Layer Approximations

The essence of the "boundary-layer approximation" is that the shear layer is thin, $\delta \ll x$. From Eq. (4-14), we see that this is true if $Re_x \gg 1$. Other scale arguments also follow from the results. First, since the velocity ratio $v/u \le d\delta^*/dx$, the outer streamline slope, it follows from Eq. (4-15) that $v \ll u$ if $Re_x \gg 1$. Second, by differentiating Eq. (4-11) we may determine that $\partial u/\partial x \ll \partial u/\partial y$ if, again, $Re_x \gg 1$, and a similar result holds for the derivatives of normal velocity v. In summary, a large Reynolds number creates the following strong inequalities:

$$Re_x \gg 1: \qquad \delta \ll x \qquad v \ll u \qquad \frac{\partial u}{\partial x} \ll \frac{\partial u}{\partial y} \qquad \frac{\partial v}{\partial x} \ll \frac{\partial v}{\partial y}$$

All of these approximations were used by Prandtl (1904) in deriving his celebrated boundary-layer equations.

4-1.6 Integral Analysis of the Energy Equation

In similar manner, the control-volume energy equation can be used to calculate approximate values for the mean and local heat transfer and the thickness of the
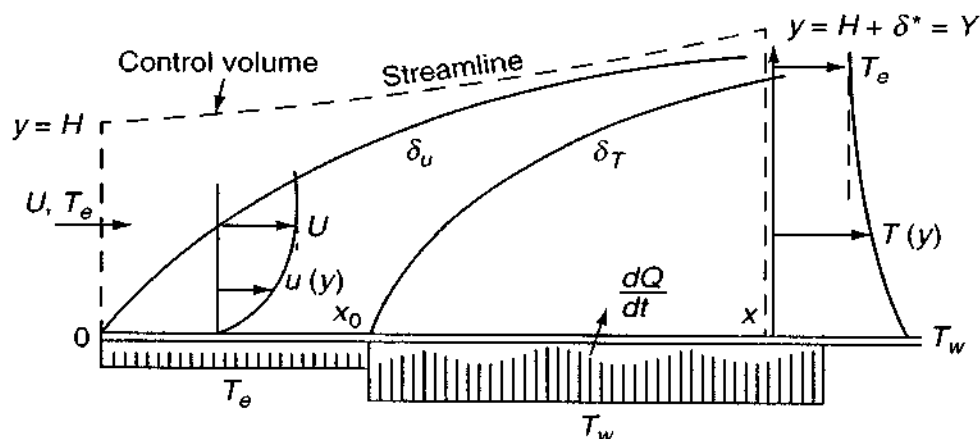
FIGURE 4-3
Sketch and control volume for the thermal boundary layer. Hot wall shown for convenience.

thermal boundary layer δ_T. The control volume chosen is shown in Fig. 4-3, where we propose that the rear portion of the plate, $x \geq x_0$, is heated (or cooled) to a temperature T_w different from the environment temperature T_e in the freestream (and on the first portion of the plate). Beginning at x_0, then, a thermal boundary layer will grow, assuming of course that the Reynolds number is large.

If we make sure that the upper streamline is outside the region of shear (the velocity boundary layer), there will be no shear work of significance at any boundary; therefore Eq. (2-139) will be valid and the shaft work will also be zero:

$$\frac{dQ}{dt} = \iint_{CS} \left(\frac{p}{\rho} + e + gy + \frac{1}{2} u^2 + \frac{1}{2} v^2 \right) \rho \mathbf{V} \cdot d\mathbf{A} \qquad (4\text{-}17)$$

At large Re_x, $\delta^* \ll x$, so that $v \ll u$ and the change in potential energy will be very small. Hence we neglect the terms gy and $\frac{1}{2}v^2$. The quantity $p/\rho + e$ is the enthalpy h, and the equation reduces to integrals over the inlet and outlet of the stagnation enthalpy $h_0 = (h + \frac{1}{2}u^2)$:

$$\frac{dQ}{dt} \approx \int_0^Y \left(h + \frac{1}{2} u^2 \right) \rho u \, dy - \int_0^H \left(h + \frac{1}{2} u^2 \right) \rho u \, dy \qquad (4\text{-}18)$$

This expression applies even for compressible flow and will be studied again in Chap. 7. Here we assume constant density. Since the conditions at the inlet are uniform (h_e, T_e, U), we obtain

Inlet: $$\int_0^H \left(h + \frac{1}{2} u^2 \right) \rho u \, dy = \left(h_e + \frac{1}{2} U^2 \right) \rho U H$$

Now the mass-flow relation from Eq. (4-3) is still valid, so that we can eliminate H

from the energy relation, giving

$$\frac{dQ}{dt} = \rho \int_0^{Y \to \infty} \left[(h - h_e) - \frac{1}{2}(U^2 - u^2) \right] u \, dy \qquad (4\text{-}19)$$

This is the overall *integral-energy* equation. Since $dQ/dt = \int q_w \, dx$, it may be differentiated and written in *local* form:

$$q_w = \frac{d}{dx} \left[\int_0^\infty \rho u \left(h + \frac{1}{2} u^2 - h_e - \frac{1}{2} U^2 \right) dy \right] = -k \frac{\partial T}{\partial y} \bigg|_{y=0} \qquad (4\text{-}20)$$

For low-speed flow, it is customary to neglect kinetic energy $u^2/2$ (i.e., $Ec \ll 1$) and to use the approximation $h \approx c_p T$:

$$q_w \approx \frac{d}{dx} \left[\int_0^\infty \rho c_p u (T - T_e) \, dy \right] \qquad (4\text{-}21)$$

This may also be written in dimensionless form as a Stanton number, with a local length scale called the *enthalpy* thickness, δ_h:

$$C_h(x) = \frac{q_w}{\rho U c_p (T_w - T_e)} = \frac{d}{dx}(x C_H) = \frac{d\delta_h}{dx} \qquad (4\text{-}22)$$

where $\qquad \delta_h = $ enthalpy thickness $\approx \displaystyle\int_0^\infty \frac{T - T_e}{T_w - T_e} \frac{u}{U} \, dy$

Note the similarity to the local momentum integral relation, Eq. (4-11). Equation (4-22) is valid for either laminar or turbulent flow.

4-1.7 A Guessed Temperature Profile Yields the Heat-Transfer Rate

We can evaluate the heat transfer approximately for laminar flow by combining the velocity estimate Eq. (4-11) with a similar second-order polynomial temperature estimate:

$$T - T_e \approx (T_w - T_e) \left(1 - \frac{2y}{\delta_T} + \frac{y^2}{\delta_T^2} \right) \qquad (4\text{-}23)$$

Substitute these approximations, Eqs. (4-11) and (4-23), into the integral relation Eq. (4-20) to obtain

$$q_w \approx \frac{d}{dx} \left[\rho c_p U (T_w - T_e) \delta \left(\frac{\zeta^2}{6} - \frac{\zeta^3}{30} \right) \right] \approx \frac{2k(T_w - T_e)}{\zeta \delta} \qquad (4\text{-}24)$$

where $\zeta = \delta_T/\delta$ is the ratio of boundary-layer thicknesses. If we assume constant wall and stream temperatures, the term $(T_w - T_e)$ drops out. Also assume that ρ, μ, k, and c_p are constant.

Let us illustrate two solutions of Eq. (4-24). First, let the thermal boundary layer start from the plate leading edge, $\delta_T = 0$ at $x = 0$. Further assume, for convenience

in the integration, that $\delta_T < \delta$. After introducing $\delta(x)$ from our momentum solution, Eq. (4-14), we obtain

$$\zeta^3 - \frac{\zeta^4}{5} \approx \frac{4\alpha}{5\nu} = \frac{0.8}{Pr} \tag{4-25}$$

An approximate solution to this polynomial, valid for Prandtl numbers not too far from unity, is

$$\zeta = \frac{\delta_T}{\delta} \approx Pr^{-1/3} \tag{4-26}$$

With ζ and δ known, the local Nusselt number may be obtained from Eq. (4-24):

$$Nu_x = \frac{q_w x}{k(T_w - T_e)} \approx 0.365 Re_x^{1/2} Pr^{1/3} \tag{4-27}$$

This is only 10 percent higher than the exact solution, for constant-T_w laminar flat-plate flow, given by Pohlhausen (1921)—the correct constant should be 0.332, not 0.365.

Second, consider an *unheated starting length*, where the wall temperature $T_w \neq T_e$ does not begin until $x = x_0$, as in Fig. 4-3. Here $\zeta(x)$ is not constant, and Eq. (4-24) must be solved:

$$\zeta\delta \frac{d}{dx}\left[\delta\left(\zeta^2 - \frac{\zeta^3}{5}\right)\right] \approx \frac{12\alpha}{U} \qquad \zeta = 0 \text{ at } x = x_0$$

This is readily solved numerically by, e.g., Subroutine RUNGE in App. C. To avoid this, a simple solution is possible if, noting that $\zeta < 1$ for $Pr > 1$, we neglect the term $(\zeta^3/5)$ and, concurrently, increase the constant 12 to 15. The differential equation then becomes

$$\zeta^3 + \frac{4}{3} x \frac{d}{dx}(\zeta^3) \approx \frac{1}{Pr}$$

or

$$\zeta^3 = \frac{1}{Pr} + \frac{C}{x^{3/4}}$$

To make $\zeta = 0$ at $x = x_0$, we require that the constant $C = -x_0^{3/4}/Pr$. The final solution may again be placed in the form of a Nusselt number for plate flow with an unheated starting length:

$$x > x_0: \qquad\qquad Nu_x \approx \frac{0.365 Re_x^{1/2} Pr^{1/3}}{\left[1 - (x_0/x)^{3/4}\right]^{1/3}} \tag{4-28}$$

Compare with Eq. (4-27) for $x_0 = 0$. If the constant 0.365 is reduced by 9 percent to 0.332, the result agrees with the formula recommended for flat-plate flow in most heat-transfer textbooks, e.g., Eq. (9-26) of Kays and Crawford (1993).

In summary, we see that simple integral techniques, using guessed velocity and temperature profiles, yield estimates for both mean and local friction and heat transfer with accuracies on the order of ± 10 percent. We shall return to these ideas in Sec. 4-6 for non-flat-plate flows.

4-2 LAMINAR-BOUNDARY-LAYER EQUATIONS

Integral analyses not only gave numbers but also yielded information about the sizes of various terms:

$$u, T, \text{ and } x = \mathcal{O}(\text{unity})$$

$$v \text{ and } y = \mathcal{O}\left(Re^{-1/2}\right)$$

(4-29)

These are solid estimates, not guesses, which can be used to derive the famous boundary-layer equations first propounded by Prandtl (1904). By redefining all variables in terms of these estimates, we can quickly spot which terms in the equations of motion are negligible if Re is large. Let us confine ourselves to two-dimensional incompressible flow, for which the relevant equations are

$$\frac{\partial u}{\partial x} + \frac{\partial v}{\partial y} = 0$$

$$\frac{\partial u}{\partial t} + u\frac{\partial u}{\partial x} + v\frac{\partial u}{\partial y} = -\frac{1}{\rho}\frac{\partial p}{\partial x} + g_x\beta(T - T_0) + \nu\left(\frac{\partial^2 u}{\partial x^2} + \frac{\partial^2 u}{\partial y^2}\right)$$

$$\frac{\partial v}{\partial t} + u\frac{\partial v}{\partial x} + v\frac{\partial v}{\partial y} = -\frac{1}{\rho}\frac{\partial p}{\partial y} + g_y\beta(T - T_0) + \nu\left(\frac{\partial^2 v}{\partial x^2} + \frac{\partial^2 v}{\partial y^2}\right)$$

(4-30)

$$\rho c_p\left(\frac{\partial T}{\partial t} + u\frac{\partial T}{\partial x} + v\frac{\partial T}{\partial y}\right) = k\left(\frac{\partial^2 T}{\partial x^2} + \frac{\partial^2 T}{\partial y^2}\right)$$

$$+ \mu\left[2\left(\frac{\partial u}{\partial x}\right)^2 + 2\left(\frac{\partial v}{\partial y}\right)^2 + \left(\frac{\partial u}{\partial y} + \frac{\partial v}{\partial x}\right)^2\right]$$

With our estimates from Eq. (4-29), we can now define dimensionless variables, all of which are sure to be of order unity if Re is large:

$$x^* = \frac{x}{L} \qquad y^* = \frac{y}{L}\sqrt{Re} \qquad t^* = \frac{tU}{L} \qquad T^* = \frac{T - T_0}{T_w - T_0}$$

$$u^* = \frac{u}{U} \qquad v^* = \frac{v}{U}\sqrt{Re} \qquad p^* = \frac{p - p_0}{\rho U^2}$$

(4-31)

where U, L, p_0, and T_0 are reference values and $Re = UL/\nu$ is the Reynolds number characterizing the flow. Now substitute these variables into Eqs. (4-30) and take

the limit of these equations as Re becomes very large. Many terms drop out, and we retain only

$$\frac{\partial u^*}{\partial x^*} + \frac{\partial v^*}{\partial y^*} = 0$$

$$\frac{\partial u^*}{\partial t^*} + u^*\frac{\partial u^*}{\partial x^*} + v^*\frac{\partial u^*}{\partial y^*} = -\frac{\partial p^*}{\partial x^*} + \frac{\beta(T_w - T_0)T^*}{Fr_x} + \frac{\partial^2 u^*}{\partial y^{*2}}$$

$$0 = \frac{\partial p^*}{\partial y^*} + \frac{\beta(T_w - T_0)}{Fr_y}T^* \qquad\qquad (4\text{-}32)$$

$$\frac{\partial T^*}{\partial t^*} + u^*\frac{\partial T^*}{\partial x^*} + v^*\frac{\partial T^*}{\partial y^*} = \frac{1}{Pr}\frac{\partial^2 T^*}{\partial y^{*2}} + Ec\left(\frac{\partial u^*}{\partial y^*}\right)^2$$

where $Ec = U^2/c_p(T_w - T_0)$ is the Eckert number and $Fr_i = U^2/Lg_i$ is the Froude number in each direction. All other terms had coefficients $1/Re$ or $(1/Re)^2$ and were dropped as asymptotically small. There are many things to notice about this simplified set of equations.

1. The continuity equation is unaffected by Reynolds number considerations.
2. The term $\partial^2 u/\partial x^2$ in the x-momentum equation has been neglected, and the buoyant term is also small if the Froude number is large (large U, small L), since $\beta(T_w - T_0)$ can only be of order unity at best (see Fig. 1-27). Therefore, except for small velocities and large sizes, free convection is negligible in the boundary-layer approximation.
3. The pressure gradient in the y direction is nearly zero, being affected only by a buoyant or stratification term that does not contribute to accelerations in the y direction. To all intents, then, in a boundary layer, the transverse pressure gradient in negligible.

$$\frac{\partial p}{\partial y} \approx 0 \qquad p = p(x) \text{ only} \qquad\qquad (4\text{-}33)$$

This splendid observation is due to Prandtl (1904), showing that pressure is a *known* variable in boundary-layer analysis, with $p(x)$ assumed to be *impressed* upon the boundary layer from without by an inviscid outer flow analysis. That is, the freestream outside the boundary layer, $U = U(x)$, where x is the coordinate parallel to the wall, is related to $p(x)$ by Bernoulli's theorem for incompressible flow. For steady flow, for example,

$$\frac{dp}{dx} = -\rho U\frac{dU}{dx} \qquad\qquad (4\text{-}34)$$

so that specifying $p(x)$ is equivalent to specifying $U(x)$ outside the boundary layer.

4. The energy equation shows that $\partial^2 T/\partial x^2$ is negligible and that only the $\partial u/\partial y$ portion of the dissipation is important. Further, it is clear that dissipation is entirely negligible if the Eckert number is small (small velocity and large temperature differences).

5. A very interesting observation is that the Reynolds number does not even appear in Eqs. (4-32). In this coordinate system, all thicknesses have been scaled to unit size, which is the only role of the Reynolds number in laminar flows.[†]

6. Perhaps most interesting, we note that all second derivatives with respect to x have been lost in the boundary-layer approximation. This has two consequences: (1) the equations are now *parabolic* instead of elliptic, so that x is now a marching variable and computer solutions are relatively easier than in Sec. 3-10; and (2) we have lost certain boundary conditions, notably those on v and x. The variable v has only one derivative left, $\partial v/\partial y$, with $\partial v/\partial x$ and the two second derivatives having been discarded. We now need only one condition on v at one y position. The obvious condition to retain is no slip: $v = 0$ at $y = 0$. We need not specify v at the outer edge of the layer. We have lost one condition each on u and T by discarding $\partial^2 u/\partial x^2$ and $\partial^2 T/\partial x^2$; therefore we disavow all knowledge of u and T at one x position, the best choice being the exit plane. The solutions will yield the correct values of u and T at the exit without our specifying them.

To sum up, the boundary-layer equations are far simpler than their parents, the Navier–Stokes equations. We can rewrite Eqs. (4-32) in the more common dimensional form for two-dimensional incompressible flow with constant properties

$$\frac{\partial u}{\partial x} + \frac{\partial v}{\partial y} = 0 \tag{4-35a}$$

$$\frac{\partial u}{\partial t} + u\frac{\partial u}{\partial x} + v\frac{\partial u}{\partial y} \approx \left(\frac{\partial U}{\partial t} + U\frac{\partial U}{\partial x}\right) + g_x\beta(T - T_0) + \nu\frac{\partial^2 u}{\partial y^2} \tag{4-35b}$$

$$\rho c_p\left(\frac{\partial T}{\partial t} + u\frac{\partial T}{\partial x} + v\frac{\partial T}{\partial y}\right) \approx k\frac{\partial^2 T}{\partial y^2} + \mu\left(\frac{\partial u}{\partial y}\right)^2 \tag{4-35c}$$

where $U = U(x, t)$, assumed known, denotes the freestream velocity just outside the boundary layer. The boundary conditions are

No slip: $u(x, 0, t) = v(x, 0, t) = 0$ $T(x, 0, t) = T_w(x, t)$

Inlet condition: $u(x_0, y, t)$, $v(x_0, y, t)$, and $T(x_0, y, t)$ known

Patching to the outer layer: $u(x, \infty, t) \rightarrow U(x, t)$ $\tag{4-36}$

$$T(x, \infty, t) \rightarrow T_e(x, t)$$

Initial condition: $u(x, y, 0)$, $v(x, y, 0)$, and $T(x, y, 0)$ known

---

[†] In turbulent flows (Sec. 6-4), the Reynolds number remains as a parameter because the turbulent inertia terms cannot be scaled by the square root of Re.

These equations, developed by Prandtl (1904), approximate the flow of a viscous fluid at high Reynolds numbers. They may be solved, at least numerically, for any practical distribution of stream velocity and temperature and of wall temperature. Some important solutions will be detailed here—for additional laminar boundary layers, see the text by Rosenhead (1963).

The limitations of the boundary-layer equations are

1. The Reynolds number must be large.
2. If the outer flow is decelerating ($dU/dx < 0$, $dp/dx > 0$), a point may be reached where wall shear approaches zero, the *separation point*. Beyond this point, the boundary-layer approximations are not accurate.
3. At some large $Re_x = \mathcal{O}(10^6)$, the laminar solutions become unstable and transition to turbulence occurs. The thin-layer approximations still hold then for the *turbulent* boundary layer.

The problem of separated flow is still frustrating because boundary-layer approximations fail. However, some newer techniques, to be discussed, have made headway on separated-flow analysis.

Here we present only two-dimensional incompressible-boundary-layer relations. They may be readily extended to three-dimensional and to compressible-flow conditions.

4-2.1   Orthogonal Curvilinear Coordinates

At first glance, Eqs. (4-35) seem to be valid only for a Cartesian system (x, y). However, they are also valid for flow along the curved wall shown in Fig. 4-4, subject only to the requirement that the boundary-layer thickness δ be much smaller than the radius of curvature $\mathcal{R}$ of the wall. The exact boundary-layer equations in such a curvilinear coordinate system were given by Tollmien (1931). After suitable order-of-magnitude assumptions, we find that the chief difference between the curvilinear and the Cartesian equations lies in the pressure gradient normal to the wall, which is no longer negligibly small for a curved body:

$$\frac{\partial p}{\partial y} \approx \frac{\rho u^2}{\mathcal{R}} \tag{4-37}$$
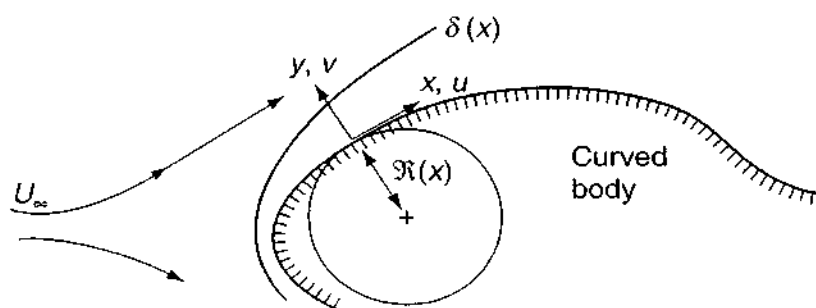

FIGURE 4-4
Boundary-layer flow over a curved body shape.

The gradient is of order unity. But if we integrate this from $y = 0$ to $y = \delta$, assuming, say, a linear distribution $u = Uy/\delta$, we obtain

$$p(\delta) - p(0) \approx \frac{\rho U^2 \delta}{3.\mathcal{R}}$$

or   (4-38)

$$\Delta p^* \approx \frac{\delta}{3\mathcal{R}}$$

which is negligibly small if $\delta \ll \mathcal{R}$. Therefore Eqs. (4-35) are valid for general curved-wall flows as long as the boundary-layer thickness is small compared to the wall radius of curvature. This would not be true at a sharp corner, but sharp corners invite immediate flow separation and are thus to be avoided.

4-2.2   General Remarks about Flow Separation

Before we attempt actual solutions, we can spot flow-separation effects from the boundary-layer equations themselves. If we apply the momentum equation at the wall, where $u = v = 0$, we find that

$$\left.\frac{\partial^2 u}{\partial y^2}\right|_{y=0} = \frac{1}{\mu}\frac{dp}{dx}$$ (4-39)

Thus the wall curvature has the sign of the pressure gradient, whereas further out the profile must have *negative* curvature when it merges with the freestream. Profile curvature is an indicator of possible boundary-layer *separation*. Three examples are shown in Fig. 4-5a. For negative (favorable) pressure gradient, the curvature is negative throughout, and no flow separation can occur. For zero gradient, e.g., flat-plate flow, the curvature is zero at the wall and negative further out; there is no separation. For positive (adverse) gradient, the curvature changes sign and the profile is
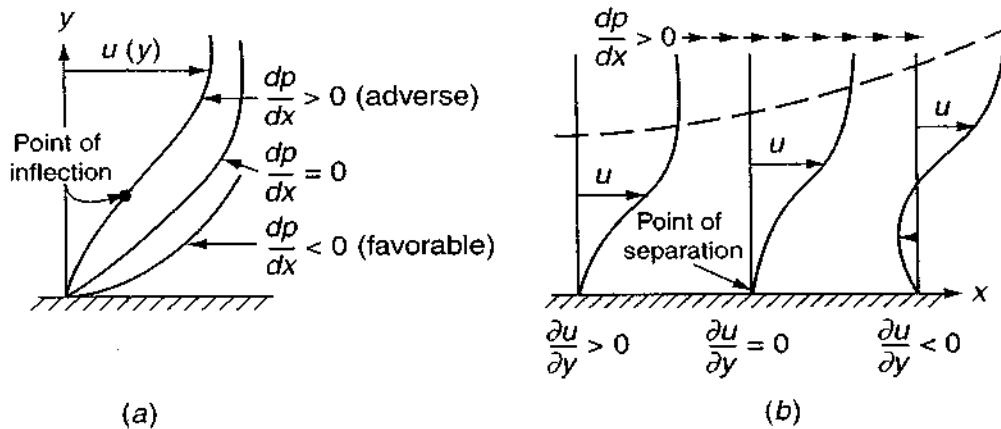

(a)   (b)

FIGURE 4-5
Geometric effects due to pressure gradient: (a) types of profile; (b) persistent adverse gradient.

S-shaped. The increasing downstream pressure slows down the wall flow and can make it go backward—flow separation.

Figure 4-5b illustrates the separation process. A persistent adverse gradient $(dp/dx > 0)$ makes the profile more and more S-shaped, reducing the wall shear to zero (the separation point) and then causing backflow, while the boundary layer becomes much thicker. Laminar flows have poor resistance to adverse gradients and separate easily. Turbulent boundary layers can resist separation longer—at the expense of increased wall friction and heat transfer.

4-2.3 Shear Stress in a Boundary Layer

After the boundary-layer equations have been solved, a major interest is shear stress, which in two-dimensional flow would be given by

$$\tau = \mu\left(\frac{\partial u}{\partial y} + \frac{\partial v}{\partial x}\right)$$

But the order-of-magnitude analysis shows that the term $\partial v/\partial x$ is two orders smaller than $\partial u/\partial y$. Hence it is quite proper in boundary-layer theory to calculate the shear stress from the approximation

$$\tau \approx \mu\frac{\partial u}{\partial y} \qquad \tau_w \approx \mu\left(\frac{\partial u}{\partial y}\right)_{y=0} \tag{4-40}$$

The friction drag would of course be the integrated value of this local shear stress. The relation also shows that the approximate point of separation in Fig. 4-5b is the point of zero shear stress, i.e., the point where τ_w passes from positive to negative.

4-3 SIMILARITY SOLUTIONS FOR STEADY TWO-DIMENSIONAL FLOW

If we neglect buoyancy in Eqs. (4-35), the velocity is uncoupled from the temperature, and we can confine our attention temporarily to the momentum and continuity equations for steady flow:

$$\frac{\partial u}{\partial x} + \frac{\partial v}{\partial y} = 0 \tag{4-41a}$$

$$u\frac{\partial u}{\partial x} + v\frac{\partial u}{\partial y} = U\frac{dU}{dx} + \nu\frac{\partial^2 u}{\partial y^2} \tag{4-41b}$$

subject to $\qquad u(x, 0) = v(x, 0) = 0 \qquad u(x, \infty) = U(x)$

This is a system of partial differential equations of the parabolic type which can be solved with finite-difference techniques by marching downstream in the x direction. However, before trying that idea in Sec. 4-5, we study here the possibility of reducing these equations to *ordinary* differential equations by similarity transformation. Similarity solutions for the full Navier–Stokes equations were discussed in Sec. 3-8, and one of those successes, stagnation flow, is also a solution of the boundary-layer

equations, as we shall see. Whole books are devoted to similarity techniques, e.g., Hansen (1964) and Sachdev (2000). We shall discuss here three similar boundary layers: the flat plate, the Falkner–Skan wedge flows, and the converging channel (sink flow). In each case the two-dimensional partial differential equations of continuity and momentum can be reduced to a single ordinary differential equation.

4-3.1 The Blasius Solution for Flat-Plate Flow

Ludwig Prandtl's first student, H. Blasius (1908), found a celebrated solution for laminar-boundary-layer flow past a flat plate, as in Fig. 4-1. If the displacement thickness is small ($Re \gg 1$), then $U = $ const and $dU/dx = 0$ in Eq. (4-41). There is a leading edge, $(x, y) = (0, 0)$, but no characteristic length "L." Therefore the local velocity profiles must all have the same dimensionless shape, $u/U = fcn(y/\delta)$. Since, from our integral analysis, Eq. (4-14), $\delta = \text{const}(\nu x/U)^{1/2}$, the appropriate dimensionless *similarity* variable should be

$$\eta = y\sqrt{\frac{U}{2\nu x}} \tag{4-42}$$

The factor "2" is not necessary—Blasius himself did not use it—but it will avoid another factor "2" in the final differential equation.

The stream function of the flow, $\psi = \int u\, dy\,|_{x=\text{const}}$, should increase as δ, or $x^{1/2}$, and has the following nondimensional form:

$$\psi = \sqrt{2\nu U x}\, f(\eta) \tag{4-43}$$

where f is a function to be determined. Note another factor "2" introduced for convenience. From the definition of stream function,

$$u = \frac{\partial \psi}{\partial y} = U f'(\eta)$$

$$v = -\frac{\partial \psi}{\partial x} = \sqrt{\frac{\nu U}{2x}}\,(\eta f' - f) \tag{4-44}$$

where the prime denotes differentiation with respect to η. We see that, as expected, u is of order U while v is of smaller order, $U/\sqrt{Re_x}$.

Substitution of u and v from Eqs. (4-44) into the boundary-layer momentum relation (4-41) yields, after considerable manipulation useful as a student exercise, the following differential equation

$$f''' + ff'' = 0 \tag{4-45}$$

Referring to Eqs. (4-44), the no-slip conditions $u(x, 0) = v(x, 0) = 0$, and the freestream-merge condition, $u(x, \infty) = U$, convert to

$$f'(0) = f(0) = 0 \qquad f'(\infty) = 1 \tag{4-46}$$

Equation (4-45) is the celebrated non-linear *Blasius equation* for flat-plate flow. Note its similar appearance to the stagnation-flow relation, Eq. (3-151), whose extra terms are due to the (favorable) pressure gradient.

The Blasius equation has never yielded to exact analytic solution. Blasius himself (1908) gave matching inner and outer series solutions. Many other methods of attack are chronicled in the text by Rosenhead (1963). One method led to a general boundary-layer technique, now outdated, outlined in the text by Meksyn (1961). With the advent of the personal computer, it is now a simple matter to program Eqs. (4-45) and (4-46) using Subroutine RUNGE from App. C. Let $f'' = Y_1$, $f' = Y_2$, and $f = Y_3$. Then the proper FORTRAN relations are

$$F(1) = -Y(1) * Y(3)$$

$$F(2) = Y(1) \tag{4-47}$$

$$F(3) = Y(2)$$

The problem is to find the correct value $f''(0) = Y_1$ ($\eta = 0$) which will make $f' = Y_2$ approach 1.0 as η approaches infinity. By a simple asymptotic analysis, we find that "infinity" is approximately $\eta = 10$, and we can run off a few solutions for various values of $f''(0)$, all of which behave beautifully. From these guesses, we can interpolate to find the value $f''(0)$ which makes $f'(\infty) \approx Y_2(10.0) \approx 1.0$. The accepted value, correct to six significant figures, is

$$f''(0) = 0.469600 \ldots \tag{4-48}$$

The complete numerical solution for the Blasius equation is given in Table 4-1. From this we can find all the flow parameters of interest to flat-plate flow.

Figure 4-6a shows a plot of the Blasius functions f, f', and f'', and Fig. 4-6b compares the profile $f' = u/U$ with the experiments of Liepmann (1943). The agreement is excellent, and we may regard this first test of the boundary-layer approximation as a success.

Other properties follow from the table. We note that $f' = 0.99$ at $\eta \approx 3.5$. Thus we have a value of the 99 percent boundary-layer thickness

$$\delta_{99\%} \approx 3.5\sqrt{\frac{2\nu x}{U}}$$

or $\tag{4-49}$

$$\frac{\delta_{99\%}}{x} \approx \frac{5.0}{\sqrt{Re_x}}$$

The momentum and displacement thickness are related to integrals of f' through their definitions from Eqs. (4-4) and (4-6):

$$\delta^*\sqrt{\frac{U}{2\nu x}} = \int_0^\infty (1 - f')\, d\eta = \lim_{\eta \to \infty} (\eta - f) = 1.21678$$

or $\tag{4-50}$

$$\frac{\delta^*}{x} = \frac{1.7208}{\sqrt{Re_x}}$$

TABLE 4-1
Numerical solution of the Blasius flat-plate relation, Eq. (4-45)

η	$f(\eta)$	$f'(\eta)$	$f''(\eta)$
0.0	0.0	0.0	0.46960
0.1	0.00235	0.04696	0.46956
0.2	0.00939	0.09391	0.46931
0.3	0.02113	0.14081	0.46861
0.4	0.03755	0.18761	0.46725
0.5	0.05864	0.23423	0.46503
0.6	0.08439	0.28058	0.46173
0.7	0.11474	0.32653	0.45718
0.8	0.14967	0.37196	0.45119
0.9	0.18911	0.41672	0.44363
1.0	0.23299	0.46063	0.43438
1.1	0.28121	0.50354	0.42337
1.2	0.33366	0.54525	0.41057
1.3	0.39021	0.58559	0.39598
1.4	0.45072	0.62439	0.37969
1.5	0.51503	0.66147	0.36180
1.6	0.58296	0.69670	0.34249
1.7	0.65430	0.72993	0.32195
1.8	0.72887	0.76106	0.30045
1.9	0.80644	0.79000	0.27825
2.0	0.88680	0.81669	0.25567
2.2	1.05495	0.86330	0.21058
2.4	1.23153	0.90107	0.16756
2.6	1.41482	0.93060	0.12861
2.8	1.60328	0.95288	0.09511
3.0	1.79557	0.96905	0.06771
3.2	1.99058	0.98037	0.04637
3.4	2.18747	0.98797	0.03054
3.6	2.38559	0.99289	0.01933
3.8	2.58450	0.99594	0.01176
4.0	2.78388	0.99777	0.00687
4.2	2.98355	0.99882	0.00386
4.4	3.18338	0.99940	0.00208
4.6	3.38329	0.99970	0.00108
4.8	3.58325	0.99986	0.00054
5.0	3.78323	0.99994	0.00026
5.2	3.98322	0.999971	0.000119
5.4	4.18322	0.999988	0.000052
5.6	4.38322	0.999995	0.000022
5.8	4.58322	0.999998	0.000009
6.0	4.78322	0.999999	0.000003

$$\eta = y \sqrt{\frac{U}{2vx}}$$

(a)

$$\sqrt{2}\,\eta = y \sqrt{\frac{U}{vx}}$$

(b)
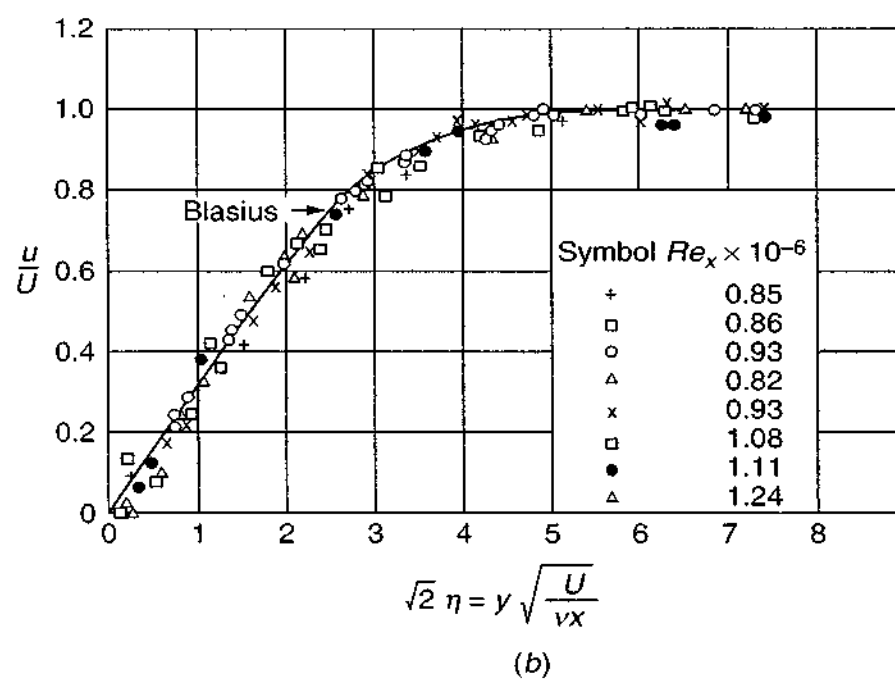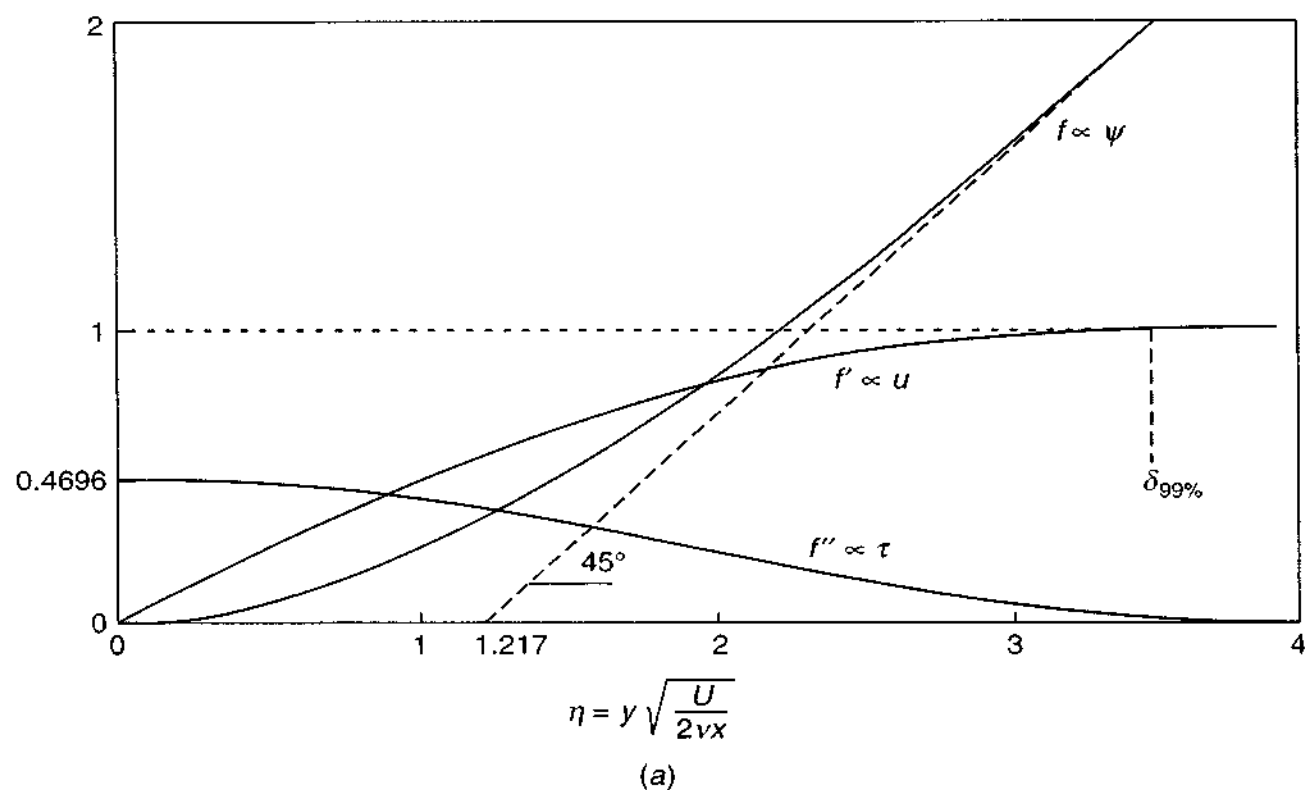
FIGURE 4-6

The Blasius solution for the flat-plate boundary layer: (a) numerical solution of Eq. (4-45); (b) comparison of $f' = u/U$ with experiments by Liepmann (1943).

The numerical value 1.21678 is shown in Fig. 4-6a to be the η intercept of a 45° line which is asymptotic to the curve $f(\eta)$ at large η. Since f is proportional to the stream function, the dashed 45° line represents an inviscid stream function displaced a dimensionless amount 1.21678 away from the plate. Similarly, we calculate

$$\theta\sqrt{\frac{U}{2\nu x}} = \int_0^\infty f'(1 - f')\,d\eta = f''(0) = 0.4696$$

or   (4-51)

$$\frac{\theta}{x} = \frac{0.664}{\sqrt{Re_x}}$$

We can also calculate the wall shear stress

$$\tau_w = \mu\left.\frac{\partial u}{\partial y}\right|_w = \frac{\mu U f''(0)}{\sqrt{2\nu x/U}}$$

or   (4-52)

$$C_f = \frac{2\tau_w}{\rho U^2} = \frac{0.664}{\sqrt{Re_x}} = \frac{\theta}{x}$$

Finally, the integrated drag coefficient on a plate of length L is

$$C_D(L) = \frac{1}{L}\int_0^L C_f\,dx = 2C_f(L) = \frac{1.328}{\sqrt{Re_L}} \qquad (4\text{-}53)$$

This is the drag on one side of the plate. Experimental values of the drag coefficient of a plate in the range $1 \le Re_L \le 2000$ are shown in Fig. 4-7 and compared with
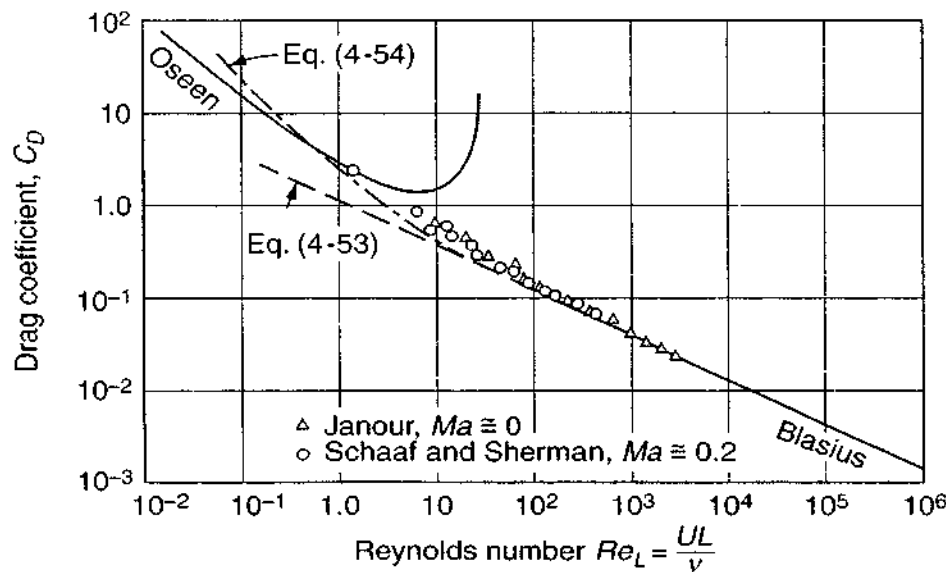

FIGURE 4-7
Theoretical and experimental drag of a flat plate.

Eq. (4-53) and also with the Oseen relation discussed in Chap. 3, Eq. (3-226). We see that the Blasius relation is accurate for $Re_L \geq 1000$, and the Oseen theory is valid for $Re_L \leq 1$.

The intermediate region $1 < Re_L < 1000$ has been the subject of many analytical and numerical studies. It may be fit reasonably well by the correction factor given in a perturbation theory by Imai (1957):

$$C_D \approx \frac{1.328}{\sqrt{Re_L}} + \frac{2.3}{Re_L} \tag{4-54}$$

This relation is also plotted in Fig. 4-7 and can be seen to fall slightly lower than the data.

Numerical solutions of the full Navier–Stokes equations for $0.1 < Re_L < 1000$ by Dennis and Dunwoody (1966) and by Brauer and Sucker (1976) verify that the drag is higher than predicted by boundary-layer theory. Figure 4-8 shows the computations of Dennis and Dunwoody (1966) for (*a*) the local friction coefficient and (*b*) the local surface pressure. For lower Reynolds numbers, there are marked effects at both the leading and trailing edges, and the boundary-layer approximation is not realized until $Re_L \geq 1000$.

It is interesting that the normal velocity v is not zero at the edge of the boundary layer. From Eq. (4-44), we compute, as $\eta \rightarrow \infty$,

$$v(x, \infty) = \frac{0.8604U}{\sqrt{Re_x}} \tag{4-55}$$

There is a slight upwelling of the flow because of displacement of the outer stream. Panton (1996, Sec. 20.7) contains a good discussion of this effect. In favorable gradients, there can be downwelling toward the wall.

4-3.2 Flat-Plate Heat Transfer for Constant Wall Temperature

If T_w and T_e are constant, the temperature profiles also satisfy similarity relations. By analogy with the stagnation-flow relation, Eq. (3-167), we define a dimensionless temperature difference

$$\Theta(\eta) = \frac{T - T_e}{T_w - T_e} \tag{4-56}$$

Assuming that u and v are known from the Blasius solution, we substitute Eq. (4-56) into the boundary-layer energy Eq. (4-35c), *neglecting dissipation*, that is, $Ec \ll 1$. The result is

$$\Theta'' + Pr f(\eta)\Theta' = 0 \tag{4-57}$$

subject to
$$\Theta(0) = 1 \qquad \Theta(\infty) = 0$$
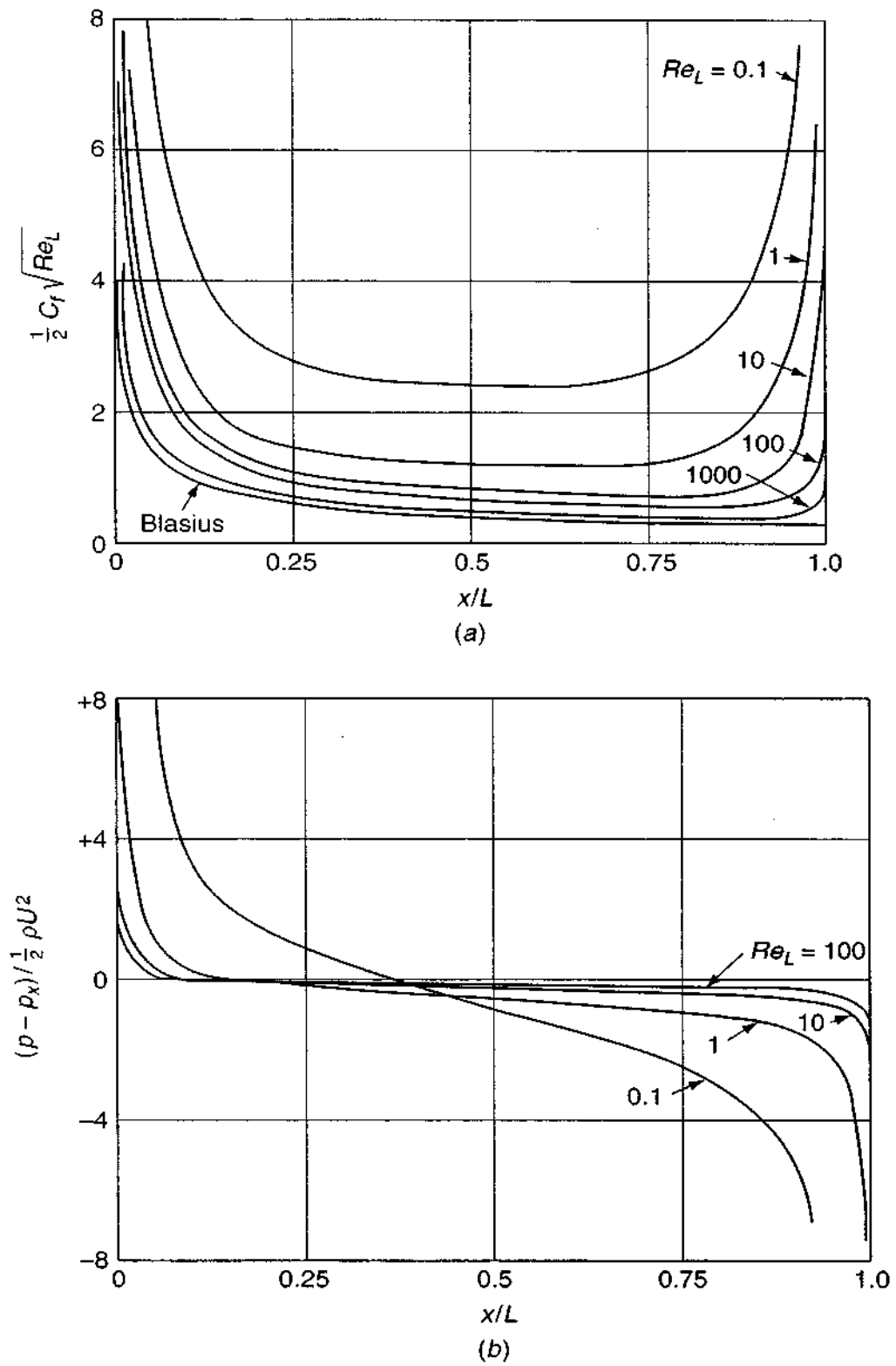
FIGURE 4-8

Numerical solution of the full Navier–Stokes equations for flat-plate flow at moderate Reynolds numbers: (a) local friction coefficient; (b) local surface pressure. [*After Dennis and Dunwoody* (*1966*).]

FIGURE 4-9
Flat-plate temperature profiles for zero dissipation.

This is identical to the stagnation-flow relation Eq. (3-168) with the boundary conditions reversed. The solution is, by analogy,

$$\Theta = \frac{\int_\eta^\infty d\eta \, \exp\left(-Pr \int_0^\eta f \, ds\right)}{\int_0^\infty d\eta \, \exp\left(-Pr \int_0^\eta f \, ds\right)} \tag{4-58}$$
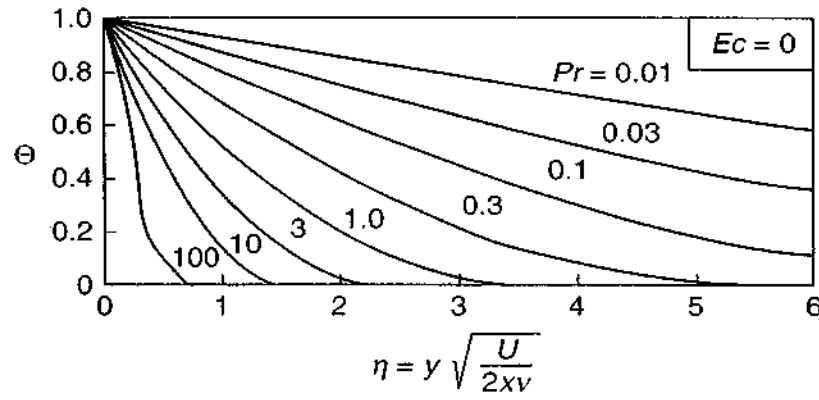
This result was given by Pohlhausen (1921). The temperature profiles computed from Eq. (4-58) are shown in Fig. 4-9 for various Prandtl numbers. Since Pr is a ratio of viscous to conduction effects, the higher the Prandtl number, the thinner the thermal boundary layer. The thickness ratio may be approximated by

$$\frac{\delta_T}{\delta} \approx Pr^{-0.4} \tag{4-59}$$

The wall heat transfer may be computed from Fourier's law:

$$q_w = -k \left.\frac{\partial T}{\partial y}\right|_{y=0} = -k(T_w - T_e)\Theta'(0)\sqrt{\frac{U}{2\nu x}}$$

or, in dimensionless form,

$$Nu_x = \frac{-\Theta'(0)}{\sqrt{2}} Re_x^{1/2} \tag{4-60}$$

As seen in Fig. 4-9, the wall temperature slope $\Theta'(0)$ is a function of the Prandtl number and from Eq. (4-56) is given by

$$-\frac{1}{\Theta'(0)} = \int_0^\infty d\eta \, \exp\left(-Pr \int_0^\eta f \, ds\right) \tag{4-61}$$

By exact analogy with the stagnation-flow relation Eq. (3-172), this parameter may be evaluated by adding two FORTRAN statements to our Blasius analysis, Eq. (4-45):

$$F(4) = Y(3)$$

$$F(5) = EXP(-PR * Y(4))$$

The output $1/Y_5(\infty)$ is the desired wall slope $|\Theta'(0)|$. Some values of this slope may be tabulated as follows:

Pr	$-\Theta'(0)/\sqrt{2}$	Pr	$-\Theta'(0)/\sqrt{2}$
0.001	0.0173	10	0.7281
0.01	0.0516	100	1.572
0.1	0.1400	1000	3.387
1.0	0.3321	10,000	7.297

For Prandtl numbers, in the range $0.1 < Pr < 10{,}000$, a good curve fit to these tabulated values is $-\Theta'(0)/\sqrt{2} \approx 0.332 Pr^{1/3}$. Therefore Eq. (4-60) for low-speed laminar flat-plate heat transfer may be written as the familiar approximate relation

$$Nu_x \approx 0.332\, Re_x^{1/2} Pr^{1/3} \tag{4-62}$$

This has the same form as our energy-integral result, Eq. (4-27). It is the accepted engineering approximation but predicts too high for liquid metals, $Pr < 0.1$.

The solution of the flat-plate energy equation when dissipation is *not* neglected is very interesting and leads to the concept of the recovery factor and the adiabatic-wall temperature. However, these concepts are realized in practice only by high-speed (compressible) boundary layers. Therefore discussion will be postponed until Chap. 7.

4-3.3 The Falkner–Skan Wedge Flows

The most famous family of boundary-layer similarity solutions was discovered by Falkner and Skan (1931) and later calculated numerically by Hartree (1937). Rather than merely "anticipating" the solution as we did with the Blasius problem, let us outline a search for similarity.

To begin with, we can eliminate v from the momentum equation by using the no-slip condition to solve continuity for v

$$v = -\frac{\partial}{\partial x}\int_0^y u\, dy \tag{4-63}$$

the integration being carried out at constant x. The problem now reduces to a single integrodifferential equation for u alone:

$$u\frac{\partial u}{\partial x} - \frac{\partial u}{\partial y}\left(\frac{\partial}{\partial x}\int_0^y u\, dy\right) = U\frac{dU}{dx} + \nu\frac{\partial^2 u}{\partial y^2} \tag{4-64}$$

We now inquire: Is there any possibility of combining x and y into a single variable $\eta(x, y)$ such that the above equation becomes an ordinary differential equation in a function of η only? If so, we have achieved similarity, but only for certain special cases of the freestream velocity distribution $U(x)$.

Let us generalize the Blasius solution to variable freestream velocity:

$$u(x, y) = U(x)f'(\eta) \tag{4-65}$$

where $\eta = \eta(x, y)$ is dimensionless but is *not* the Blasius variable from Eq. (4-42). With careful chain-rule differentiation, we can substitute this in the momentum Eq. (4-64). For example, if $u = Uf'$, then

$$\frac{\partial u}{\partial x} = U'f' + Uf''\frac{\partial \eta}{\partial x}$$

$$\frac{\partial u}{\partial y} = Uf''\frac{\partial \eta}{\partial y}$$

$$(4-66)$$

and likewise for the second derivatives. An especially appealing form is linear in y, so that $(\partial^2 \eta / \partial y^2)$ vanishes:

$$\eta = yg(x) \tag{4-67}$$

Substitute Eq. (4-67) into the momentum relation, Eq. (4-64), evaluating the integral by Leibnitz' rule, using integration by parts. The result may be rearranged as follows:

$$f''' = ff''\left(\frac{Ug'}{\nu g^3}\right) + (f'^2 - ff'' - 1)\left(\frac{dU/dx}{\nu g^2}\right) \tag{4-68}$$

Similarity is achieved if each of the two coefficients in this relation is such that all x's disappear, leaving only constants. For Eq. (4-68), this implies that $\ln(U)$ is proportional to $\ln(g)$.

Falkner and Skan (1931) found that similarity was achieved by the variable $\eta = Cyx^a$, which is consistent with a power-law freestream velocity distribution:

$$U(x) = Kx^m \qquad m = 2a + 1 \tag{4-69}$$

The exponent m may be termed the Falkner–Skan *power-law parameter*. The constant C must make η dimensionless but is otherwise arbitrary. The best choice is $C^2 = K(1 + m)/2\nu$, which is consistent with its limiting case for $m = 0$, the Blasius variable from Eq. (4-42). Thus we choose

$$\eta = y\sqrt{\frac{m + 1}{2}\frac{U(x)}{\nu x}} \tag{4-70}$$

Substituting this particular C into g_2 and g_3 in Eq. (4-67) gives the most common form of the Falkner–Skan equation for similar flows:

$$f''' + ff'' + \beta(1 - f'^2) = 0$$

$$(4-71)$$

where

$$\beta = \frac{2m}{1 + m}$$

The boundary conditions are exactly the same as for the flat plate:

$$f(0) = f'(0) = 0 \qquad f'(\infty) = 1 \tag{4-72}$$

The parameter β is a measure of the pressure gradient dp/dx. If β is positive, the pressure gradient is negative or favorable, and negative β denotes an unfavorable positive pressure gradient. Naturally, $\beta = 0$ denotes the flat plate. A priori, we

expect the case $m = -1$ ($\beta = \pm\infty$) to be a trouble spot, but it is not: This case (U inversely proportional to x) is handled by a different choice of the constant C.

4-3.3.1 INVISCID FLOW PAST WEDGES AND CORNERS. The Falkner–Skan solution illustrates both favorable and adverse pressure gradients and is a realistic engineering flow pattern. The power-law freestream, $U = Kx^m$, is the exact solution to inviscid flow past a wedge or corner shape. In plane polar coordinates, Laplace's equation for the stream function $\psi(r, \theta)$ is

$$\frac{1}{r}\frac{\partial}{\partial r}\left(r\frac{\partial\psi}{\partial r}\right) + \frac{1}{r^2}\frac{\partial^2\psi}{\partial\theta^2} = 0$$

As shown in texts covering potential flow, e.g., White (2003), p. 546, an exact solution is

$$\psi(r, \theta) = const\ r^{m+1}\sin[(m + 1)\theta] \tag{4-73}$$

This formula has certain radial streamlines that can be interpreted as the "walls" of a wedge or a corner, as in Fig. 4-10, depending upon the value of $\beta = 2m/(m + 1)$. The velocity along these walls has the form $U = Kx^m$ and represents the freestream driving the boundary layer on the wall, with $x = 0$ at the tip of the wedge. We may list the following cases:

$-2 \le \beta \le 0, -\frac{1}{2} \le m \le 0$: flow around an expansion corner of turning angle $\beta\pi/2$

$\quad\beta = 0, m = 0$: the flat plate

$\quad 0 \le \beta \le +2, 0 \le m \le \infty$: flow against a wedge of half-angle $\beta\pi/2$

$\quad\beta = 1, m = 1$: the plane stagnation point (180° wedge)

$\quad\beta = +4, m = -2$: doublet flow near a plane wall

$\quad\beta = +5, m = -\frac{5}{3}$: doublet flow near a 90° corner

$\quad\beta = +\infty, m = -1$: flow toward a point sink [the boundary-layer version of the Jeffery–Hamel flow in a convergent wedge (Sec. 3-8)]

These are *similar* flows, i.e., for a given β the velocity profiles all look alike when scaled by $U(x)$ and $\delta(x)$. They may also be used, with modest success, to predict the behavior of nonsimilar flows.
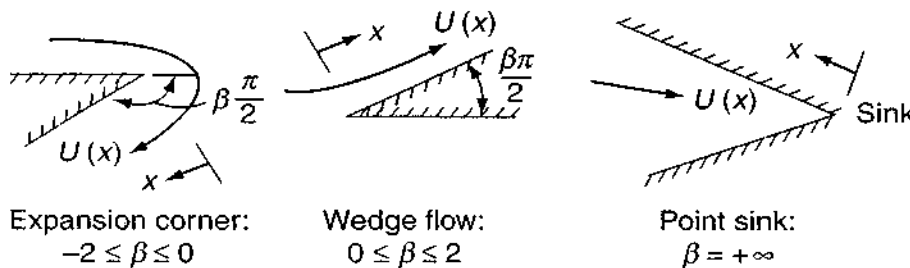

FIGURE 4-10
Some examples of Falkner–Skan potential flows.

Equation (4-71) obviously yields to a digital-computer solution simply by adding the term $\beta(1 - f'^2)$ to the FORTRAN relations of Eq. (4-47) for the Blasius equation:

$$F(1) = -Y(1) * Y(3) - BETA * (1. - Y(2) * Y(2))$$

$$F(2) = Y(1) \tag{4-74}$$

$$F(3) = Y(2)$$

As before, we select β and try to find the proper value of f_0'' that makes $f'(\infty)$ asymptotically approach unity.

Although we could easily attack Eq. (4-71) with our personal computers, in fact, the Falkner–Skan solutions have been well tabulated and charted. Extensive results are given in the text by Evans (1968). The most important results are plotted in Fig. 4-11, spanning the range from the stagnation point ($\beta = m = 1$) down through flat-plate flow ($\beta = m = 0$) to the separation point ($\beta = -0.19884$, $m = -0.09043$). Figure 4-11a shows the velocity profiles $u/U = f'$, which grow thicker as β decreases and, for $\beta < 0$, become S-shaped as in Fig. 4-5b and separate ($\tau_w = 0$) for $\beta = -0.19884$. Separation corresponds to an expansion angle in Fig. 4-10 of only 18°.

Figure 4-11b shows the shear-stress profiles $f''(\eta)$. Note that shear, in accelerated (favorable) flows, falls away from the wall value but instead rises from the wall in decelerated (adverse) flows. This is a consequence of the momentum-equation condition $\partial \tau / \partial y |_{wall}\, dp/dx$ and is true also in turbulent boundary layers. Note in passing that the solution for $\beta = \frac{1}{2}$, $m = \frac{1}{3}$ corresponds to the axisymmetric stagnation flow from Sec. 3-8.1.3.
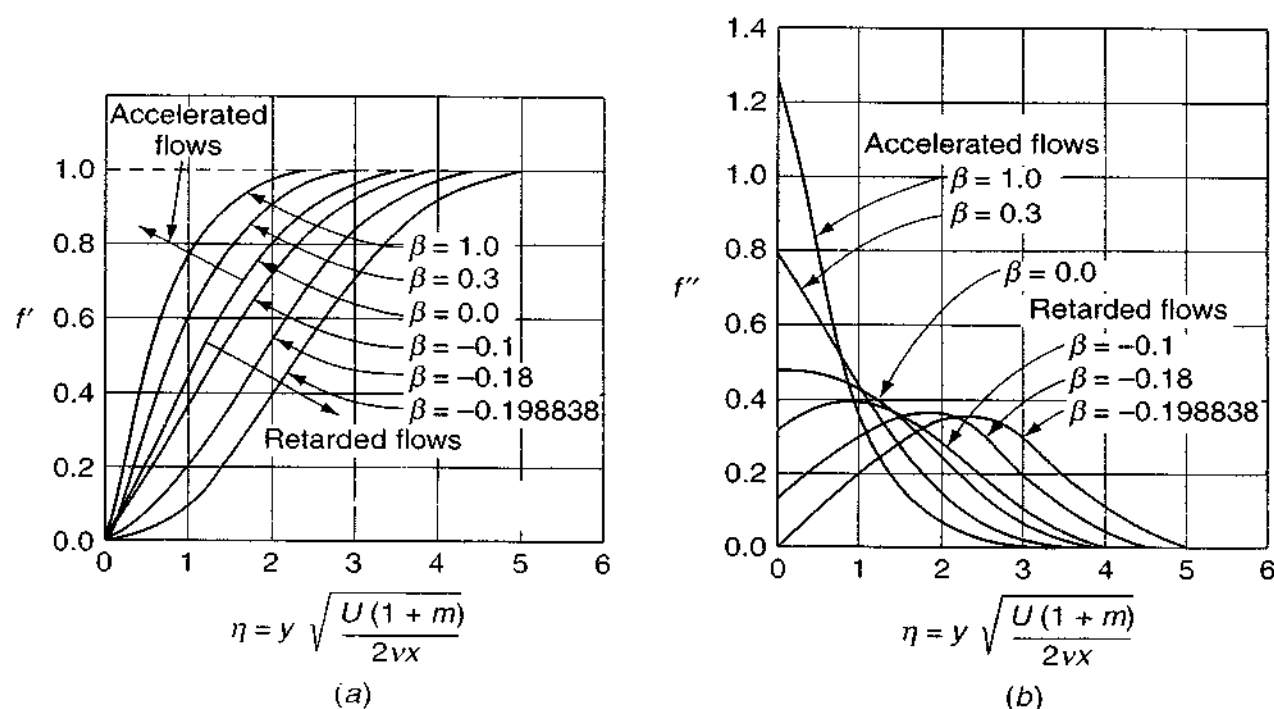

FIGURE 4-11
(a) Velocity profiles and (b) shear-stress profiles for the Falkner–Skan equation.

TABLE 4-2
Numerical values of the streamwise velocity $f'(\eta)$ for Falkner–Skan similarity flows

η	β f_0'' η^* θ^*	−0.19884 0.0 2.35885 0.58544	−0.18 0.12864 1.87157 0.56771	0.0 0.46960 1.21678 0.46960	0.3 0.77476 0.91099 0.38574	1.0 1.23259 0.64790 0.29235	2.0 1.68722 0.49743 0.23079	10.0 3.67523 0.24077 0.11523
0.0		0.0	0.0	0.0	0.0	0.0	0.0	0.0
0.1		0.00099	0.01376	0.04696	0.07597	0.11826	0.15876	0.31843
0.2		0.00398	0.02933	0.09391	0.14894	0.22661	0.29794	0.54730
0.3		0.00895	0.04668	0.14081	0.21886	0.32524	0.41854	0.70496
0.4		0.01591	0.06582	0.18761	0.28569	0.41446	0.52190	0.81043
0.5		0.02485	0.08673	0.23423	0.34938	0.49465	0.60964	0.87954
0.6		0.03578	0.10937	0.28058	0.40988	0.56628	0.68343	0.92414
0.7		0.04868	0.13373	0.32653	0.46713	0.62986	0.74496	0.95259
0.8		0.06355	0.15975	0.37196	0.52107	0.68594	0.79587	0.97057
0.9		0.08038	0.18737	0.41672	0.57167	0.73508	0.83767	0.98185
1.0		0.09913	0.21651	0.46063	0.61890	0.77787	0.87172	0.98888
1.2		0.14232	0.27899	0.54525	0.70322	0.84667	0.92142	0.99591
1.4		0.19274	0.34622	0.62439	0.77425	0.89681	0.95308	0.99856
1.6		0.24982	0.41691	0.69670	0.83254	0.93235	0.97269	0.99957
1.8		0.31271	0.48946	0.76106	0.87906	0.95683	0.98452	0.99998
2.0		0.38026	0.56205	0.81669	0.91509	0.97322	0.99146	0.99999
2.2		0.45097	0.63269	0.86330	0.94211	0.98385	0.99542	
2.4		0.52308	0.69942	0.90107	0.96173	0.99055	0.99761	
2.6		0.59460	0.76048	0.93060	0.97548	0.99463	0.99879	
2.8		0.66348	0.81449	0.95288	0.98480	0.99705	0.99940	
3.0		0.72776	0.86061	0.96905	0.99088	0.99842	0.99972	
3.2		0.78578	0.89853	0.98037	0.99471	0.99919	0.99987	
3.4		0.83635	0.92854	0.98797	0.99704	0.99959	0.99995	
3.6		0.87882	0.95138	0.99289	0.99840	0.99980	0.99998	
3.8		0.91315	0.96805	0.99594	0.99916	0.99991	0.99999	
4.0		0.93982	0.97975	0.99777	0.99958	0.99996		
4.5		0.97940	0.99449	0.99957	0.99994	0.99999		
5.0		0.99439	0.99997	0.99994	0.99999			

Table 4-2 lists the values of $u/U = f'(\eta)$ for a variety of solutions. Also tabulated are the proper initial conditions $f''(0)$, plus the dimensionless displacement and momentum thicknesses:

$$\eta^* = \int_0^\infty (1 - f')\, d\eta = (\eta - f)|_{\eta \to \infty}$$

$$\theta^* = \int_0^\infty f'(1 - f')\, d\eta = \frac{f_0'' - \beta \eta^*}{1 + \beta}$$

(4-75)

The ratio of these two, the shape factor H, will be especially useful in some approximate theories to be discussed.

In keeping with our constant reminders that the Navier–Stokes equations are nonunique, the boundary-layer equations also show multiple solutions. Stewartson (1954) pointed out the following pathology of the Falkner–Skan equation for negative β:

1. For $-0.19884 \le \beta \le 0$, there are (at least) two solutions of Eq. (4-71) for any given β, one of which is of the type shown in Fig. 4-11a and the second of which always shows a backflow at the wall. The two types of solution are identical at $\beta = -0.19884$ but are entirely different at $\beta = 0$.

2. For $\beta < -0.19884$, a multiple (probably an infinity) of solutions to Eq. (4-71) exists for any given value of the wall gradient f_0''. For example, Fig. 4-12b shows a family of separating profiles ($f_0'' = 0$) calculated by Libby and Liu (1967);
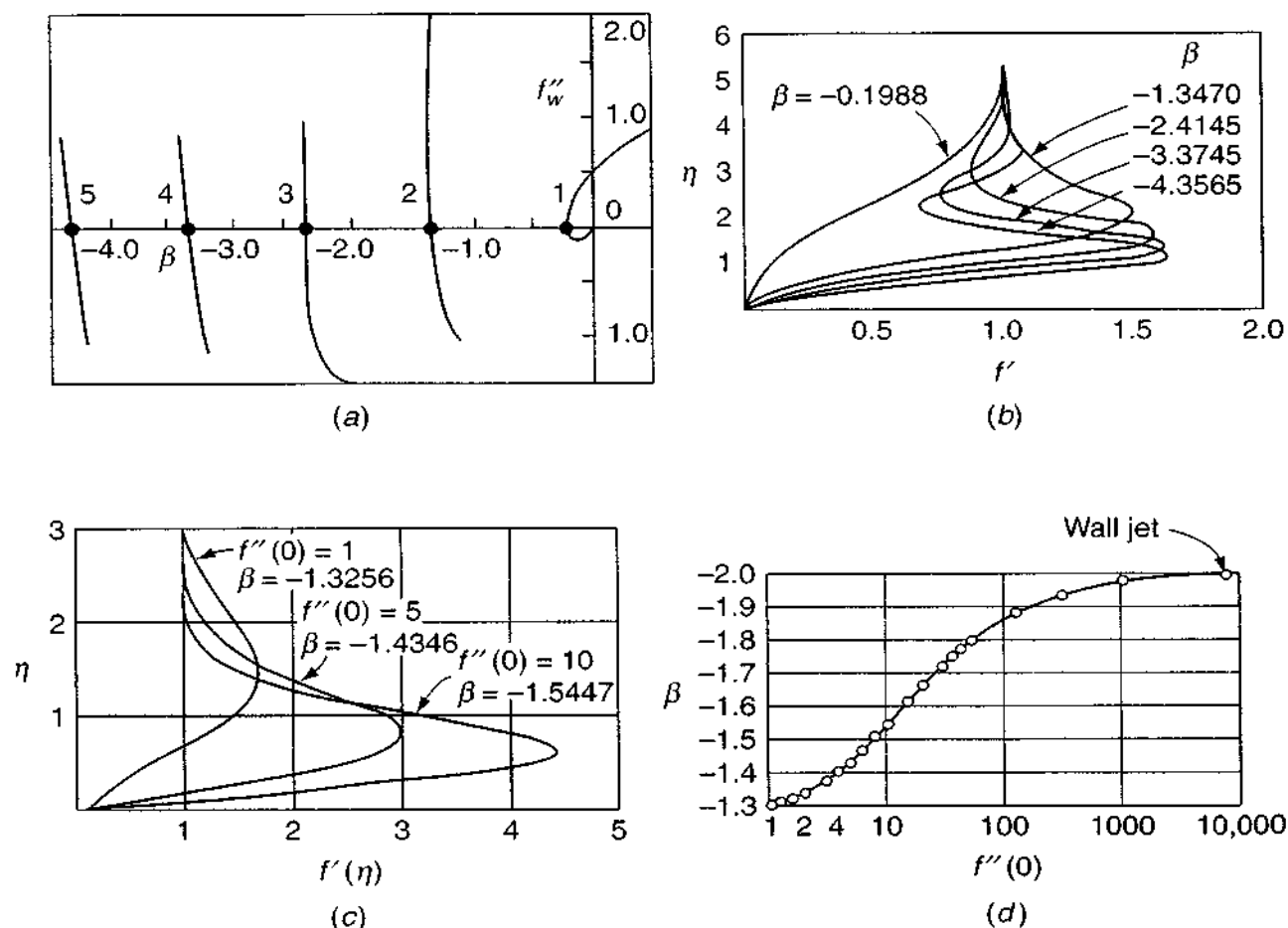

(a)

(b)

(c)

(d)

FIGURE 4-12

The multiplicity of Falkner–Skan solutions for negative β: (a) five branches of solutions for negative β, as found by Libby and Liu (1967); (b) five separating profiles corresponding to the five heavily marked intercepts in (a); (c) three overshoot profiles without backflow, calculated moving up along branch 2 [*After Steinheuer (1968)*]; (d) solution sets along upper branch 2 as calculated by Steinheuer (1968), showing asymptotic approach to the wall jet solution found by Glauert (1956).

presumably there are even more of this same family; for $\beta \approx -5.3, -6.3$, etc., Stewartson (1954) has proved that all solutions in this range of β must show velocity overshoot, that is, f' greater than 1.0, at some point in the boundary layer.

The gist of these remarks is shown in Fig. 4-12a, which gives a polar plot of β vs. f_0'' for the first five branches of solutions for negative β found by Libby and Liu (1967). Figure 4-12c shows some profiles for positive f_0'' along branch 2 as computed by Steinheuer (1968); these, like the separating profiles, show overshoot but no backflow. Libby and Liu (1967) liken these profiles to streamwise blowing into a moving stream—a wall jet. Indeed, as $f''(0)$ becomes very large along branch 2 of Fig. 4-12a, β approaches -2.0 and, as pointed out by Steinheuer (1968), the velocity profile becomes identical with the pure laminar-wall-jet solution found by Glauert (1956). This effect is shown in Figs. 4-12c and d.

4-3.4 Heat Transfer for the Falkner–Skan Flows

If we neglect dissipation and assume constant wall and stream temperature, the flat-plate analysis of Sec. 4-3.2 holds in exactly the same form:

$$\Theta'' + Prf(\eta, \beta)\Theta' = 0 \tag{4-76}$$

where $\Theta = (T - T_e)/(T_w - T_e)$ as before. Here $f(\eta, \beta)$ is the Falkner–Skan stream function—the output Y_3 from Eq. (4-74)—defined as

$$\psi(x, y) = f(\eta)\sqrt{\frac{2}{m + 1} \nu x U(x)} \tag{4-77}$$

Compare with Eq. (4-43). The solution is given by Eq. (4-58), and the local Nusselt number may be written in the form

$$Nu_x = \sqrt{\frac{m + 1}{2}} G(Pr, \beta)Re_x^{1/2} \qquad Re_x = \frac{xU(x)}{\nu} \tag{4-78}$$

where
$$\frac{1}{G(Pr, \beta)} = \int_0^\infty \exp\left(-Pr\int_0^\eta f\, ds\right) d\eta$$

A plot of $G(Pr, \beta)$ for various β is given in Fig. 4-13, and tabulated values are given in Table 4-3. For a given β, the variation with Pr is nearly a power law, as in Eq. (4-62). Three examples would be

$$\frac{Nu_x}{Re_x^{1/2}} \approx \begin{cases} 0.22\, Pr^{0.27} & \text{(separation, } \beta = -0.1988) \\ 0.332\, Pr^{1/3} & \text{(flat plate, } \beta = 0) \\ 0.57\, Pr^{0.4} & \text{(stagnation, } \beta = 1) \end{cases} \tag{4-79}$$

Note that separation flow, where skin friction is *zero*, supports considerable heat transfer. In fact, heat transfer in general (nonsimilar) separated-flow regions is substantial for both laminar and turbulent flows, e.g., the rear of bluff bodies.

TABLE 4-3

Numerical values of the heat-transfer parameter $G(Pr, \beta)$ from Eq. (4-78)

|	β	−0.19884	−0.18	0.0	0.3	1.0	2.0	10.0
	f_0''	0.0	0.12864	0.46960	0.77476	1.23259	1.68722	3.67523
Pr	η^*	2.35885	1.87157	1.21678	0.91099	0.64790	0.49743	0.24077
0.001		0.02383	0.02410	0.02449	0.02467	0.02483	0.02492	0.02508
0.003		0.03967	0.04047	0.04154	0.04206	0.04252	0.04278	0.04325
0.006		0.05409	0.05555	0.05759	0.05859	0.05947	0.05999	0.06091
0.01		0.06745	0.06972	0.07296	0.07455	0.07597	0.07681	0.07831
0.03		0.10547	0.11109	0.11935	0.12353	0.12734	0.12972	0.13385
0.06		0.13666	0.14619	0.16050	0.16791	0.17480	0.17903	0.18693
0.1		0.16339	0.17709	0.19803	0.20908	0.21950	0.22600	0.23843
0.3		0.23180	0.25971	0.30371	0.32783	0.35147	0.36681	0.39801
0.6		0.28318	0.32498	0.39168	0.42892	0.46633	0.49130	0.54459
Air 0.72		0.29777	0.34400	0.41786	0.45929	0.50113	0.52928	0.59054
1.0		0.32581	0.38112	0.46960	0.51952	0.57047	0.60520	0.68219
2.0		0.39145	0.47090	0.59723	0.66905	0.74372	0.79599	0.91815
3.0		0.43478	0.53224	0.68596	0.77344	0.86522	0.93036	1.0872
6.0		0.51896	0.65591	0.86728	0.98727	1.1147	1.2069	1.4396
10.0		0.59054	0.76545	1.02974	1.1791	1.3388	1.4557	1.7597
30.0		0.77839	1.0703	1.4873	1.7198	1.9706	2.1577	2.6682
60.0		0.92602	1.3260	1.8746	2.1776	2.5054	2.7520	3.4395
100.0		1.0523	1.5550	2.2229	2.5892	2.9863	3.2863	4.1332
400.0		1.4885	2.4098	3.5292	4.1331	4.7894	5.2890	6.7332
1000.0		1.8717	3.2319	4.7901	5.6230	6.5291	7.2212	9.2401
4000.0		2.6471	5.0631	7.6039	8.9481	10.4112	11.5320	14.8312
10,000.0		3.3285	6.8289	10.3201	12.1577	14.1583	15.6928	20.2262
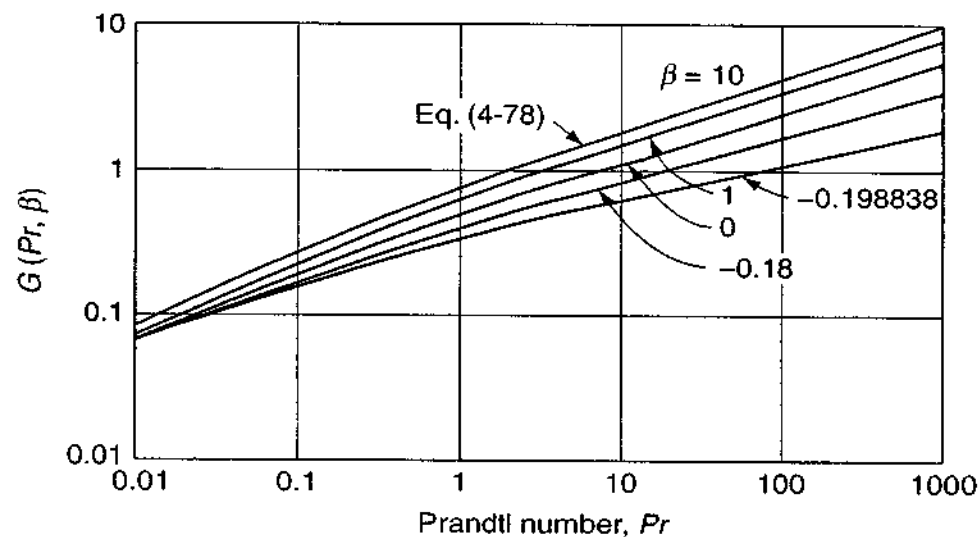
FIGURE 4-13

Heat-transfer parameter $G(Pr, \beta)$ for Falkner–Skan similarity flows with constant wall temperature and negligible dissipation.

4-3.5 The Reynolds Analogy as a Function of Pressure Gradient

We saw in Sec. 3-8.1.5 that there is a proportionality between friction and heat transfer in stagnation flow. A comparable Reynolds analogy holds in flat-plate flow. If we divide Eq. (4-52) by Eq. (4-62), we obtain

$$\frac{C_f}{C_h} \text{ (flat plate)} = 2Pr^{2/3} \tag{4-80}$$

This is a pure proportionality, valid for laminar or turbulent flow, independent of the Reynolds number. It is often used as an approximation in other (nonsimilar, non-flat-plate) situations, such as duct flow. But Eq. (4-79) alerts us that there is a pressure gradient effect.

Let us see if the Reynolds analogy holds for the Falkner–Skan solutions. The skin friction for these flows is given by

$$C_f(x) = \frac{2\mu(\partial u/\partial y)_w}{\rho U^2(x)} = f_0'' \sqrt{\frac{2(1 + m)\nu}{Ux}} \tag{4-81}$$

and the Stanton number C_h is given by Eq. (4-78). If we adopt the usual power-law approximation near Prandtl number unity

$$G(Pr, \beta) \approx G(1, \beta)Pr^{1/3} \tag{4-82}$$

we find that the ratio of skin friction to heat transfer for the Falkner–Skan flows is given by

Gases: $$\frac{C_f(x)}{C_h(x)} \approx 2Pr^{2/3}\frac{f_0''}{G(1, \beta)} \tag{4-83}$$

and the simple Reynolds analogy will be valid only if the factor $f_0''/G(1, \beta)$ is unity, which indeed it is for $\beta = 0$. However, this "analogy factor" varies strongly with β, as shown in Fig. 4-14. It is zero at the separation point, where C_f is zero but C_h
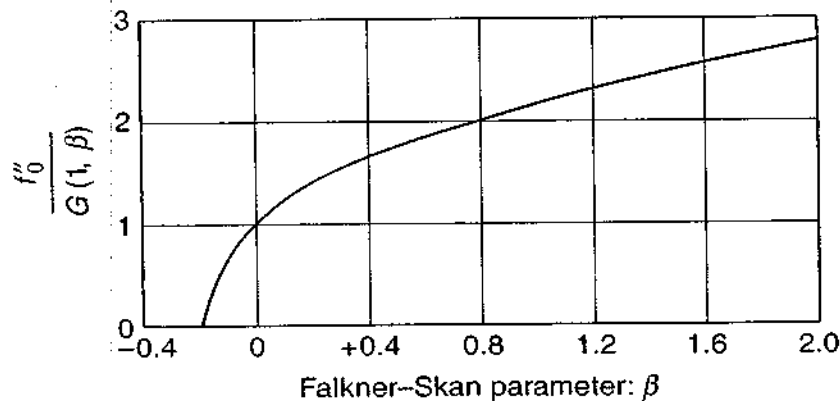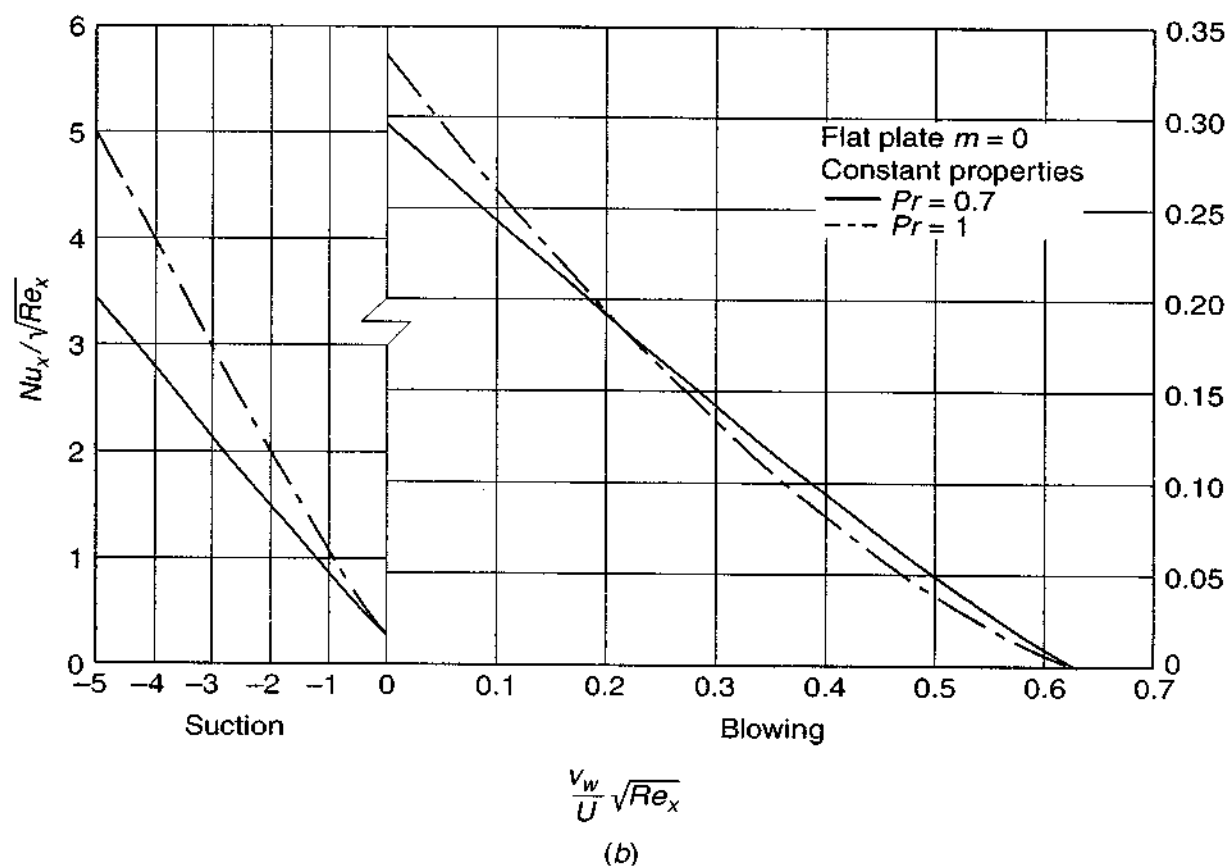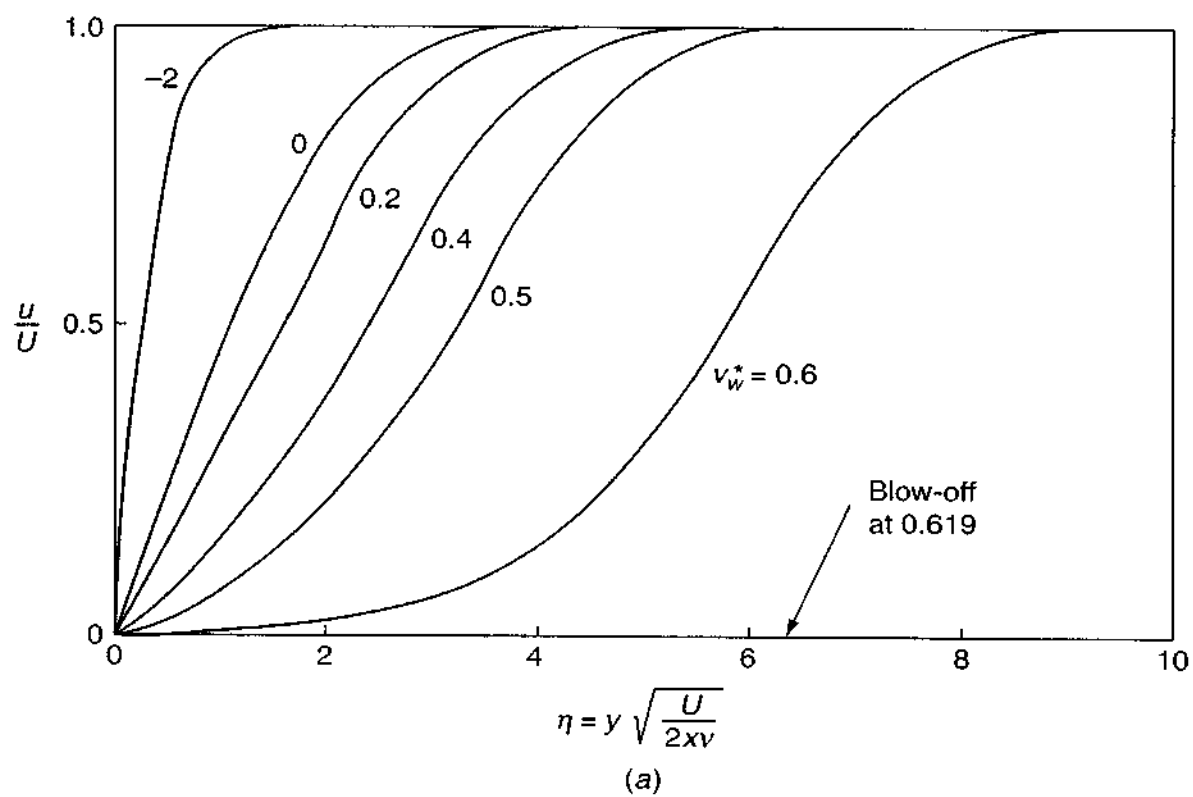

FIGURE 4-14
Variation of the Reynolds analogy from Eq. (4-83) with pressure gradient β for the Falkner–Skan solutions.

FIGURE 4-15

Flat-plate flow with suction or blowing: (a) velocity profiles; (b) local heat-transfer rates [*After Hartnett and Eckert (1957).*]

is finite, and increases without bound as β becomes large. The analogy is thus reliable only for modest, near-zero pressure gradients. It breaks down completely for nonsimilar flows or if the wall temperature varies.

4-3.6 The Flat Plate with Wall Suction or Blowing

The Blasius solution can be extended to nonzero wall velocity, $v_w \ll U$, either positive (blowing) or negative (suction). The streamwise wall velocity, u_w, is still zero from the no-slip condition. This has practical application to many problems: mass transfer, drying, ablation, transpiration cooling, and boundary-layer control. For similarity, only a certain variation $v_w(x)$ is allowed. From Eq. (4-44), at $\eta = 0$, the wall velocity $v_w = -f(0)\sqrt{\nu U/2x}$. Therefore suction and blowing can be simulated by a nonzero value of the Blasius stream function, $f(0)$, and v_w must vary as $x^{-1/2}$. We solve the Blasius Eq. (4-45) with

$$f'(0) = 0 \qquad f'(\infty) = 1 \qquad f(0) \neq 0 \qquad \text{(4-84)}$$

The results will vary with the *suction-blowing parameter*, v_w^*.

$$v_w^* = \frac{v_w}{U}\sqrt{Re_x} = \frac{-f(0)}{\sqrt{2}} \qquad \text{(4-85)}$$

The momentum problem was studied by Schlichting and Bussmann (1943), with heat-transfer results added by Hartnett and Eckert (1957).

Figure 4-15 shows the basic results. The velocity profiles in Fig. 4-15a are strongly affected by v_w^*. Suction thins the boundary layer and greatly increases the wall slope (friction, heat transfer). The suction profiles have strong negative curvature, like a favorable gradient, and are very stable and delay transition to turbulence (see Fig. 5-12). Blowing thickens the boundary layer and makes the profile S-shaped, less stable, and prone to transition to turbulence (look again at Fig. 5-12). At a finite value $v_w^* = +0.619$, the solution yields $\partial u/\partial y = 0$ at $y = 0$, with $u = 0$ for all finite y. The boundary layer is said to be "blown off" by the wall effect, and both the heat transfer and friction are zero. (The boundary-layer approximations fail, of course, for this extreme case.) Figure 4-15b shows the heat transfer $Nu_x/\sqrt{Re_x}$ versus the suction-blowing parameter. The effect of the Prandtl number is seen to be slight, at least for gases. The dash-dot lines in Fig. 4-15b also represent the skin friction $C_f/2$, since the Reynolds analogy is exactly valid if $Pr = 1$ in flat-plate flow.

4-3.7 Flow toward a Point Sink

Figure 4-10 indicated that the limiting case $\beta = +\infty, m = -1$ corresponds to flow toward a point sink. However, the Falkner–Skan approach is inappropriate,
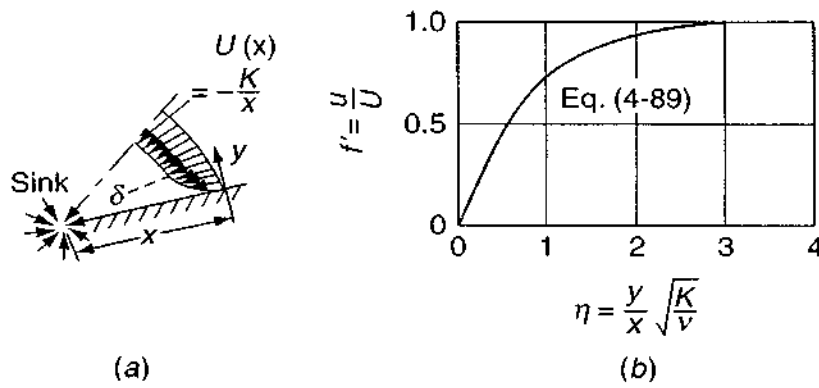
$$\eta = \frac{y}{x}\sqrt{\frac{K}{\nu}}$$

(a)   (b)

FIGURE 4-16
Boundary-layer similar solution for a
point sink: (a) geometry; (b) solution.

since the similarity variable in Eq. (4-70) is squeezed to nothing when $(1 + m) = 0$. The remedy is to redefine the similarity variable for this case. For the point-sink coordinates in Fig. 4-16a,

$$U(x) = -\frac{K}{x} \tag{4-86}$$

Comparison with Eq. (4-68) reveals that similarity is achieved if η is proportional to y/x. For the nicest constants, we choose

$$\eta_{\text{point sink}} = \frac{y}{x}\sqrt{\frac{K}{\nu}} \tag{4-87}$$

Substitution in Eq. (4-67) gives the following differential equation for flow into a convergent channel:

$$f''' - f'^2 + 1 = 0 \tag{4-88}$$

subject to $f(0) = f'(0) = 0$ and $f'(\infty) = 1$. An exact solution may be found if one resists the temptation to retreat into Subroutine RUNGE:

$$f' = \frac{u}{U} = 3\tanh^2\left(\frac{\eta}{\sqrt{2}} + \tanh^{-1}\sqrt{\tfrac{2}{3}}\right) - 2 \tag{4-89}$$

where the constant $\tanh^{-1}\sqrt{\tfrac{2}{3}} = 1.146$. A plot of this relation is given in Fig. 4-16b. We have $f' = 0.99$ at $\eta \approx 3.4$, so that once again we have the customary inverse square-root relationship

Point sink: $$\frac{\delta_{99\%}}{x} \approx \frac{3.4}{\sqrt{-Ux/\nu}} \tag{4-90}$$

the minus sign merely denoting that U is opposite to x, as shown in Fig. 4-16a. It is interesting that the sink-flow profile in Fig. 4-16b is the same as the Jeffery–Hamel wedge-flow profiles of Sec. 3-8.3.1 for large negative $Re\alpha$. See, e.g., the profile for $Re\alpha = -100$ in Fig. 3-34. Note, however, that η is defined quite differently for Jeffery–Hamel flow.

4-4 FREE-SHEAR FLOWS

Free-shear layers are unaffected by walls and develop and spread in an open ambient fluid. They possess velocity gradients, created by some upstream mechanism, that they try to smooth out by viscous diffusion in the presence of convective deceleration. Three examples are (1) the free-shear layer between parallel moving streams, (2) a jet, and (3) the wake behind a body immersed in a stream.

Let the dominant free-shear velocity be u in the x direction. Then, if the Reynolds number is large, the boundary-layer approximations will hold: $v \ll u$, $\partial u/\partial x \ll \partial u/\partial y$, $\partial p/\partial y \approx 0$. Further, if there are no confining walls, the pressure gradient dp/dx will be essentially zero. Then plane free-shear flows satisfy the flat-plate equations

$$\frac{\partial u}{\partial x} + \frac{\partial v}{\partial y} = 0$$

$$u\frac{\partial u}{\partial x} + v\frac{\partial u}{\partial y} \approx \nu\frac{\partial^2 u}{\partial y^2}$$

(4-91)

except of course there are no walls to enforce a no-slip condition.

Just downstream of the disturbance that caused the velocity gradients (the meeting point of the two parallel streams, the jet exit, the rear of the immersed body), the flow will be *developing* and nonsimilar. Further downstream, the flow will be *similar* and the velocity profiles will all look alike when suitably scaled. Here we discuss only the similar solutions for the shear layer, the jet, and the wake.

4-4.1 The Free-Shear Layer between Two Different Streams

Figure 4-17a shows two parallel uniform streams, U_1 (upper) and U_2 (lower), meeting at $x = 0$. As we move downstream, the discontinuity between U_1 and U_2 is smoothed out by viscosity into an S-shaped *free-shear layer* between the two. The simplest application would be for $U_2 = 0$, such as a plane airflow emerging from a slot into ambient air at rest. Lock (1951) generalized this into two different fluids with physical properties (ρ_1, μ_1) and (ρ_2, μ_2), respectively—also shown in Fig. 4-17a. He defined a Blasius-type similarity variable for each stream:

$$\eta_j = y\sqrt{\frac{U_1}{2x\nu_j}}$$

$$f_j' = \frac{u_j}{U_1} \qquad j = 1, 2$$

(4-92)

Note that U_1, not U_j, is specified in both variables. Substitution in Eqs. (4-92) yields a Blasius-type equation for each layer:

$$f_j''' + f_j f_j'' = 0 \qquad j = 1, 2$$

(4-93)
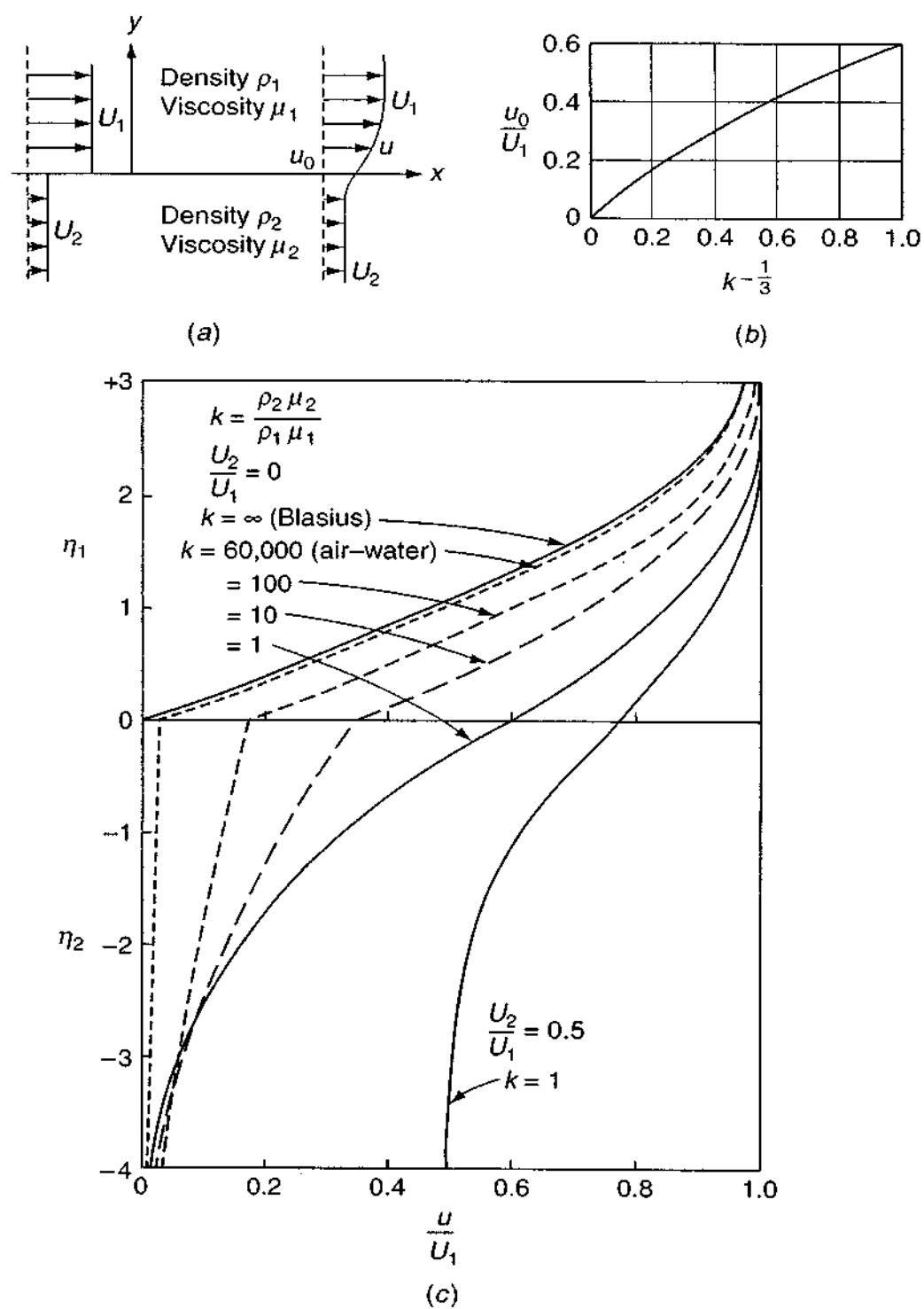
FIGURE 4-17
Velocity distribution between two parallel streams of different properties: (a) geometry; (b) velocities at the interface ($U_2 = 0$) (c) representative velocity profiles. [*After Lock (1951).*] (*By permission of The Clarendon Press, Oxford.*)

The boundary conditions are of three types. First, an asymptotic approach to the two stream velocities:

$$f_1'(+\infty) = 1 \qquad f_2'(-\infty) = \frac{U_2}{U_1} \tag{4-94}$$

Second, there should be kinematic equality, $u_1 = u_2$ and $v_1 = v_2$, at the interface, taken to be at $\eta_j = 0$:

$$f_1(0) = f_2(0) = 0$$
$$f_1'(0) = f_2'(0) \neq 0 \tag{4-95}$$

Third, there should be equality of shear stress at the interface:

$$\mu_1 \frac{\partial u_1}{\partial y}(0) = \mu_2 \frac{\partial u_2}{\partial y}(0)$$

or

$$\tag{4-96}$$

$$f_1''(0) = k^{1/2} f_2''(0)$$

where $k = (\rho_2 \mu_2 / \rho_1 \mu_1)$. The most practical cases, since we are neglecting mass transfer between the two fluids, are $k = 1$ (identical fluids) or $k \gg 1$ (a gas flowing over a liquid). For the air–water interface, $k \approx 60{,}000$ or $k^{1/2} \approx 245$.

Some solutions computed by Lock (1951) for various k are shown in Fig. 4-17c. As k increases, the lower layer moves more slowly. The air–water case, $k = 60{,}000$, gives a good physical picture of slow "wind-driven" flow in the surface layer of a lake or ocean—although *that* large-scale flow would likely be turbulent, not laminar. The interface velocity when $U_2 = 0$ is shown in Fig. 4-17b as a function of k.

The classic case $k = 1$, $U_2 = 0$ in Fig. 4-17c has two interesting facets. First, it is not antisymmetric. The interface velocity is greater than $0.5\,U_1$ because the two layers have different convective deceleration. Second, the asymptotic value $f_2(-\infty)/\sqrt{2} = -0.619$, which represents a flat plate at $(-\infty)$ with its boundary layer "blown off" as in Fig. 4-15a.

4-4.2   The Plane Laminar Jet

Consider a plane jet emerging into a still ambient (identical) fluid from a (two-dimensional) slot at $x = 0$, as shown in Fig. 4-18. Since the jet spreads at constant pressure and there are no bounding walls, it satisfies Eqs. (4-91) and must also have constant momentum flux across any ($x = $ const) cross section:

$$J = \rho \int_{-\infty}^{+\infty} u^2 \, dy = \text{const} \tag{4-97}$$

which is the zero-drag, zero-freestream version of Eq. (4-5) for a constant-pressure control volume. Schlichting (1933a) showed that if boundary-layer approximations
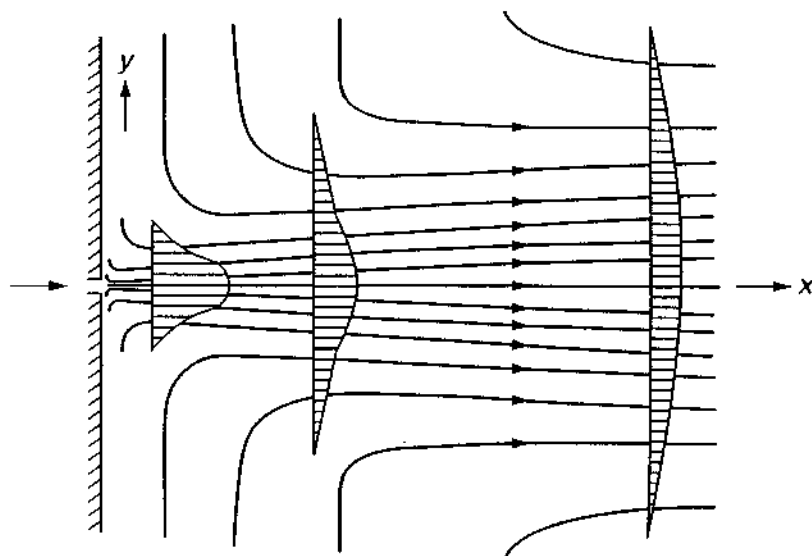
FIGURE 4-18
Definition sketch for a two-dimensional laminar free jet. [*After Schlichting (1933a).*]

are valid, the jet entrainment spreads as the cube root of x, and the proper stream function is

$$\psi = \nu^{1/2} x^{1/3} f(\eta) \tag{4-98}$$

where

$$\eta = \frac{y}{3\nu^{1/2} x^{2/3}}$$

The corresponding velocity components are

$$u = \frac{f'(\eta)}{3x^{1/3}}$$

$$v = \frac{-\nu^{1/2}}{3x^{2/3}} (f - 2f'\eta) \tag{4-99}$$

Substitution in Eq. (4-91) gives the following relation to be solved:

$$f''' + ff'' + f'^2 = 0 \tag{4-100}$$

The boundary conditions are symmetry about the x axis ($v = 0$ and $\partial u/\partial y = 0$ at $y = 0$) and a quiescent ambient fluid ($u = 0$ at $y = \infty$). This translates in the similarity variables to

$$f(0) = f''(0) = 0$$

$$f'(\infty) = 0 \tag{4-101}$$

With all zero boundary conditions, it looks as if we have no driving force for the equation. Upon reflection, we see that the driving potential is the momentum flux J, rather analogous to the Jeffery–Hamel wedge flows of Chap. 3.

Equation (4-100) contains the same two non-linearities as the Falkner–Skan equation (4-69), thus issuing a seductive call for Subroutine RUNGE. In fact,

however, Schlichting (1933a) deduced the exact analytic solution, which is strikingly simple:

$$f(\eta) = 2a \tanh(a\eta)$$

or

$$f'(\eta) = 2a^2 \operatorname{sech}^2(a\eta)$$

(4-102)

The jet velocity profile thus has the symmetrical $\operatorname{sech}^2 y$ shape, reminiscent of a Gaussian probability distribution. The constant a is determined by evaluating the momentum flux J from Eq. (4-97):

$$J = \rho \int_{-\infty}^{+\infty} \left(\frac{2a^2}{3x^{1/3}} \operatorname{sech}^2 a\eta \right)^2 3\nu^{1/2} x^{2/3} d\eta = \tfrac{16}{9} \rho \nu^{1/2} a^3$$

or

(4-103)

$$a = \left(\frac{9J}{16\sqrt{\rho\mu}} \right)^{1/3} \approx 0.8255 \frac{J^{1/3}}{(\rho\mu)^{1/6}}$$

Since $\operatorname{sech} 0 = 1$, the maximum or centerline velocity is seen to be

$$u_{max} = \frac{2a^2}{3x^{1/3}} = \frac{2}{3} \left(\frac{9}{16} \right)^{2/3} \frac{J^{2/3}}{(\rho\mu x)^{1/3}} \approx 0.4543 \left(\frac{J^2}{\rho\mu x} \right)^{1/3} \quad (4\text{-}104)$$

Thus the jet spreads so that the centerline velocity drops off as $x^{-1/3}$. The velocity distribution is

$$u(x, y) = u_{max} \operatorname{sech}^2 a\eta = u_{max} \operatorname{sech}^2 \left[0.2752 \left(\frac{J\rho}{\mu^2 x^2} \right)^{1/3} y \right] \quad (4\text{-}105)$$

We may define the width of the jet as twice the distance y where $u = 0.01 u_{max}$. Noting that $\operatorname{sech}^2 3 \approx 0.01$, we have

$$\text{Width} = 2y|_{1\%} = b \approx 21.8 \left(\frac{x^2 \mu^2}{J\rho} \right)^{1/3} \quad (4\text{-}106)$$

and thus the jet spreads as $x^{2/3}$. The mass rate of flow across any vertical plane is given by

$$\dot{m} = \rho \int_{-\infty}^{+\infty} u \, dy = (36 J \rho \mu x)^{1/3} \approx 3.302 (J\rho\mu x)^{1/3} \quad (4\text{-}107)$$

which is seen to increase with $x^{1/3}$ as the jet entrains ambient fluid by dragging it along. This result is correct at large x but implies falsely that $\dot{m} = 0$ at $x = 0$, which is the slot where the jet issues. The reason is that the boundary-layer approximations fail if the Reynolds number is small, and the appropriate Reynolds number here is $\dot{m}/\mu \sim (J\rho x/\mu^2)^{1/3}$. Thus the solution is invalid for small values of $J\rho x/\mu^2$, meaning that we cannot ascertain any details of the flow near the jet outlet with a boundary-layer theory.

Since jet velocity profiles are S-shaped (i.e., have a point of inflection), they are unstable and undergo transition to turbulence early—at a Reynolds number of about 30, based on exit slot width and mean slot velocity. Thus although there is further analysis of laminar jets in the literature [Pai (1954)], jets are more likely to be turbulent. Textbooks treating turbulent-jet analysis and experiments are by Abramovich (1963), Schetz (1980), and Morris et al. (2002).

The analysis of axisymmetric (round) jets and wakes will be discussed in Sec. 4-10.

4-4.3 The Plane Laminar Wake: Far-Field Approximation

A wake is the *defect* in stream velocity behind an immersed body in a flow, as sketched in Fig. 4-19. A slender plane body with zero lift, such as the airfoil parallel to the stream in Fig. 4-19, usually produces a smooth wake whose velocity defect u_1 decays monotonically downstream. A blunt body, such as a cylinder, has a wake distorted by an alternating shed vortex structure—the picture in Fig. 4-19 would be a time-average wake.

Immediately downstream of the body in Fig. 4-19, the wake is developing and nonsimilar. About three body-lengths downstream, the wake becomes developed, with similar profiles. Here we make only a simple far-field approximation for a developed wake by assuming that the velocity defect is very small:

$$u_1(x, y) = U_0 - u(x, y) \ll U_0 \tag{4-108}$$

in which case the convective acceleration can be linearized in the manner of the Oseen approximation, Sec. 3-9.4. The momentum Eq. (4-91) simplifies to

$$U_0 \frac{\partial u_1}{\partial x} \approx \nu \frac{\partial^2 u_1}{\partial y^2} \tag{4-109}$$
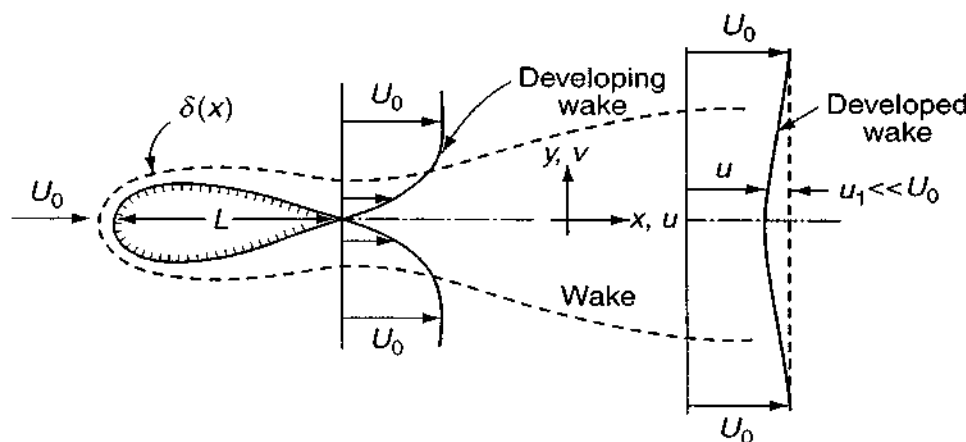

FIGURE 4-19
Flow in the wake of a body immersed in a stream.

subject to $u_1(x, \pm\infty) = 0$ and $\partial u_1/\partial y = 0$ at $y = 0$. This is the linear heat-conduction equation, and the solution is

$$u_1 = BU_0 x^{-1/2} \exp\left(-\frac{U_0 y^2}{4x\nu}\right) \qquad (4\text{-}110)$$

where B is a constant. In the far field, then, the wake has a Gaussian velocity distribution whose centerline value drops off as $x^{-1/2}$. The constant B is evaluated from the condition that the body drag force F equals the momentum flux defect in the wake:

$$F = \int_{-\infty}^{\infty} \rho u u_1 \, dy \approx \rho U_0 \int_{-\infty}^{\infty} u_1 \, dy = 2\rho U_0^2 B \sqrt{\frac{\pi\nu}{U_0}} \qquad (4\text{-}111)$$

Meanwhile, this force is correlated by the body drag coefficient:

$$F = C_D \tfrac{1}{2}\rho U_0^2 L$$

per unit depth into the paper. Equate this to Eq. (4-111) and solve for B, after which the wake velocity may be written in the form

$$\frac{u_1}{U_0} = C_D\left(\frac{Re_L}{16\pi}\right)^{1/2}\left(\frac{L}{x}\right)^{1/2} \exp\left(-\frac{U_0 y^2}{4x\nu}\right) \qquad (4\text{-}112)$$

where $Re_L = U_0 L/\nu$ is the body Reynolds number. The wake defect is thus proportional to the body drag coefficient. For a flat plate wetted on both sides, $C_D = 2.656/\sqrt{Re_L}$ from Eq. (4-53), the centerline velocity defect becomes

$$\left.\frac{u_1(x, 0)}{U_0}\right|_{\text{flat plate}} = \frac{0.664}{\sqrt{\pi}}\left(\frac{L}{x}\right)^{1/2} \qquad (4\text{-}113)$$

a result given by Tollmein (1931) and valid for $x > 3L$.

A complete review of laminar wakes, including near-field and three-dimensional geometries and compressible flows, is given in the monograph by Berger (1971). Like jets, wakes are unstable and are more likely in practice to be turbulent than laminar.

4-5 OTHER ANALYTIC TWO-DIMENSIONAL SOLUTIONS

It is clear that the similarity solutions of Secs. 4-3 and 4-4 are very special, in that their profile shapes remain the same (in the dimensionless sense) as we move downstream. It is far more likely that typical flow in practice is nonsimilar and changes from adverse to favorable gradients and perhaps back again. For example, the freestream flow near a cylinder has a favorable gradient near the nose which changes continuously to an adverse gradient (with separation) as we move toward the rear. No similarity technique can attack such a flow.

In the first 50 years after Prandtl's development of boundary-layer theory, nonsimilar flows were vexing and had to be computed laboriously by hand using analytic methods. Computed results, such as the boundary layer over a cylinder, were

cherished and used as examples over and over. Now, however, in this personal-computer era, any practical laminar freestream distribution $U(x)$ can be computed swiftly and accurately by numerical methods which we illustrate in Sec. 4-7. (The same computational power is also available for turbulent boundary layers, but in that case the equations themselves are less reliable.)

Three basic approaches have been used to analyze nonsimilar boundary layers:

1. Analytic continuation by series expansion, e.g., Howarth (1938), Görtler (1957), and Meksyn (1961). These methods are now obsolete.

2. Approximate integral methods—an extension of Sec. 4-1.1 An amazing number of these techniques are discussed by Rosenhead (1963). We will discuss here the simple and accurate laminar-flow correlation of Thwaites (1949), which seems to serve well for any $U(x)$.

3. Numerical modeling on a digital computer. Scores of these numerical techniques, both finite-difference and finite-element, are reported in recent literature, e.g., Schetz (1992) and Cebeci and Cousteix (1998). We will outline a simple finite-difference method easily implemented on a personal computer.

Although approaches 2 and 3 above can handle any new problem with proper care, two classic results are worth a brief description here.

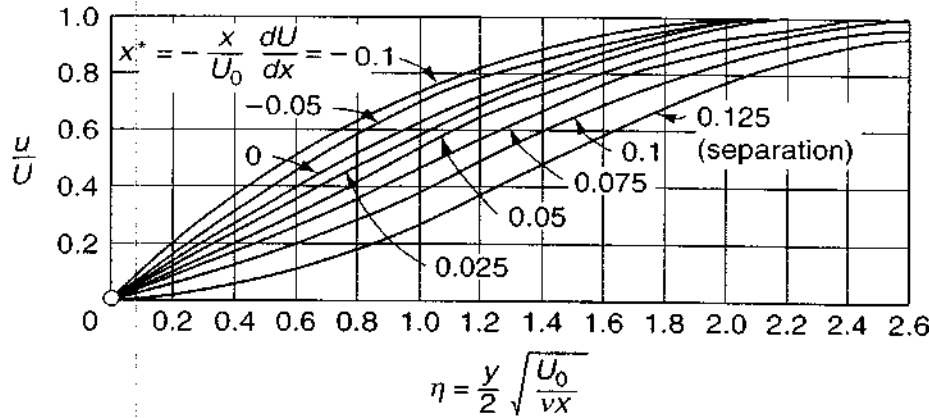### 4-5.1 The Linearly Retarded Flow of Howarth

A simple decelerating nonsimilar freestream distribution,

$$U(x) = U_0\left(1 - \frac{x}{L}\right) \tag{4-114}$$

was studied by Howarth (1938) to illustrate adverse gradients and laminar-boundary-layer separation. Howarth expanded the stream function into a power series in x/L whose coefficients were Blasius-type functions of $[y\sqrt{U_0/\nu x}]$. He kept seven terms—each a complicated function—and plotted the velocity profiles shown in Fig. 4-20. The curve for $x/L = 0$ is the Blasius profile, downstream of which the profiles become increasingly S-shaped and finally separation occurs at $x/L \approx 0.125$, according to Howarth's estimate.

The series-expansion approach is definitely obsolete now, but even the most accurate numerical solution of boundary-layer equations is invalid and inappropriate at separation and beyond. No matter how the external potential flow $U(x)$ varies, the wall shear stress at the separation point comes in vertically to zero, that is, $\partial\tau_w/\partial n = 0$ at separation.[+] This is known as the *Goldstein singularity*, after Goldstein (1948), who showed that, in boundary-layer theory, the wall shear stress

---

[+]Look ahead to see similar singular wall shear stress behavior on a cylinder, Fig. 4-24b.

FIGURE 4-20

Velocity profiles from a series expansion of linearly retarded flow $U(x) = U_0(1 - x/L)$. [*After Howarth (1938)*.]

has square-root behavior near separation:

$$\mu\frac{\partial u}{\partial y}\bigg|_{y=0} = \text{const}(x_{\text{sep}} - x)^{1/2} \tag{4-116}$$

Though interesting mathematically, this is unrealistic physically and is a fundamental limitation of boundary-layer theory. The dilemma was resolved by Sychev (1972), who showed that a *free-streamline potential theory*, discussed, e.g., in Milne–Thomson's text (1968), plus a rescaled boundary-layer approximation in the immediate vicinity of separation, removes the singularity. The wall shear stress then varies smoothly through zero. Another example of this rescaling technique is given later in Sec. 4-11.5. In the separated region, higher order theory and, indeed, the full Navier–Stokes equations should replace boundary-layer approximations. Additional detailed calculations of the separation region structure are given by Smith (1977). The Sychev–Smith theory is most appropriate for bluff-body flows, where the free streamline produces an adverse pressure gradient just sufficient to cause flow separation. For further discussion, see Chap. 14 of the monograph by Schlichting and Gersten (2000).

4-5.2 The Flat Plate with Uniform Wall Suction

In another series solution of an important case, Iglisch (1944) studied boundary-layer flow past a flat plate with uniform suction, as in Fig. 4-21. Wall suction is a very practical means of delaying boundary-layer transition to turbulence. Iglisch solved the boundary-layer Eqs. (4-91) for constant pressure, $dU/dx = 0$, and a wall-suction boundary condition:

$$u(x, 0) = 0 \qquad u(x, \infty) = U_\infty \qquad v(x, 0) = v_0 = \text{const} < 0 \tag{4-117}$$

The flow is nonsimilar, and the velocity profiles in Fig. 4-21 gradually change shape from near-Blasius flow at the leading edge to the asymptotic exponential
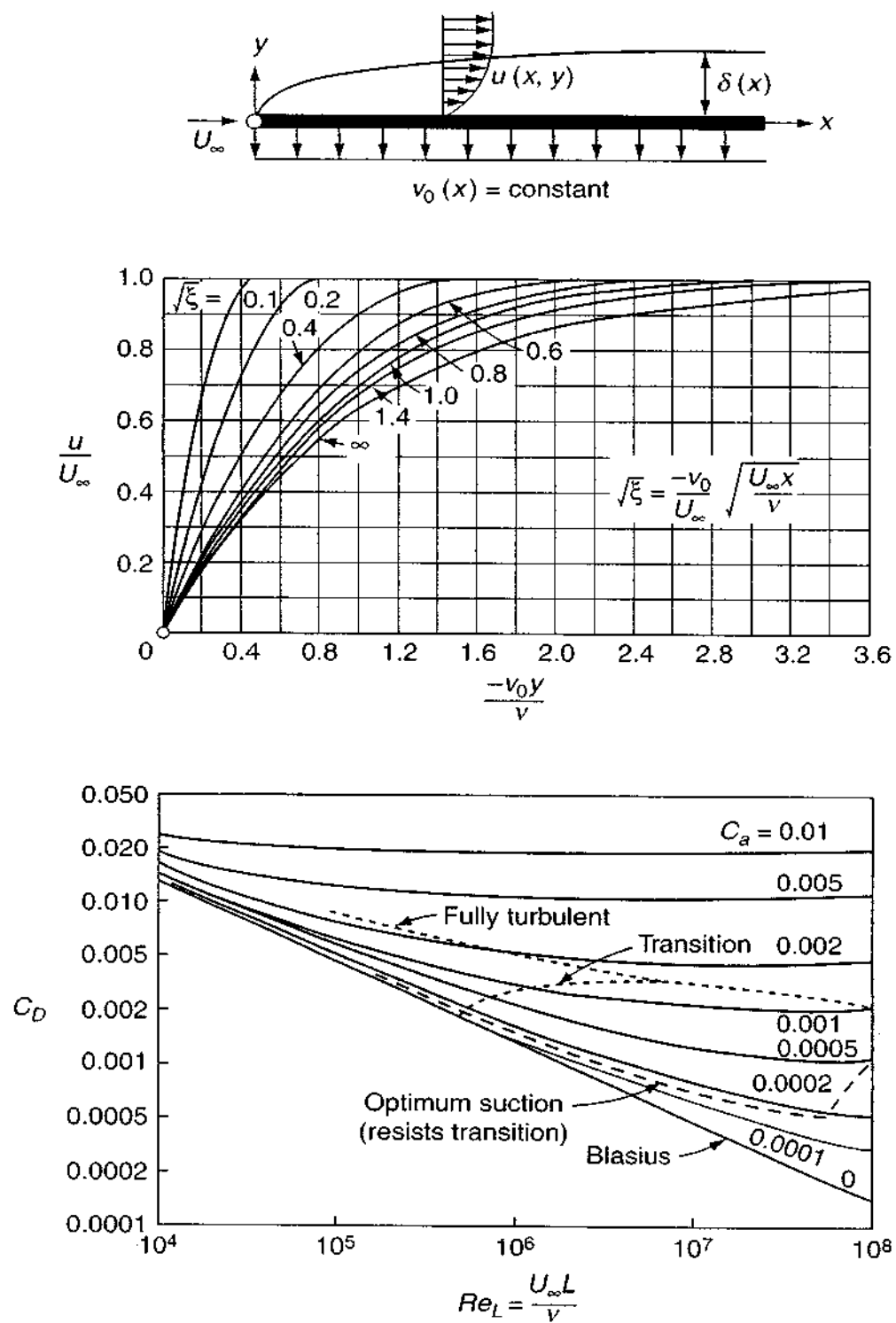
FIGURE 4-21
Velocity profile and drag coefficient of a flat plate with uniform suction. [*After Iglisch* (*1994*).]

profile of Eq. (3-121) far downstream. The asymptotic condition is reached at about $(-v_0/U_\infty)\sqrt{Re_x} \approx 2.0$. If the suction rate is a typical value, $(-v_0/U_\infty) = 0.001$, in air at 22°C with $U_\infty = 10$ m/s, this corresponds to a distance $x = 6$ m. But the third chart in Fig. 4-21 shows that increasing suction raises the plate drag, possibly even above the turbulent-flow drag that we are trying to avoid with suction. The reader may show as an exercise (from a control volume similar to Fig. 4-1) that the drag coefficient on the plate is increased by suction, due to swallowing tangential momentum through the wall:

$$C_D = \frac{1}{L}\int_0^L C_f(x)\,dx + 2C_Q$$

$$C_Q = -\frac{v_0}{U_0}$$

(4-118)

Here C_f is the local viscous shear, $2\tau_w/\rho U_0^2$. Iglisch's drag computations are shown in Fig. 4-21. The dashed line shows the optimum suction, the locus of points of minimum suction required to maintain laminar flow, according to the transition theory of Chap. 5. For further study, the reader is referred to the excellent review by Wuest in Lachmann (1961).

4-5.3   Other Classical Analytic Solutions

There are quite a few other published classical solutions of boundary-layer equations for special $U(x)$. Some of these are theoretical:

1. Tani (1949): $U = U_0(1 - x^{*n})$, $n = 2, 4, 8$, and $x^* = x/L$
2. Görtler (1957): $U/U_0 = (1 - x^*)^n$, $n = \frac{1}{2}, 2$; $(1 + x^*)^m$, $m = -1, -2, \cos(x^*)$
3. Curle (1958): $U = U_0(x^* - x^{*3} + ax^{*5})$, $a = 0, +0.07885, -0.12156$
4. Terrill (1960): $U = U_0 \sin(x^*)$

Two of them are experiments used for comparison with theory:

5. Hiemenz (1911): Flow past a circular cylinder
6. Schubauer (1935): Flow past a slender elliptical cylinder

All of these laminar flows are driven to separation and make good test cases for an alternate method. The reader will appreciate that they also make good problem exercises for integral or finite-difference methods.

4-6   APPROXIMATE INTEGRAL METHODS

The control-volume approach of Sec. 4-1 is exact in principle—if exact velocity and temperature distributions are used—but is approximate in practice, using

guessed profiles and other correlations. A wide variety of these "integral methods" are discussed in the text edited by Rosenhead (1963). Here we present only this writer's favorite method, due to Thwaites (1949).

4-6.1   The Boundary-Layer Integral Equations

All integral methods use partially integrated forms of the continuity, momentum, and energy equations, which for two-dimensional incompressible flow are Eqs. (4-35). Continuity is eliminated during the derivation, so that the two basic results are (1) the *momentum* integral relation [Kármán (1921)] and (2) the *thermal-energy* integral relation [Frankl (1934)]. Some workers also use a third, called the *mechanical-energy* integral relation [Leibenson (1935)]. The mechanical-energy equation is the x-momentum equation multiplied by u, that is, it changes forces into the rate of work done by those forces. It is not a fundamental relation but can be useful as a correlation tool, especially for turbulent boundary layers.

We may derive the integral relations by direct integration, in the y direction, of the boundary-layer equations, repeated here for convenience:

Continuity:
$$\frac{\partial u}{\partial x} + \frac{\partial v}{\partial y} = 0 \tag{4-35a}$$

Momentum:
$$\frac{\partial u}{\partial t} + u\frac{\partial u}{\partial x} + v\frac{\partial u}{\partial y} \approx \left(\frac{\partial U}{\partial t} + U\frac{\partial U}{\partial x}\right) + \frac{1}{\rho}\frac{\partial \tau}{\partial y} \tag{4-35b}$$

Thermal energy:
$$\rho c_v\left(\frac{\partial T}{\partial t} + u\frac{\partial T}{\partial x} + v\frac{\partial T}{\partial y}\right) \approx -\frac{\partial q}{\partial y} + \tau\frac{\partial u}{\partial y} \tag{4-35c}$$

We have neglected buoyant forces and have used τ and q to represent shear stress and heat transfer, because then the equations are valid, as we shall see, for turbulent boundary layers also. In the laminar case, $\tau = \mu\,\partial u/\partial y$ and $q = -k\,\partial T/\partial y$.

4-6.2   The Momentum-Integral Relation

To obtain the momentum-integral relation, we first multiply continuity by $u - U$ and subtract from momentum, with the result

$$-\frac{1}{\rho}\frac{\partial \tau}{\partial y} = \frac{\partial}{\partial t}(U - u) + \frac{\partial}{\partial x}(uU - u^2)$$
$$+ (U - u)\frac{\partial U}{\partial x} + \frac{\partial}{\partial y}(vU - vu) \tag{4-119}$$

We allow unsteady flow and the possibility of a porous wall with normal velocity $v_w(x)$ which is positive for injection. We then integrate from the wall to infinity, noting that

τ vanishes at infinity in the boundary-layer approximation. The result is

$$\frac{\tau_w}{\rho} = \frac{\partial}{\partial t}\int_0^\infty (U - u)\,dy + \frac{\partial}{\partial x}\int_0^\infty u(U - u)\,dy$$

$$+ \frac{\partial U}{\partial x}\int_0^\infty (U - u)\,dy - Uv_w \tag{4-120}$$

This a fairly general form of the momentum-integral relation, often called the Kármán integral relation after T. von Kármán, who first suggested this approach in boundary-layer analysis (1921). As might be expected, the integrals of $U - u$ and $u(U - u)$ are equivalent to the displacement and momentum thicknesses, Eqs. (4-4) and (4-6). Hence we can rewrite the momentum relation in the more compact form

$$\frac{\tau_w}{\rho U^2} = \frac{C_f}{2} = \frac{1}{U^2}\frac{\partial}{\partial t}(U\delta^*) + \frac{\partial \theta}{\partial x} + (2\theta + \delta^*)\frac{1}{U}\frac{\partial U}{\partial x} - \frac{v_w}{U} \tag{4-121}$$

For steady flow with an impermeable wall, this reduces to

$$\frac{C_f}{2} = \frac{d\theta}{dx} + (2 + H)\frac{\theta}{U}\frac{dU}{dx} \qquad H = \frac{\delta^*}{\theta} \tag{4-122}$$

which is the most heavily analyzed and most commonly seen form of the Kármán integral relation. The so-called shape factor H is always greater than unity, as seen from the geometry of Fig. 4-2, and varies for laminar flow from about 2.0 at the stagnation point to about 3.5 at the separation point. In turbulent flow, the variation is even less (about 1.3 to 2.5), but, paradoxically, determining the exact value of H in turbulent flow is critical to an accurate analysis of this type.

4-6.3 The Thermal-Energy Integral Relation

The thermal-energy integral is most easily derived by first multiplying the momentum Eq. (4-35b) by u and adding this to the thermal-energy Eq. (4-35c). The result is

$$\rho\frac{\partial h_0}{\partial t} + \rho\left(u\frac{\partial h_0}{\partial x} + v\frac{\partial h_0}{\partial y}\right) = \frac{\partial}{\partial y}(-q + u\tau) \tag{4-123}$$

where $h_0 = c_pT + u^2/2$ is the total, or stagnation, enthalpy of the flow—neglecting $v^2/2$, naturally. This equation will have important consequences in laminar compressible flow (Chap. 7) of gases. Presently, we merely wish to integrate the equation from zero to infinity, including porous walls and unsteady flow. The result is

$$q_w = \frac{\partial}{\partial t}\int_0^\infty \rho c_pT\,dy + \frac{\partial}{\partial x}\int_0^\infty \rho u(h_0 - h_{0e})\,dy - \rho c_p v_w(T_w - T_e) \tag{4-124}$$

This is the general form of the thermal-energy integral relation, derived by Frankl (1934). For steady flow with impermeable walls and negligible dissipation, we have

the simpler form

$$q_w = \frac{d}{dx} \int_0^\infty \rho c_p u (T - T_e)\, dy \tag{4-125}$$

which was used earlier in our flat-plate analysis, Eq. (4-21), and in fact is valid for any low-speed laminar or turbulent boundary layer.

4-6.4   The Mechanical-Energy Integral Relation

To derive the mechanical-energy integral relation, we multiply continuity by $u^2 - U^2$ and momentum by $2u$, subtract, and integrate as before from the wall to infinity. The result is

$$\frac{2}{\rho} \int_0^\infty \tau \frac{\partial u}{\partial y}\, dy = \frac{\partial}{\partial t} \int_0^\infty u(U - u)\, dy + U^2 \frac{\partial}{\partial t} \int_0^\infty \left(1 - \frac{u}{U}\right) dy$$

$$+ \frac{\partial}{\partial x} \int_0^\infty u(U^2 - u^2)\, dy - U^2 v_w \tag{4-126}$$

The integral on the left-hand side is often called the *dissipation integral*:

$$\mathcal{D} = \int_0^\infty \tau \frac{\partial u}{\partial y}\, dy \tag{4-127}$$

On the right-hand side, we recognize the momentum thickness, the displacement thickness, and a third integral related to the so-called kinetic-energy thickness (sometimes called the dissipation thickness):

$$\delta_3 = \int_0^\infty \frac{u}{U}\left(1 - \frac{u^2}{U^2}\right) dy \tag{4-128}$$

With this notation, Eq. (4-126) can be rewritten in the compact form

$$C_{\mathcal{D}} = \frac{2\mathcal{D}}{\rho U^3} = \frac{1}{U}\frac{\partial}{\partial t}(\theta + \delta^*) + \frac{2\theta}{U^2}\frac{\partial U}{\partial t} + \frac{1}{U^3}\frac{\partial}{\partial x}(U^3 \delta_3) - \frac{v_w}{U} \tag{4-129}$$

This is the mechanical-energy integral relation, first derived by Leibenson (1935) and valid for laminar or turbulent flow. The relation has been used in laminar flow but is more appropriate for turbulent flow, where an extra correlation can help make up for uncertain modeling laws.

4-6.5   One-Parameter Integral Methods

The three integral relations derived before are exact but are used in *approximate* methods, and many have been published. There are two basic categories: (1) guessed velocity and temperature profiles and (2) empirical correlations among the integral parameters.

For momentum analysis, Eq. (4-122), one could approximate u by a one-parameter family of velocity profiles:

$$u(x, y) \approx U(x)f[\eta, P(x)] \tag{4-130}$$

where $\eta = y/\delta$ and P is a suitable dimensionless parameter. From such a profile we could then compute θ, δ^*, H, and τ_w and substitute in Eq. (4-122) to obtain a first-order differential equation for, say, $\delta(x)$.

The guessed-profile idea was dominated for decades by the first such method, developed by Pohlhausen (1921). Guided by the concurrent paper of Kármán (1921), Pohlhausen proposed a fourth-order polynomial:

$$\frac{u}{U} \approx 2\eta - 2\eta^3 + \eta^4 + \frac{\Lambda}{6}[\eta(1 - \eta)^3] \tag{4-131}$$

where $\Lambda = \delta^2(dU/dx)/\nu$ varies with the local pressure gradient and is now called the *Pohlhausen parameter*. Equation (4-131) looks good when plotted, fits five realistic profile boundary conditions, and, when substituted into the momentum-integral relation (4-122), produces a differential equation that is easy to solve on a personal computer. Unfortunately, it is *not* very accurate and thus should be discarded.

There have been many other methods using profile assumptions, some involving multiple parameters [Rosenhead (1963)]. But this writer believes that the correlation idea of Thwaites (1949) is excellent and sufficient for laminar flow and need not be supplemented by any other approximation.

4-6.6   The Correlation Method of Thwaites

Thwaites (1949) modified and improved an idea of Holstein and Bohlen (1940), who cleverly rewrote the momentum-integral Eq. (4-122) in terms of a better parameter λ, defined as

$$\lambda = \frac{\theta^2 U'}{\nu} = \left(\frac{\theta}{\delta}\right)^2 \Lambda \tag{4-132}$$

Their simple but inspired idea was to multiply the momentum-integral relation, Eq. (4-122), by $U\theta/\nu$, with the result

$$\frac{\tau_w \theta}{\mu U} = \frac{U\theta}{\nu}\frac{d\theta}{dx} + \frac{\theta^2 U'}{\nu}(2 + H) \tag{4-133}$$

Now H and the left-hand side of this equation are dimensionless boundary-layer functions and thus, by assumption, are correlated reasonably by a single parameter (λ in this case). Thus we assume, after Holstein and Bohlen (1940), that

$$\frac{\tau_w \theta}{\mu U} \approx S(\lambda) \qquad \text{shear correlation}$$

$$H = \frac{\delta^*}{\theta} \approx H(\lambda) \qquad \text{shape-factor correlation} \tag{4-134}$$
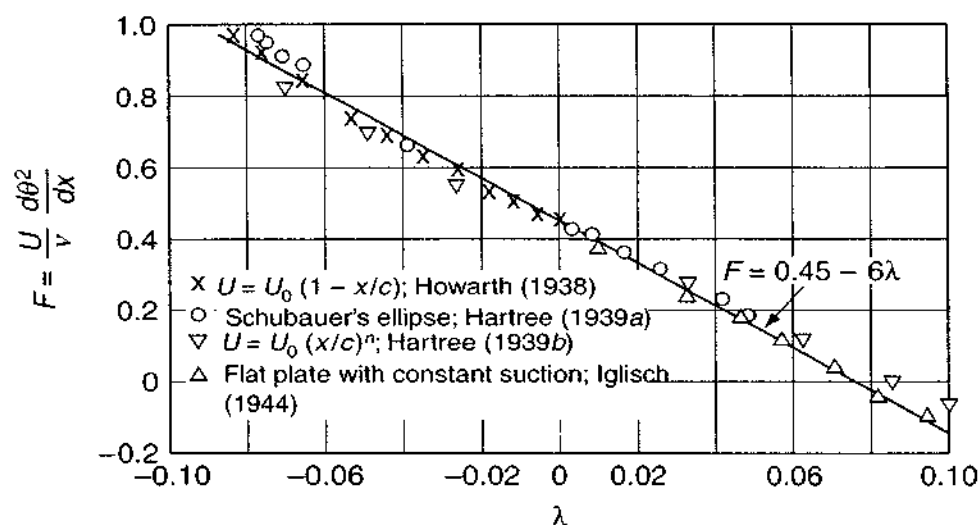
FIGURE 4-22
Empirical correlation of the boundary-layer function $F(\lambda)$ in Eq. (4-135). [*After Thwaites (1949)*.]

and further note that $\theta \, d\theta = d(\theta^2/2)$. Equation (4-133) may thus be rewritten in the very neat form

$$U \frac{d}{dx}\left(\frac{\lambda}{U'}\right) \approx 2[S(\lambda) - \lambda(2 + H)] = F(\lambda) \qquad (4\text{-}135)$$

Whereas earlier workers would have proposed a family of profiles to evaluate the parametric functions in Eq. (4-135), Thwaites (1949) abandoned the favorite-family idea and looked at the entire collection of known analytic and experimental results to see if they could be fit by a set of average one-parameter functions. As shown in Fig. 4-22, he found excellent correlation for the function F and proposed a simple linear fit

$$F(\lambda) \approx 0.45 - 6.0\lambda \qquad [\text{Thwaites (1949)}] \qquad (4\text{-}136)$$

If $F = a - b\lambda$, Eq. (4-135) has a closed-form solution which the reader may verify as an exercise:

$$\frac{\theta^2}{\nu} = aU^{-b}\left(\int_{x_0}^{x} U^{b-1}\,dx + C\right) \qquad (4\text{-}137)$$

If x_0 is a stagnation point, the constant C must be zero to avoid an infinite momentum thickness where $U = 0$. Thus Thwaites has shown that $\theta(x)$ is predicted very accurately (± 3 percent), for all types of laminar boundary layers, by the simple quadrature

$$\theta^2 \approx \frac{0.45\nu}{U^6}\int_{0}^{x} U^5 \, dx \qquad (4\text{-}138)$$

TABLE 4-4
Shear and shape functions correlated by Thwaites (1949)

λ	$H(\lambda)$	$S(\lambda)$	λ	$H(\lambda)$	$S(\lambda)$
+0.25	2.00	0.500	−0.056	2.94	0.122
0.20	2.07	0.463	−0.060	2.99	0.113
0.14	2.18	0.404	−0.064	3.04	0.104
0.12	2.23	0.382	−0.068	3.09	0.095
0.10	2.28	0.359	−0.072	3.15	0.085
+0.080	2.34	0.333	−0.076	3.22	0.072
0.064	2.39	0.313	−0.080	3.30	0.056
0.048	2.44	0.291	−0.084	3.39	0.038
0.032	2.49	0.268	−0.086	3.44	0.027
0.016	2.55	0.244	−0.088	3.49	0.015
0.0	2.61	0.220	−0.090	3.55 (Separation)	0.000
−0.016	2.67	0.195			
−0.032	2.75	0.168			
−0.040	2.81	0.153			
−0.048	2.87	0.138			
−0.052	2.90	0.130			

Having found θ from this relation, one calculates $\lambda = \theta^2 U'/\nu$ and calculates the skin friction and displacement thickness from the assumed one-parameter correlations

$$\tau_w = \frac{\mu U}{\theta} S(\lambda)$$
$$\delta^* = \theta H(\lambda)$$

(4-139)

Thwaites' suggested correlations for $S(\lambda)$ and $H(\lambda)$ are listed in Table 4-4 and plotted in Fig. 4-23. A simple and accurate curve fit to the shear function, shown in Fig. 4-23b, is

$$S(\lambda) \approx (\lambda + 0.09)^{0.62}$$

(4-140)

Being unable to divine a comparably simple formula for the shape-factor function $H(\lambda)$, this writer offers the following desperation polynomial:

$$H(\lambda) \approx 2.0 + 4.14z - 83.5z^2 + 854z^3 - 3337z^4 + 4576z^5$$

(4-141)

where $z = (0.25 - \lambda)$. The fit in Fig. 4-23a is good, though laborious.

The accuracy of the Thwaites method is about ±5 percent for favorable or mild adverse gradients but may be as much as ±15 percent near the separation point. Nevertheless, since the method is an average of many exact solutions, it can be regarded as a best available one-parameter method. If more accuracy is desired, the finite-difference computer method of Sec. 4-7 is recommended.

$$\lambda = \frac{\theta^2 \, (dU/dx)}{\nu}$$

(a)

λ

(b)
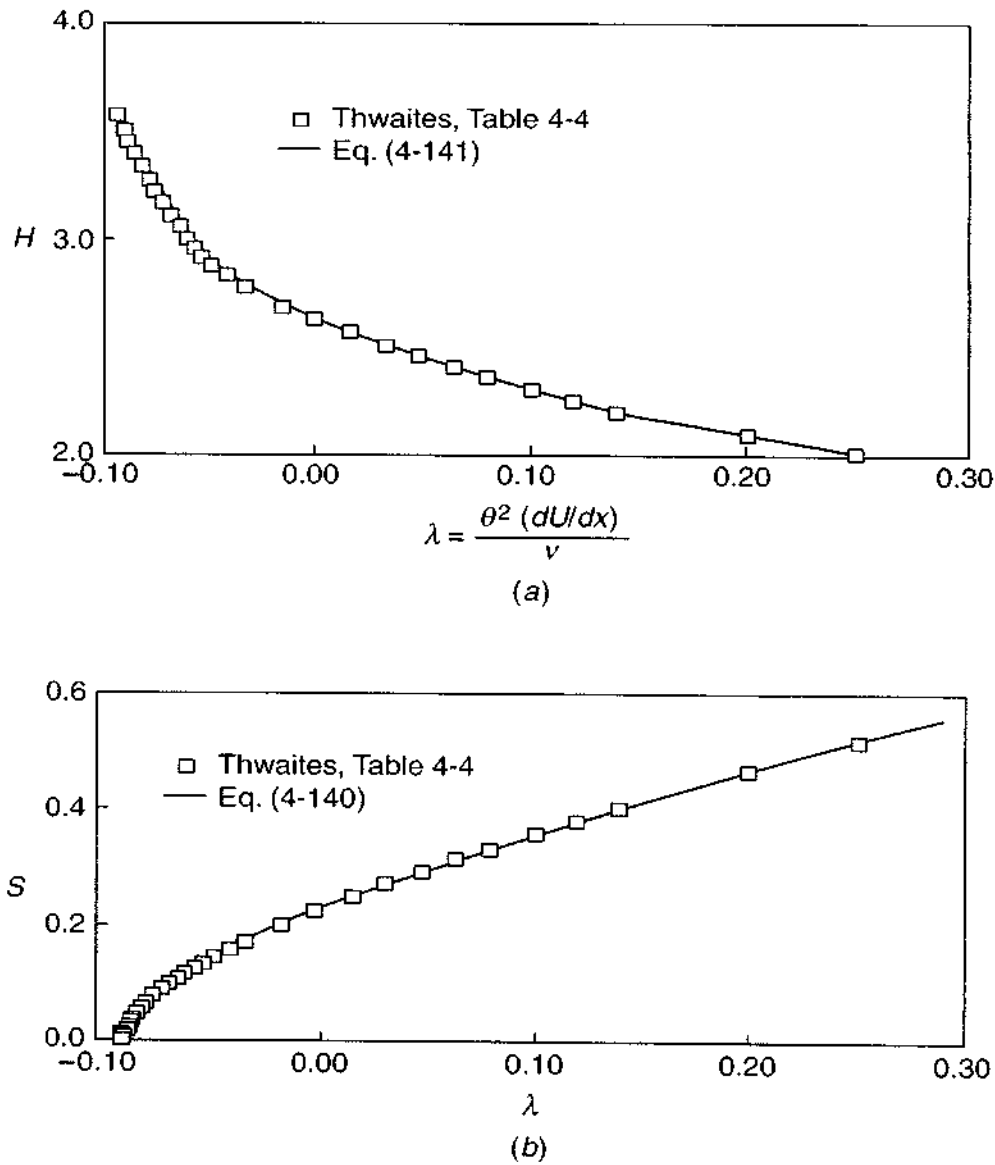
FIGURE 4-23

The laminar-boundary-layer correlation functions suggested by Thwaites (1949): (a) shape factor; (b) shear stress, with curve fits.

4-6.7 Application to the Howarth Decelerating Flow

To illustrate the simplicity and accuracy of Thwaites' method, we apply it to the Howarth linearly decelerating flow of Eq. (4-114) and Fig. 4-20, with $dU/dx = -U_0/L = $ const. The momentum thickness is computed, approximately, from Eq. (4-138):

$$\theta^2 = \frac{0.45\nu}{U_0^6(1 - x/L)^6} \int_0^x U_0^5 \left(1 - \frac{x}{L}\right)^5 dx = 0.075 \frac{\nu L}{U_0}\left[\left(1 - \frac{x}{L}\right)^{-6} - 1\right]$$

from which, by definition,

$$\lambda = \frac{\theta^2}{\nu}\frac{dU}{dx} = -0.075\left[\left(1 - \frac{x}{L}\right)^{-6} - 1\right]$$ (4-142)

With $\lambda(x)$ given by this (approximate) expression, we could then compute the wall shear $\tau_w(x)$ from the function $S(\lambda)$ in Table 4-4 or Fig. 4-23b. Let us save that until Sec. 4-7 as a comparison.

Given $\lambda(x)$, the separation point is predicted by

$$\lambda_{sep} \approx -0.09$$

or

$$\frac{x_{sep}}{L} = 1 - (2.2)^{-1/6} = 0.123$$

This is within 3 percent of the exact finite-difference result $x_{sep} = 0.120\,L$, achieved with very modest computational effort. This is better accuracy than the ± 10 percent that one might expect in any given case. Further, if $U(x)$ is complicated algebraically, it may be necessary to carry out the integral of U^5 in Eq. (4-138) numerically—which is still much simpler than a full-blown finite-difference computer attack.

4-6.8   Application to Laminar Flow Past a Circular Cylinder

Both the accuracy and the dilemma of a bluff-body boundary-layer calculation are illustrated by the circular cylinder. In terms of the dimensionless arc length $x^* = x/a$, where a is the cylinder radius, the potential-flow velocity distribution is

$$\frac{U}{U_\infty} = 2\sin x^* = 2.0x^* - 0.333x^{*3} + 0.0167x^{*5}\ldots$$ (4-143)

from which we can easily generate boundary-layer solutions of any type (integral, series, or digital computer). Calculations of this type have been made. Separation is predicted at an angle $x^* = \phi = 104.5°$ in numerical results by Terrill (1960), which we might (mistakenly) think would be reproduced in an experimental laminar cylinder flow.

Unfortunately, as discussed earlier in Sec. 1-2, the broad wake caused by bluff-body separation is a *first-order effect*, i.e., it is so different from potential flow (see Figs. 1-5 and 1-6) that it alters $U(x)$ greatly everywhere, even at the stagnation point. For example, the experiment of Hiemenz (1911) for a cylinder at a Reynolds number $Re_a = U_\infty a/\nu = 9500$ fit the polynomial

$$\frac{U}{U_\infty} \approx 1.814x^* - 0.271x^{*3} - 0.0471x^{*5}$$ (4-144)

which is quite different from potential flow. Even the stagnation velocity gradient
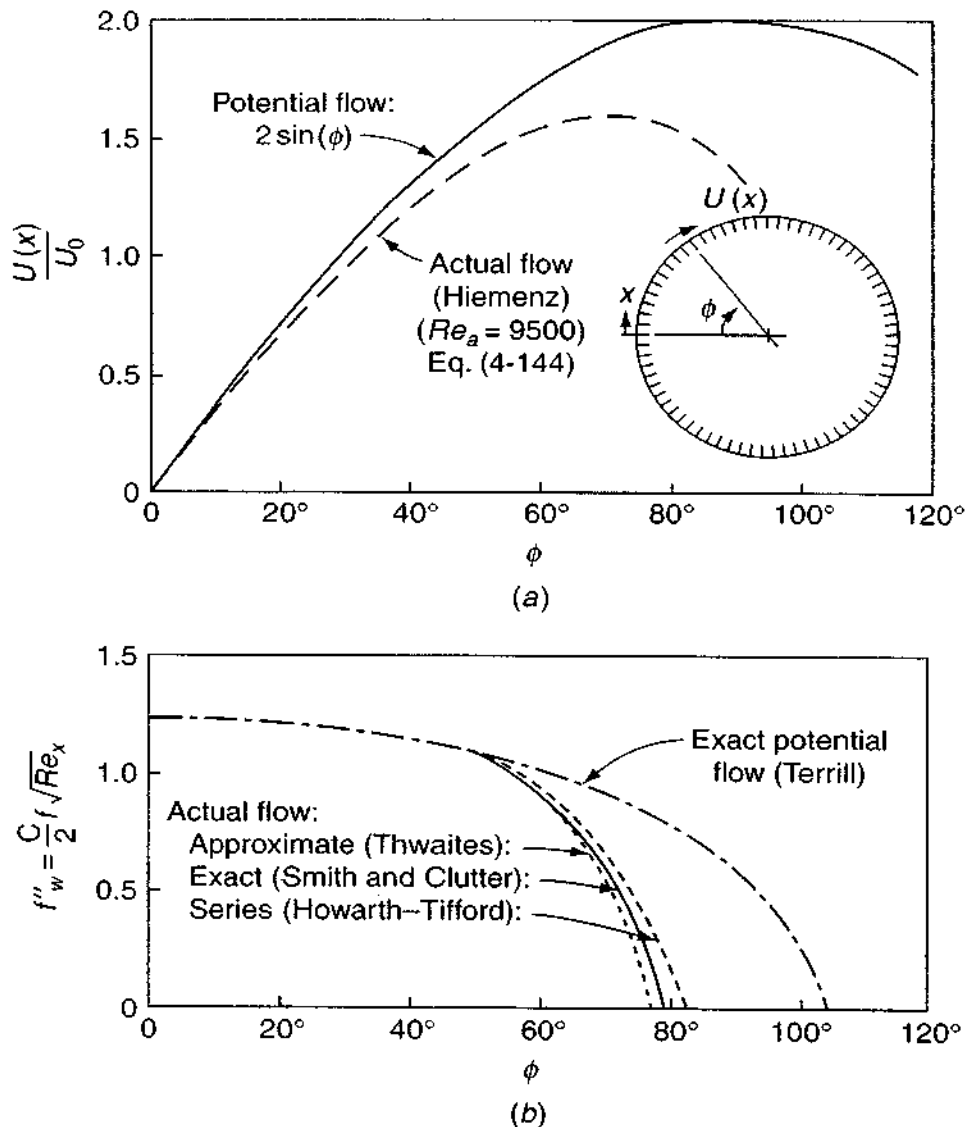
FIGURE 4-24

Comparison of potential-flow and actual-flow computations for a circular cylinder: (*a*) potential and actual velocity distributions; (*b*) potential-flow and actual-flow skin friction.

(1.814) is 9.3 percent less than the potential-flow value (2.0), and the maximum velocity ($1.595U_\infty$) occurs at $\phi = 71.2°$, instead of $2.0U_\infty$ at $\phi = 90°$. The two distributions are illustrated in Fig. 4-24*a*. It is clear that the potential flow is not a suitable input for the boundary-layer calculation. Once the actual $U(x)$ is known, the various theories are accurate, as seen in Fig. 4-24*b*. The finite-difference method of Smith and Clutter (1963) places ϕ_{sep} at 80°, whereas Thwaites' integral method, Eq. (4-138), predicts 78.5° and a Howarth–Tifford series (including 19 terms) predicts 83°. All three are in reasonable agreement with the Hiemenz (1911) experimental observation $\phi_{sep} \approx 80.5°$.

All laminar-boundary-layer computations hinge upon knowing the correct $U(x)$, however. It is presently a very active area of research to develop coupled methods in which a separating boundary layer interacts with and strongly modifies the external inviscid flow.

TABLE 4-5
**Laminar-separation-point prediction by Thwaites'
method**

U(x)	x_{sep} (exact)	Thwaites x_{sep}	Error, %
Howarth (1938)			
$1 - x$	0.120	0.123	+2.5
Tani (1949)			
$1 - x^3$	0.271	0.268	−1.1
$1 - x^4$	0.462	0.449	−2.8
$1 - x^8$	0.640	0.621	−3.0
Terrill (1960)			
$\sin(x)$	1.823	1.800	−1.3
Curle (1958)			
$x - x^3$	0.655	0.648	−1.1
Görtler (1957)			
$\cos(x)$	0.389	0.384	−1.3
$(1 - x)^{1/2}$	0.218	0.221	+1.3
$(1 - x)^2$	0.0637	0.0652	+2.4
$(1 + x)^{-1}$	0.151	0.158	+4.6
$(1 + x)^{-2}$	0.0713	0.0739	+3.6

4-6.9 Laminar-Separation-Point Prediction

One test of the general effectiveness of Thwaites' theory Eq. (4-138) is to see how well it predicts laminar separation for a variety of $U(x)$ freestream velocity distributions. Apply Eq. (4-138) to the distribution, compute $\theta(x)$, and note the position where $\lambda_{sep} = \theta^2(dU\,dx)/\nu \approx -0.09$. Some results are shown in Table 4-5 for eleven different flows with adverse pressure gradients. The separation position error is less than 4 percent, but this success is tempered by our previous observation that large-scale separation greatly changes the external velocity and pressure distribution. The boundary-layer approximation is inadequate in the vicinity of separated flow.

4-7 DIGITAL-COMPUTER SOLUTIONS

The integral methods discussed in Sec. 4-6 are easy to use but limited in accuracy. The similarity solutions of Sec. 4-3 are accurate but limited in applicability. If one is faced with a heavy-duty study of nonsimilar boundary layers and needs great accuracy, then a digital-computer numerical model is required.

For convenience, let us repeat the two-dimensional, steady, laminar, boundary-layer equations that we wish to solve:

Continuity:
$$\frac{\partial u}{\partial x} + \frac{\partial v}{\partial y} = 0 \qquad (4\text{-}41a)$$

Momentum:
$$u\frac{\partial u}{\partial x} + v\frac{\partial u}{\partial y} = U\frac{dU}{dx} + \nu\frac{\partial^2 u}{\partial y^2} \qquad (4\text{-}41b)$$

These equations are *parabolic* in x, so the numerical models are all of the downstream-marching type. The usual inputs for any method are (1) known upstream profiles $u(0, y)$ and $v(0, y)$, (2) known freestream velocity $U(x)$, and (3) known wall conditions $u(x, 0) = 0$ and $v(x, 0) = v_w(x)$.

The laminar-boundary-layer equations are *parabolic* or "marching" in character and thus relatively easy to model with CFD. The literature contains scores of numerical models, many of which are summarized in three boundary-layer texts: Schetz (1992), Cebeci and Cousteix (1998), and Schlichting and Gersten (2000). The first two of these texts include FORTRAN codes for various boundary-layer models. Moreover, Schetz' work has been extended, as sponsored by the National Science Foundation, in the form of Internet Boundary Layer Applets,[*] Devenport and Schetz (2002), which anyone can access and run on their own PC. These excellent Applets are JAVA codes that include laminar and turbulent flows, both incompressible and compressible. With such resources available, the present text will not attempt to become a CFD monograph. We will simply present a simple, direct boundary-layer model that is effective and useful. The reader may wish to learn from this simple method and then graduate to more advanced codes.

There are two types of marching schemes: *explicit* and *implicit*. In the explicit methods, the downstream profiles $u(x + \Delta x, y)$ and $v(x + \Delta x, y)$ are calculated immediately from the known upstream profiles $u(x, y)$ and $v(x, y)$ by direct application of an algebraic model of Eqs. (4-41). Explicit models are simple but become unstable numerically unless small step sizes Δx are used, which may mean excessive computer time.

An implicit method is also an algebraic model of Eqs. (4-41), but points on the downstream profile $u(x + \Delta x)$ must be *solved simultaneously* by either iteration or matrix inversion. Computation time per step Δx is larger than for explicit schemes, but there is no numerical instability. The step size may be as large as one likes, subject only to the normal truncation errors that do not diverge or oscillate. We will illustrate both an explicit and an implicit model.

The methods we illustrate are *finite-difference* schemes, modeling derivatives by differences between nodal points on a rectangular (x, y) mesh. There are also numerous schemes using the *finite-element* method Beer (2001) or Löhner (2001) that is quite different in principle—simulating whole fields or "elements" of flow bounded by mesh points. We shall not discuss finite-element models here.

4-7.1   An Explicit Finite-Difference Model for Plane Flow

For both of our methods, we use the rectangular finite-difference mesh shown in Fig. 4-25. Subscripts are convenient: $u_{m, n}$ means the velocity u at mesh point

---

[*]An Applet is an Internet software program that a browser can download and use interactively. Not all Applets are excellent. Poorly constructed Applets can slow or crash PCs and are known as "craplets."
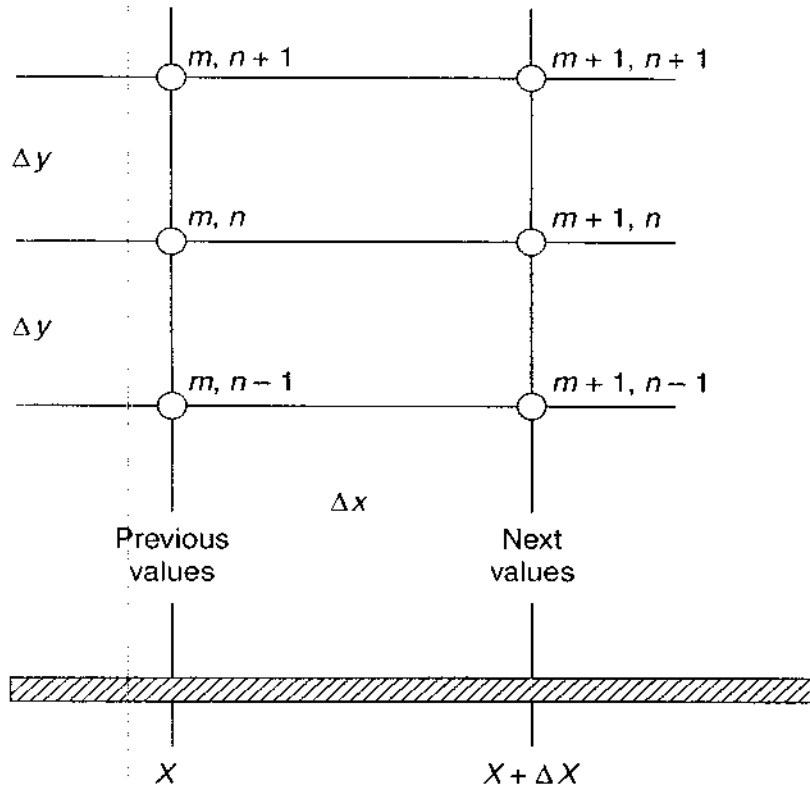
FIGURE 4-25
Finite-difference mesh for a two-dimensional boundary layer.

(m, n), located at $(x, y) = [(m - 1) \Delta x, (n - 1) \Delta y]$. Thus $(m, n) = (1, 1)$ locates the origin, $(x, y) = (0, 0)$. The step sizes Δx and Δy need not be equal. We also locate vertical velocity $v_{m,n}$ and (later) temperature $T_{m,n}$ at the same mesh points. All values at station m are assumed known or "previous," and we use them to march downstream and predict the "next" station values at $(m + 1)$. Let the total mesh be $M \times N$ large, where $m = M$ is the exit, $n = N$ is the freestream, $m = 1$ is the inlet, and $n = 1$ is the wall.

Let us begin by writing a finite-difference model of the momentum Eq. (4-41b) representing level n of the mesh:

$$u_{m,n} \frac{u_{m+1,n} - u_{m,n}}{\Delta x} + v_{m,n} \frac{u_{m,n+1} - u_{m,n-1}}{2 \Delta y}$$

$$\approx \frac{U_{m+1}^2 - U_m^2}{2 \Delta x} + \nu \frac{u_{m,n+1} - 2u_{m,n} + u_{m,n-1}}{\Delta y^2} \qquad (4\text{-}145)$$

Now, moving from left to right, let us remark about each term. The first term uses a *forward* difference to model $\partial u/\partial x$. The second term uses a *central* difference to represent $\partial u/\partial y$, thus keeping the model at level "n." The third term is the pressure gradient, using the form $U(dU/dx) = d(U^2/2)/dx$ and writing this as a forward difference—note that U_{m+1} is *known* because $U(x)$ is the freestream velocity. Finally, the fourth term is a central-difference model of $\partial^2 u/\partial y^2$. All terms center about level "n," which is good practice for numerical accuracy. The only unknown velocity in the model is $u_{m+1,n}$, which we may solve for and write

as follows:

$$u_{m+1,n} \approx (\alpha - \beta)u_{m,n+1} + (1 - 2\alpha)u_{m,n} + (\alpha + \beta)u_{m,n-1} + \frac{U_{m+1}^2 - U_m^2}{2u_{m,n}}$$

(4-146)

where $\qquad \alpha = \dfrac{\nu \Delta x}{u_{m,n}\Delta y^2} \qquad$ and $\qquad \beta = \dfrac{v_{m,n}\Delta x}{2u_{m,n}\Delta y}$

The right-hand terms in Eq. (4-146) are all known from the "previous" station. Therefore we may solve for $u_{m+1,n}$ immediately—the model is *explicit*. However, algebraic recurrence relations such as Eq. (4-146) require, for numerical stability, that all the coefficients of the previous values u_m be positive. In this case, $\alpha < \frac{1}{2}$ and $\beta < \alpha$. The restraints limit both step sizes in the mesh:

$$\Delta x < \frac{u_{\min}\Delta y^2}{2\nu} \qquad \Delta y < \frac{2\nu}{|v_{\max}|}$$

(4-147)

We need the absolute value on $v_{\max}$ because v is positive in adverse gradients but may be negative in favorable gradients. Usually $u_{\min}$ occurs near the wall and $v_{\max}$ near the freestream. During this explicit computation, we have to monitor $\alpha(y)$ and $\beta(y)$ to make sure that Eqs. (4-147) are satisfied.

With $u_{m+1,n}$ known from Eq. (4-146), we find $v_{m+1,n}$ by modeling the continuity Eq. (4-41a). The simplest way would be a forward difference for both terms:

$$\frac{u_{m+1,n} - u_{m,n}}{\Delta x} + \frac{v_{m+1,n} - v_{m+1,n-1}}{\Delta y} \approx 0$$

We start with $n = 2$ to compute $v_{m+1,2}$ because $v_{m+1,1} = v_w$ is known. However, let's not bother: The first term is at level n, and the second is at level $n - \frac{1}{2}$; numerical accuracy will be poor. Moving $\partial v/\partial y$ up to a central difference $[v_{m+1,n+1} - v_{m+1,n-1}]/2\Delta y$ at level n is self-defeating because we skip the value we wanted, $v_{m+1,n}$. Wu (1961) suggested that we move $\partial u/\partial x$ *down* to level $n - \frac{1}{2}$ by using an average value:

$$\left.\frac{\partial u}{\partial x}\right|_{\text{avg}} \approx \frac{1}{2}\left[\frac{u_{m+1,n} - u_{m,n}}{\Delta x} + \frac{u_{m+1,n-1} - u_{m,n-1}}{\Delta x}\right]$$

We use this expression instead in the continuity model and solve explicitly for the next vertical velocity:

$$v_{m+1,n} \approx v_{m+1,n-1} - \frac{\Delta y}{2\,\Delta x}[u_{m+1,n} - u_{m,n} + u_{m+1,n-1} - u_{m,n-1}] \quad (4\text{-}148)$$

There is no instability in this relation other than that already required by Eqs. (4-147). We begin at $n = 2$ and move upward.

Equations (4-146) and (4-148) constitute a satisfactory, explicit, laminar, boundary-layer model which may easily be programmed on a personal computer.

Since we are "marching," there is really no need to use the "m" subscript, e.g., to dimension $u(1000, 50)$ and $v(1000, 50)$ for 1000 downstream steps. One can merely denote station m as $up(50)$ and $up(50)$ for "previous" and station $m + 1$ as $un(50)$ and $vn(50)$ for "next," keep the results long enough to print them, reinitialize $up(n) = un(n)$ and $vp(n) = vn(n)$, and move on. During the computation, one should constantly monitor the stability conditions Eqs. (4-147) and also check to see that the outer values $u_{m,N-1}$ and $u_{m,N}$, etc., merge smoothly with the freestream velocity U_m, since the boundary-layer thickness is *a priori* unknown.

4-7.1.1 APPLICATION TO HOWARTH LINEARLY DECELERATING FLOW. For illustration, Eqs. (4-146) and (4-148) were programmed to solve the Howarth problem $U = U_0(1 - x/L)$ from $x = 0$ until separation. Arbitrary values can be taken for U_0, L, and ν, since the results will be nondimensionalized. Figure 4-26 shows the computed values of normalized skin friction $C_f/C_f(0)$ compared with the Howarth series solution, and Thwaites' method using $S(\lambda)$ when λ is given by
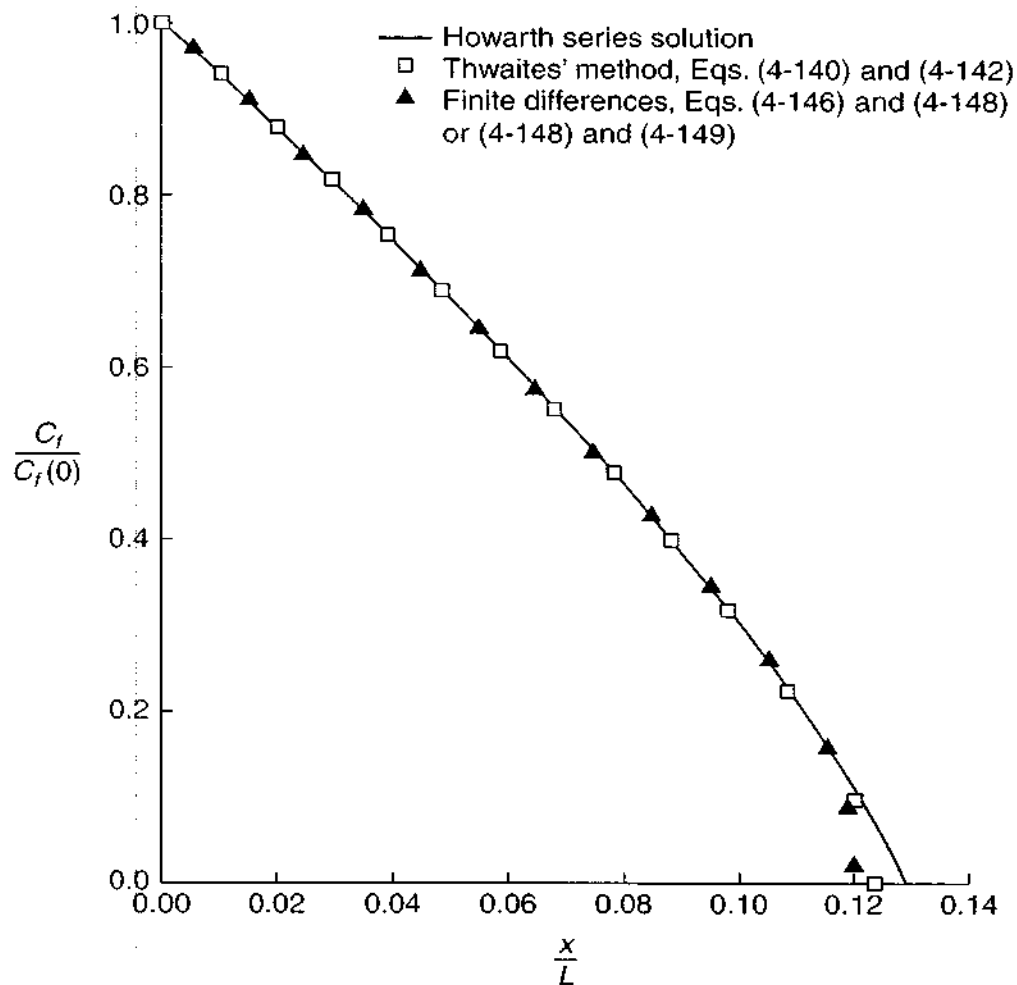

FIGURE 4-26

Comparison of finite-difference, integral, and series solutions for wall friction in the Howarth linearly decelerating flow of Eq. (4-114).

Eq. (4-142). We see that the computer solution equals the Howarth series for $x/L \leq 0.1$ and then is more accurate near separation, $x_{sep}/L \approx 0.120$. Thwaites' method is quite good (± 5 percent) over the entire range. The explicit computer method required 3000 steps, with Δx being extremely restricted by Eqs. (4-147) near separation.

4-7.2 An Implicit Finite-Difference Model

In an implicit model, more of the "next" terms are used to approximate the derivatives, resulting in simultaneous algebraic equations. In the present application, we model the viscous or second-derivative term in the momentum equation at the next station, $m + 1$:

$$\frac{\partial^2 u}{\partial y^2} \approx \frac{u_{m+1, n+1} - 2u_{m+1, n} + u_{m+1, n-1}}{\Delta y^2}$$

When this replaces the "previous" second derivative used in the explicit model, the result is that each nth-level equation has three unknowns:

$$-\alpha u_{m+1, n+1} + (1 + 2\alpha)u_{m+1, n} - \alpha u_{m+1, n-1}$$

$$\approx u_{m, n} - \beta(u_{m, n+1} - u_{m, n-1}) + \frac{U_{m+1}^2 - U_m^2}{2u_{m, n}} \qquad (4\text{-}149)$$

where α and β have the same meaning as before, Eq. (4-146). Now we must solve simultaneously for the $u_{m+1, n}$—the method is *implicit*. The benefit is that the results are unconditionally stable, regardless of the step sizes Δx and Δy—no need to use conditions Eqs. (4-147). We should select Δy small enough that, say, 20 or more points are within the boundary layer, and Δx should be small enough that changes in $u_{m, n}$ from station to station are small, say, less than 5 percent.

One way to solve Eq. (4-149) is by Gauss–Seidel iteration: Solve for the dominant term $u_{m+1, n}$, moving $u_{m+1, n\pm1}$ over, and sweep the right-hand side repeatedly until the values of u do not change. Convergence is not guaranteed unless Δx and Δy are relatively small. A second method is direct solution by Gauss elimination or matrix inversion.

4-7.2.1 INVERSION OF A TRIDIAGONAL MATRIX. Assuming that $n = 1$ is the wall and $n = N$ is the freestream, Eqs. (4-149) represent $(N - 2)$ equations, each with three unknowns: The matrix is thus *tridiagonal*. Such matrices are easy to invert by a procedure, called the tridiagonal matrix algorithm (TDMA), very nicely described in Sec. 4.2-7 of the text by Patankar (1980). It works because there are only two unknowns at the bottom, $n = 2$, where $u_{n=1} = 0$ (no slip), and only two at the top, $n = N$, where $u_N = U(x)$. Thus we can begin at the bottom and eliminate one variable at a time until we reach the top, where u_{N-1} is immediately found.

We then work our way back to the bottom ("back substitution"), picking up u_n in terms of u_{n+1} until we secure the final value, u_2.

The TDMA is outlined as follows. Dropping the "m" subscripts as superfluous, Eq. (4-149) may be written, at any n, as

$$(1 + 2\alpha_n)u_n = \alpha_n u_{n+1} + \alpha_n u_{n-1} + C_n$$

where C_n denotes the entire right-hand side of Eq. (4-149). The desired back-substitution recurrence relation has the form

$$u_n = P_n u_{n+1} + Q_n \tag{4-150}$$

First calculate P_n and Q_n. Begin at the bottom, $u_1 = 0$, by computing

$$P_2 = \frac{\alpha_2}{1 + 2\alpha_2}$$

$$Q_2 = \frac{C_2}{1 + 2\alpha_2} \tag{4-151}$$

Then calculate the remaining P's and Q's by recurrence relations:

$$P_n = \frac{\alpha_n}{1 + 2\alpha_n - \alpha_n P_{n-1}}$$

$$Q_n = \frac{C_n + \alpha_n Q_{n-1}}{1 + 2\alpha_n - \alpha_n P_{n-1}} \tag{4-152}$$

At the top, since $u_N = U$, the value of velocity follows immediately:

$$u_{N-1} = \frac{\alpha_{N-1}U + \alpha_{N-1}Q_{N-2} + C_{N-1}}{1 + 2\alpha_{N-1} - \alpha_{N-1}P_{N-2}} \tag{4-153}$$

where U is the freestream velocity at that station. With u_{N-1} known, plus all the P's and Q's, we work our way downward using Eq. (4-150) until we reach the final unknown, u_2. The algorithm works extremely well for a well-behaved matrix such as Eq. (4-149). Remember that the coefficient α itself varies with n because it contains $u_{m,n}$.

The implicit method was also applied to the Howarth distribution and results of accuracy equal to the explicit method, plotted in Fig. 4-26, were obtained with $\Delta x/L = 0.001$. Run time on a personal computer was less than the explicit method. There is no instability and no special need for decreased Δx near separation.

Finally, to illustrate the yin and yang of nonsimilar boundary layers, the method was run for a circular cylinder with the Hiemenz experimental velocity distribution, Eq. (4-144). Boundary-layer profiles are plotted in Fig. 4-27 for every $\Delta\theta = 10°$, measured from the stagnation point. Separation was predicted at $\theta = 81°$ (see Fig. 4-24b). The nominal Reynolds number was taken as $U_0 R/\nu = 10^5$ to show the actual boundary-layer thickness, which is about 1 percent of the cylinder radius. In the favorable gradient for θ up to 60°, the profiles are strongly curved and have increasing wall shear stress. From 60° on, as the freestream levels off and begins to decelerate, the profiles become thicker and then S-shaped, with an early separation.
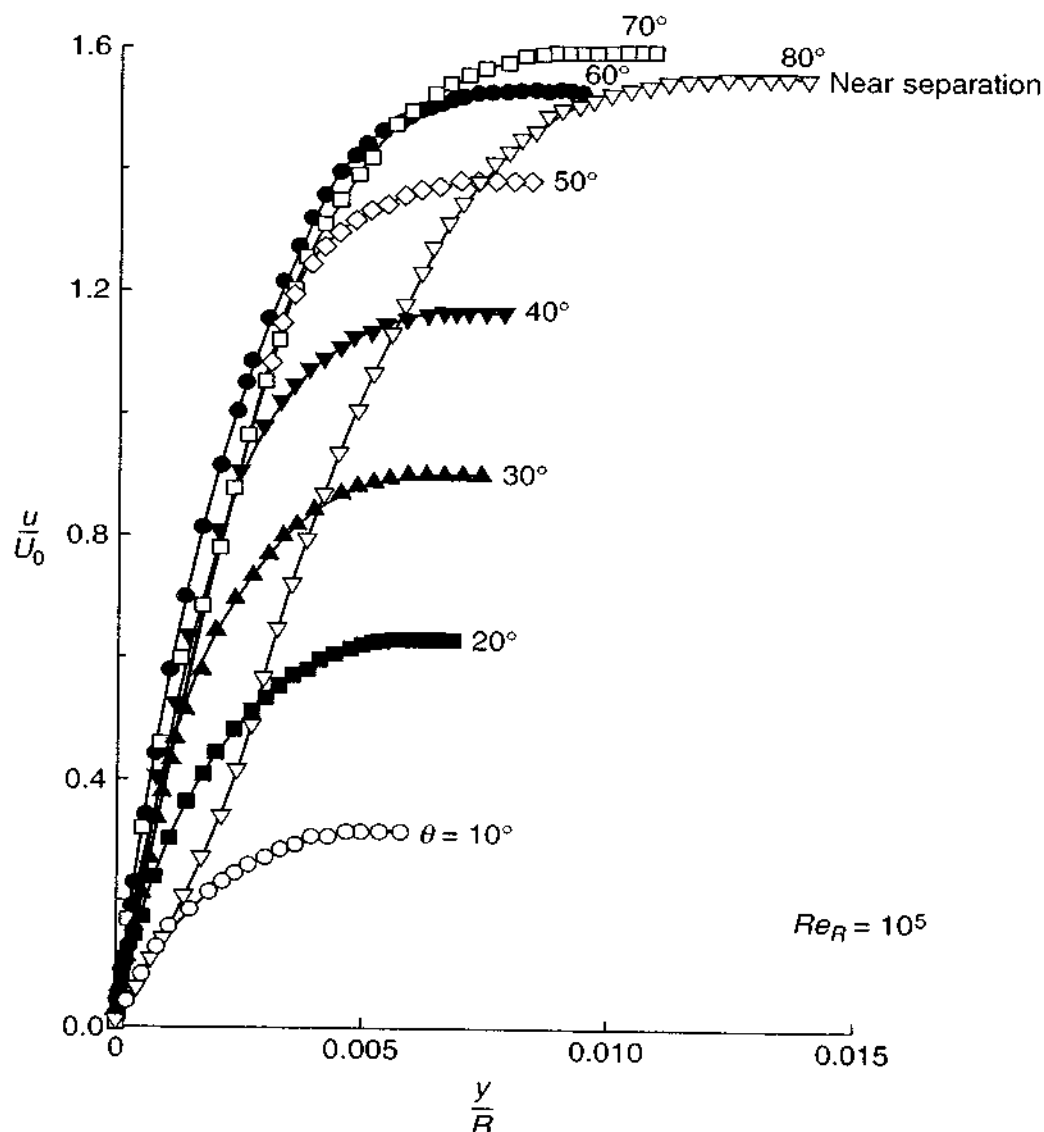
FIGURE 4-27

Laminar boundary layers on a cylinder computed by the implicit numerical method of Eqs. (4-148) and (4-149). Freestream velocity given by Eq. (4-144).

4-8 THERMAL-BOUNDARY-LAYER CALCULATIONS

The previous three sections were devoted to velocity calculations, because the assumption of incompressible flow with constant viscosity uncouples the velocity and enables it to be calculated independent of temperature. Afterward, the temperature can be calculated from the thermal-energy equation (4-35c) and the known velocity solution. We now review some of the methods of making temperature calculations under fairly arbitrary conditions.

Almost all analyses of incompressible flow assume that dissipation is negligible and work with the simplified thermal-energy equation

Differential form:
$$u \frac{\partial T}{\partial x} + v \frac{\partial T}{\partial y} \approx \frac{k}{\rho c_p} \frac{\partial^2 T}{\partial y^2} \tag{4-154a}$$

Integral form:
$$q_w = \frac{d}{dx}\left[\int_0^\infty \rho u c_p (T - T_e)\, dy \right] \tag{4-154b}$$